UNIVERSITY OF CAPE TOWN

IYUNIVESITHI YASEKAPA • UNIVERSITEIT VAN KAAPSTAD

The effect of blast loading on composites that contain sustainable materials

Student: Sherlyn Gabriel

GBRSHE003

Supervisor: Prof Genevieve Langdon

Co-supervisors: A/Prof Chris von Klemperer & A/Prof Steeve Chung Kim Yuen

BLAST IMPACT & SURVIVABILITY RESEARCH UNIT

Thesis Presented for the Degree of

DOCTOR OF PHILOSOPHY

in the Department of Mechanical Engineering

UNIVERSITY OF CAPE TOWN

March 2020

Declaration

I, Sherlyn Gabriel, hereby declare that the work which this thesis is based is my original work (except where acknowledgements indicate otherwise) and that neither the whole work nor any part of it has been, is being, or is to be submitted for another degree in this or any other university. I authorise the University to reproduce for the purpose of research either the whole or any portion of the contents in any manner whatsoever.

Signature: Signed by candidate Date: 2022/04/06

Abstract

In the pursuit of global environmental sustainability, bio-based resins, and natural fibres as reinforcements in Fibre Reinforced Polymer (FRP) composites offer potential benefits, and some of these can be used in different applications particularly when strength is of secondary importance (such as automotive, architecture, and mass-transportation industries). However, there is a constant possibility of explosive threats, and little is known about the blast response of these materials. This study focusses on the effect of blast loading on composites with sustainable constituent materials.

Seven different FRP composites were examined. Two were chosen as control materials, namely glass fibre reinforced epoxy composite and a common medium density fibreboard (MDF). The five sustainable materials were: vacuum infused flax fibre reinforced epoxy using both bio-epoxy and conventional epoxy, vacuum infused jute fibre reinforced epoxy, flax fibre reinforced epoxy made using hand lay-up and glass fibre epoxy manufactured using a bio-epoxy. These composites were subjected to quasi-static and blast loading conditions.

Initially, some of the material properties of the seven composite systems were characterised though a series of quasi-static tensile, flexural and interlaminar fracture tests. Blast testing was undertaken on a ballistic pendulum facility, capable of measuring the impulse imparted by the plastic explosive.

The glass fibre reinforced composites had better blast resistant properties in comparison to natural fibre composites, following the trends observed during quasi-static testing. Delamination was observed on the glass fibre reinforced composites and the damage tended to increase progressively. Large amounts of inelastic deformation, surface and through-thickness cracking were observed on the natural fibre composites. The jute fibre reinforced composites tended to have a sudden destructive failure whereas the flax fibre reinforced composites and, to some extent, MDF sustained progressive damage. Substituting the epoxy resin for the more sustainable bio-based resin had little effect on the blast resistance for both glass and flax fibre reinforced composites, which is encouraging because this suggests that a sustainable resin can be substituted in those panels without significant degradation in blast protection properties. The manufacturing method played a role for the flax fibre reinforced composites, with hand lay-up specimens exhibiting a lower level of protection and inconsistent properties compared to the vacuumed infused panels. The results also indicated that the addition of more glass fibre plies enhanced the blast resistance considerably. Of the composites tested, the best performing composite that takes sustainability into account was the glass fibre reinforced bio-based epoxy composite. The results of the experimental study presented discusses the blast behaviour of these materials which are relevant to engineers considering alternative sustainable materials in various applications where explosive loading is a threat.

Acknowledgements

Foremost, I would like to express my deepest gratitude to my supervisors, Professor Langdon, Associate Professor von Klemperer and Associate Professor Chung Kim Yuen for their support and guidance throughout the years. This research would not have been possible without their persistent help and advice.

I also wish to thank the Mechanical Engineering workshop staff, particularly Pierre Smith, Dillon Jacobs, Gavin Doolings, Willie Slaverse and Peter Jacobs. Whether it be drilling holes, cutting boards, fetching materials or manufacturing rigs, their willingness to provide assistance and eagerness to teach me new skills is highly appreciated. I would also like to extend my gratitude to the Centre of Materials Engineering (CME) staff, particularly Penny Louw and Soraya von Willingh, for the assistance with microscopy work and quasi-static testing.

My sincere thanks go to Professor Nawawi and Wenjie Wang from the University of Auckland for the flax fibre reinforced composites and flax textiles. I would also like to thank them for being wonderful hosts during my time as a visiting student in New Zealand.

I cannot express enough my thanks to the BISRU staff and students, so many of whom have helped in some way or another. I would like to single out my manufacturing buddies Ismail Ghoor and Vinay Shekhar, for the DIC assistance, Richard Curry, and Dustin Fischer, for keenly acting as a sounding board in the office. I would also like to thank Rendani Khobo and Lindsay Kotze who, while not BISRU students, were always willing to offer a helping hand in editing documents and presentations, setting experiments and making sure I was not alone in the lab or office late at night.

I am grateful for financial support provided by the National Research Foundation and Worldwide Universities Network (WUN) Research Development Fund, without which this project would have not been possible.

Special thanks go to my friends for all the support, fruitful discussions, and providing some happy distractions outside my research. Last but not least, I am deeply indebted to my family: my mother Mary Jean, my late aunt Mary Anne and my brother Sherwin, for all the support and love shown to me throughout my life, for always being there for me, offering wise counsel and a sympathetic ear.

Dedication

In loving memory of Mary Anne Groepe.

Thank you for being a mother and, throughout this PhD journey,

an advisor to me.

Table of Contents

List of Figures

List of Tables

Nomenclature and Abbreviations

CFRP	Carbon fibre reinforced polymer
CJ	Chapman-Jouguet minimum detonation velocity
CLS	Clear slow hardener
DCB	Double cantilever beam
DIC	Digital image correlation
EOS	Equation of States
FRP	Fibre reinforced polymer
GFRP	Glass fibre reinforced polymer
INH	Inhibitor
JWL	Jones-Wilkins-Lee
LCA	Life cycle assessment
LSTC	Livermore software technology Corp
MBT	Modified beam theory
MDF	Medium density fibreboard
MMALE	Multi-material arbitrary Lagrangian-Eulerian
MSDS	Material safety data sheet
NFC	Natural fibre composites
PE4	Plastic Explosive number 4
PEI	Poly-ether-imide
prepreg	Pre-impregnated
pty	Proprietary
SDG	Sustainable development goals
SEM	Scanning electron microscope
SOD	Stand-off Distance
UF	Urea formaldehyde
VI	Vacuum infusion
VOC	Volatile organic compound
WCED	World Commission on Environment and Development

1 Introduction

Sustainable development is defined simply as the “development that meets the needs of the present without compromising the ability of future generations to meet their own needs by the World Commission on Environment and Development (WCED) [1],”. While recently, sustainability has been considered a “megatrend” and the term, itself, only appeared in the Oxford English Dictionary in the late 20th century[2]. The motivation to live sustainably dates to early civilisations [2], [3]. The demand for raw materials and environmental impact of extracting said materials have been a constant issue throughout human history. Fears over shortages of raw materials, which threatens the quality of life, encouraged earlier civilisations to consider the responsible use of natural resources similarly to the rationale of sustainable development today [3]. The concept and practice of sustainability has generated environmental standards and regulatory frameworks by governments, protocols and agreements by international organisations, lifestyle changes for individuals, and widespread initiatives and innovations within civil society and business [1], [2]. Furthermore, it will continue to be advocated for as the problems of population growth, raw material depletion, increase in energy demand, rapid environmental deterioration and climate change cannot be denied [1]–[4].

Sustainability is not often discussed in blast applications. Lori et al [6] investigated sustainable glazed facade systems and developed enhancements to these systems to obtain higher blast protection levels. Kim and Park [7] discussed new design procedures for military protective structures in South Korea that will have a reduced environmental impacts and cost in comparison to conventional methods, while still providing reasonable levels of protection. These studies embrace innovative materials and components to achieve excellent blast protection performance in a sustainable manner [6], [7].

The drivers that invoke terrorist activity are complex and multidimensional, making prediction very difficult [8]. Furthermore, accidental explosions can also have serious impact on the public as observed in the 2020 Beirut explosion where nearly 200 people were killed, and thousands of residents lost their homes [9]. In addition, this resulted in loss of business and the incurring of associated costs. The effects of blasts on structures and humans can lead to catastrophic consequences. Safety and protection are driving forces to improve the resistance of structures subjected to blasts. While there is a need to design and incorporate materials that can reduce the damage caused by a blast event, there should also be considerations for sustainability. Furthermore, as the demand and use of sustainable materials (like natural fibres composites [10] and environmentally friendly resins [11]) increase, so does the likelihood of these materials be exposed to blast loading. Sustainable materials offer a myriad of solutions in diverse applications including automotive [12], [13], built

environment[14]–[16], ballistic armour [17]–[19] and others[20]–[22]. Therefore, the behaviour of such materials when subjected to blast needs to be understood, both for their blast behaviour properties and potential use in blast resistant applications.

1.1 Thesis objective

The aim of this project was to understand the blast response of a range of composites containing materials deemed sustainable and to compare them to baseline composites. Two types of baseline material were chosen: a fully synthetic glass fibre reinforced epoxy composite as a material that has the lowest sustainability rating of those tested in this project; and a medium density board, a popular, inexpensive, readily available composite made from wood fibres. This will address the gap in literature on the impact of substituting either fibre or matrix for an environmentally friendly option (such as natural fibres and plant-based resins) in blast applications. It will also present how cheap medium density fibreboards respond to blast in comparison to laminates made with natural fibres.

The three objectives required to meet this aim are to:

- Investigate the influence of fibre type on blast response
- Investigate the effect of replacing a conventional resin with a plant based alternative bio-resin
- Evaluate the failure progression in composites containing sustainable materials

It was hypothesised that the natural fibre composites would have lower blast protection properties compared to the glass fibre reinforced composites. Furthermore, there would be a minimal effect on blast related properties of composites when replacing the resin for a more sustainable alternative provided the resins were formulated similarly.

1.2 Scope and limitations

Small scale explosive charge detonations, using Plastic Explosive number 4 (PE4), were performed in air to investigate the permanent damage and transient deformation response of the test panels. The test parameters were determined using simple numerical simulations on LS-Dyna. Quasi-static tests, including flexural, tensile and interlaminar fracture testing, were performed using a Zwick universal testing machine to gain insight into the material characteristics and manufacturing consistency of the test panels.

This investigation was limited to fibre reinforced composites with polymeric resins. The manufacturing methods considered were vacuum infusion and hand lay-up. Panels were manufactured to an overall size of 300 x 300 mm with a square exposed area of 200 x 200 mm. The size of the exposed area exceeds the recommended ratio of specimen width to unit cell of 2:1 found in ASTM D6856.

The fibres used were limited to glass, jute, and flax fibre, all of which were woven textiles and ready to be processed in composites. No further surface treatments were implemented onto the fibres. The resins used were limited to epoxy resins, namely Gurit's Prime 20LV (fossil-fuel based resin) and Entropy Resins' Super Sap (bio-based resin). The medium density fibreboard used as a control material is locally available in South Africa and known as Supawood. Flax fibre reinforced composites and flax fabric were donated by the University of Auckland. Jute fabric was donated by the University of Liverpool. For both materials, limited quantities were available which limited the number of tests that could be performed.

The panels were tested under a uniform blast loading condition. PE4 charges of varying masses were detonated at a fixed stand-off distance of 200 mm where the maximum charge mass tested was 40 g. The transient response of the panels was measured using a high-speed camera system.

1.3 Thesis development

This thesis consists of twelve chapters in total. A detail of work flowchart is shown in Figure 1-1. Chapter 2 contains a literature review, which covers the background to fibre reinforced composites and their characteristics, manufacturing methods and sustainability aspects. A brief background on the response of composites to blast loading and the response of natural fibre composites to different types of impact loading is also given.

Chapter 3 covers the different materials used in this work. The information found in the manufacturers' datasheets is presented. Additionally, reasons for why some of the materials were considered sustainable are provided.

Chapter 4 describes the numerical simulations that were generated to define the blast loading conditions and panel thickness of the natural fibre laminates. Simplified numerical models were made and checked using the results of previous work that use similar set-ups.

Chapter 5 describes the manufacturing methods used for the blast panels. It also includes manufacturing details for the quasi-static test specimens. The quasi-static material testing results are found in Chapter 6. These results were used to characterise some material properties of the different composites tested and determine the consistency of manufacturing.

Chapter 7 describes the experimental blast method. The clamping arrangement and experimental equipment used are explained. The results of the blast loaded panels were spilt into two chapters, one describing the results more qualitatively and the other presenting measured damage. Chapter 8 contains the qualitative experimental results and observations made on the blast tested materials.

The results are grouped by fibre type, and descriptions are given on the appearance of the panels. Simple descriptions on microscopic images are also presented. Thereafter, Chapter 9 contains the results of quantifiable damage presented in chapter 8. The transient results obtained from DIC are also presented in Chapter 9.

Chapter 10 covers the discussion of the experimental blast results, and compares the different composites tested. The differences in the fibre type, resin type and manufacturing methods are highlighted. A simple sustainability assessment, based on the cost, blast performance and environmental impact of the composites tested, is presented. Finally, the conclusions and recommendations are presented in Chapters 11 and 12.

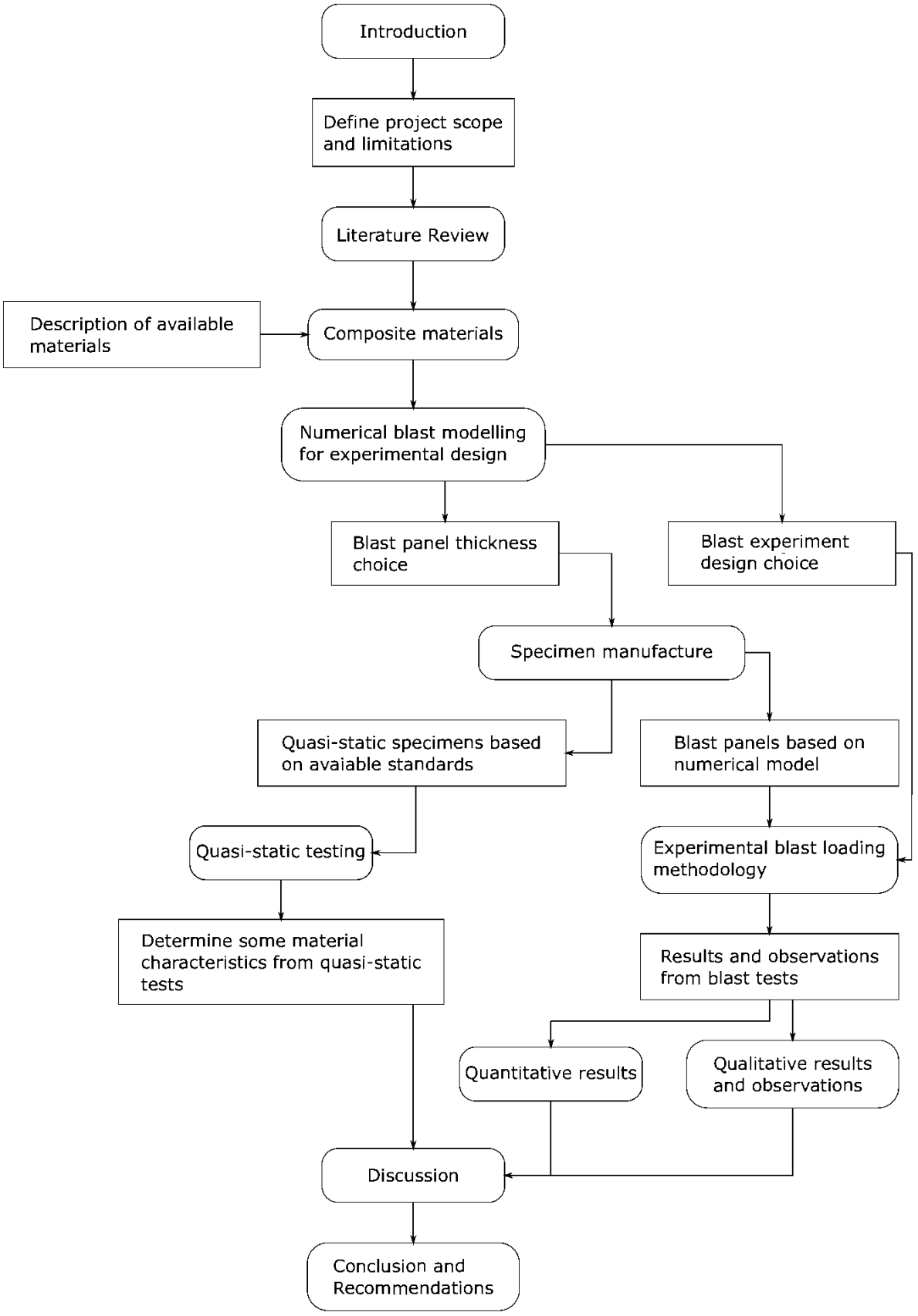

Figure 1-1: Detail of work flowchart

2 Literature review

This section contains the literature survey pertaining to fibre-based polymeric composites and their response to different loading conditions. The constituents of the composites deemed relevant to this project are described. These include synthetic fibres, natural fibres derived from plants and polymeric matrices. The various methods used to manufacture laminate composites and Medium Density Fibreboards (MDFs) are reviewed. The sustainability of the constituent materials and composites are also described. The characteristics of composites, such as their material properties and failure mechanisms, are described thereafter. The response of composites to blast in air was analysed. However, only Fibre Reinforced Polymeric (FRP) composites with randomly orientated fibres, unidirectional fibres and woven fabrics, as well as wood-based products were considered. This chapter highlights the lack of information for the blast behaviour of Natural Fibre Composites (NFCs); however, the impact behaviour from non-explosive tests of NFCs is discussed where it could provide some insight to how NFCs could respond to blast.

2.1 Composite material constituents

Composites are described as a combination of two or more dissimilar materials where the mechanical properties are significantly different from those of the constituent components. By combining the different materials, it is possible that a better product can be yielded as the individual materials can compensate and complement each other [23].

In composites, there are traditionally two main types of constituents, namely: a reinforcement and a matrix. The type and quantity of reinforcement significantly impacts the mechanical properties of the composite by providing the strength and stiffness. On the other hand, the matrix acts as a medium that surrounds the fibres and keeps the composite together [23]. Assessing the different constituents, prior to manufacturing the composite, helps develop a better understanding of the characteristics of the final composite. While there are different types of reinforcements used in composites (such as particulates, plates and fibrous) only fibrous reinforcements were considered in this work.

2.1.1 Fibres as reinforcements

Broadly speaking, there are two types of fibres: synthetic and natural fibres. Synthetic fibres are man-made from raw materials, often derived from petrochemicals, which are modified through chemical processes and manufacturing methods [24] prior to the inclusion in an FRP. The material properties of the synthetic fibres tend to be more controllable. If the same procedure was used to manufacture the fibres, these properties are expected to be consistent between batches. In comparison, natural fibres derived from plants, are not man-made, and are influenced by external factors such as the

geographical, climate and environment in which they grow [25]. The cross-sections of different synthetic [26] and natural fibres [27] are shown in Figure 2-1 and Figure 2-2 to highlight the geometric differences of the fibres. As shown in Figure 2-1, the cross sections of the carbon and glass fibre are smooth and circular. In comparison to the natural fibres (shown in Figure 2-2), non-unform cross sections are observed.

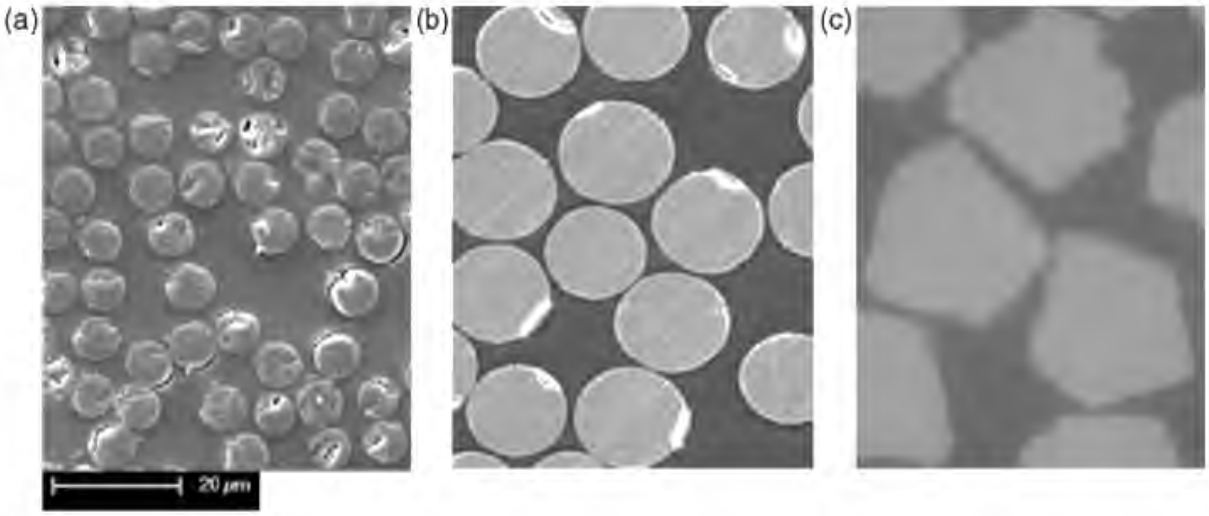

Figure 2-1: Scanning electron microscope (SEM) images of composites reinforced with a) carbon, b) glass and c) steel fibres under the same scale[27]

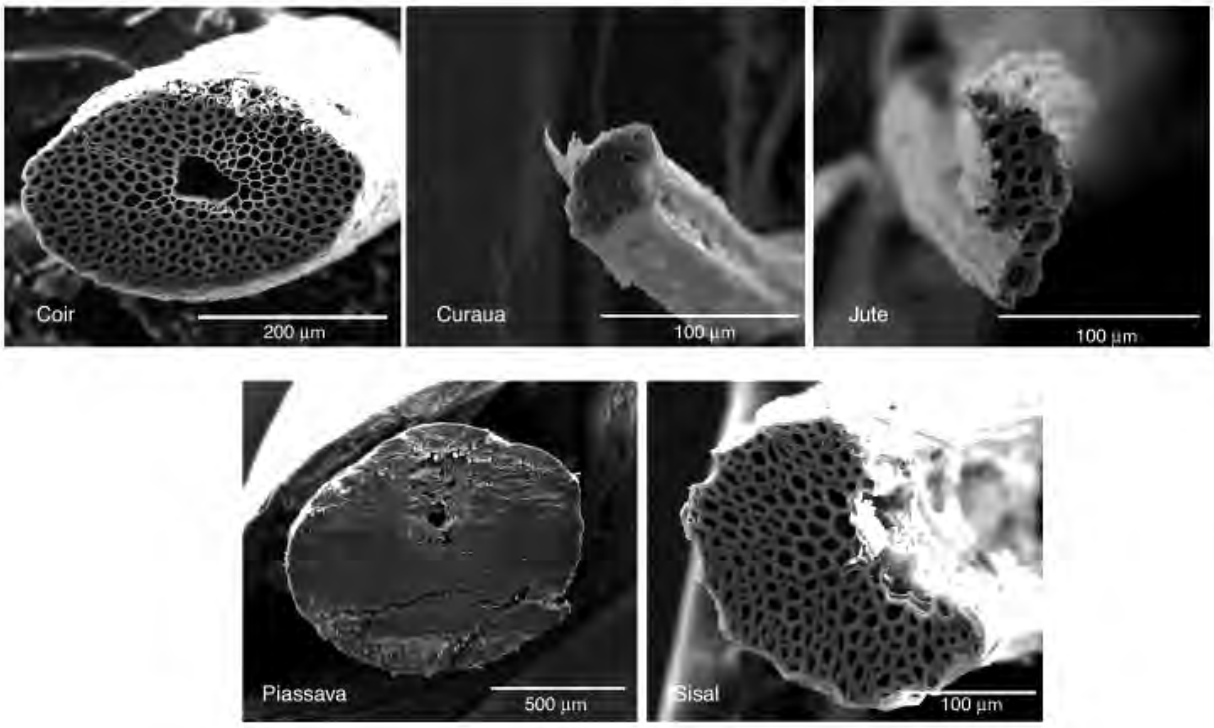

Figure 2-2: Micrographs of the cross-section of different natural fibres (coir, curaua, jute, piassava, sisal)[28]

The physical properties of plant fibres (such as: morphology, regularity/irregularity along and across its main axis, crystalline packing order, amorphous content, and chemical composition) affect the mechanical properties of the fibre. Additionally, these properties can also be different within a plant structure. While treatments and chemical sizing of the natural fibres do help control the stability of the fibres and improve properties, it is very difficult to get the same level of material consistency between natural fibres when compared to synthetic fibres [29]–[31]. Furthermore, both the elastic and viscous behaviour of natural fibres depend on all these aspects.

Table 2-1 lists the properties of some common fibre materials and commonly used metals for comparison [30]–[35]. These fibres are frequently chosen due to their unique and favourable properties such as high specific strength or stiffness. Approximations and ranges are given for the properties of flax, jute, sisal and coir as it was found that there are difficulties presenting data on plant-based fibres as the fibres, conditions and preparations used are diverse.

Table 2-1: Properties of synthetic and natural fibre materials and commonly used metals [30]–[35]

Material	Density (kg/m^3)	Elastic modulus (GPa)	Ultimate tensile strength (MPa)	Specific strength ($MPa/g/ cm^3$)	Specific modulus ($GPa \cdot cm^3/g$)
R-Glass	2550	86	4400	1730	34
E-Glass	2600	74	2500	666 -1400	29
Carbon “HT”	1750	230	3200	3880	162
Carbon “HM”	1800	390	2500	1850	238
Flax	~1400	27.6	345 – 1035	227 -1220	18 - 53
Jute	~1200	26.5	393 – 773	140 - 610	7.1 - 39
Sisal	1300	9.4 - 22.0	511 – 635	55 - 610	6 - 20
Coir	1200	4.0 - 6.0	175	92 - 180	3.3 - 5.2
Common steel alloys	7800	200 - 206	300 - 630	50	26
Aluminium alloy 2024	2780	73.1	450	250	36

Compared to the material properties of the synthetic fibres, natural fibres tend to have lower values for the elastic modulus and tensile strength. However, in low load bearing applications, it was found that natural fibres could provide reasonable tensile strength properties and be an environmentally friendly alternative to conventional materials [30]. In comparison to some steels and aluminium alloys

(like those listed in Table 2-1) natural fibres offer favourable properties at a lower density. Some of the advantages and disadvantages for the synthetic (particularly glass and carbon fibres) and natural fibres are summarised in Table 2-2 [30]–[32], [36]–[38].

Table 2-2: Advantages and disadvantages of synthetic and natural fibres [29]–[31], [35]–[37]

	Advantage	Disadvantage
Synthetic Fibres	• High specific strength and stiffness • High chemical and biological resistance • Reasonable density • Some are hydrophobic and fibres do not change dimensions in water • High thermal resistance	• Can be brittle • Sensitive to surface damage • Conventional methods of manufacturing fibres are environmentally unsustainable and require large amounts of energy • Difficult to recycle
Natural Fibres	• High acoustic damping which results in good sound properties • Competitive strength and stiffness values with plastics • Biodegradable and easily combustible, thus waste disposal methods are less energy consuming • Materials are abundant, cheap, and renewable • Very low density	• Dimensional stability of the fibres needs to be controlled by treatments to improve its properties • Temperatures about 240^{o}C degrade fibres • High moisture absorption if not treated • Shorter service life • Non-homogenous properties

2.1.2 Polymeric matrices

The matrix component of a composite offers the following characteristics [23]:

1) Ensuring fibres maintain their position and orientation.
2) Transferring the loads on the part to the fibres.
3) Providing a barrier against adverse environments; and
4) Protecting fibre surfaces against mechanical degradation.

The selection of the matrix therefore influences the overall properties of the composite, particularly the compressive strength (as it provides the lateral support), interlaminar shear and in-plane shear properties (especially during bending and torsional loads), and a lesser portion of the tensile load-carrying capacity of a composite structure [23].

There are two main types of polymeric matrices: thermoplastics and thermoset. Thermoplastic matrix composites have favourable fabrication technologies in comparison to thermosetting matrices from the point of view of eco-sustainability [37], [38]. This is because, unlike thermosets which contain long

polymer cross-linked chains, thermoplastics can be re-melted and re-shaped to form new parts [25]. However, some processes for thermoplastic composites require high pressures and high temperatures, exceeding 200°C [37], which can negatively impact the natural fibres. Thermosets tend to have more favourable mechanical, chemical, electrical insulating and thermal properties when compared to thermoplastic matrices [24]. Thermosets are also usually more dimensionally stable and, have less creep and stress relaxation than thermoplastics. The limitations are that thermosets require long curing times, have limited storage life and usually exhibit a low strain-to-failure [24].

Epoxy resin is a popular thermoset resin, used as a matrix for fibre reinforced composites, due to its ability to be cured at room temperatures [40]. Liquid epoxy resins require a hardener which starts the exothermic curing reaction, permanently setting the resin during polymerisation [40], [41]. Epoxy resins do not have sharply defined glass-transition temperature which is favourable in aerospace applications [41].

Thermosetting resins are also widely used in manufacturing MDF's, particularly Urea Formaldehyde (UF) resins which contains urea and formaldehyde to act as the crosslinker [42]. Favourable properties include low viscosity and high polarity which helps coat wood fibres to produce a strong adhesive bond. Urea formaldehyde resins also are one of the fastest curing resins available and thus can be cost-effective [42].

2.2 Composite manufacturing

Different manufacturing methods can be used to make fibre reinforced polymer composite panels. These methods include autoclave curing of fibres pre-impregnated with resin (known as prepreg materials), hand lay-up with liquid resins, resin transfer moulding and compression moulding. According to refs [30], [43], challenges that may arise when manufacturing natural fibre reinforced composites, include:

- Adhesion between the fibre surface and matrix
- High temperatures degrade cellulose in plant fibre which negatively affects the mechanical properties of the fibres.
- Loading limitations during compression moulding as natural fibres are more susceptible to breakages at lower loads in comparisons to synthetic fibres.
- Availability of different natural fibre material for prepreg and even ready-for-use fabrics for composites.

The manufacturing methods discussed further are focussed on hand lay-up and vacuum infusion (VI). Both these manufacturing methods do not require high pressures or temperatures which is favourable for processing natural fibre composites. The manufacturing of MDF is also described.

2.2.1 Hand lay-up

Hand lay-up is a labour-intensive manufacturing method. It involves manually infusing the dry fabric with resin using a roller or brush. A single layer of fibre fabric, cut to the correct size, is placed on a mould or tool surface. Resin is then applied onto the fabric using the roller. Once a layer is considered well impregnated with resin, another single layer is placed on top of the existing infused fabric and the process is repeated until the desired thickness or number of layers has been reached. Figure 2-3 illustrates the main steps of a hand lay-up [44].

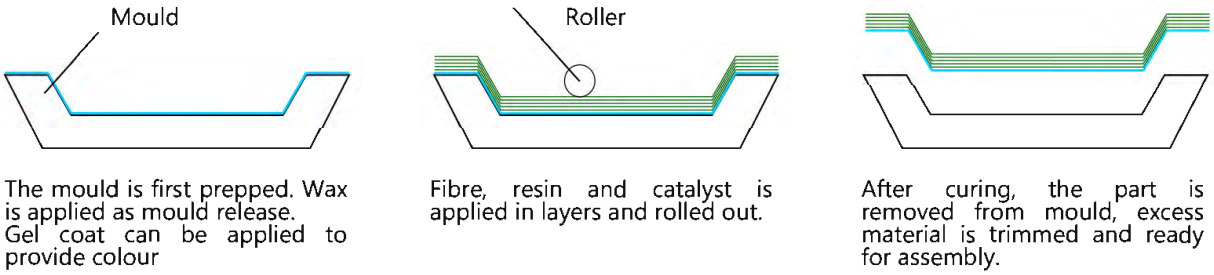

Figure 2-3: Step guide of hand lay-up manufacturing method (adapted from [43]**)**

During manufacturing, the roller can be used to spread any excess resin and compact the sample by squeezing out any air pockets that may have been formed. Additional consumables and equipment, such as a vacuum pump and bleeder cloth, can also be used to remove the excess air and resin to yield a better part [43]. This would then be a vacuum bagging manufacturing process, which is a development of the simple hand lay-up process. Importantly, the vacuum bag process allows for higher compaction and the removal of excess resin to produce a better part. The main advantages and disadvantages of hand lay-up manufacturing are listed in Table 2-3[44].

Table 2-3: Advantages and disadvantages of manufacturing composites with hand lay-up [44]

Advantages	Disadvantages
• Simple manufacturing method therefore relatively easy to teach and learn • Possible low-cost tooling • Wide choice of suppliers and material types	• Sensitive to environmental conditions, labourer and skill level • Can be physically demanding and time consuming • Health and safety considerations of resins used with open moulds releasing volatiles into the workspace

2.2.2 Vacuum Infusion

Vacuum infusion (VI) is a closed mould technique where resin is drawn into the mould to coat the fibres. The resin front, driven by the vacuum, pushes the air out and infuses the fibres. High-performance components of different sizes can be manufactured using VI without the time pressure associated with the hand lay-up method [45].

Pre-shaped fibre reinforcement (as known as fibre preform), which could consist of multiple layers or materials, is loaded into a mould. A single sided mould can be used and sealed with a vacuum bag plastic. The resin pot is connected to an inlet pipeline and resin is transferred through the reinforcements. The vacuum provides compaction removing excess air prior to infusion and helps draw the resin into and through the preform. Once all the fabric is wetted out, the inlet is closed and left to cure under vacuum [45]–[47]. A diagram showing part manufacture using VI in Figure 2-4 illustrates how the resin is drawn through the fibre reinforcement [46]. Consumables like peel ply and resin distribution fabric can be used to give the part a smoother exterior surface and improve resin flow.

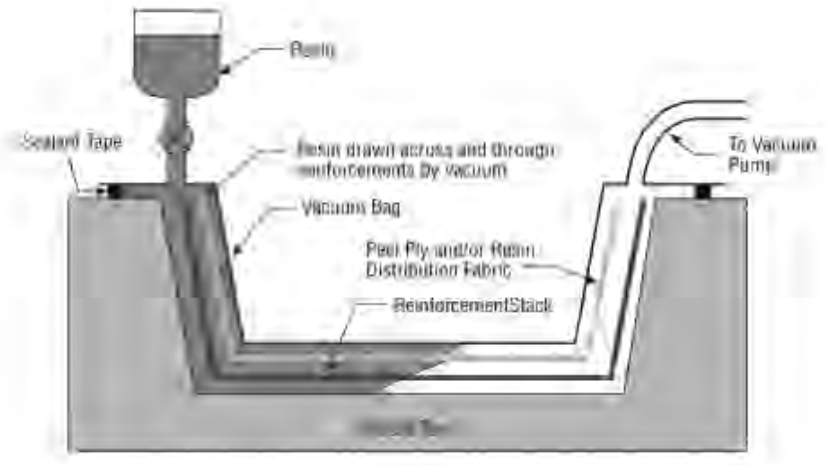

Figure 2-4: Schematic representation of a VI process [46]

There are several advantages to VI over simple hand lay-up. Less time is taken to infuse fibres compared to the hand lay-up method [47]. The vacuum bag reduces the number of volatiles released into the atmosphere during curing [49]. VI manufactured parts can usually have higher fibre and lower void content which enhances the mechanical properties [49]. Fibres are well saturated with resin and the resin distribution is uniform [49], [50]. In some cases, a weight savings of 15 % have been found on parts manufactured using VI compared to hand lay-up parts [50]. In general, research suggests that VI has the advantage, especially with quality control and consistency, over hand lay-up [51].

2.2.3 Medium Density Fibreboard manufacture

There are several steps used to manufacture Medium Density Fibreboard (MDF) that include: fibre preparation, resin incorporation and mat compression and forming. Initially, wood chips are crushed into fibres using essentially a thermomechanical pulping process [52] (in the pressured digester and refiner shown in Figure 2-5). The fibres are then combined with resin and other additives via a sequence of blending operations. The blended fibres are dried and formed into mats before being hot pressed into boards. This operation is performed under high pressures (6 – 8 bar) and temperatures (160 – 180^{o}C) so that the resin and fibres bond to form a solid panel. Finally, the board is sanded, trimmed and sawed to the final dimensions [51]–[54].

A detailed process diagram of the different steps in manufacturing MDFs is illustrated in Figure 2-5 [53]. In the diagram, resin and other additives are introduced in the blowline and blender. It also shows the stages where discarded fibre and wood waste can be recycled, usually materials found in the fibre recovery cyclone.

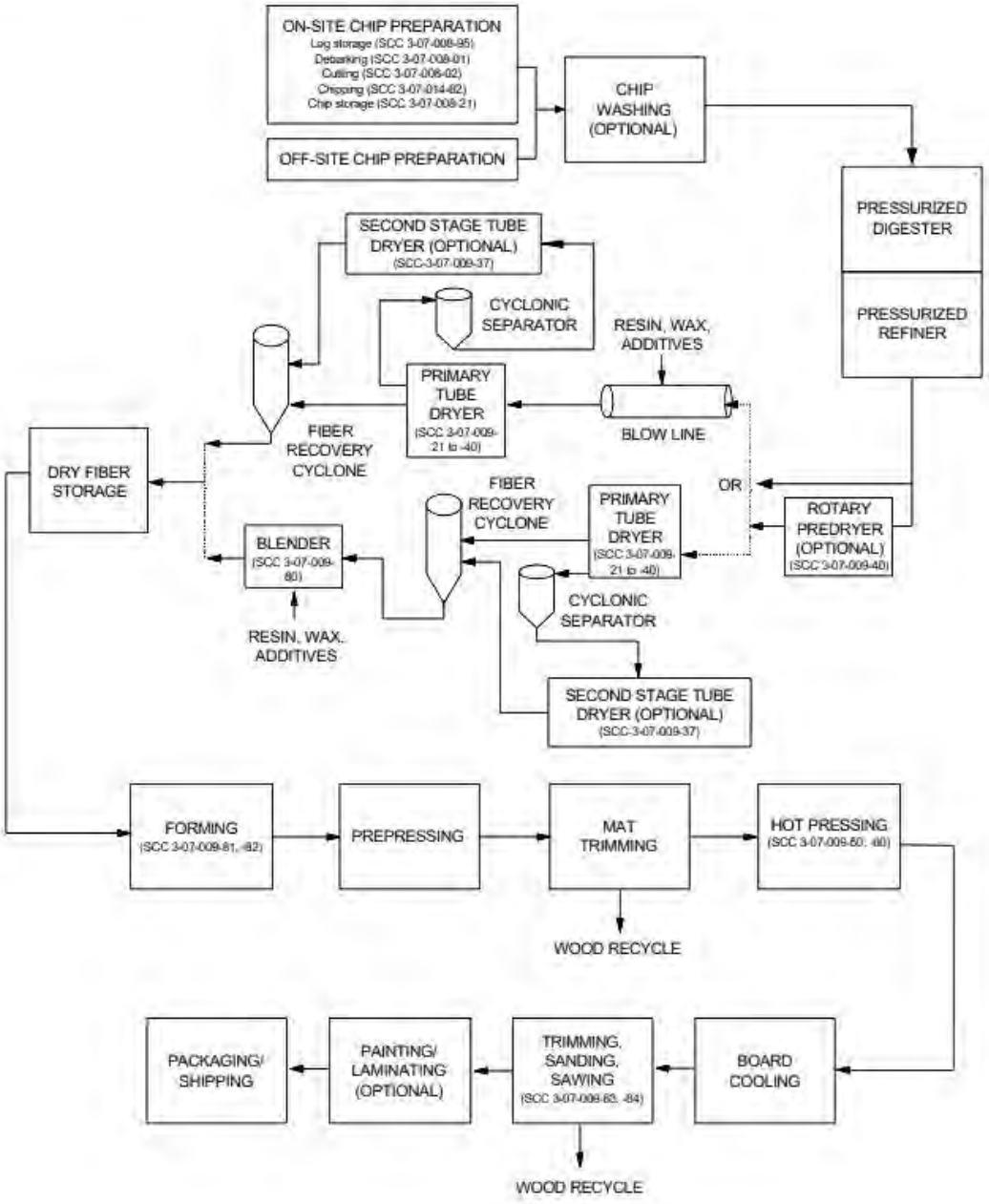

Figure 2-5: Typical process flow diagram for MDF plant [53]

2.3 Sustainability of materials

Sustainable development consists of three aspects: society, environment, and the economy. According to Thakur et al [55], the combination of these three elements must work together to "meet the needs of the present without compromising the ability of future generations to meet their own needs". The effect on the environment, societal concerns and economic impact should be considered when designing for composite materials along with mechanical and chemical properties, material purchase costs and availability of resources. These considerations should include the sourcing and manufacturing of base materials of a product, full life cycle of the product and actions at the end of the product life.

2.3.1 Natural fibres as sustainable materials

Natural fibres are typically considered "environmentally friendly" due to abundance and renewability, low CO_2 emissions in processing, being biodegradable, low energy consumption, relatively good mechanical properties (with improvements from treatments), and with minimal health hazards during its processing [56], [57]. There has been a growing interest in natural fibres, because of environmental reasons, particularly in the automotive industry [58]. In 2016, the global natural fibre composite market size was valued at USD 4.46 billion, and it is projected that the market will grow at a compound annual growth rate of 11.8 % from 2016 to 2024 [59]. Furthermore, the use of natural fibres can support developing countries as over 60 % of natural fibre production is carried out in those countries, which positively affects the economy of those countries in terms of overall Gross Domestic Product and employment rates [60], [61]. The agriculture sector contributes around 2 % of the GDP in South Africa [62]. Considering this sector is one of the world's most diverse due to the rich biodiversity of the country [63], there are potential opportunities to tap into to the emerging natural fibre market in a sustainable and profitable manner.

There are several studies that seem to support the idea that natural fibres are sustainable materials. Joshi et al [10] suggested that natural fibre reinforced composites are likely to be environmentally superior to glass fibre reinforced polymer composites (GFRPs) in low load bearing applications, as the overall fibre production environmental impacts are less for natural fibres, similar parts made from natural fibres often weigh less which can reduce costs and emissions associated with handling and transportation, and the disposal of material requires less energy. Similar findings were observed by Le Duigou et al [64] on flax fibres, and Wotzel et al [65] and, Schmidt and Beyer [66] considering hemp fibres as a reinforcement. Table 2-4 shows an environmental impact analysis, by Le Duigou et al [64], for the production of one tonne flax and glass fibres to be used as a composite reinforcement. The impact categories are explained in Table 2-5. The flax fibres were also assessed under two mechanical treatments: scutching (mechanical separation of non-fibrous material to extract fibres) and hackling (performed after scutching, hackling separates fibre bundles and improves fibre quality). Considering the production of flax fibre is dependent on yield, an economic coefficient was allocated and compared to the glass fibres.

Table 2-4: Environmental impacts of flax fibres compared to glass fibres [64]

Impact Category	Units	Glass Fibres (by Mass)	Scutched Flax (by Mass)	Hackled Flax (by Mass)	Hackled Flax (by Economic Value)
Abiotic depletion	$x10^{-3}$kg Sb eq./kg	19	1.3	1.7	6.5
Acidification	$x10^{-3}$kg SO_2 eq./kg	16	1.8	2.2	6.2
Eutrophication	$x10^{-3}$kg PO_4 eq./kg	1.2	1.4	1.4	6.2
Global warming (GWP100)	kg CO_2 eq./kg	2.65	-1.45	-1.4	-6.4
Ozone layer depletion	$x10^{-9}$kg CFC.11 eq./kg	200	2.1	24	98
Human toxicity	kg 1.4-DB eq./kg	9.1	0.15	0.215	0.77
Fresh water aquatic ecotoxicity	$x10^{-3}$kg 1.4-DB eq./kg	170	54	59	240
Non-renewable energy consumption	GJ/tonne	45	4.4	11.7	-
Land use	$x10^{-3}$ m^2/year/kg	7	970	850	3800

Table 2-5: Definitions of different impact categories used in LCAs [64]

Impact Category	Description
Abiotic depletion	Attribution to the decrease in the nonbiological resources of the environment
Acidification	Acid deposited onto the soil, water and atmosphere which negatively affects the environment
Eutrophication	Overfertilization leading to increased biomass which can be harmful for the environment
Global warming (GWP100)	Contribution of emissions and the effects on the atmosphere
Ozone layer depletion	Halocarbon carbons and emissions that lead to rapid depletion of the ozone layer
Human toxicity	Chemicals involved and potential interactions that negatively affects human life
Fresh water aquatic ecotoxicity	Chemicals involved and potential interactions that negatively affects freshwater aquatic life
Non-renewable energy consumption	Consumption from non-renewable resources and non-renewable energy
Land use	Amount of land/space required for production per year

In Table 2-4, the environmental impact to produce fibres is less for the flax fibres for every category except land use and eutrophication, suggesting that flax fibres are an environmentally-friendlier material compared to glass fibres. Similar results were found in Life Cycle Assessments (LCA) studies

by Wotzel et al [65] and Schmidt and Beyer [66] when considering certain components used in cars (typically as low-load structural parts) that can be made from hemp fibre reinforced composites. There are limitations with the LCA studies as a way to measure the environmental impacts as it can be difficult to quantify some impact categories [67]. However, it seems that in comparison to conventional synthetic materials, natural fibres are environmentally friendlier.

A great concern regarding the use of natural fibres is that the agriculture fibre cultivation requires fertilisers, pesticides and herbicides [64]–[67]. This can lead to higher nitrate and phosphate emissions that may contaminate local water supplies causing eutrophication and degradation to the environment [68]. However, with further research, different strategies and developments can be implemented to improve the harmful impact that chemical products have [64]–[67].

2.3.2 Environmental impact of resins

Typically, fully cured products using resins are regarded as non-hazardous to the environment. However, during the manufacturing process, these materials can produce harmful by-products [69], [70]. Prior to curing, liquid epoxy resins and urea formaldehyde (UF) resins (commonly used in MDFs) are classified as hazardous to the environment according to the European Chemicals Agency [71], [72]. Additionally, these resins and reactive diluents are not readily biodegradable and considered toxic to aquatic organisms [71], [72]. With most (if not all) resins, proper handling procedures and waste management should always be performed when handing these materials.

The raw materials used to manufacture resin also have a significant impact on the environment. McDevitt and Grigsby [73] calculated that the life cycle impact for MDF manufacture was 22 % lower for a bio-based (theoretically composed only of bio-based ingredients) adhesive compared to a petrochemical adhesive based on environmental impact points assigned to a conventional UF resin and a fully bio-based resin shown in Figure 2-6. The constituents of such a bio-based adhesive originate from biological feedstocks, and with that arise associated ecosystem degradation such as land use, similarly to natural fibres. However, the petrochemical adhesive had a higher impact overall and a key advantage from using bio-based resins was that no toxic formaldehyde substances are present.

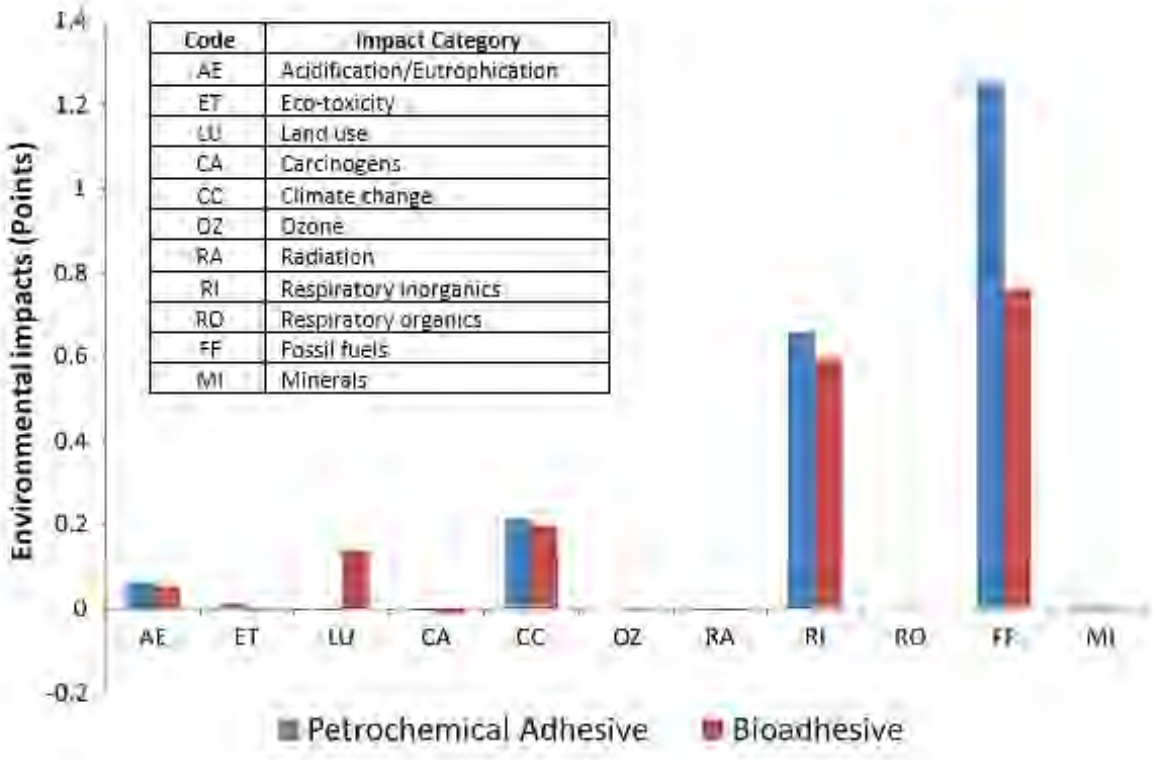

Figure 2-6: Midpoint environmental impact results for petrochemical adhesives and bio adhesives [73]

One of the biggest concerns highlighted for epoxies and UF resins is that volatile organic compound (VOC) emissions can be released during manufacture and processing, causing health effects such as irritation to the skin, eyes and throat [69], [70]. Some of the deleterious effects of VOCs include cancer, liver and kidney damage and central nervous system damage [74]. Formaldehyde, a suspected carcinogen [75] found in UF resin, is released from wood-based panels and recognised as a major cause of poor indoor air quality [76]. The emission of VOCs from resins should be as low as possible. Most countries have legal limits on the quantities of these emissions which can be released into the atmosphere [69].

The use of bio-based resins could target two Sustainable Development Goals (SDGs) (SDG 12, on responsible consumption and production, and SDG 13, on climate change [77]) set by the United Nations General Assembly. Currently, there are epoxy resins that contain some biological ingredients and claim to have environmental benefits, such as reduced consumption of fossil fuels and carbon footprint [78], [79]. Modified UF resins with additives and alternative formaldehyde resins that reduce the rate of emissions or alternative binders that contain no added formaldehyde are more environmentally friendly [80] and considered as an eco-sustainable alternative. Fully bio-based resin may not necessarily be the sole solution for sustainable composites, however resins with biological ingredients and innovations warrant further investigation with sustainability performance in mind.

2.3.3 Recycling with composites

The recyclability of a material contributes to the sustainable development of industrial processes and adds to the overall sustainability. However, recycling (FRP) composites, in comparison to other engineering materials like metals and glass, is complex due to the heterogeneous nature of the material [81], [82]. Thus, the characteristics of the constituent materials in a composite affects the recyclability. Unfortunately, thermoset resin-based composites are very difficult to recycle as they cannot be melted [81], [82]. Table 2-6 shows some options that are available for the recyclability and disposal of different composites [81].

Table 2-6: Recycle and disposal options for composites (adapted from [81]**)**

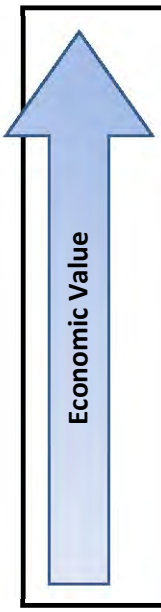

Post-consumer application	Compatible composite materials
Recycle into the same product	Thermoplastic matrix, short fibres of any composition
Recycle into lower performance composite	Thermoplastic matrix, short fibres of any composition
Melt and recycle as a thermoplastic	Thermoplastic matrix and thermoplastic fibres; long or short fibres that can be nonwoven or woven
Recycle as filler for other composites	Thermoplastic or thermoset matrix with any fibre reinforcement
Shred composite and use as fuel	Thermoplastic or thermoset matrix with any fibre reinforcement
Dispose composite as degradable waste	Natural fibre-biopolymer composites or natural fibre composites

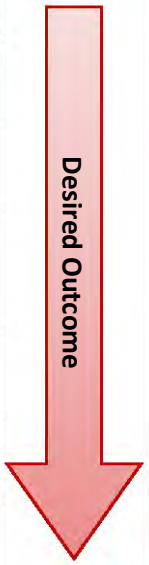

According to Shanks [81], it is only viable to recycle thermoset based composites as filler. For GFRP, the value and usefulness of the recycled material tends to be low. Furthermore, it requires large amounts of energy and processing to yield raw material. For each of these products, the recycled composite will likely be weaker [81]–[83]. Even for thermoplastics with short fibres recycled into the same product, some loss of fibre length (due to shear) occurs as it is reprocessed [81]. The desired outcome (see Table 2-6) decreases significantly as a thermoset matrix is used [81]–[83]. Unfortunately, in cases where high temperatures and large crushing forces are required to recycle the composite, the costs can exceed the value of the recycle material, making recycling economically unjustifiable [83]. However, due to the concerns of composite waste and environmental impact, there continues to be incentives to develop recyclability solutions. In 2017, a company called MDF Recovery claimed to have developed a process to recover wood fibre from recycled MDF while maintaining the properties of the fibre [84]. As research in materials and new processing techniques are developed, more options will be available such that greater sustainability can be achieved.

2.4 Mechanical response of FRPs

The typical mechanical failure modes that can occur in any fibre reinforced composite after initial elastic deformations are [85]:

- Fibre failure and fracture
- Matrix failure (such as matrix rupture, micro-cracking, and gross fracture)
- Fibre pull-out and debonding between the fibre and matrix
- Delamination between adjacent plies in the composite laminate

A schematic of some typical failure modes in composites (such as fibre rupture, debonding, matrix rupture, delamination and bridging) are illustrated in Figure 2-7 [86]. In addition, examples of some failure modes observed on micrographs for jute fibre reinforced composites [87] and carbon fibre reinforced composites [88] are shown in Figure 2-8 and Figure 2-9 respectively.

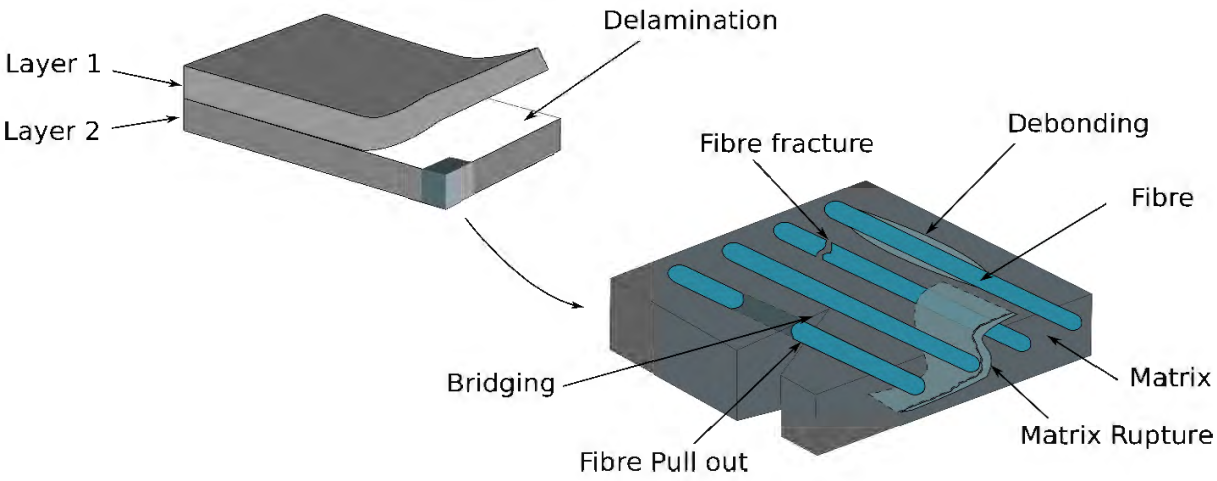

Figure 2-7: Mechanical failure modes that can occur in a composite (adapted from[86]**)**

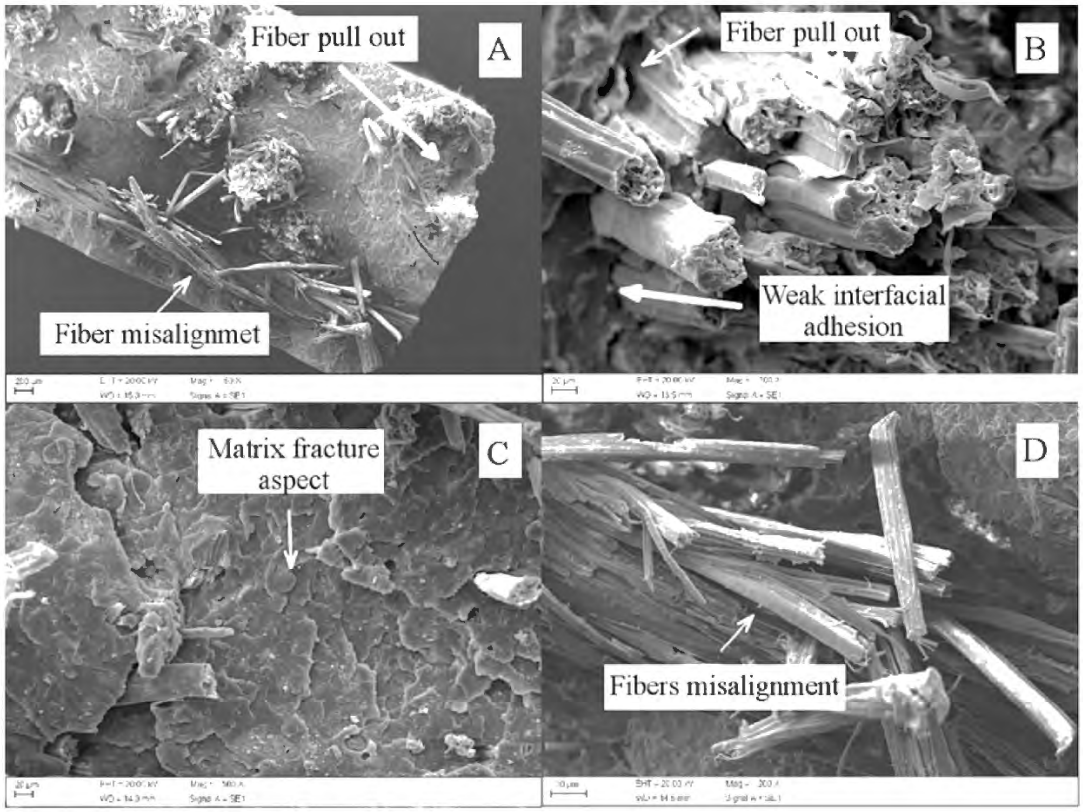

Figure 2-8: Micrographs showing failure modes in jute fibre reinforced composites [87]

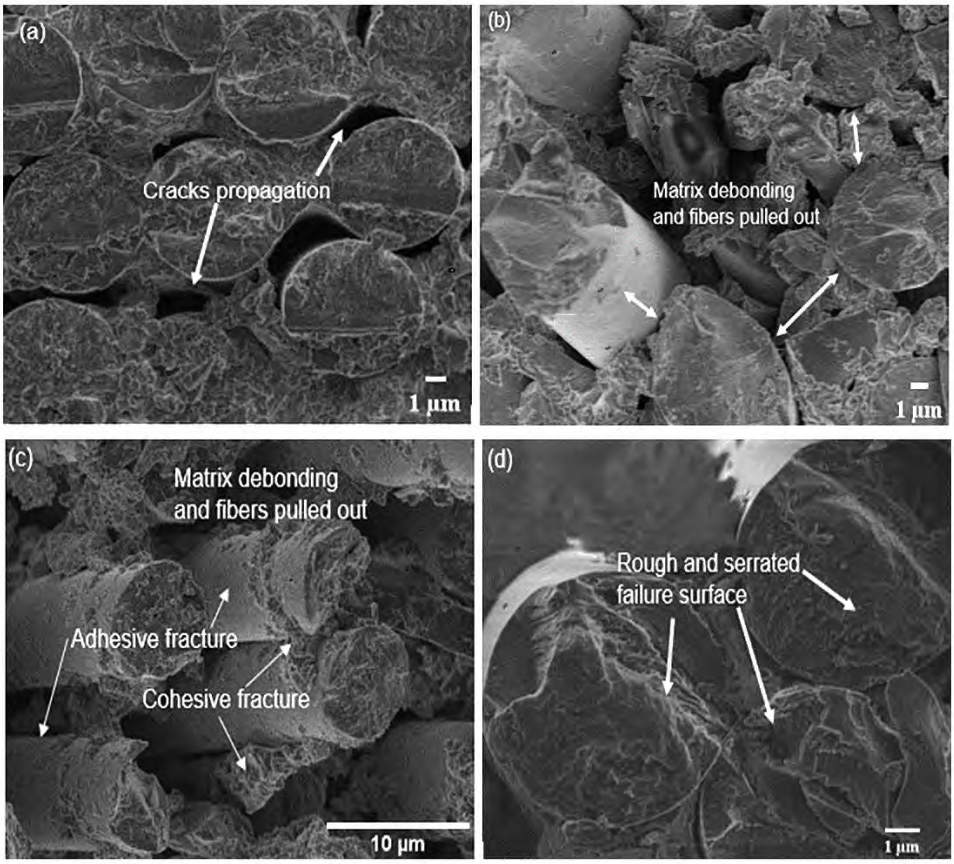

Figure 2-9: Micrographs showing failure modes in carbon fibre reinforced composites [88]

The failure modes occur either in the matrix, reinforcement or at the interfaces between the constituent materials. The mechanical failure modes are highly dependent on the constituent materials used and their properties and can give insight to which material dominates the overall properties of the composite. Additionally, damage in a composite could also occur due to defects from fabrication and handling. Figure 2-10 summarises the factors that affect the mechanical properties and tribology of natural fibre composites [89]. However, similar parameters affect synthetic fibre composites as well [32].

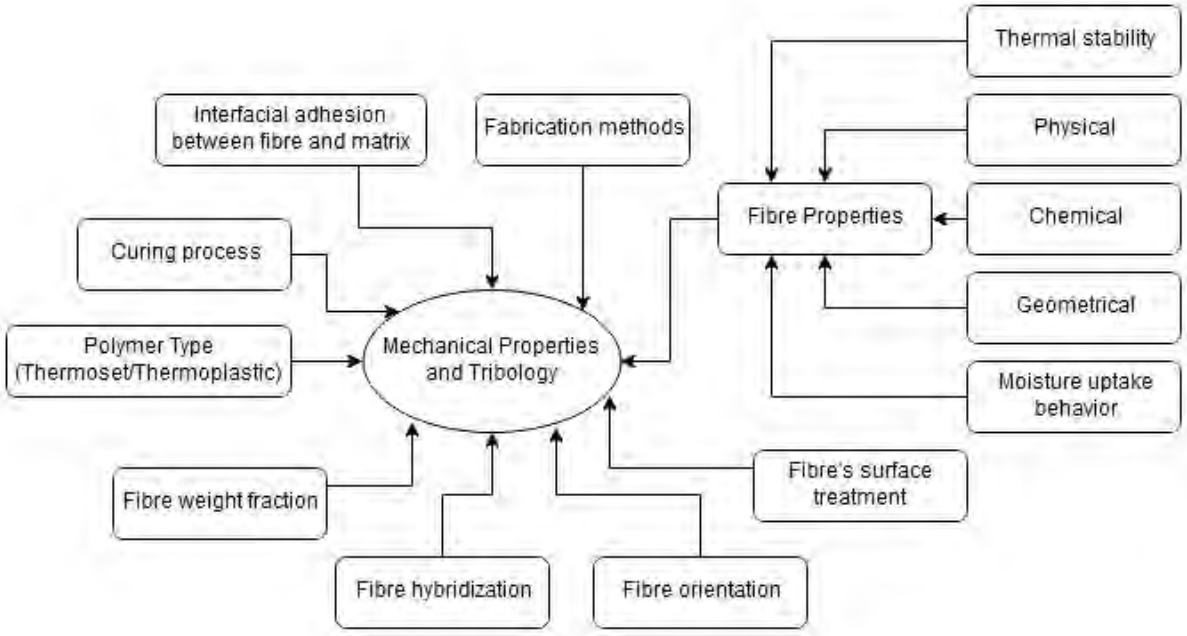

Figure 2-10: Parameters affecting properties of natural fibre composites (adapted from [89]**)**

The factors that influence the mechanical properties of fibre reinforced polymer composites mainly depend on the following: matrix properties, fibre properties, fibre configuration (such as woven fabric or randomly orientated mat), interfacial adhesion between the fibre and matrix, voids, and manufacturing methods used [32], [89], [90]. These influences tend to be related to one another. The effects of these factors on the characteristics of material properties of composites, with attention paid to natural fibre composites, is discussed further in this section.

2.4.1 Fibre properties

There are several factors that influence fibre properties. These factors include thermal stability, physical and chemical fibre properties, fibre geometry such as length and diameter and ability to absorb moisture [89]. The poor thermal stability and high moisture absorption potential of the fibres are two prominent difficulties with using natural fibres [55].

High temperatures can assist bonding between the reinforcement and polymer matrix. Unfortunately, the structural constituents of plant fibres start to degrade at high temperatures around 200°C, adversely affecting the mechanical properties [30]. Technical thermoplastics that require processing temperatures above 250°C, like polyamides, polyesters and polycarbonates, are therefore unsuitable for most natural fibres [30], [91]. Glass fibres, which have higher strength properties compared to natural fibres, can retain 50 % of room temperature tensile strength at 370°C, have a softening point of 846°C and good thermal conductivity [92], and thus can be used with most thermoplastic matrixes.

Plant fibres are hydrophilic and are prone to absorbing moisture if not treated. They contain hydroxyl (-OH) and other oxygen-containing groups that attract water molecules through hydrogen bonding [29]. When processing natural fibre composites with thermoset resins, the two groups form hydrogen bonds as shown in Figure 2-11 [93]. In the presence of water molecules, void formation occurs and poor interfacial adhesion results between the fibre and resin.

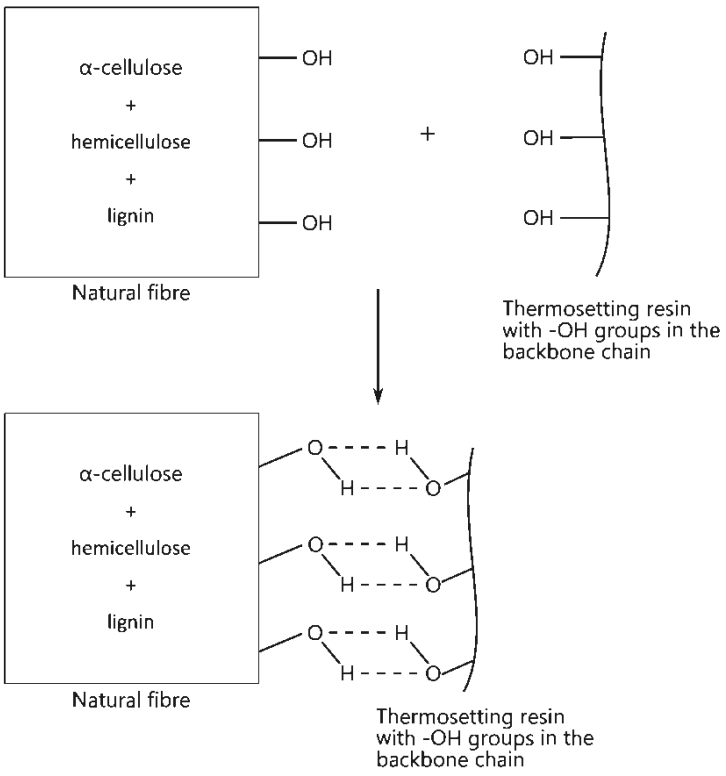

Figure 2-11: Formation of hydrogen bonds between the hydroxyl groups of natural fibres and thermosetting resins (redrawn from [93]**)**

2.4.2 Fibre configuration

The different configurations of fibres used for laminated composite panels include unidirectional tapes, woven fabrics, or short fibres in random-oriented fibre mats. The fibre orientation in the laminates determines whether the response of the composite is isotropic, transversely isotropic, orthotropic, or anisotropic material. Composite laminates manufactured with unidirectional tape laid in a single direction are highly anisotropic therefore will have high longitudinal tensile strength and a low transverse tensile strength. Short randomly orientated fibre reinforced composites tend to have low strength properties but will be isotropic and cheaper [31], [94]. Figure 2-12 shows the effect of the configuration of fibre (unidirectional, multiaxial or nonwoven on the tensile properties such strength and modulus) for both the glass and natural reinforced plastics [28]. Nonwoven fibre reinforced plastics were found to have a lower tensile strength than multiaxial and unidirectional reinforced composites, irrespective of how the fibre was sourced and which polymeric resin used.

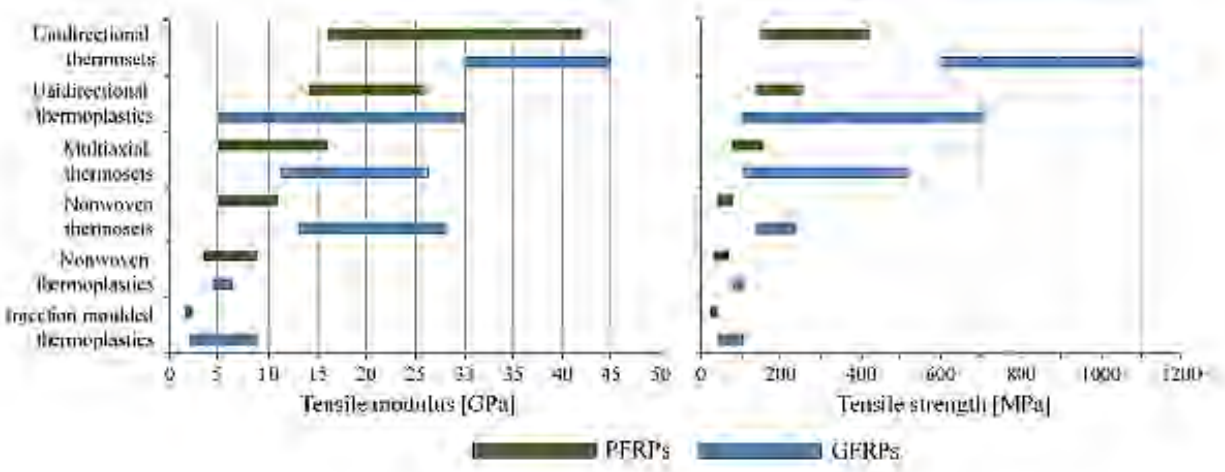

Figure 2-12: Tensile strength and modulus ranges for plant fibre reinforced polymers (PFRPs) with glass fibre reinforced polymers (GFRPs) [28]

2.4.3 Properties of MDF

Medium density fibreboards are described as a fibre composite material, as such the properties would depend on the raw materials used to manufacture the component. The main lignocellulosic material used in MDF is wood, however other lignocellulosic materials have also been considered to combat shortages of forest resources [95]. In addition to this, defibration conditions, refining parameters, other manufacturing methods and conditions, and treatments affect the properties of the MDF [95]–[99]. Table 2-7 shows some properties of MDF panels manufactured and tested under various conditions.

Table 2-7: Internal bond and modulus of rupture of different MDF panels

Fibre	Resin	Primary testing parameter	Internal bond (MPa)	Modulus of rupture (MPa)	Ref
Rice Straw	UF	Oxalic acid and steam pretreatment	0.5-0.6	12-17	[95]
Kenaf	UF	Various fibre geometry and refining conditions	0.5-0.8	24.8-32.6	[99]
Wheat Straw	Urea melamine formaldehyde and urea melamine phenol formaldehyde	Various resin contents and qualities of wheat straw	0.4-1.3	25-50	[100]
Wood-based MDF product from "MDF Hallein GmbH & Co KG", Austria		Commercially produced MDF tested to determine suitability for furniture production	0.5-0.8	31.4-39.9	[101]

2.4.4 Interfacial adhesion between fibre and matrix

The interfacial adhesion between the fibre and matrix depends on the fibre/matrix selection, manufacturing process and surface treatment of the fibre. The overall properties, such as strength, fracture toughness and environment stabilities, of fibre reinforced composites are highly dependent on the interfacial adhesion [102]. The presence of voids between the fibre and matrix could also act as crack initiators which weaken the composite and can allow for an increase in the moisture uptake for the composite, making it more susceptible to premature degradation [87], [103]–[105]. This is a greater concern for natural fibres as they are hydrophilic and dimensionally unstable in water. Figure 2-13 shows an example of a jute fibre reinforced composite where there was lack of adhesion between fibre and matrix [87].

There was a distinct gap between the fibre and resin, as highlighted by the arrow in Figure 2-13. Without proper interfacial adhesion, the load will not be transferred from the polymer matrix to the reinforcing fibres. The poor interfacial stress transfer capability consequently affects the mechanical properties of the jute fibre composite.

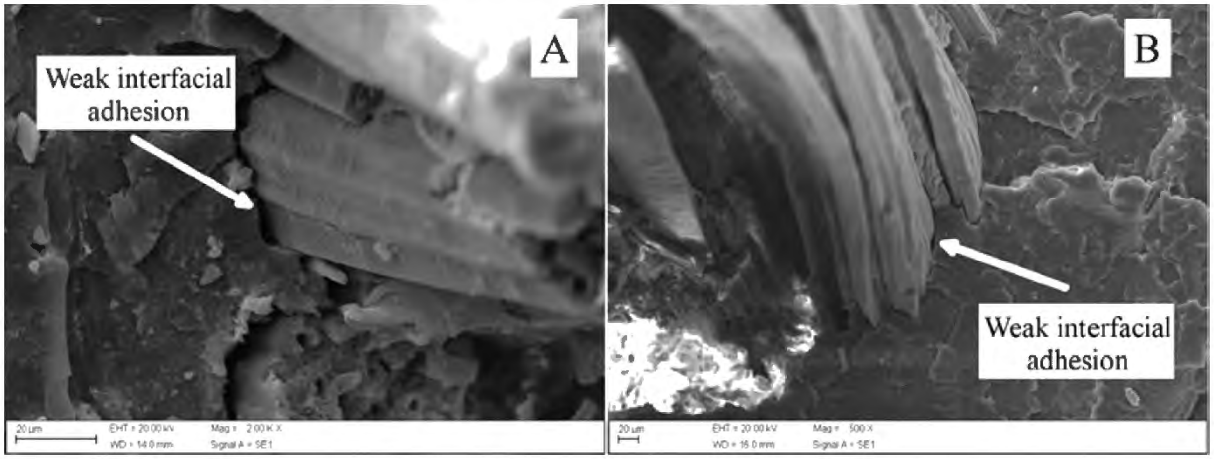

Figure 2-13: SEM of fracture surfaces showing the weak interfacial adhesion of jute fibre reinforced composites at a) 2000x and b) 500x magnification [87]

2.4.5 Voids

The presence of voids has a significant influence on the physical and mechanical properties of composites [29], [106]–[108]. In VI, the main cause for void formation is mechanical air entrapment during resin flow as illustrated in Figure 2-14 where micro-voids (between the fibre) and meso-voids (between tows) are formed [106]. In addition, gas created during the curing process and nucleation of dissolved gases in the resin can also lead to the formation of voids[106].

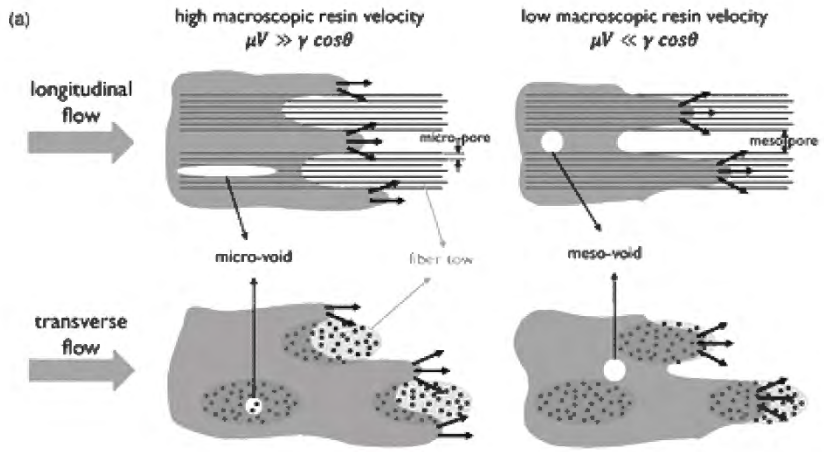

Figure 2-14: Schematic of void formation during longitudinal and transverse flow in liquid composite moulding manufacturing methods [106]**.**

Estimating values for the void and fibre volume fraction provides insight as to how the material will perform. The most commonly used methods of determining the fibre volume fraction of a composite uses burn off tests or acid digestion to remove the matrix [109]. Unfortunately, both these methods are unsuitable for natural fibre composites, and determining the void and fibre volume fraction for these materials is challenging [110]. Typically, void and fibre fractions of natural fibre composites are

determined by weight fractions (rather than volume) however this approach is less accurate [111]. Amiri and Ulven [110] suggested that a reliable method to evaluate natural fibre composites and calculate void fractions was by micro-CT technology. Unfortunately, this technique requires specialised equipment and is more complicated and expensive than burn off tests or acid digestion [111].

2.4.6 Effect of manufacturing methods on properties

Reducing voids and ensuring uniform distribution of resin and fibres is a requirement of any FRP manufacturing process. Void formation can be a significant problem when manufacturing composites. As discussed, voids create stress concentration zones within the composite that negatively influences material properties. These voids can be introduced while mixing resin formulations or filling cavities in more complex components. Air can be trapped in the interstices of fibre structures which can also lead to poor interfacial bonding. For some thermosetting resins, during the curing process, volatile gases are released as bubbles that can be trapped in the resin. While the fibre/resin selection impacts the properties of the composites, the manufacturing processing technique is also a major factor [112].

Hand lay-up natural fibre composites tend to be more susceptible to errors and defects [113]. However, in comparison to wet lay-up, VI can increase the component mechanical properties and fibre content as the void content is reduced and fibre volume fraction is improved. This is usually found to be true for both synthetic and natural fibre composites [114]. Yuhazri and Phongsakorn [115] found that kenaf/polyester composites manufactured using a VI process had a higher tensile property than the ones manufactured using wet lay-up as shown in Figure 2-15. Similar findings for jute/styrene composites were found by An et al [116] and cotton/epoxy composites by Tafur et al [113]

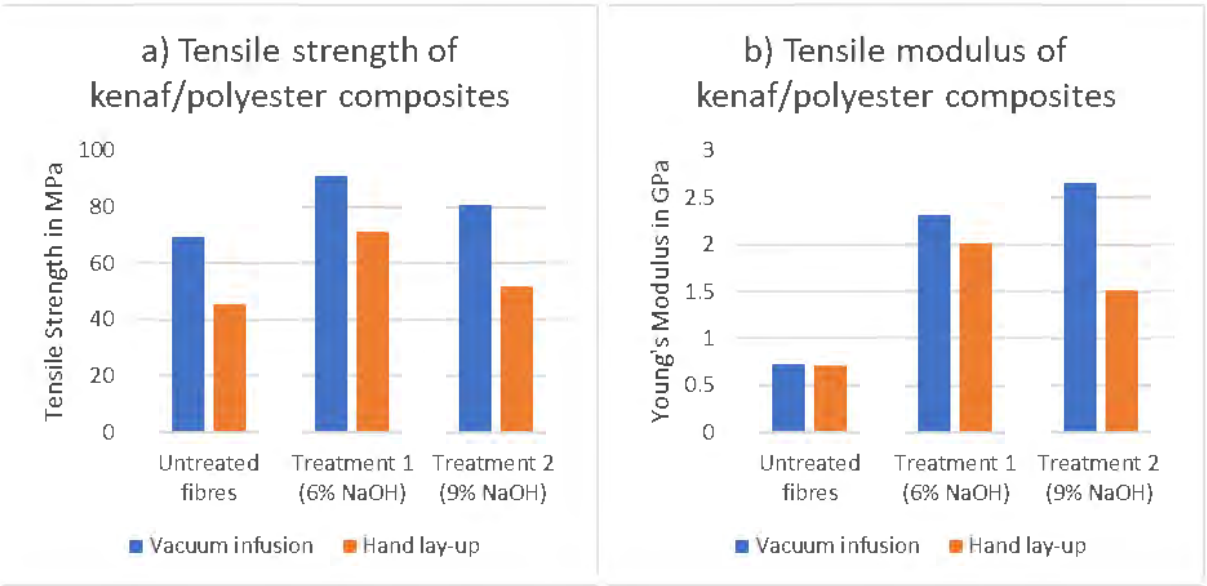

Figure 2-15: Comparison of the a)tensile strength and b) Young's Modulus of kenaf/polyester composites between VI and hand lay-up method (redrawn from [115]**)**

Removing trapped air by hand using an aluminium roller was found to be difficult as it was not possible to provided sufficient compaction [115]. This led to a higher void content in the hand lay-up samples compared to the VI samples. The material was also exposed to the environment during manufacture therefore it was possible for moisture to affect the composite [115]. Sharba et al [117] found that combining hand lay-up method with hydraulic cold press significantly improved the fibre-matrix adhesion and yielded better tensile properties compared to VI manufactured specimens. Scanning electron microscope (SEM) images of a failed tensile section are shown in Figure 2-16 where more voids and fibre pull-out were observed for the VI manufactured specimens [117]. It was also reported that impact properties were not influenced by the fabrication method (hand lay-up with cold press and VI) [117].

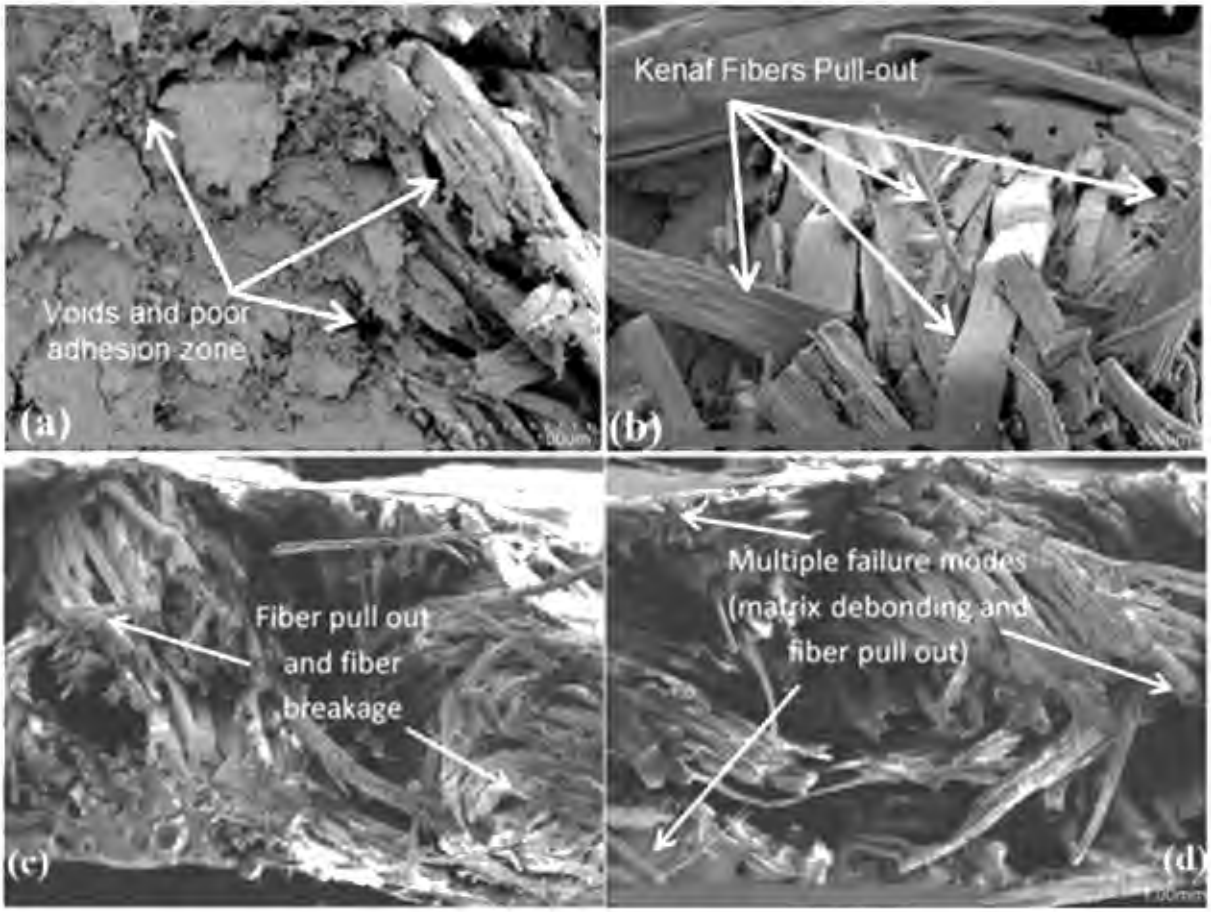

Figure 2-16: SEM images of tensile failure section of kenaf/polyester composites manufactured (a) and (b) using VI, and (c) and (d) hand lay-up with cold press [117]

2.5 Air blast theory

An explosion is defined as a rapid release of energy in a short period of time. During an explosion, a substance (for example, explosives and fuels) detonates or an event (for example, volcano eruption and failed pressured steam vessel) occurs that causes a sudden outward projection that rapidly expels matter [118]. The quick release of energy dissipates as light, heat and/or motion depending on the environment and conditions of the explosion [119].

There are several important factors such as surrounding medium and environment, explosive materials that affects the nature of an explosive blast and its subsequent effects on the blast loading (blast waves; pressure profiles, duration, and magnitude) has on structures. The characteristics of the blast waves and its ensuing effects on structural response of the composites are hereby reported.

2.5.1 Explosives and detonation

Most explosive compositions contain varying amounts of fuel elements such as carbon, nitrogen and hydrogen atoms[120]. A blast load that arises from explosive detonation is characterised as a high-rate exothermic reaction which produce high temperatures and high pressures in the surrounding environment due to the large volume of gaseous product evolved[120].

An important factor in the design calculations of explosions is the minimum detonation velocity known as the Chapman-Jouguet (CJ) point [121]. It describes the state of the products behind the detonation front and, in many cases, is used to classify explosives into low or high explosives. Low explosives are typically used as propellants and burn slower than high explosives. Low explosives tend to deflagrate rather than detonate. High explosives are used in military and mining applications which was of interest in this project [120], [122], [123]. Table 2-7 lists the experimental data found for common explosive materials at the CJ state [120].

Table 2-8: Experimental data range of detonation parameters at Chapman-Jouguet state [120]

Explosive	Initial density, ρ_0 [g/cm^3]	Detonation Velocity, D [km/s]	Pressure at CJ state, P_{CJ} [GPa]
TNT	0.624 – 1.64	3.82 – 6.95	2.62 – 19.8
RDX	0.56 – 1.8	4.05 – 8.754	3.19 – 34.7
PETN	0.2 – 1.77	0.93 – 8.27	0.051 – 33.7
Comp-B	1.67 – 1.733	7.69 – 8.022	25.65 - 30

When an explosive is detonated, a shock wave moves through the explosive with the shock front driven forward due to the energy released [120], [122]. This initial phase is known as the detonation. To enable modelling of an explosive detonation for a steady state condition, several assumptions are made, including [120]:

1. The flow of the detonation product is one-dimensional.
2. The front of the detonation is a jump discontinuity and is treated as a non-reactive shock wave.
3. Chemical and thermodynamic equilibrium is assumed for the reaction-product gasses leaving the detonation front and chemical reaction is complete.
4. The length of the chemical reaction zone is zero.
5. Detonation is a steady state process therefore the detonation velocity is constant.
6. Gaseous reaction products leaving the detonation front may be time-dependent and are affected by the surroundings.

2.5.2 Blast waves

Blast waves form as a compressed layer of air in front of the expanded hot gas from a detonated explosive. Most of the energy from the explosion is contained in the layer of compressed gas. In ideal cases, the detonation of spherical explosives in air at a large stand-off distance, the blast wave immediately reaches a pressure higher than ambient pressure before dissipating outwards away from the source as a shock wave [124], [125]. Blast waves are described by three main independent variables: initial shock intensity, duration of the blast and impulse from the pressure forces generated in the explosion [119].

A typical pressure-time history curve for a fully developed blast wave system is shown in Figure 2-17 [126]. Initially, the blast wave arrives at the location at time t_a at which the pressure instantaneously peaks to a value P_{max} known as overpressure. Any object in its path will experience an abrupt lateral force over its exposed area. The pressure, thereafter, decays quasi-exponentially to a negative phase [119]. During the negative phase, surrounding pressure falls below ambient pressure for a short period as the distance of the blast wavefront increases and the gas cools. Overexpansion due to the momentum of the gas molecules causes differential pressure between the gas pressure and ambient pressure, causing a partial vacuum. The surrounding air is sucked in during this negative phase before the pressure returns to ambient conditions [127]. The positive phase duration, t_d, and the peak positive overpressure (P_{max}) are used to characterise a blast event and the negative phase is often neglected. The pressure-time characteristic of the blast wave is often described as the Friedlander form [119], given in Equation 2.1.

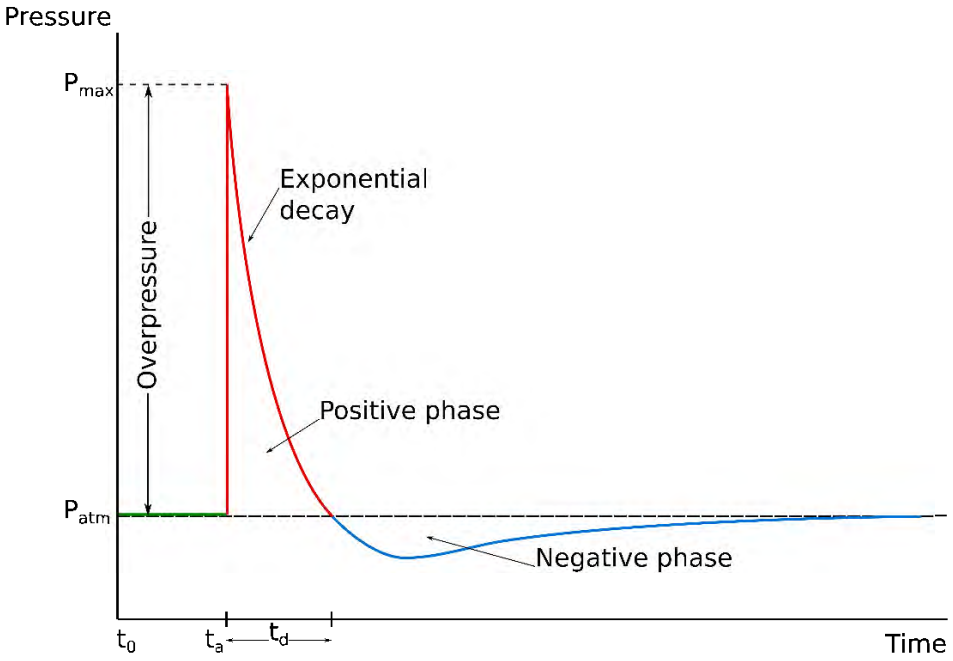

Figure 2-17: Blast wave pressure-time history from a typical far-field explosion (adapted from [126]**)**

$$p_s(t) = P_{max}(1 - t/t_d)e^{-\alpha t/t_d} \qquad 2.1$$

where P_{max} is the peak pressure and α is a decay parameter.

2.5.3 Cylindrical charges in air

Traditionally, comparisons of explosives and produced pressure waves are based on spherical charges. For a spherical charge, the resulting shock wave, when initiated at the centre of the charge, producing a uniform spherical wave. Similar shock waves can be produced, with different charge masses detonated at different positions, if the scaled distance Z, given by Equation 2.2, is the same [128], [129].

$$Z = \frac{R}{\sqrt[3]{W}} \qquad 2.2$$

where R is the radial distance from the centre of the explosion (stand-off distance) and W is the TNT equivalent charge mass.

For a cylindrical charge mass of the same mass, the resulting pressure waves may be amplified and dampened in certain areas because of the blast waves interactions with each other. The geometry and point of initiation of the explosion influence the shape and size of a shock wave [128], [129]. For an ignition point at the centre of the base of a cylinder, the development of the shock wave and bridge

wave is illustrated in Figure 2-18 [130] where the primary side and end waves interact, causing bridge waves.

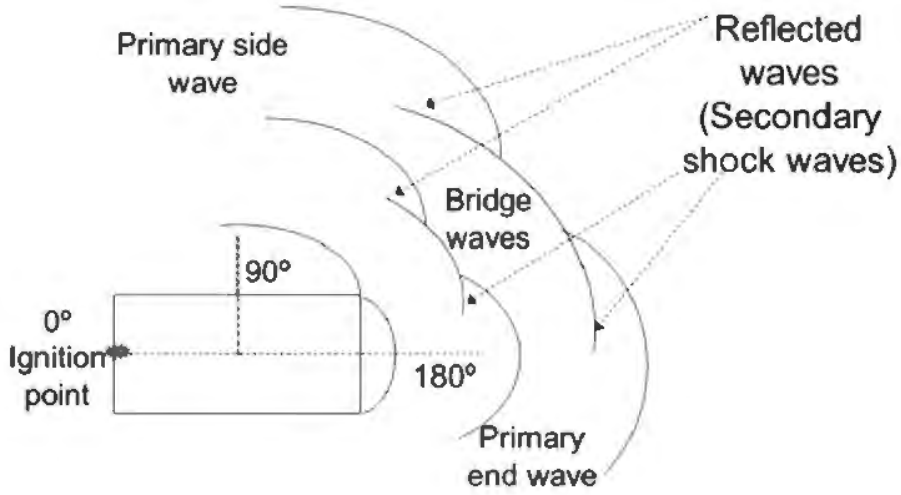

Figure 2-18: Development of shock and bridge from a cylindrical explosive charge [130]

According to Knock et al [130], the impulse from a curved surface of the charge appeared to be independent on the length to diameter ratio and is given by Equation 2.3. It is inversely dependant on the stand-off distance. Therefore, the shape of explosives has a higher influence at shorter stand-off distance; at larger stand-off distances, there are no significant differences in blast loading [130].

$$I = \frac{K'_1 M^{2/3}}{R} = \frac{K_1 M^{1/2}}{R} \qquad 2.3$$

where K'_1 and K_1 are explosive dependant coefficients.

2.6 Blast response of composites

During explosive loading, significant damage can occur to the affected structures. The blast impulse can cause deformations and eventual failure at high blast loads. Therefore, it is important to understand the extent of the type of damage that can be exerted on different materials and their blast resistance properties. This section evaluates experimental testing techniques used to generate a blast load onto composite specimens and reports on observations made concerning the blast response of different fibre reinforced polymer composites (namely those reinforced with glass and carbon fibre) and natural fibre composites.

2.6.1 Experimental testing methods

There are several experimental testing methods to determine the structural response of different materials and structures. Some methods include full-scale open-arena air blasting, small-scaled blast testing and shock tube testing. Each method has their own advantages and drawbacks.

An ideal method of blast testing structures is full-scale open-arena air blast tests, as the conditions are more representative of real-life explosions. However, they require a large amount of open land with no obstructions to reflect the blast wave and depend upon prevailing weather conditions. Furthermore, full scale tests are very expensive and difficult to set-up and perform [131]. For most research purposes, it is more feasible to perform smaller scaled (laboratory) explosion tests. Small-scale experiments are easier to perform and carefully control, for excellent potential of repeatability. However, the reliability and accuracy of these testing methods depends on the boundary conditions and equipment [132]. There are concerns especially for fibre-reinforced polymer composite structures, that the mounting and clamping options in small-scale tests are not representative of real-life connections used in structures. These can cause premature failures [133]. In blast chambers with hardened walls, small-scaled explosive testing can be safely conducted on scaled specimens. It is possible to have consistent loading conditions; therefore, tests have a high repeatability. Unfortunately, complex test configurations are difficult to perform in blast chambers [131].

Shock tubes generate simulated blast pressures using a fluid system that consists of driver and driven fluids at different pressures, facilitating the production and propagation of a shock wave [131]. A simplified schematic of a shock tube facility is shown in Figure 2-19 [134]. When the diaphragm ruptures, high pressured gas (indicated by yellow) flows into the lower pressured gas (blue) generating a high velocity region (purple) with an incident shock front. Expansion waves occur as the pressured reduces at the back of the shock wave. The disadvantages of shock tubes are the resulting lower pressures and longer durations than those encountered during explosive detonations, making them not representative of realistic explosions [131].

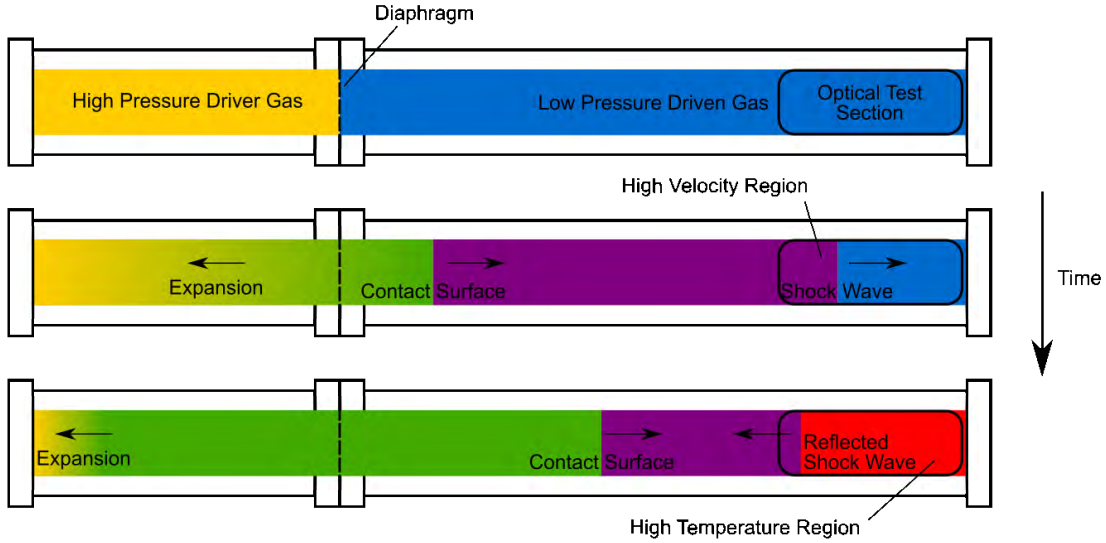

Figure 2-19: Schematic of a shock tube facility (redrawn from [134]**)**

2.6.2 Classification of blast loading based on standoff distance

The positioning of the structure from the centre of explosion has a critical influence on damage observed. By varying the stand-off distance of the explosive, the spatial distribution of the blast on a test specimen affects the response of the material which was found to also influence the loading conditions on a specimen [135].

The two categories that are often used, based on stand-off distance, are localised explosive loading and uniform explosive loading [133], [135]. During localised blast loading, the resulting shock wave is localised over a target area of the structure as opposed to the full exposed surface of a specimen. In these instances, the explosive is positioned near to the specimen, typically within 10 to 20 times of the (spherical) charge radii [133]. However, as the stand-off distance increases, it decreases the load localisation and changes the type of failure modes observed [135]. Once the stand-off distance exceeds the largest plate dimension, the loading can be considered as uniform [135].

2.6.3 Blast loading of glass and carbon fibre reinforced composites

There have been several blast loading experimental tests and numerical analyses conducted on composites primarily made from synthetic materials. Some of these tests include materials like glass fibre reinforced polymer composites (GFRPs) and carbon fibre reinforced polymer composites (CFRPs).

Franz et al [136] investigated the response of chopped strand mat glass fibre reinforced polyester composites in 2002, with differing areal densities (namely 600, 750, 900 and 1200 g/m^2) and test lay-up configurations, to localised explosive loading. Figure 2-20 and Figure 2-21 show the observed failures of some of the 600 g/m^2 and 1200 g/m^2 GFRPs respectively [136].

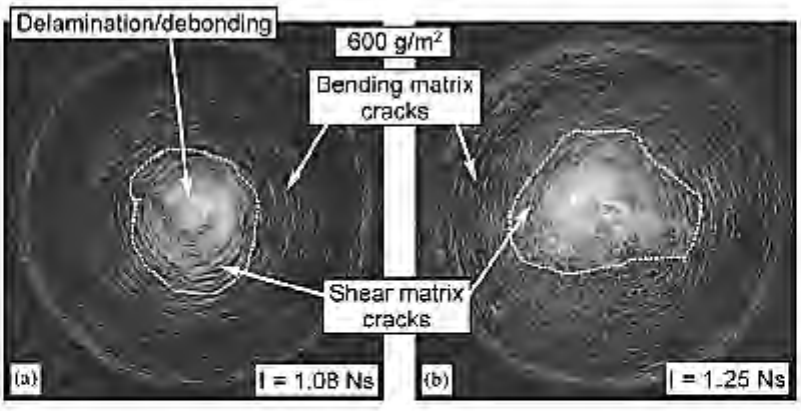

Figure 2-20: Photographs of the rear side of blast loaded 600g/m^2 glass fibre reinforced composites [136]

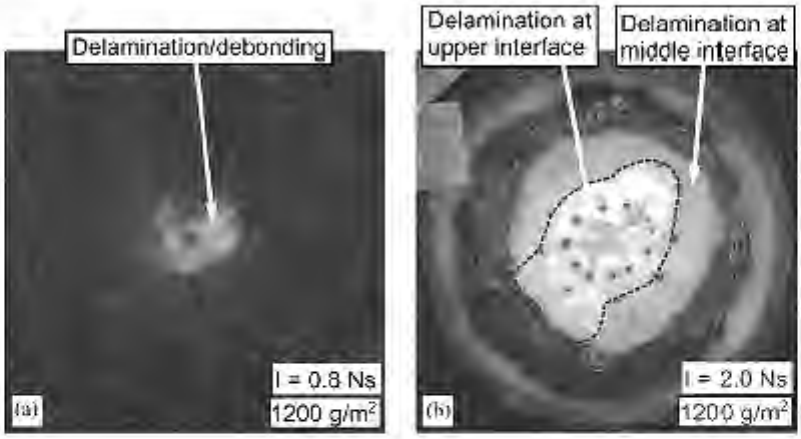

Figure 2-21: Photographs of the rear side of blast loaded 1200g/m^2 glass fibre reinforced composites [136]

As shown in Figure 2-20 and Figure 2-21, the damage distribution on the plates were mostly around the loading location. At relatively high impulses (Figure 2-20 (b) and Figure 2-21 (b)), significant damage also occurred along the clamped boundary. The main observed failure modes were matrix cracking, delamination/debonding and penetration. Matrix cracking increased with increasing impulse for the specimens depending on the areal density. Additionally, the resistance to matrix cracking was found to improve with areal density. Delamination was predominantly observed on thicker specimens as the flexural rigidity was larger in thicker specimens than thinner ones. Furthermore, Franz et al [136] found that layered composites could offer improved blast resistant properties in comparison to monolithic composite plates [136].

Comtois et al [137] investigated the effect of standoff distance and clamping arrangement carbon (unidirectional prepregs) and glass (woven) fibre reinforced epoxy composites. Predominately delamination between the layers was found. The results showed that the stand-off distance influenced the extent of damage as it was related to the imparting impulse and pressures. On localised blast loading conditions (where the charge was detonated close to the panel), penetration occurred. The holes caused by the localised load were found to be larger than those observed on metallic sheets tested under similar conditions. However, unlike in metallic sheets, tearing was not observed on the composites tested. The testing conditions, particularly the clamping arrangement, were found to have a greater influence on the damage pattern and failure. Bonded specimens allowed the plate to bend under the applied loading without generating large in-plane stretching strains. For clamped specimens, less damage was observed as shown in Figure 2-22. In addition, at the attachment point on the adhesively bonded composites, less fibre breakage was observed on the CFRPs than the lower strength GFRP.

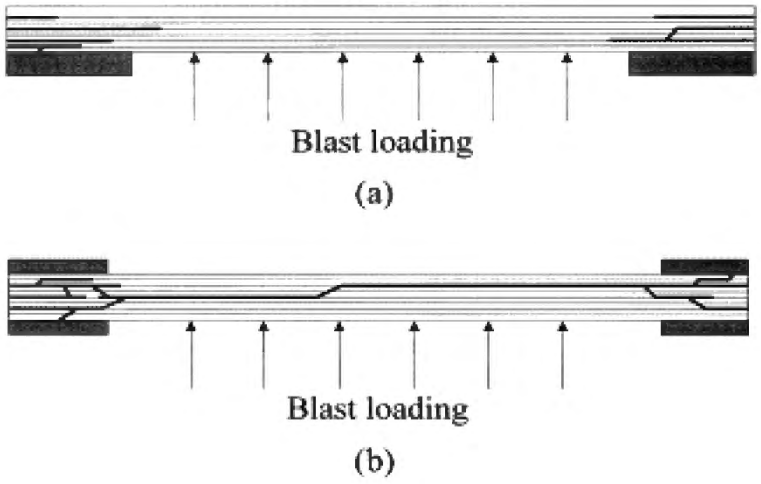

Figure 2-22: Schematic of delamination for a) bonded and b) clamped specimens[137]

Tekalur et al [138] found that, despite the superior tensile strength and modulus of the carbon fibre reinforced composite, the blast resistant properties were better for glass (woven) fibre reinforced vinyl ester composites than the carbon (stitch bonded) fibre vinyl ester composites. A continuous damage progression was observed on the GFRP tested whereas, the CFRPs showed no signs of external damage until a certain threshold shock pressure where the panel failed. Photographs of the failure modes and damage progression for the GFRPs and the CFRPs panels tested are shown in Figure 2-23 and Figure 2-24 [138]. In Figure 2-23, delamination was observed in the centre of the GFRP panels with damage found at the clamped boundary. A central burn region on the front surface, where the matrix possibly burned, was also observed. In comparison, the predominant failure modes observed on the CFRPs was fibre breakage and delamination on the front surface of the panels [138].

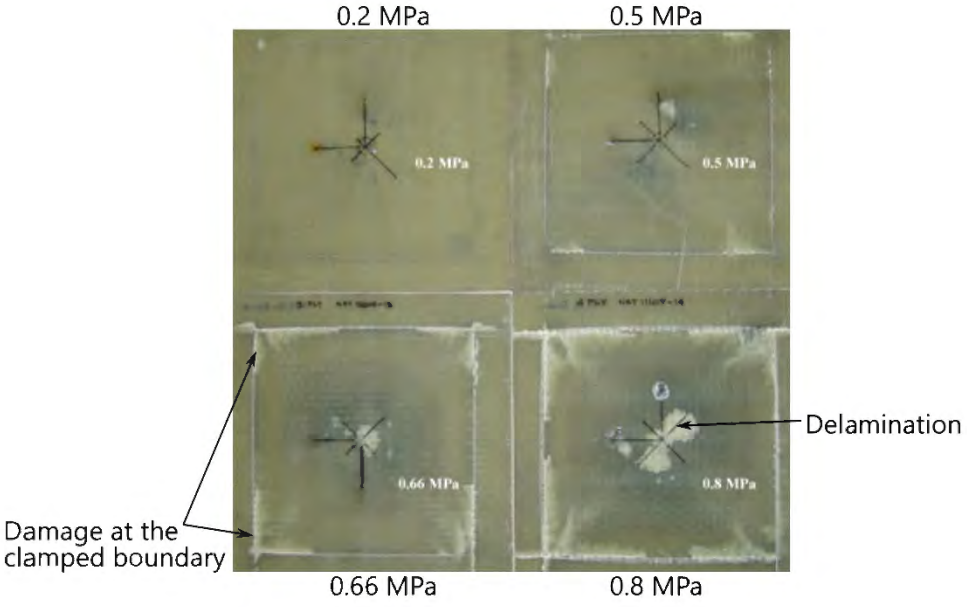

Figure 2-23: Back surface of E-Glass/Vinyl Ester composite subjected to different shock pressures [138]

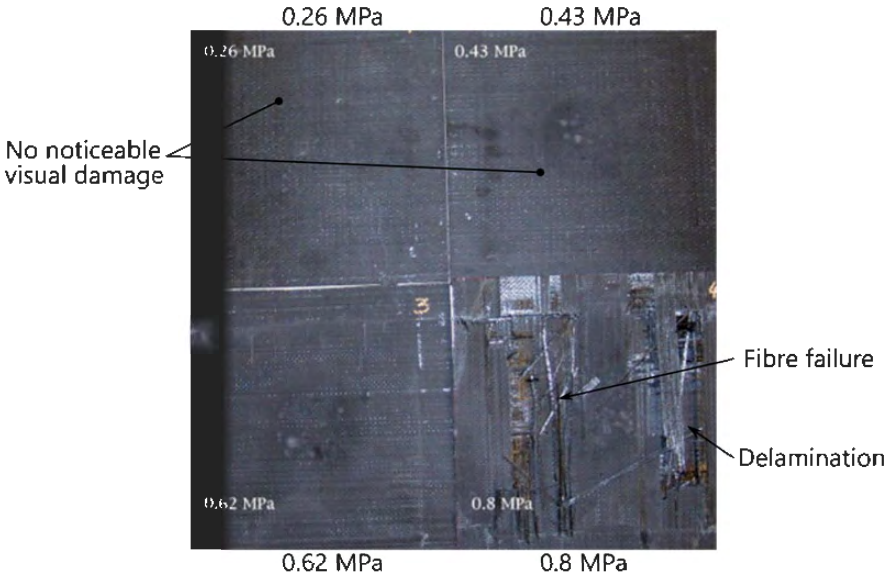

Figure 2-24: Front surface of Carbon/Vinyl Ester composite subjected to different shock pressures [138]

Similar conclusions as Tekalur et al [138] were drawn with regards to the GFRPs having a superior blast resistant ability in comparison to CFRPs by Yahya et al [139]. Yahya et al [139] investigated the effect of glass (woven) and carbon (woven prepreg) fibre reinforced poly-ether-imide (PEI) thermoplastic composites of different thicknesses under a uniform blast load. On the CFRPs tested, the failure modes observed were fibre fracture on the back surface, localised delamination and fibre buckling at the front surface. For CFRP panels tested at high impulses, shear out and fragmentation were observed. The progression of damage increased rapidly after a threshold impulse depending on the thickness of the panel. In the GFRP panels, fibre fracture (Figure 2-25c and d) and small amounts of delamination were found. The lower quantity of delamination was due to the higher values of interlaminar fracture energy reported. This was a disadvantage as multiple delaminations across the panel indicates as a considerable energy absorption ability. However, the superiority of the GFRPs was likely due to the higher strain to failure values for glass fibre. Furthermore, the blast energy exerted onto the panels was absorbed in other mechanisms such as elastic deformation, fibre buckling (Figure 2-25b) and plastic shear flow in the thermoplastic matrix. Photographs of some of the damage on the glass and carbon fibre reinforced composites are shown on Figure 2-25 [139].

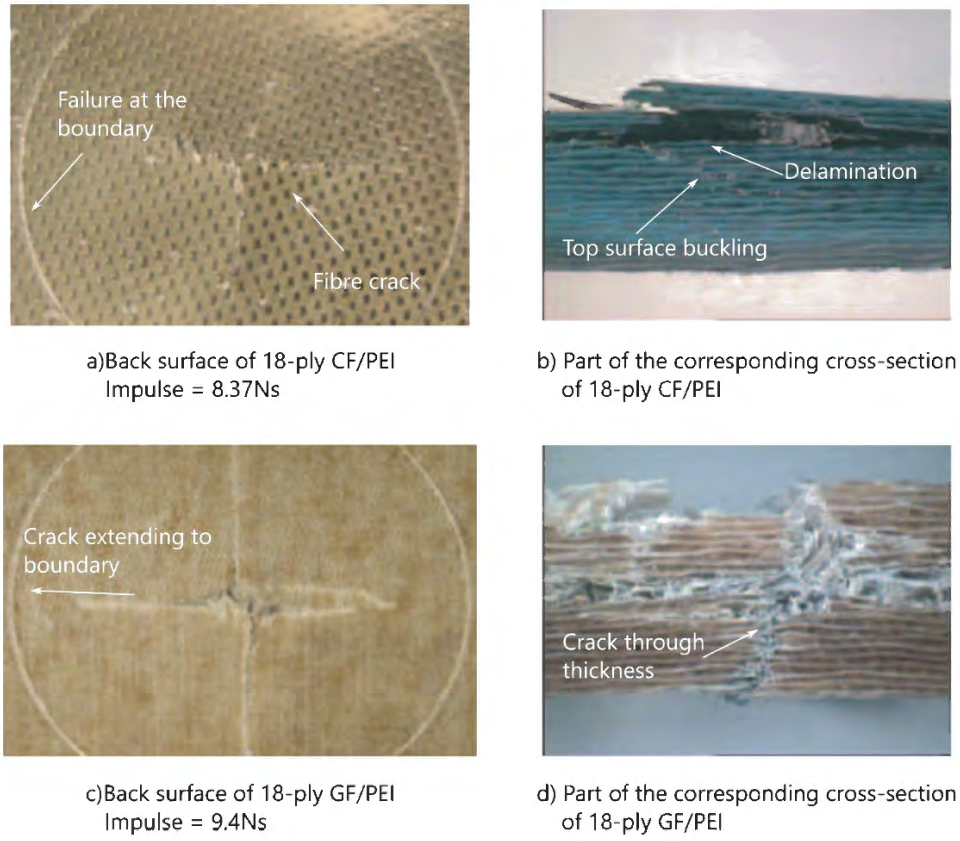

a)Back surface of 18-ply CF/PEI
Impulse = 8.37Ns

b) Part of the corresponding cross-section of 18-ply CF/PEI

c)Back surface of 18-ply GF/PEI
Impulse = 9.4Ns

d) Part of the corresponding cross-section of 18-ply GF/PEI

Figure 2-25: Some of the different failure modes found on fibre reinforced thermoplastic composites (adapted from [139]**)**

In terms of the influence of thickness, the graph shown in Figure 2-26 depicts the impulse required to initiate fibre damage and the impulse required for complete failure [139]. The arrows in Figure 2-26 indicate where complete failure was not observed during experimental testing. The distance between complete failure and initiating fibre damage increased as the thickness of the panel was increased for the carbon fibre reinforced composites. With increasing thickness, higher blast loads were required to destroy the panels. There was also significantly more indication of increased damage before the panel was destroyed. The results for glass fibre reinforced composite, around 4 mm thickness, had a higher impulse threshold than the carbon fibre reinforced composite with a similar thickness. Moreover, thinner panels had a lower ability to absorb energy [139].

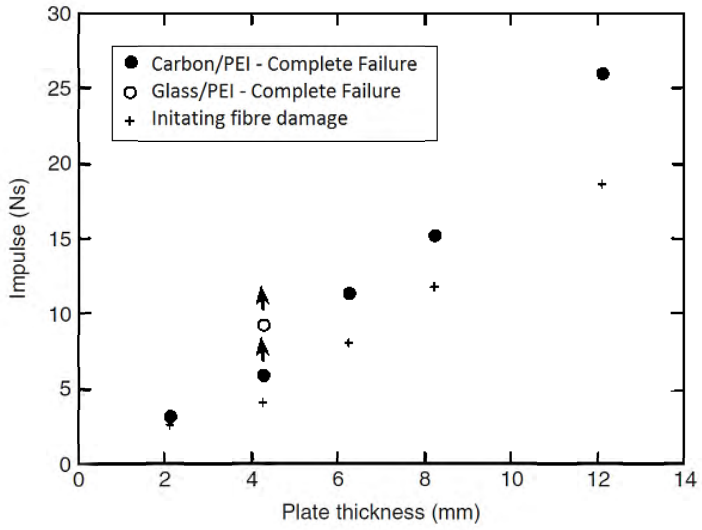

Figure 2-26: Complete failure limit illustrated on impulse versus plate thickness graph [139]

The influence of resin on carbon reinforced composites was also investigated. The polyester resin was substituted with an epoxy resin. The results did not show any significant influence of the different resin on the blast resistant properties of the composites [139], [140]. However, fibre (both glass and carbon) polymers with vinyl ester matrices exhibited lower amounts of delamination than their polyester counterparts [141]. Gargano et al [141] found that when the bond strength between the fibre and the matrix was greatly affected by the choice of polymer matrix, this would in turn influence the damage tolerance to blast loading. Fibre-matrix interfacial cracks and cracks within the polymer-rich regions and fibre tows-initiated damage in the panels. That said, the superior fibre material for blast applications was glass as the resistance to permanent deformation and damage was higher for the GFRPs than the CFRPs [141].

In summary, damage caused by explosive loading on fibre reinforced composites, particularly those reinforced with glass or carbon fibre, would be delamination, fibre fracture, matrix cracking, and penetration or shearing at the boundary. The initiation, progression, and extent of these failure types were influenced by explosive charge mass, standoff distance, fibre type, specimen dimensions and clamping arrangement (among others). Similar conclusions were found by Mouritz [133] when reviewing the blast behaviour of fibre-based composites. The sequence of damage for the fibre reinforced composite laminates were found to start as dynamic elastic deformation and end by complete rupture as indicated by the progress chart shown in Figure 2-27. Mouritz [133] also acknowledged that further research was needed to fully understand the effect of blast loading on fibre reinforced composites as there were a range of different fibre types and arrangements.

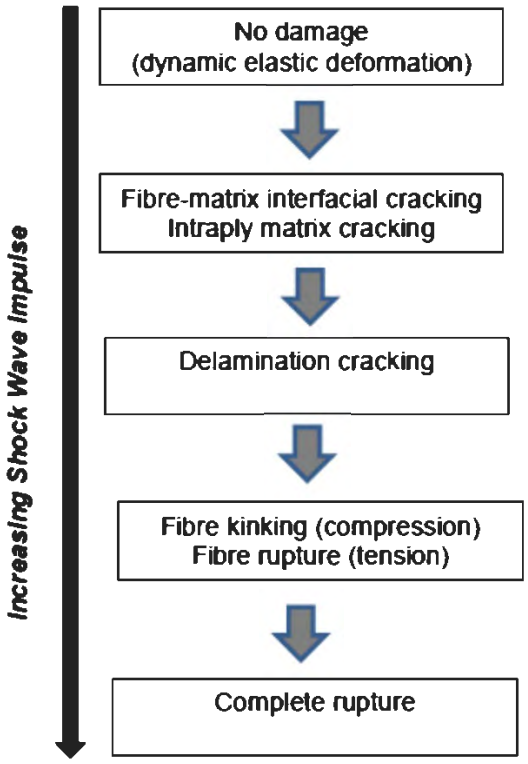

Figure 2-27: Development of damage in fibre reinforced composites due to explosive loading [133]

2.6.4 Blast loading of composites containing sustainable materials

Limited research had been conducted to investigate the blast related properties of natural fibre composites and other green composites. Experimental studies have been performed on wood [142]–[145] and flax-based composites [146].

Several studies on wood appeared to be focused on how construction timber structures behaved under blast load [142]. Wall sheathing, load bearing elements, boundary connections and debris mitigation were studied to understand the dynamic behaviour of the construction system. It was found that thicker wood sections would be capable of resisting a blast load with acceptable damage levels [142]. Photographs of the light-frame wood stud walls subjected to simulated shock waves similar to those found in far-field explosions is shown in Figure 2-28 [142].It shows the sequence of failure for the different construction detailing where with increasing load, blowout occurred.

Figure 2-28: Damage observed in light-frame wood stud walls subjected to different simulated blast loads[142]

Buchar et al [143] investigated localised blast loading of five different woods (namely Oak, Beech, Pine, Spruce and Birch). The behaviour was different between the wood types. Furthermore, describing the materials' response were complex due to its anisotropic nature and characteristics. As found by Bol'shakov et al [145], the strength—deformation properties were dependent on wood type, orientation angle, and environmental factors such as temperature and humidity. It was for these reasons that predicting their behaviour with numerical analysis would be difficult [143], [144].

Huang et al [146] conducted simulated blast loading tests, using a shock tube facility, on flax/epoxy and flax/polypropylene composites in unidirectional and cross-ply orientations. The damage visually observed for the specimens were cracks at the fibre/matrix interface (shown in Figure 2-29), permanent deformation and, in the case of flax/polypropylene composites, delamination. At a pressure of 0.592 MPa, flax/epoxy specimens fractured as shown in Figure 2-29d, in a brittle manner as observed for carbon fibre reinforced composites [139]. Cross-ply composites were found to have superior impact and shock load resistance properties compared to the unidirectional composites. Additionally, the resin type mattered - the polypropylene-based composites had better impact resistance then the epoxy-based panels, since polypropylene behaved in a less brittle manner [146].

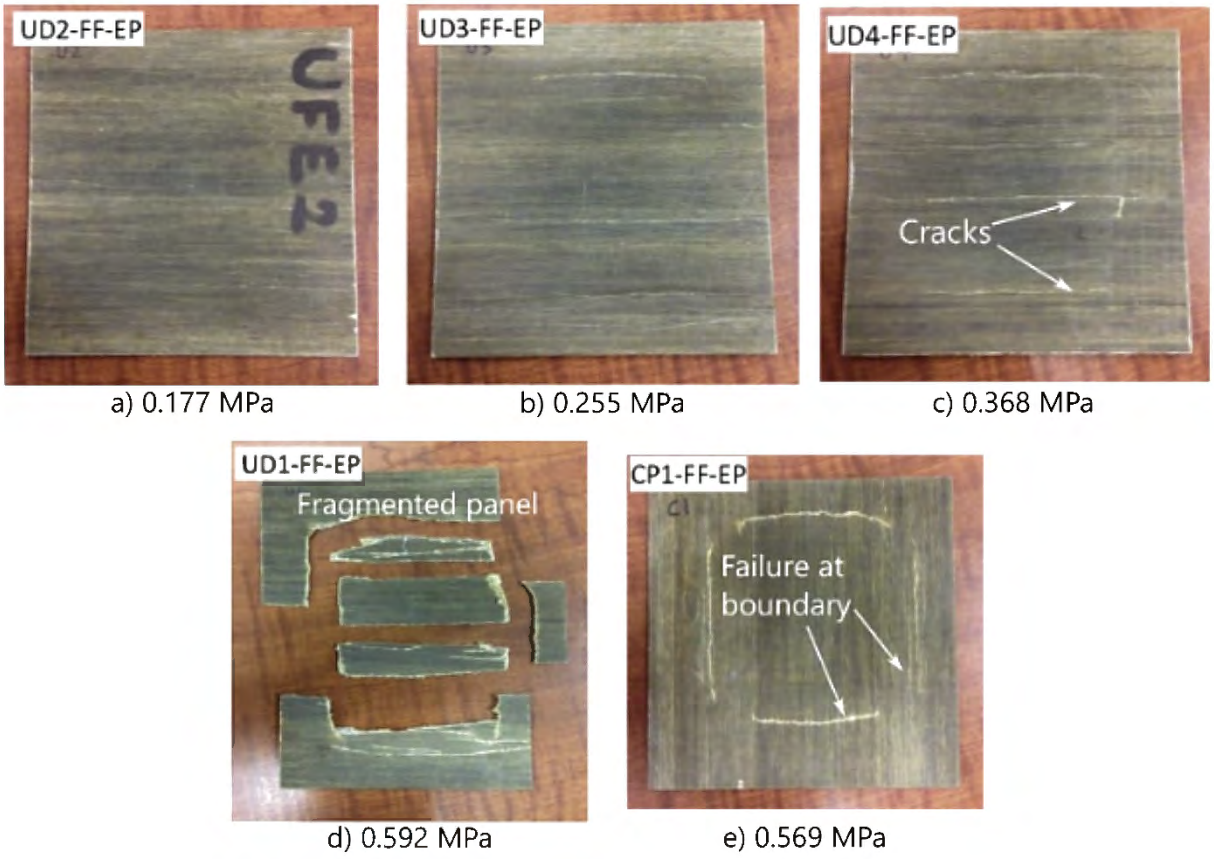

Figure 2-29: Damage on (a - d) unidirectional and (e) cross-ply orientations flax fibre reinforced epoxy specimens (adapted from [146]**)**

2.7 Impact behaviour of NFCs

Due to the nature of natural fibres, studies on synthetic fibre-based composites may not be applicable to understanding the blast behaviour of a natural fibre-based composite. However, numerous studies (not including explosive loading) have been conducted to characterise the impact behaviour of various natural fibre composites. Evaluating data from these studies could provide a means for estimating types of damage from blast loading and, at the very least, show how natural fibre composites respond to a dynamic load.

Figure 2-30 shows a schematic of the expected impact damage observed in fibre reinforced composite laminates irrespective of the constitute materials used [147]. Delamination and matrix -cracking tends to occur in the different plies because of bulk shear and bending. Moreover, the impact tool used can also affect the types and severity of damage observed. Surface buckling tends to occur around the indentation from the impact tool. It is also likely that a concentration of micro-cracks and fibre failure will occur around the indentation while the damage usually tends to disperse away from the indentation [147].

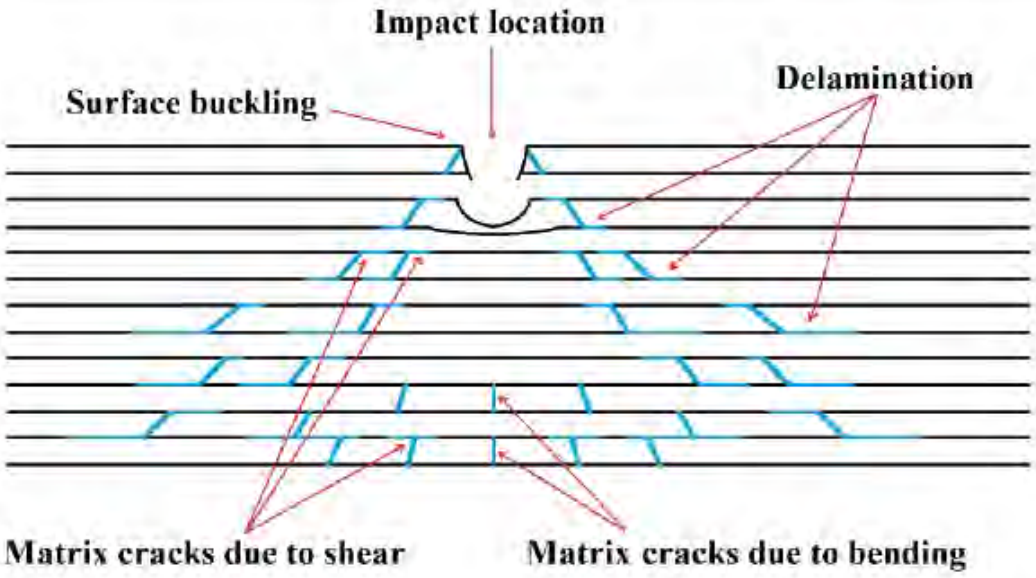

Figure 2-30: Typical impact damage modes in fibre-reinforced composite laminates [147]

The damage that initiates on a natural fibre composite is dependent on the impact energy (or velocity) [148] and characteristics of the composite (which was discussed in section 2.4). As expected, damage on natural fibre composites is more extensive than that of synthetic composites and results in more catastrophic failures such as through thickness cracking and rupture. For low-energy impact loads, the observed damage modes are matrix cracking, fibre-matrix debonding and delamination; at higher impact loads, fibre facture and fibre pull-out also starts to occur.

The severity of the damage is influenced by the interfacial adhesion between the fibres and matrix [148]. Poor interfacial adhesion would result in large amounts of delamination and splitting. Scarponi [148] found that the observed typical sequence of impact damage on a natural wood fibre composite from low velocity impact test was:

1. Cracks between plies (intraply matrix cracks) appear after impact.
2. Delamination occurs due to the intraply matrix cracks which spreads through the fibre-matrix interface.
3. Formation of new micro-cracks start to occur due to the propagation of delamination
4. Delamination initiated along the lower interface of the ply as shear cracks propagate in the material.
5. Lastly, delamination initiates along the upper interface of the ply as bending cracks propagate in the material.

Few studies have been reported on the potential of using natural fibre composites in resistant ballistic applications [149], [150]. Preliminary investigations on bulletproof panels made from ramie fibre

reinforced composites and steel plates were conducted by Marsyahyo et al [149] with the aim to reduce the weight of bulletproof vests. Debonding occurred between the steel plates and composite panels due to weak bonding strength and stretching. It was concluded that while natural composites decreased the overall weight, further investigations were required to meet the high standard of military equipment [149]. Wambua et al [150] performed ballistic tests on different natural fibre composites such as flax, hemp and jute fibre reinforced composites and natural fibre/steel composite hybrids. The failure modes observed were fibre fracture, delamination and shear as shown in Figure 2-31. The velocity of the projectile to penetrate the material was found to increase non-linearly with increasing areal density and composite thickness. Moreover, jute fibre-based specimens had inferior impact resistant properties compared to the other natural fibres tested [150].

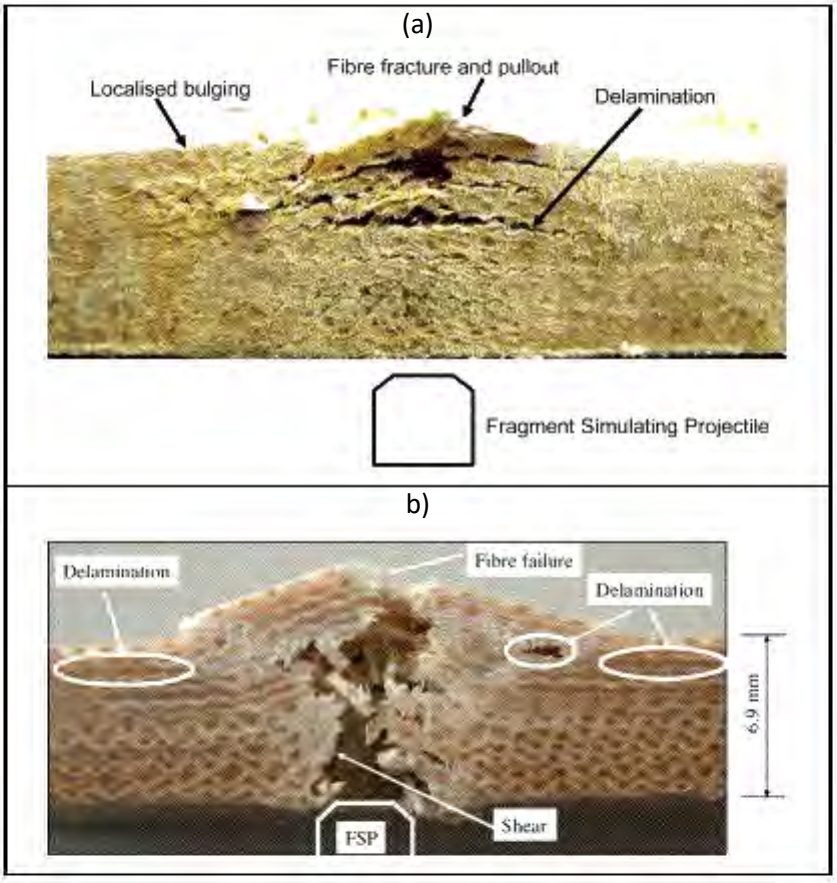

Figure 2-31: Photograph showing a a) jute and b) hemp fibre reinforced composite specimen under ballistic loading [150]

Koene and Broekhuis[151] investigated the bullet penetration into flat MDF targets. In the hardness measurement tests, it was found that the hardness of the MDF decreased with depth. However, the there was no apparent correlation between the change of hardness (hence, density) within a target and projectile penetration depth. While this suggests that the hardness variation over the thickness does not influence the impact properties, further research is necessary [150].

In general, studies on the impact properties of natural fibres typically focussed on the surface and subsurface damage, penetration, and fragmentation. One of the biggest concerns noted with natural fibre reinforced composites was poor interfacial adhesion between the fibre and matrix. It was commented that the interfacial adhesion was often found to improve with additional fibre treatments [152]–[156]. An overview of the factors and process parameters found to affect impact properties of natural fibre composites are shown in Figure 2-32 [156]. These parameters influencing the impact properties (such as work of fracture, penetration, damage characterisation and residual properties) have been discussed in section 2.4.

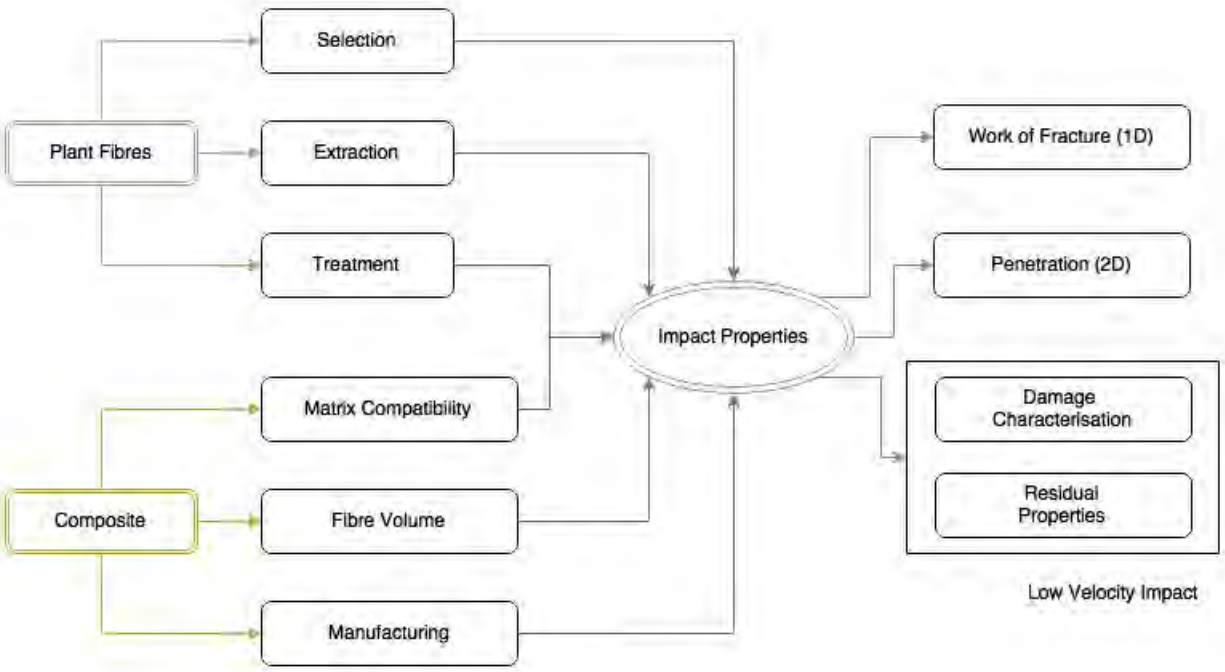

Figure 2-32: Factors affecting impact properties of plant fibre reinforced composites (adapted from [156]**)**

While there is more data on the impact loading of natural composites compared to blast loading, the impact and high stain rate behaviours of natural fibre composites are not fully understood. This is mostly due to fibre variability and other parameters that affect their mechanical performances. Further research is needed to understand how natural fibre composites respond to impact and shock loading.

2.8 Summary of chapter

While there have been major advancements in understanding the mechanical properties of different fibre reinforced composites, very little is known about alternative environmentally friendly options like bio-resin and the high strain deformation response of natural fibre composites. The following conclusions can be drawn from the literature review:

- Composite materials contain two types of constituents, matrix, and reinforcement. Either one can be obtained from plant resources which can yield a sustainable product.
- Natural fibres tend to have inferior strength properties compared to synthetic fibres like glass and carbon fibre. However, they are more environmentally friendly.
- The properties of natural fibres are heavily dependent on environmental factors and structural attributes of the plant and therefore fibres can be inconsistent between batches and have a wider range of property values.
- Different methods of manufacturing can be used to make composites, however VI can produce more favourable properties for natural fibre composite laminates in comparison to conventional hand lay-up.
- The typical failure modes observed in blast loading of composites are, matrix cracking, fibre failure and delamination. The failure progresses to penetration, shearing at the boundary or fragmentation. These are influenced by fibre type, resin, explosive charge mass, standoff distance, specimen dimensions and clamping arrangement. The choice of resin may have a greater influence for natural fibre composites than their synthetic counterpart.
- In general, damage on natural fibre composites is more critical than that of other composites, as the fibres are highly irregular.

In general, it is unlikely that current natural plant-based fibres will replace glass and carbon fibres for reinforced composite structures requiring superior mechanical properties. However, there is a growing interest in the possibility of using natural fibres for a wide range of applications [157], some of which have been briefly discussed such as the automotive and construction industry, and in resistant ballistic applications. Moreover, despite developments in more sustainable resins, their response to blast is virtually unreported. Further research is required to understand the influence of natural fibres and sustainable resins on the blast response of environmentally friendly composite alternatives.

3 Composite materials

Glass, flax, and jute woven fabrics were selected as textile reinforcements. Each of the reinforcements were, according to their manufacturers ready for FRP manufacturing processes and no additional treatments or processes were needed prior to manufacturing the fibre reinforced polymeric composites [158]–[160]. A medium density wood fibreboard, Supawood, was selected as a sustainable composite control material. Supawood and glass fibre, particularly infused with Prime 20LV, were considered as control materials for this project. Table 3-1 lists the manufacturers' claimed properties, where possible, for the different fibre reinforced composites (as the technical data sheets list the properties of composites rather than fibre for the natural fibres) [158]–[162]. Prime 20LV epoxy resin and an environmentally friendlier option named Super Sap Epoxy resin were used in conjunction with these textile fibres. The manufacturers' claimed properties for Prime 20LV [163] and Super Sap [164] are listed Table 3-2. This chapter further describes the characteristics of the materials used.

Table 3-1: Specifications and mechanical properties of materials chosen

	Glass fibre[158]	Flax fibre [159]	Jute fibre [160]	Supawood [162]
Areal density	400 g/m^2	550 g/m^2	400 g/m^2	780 kg/m^3 [a]
Weave type	Plain weave	2x2 Twill	2x2 Twill	Random
Fibre treatment	Silane	Pre-treated fibres[b]	No additional treatment [c]	N/A
Tensile strength	44 kN/m [d] [161]	330 MPa [e]	59 MPa [f]	0.5 MPa [g]
Young's Modulus	-	35 GPa [e]	8.1 GPa [f]	-
Flexural Strength	-	300 MPa [e]	87 MPa [f]	30 MPa

a – Volumetric density is given for Supawood boards

b – Using LINEO patented sizing technology

c – Not specifically given an additional sizing treatment but was "ready for processing" in the same way as glass fibre according to manufacture

d – Warp tensile strength of the fabric

e – Data from pressed laminates comprising of unidirectional flax fibres of 180g/m^2 and epoxy resin

f – Data from VI laminates using unsaturated polyester resin

g – Internal bond strength

Table 3-2: Cured system mechanical properties for Prime 20LV and Super Sap resin

	Prime 20LV Epoxy with slow hardener	Super Sap CLR with CLS hardener
Mix Ratio by Weight (Resin: Hardener)	100:26	100:47
Cured Mixed Density	1144 kg/m^3	1080 kg/m^3
Tensile Strength	73 MPa	67.6 MPa
Young's Modulus	3.5 GPa	3.2 GPa
Strain to Failure	3.5 %	4.6 %
Flexural Strength	82 MPa	100.5 MPa

3.1 Reinforcements of panels

3.1.1 Glass fibre

Glass fibres are commonly used in FRP composites for applications in automobile, aerospace and marine industries [165], [166]. A brief list of advantages and disadvantages of glass fibres is given in Table 3-3 [23]. Plain weave 400 g/m^2 E-glass fabric, shown in Figure 3-1, was purchased from Aerontec South Africa. This glass fibre is deemed suitable for all polymer composite applications and compatible with epoxy resin [158].

Table 3-3: Summary of advantages and disadvantages of using glass fibre as reinforcement

Advantages	Disadvantages
• Low-cost synthetic fibre • High tensile strength • High chemical resistance • Excellent insulating properties	• High density • High abrasion sensitivity • Low fatigue resistance

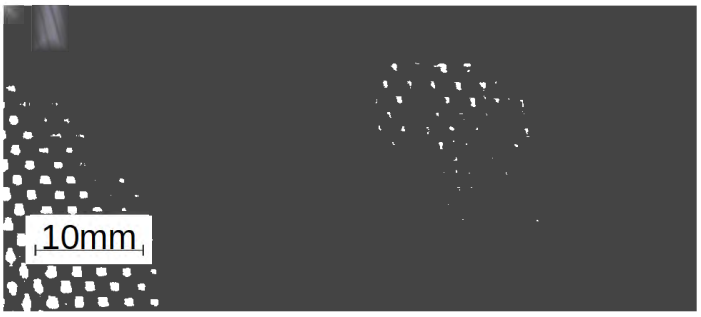

Figure 3-1: Photograph of plain weave 400 g/m^2 glass fibre fabric

As described in the literature survey, several studies have been conducted on GFRP to determine the blast resistance properties ([127], [131], [133], [136], [167]). Moreover, the same material sourced from the same supplier, was used by Langdon et al [168] and Ghoor [169] amongst others in other blast related work at UCT. It was for these reasons that this material was chosen as a suitable control material.

3.1.2 Flax fibre

Flax fibres are mainly used in the textile industry but are gaining popularity as reinforcements in FRP composites [170]. According to Moudood et al [171], flax fibre reinforced composites have the potential for wide range of usage in sport, maritime and automotive applications. Additionally, this reinforcement is currently in the development stages for future applications in the aeronautical industry [171]. It seems that flax fibres are promising reinforcement for biocomposites and can be used in a range of applications as an eco-friendly and biodegradable raw reinforcement material [172], [173].

A balanced twill weave 550 g/m^2 flax fabric, produced by Lineo Belgium Limited, was used in this project as a possible sustainable reinforcement material alternative to glass fibres. According to Lineo [159], the main advantages to using their flax fabric are that it is easy and ready to use with conventional manufacturing processes. It also has good vibration absorption, low density that can enable weight reduction and can be combined with other fabrics (like glass etc). It is also deemed eco-friendly and carbon neutral as it was made with natural and renewable resources [174]. The weave pattern and size of the tows are shown in Figure 3-2. It was found that the fabric had a waxy feel to the touch which was likely due to its sizing process.

Figure 3-2: Photograph of twill 550 g/m^2 flax fabric

3.1.3 Jute fibre

Similar to flax fibre, jute fibre is also considered as an environmentally friendly and biodegradable raw material. Currently, the biggest consumer for jute fibres is the bag cloth industry as they provide a greater eco-friendly advantage over both nonbiodegradable poly bags and paper bags [175]. According to Aly-Hassan [175], the potential applications for jute fibre reinforced composites include barrier walls against the thermal and acoustic energies for interior construction, lightweight panels for furniture construction, and housings for electronic equipment.

Biotex Jute 400 g/m^2 2x2 Twill fabric, pictured in Figure 3-3, produced by UK-based manufacturer Composites Evolution, was also used a possible sustainable reinforcement material alternative to glass fibres. Unfortunately, this product was discontinued during this project, therefore only limited quantities were available. In comparison to the two other (glass and flax fibre) reinforcements, there appeared to be a lot of open spaces in the jute fibre fabric as shown in Figure 3-3. In addition, the jute fabric was thinner than the flax fabric.

Figure 3-3: Photograph of twill 400 g/m^2 jute fabric

3.2 Supawood

Supawood is a medium density fibreboard (MDF) locally manufactured in South Africa by PG Bison (Pty) Ltd. It is inexpensive and easily available in hardware stores as it is often used for home furnishing applications. Currently, boards are available in various set thicknesses between 3 – 30 mm [176]. The main composition of Supawood is 82 – 84 % wood fibres and 8 – 10 % UF resin [177]. Supawood is made from wood chips ground into fibre and blended with resin before being bonded together through heat and pressure to yield a nominally homogenous density profile [52]. A cross section of a 16 mm Supawood piece is shown in Figure 3-4.

Figure 3-4: Photograph of the cross section of a 16 mm thick Supawood board

As stated in the Material Safety Data Sheet (MSDS)[177], no quantitative data on the ecological impact of Supawood was available. However, the manufacturers stated that it was unlikely that the Supawood had a negative effect on the environment when used appropriately [177]. The material can also be recycled or sent for energy recovery at the end of the life cycle of the product [177]. The properties of a Supawood board are homogenous and more consistent compared to wood panels. In addition, advantages claimed for the material include high impact strength, price stability, availability, locally produced and consistent board density profile [176]. All of which make Supawood an attractive option as a sustainable second control material.

3.3 Polymeric matrices

3.3.1 Prime 20LV epoxy system

Prime 20LV is a fossil fuel-based epoxy infusion system manufactured by Gurit. With very low viscosity properties and long working times, this product is ideal for large panel infusions and hand lay-up [163]. It also has low exothermic characteristics [163]. This means that the manufacturing of thick sections is possible without large amounts of heat being generated while curing, a significant concern for the natural fibres. The resin has been used with a range of fibres, including natural fibres, under various loading conditions, many of which are discussed in the literature chapter. Furthermore, some previous blast work [168], [169] was conducted on glass fibres infused with Prime 20LV. Therefore, it was chosen as a suitable control matrix material.

3.3.2 Super Sap CLR Epoxy

Super Sap CLR, from Entropy Resins, is a clear epoxy infusion system used for laminating and epoxy coating. It is compatible with a range of fibres including glass fibre, carbon and natural fibres [164]. Super Sap CLR has low viscosity properties and long workable times, like Prime 20LV, which is suitable in manufacturing large panel by infusion or hand lay-up.

Twenty nine percent of the carbon content of Super Sap is from renewable plant-based (bio-based) sources, whereas conventional epoxies are typically formulated using petroleum [79]. The resin is

described by Entropy Resins Inc. [79], to have a lower carbon footprint compared to other conventional epoxies. Products made with Super Sap tend to have a perceived reduced environmental impact. Results of the LCA data provided by Entropy Resins are shown in Table 3-4 to compare their formulated bio-based liquid epoxy system to the same formulation using industry average petrochemical-based components [178]. The descriptions for the impact categories listed in Table 3-4 are shown in Table 3-5.

Table 3-4: Comparative analysis of the bio-based resin by Entropy Resins compared to the industry average petrochemical based resin formulation equivalent [178]

	Human health (DALY[a])	Ecosystems (Species *yr)	Resources ($/kg)	Cumulative Energy demand (MJ)	Climate Change (kg CO_2 eq.)	Water use (m^3)
Bio-based product	$1.09x10^{-5}$	$2.10x10^{-8}$	0.604	91	4.54	0.047
Industry average petrochemical-based product	$1.25x10^{-5}$	$2.42x10^{-8}$	0.681	103	5.28	0.056
Percentage difference	-13 %	-13 %	-11 %	-12 %	-14 %	-16 %
a – Disability adjusted life years						

Table 3-5: Descriptions of the relevant impact properties [178]

Impact category	Method	Description
Human health	ReCiPe 2016 Endpoint (H) v1.03	Human health impacts from climate change, human toxicity, photochemical oxidant formation, particulate matter formation, ionizing radiation and ozone depletion
Ecosystems	ReCiPe 2016 Endpoint (H) v1.03	Ecosystem impacts from climate change, terrestrial acidification, freshwater eutrophication, ecotoxicity, agricultural land occupation, urban land occupation and natural land transformation
Resources	ReCiPe 2016 Endpoint (H) v1.03	Resource impacts from fossil depletion and metal depletion
Cumulative Energy demand	CED v1.11	Non-renewable and renewable energy sources required
Climate Change	IPCC 2013 GWP 100a v1.03	Combination of the effect of the periods of time that the various greenhouse gases remain in the atmosphere and their relative effectiveness in absorbing outgoing infrared radiation
Water use	ReCiPe 2016 Midpoint (H) v1.03	Amount of fresh water consumed

3.4 Summary of chapter

The different materials used for the project (glass, flax and jute fibre as reinforcements, and Prime 20LV and Super Sap epoxy resins, and Supawood) are introduced with their reported property values

found in Table 3-1 and Table 3-2. Three materials were chosen as control materials namely glass fibre, Prime 20LV and Supawood. The manufacturers' claimed properties (particularly tensile strength and Young's modulus) for the epoxy resins seemed similar. Unfortunately, the reported mechanical properties of the reinforcements could not be compared, based on the product information, as conditions were different. However, based on the literature review and the reported strength of the glass fibre, composites made with glass fibre would have higher strength properties compared to the natural fibre composites. With the exception of the Supawood, which was bought in boards, the constituent materials were used to manufacture flat panel composites further described in chapter 5.

4 Numerical blast modelling for experimental design

Limited quantities of flax and jute fibre were available for this project. Consequently, basic numerical simulations were used to help define design parameters with a view to reducing the number of blast experiments. This included determining the minimum thickness of the flax and jute fibre composite panels and the parameters of the experiments saving any associated costs relating to the experiments including the cost of materials and labour. LS-DYNA V971 R8.10, a commercial solver developed by the Livermore Software Technology Corp (LSTC), was used to simulate the experimental blast loading. LS-DYNA R810 has been extensively used to model composites subjected to a range of loads and has demonstrated usefulness for non-linear response as a result of blast loading [179]. In a literature survey conducted by Shekhar [180], the Multi-Material Arbitrary Lagrangian-Eulerian (MMALE) approach showed a good correlation with blast experimental results, and this approach was followed here. Experimental blast results for GLARE were used to validate the numerical results. The simulation input deck can be found in Appendix A.

4.1 Basic model description

Quarter symmetry models were used to simulate the blast loading experiments to reduce the computational cost associated with a full model. The expected experimental tests conducted were on square, flat panels of size 300 x 300 mm with an exposed area of 200 x 200 mm. Although improved accuracy comes from modelling the full clamp boundary conditions, only the exposed area of the panel was modelled in this work for simplification and to further reduce the computational cost. This was considered adequate for the design of the blast experiments. Only two stand-off distances for the explosives were considered; a stand-off distance (SOD) of 20 mm to simulate a localised blast load, and a SOD of 200 mm to simulate a uniform blast load. These models are referred to as the localised and uniform blast loading from herein. The positions of the panel and explosive in an air mesh are shown in Figure 4-1 and Figure 4-2 for localised and uniform blast loading respectively. The air and explosive were modelled using a Eulerian mesh whereas the plates use a Lagrangian mesh.

At the edge of the panel, rotational constraints and translation constraints were imposed to simulate the edge being clamped as shown in Figure 4-2 and Figure 4-2. Unlike metal panels (where plastic deformation in the form of thinning and bending can be observed along the clamped area), a fully constrained boundary condition was chosen due to the brittle nature of composites as the composite panels were likely to shear at the boundary. While there may be some materials pull in for some of the thinner composite panels, the intent of the numerical simulation was to simplify the model for the design of the experiments as opposed to interrogating the results to gain more insights or investigating

the influence of different parameters (parametric study). Based on the constraints and parameters chosen, it was felt likely that the numerical results from the modelling would be conservative.

Symmetry boundary conditions were imposed on XZ and YZ planes for both the panel and air meshes. Depending on the type of loading, different boundary conditions were used on the air mesh to mimic the experimental environment for the panel. As shown in Figure 4-1 and Figure 4-2, non-reflective boundaries were placed on open sections where the explosive products would be free to exit. This included the top and bottom faces of the air mesh. In Figure 4-2, a reflective boundary was imposed on the outer surfaces of the air mesh, indicated in red, because a square tube would be used to direct the blast load onto the specimen for the uniform blast load (see Figure 7-1). On those faces, explosive products and pressures would be reflected. For the localised blast load, non-reflective boundary condition was imposed on the outer surfaces of the air mesh (Figure 4-1) as the charge would be placed in close proximity to the panel without the need of the square tube.

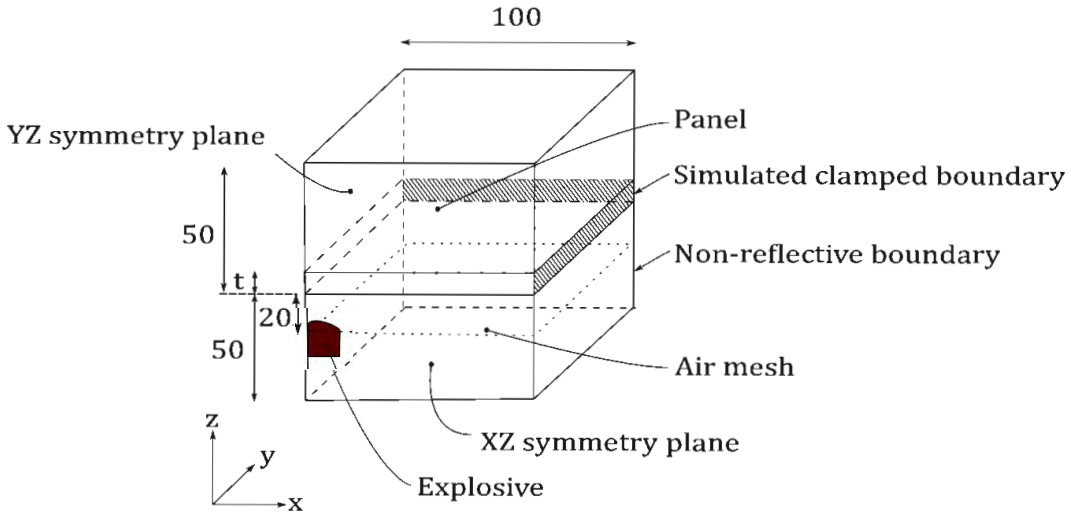

Figure 4-1: Schematic of basic numerical model used for a panel subjected to localised blast loading (dimensions in mm, not to scale)

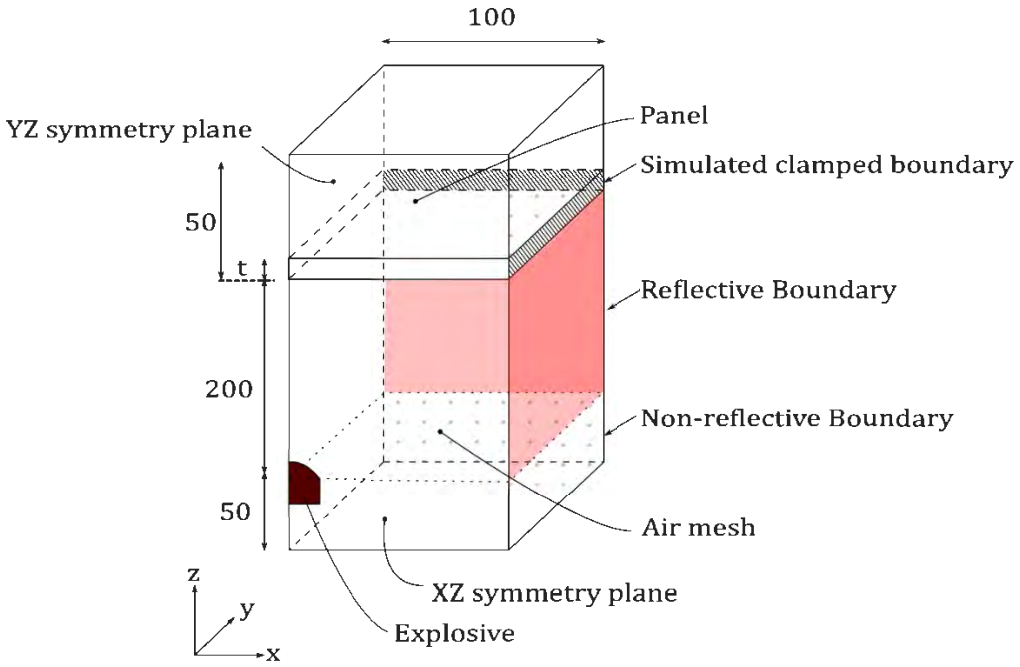

Figure 4-2: Schematic of the basic numerical model used for a panel subjected to uniform blast loading (dimensions in mm, not to scale)*

A displacement- time history result for each of the loading conditions on GLARE is shown Figure 4-3 to ensure that the run times of the simulation were sufficient. The deflections measured for the localised loading condition were higher compared to the results found for uniform blast loading condition. The deflection for the localised blast loading settled at around 0.28 microseconds for a 5g charge and at 0.35 microseconds for a 10g charge (Figure 4-3a). For the uniform blast loading model, the deflection appeared to have levelled off at 0.50 microseconds (Figure 4-3b). The termination time for the localised and uniform blast loading simulation were, therefore, set at 0.35 microseconds and 0.55 microseconds respectively.

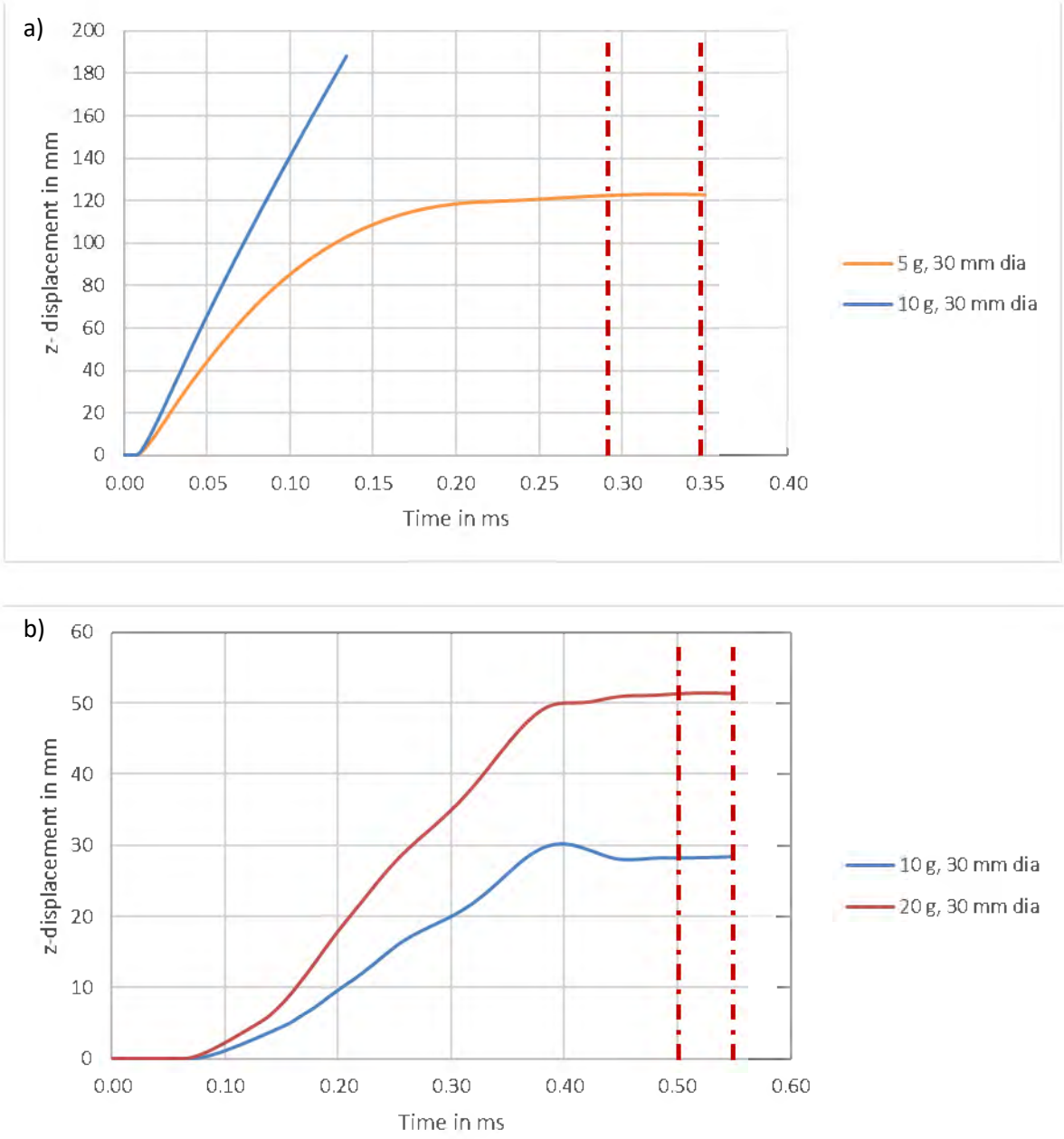

Figure 4-3: Displacement time history for a) localised and b) uniform blast loading

4.2 Air and explosive mesh description

The equation of states (EOS) and material models for the air and explosive were similar to those implemented by previous authors [180]–[182] where a similar experimental set-up was used. Therefore, the same values were adopted in the models presented.

4.2.1 Air mesh description

Two 100 mm x 100 mm air blocks of differing heights, 100 mm and 300 mm were used to simulate localised and uniform blast loading respectively using cubic elements of size 2 mm. Convergence and mesh sensitivity analysis for the ALE air mesh by Volschenk [181] found that the element size was

appropriate for a similar experimental set-up and charge masses. The criteria used to determine the most suitable ALE element size was stability of the simulations, run time and total experienced impulse values [181].

Air was modelled as an ideal gas with the characteristic equation given in Equation 4-1 and described in LS-DYNA using a linear polynomial EOS card, specified by Equation 4-2 [183], where C_4 and C_5 were set to $(\gamma - 1)$ with the other C constants set to zero. The μ value is known as a volumetric parameter based on the density of the air material. The property values for the air mesh are listed in Table 4-1 [119].

$$p = (\gamma - 1)\frac{\rho}{\rho_0}E \qquad 4\text{-}1$$

$$p = C_0 + C_1\mu + C_2\mu^2 + C_3\mu^3 + (C_4 + C_5\mu + C_6\mu^2)E \qquad 4\text{-}2$$

Table 4-1: Material and EOS properties for the modelled air mesh [119]

Initial density, ρ_0 $(\mathrm{kg/m^3})$	Specific heat ratio, γ	Initial internal energy per volume, $E_0(\mathrm{kJ/m^3})$
1.184	1.4	253.3

4.2.2 Explosive description

Cylindrical disks, to mimic the conditions of the experimental testing using INITIAL_VOLUME FRACTION, were implemented to discretise the volume of the explosive into elements and fill the Eulerian air mesh with explosive material. Similar explosive descriptions were used by Curry and Langdon [184] and Volschenk [181] where the volume of the explosive was based on the charge mass and density. The charge masses simulated for the different scenarios are listed in Table 4-2.

Table 4-2: Charge masses simulated for the different models

Charge mass (g)	Simulation	Ref.
6, 10, 15	Impulse validation	[185]
10	Initial model – Localised and Uniform	[181]

The charge masses for the impulse validation models were determined using existing experimental data [181], [185], from a similar uniform blast loading experimental set-up and panel size, where the explosive mass of the leader was included in the total charge mass detonated. A 10 g explosive charge mass for the initial models as a baseline.

The PE4 plastic explosive was modelled using the Jones-Wilkins-Lee (JWL) EOS as described in Equation 4-3 [183]. The property values of C4 explosives listed in Table 4-3 [186], were implemented as the PE4 as successfully used in previous studies [187]. C4 and PE4 explosives only differ in the plasticisers used.

$$p = A\left(1 - \frac{\omega}{R_1 V}\right)e^{-R_1 V} + B\left(1 - \frac{\omega}{R_2 V}\right)e^{-R_2 V} + \frac{\omega E}{V} \qquad 4\text{-}3$$

Table 4-3: Material and EOS properties for the explosive [186]

ρ_0 (kg/m^3)	D (m/s)	P_{CJ} (GPa)	A (GPa)	B (GPa)	R_1	R_2	ω	E_0 (GJ/m^3)
1601	8193	28	609.77	12.95	4.5	1.4	0.25	9

4.3 GLARE material description for numerical validation

The numerical models were validated by comparing the impulse and midpoint displacement from published experimental data on GLARE panels presented by Langdon et al [185]. The material behaviour was not the focus, rather, it was important to determine the differences between the experimental results and the impulse and midpoint deflections obtained on that material with smeared properties. The GLARE panels were 1.42 mm thick. Quarter symmetry exposed area (of 100 x 100 mm) was modelled using solid elements as the simplified numerical model used for this work. An element length of 1 mm through the length and width and, 0.71 mm through the thickness was used. The panel was modelled as a homogenous material using ISOTROPIC_MATERIAL_ELASTIC_PLASTIC (MAT 12) [183] description with estimated smeared material properties, listed in Table 4-4, reported by Langdon et al [185]. From the information given, the shear modulus and bulk modulus were calculated by using Equation 4-4 and Equation 4-5 for an isotropic material respectively.

$$G = \frac{E}{2(1+\nu)} \qquad 4\text{-}4$$

$$K = \frac{E}{3(1-2\nu)} \qquad 4\text{-}5$$

Table 4-4: Material properties for GLARE

Composite	Mass density (kg/m^3)	Shear modulus (GPa)	Yield stress (MPa)	Poisson's ratio	Bulk modulus (GPa)
GLARE	2500 [185]	23.32 [185]	306 [185]	0.25 [188]	38.87 [185]

4.4 Numerical validation results

The impulse and back-face permanent deformation for the experimental results presented by Langdon et al [185] were compared to the results from the numerical simulation. The percentage variation of the two parameters was calculated using Equation 4-6. The results from the numerical simulations are listed in Table 4-5. The impulse variation decreased as the charge mass increased. A maximum variation of 16 % suggested that the mechanics of the air mesh and explosive interaction were modelled with sufficient accuracy for use in experimental design. For the 10 g charge mass, there was a 13 % variation between the experimental and numerical value, which was considered low as it was possible that the range of experimental values for 10 g test would deviate by a similar amount. The numerical model overestimated the damage sustained by the panel, as expected, due to the simplified material model and clamping simplifications. Based on these results, the numerical model for the experimental design would give conservative results, which is considered acceptable for this application. A 15 % variation was deemed acceptable for the nature of the experiments as there was variation in both the explosive loading and the composite panels.

$$\%Variation\ (V) = \frac{|A_E - A_N|}{A_E} \qquad 4\text{-}6$$

Where A_E is the value found from experimental value and A_N is the numerical value.

Table 4-5: Comparison of the impulse and back-face displacement

Charge Mass	Impulse, I (Ns)		I % V	Back-face displacement, d (mm)		d % V
	Experimental	Numerical		Experimental	Numerical	
6	17.3	14.6	+ 16	17.0	15.6	- 8
10	**25.5**	**22.3**	**+ 13**	**24.1**	**28.4**	**+ 18**
15	31.9	31.8	+ 0.3	31.2	36.5	+ 17
+ refers to an over-estimation; - refers to an under-estimation						

4.5 Natural fibre composite panel model description

The flax and jute fibre reinforced composites were modelled as isotropic materials, similar to the description used for the GLARE panels with a failure criterion. The material card ISOTROPIC_ELASTIC_FAILURE (MAT 13), non-iterative model with a simple plastic strain failure [183], was used. It differed from ISOTROPIC MATERIAL_ELASTIC_PLASTIC by deleting elements that exceeded the plastic strain failure value [183]. The material properties for flax and jute are shown in Table 4-6. The bulk and shear modulus were calculated the same way as described for GLARE.

Table 4-6: Material properties for the natural fibre composite panels

Composite Fibre	Mass density (kg/m^3)	Shear modulus (GPa)	Yield stress[(a)] (MPa)	Plastic failure strain	Poisson's ratio [189]	Bulk modulus (GPa)
Flax [159]	1330	12.7	330	1.8 %	0.375	46.7
Jute [160]	1270	3.02	59	1.3 %	0.34	8.44
a - Reported tensile strength was used as the yield stress						

Two flat composite panels of 5 mm and 10 mm thick were modelled to determine which geometry would be best suited for the experiments. Thicker panels for the flax and jute fibre reinforced composites could not be considered due to the limitations of the material availability. The composite meshes were modelled as cubic with an element length of 1 mm. 6

4.6 Numerical results for natural fibre composites

4.6.1 Explosive development and panel response for localised blast loading

The transient response of the explosive material (shown in red) and the response of the 5 mm flax and jute FRP panel (shown in green) is shown in Figure 4-4. The results of the simulations showed that explosive products had perforated the composite panel within a time frame of 20 µs as indicated in Figure 4-4. A large amount of cracking and damage spread across the panel. By end of the simulation, the panels had fragmented and cracks extending towards the boundary were observed.

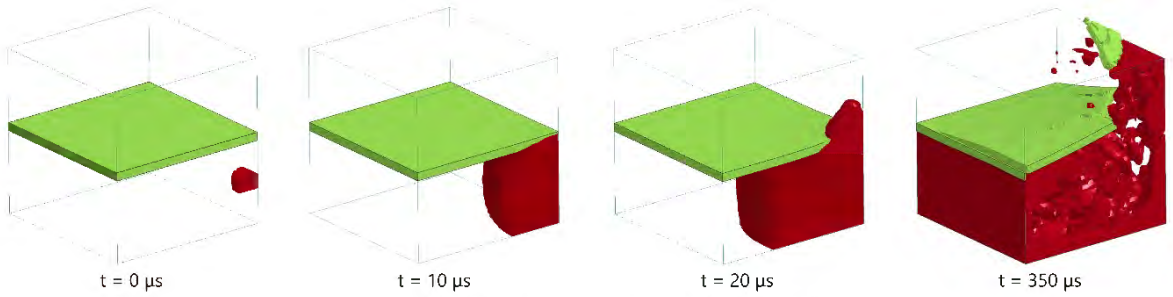

a) Transient response of the 5 mm flax FRP panel

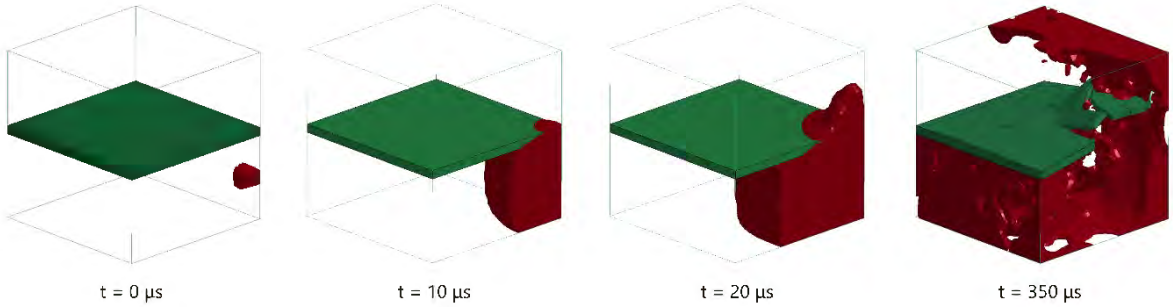

b) Transient response of the 5 mm jute FRP panel

Figure 4-4: Transient response for a blast loaded a 5 mm a) flax FRP and b) jute FRP composite with a localised 10 g charge mass

The transient response of the explosive material and the response of the 10 mm thick flax and jute FRP panel is shown in Figure 4-5 for localised blast loading. The results were similar to the 5 mm thick panels as explosive products had perforated the panel within a time frame of 20 µs. Significant damage was observed on the panels due to the impact of the explosive products. On the 10 mm flax FRP panel, a significant amount of element erosion causing the explosive products to obscure the deformation of the panel at 350 µs. In comparison, the cracking mostly occurred at the centre for the jute FRP panel.

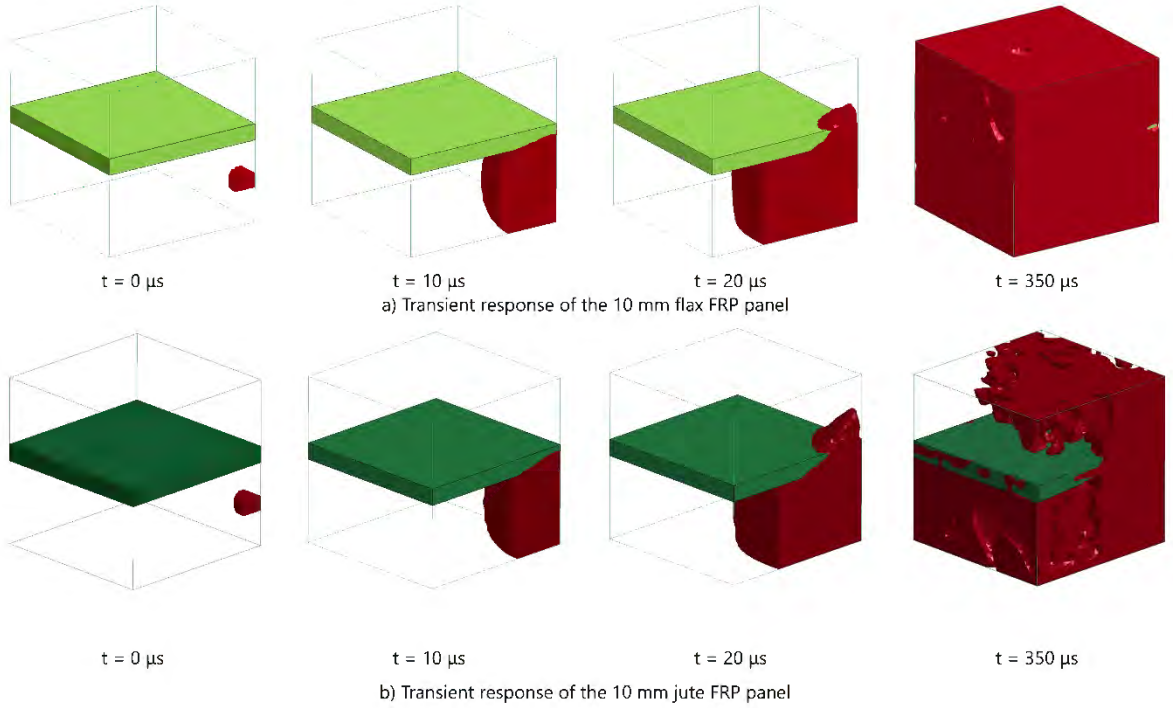

Figure 4-5: Transient response for a blast loaded a 10 mm a) flax FRP and b) jute FRP composite with a localised 10 g charge mass

At a lower charge mass of 5 g for the 10 mm flax FRP panel (as it was stronger than the jute) explosive products were observed to still travel through the composite indicating perforation, as observed in Figure 4-6.

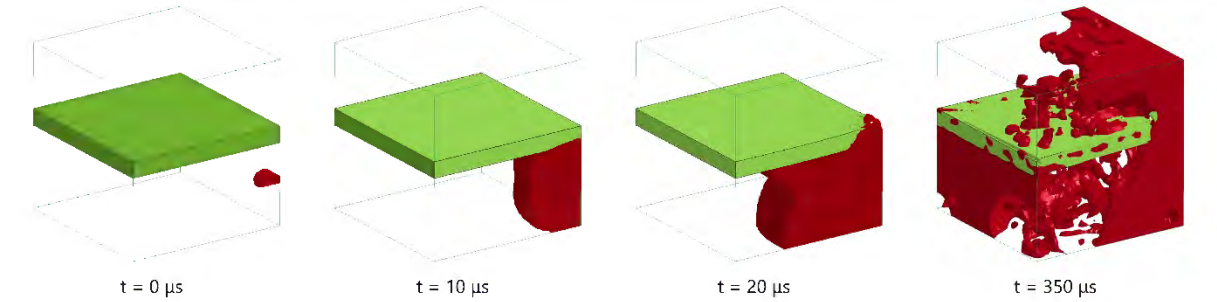

Figure 4-6: Transient response for a blast loaded a 10 mm flax FRP composite with a localised 5 g charge mass

Less damage was observed in the thicker panels as expected. Figure 4-7 shows the top view of the two jute FRP panels, without the explosive products, at t = 350 µs. Similar observations were made on the flax FRP panels. For both panels, at the centre of the panel (top right corner on the top view), a portion of the panel had lifted. The 5 mm exhibited large regions of cracking and fragmentation with a centrally capped region. Less damage was evident in the 10 mm thick panel. There were also lines with elements missing near the panel boundaries for both thicknesses, indicating potential failure along the clamped boundary highlighted in Figure 4-7.

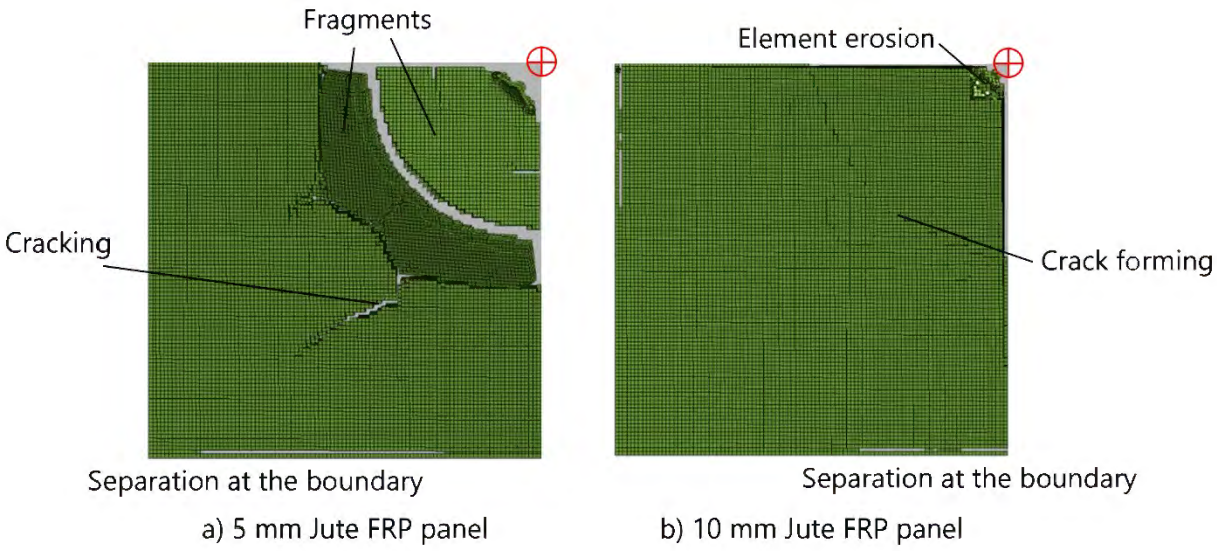

Figure 4-7: Top view of the jute fibre reinforced composites at t = 350 µs

4.6.2 Explosive development and panel response for uniform blast loading

The transient response both for the 5 mm and 10 mm thick flax and jute FRP panels subjected to uniform blast loading are shown in Figure 4-8 and Figure 4-9. For the 5 mm thick panels, significant damage occurred at the boundary. Strain obtained in the elements at the boundary exceeded the threshold, indicating failure and shearing at the boundary before t = 200 µs. The panels deflected more than 30 mm, five times the thickness of the panel.

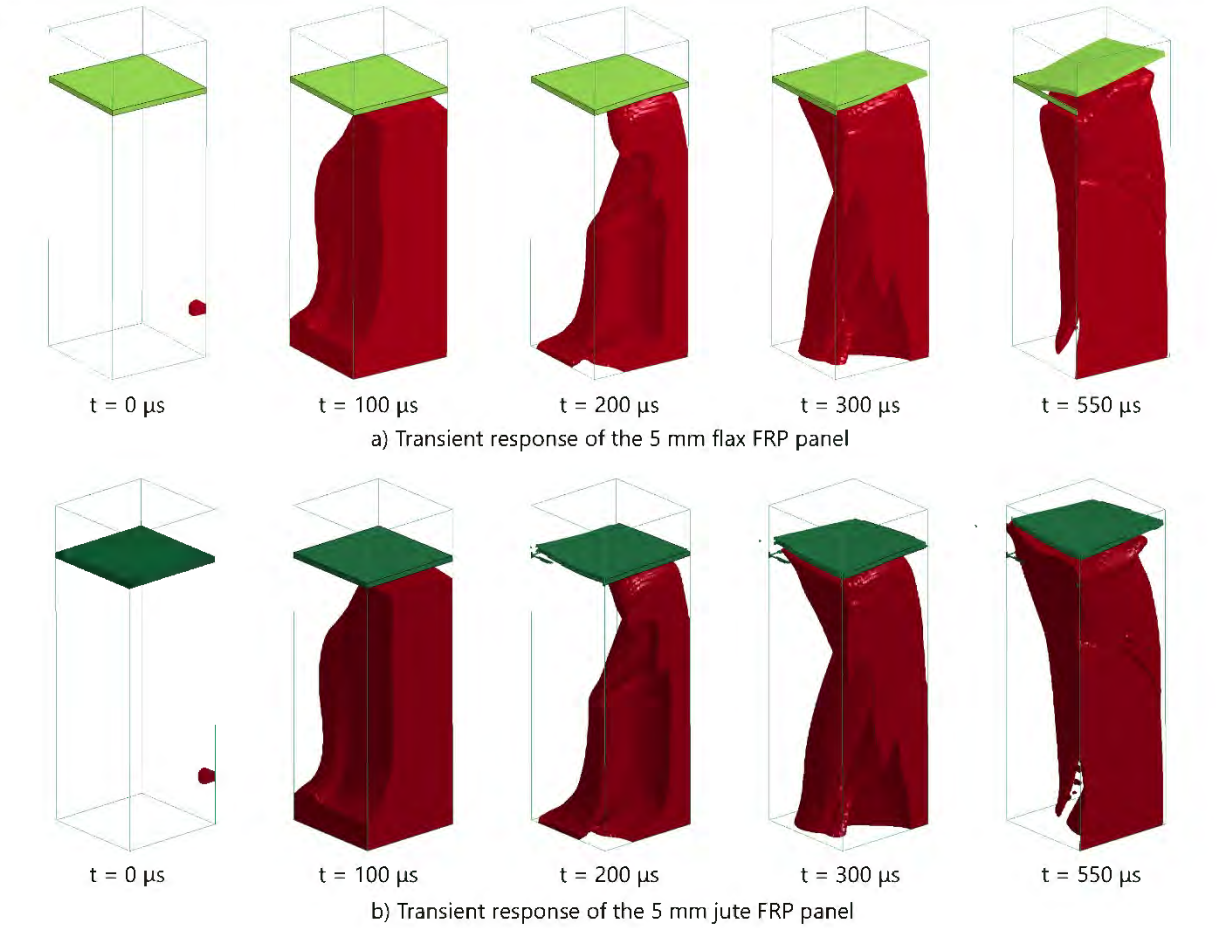

Figure 4-8: Transient response for a uniformly blast loaded 10 mm a) flax FRP and b) jute FRP composite with a 10 g charge mass

The 10 mm flax fibre reinforced composite panel did not separate from the boundary (Figure 4-9a). Damage and element erosion were observed on the flax panel; however, the simulated blast did not fragment the panel. The 10 mm jute fibre reinforced composite panel separated at the boundary at 300 µs (Figure 4-9b). At the end of the simulation, the jute fibre reinforced composite panel travelled less than 20 mm. The damage appeared to be less than that observed in the 5 mm panels.

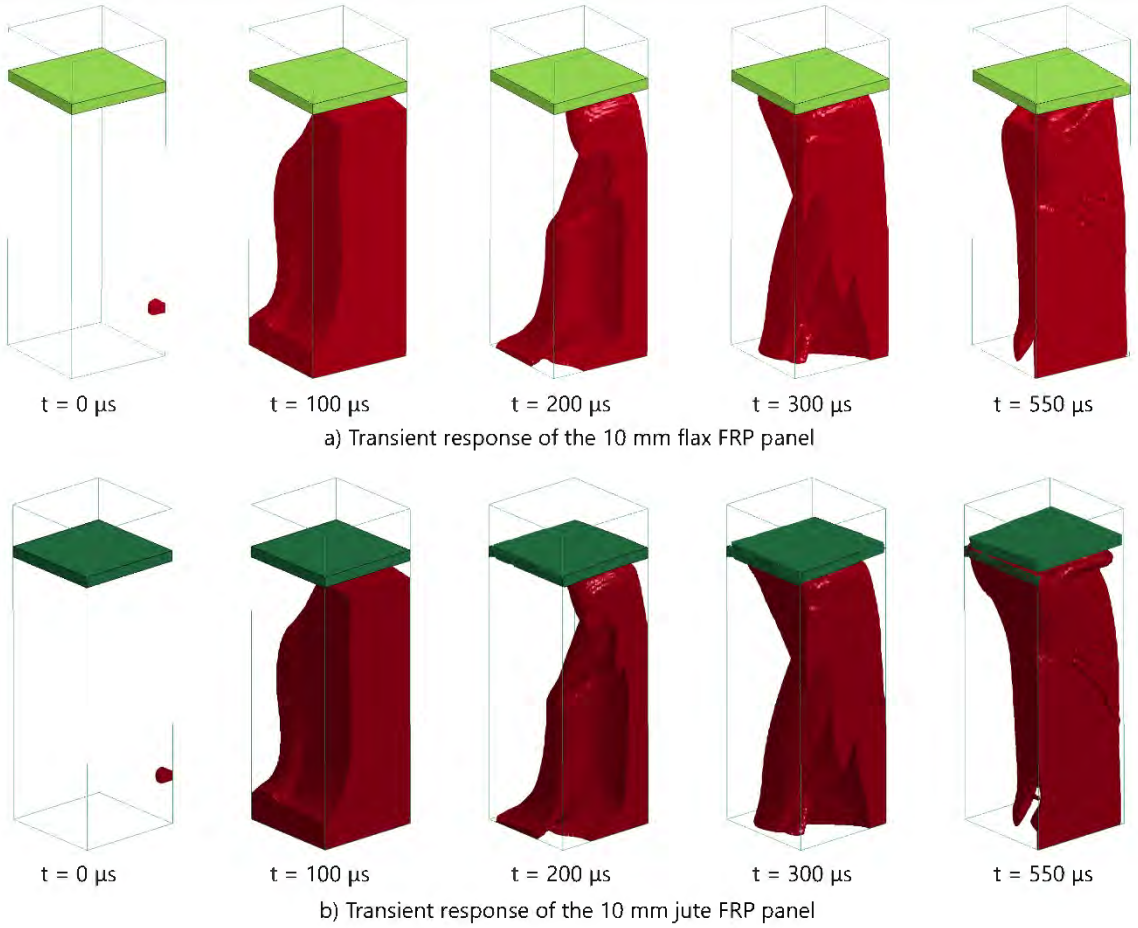

Figure 4-9: Transient response for a uniform blast loaded 10 mm 10 mm a) flax FRP and b) jute FRP composite with a 10 g charge mass

4.6.3 Overview of simulation results for NFCs

A total of eight simulations were performed. A summary of the results is given in Table 4-7. Each panel was subjected to a 10 g explosive charge detonation. The impulse was found by integrating the applied force with respect to time acting on the panel. The final midpoint deflection was obtained from the element located at the centre of the panel. The values for the midpoint deflection that are bracketed are for the panels that separated at the boundary.

Table 4-7: Simulation results for the natural fibre composites subjected to charge mass of 10 g

Fibre	Thickness (mm)	Loading	Impulse (Ns)	Midpoint deflection (mm)	Comments
Jute	5	Local	10.3	-	Broken off pieces, cracks, explosive perforated,
Jute	5	Uniform	22.8	(34.8)	Complete failure at boundary
Flax	5	Local	10.3	-	Broken off pieces, cracks, explosive perforated,
Flax	5	Uniform	25.5	(34.3)	Complete failure at boundary
Jute	10	Local	10.3	-	Cracking, explosive perforated
Jute	10	Uniform	22.8	(15.3)	Complete failure at boundary
Flax	10	Local	10.3	-	Cracking, explosive perforated
Flax	10	Uniform	25.9	3.7	Some elements eroded at boundary and centre

Denotating the charge at different SOD affected the impulse. Higher impulses were obtained at larger SOD. The 5 mm panels underwent significant amounts of damage with multiple element erosion due to large strains. In the central region of every locally loaded panel, the midpoint deflections were not recorded in Table 4-7 due to the multiple element erosions within 100 μs of the blast impacting the panel.

The 10 mm panels were able to withstand the load better than the 5 mm panels. With increased material thickness, the panels were able to absorb more damage. Despite complete boundary failure for the jute fibre reinforced composites, the centre displacement dropped by more than half when the thickness of the panel increased from 5 mm to 10 mm. Additionally, the 10 mm flax fibre reinforced composite panel did not completely fail and appeared to near a threshold of failure when tested under uniform blast loading conditions. Therefore, for the flax and jute fibre reinforced composites, it was decided that localised blast loading would not be performed. In addition, panels made from jute and flax would be manufactured to be 10 mm thick based on the numerical results.

4.7 Numerical simulations of the control composites

4.7.1 Control panel description

According to the reported densities of the jute and flax fibre reinforced composite, the mass of the panels would be between 1.1 – 1.2 kg. Using a similar mass approach, the thickness of GFRP and Supawood were determined to be 5 mm and 16 mm respectively.

The same material description and element size for the flax and jute fibre reinforced composites (described in section 4.5) were used to describe the material properties of the GFRP and Supawood.

The tensile properties, reported by Ghoor [169] for 400g/m^2 glass fabric and Prime 20LV epoxy resin sourced from the same supplier, were implemented into the numerical model. The tensile properties for Supawood were not available in the manufacturer's data sheet [190] and were taken from [191]. The material properties for both materials are listed in Table 4-8. The shear modulus and bulk modulus were calculated from Equation 4-4 and Equation 4-5, similar to the other panels described in this chapter.

Table 4-8: Material properties for the Supawood and GFRP

Composite	Mass density (kg/m^3)	Shear Modulus (GPa)	Yield Stress (MPa)	Plastic failure strain	Poisson's Ratio	Bulk Modulus (GPa)
GFRP [169]	1840	30.3	424	6.9 %	0.22	44.0
Supawood [191]	780	1.6	18	0.5 %	0.25	2.66

4.7.2 Explosive development and panel response

The development of the explosive material and the response for the 16 mm Supawood and 5 mm GFRP panels are shown in Figure 4-10 and Figure 4-11.

There was a large amount of damage in the Supawood as shown in Figure 4-11, as expected due to the lower reported yield stress of 18MPa, almost 70 % lower than the value reported for the next weakest composite - jute. Significant element deletions extending from the boundary and centre of the panel were observed. The plastic failure strain for the Supawood was also the lowest out of all materials evaluated.

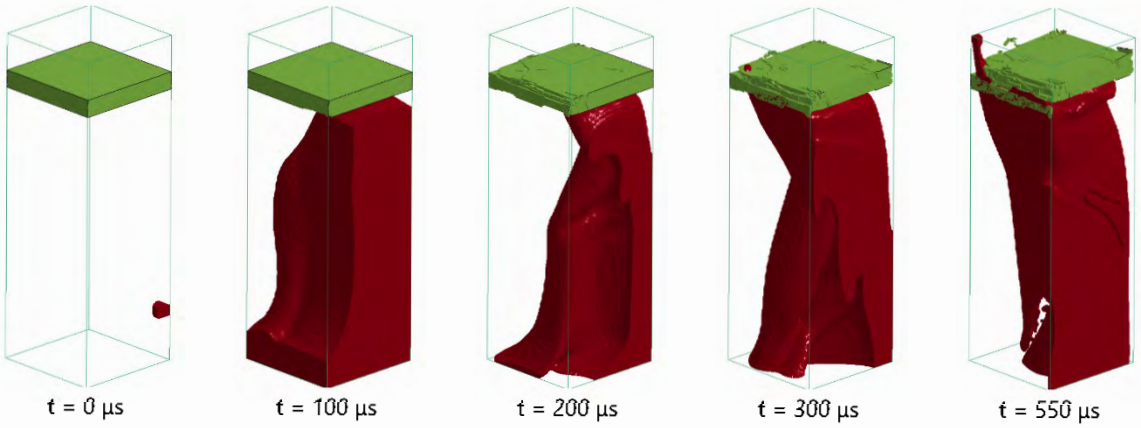

Figure 4-10: Transient response for a uniformly blast loaded 16 mm Supawood panel with a 10 g charge mass

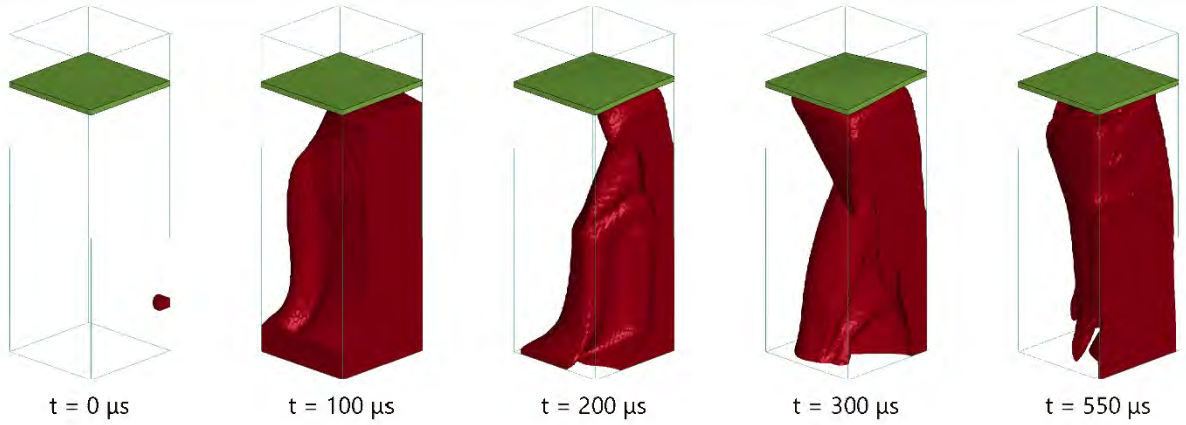

Figure 4-11: Transient response for a uniformly blast loaded 5 mm GFRP with a 10 g charge mass

Minor damage in the form of element deletion at the fixed boundary occurred in the 5 mm GFRP panel as shown in Figure 4-12. In comparison to the results found for the flax fibre reinforced composites, fragmentation and perforation of explosive products did not occur in the GFRP model. The crack formed (from the elements deleted) on the GFRP panel did not appear to extend past half the length and thickness of the panel as shown in Figure 4-12.

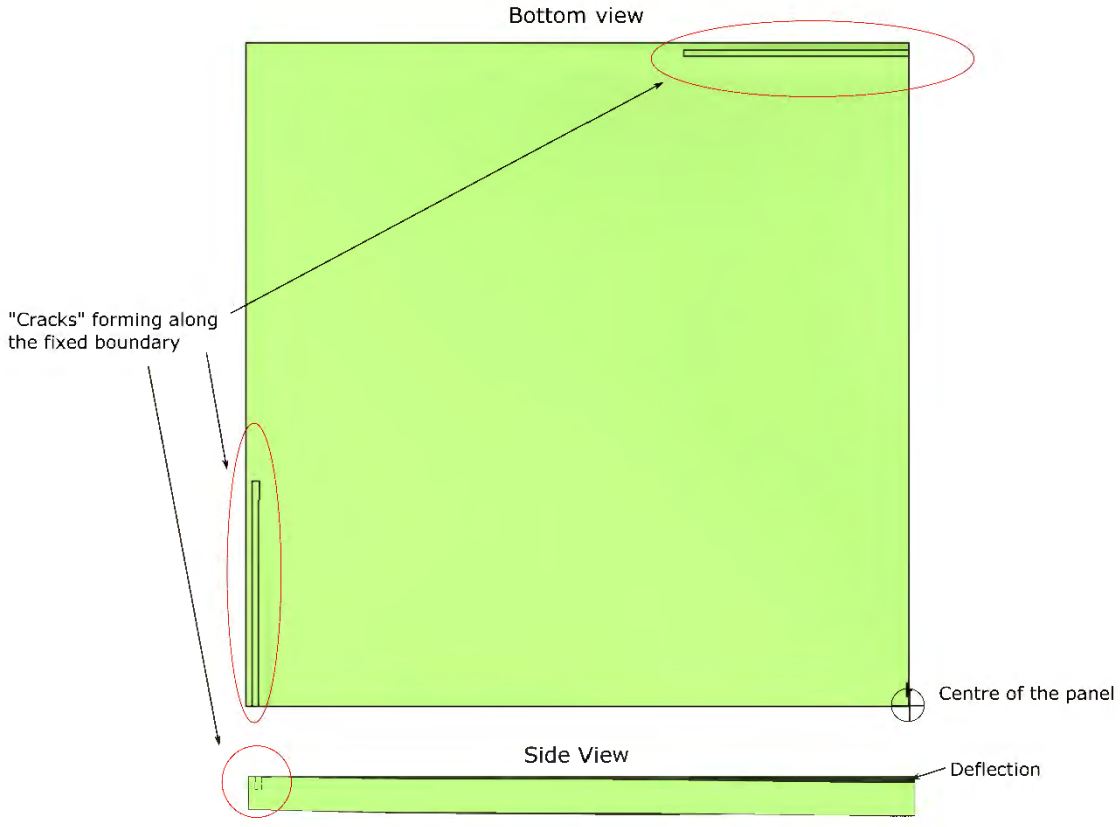

Figure 4-12: Bottom and side view of a GFRP numerical panel subjected to a charge mass of 10 g at the end of the simulation (t = 550 µs)

4.7.3 Overview of the control simulation results

A total of three simulations were performed on the control materials, each subjected to uniform blast loading conditions. A summary of the results is listed in Table 4-9.

Table 4-9: Simulation results for the control composites

Fibre	Thickness (mm)	Impulse (Ns)	Midpoint deflection at the end of simulation (mm)	Comments
Glass	5	26.6	0.93	Minor element deletion detected at the boundary; displacement decreases to original after max deflection of 9 mm was observed
Supawood	16	19.4	(17.9)	Complete boundary failure, explosive perforation, cracks at boundary

From the simulations, Supawood appeared to have the lowest blast resistant properties. Despite being the thickest panel, the amount of cracking and damage on the boundary was significantly more than those observed in the other composites. The midpoint deflection, 17.9 mm, was the largest value compared to all of the material models, as expected because the material properties for Supawood were significantly lower than the other composites.

4.8 Experimental plan based on numerical simulations

Despite the difference in thickness, the strength properties and limitations on the plastic failure strain of the material dominated the resistance towards blast loading. The recommended parameters of the blast tests are listed in Table 4-10. All tests would be subjected to uniform blast loading conditions, where the stand-off distance would be set at 200 mm. The explosive charge would be shaped as cylindrical discs.

Table 4-10: Recommended testing matrix

Composite	Control	Panel Thickness (mm)	Expected Charge Range (g)	Expected Number of Tests
Glass fibre/ Prime 20LV	✓	5	4 – 20	10
Glass fibre/ SuperSap		5	4 – 20	10
Supawood	✓	16	4 – 6	4
Flax fibre/ Prime 20LV		10	4 – 12	8
Flax fibre/ SuperSap		10	4 – 12	8

Jute fibre/ Prime 20LV		10	4 – 10	6

The explosive charge mass would vary more for the glass fibre reinforced composites, irrespective of the resin used. It was anticipated that very little damage would occur at low charges for the glass fibre reinforced composites. Supawood would likely be very weak and have a short range where testing could be performed. Lastly, the limit for the charge mass that can fragment a natural fibre reinforced composite laminates was approximately 10 g. It was possible that jute fibre reinforced composite could have a lower limit than flax fibre reinforced composite.

4.9 Summary of chapter

The goal of the numerical simulations was to obtain a particular thickness and weight for the natural fibre composites panels and to establish the stand-off distance for the explosive. A MMALE approach was used to model a total of 18 simulations. Three of which were used as numerical validation models to compare the impulse and permanent back face displacement with experimental blast results found for GLARE. Three additional models (5 g and 10 g localised charge mass, and 20 g uniform loading condition) were simulated on GLARE to determine the required runtime of the simulations. The panels, except for GLARE, were all modelled with 1mm cubic Lagrange elements. The different materials were described as isotropic. The composites were assigned a maximum strain value as a failure criterion. The elements would be deleted once the strain had reached the assigned maximum strain value to indicate cracking. Based on the numerical simulations conducted on the flax and jute fibre reinforced composites, the uniform blast loading test method was chosen and a thickness of 10 mm for those composites. Subsequently, the thickness of the GFRP (5 mm) and Supawood (16 mm) was determined by equivalent mass. It was found that the order of which the materials would likely fail was Supawood, jute, flax and lastly glass fibre reinforced composites.

5 Specimen manufacture

This chapter details the methods and processes used to manufacture specimens, including those used to help characterise the material, for this project. Based on the results from the numerical simulations, the flax and jute fibre reinforced blast specimens were designed to be nominally 10mm thick. The control glass fibre reinforced Prime 20LV composite panels were manufactured, and in the case of Supawood chosen to be of a similar weight. Additionally, ten donated flax fibre reinforced composite blast panels were manufactured using hand lay-up as described by Wang et al [192].

5.1 VI manufacturing procedure

Vacuum Infusion (VI) was used to manufacture most of the specimens. As described in Chapter 2, this technique produces consistent panels with less time is required to infuse dry fabric compared to hand lay-up specimens [115], [116]. Therefore, it was chosen as a suitable manufacturing method for all composites manufactured except for the donated flax fibre reinforced composites panels which were used as a comparative manufacturing method.

A cross section of the set-up for VI is shown in Figure 5-1 which illustrates the lay-up of the fabric and the different consumables used for the processing method. These consumables included resin distribution media, peel ply, vacuum bag, piping, and sealant tape. Large panels (0.7 x 1 m and larger), with the required thickness, were manufactured. Individual blast panels and flexural quasi-static specimens were cut from these large panels. The same manufacturing method was used to form smaller panels (approximately 0.6 x 0.7 m) to obtain the quasi-static tensile and double cantilever beam (DCB) specimens.

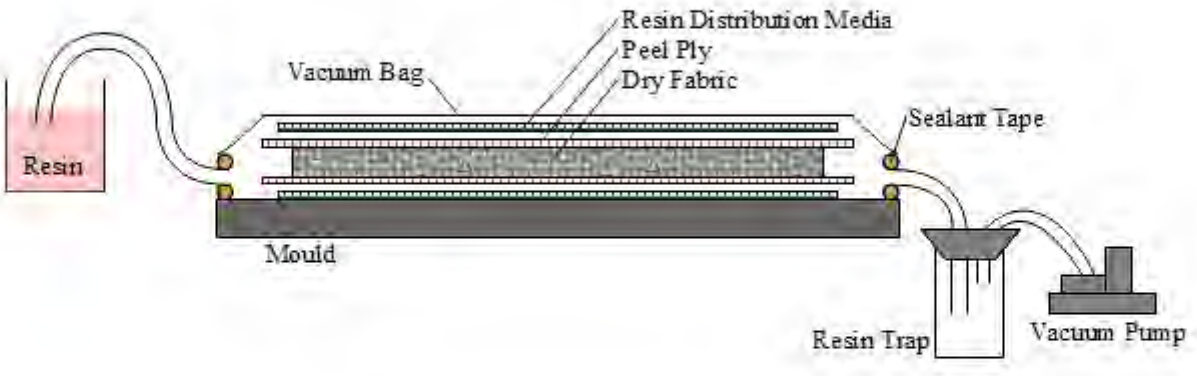

Figure 5-1: Schematic of VI

The order and process on how VI was used to manufacture the panels are summarised in Figure 5-2. The flat moulding surfaced was initially prepped by scrapping excess material, thereafter, cleaned with a solvent. The surface was waxed several times and polished before a final layer of wax was applied

to leave a light layer of wax to help release the infused composite. Fabric and consumables were cut to the appropriate size and assembled as shown in Figure 5-1. Piping networks to allow for the feed and vacuum were arranged to ensure a consistent and fast infusion across the entire panel.

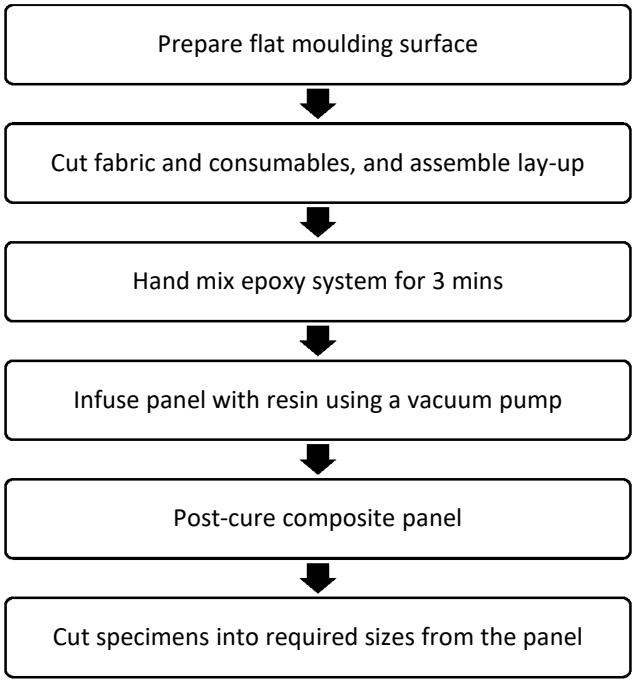

Figure 5-2: Basic VI procedure

The resin and hardener (Super Sap resin + CLS hardener + INH inhibitor or Prime 20LV + slow hardener) were prepared and mixed into containers in small quantities to avoid exothermic reactions causing high temperatures. These mixtures were gradually added to the feed bucket during infusion. Once the resin was infused to the end of the panel, the feedline was clamped, and the lay-up left under vacuum overnight. Finally, the specimens were allowed to post cure at an elevated temperature, based on resin suppliers' datasheets [163], [193] using an oven and then allowed to rest at room temperature.

The post curing profiles of Prime 20LV and SuperSap were shown in Figure 5-3. Both post cure cycles have the same ramp rate for increasing and decreasing temperatures of 1 ^{o}C/min. As shown in Figure 5-3, the temperature to post cure for Prime 20LV infused specimens was 50 ^{o}C [163] and 80 ^{o}C for Super Sap infused specimens [193]. The SuperSap composites were also left to post cure at room temperature for 7 days afterwards.

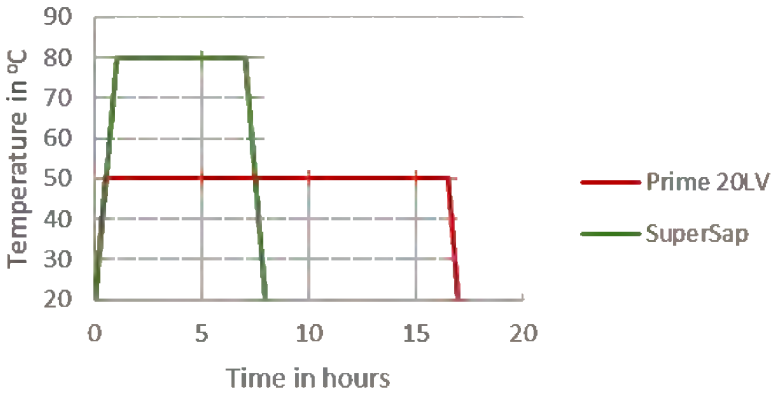

Figure 5-3: Graph showing the post cure cycle for Prime 20LV and SuperSap resin

Large panels exceeding 1000 mm in width required two inlet pipes were used to infuse the panel. This was performed to avoid the possibility of the resin gelling before all the fibres were well saturated, leaving dry spots in the fabric. An infused jute fibre reinforced composite, left under vacuum, is shown in Figure 5-4 where two inlet pipes, positioned 500 mm apart, were needed.

Figure 5-4: Photograph of an infused natural fibre composite on a flat moulding surface

While manufacturing, the panels were monitored during the infusion process and for approximately two hours after infusion was complete. The vacuum bag was continuously checked for holes and ruptures. Any leaks were sealed using sealant tape. During the entire process, the temperature at the top surface of all the natural fibre composites was monitored and was observed to be less than 50 °C. At the end of infusion and any post curing, the panels were visually inspected for sizeable defects such as large cracks or areas of dry fabric. Sections with such defects were disregarded. Specimens were cut at least 50 mm away from any free edges for large panels. For smaller panels, specimens were cut at least 20 mm away from edges. This was to avoid any thickness changes which can occur at the edges.

5.2 Relationship between thickness and plies for natural fibre laminates

The relationship between the thickness and number of plies for the natural fibre composites (both flax and jute) was determined by manufacturing three small sample panels (size 200 x 150 mm). It was unclear how much the textiles would compress under vacuum and consequently affected the thickness of the resulting panel.

The thickness of the samples was measured at five different locations with a micrometre and the average value was plotted in Figure 5-5. In the region of interest between 5 to 16 plies, a linear relationship between the parameters was observed. The R^2 value was 0.9999 and 0.9978 for flax and jute fibre reinforced composite, respectively. While this was a small data sample, the linear model was a good fit in this data range.

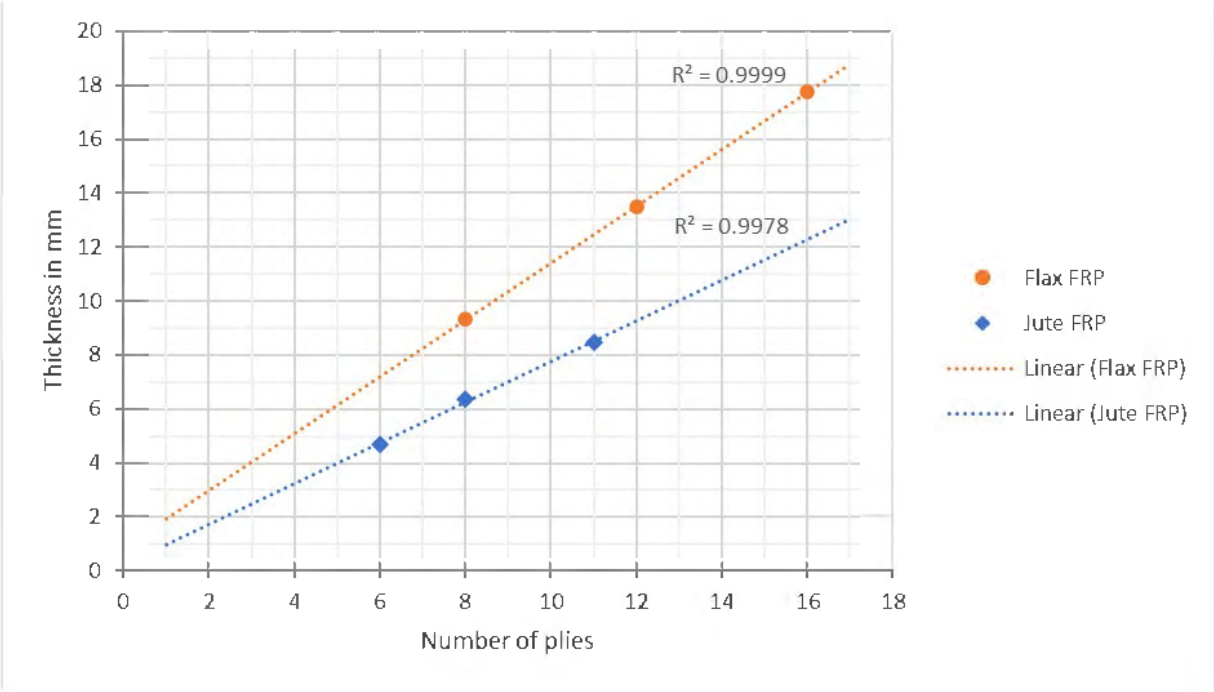

Figure 5-5: Graph showing thickness versus number of piles for jute and flax reinforced composites

From Figure 5-5, the number of plies required to make a 10 mm thick composite panel was found to be 9 and 13 plies for flax and jute textiles respectively. In comparison to the hand lay-up flax fibre reinforced composites, one more ply was required for the VI method. The number of layers directly affected the number of panels which could be manufactured due to the availability of material.

5.3 Hand lay-up specimen information

Ten blast panels of size 300 x 300 mm of hand lay-up flax fibre reinforced Prime 20LV composites were donated by the University of Auckland, along with flax textile, towards this work. These panels were manufactured to be nominally 10 mm thick and contained eight layers of flax textile. One of the

provided panels was cut up to obtain specimens that would be tested under quasi-static flexural loading conditions. In addition to the blast panels, different sizes of quasi-static tensile specimens (also made from hand lay-up flax fibre reinforced Prime 20LV composites) were received to determine the influence of the manufacturing process with increasing thickness. The number of layers, average width, average thickness, and number of tensile specimens is listed in Table 5-1.

Table 5-1: Hand lay-up flax fibre reinforced Prime 20LV tensile specimen detail

Number of layers	Average width (mm)	Average thickness (mm)	Number of specimens available
6	29.9	7.4	4
4	25.4	5.0	5
2	25.3	2.6	5

For convenience, the manufacturing process as described by Wang et al [192], [194] is detailed herein. Initially, a number of large pieces of flax textile were cut and a flat base table was covered with a plastic sheet. Prime 20LV epoxy resin was mixed with its slow hardener thoroughly for three minutes. A layer of flax textile was placed onto the plastic sheet then, by hand, fully impregnated with the epoxy using a brush. Thereafter another layer of flax textile was placed on top of the saturated layer and impregnated with resin using a brush. This process was repeated until the final layer where the remaining epoxy was evenly spread over the fibre sheet before it was covered by another plastic layer. The laminates were left to cure under standard atmospheric conditions and at room temperature for at least 48 hours. Once this was complete, laminates were cut into the required dimensions for the blast panels and tensile specimens [192], [194].

With the hand lay-up panels and VI panels, it was possible to determine whether manufacturing method has an influence on blast resistant properties of natural fibre composites. While findings on the comparisons of the two manufacturing methods typically show that VI specimens produce higher mechanical properties [50] (as discussed in the literature review chapter), it was not certain whether the advantages of VI would be applicable to the blast behaviour of natural fibre composites.

5.4 Manufacturing for blast specimens and quasi-static flexural tests

Table 5-2 lists the number of plies, and the resulting nominal thickness and mass for the blast specimens. The Supawood, also included in Table 5-1, was purchased as a ready-to-use product. Modifications on the Supawood samples were only performed for quasi-static tensile specimens as a soft centre was observed on the panels, and the modifications could provide insight with regards to this. For all materials, at least five quasi-static flexural test specimens were cut from the same large

panel that was used to get the blast test panels such that the material consistency of the panel could be verified.

Table 5-2: Details for the blast specimens

Composite Type	Number of plies	Nominal Thickness (mm)	Nominal mass (kg)	Number of blast panels available
Glass fibre/ Prime 20LV (1)	17	5	0.77	10
Glass fibre/ Prime 20LV (2)	19	6	1.00	10
Glass fibre/ SuperSap	17	5	0.85	10
Hand lay-up Flax fibre/ Prime 20LV	10	10	0.97	9
Flax fibre/ Prime 20LV	9	10	1.10	6
Flax fibre/ SuperSap	9	10	1.10	6
Jute fibre/ Prime 20LV	13	10	1.02	6
Supawood	-	16	1.01	12

5.5 Double Cantilever Beam (DCB) specimen manufacture

DCB bending test was used to characterise the interlaminar fracture toughness of the composites. Panels were manufactured using the VI process where a non-perforated release film was placed in mid-plane section of the panel to create a crack in the material. Specimens were waterjet cut from the manufactured panel using the dimensions based on ASTM D5528 [195] standards and loading blocks bonded on. A schematic of a DCB specimen is shown in Figure 5-6, showing the loading blocks attached at the crack end of the specimen.

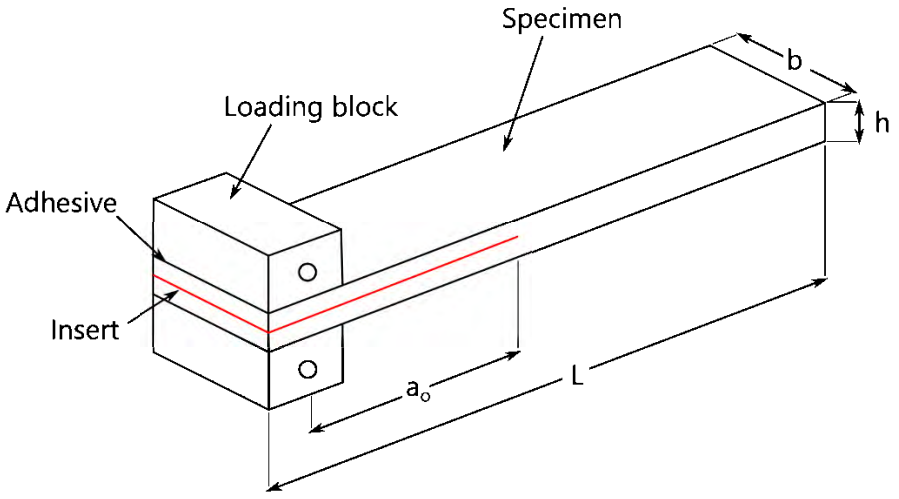

Figure 5-6: Schematic of a DCB specimen with loading blocks attached (adapted from [195]**)**

The same manufacturing process, as described in Section 5.1, was used to fabricate the specimens. Loading blocks were adhesively bonded to the specimens using a 3-d printed jig, shown in Figure 5-7, which positioned and glued the two loading blocks onto each specimen.

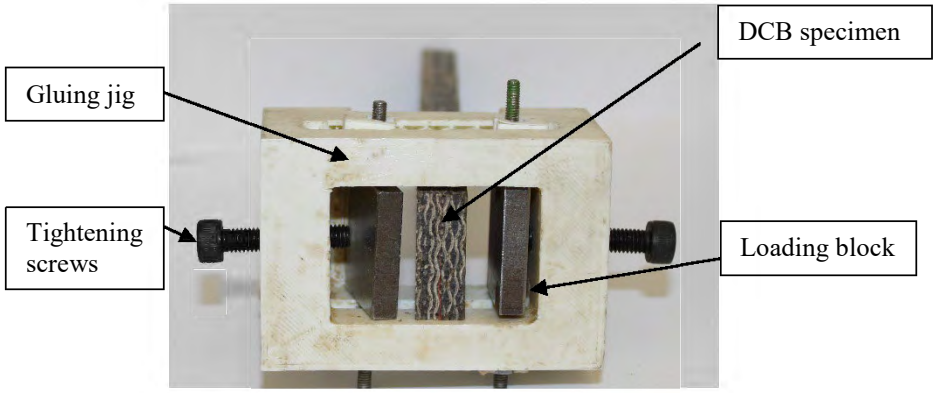

Figure 5-7: Photograph of DCB jig used to glue the loading blocks

The jigs, loading blocks and specimens were all cleaned and wiped down with alcohol to remove any oil or residue from the surface. A mould release wax was applied to the jig. The loading blocks and specimen with the artificial crack were placed into the jig as shown in Figure 5-7. A thin layer of Spabond 340 epoxy (with fast hardener) adhesive, was applied to both sides of the specimen and loading blocks. The two opposing screws located on both sides of the jig were tightened to apply a constant force onto the loading blocks and specimen for consistent adhesion. The assembled fixture was then placed in the oven at 35 °C reduce the clamp time to 2.5 hours. The specimens were thereafter initially cured at room temperature for 24 hours before a second post curing in an oven at a temperature of 50 °C for 16 hours as recommended by the adhesive supplier's datasheets [196] .

5.6 Manufacturing for quasi-static DCB and tensile tests

Separate panel infusions were performed for the DCB specimens and tensile specimens as the required thickness varied compared to the blast specimens. For DCB specimens, an even number of layers were required for the non-perforated insert to be placed mid-plane. The tensile specimens were manufactured according to ASTM 3039 [197] standards. The dimensions of the specimens were based on ASTM D5528 [195] and ASTM 3039 [197] for DCB and tensile testing respectively and are detailed in Chapter 6. Table 5-3 shows the number of plies used the specimens manufactured under VI.

Table 5-3: Number of plies used for DCB and tensile test specimens

	Number of plies	
	DCB	Tensile
Glass fibre/ Prime 20LV	12 (6/6)	8
Glass fibre/ SuperSap	12 (6/6)	8
Flax fibre/ Prime 20LV	8 (4/4)	2
Flax fibre/ SuperSap	8 (4/4)	2
Jute fibre/ Prime 20LV	10 (5/5)	4

For Supawood, two thicknesses were tested under the quasi-static tensile loading condition: 3 mm (which was the closest thickness for a board to the recommended specimen thickness in ASTM 3039 [197] available) and 12 mm. A ready-to-use 12 mm board, as well as a 16 mm board were purchased. 2 mm was machined off both sides of the 16 mm board, resulting in a 12 mm thick Supawood specimen without the hard compressed outer layer.

5.7 Summary of chapter

Flat composite panels were manufactured using primarily VI and hand lay-up. Large panels were made, and specimens were cut out. Each textile (glass, flax, and jute fibre) was infused with Prime 20LV resin. Only two fibres, glass, and flax, were infused with SuperSap. Only flax fibre reinforced Prime 20LV blast panels and tensile specimens were manufactured via hand lay-up. All the VI manufactured composites were post-cured at an elevated temperature (50 °C and above), and all composites were post-cured at room temperature at least. No further processes or treatments, except for the addition of loading blocks for DCB specimens, were conducted on the specimens post or prior manufacturing. Supawood was purchased as a ready-to-use product, except for a series of tensile specimens where the outer layers were shaved down.

6 Quasi-static testing

A range of quasi-static materials tests were performed on the manufactured materials to determine their behaviour in different loading conditions. These tests were used to ensure consistency in the manufacture of the fibre reinforced polymer composites and to provide insight into the damage mechanisms observed during the blast testing. These tests were performed using a Zwick Roell 1484 universal testing machine and according to relevant standards. Tests on the fibre reinforced polymer composites include flexural, tensile and interlaminar delamination tests. The glass fibre reinforced Prime 20LV composite specimens for tensile and interlaminar tests were performed in conjunction with a fellow PhD student, Shekhar [198]. Similar tests were conducted on Supawood, except for interlaminar testing whereby through-thickness compression and tensile tests were performed. The types of quasi-static tests performed on each material are listed in Table 6-1. In this chapter, different sections outline the type of testing used, describes the procedures followed and discusses the results from testing. These findings aid to understand the damage mechanisms in blast loaded specimens.

Table 6-1: Quasi-static tests performed on the different materials.

	Flexural	Tensile		DCB	Through thickness compression
		In-plane	Through thickness		
Glass FRP	✓	✓		✓	
Flax FRP	✓	✓		✓	
Jute FRP	✓	✓		✓	
Supawood	✓	✓	✓		✓

6.1 Quasi-static flexural tests

Quasi-static flexural tests were performed to determine the behaviour and flexural properties such as the flexural elastic modulus, stress and strain. Additionally, to the flexural behaviour, these tests were also carried out to determine the consistency of properties within a composite panel as several specimens were cut from the same large manufactured composite panel (in the case of the VI manufactured panels) or MDF sheet as the blast specimens. A hand lay-up panel, similar to one that would be used for blast testing, was cut up into flexural specimens for similar reason to determine the consistency of hand lay-up specimens.

6.1.1 Specimen preparation and test method

Specimen sizes were based on panel thickness. Test specimens had a nominal support span-to-thickness ratio of 16:1, with the overall length being at least 20 % greater than the support span based on ASTM D7264 [199].

The specimen was placed on adjustable supports that were placed equidistant from the central loading nose. For each configuration, the supports were fixed according to the relevant span of the specimen based on the average thickness of that configuration. The three-point loading configuration, shown in Figure 6-1, was used to measure the displacement history versus force. From the specimen dimensions, displacement and force history, the flexural strength at the centre of the beam was determined. The specimen dimensions are listed in Table 6-2.

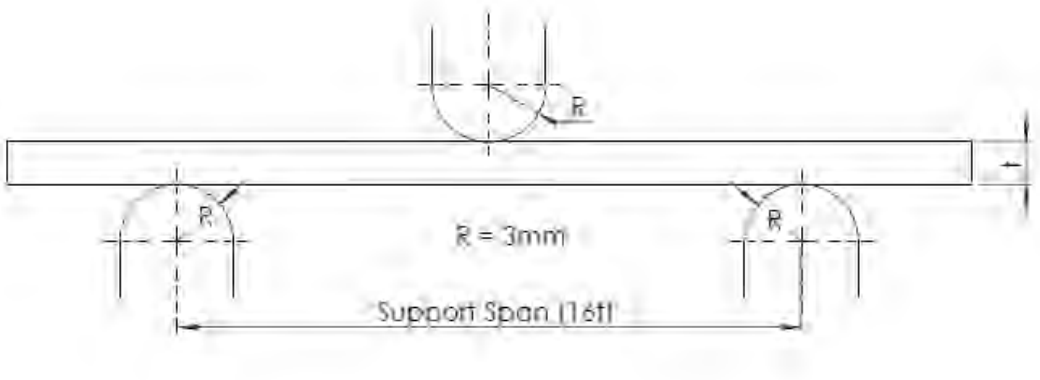

Figure 6-1: Three-point bend loading configuration with supports and centre loading nose (Redrawn from Ref [199]**)**

Table 6-2: Dimensions for the flexural specimens

	Nominal thickness, mm	Nominal width, mm	Nominal support span, mm
Glass 19/Prime 20LV	6	32	100
Glass 17/Prime 20LV	5	30	79
Glass 17/Super Sap	5	32	80
Flax 9/Prime 20LV	10	24	156
Flax 9/Super Sap	10	30	159
Hand lay-up Flax 8/Prime 20LV	10	34	155
Jute 13/Prime 20LV	10	36	160
Supawood	16	55	260

During testing, the bottom plate moved upwards at a constant displacement rate of 3 mm/min towards the centre loading nose, causing an applied force that flexed the specimen. The centre force and crosshead deflection were recorded until the specimen failed. The bending stress and corresponding strain at a given time, on the outer surface at mid-span, was calculated using Equation 6-1 and 6-2. The maximum flexural stress, also known as the flexural strength, was calculated at peak stress prior to specimen failure.

$$\sigma = \frac{3\mathrm{PL}}{2\,\mathrm{w}t^2} \qquad 6\text{-}1$$

$$\varepsilon = \frac{6\delta\mathrm{t}}{\mathrm{L}^2} \qquad 6\text{-}2$$

where P = measured force, L = support span of the specimen, w = average width of the specimen, t = average thickness of the specimen and δ= mid-span deflection.

The ratio between stress and strain in the elastic range of the material, known as the flexural chord of elasticity, was found using Equation 6-3. The modulus was calculated between two selected strain points during which the response was linear.

$$\mathrm{E}^{\mathrm{f}}_{\mathrm{chord}} = \frac{\Delta\sigma}{\Delta\varepsilon} \qquad 6\text{-}3$$

6.1.2 Observed failure modes

Top surface buckling directly beneath the central support was evident on all the GFRP composite specimens subjected to three-point bending. This top surface buckling at the centre of the specimen is shown in Figure 6-2 on two different GFRP specimens. White areas in that region showed delamination occurred along with the buckling. At the end of testing, the glass fibre composite reinforced specimens permanently deformed but remained as one piece.

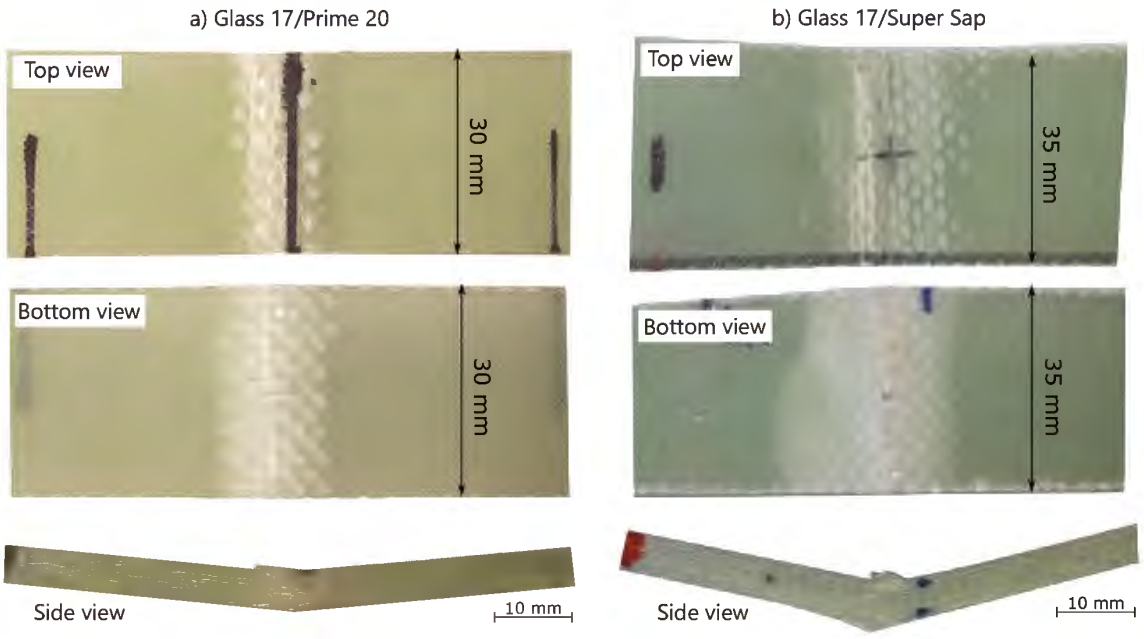

Figure 6-2: Photographs of different flexural glass fibre reinforced composites specimens subjected to flexural loading around the central region

For the laminated flax fibre composites, there was also some evidence of fibre pull-out and fibre breakages in the flax fibre reinforced composites near the centre of the specimen as shown in Figure 6-3. There did not appear to be significant differences in the damage observed based on manufacturing methods as similar failure modes were observed on the hand lay-up flax fibre reinforced composite specimens. Usually, a crack spanning the width of the specimen on the bottom surface was observed. On the side profile, the crack appeared to extend up from the bottom surface through the thickness of the specimen. Therefore, it was likely that specimens failed due to the tensile stress from the flexural load. The crack did however not always completely snap the specimens into two parts. Most specimens, while permanently deformed, remained as one piece.

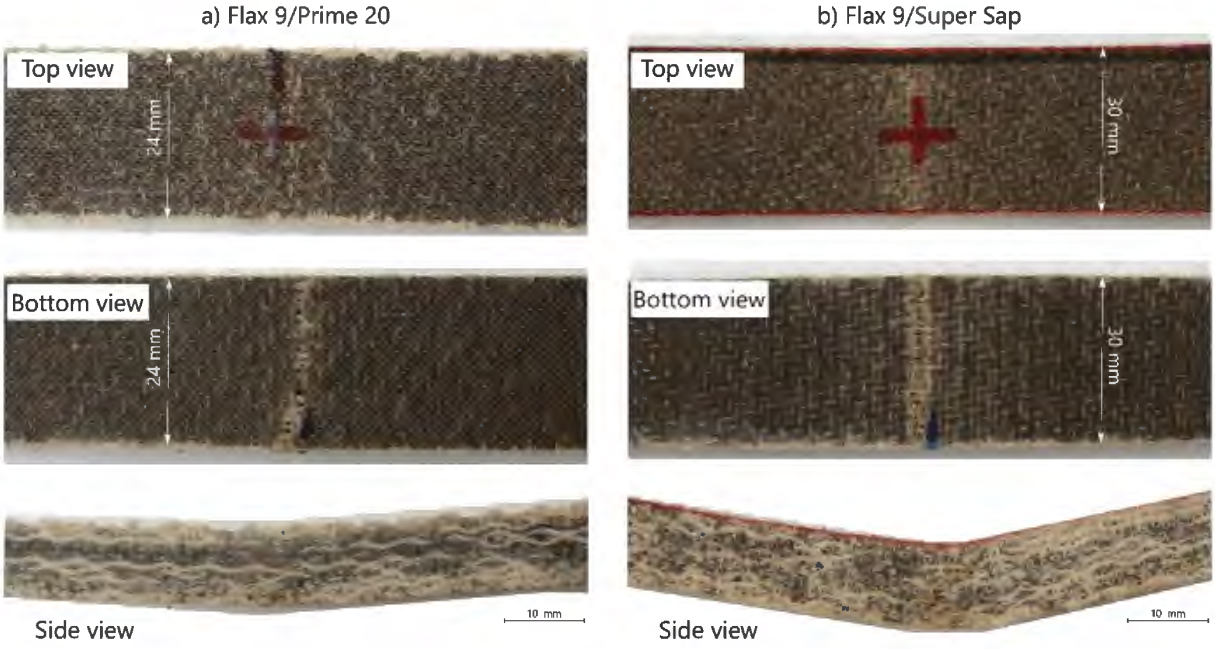

Figure 6-3: Photographs of different flexural flax fibre reinforced composites specimens subjected to flexural loading around the central region

For the Supawood, no evidence of damage was observed on the top surface as shown in Figure 6-4a. A crack on the bottom surface shown in Figure 6-4b and Figure 6-4c was observed to propagate to the top surface. Similar crack formation was observed in the flax fibre reinforced composites.

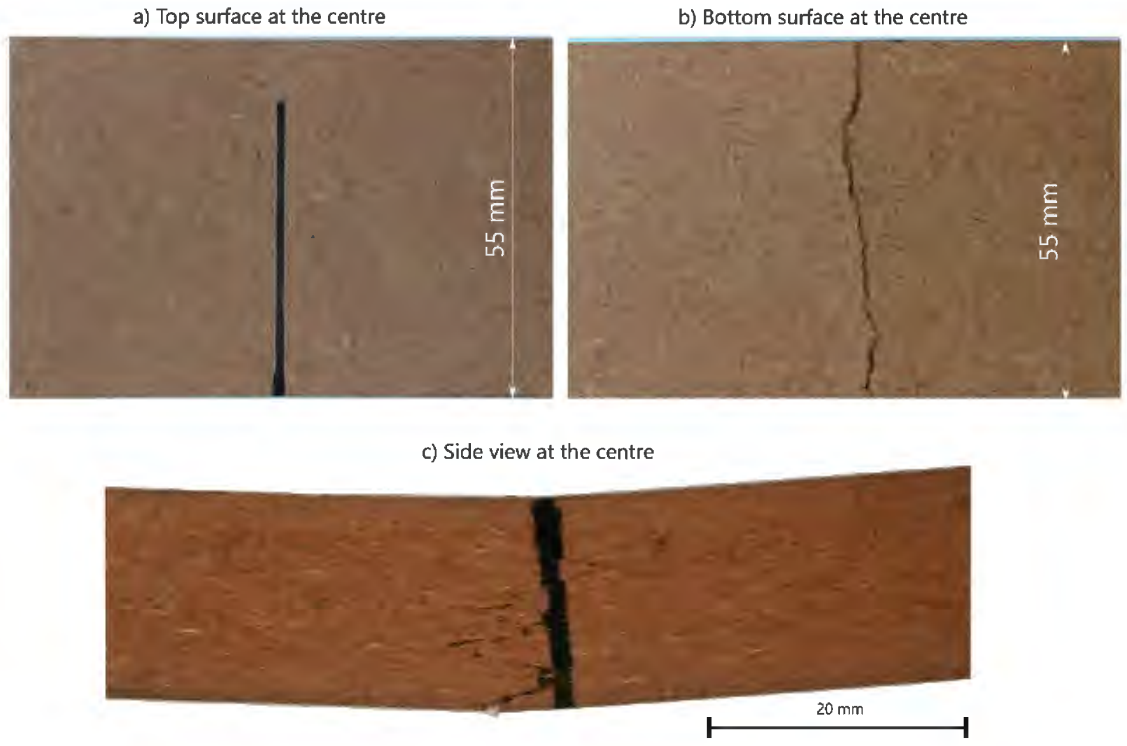

Figure 6-4: Photographs of the central region of a Supawood bend specimen after testing

For the jute fibre reinforced composites, each specimen behaved in brittle manner. A clean fracture through the thickness, as shown in Figure 6-5, was observed in all specimens. There was no other visible damage on either the bottom or top surfaces of the specimens.

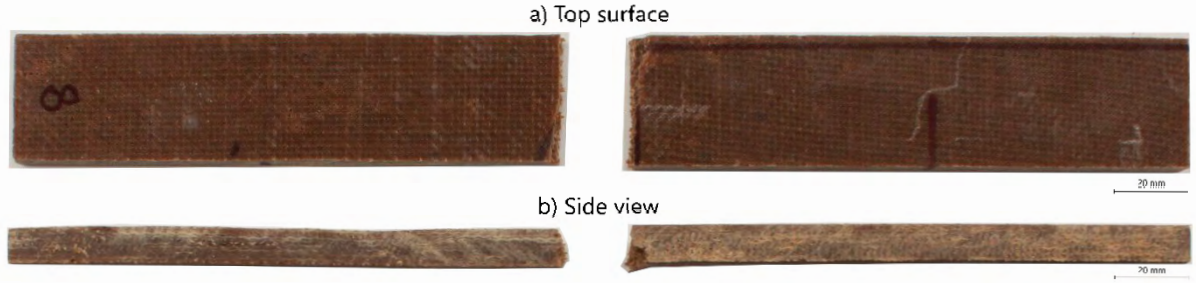

Figure 6-5: Snapped jute fibre reinforced composite bend specimen after testing

The majority of the damage observed on the flexural specimens was located at the centre of the specimen where the top centre loading nose was positioned, as expected. It seemed that how the specimen failed (either tension or compression) was dependent on the type of fibre. The flax, jute fibre reinforced and Supawood specimens all failed under tension, whereas the GFRP specimens failed under compression.

6.1.3 Flexural stress strain curves

Representative stress-strain curves for the glass and natural fibre reinforced composites are shown in Figure 6-6 and Figure 6-7. The number of layers used for a laminate is given next to the fibre in brackets. The nominal thicknesses for the different composites are also displayed. The 0^o and 90^o notation in the legend refers to glass fibre reinforced composite specimens (that were nominally 5 mm thick) cut from two separate orthogonal directions aligned with the warp and weft of the weave of the fabric. The results for GFRP are shown separately from the natural fibre reinforced composites due to the large difference in the flexural strength and strain magnitude at failure. The results were considered independent of specimen orientation as 0° and 90° specimens gave similar values. Considering that the natural fibre textiles were balanced, it was assumed that the warp and weft directions would have had similar properties as well.

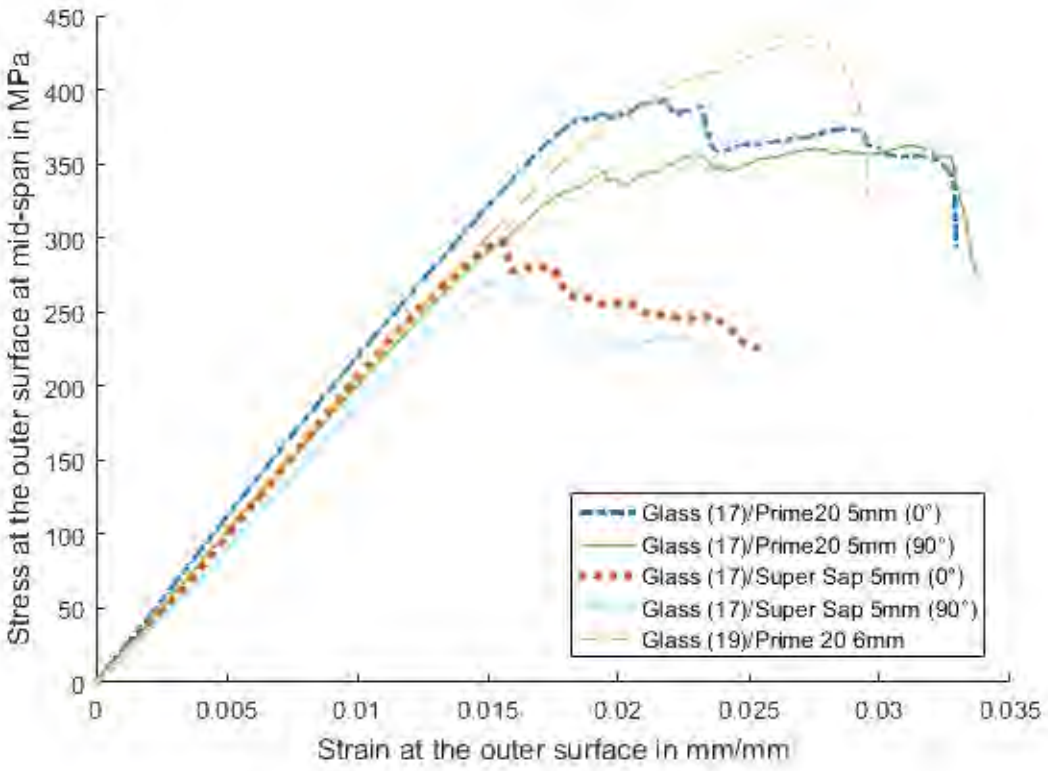

Figure 6-6: Representative flexural stress and strain curves for glass fibre reinforced composites

The initial section of the curves, up to a strain of approximately 0.015, remained linear. Afterwards, there were different responses between the different types of composites. In most cases, the stress for the glass fibre reinforced Prime 20LV composites approached the maximum value at 0.025 m/m strain before the stress sharply dropped as observed in Figure 6-6 due to failure. The stress for the glass fibre reinforced SuperSap composites, which had the lowest maximum stress values from the glass fibre composites tested, tailed off slightly after the maximum stress was reached.

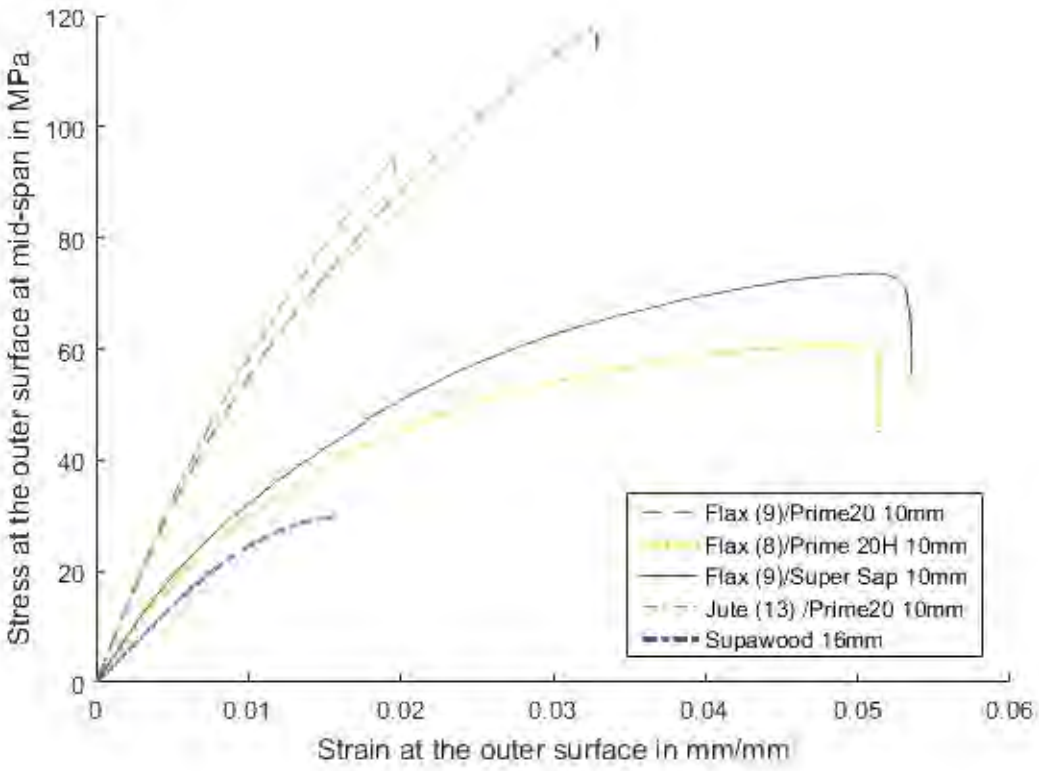

Figure 6-7: Representative flexural stress and strain curves for natural fibre reinforced composites

In comparison, the natural fibre composites were significantly weaker, failing between 30 and 120 MPa in wider range of strain (0.015 – 0.055). Supawood had the lowest flexural strength and strain to failure. All natural fibre composites tested appeared to have a curvilinear relationship between the flexural stress and strain followed by a steep drop in stress after the peak as shown in Figure 6-7. The slope and maximum stress were lower for the VI manufactured flax fibre reinforced Super Sap composites compared to VI manufactured flax fibre reinforced Prime 20LV composites. The variation is further discussed in section 6.1.4. Additionally, the hand lay-up flax fibre reinforced composites also had a lower gradient and lower maximum stress. When testing, cracking was often heard in the natural fibre composite tests indicating that fibre breakage or pull-out and / or matrix cracking occurred which would contribute to the reduction in stiffness.

6.1.4 Overview of flexural test results and discussion

A summary of results for flexural strength and corresponding strain, flexural chord of elasticity and strain at failure are listed in Table 6-3. The mean and sample standard deviations are shown for each material system. The individual test results for can be found in Appendix B. For the glass fibre reinforced composites, the results of the 0^o and 90^o specimens were combined.

Table 6-3: Mean and standard deviations of flexural properties

	Flexural strength, σ^f_{max} [MPa]		Strain at σ^f_{max}, $\varepsilon^f_{\sigma max}$ [m/m]		Flexural chord of elasticity, E^f_{chord} [GPa]		Strain at failure, ε^f_{fail} [m/m]	
	mean	*Std Dev*	*mean*	*Std Dev*	*mean*	*Std Dev*	*mean*	*Std Dev*
Glass (19)/Prime 20LV 6mm	452	12	0.026	0.001	21.3	0.6	0.029	0.001
Glass (17)/Prime 20LV 5mm	399	34	0.025	0.004	21.9	0.7	0.032	0.003
Glass (17)/ Super Sap 5mm	276	13	0.015	0.001	20.2	0.9	0.023	0.004
Flax (8)/Prime 20LV 10mm Hand Lay-up	58	5	0.045	0.004	3.4	0.3	0.050	0.006
Flax (9)/Prime 20LV 10mm	112	6	0.030	0.002	6.3	0.5	0.030	0.002
Flax (9)/SuperSap 10mm	77	6	0.042	0.007	3.9	0.5	0.044	0.008
Jute (13)/Prime 20LV 10mm	89	10	0.019	0.001	6.2	0.9	0.019	0.001
Supawood 16mm	30	0.4	0.015	0.0004	27.6	0.03	0.017	0.001

As expected, the 6mm glass fibre reinforced Prime 20LV composite exhibited the highest flexural strength (at a mean value of 452 MPa) from all GFRP tested. This showed that increasing the number of plies (i.e., more glass fibre in the specimen) increased the flexural strength of the material. The specimens with more glass fibre seemed to have had a better compaction and the resin rich areas, typically found on the top and bottom surfaces of a specimen, would have contributed less to the over material properties. However, the increase in thickness may decrease the maximum strain at failure. A slight decrease in values was observed for the two types of glass fibre reinforced Prime 20LV composites (0.029 for Glass/Prime 20LV 6 mm and 0.032 for Glass/Prime 20LV 5 mm). The flexural strength of the glass fibre reinforced SuperSap composites was less than the Prime 20LV counterpart by a margin of ~110 MPa. For both strain at maximum flexural strength and failure, glass fibre reinforced Prime 20LV composites had higher values than the glass fibre reinforced SuperSap composites. However, the flexural chord of elasticity was similar for all GFRPs despite differences in thickness and resin.

The VI manufactured flax fibre reinforced Prime 20LV composite had the highest flexural strength value of all natural fibre composites tested. The hand lay-up flax fibre reinforced composites were weaker than the infused specimens. The flexural strength was 48 % lower, (112 MPa to 58 MPa). The strain at failure and flexural chord of elasticity were noticeably higher and had a significantly larger range. Additionally, as in GFRPs, Prime 20LV flax fibre reinforced composites had higher values compared to SuperSap flax fibre reinforced composites. The jute fibre reinforced Prime 20LV composite also had a higher flexural strength than the SuperSap flax fibre reinforced composite. The strain at failure was lower, however, in comparison. Supawood had the lowest values for all the results reported, with a mean experimental maximum flexural stress value of 30 MPa matching the values reported by the manufacturer's [2].

There were larger deviations in the results for the natural fibre composites, particularly for the flexural strength values of the jute fibre reinforced composite and hand lay-up flax fibre reinforced composite. This was expected due to the nature of the material and manufacturing process. Despite this, the results for each test series were considered consistent, confirming the regularity of the manufactured specimens and suitability for blast testing.

The choice of fibre, resin, number of plies and manufacturing all affected the flexural properties. The values for the maximum flexural stress followed the expected strength of the fibre, as expected. Glass fibre was the strongest fibre followed by flax, and then jute fibre. The control material, Supawood, was significantly weaker compared to all other materials. When Prime 20LV resin was used with flax and jute fibres, the resulting composites behaved similarly in terms of elastic modulus despite different fibres. However, in comparison, the flax fibre reinforced SuperSap composite had very different properties, for both flexural chord of elasticity and flexural strength. Moreover, SuperSap resin appeared to decrease the flexural strength of the GFRPs but not the flexural chord of elasticity. The different manufacturing methods used to make flax fibre reinforced composites seemed to have a significant difference on both the flexural strength and strain, with hand lay-up resulting in lower values. It should be noted that there was one less flax ply in the hand lay-up specimens. Lastly, flax fibre reinforced composites had a larger strain at failure range than the other materials tested.

6.2 Quasi-static tensile tests

Quasi-static tensile tests were performed to determine the tensile behaviour and material properties, such as ultimate tensile strength, yield stress and tensile modulus. The specimen orientation typically affects the mechanical properties in woven fibre reinforced composites; therefore, three different orientations were considered, parallel to the warp, parallel to the weft and at 45°to the warp and weft of the fabric. The intention of these tests was primarily to gain insight into the consistency of the

materials and manufacturing methods like flexural tests. It should be noted that the tensile test specimens could not be cut from the same panels as the blast and flexural test specimens. New panels were manufactured for the tensile test specimens.

6.2.1 Specimen preparation

For the VI manufactured specimens, panels were manufactured according to the recommended panel thickness of 2.5 mm found in ASTM D3039 [197]. Tensile tests were performed on specimens cut at three fibre orientations, namely 0°, 90° and 45° relative to the woven fabric warp direction as indicated in Figure 6-8. Similarly, the Supawood specimens were also cut from three orientations relative to the supplied panel straight edge for each thickness tested. Figure 6-8 depicts a cutting schematic for a CNC router, using a 6 mm diameter end mill, for one of the manufactured panels. The dimensions for tensile specimens of this manufacturing type were nominally 25 x 250 mm. At least 5 specimens in each orientation were tested.

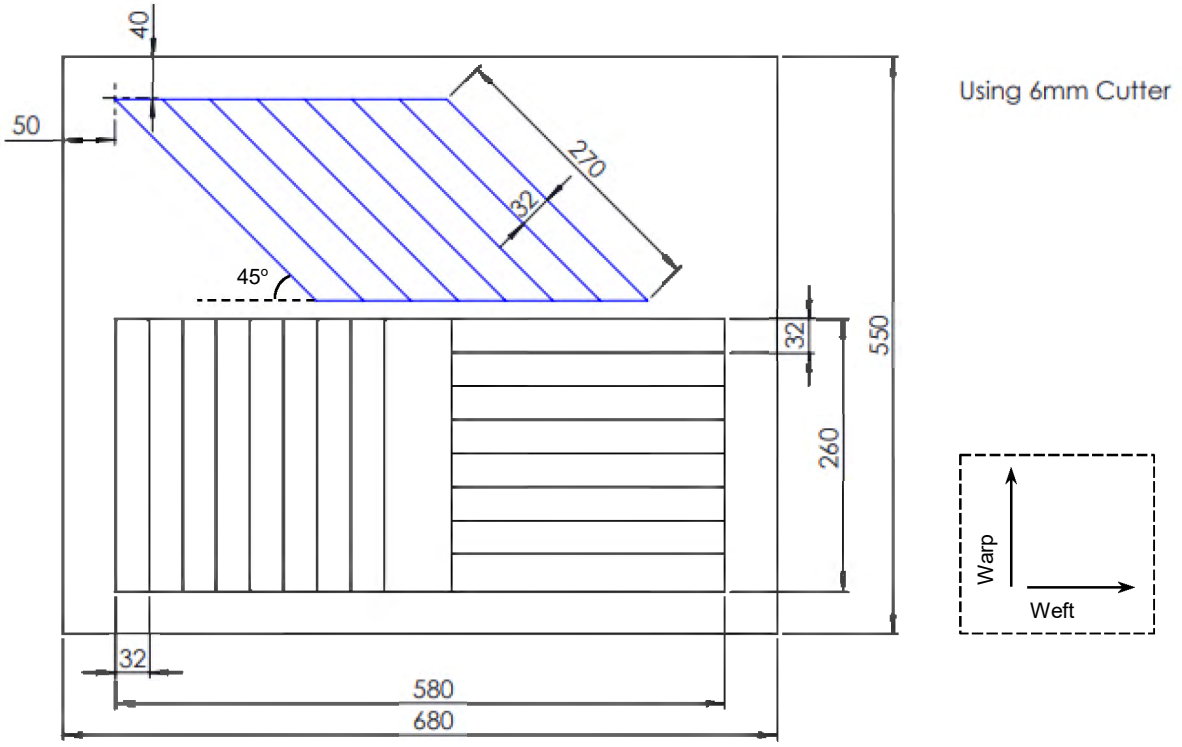

Figure 6-8: Router tensile specimen cut out schematic for a glass fibre reinforced composite

The tests performed on the glass fibre reinforced Prime 20LV composites were in conjunction with Shekhar [198]. For those tests, it was decided that a two orientation (0° and 45°) was sufficient as 0° and 90° gave similar results for the glass fibre reinforced Super Sap composites suggesting no noticeable variation between the warp and weft of the 400 g/m^2 GF fabric. A summary of the tensile tests is listed in Table 6-4.

Table 6-4: Different types of composites tested under quasi-static tensile testing

	Conditioning	Orientations tested			Nominal thickness (mm)	Number of tests
Glass Fibre, Prime 20LV	VI	0°		45°	2.5	12
Glass Fibre, SuperSap	VI	0°	90°	45°	2.5	21
Flax Fibre, Prime 20LV	VI	0°	90°	45°	2.5	17
	Hand lay-up	0°			2.5	5
	Hand lay-up	0°			5	5
	Hand lay-up	0°			7.5	4
Flax Fibre, SuperSap	VI	0°	90°	45°	2.5	18
Jute Fibre, Prime 20LV	VI	0°	90°	45°	3	17
Supawood	Plain	0°	90°	45°	3	18
	Plain	0°	90°	45°	12	18
	Shaved	0°	90°	45°	12	16

6.2.2 Testing method

The general test procedure was based on guidelines from ASTM D3039 [197]. Emery cloth was wrapped around the edges of the specimen to provide additional friction to hold the specimen between two grips on the Zwick machine. The top grip was fixed to the loadcell while the bottom grip was attached to the movable plate. During testing, the bottom grip moves away at a constant crosshead speed of 2 mm/min from the top grip, pulling the specimen whilst applying tensile force. The tensile stress and strain at a given time was calculated using Equations 6-4 and 6-5 respectively. From the stress strain values, tensile properties including ultimate tensile strength, yield stress and Young's modulus were determined.

$$\sigma = \frac{P}{(wh)} \qquad 6\text{-}4$$

$$\varepsilon = \frac{l_i - L_g}{L_g} \qquad 6\text{-}5$$

Where P = measured tensile force at the corresponding time, w = average width of the specimen, h = average thickness of the specimen, l_i = length of the gauge at the corresponding time, and L_g = initial length of the gauge at the start of the test.

The Zwick testing machine was used to record and report the force and displacement of the specimen as the lower crosshead moved. The displacement of the specimen was also found using DIC with a single camera at a sampling rate of 3 images per second. A 2D image of the specimen, which had been painted with speckles, was captured. Subsequently digital image processing was performed to obtain the full displacement field without the need to correct for machine compliance. Prior to each test being conducted, calibration photos were taken of the region of interest.

The images of the specimen captured during testing were used to calculate displacement and strain. Figure 6-9 shows the progression of a tensile test. The strain increased as the specimen was loaded. Initially, the strain was greatest near to the bottom edge at the grip as shown in Step 0 and Step 100 in Figure 6-9. In the region of interest, indicated by the vertical line in Figure 6-9, the strain distribution was uniform at each snapshot.

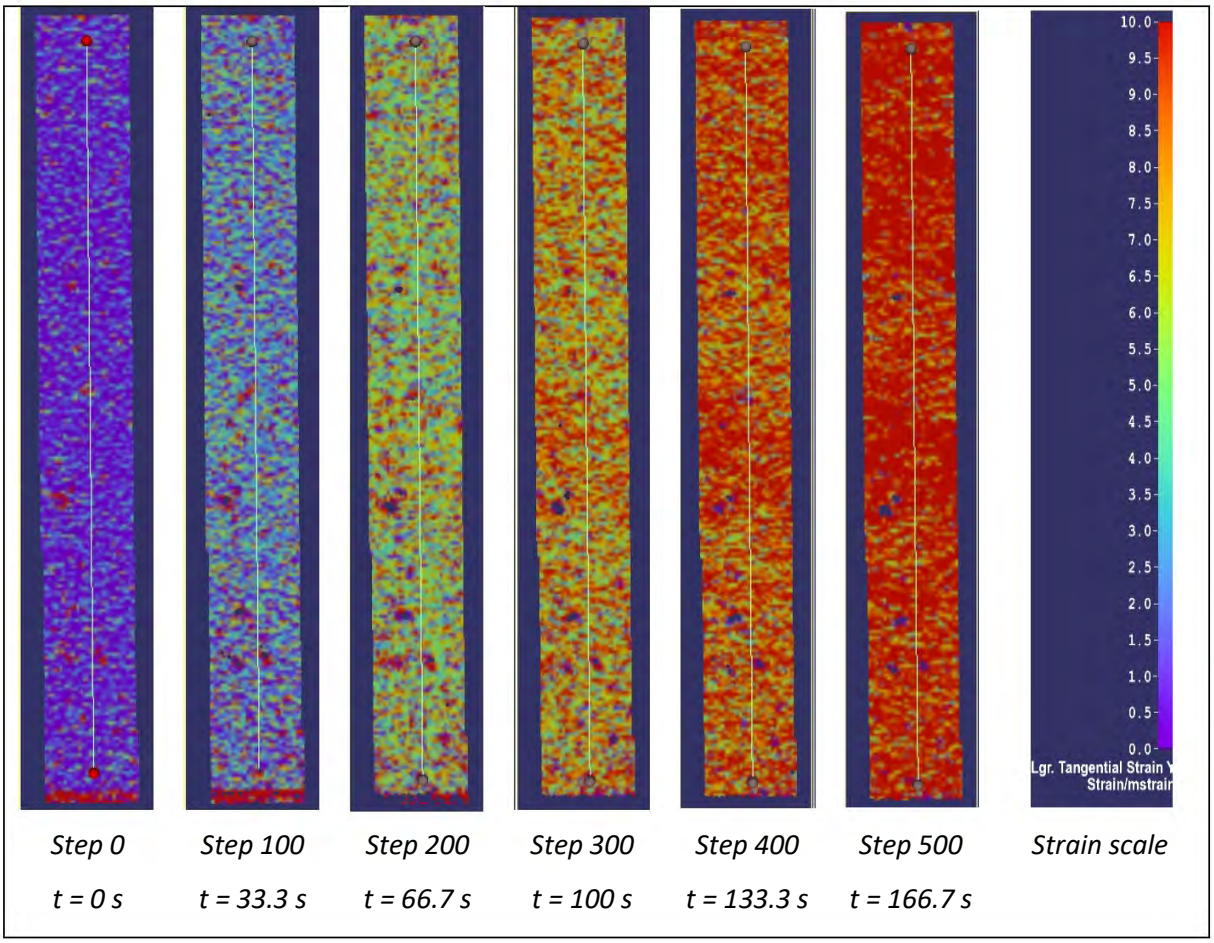

Figure 6-9: Visual graphic of the Lagrange strain in the y-direction at different time intervals

There were limitations at large strains as some of the speckles on the specimens became highly distorted. This primarily affected the 45° glass fibre reinforced composite specimens as illustrated in Figure 6-10. As shown in Figure 6-10 at t = 917.6 s, speckles were less defined and distorted, with

larger areas were missing paint. In these large deformations, the dominating modes were fibre shifting and pull-out as well as shear, rather than pure tensile.

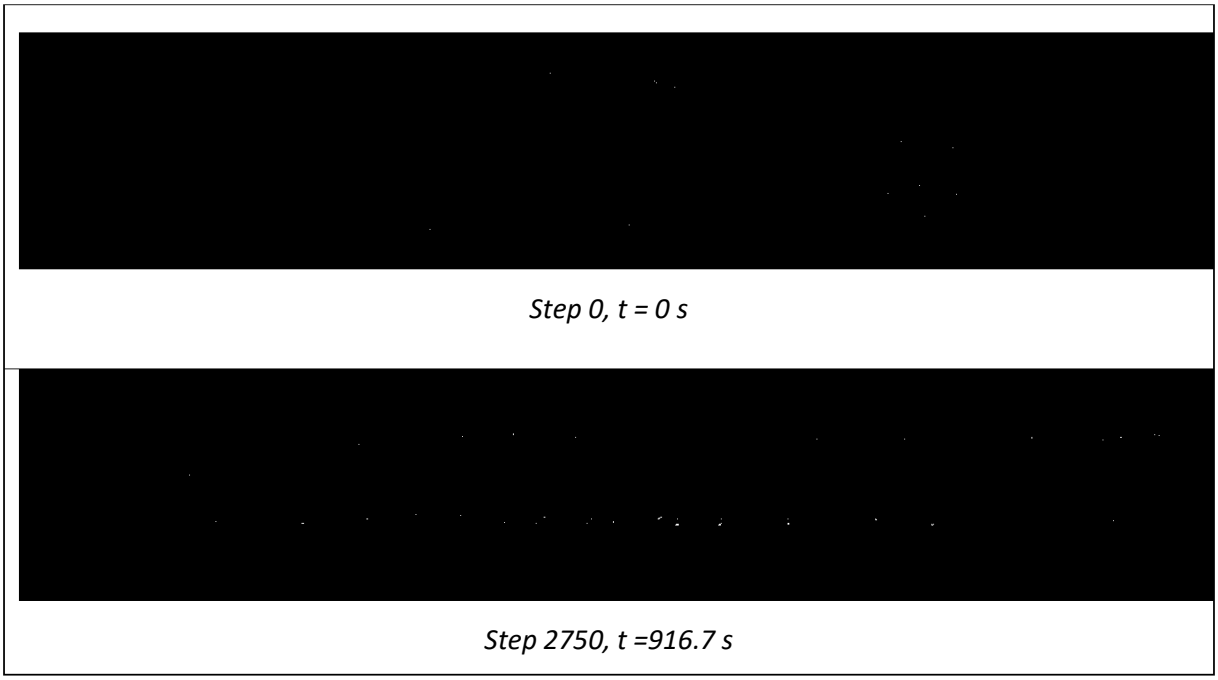

Figure 6-10: Photographs of a 45° glass fibre reinforced SuperSap specimen at two-time intervals

6.2.3 Observed failure modes

The specimens were visually inspected after testing and a three-character tensile test failure codes was recorded. The tensile test failure codes, illustrated in Figure 6-11, shows the relevant modes of failure that were applicable to the tests conducted as well as schematics of how the specimens could look [197]. For example, a LIT specimen means that the specimen failed by a lateral crack, inside the tab, at the top of the specimen. The failure code for each specimen can be found in Appendix B.

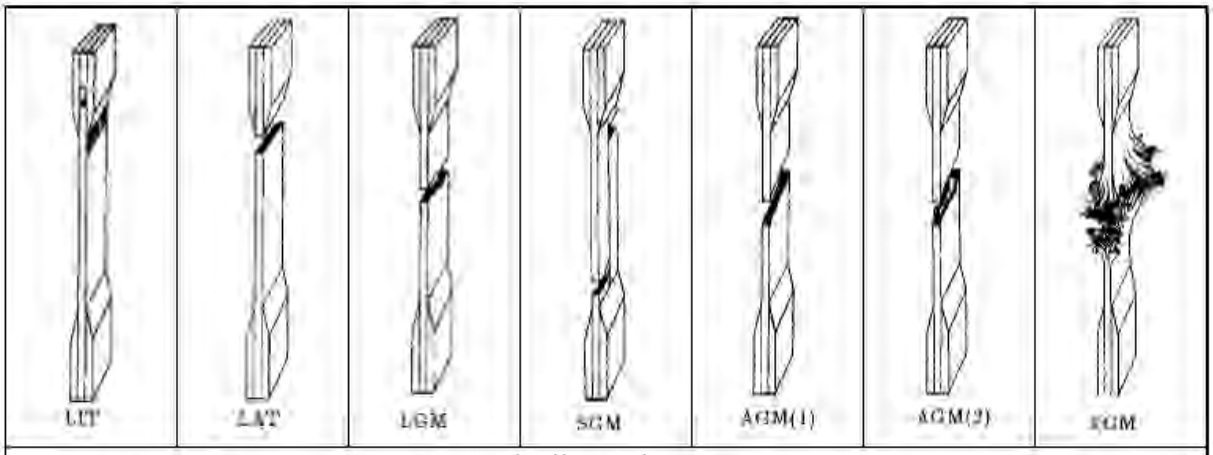

Examples of different failed specimens

Tensile test failure codes

First Character		Second Character		Third Character	
Failure Type	Code	Failure Area	Code	Failure Location	Code
Angled	A	At grip	A	Bottom	B
Lateral	L	Within gauge length	G	Middle	M
Multi-mode	M	< One width from a grip	W	Top	T
Split	S				
Explosive	X	Inside the tab	I		

Figure 6-11: Tensile test failure codes/typical modes (adapted from Ref. [197]**)**

Table 6-5 summarises the different characters for the tensile test failure code (type, area, and location) for different configurations, where the most common mode is noted by the character in bold. In general, most composites failed at the bottom or top, near the grips. Likely because of the higher stress concentration at the clamped area. Additionally, a lateral crack was commonly observed for the natural fibre composites and particularly for the flax fibre Prime 20LV and 12 mm Supawood specimens where only a lateral crack failure occurred.

Table 6-5: Summary of the different tensile test failure codes identified for each test material

		Tensile Test Failure Codes		
		Failure Type	Failure Area	Failure Location
Glass/SuperSap	0°	**A**, L, M, X	A, **W**	**B**, T
	90°	A, **L**, M, X	**G**, W	B, **M**, T
	45°	**A**, L	G, **W**	B, **T**
Flax/Prime 20LV	0°	**L**	G, **W**	**B**, T
	90°	**L**	**G**, W	**B**, M, T
	45°	**L**	A, G, **W**	**B**, T
Flax/SuperSap	0°	**L**	A, **I**, **G**, W	**B**, M, T
	90°	**L**	A, **G**, W	**B**, **T**
	45°	**A**, **L**	A, G, **W**	**B**, M, T
Flax/Prime 20LV -hand lay up	0° (2.5mm)	**L**	**G**, W	**T**
	0° (5 mm)	**L**	G, **W**	B, M, **T**
	0° (7.5 mm)	**L**	**G**, W	**B**, M, **T**
Jute/ Prime 20LV	0°	**L**	**A**, W	**B**, **T**
	90°	**L**	A, G, **W**	**B**, T
	45°	**A**, L	**A**, G, W	**B**, M, T
Supawood - 3 mm plain board	0°	A, **L**	**G**, W	B, **M**, T
	90°	A, **L**	A, **G**, W	**B**, M, T
	45°	A, **L**	**A**, G, W	B, **T**
Supawood - 12 mm plain board	0°	**L**	**G**, W	**M**, T
	90°	**L**	A, **G**, W	B, **M**, T
	45°	**L**	**A**, **G**, **W**	**B**, M, T
Supawood – 12 mm shaved	0°	**L**	G, **W**	B, **T**
	90°	**L**	A, G, **W**	**B**, T
	45°	**L**	A, **G**, **W**	**B**, T

Fibre pull-out and fibrous edges, as shown in Figure 6-12, were observed on the glass fibre reinforced SuperSap composites, regardless of orientation, particularly on the cracked surface. Delamination, debonding or a combination of the two were identified by the lighter colour and appeared along the specimen except at the gripped ends.

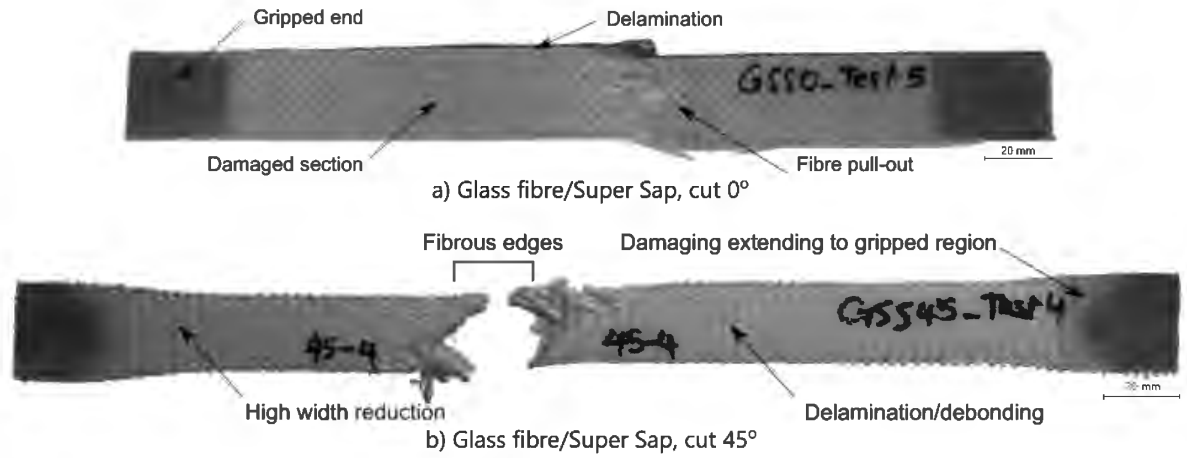

Figure 6-12: Photographs of a a) 0° and b) 45° orientated glass fibre reinforced SuperSap composite specimen subjected to tensile loading

In contrast, it was difficult to determine whether any delamination and debonding occurred in the natural fibre laminates due to the composites' opaqueness. There appeared to be some discolouration between the weaving on some of the flax fibre reinforced composites, as shown in Figure 6-13 – Figure 6-15, that could be the result of delamination or debonding. It was also possible that micro tensile failure of the matrix occurred. There did not seem to be any significant differences between the VARTM flax fibre reinforced composites and the hand lay-up flax fibre reinforced composites. Some fibre pull-out was also observed on the hand lay-up flax fibre reinforced composites, particularly on the 6 ply hand lay-up flax fibre reinforced composite shown in Figure 6-15, where the most specimens remained as one piece. This was due to the thickness of the specimen. The thinner flax fibre reinforced composites (5mm and less), irrespective of resin type and manufacturing method, had snapped into two pieces during testing.

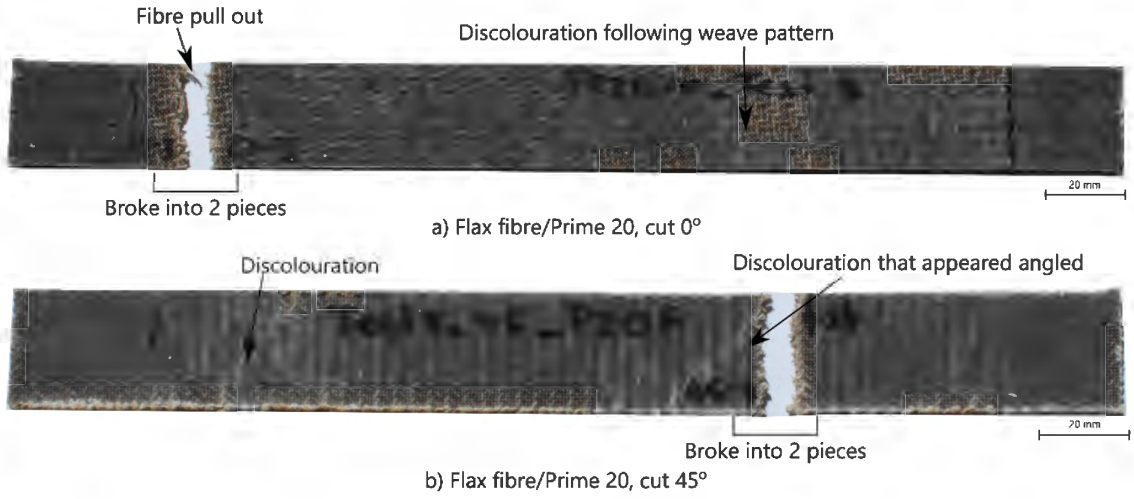

Figure 6-13: Photographs of a a) 0° and b) 45° orientated flax fibre reinforced Prime 20LV composite specimen subjected to tensile loading

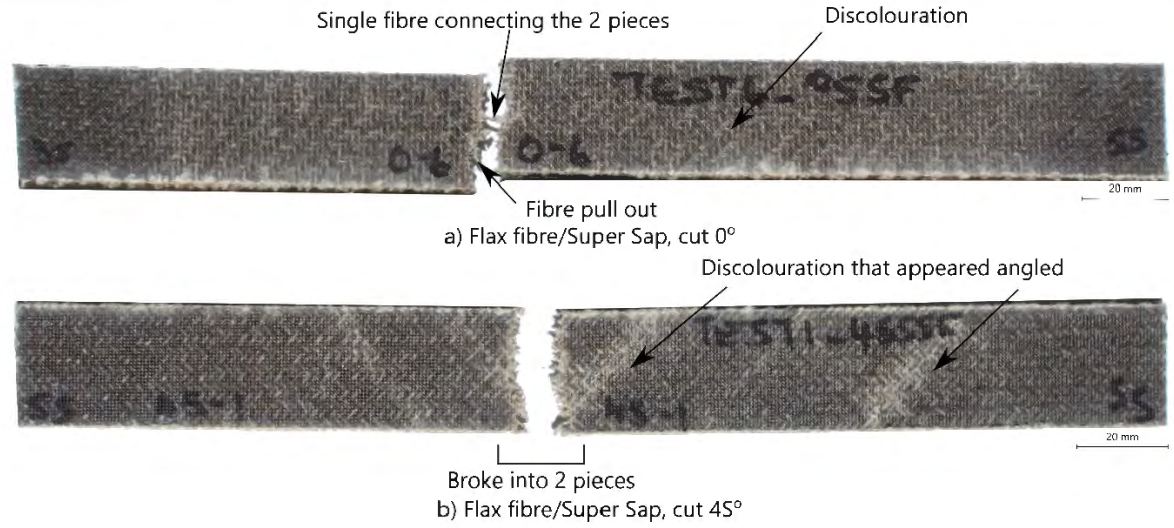

Figure 6-14: Photographs of a a) 0° and b) 45° orientated flax fibre reinforced Super Sap composite specimen subjected to tensile loading

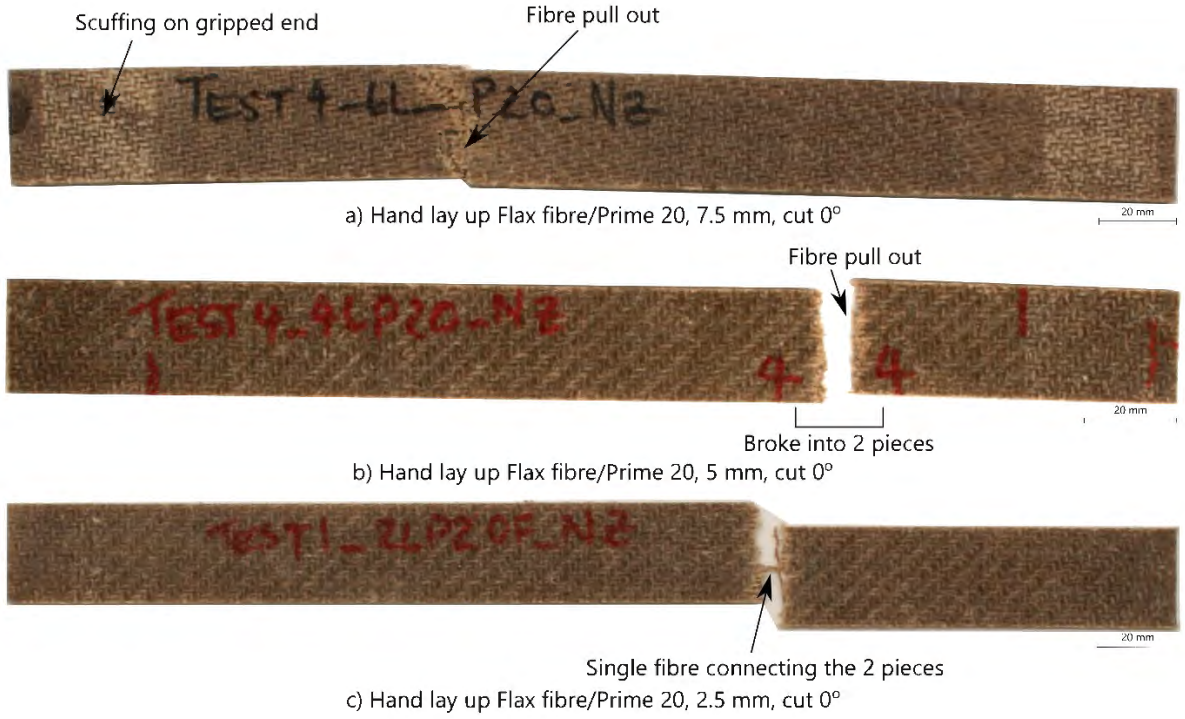

Figure 6-15: Photographs of different hand lay-up flax fibre reinforced composites (orientation 0/90°) with varying thicknesses subjected to tensile loading

The jute specimens failed in a brittle manner with a single crack found in the specimen as shown in Figure 6-16. It was particularly difficult to identify any other failure modes apart from the crack in these two types of materials. Upon visual inspection, no other areas changed colour. It was unclear whether delamination or debonding had occurred and further analysis would be required to determine the interlaminar and interfacial responses between the resin and fibres on the jute fibre reinforced composites.

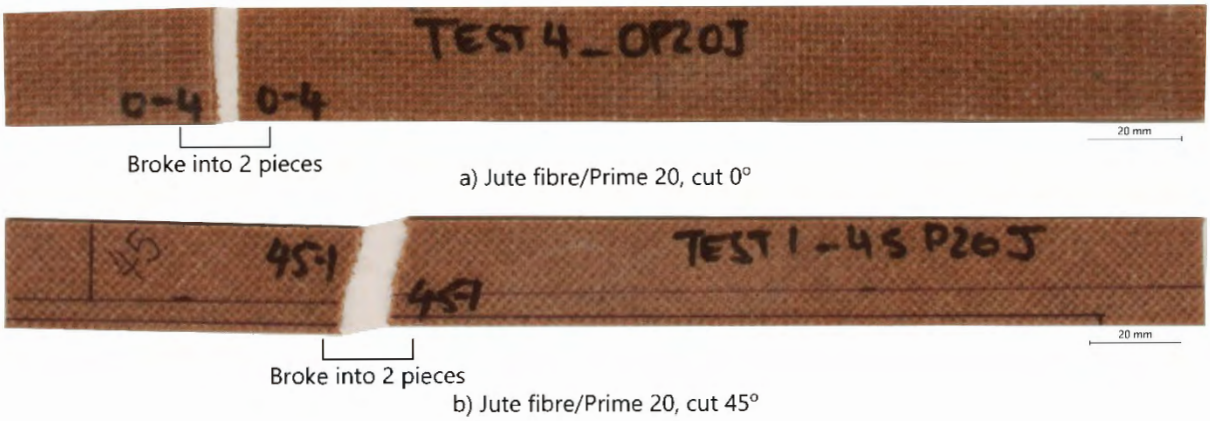

Figure 6-16: Photographs of a a) 0° and b) 45° orientated jute fibre reinforced Prime 20LV composite specimen subjected to tensile loading

Furthermore, there did not appear to be distinct dominating failure modes based on orientation or resin type for the natural fibre laminates. The main difference was that the crack was mostly angled for specimens oriented 45°. This was different to the damage observed for the 45° glass fibre composites, which included noticeable changes in specimen shape, both in length extension and width reduction, with damage extending into the gripped area and large amounts of fibre pull-out.

Similar to the jute fibre reinforced composites and thin flax fibre reinforced composites, all the Supawood specimens snapped into two pieces, irrespective of thickness as observed in Figure 6-17. The appearance of the cracks on the two types of 12 mm Supawood specimens did not seem to be different from each other. Due to the nature of the composites, specimen orientation did not appear to have an influence of the cracks observed. Furthermore, no other failure modes were observed on the specimens.

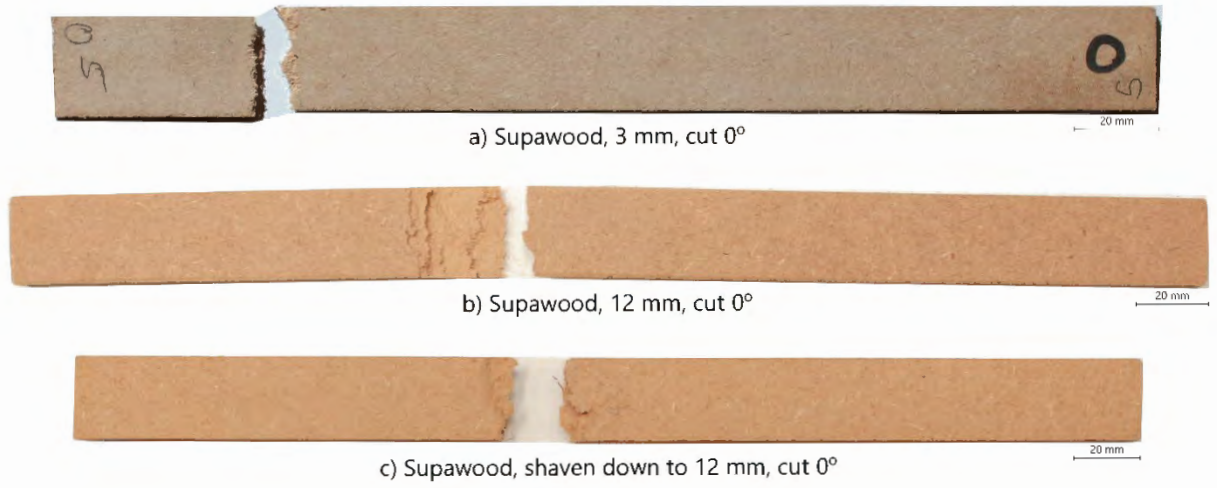

Figure 6-17: Photographs of different Supawood specimens subjected to tension

6.2.4 Tensile stress strain curves

Representative stress-strain curves are shown in Figure 6-18 to Figure 6-20. The glass fibre reinforced composites, natural fibre reinforced laminate composites and Supawood results were separated for clarity due to the differences in magnitude of the tensile strength and strain.

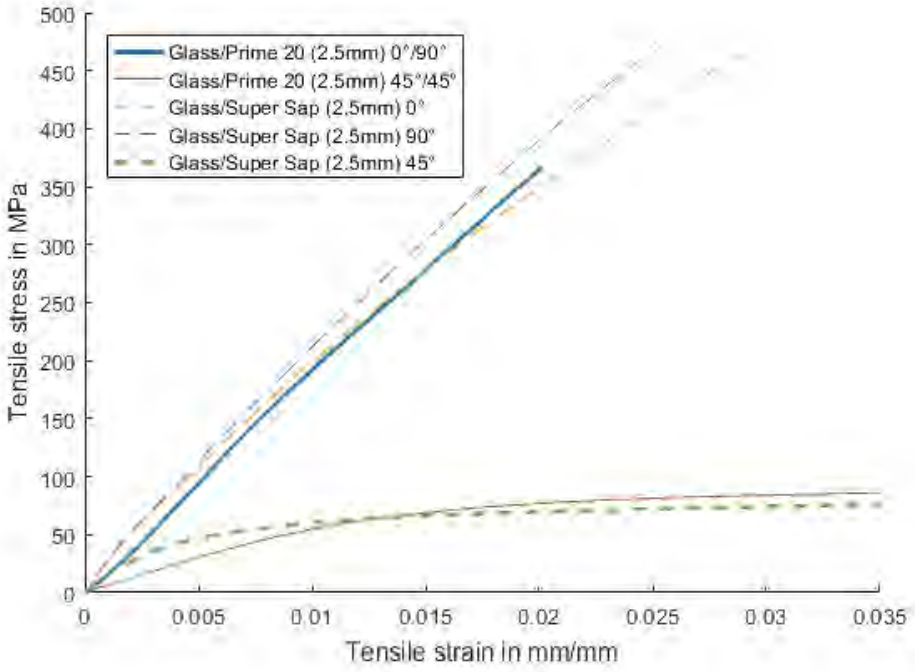

Figure 6-18: Representative tensile stress and strain curves for glass fibre reinforced composites tested (x-axis was cropped at 0.035 strain)

There was a distinct difference for the curves between the 0°/90° and 45 ° orientations. The curves for the specimens cut in the 0° and 90° orientation were similar in shape; both curves initially had a linear curve up to a point, thereafter the curve diverged slightly, and the slope decreased. It was possible that the fibres were beginning to fracture during this transition. The 45° cut specimens had a clear bilinear response, where the curve appeared to plateau after a period. It was also significantly weaker compared to the other specimens cut in the 0°/90° directions. The 45° specimens were elongated by at least 20 % of their original lengths. The change of resin did not seem have a measurable impact on the shape of the curve of the 0°/90° specimens. The initial gradient between the 45° specimens was slightly different, where the Prime 20LV specimens were longer with a shallower gradient.

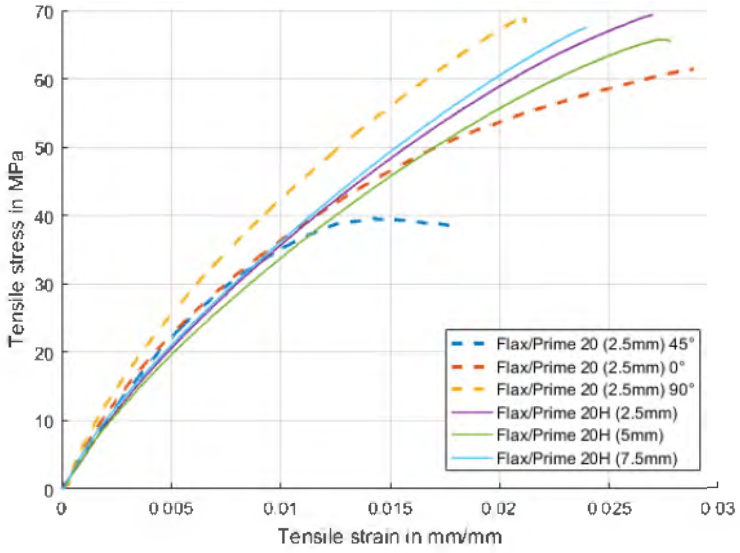

a) Hand lay-up and VI flax fibre reinforced Prime 20LV composites

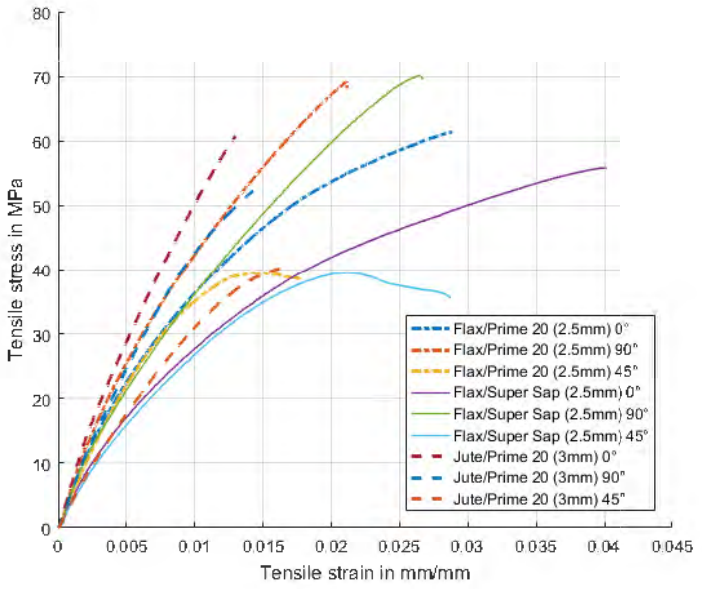

b) VI flax and jute fibre reinforced composites

Figure 6-19: Representative tensile stress and strain curves for flax and jute fibre reinforced composites tested

The stress – strain responses for the 0°/90° laminate natural fibre composites were non-linear with a lower maximum stress value and longer strain to failure in comparison to the 0°/90° GFRP. In Figure 6-19a, the curves for the hand lay-up flax fibre reinforced composites were in the same range as the 0°/90° VI flax fibre reinforced composites. Additionally, noticeable changes in the shape of the curve were not apparent, despite the increasing thickness of the hand lay-up specimens. In Figure 6-19b, it

was difficult to determine what effect the resin had on the flax fibre reinforced composites, but a steeper gradient was noticeable in the Prime 20LV composites. The jute fibre reinforced composites had lower strain to failure and lower failure strength compared to the flax fibre reinforced composites, but the shape appeared similar. The orientation of the fibre affected the results for the natural fibre laminates. The 45° specimens, despite having a lower strain capacity and stress magnitude, behaved similarly to the 45° GFRP with a slight plateau after reaching maximum stress.

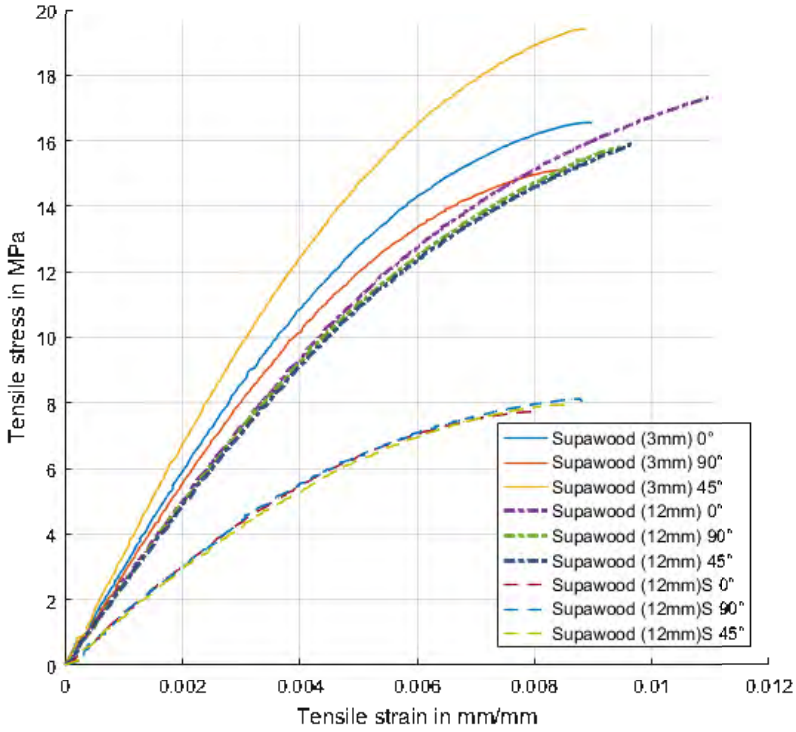

Figure 6-20: Representative tensile stress and strain curves for Supawood boards tested

Similar to the flax and jute fibre reinforced composites, the curves for the Supawood specimens were non-linear. No obvious variation between the orientation was observed, as expected, considering the fibres are randomly orientated. The shaven Supawood specimens had a significantly lower slope and lower strength compared to plain 12 mm Supawood board indicating that the more compressed outer edges contributed to the tensile strength of the board. The strain to failure was, however, similar.

6.2.5 Overview of tensile test results and discussion

The mean and standard deviation for the tensile properties are listed for the laminate composites in Table 6-6, and Supawood in Table 6-7. These properties, found from the stress-strain curve, include the modulus of elasticity, apparent elastic limit, ultimate tensile strength, and strain at failure.

With regards to the effect of specimen orientation, there did not appear to a measurable difference between the 0° and 90° specimens for the laminated fibre composites. However, as expected the 45°

specimens all tended to have lower tensile stress and a higher strain at failure value, particularly for the glass fibre reinforced composite specimens. The elastic limit for 45° GFRP and jute fibre reinforced composites were less than a third of their ultimate tensile strength. It was likely that the fibre load direction and the strength of the fibres, especially whether the specimen had resin dominated properties, contributed to the elastic limit of the materials.

The results from the tensile testing were thus similar to the flexural results. The tensile strength for GFRP were significantly greater than the natural fibre composites, and Supawood had the lowest property values overall. In general, the tensile properties did not appear to be dependent on the type of manufacturing used unlike the flexural properties. Tensile proprieties were influenced by the fibre and resin type. Additionally, off-axis loading (45°) in the composites reinforced with woven textiles typically had weaker property values.

Table 6-6: Average and standard deviations of tensile properties for laminate fibre reinforced composites

	Modulus of elasticity, E^T [GPa]		Apparent elastic limit, σ^T_Y [MPa]		Ultimate tensile strength, σ^T_U [MPa]		Strain at failure, ε^T_{fail} [m/m x10^3]	
	mean	*Std Dev*	*mean*	*Std Dev*	*mean*	*Std Dev*	*mean*	*Std Dev*
Glass/SuperSap 2.5mm 0°	19.17	0.29	214.5	12.3	449.3	12.0	26.5	4.3
Glass/SuperSap 2.5mm 90°	20.57	0.36	223.8	24.5	445.7	21.7	22.2	5.3
Glass/SuperSap 2.5mm 45°	8.89	0.22	45.9	1.3	146.8	4.4	>110	-
Glass/Prime 20LV 2.5mm 0°/90°	20.36	0.34	164	27.7	359	9	19.6	0.6
Glass/Prime 20LV 2.5mm 45°/45°	6.68	0.67	45.5	2.2	109.7	2.0	> 80	-
Flax/SuperSap 2.5mm 0°	2.95	0.13	20.6	1.3	55.6	1.5	40.1	3.8
Flax/SuperSap 2.5mm 90°	3.65	0.07	31.5	0.5	69.2	0.9	26.1	1.1
Flax/SuperSap 2.5mm 45°	2.87	0.04	19.7	0.5	39.2	0.9	33.1	6.3
Flax/Prime 20LV 2.5mm 0°	4.08	0.18	28.2	1.6	60.4	2.3	29.0	2.5
Flax/Prime 20LV 2.5mm 90°	4.56	0.12	33.4	1.1	70.0	2.7	21.8	0.9
Flax/Prime 20LV 2.5mm 45°	3.88	0.21	23.0	2.3	39.9	0.5	21.7	0.9
Flax/Prime 20LV 2.5mm	3.86	0.61	28.5	5.5	66.2	3.0	25.6	1.6
Flax/Prime 20LV 5mm	3.76	0.22	27.3	1.9	66.7	1.8	26.1	1.5
Flax/Prime 20LV 7.5mm	3.82	0.06	28.8	0.8	64.9	2.4	22.1	2.6
Jute/Prime 20LV 2.5mm 0°	6.52	0.25	12.6	0.6	61.9	6.2	14.0	1.3
Jute/Prime 20LV 2.5mm 90°	5.44	0.24	10.8	0.6	50.9	3.1	14.3	1.1
Jute/Prime 20LV 2.5mm 45°	3.84	0.21	9.5	1.0	41.2	0.9	17.6	1.2

Table 6-7: Average and standard deviations of tensile properties for Supawood specimens

	Modulus of elasticity, E^T [GPa]		Apparent elastic limit, σ^T_Y [MPa]		Ultimate tensile strength, σ^T_U [MPa]		Strain at failure, ε^T_{fail} [m/m x10^3]	
	mean	*Std Dev*	*mean*	*Std Dev*	*mean*	*Std Dev*	*mean*	*Std Dev*
Supawood 3mm 0°	2.95	0.05	7.3	0.4	16.8	0.5	8.9	1.0
Supawood 3mm 90°	2.78	0.07	6.7	0.2	15.0	0.4	8.4	0.5
Supawood 3mm 45°	3.33	0.06	8.3	0.4	19.7	0.7	9.3	1.0
Supawood 12mm 0°	2.52	0.04	7.3	0.6	18.0	0.5	12.0	0.7
Supawood 12mm 90°	2.41	0.08	7.5	1.4	15.6	0.6	10.0	1.0
Supawood 12mm 45°	2.44	0.04	8.0	0.5	17.2	0.8	11.2	1.3
Supawood 12mm-S 0°	1.55	0.04	3.9	0.2	7.4	0.2	7.0	1.0
Supawood 12mm-S 90°	1.58	0.09	4.1	0.6	8.2	0.2	8.7	0.5
Supawood 12mm-S 45°	1.51	0.05	3.9	0.7	7.8	0.2	8.1	0.8

6.3 Fibre reinforced composite interlaminar Mode I tests

As discussed in the literature review (chapter 2), delamination was a common failure mode observed in the blast loading of both carbon and glass fibre reinforced composites. Mode I DCB tests were conducted on the different laminates to characterise the delamination resistance. Mode I describe the opening or tensile mode of propagation of a crack [23]. While specimen geometry and loading conditions play a significant role in interlaminar stress, the interlaminar strength is a material dependant value [200]. Therefore, determining the interlaminar strength from Mode I DCB tests of the different composites will provide insight on how resistant the composite is to delamination and consequently blast damage (which has been shown to cause significant delamination in many FRP composites [133]).

6.3.1 Mode I DCB specimens and test method

Specimens were manufactured and prepared as described in Chapter 5 where loading blocks were glued onto the specimens. The specimens tested, 125 mm in length and 25 mm wide, were manufactured with a thin film at the mid plane. This acted as a pre-crack in the middle of the laminate.

The laminate thickness was dependent on the composite and number of plies as shown in Table 6-8. According to //9996 [195], the thicknesses of DCB specimens are normally between 3 and 5 mm, which is suitable for the glass fibre reinforced composites. However, the recommended thickness was doubled (between 6 and 10 mm) for the flax and jute fibre reinforced composites so that there were enough plies in the laminate to make stiffer specimens. According to Zulkifli et al [201], while the number of plies affected the interlaminar fracture toughness, during testing the delamination damage tended to grow slowly and more stably with an increasing number of plies.

Table 6-8: Number of plies, thickness and length of initial crack in DCB specimens

Material	Total number of plies	Average thickness [mm]
Glass fibre/ Prime 20LV	12 (6/6)	4.02
Glass fibre/ SuperSap	12 (6/6)	3.65
Flax fibre/ Prime 20LV	8 (4/4)	9.00
Flax fibre/ SuperSap	8 (4/4)	9.01
Jute fibre/ Prime 20LV	10 (5/5)	7.62

The specimens were attached to the Zwick machine using pins in the loading blocks. The bottom plate moved downwards at a constant displacement rate of 2 mm/min allowing the composite to separate at the crack position. Figure 6-21 shows a flax fibre reinforced composite specimen during testing. The composite split into two halves because of the resulting load and the test continued until the crack extended through the whole specimen.

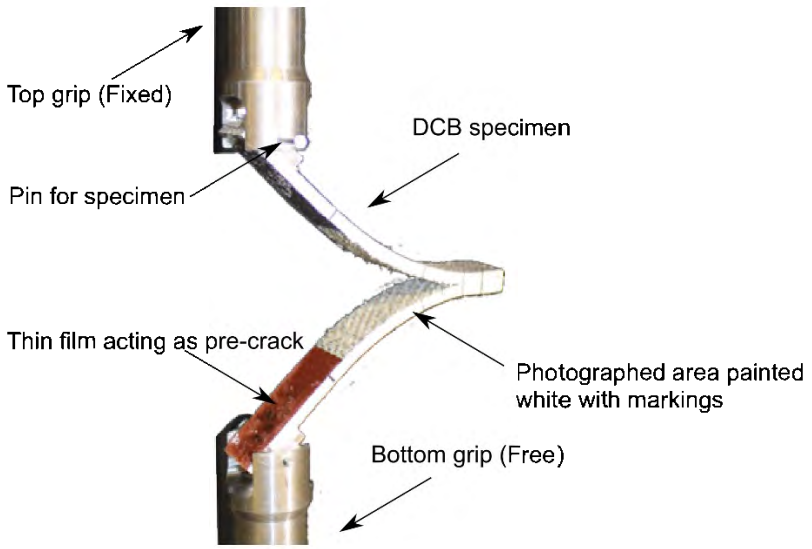

Figure 6-21: DCB test of a flax fibre reinforced composite specimen

During testing, the deformation of the specimen was recorded using a camera at a rate of one frame every 15 seconds. The rate was increased for the jute fibre reinforced composites to a frame every 10 seconds, because these specimens broke earlier on. From these images, the crack length was determined, using image processing techniques. In conjunction with the force and load point displacement data from the Zwick. An example of the results for a test is shown in Figure 6-22.

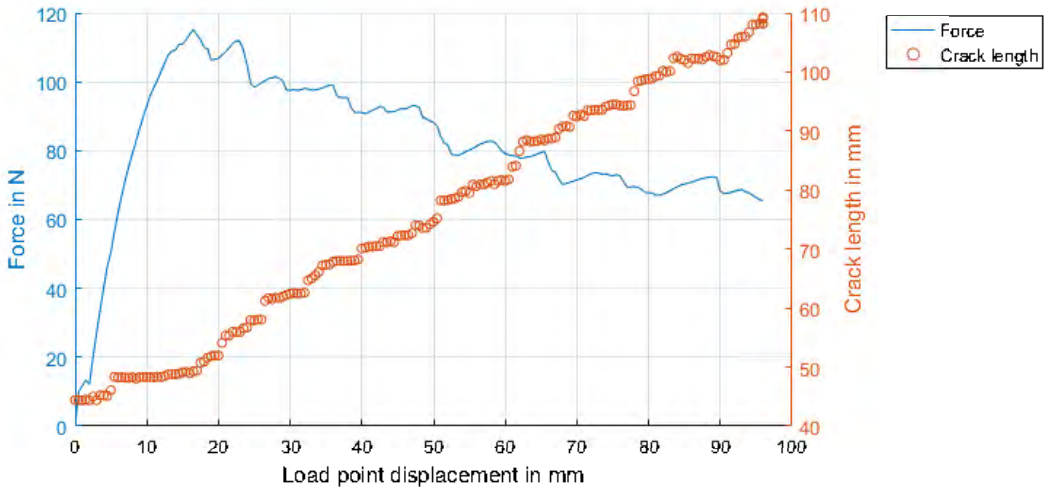

Figure 6-22: Plot of force and crack length versus load point displacement for a flax fibre reinforced Prime 20LV specimen

In a review conducted by Nasuha et al [200], Modified Beam Theory (MBT) was found to yield conservative values for strain energy release rate for a double cantilever beam, G_I. Therefore Equation 6-6 [195] was used to determine G_I. The equation elongates the delamination term $(a + |\Delta|)$ to compensate for rotations that may occur on the delamination front.

$$G_I = \frac{3P\delta}{2b(a + |\Delta|)} \qquad 6\text{-}6$$

where P = measured force, δ= measured deflection, b = average width of the specimen, and a = delamination (crack) length.

The Δ value is the x-intercept from the linear graph where delamination length is plotted as a function of the cubic root of compliance, C, where C is the ratio of the load point displacement to the measured force, δ/P, [195]. Using least squares regression to determine a linear line that best fits the data, Δ was found using Equation 6-7.

$$\text{Slope, } m = \frac{N\sum\left(aC^{\frac{1}{3}}\right) - \sum a \sum C^{\frac{1}{3}}}{N\sum(a^2) - (\sum a)^2}$$

$$Intercept, c = \frac{\sum C^{\frac{1}{3}} - m\sum a}{N}$$

$$\therefore \Delta = \frac{-c}{m} \qquad 6\text{-}7$$

where N = total number of data points

Large displacement and end block corrections were implemented by including the parameters F and N described by Equations 6-8 and 6-9 respectively. The corrected compliance, C/N, was used to determine the Δ value, then G_I was multiplied by F/N to obtain the corrected value of G_I.

$$F = 1 - \frac{3}{10}\left(\frac{\delta}{a}\right)^2 - \frac{3}{2}\left(\frac{\delta t}{a^2}\right) \qquad 6\text{-}8$$

$$N = 1 - \left(\frac{L'}{a}\right)^3 - \frac{9}{8}\left[1 - \left(\frac{L'}{a}\right)^2\right]\left(\frac{\delta t}{a^2}\right) - \frac{9}{35}\left(\frac{\delta}{a}\right)^2, if \ \ a < 50\ mm$$

$$N = 1, a \geq 50\ mm \qquad 6\text{-}9$$

where, in this case, L' is half the length of the end block and t is the addition of half the thickness of the end block and a quarter of thickness of the specimen.

6.3.2 Results of the DCB tests

Figure 6-23 shows a representative curve taken from one of the specimens from a test series showing the force and the corresponding crack length with respect to the load point displacement. The results obtained from Zwick data showed that the force for GFRP were lower than those of the natural fibre composites, as depicted in Figure 6-23a. It appeared that at a load point displacement of about 20 mm, all composites except for the jute fibre reinforced composites (which failed at this point) had reached their maximum stress. For GFRP, the crack length grew noticeably after this period whereas the crack growth seemed to start earlier in the test as shown in Figure 6-23 (b). The crack growth was more stable during testing for all the specimens tested.

Subplots for all the quasi-static DCB tests on the different materials presenting G_I as the function of crack length are shown in Figure 6-24. In GFRP (see Figure 6-24a and Figure 6-24b), the data exhibited similar tendencies: the crack length remained constant initially while G_I increased. After reaching a point, the crack length increased while values for G_I fluctuated within a range from this point. However, G_I seemed to increase with increasing crack length for the flax fibre Prime 20LV reinforced composites until it eventually started to plateau as shown in Figure 6-24c after a crack length of 60 mm. For the flax fibre reinforced Super Sap composites, the G_I initially appeared to plateau at 60 mm

but increased after reaching a crack length of 80 mm. A limited amount of data was obtained for the strain energy release rate of jute fibre reinforced composites, as shown in Figure 6-24e.

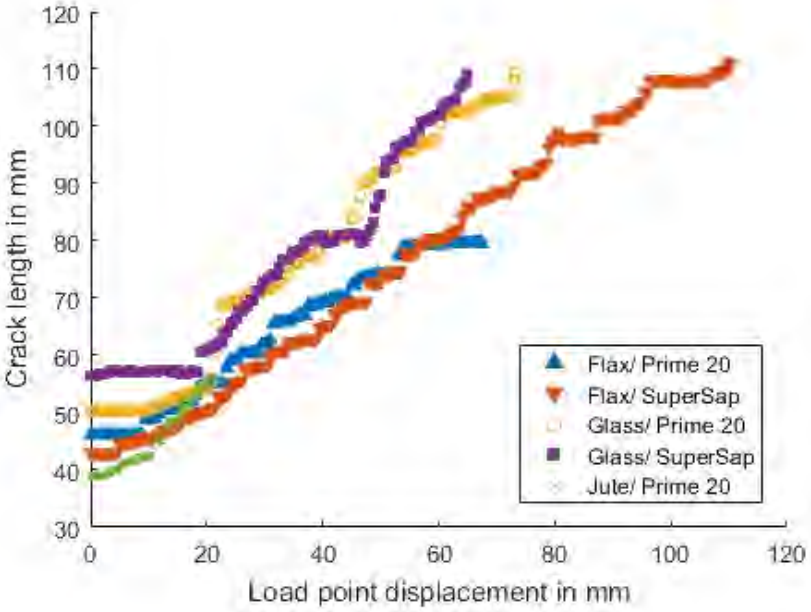

a) Crack length versus load point displacement

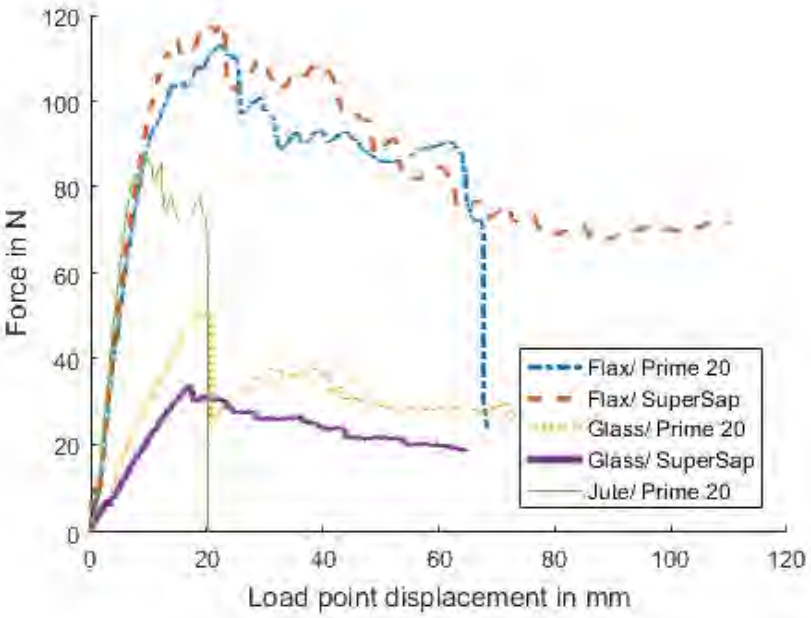

b) Force versus load point displacement

Figure 6-23: Plots of crack length and corresponding force against load point displacement

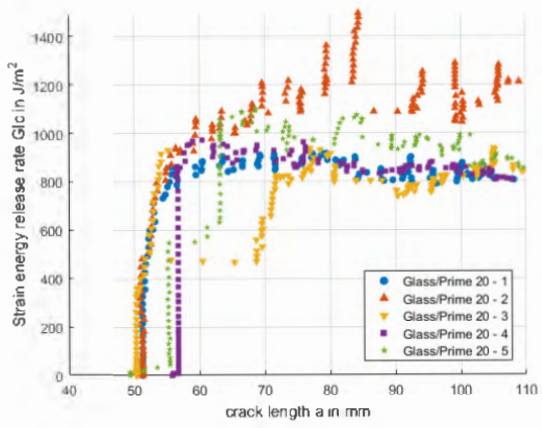

a) Glass/ Prime 20LV

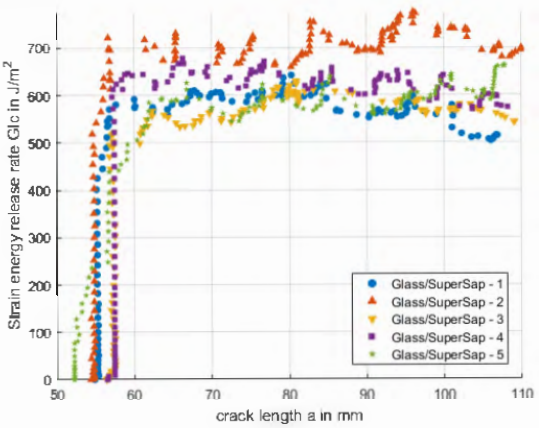

b) Glass/ SuperSap

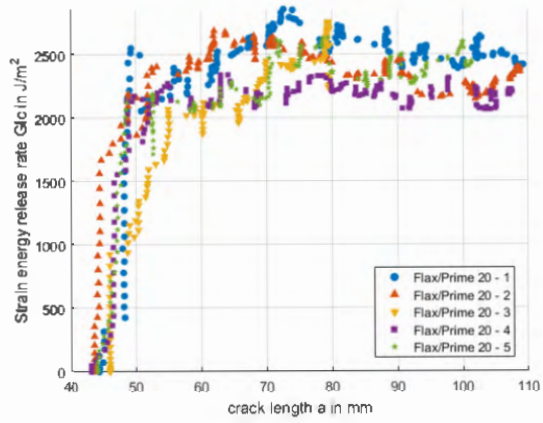

c) Flax/ Prime 20LV

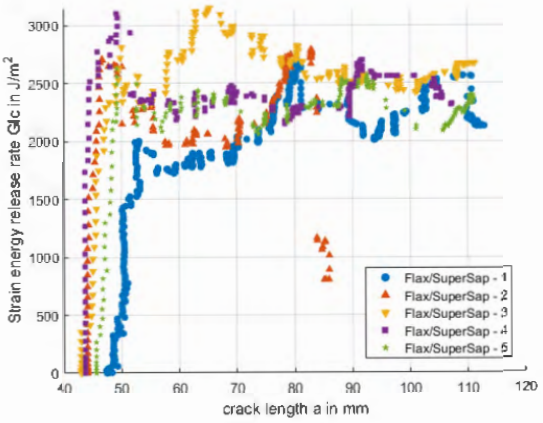

d) Flax/ SuperSap

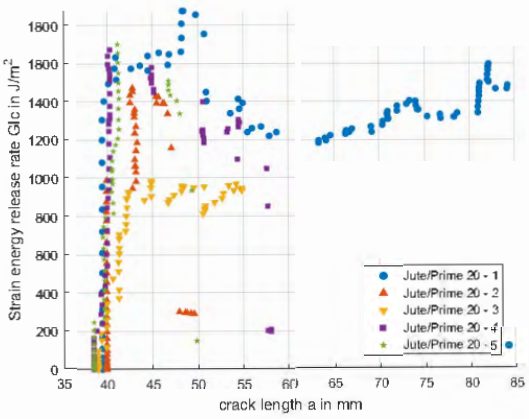

e) Jute/ Prime 20LV

Figure 6-24: Plot of strain energy release rate against crack length for all DCB specimens

The jute fibre reinforced composites specimens broke early on during testing shown in Figure 6-25. The specimens had a crack through its thickness rather than propagating throughout the mid plane of the specimen. This indicated that the energy required to propagate a crack was higher than the shear

stress. Figure 6-26 depicts photographs of the tested specimens made from the different materials. It can be observed that the crack growth was within the centre of the specimen.

Figure 6-25: Photograph of broken DCB tested jute fibre reinforced composite specimens

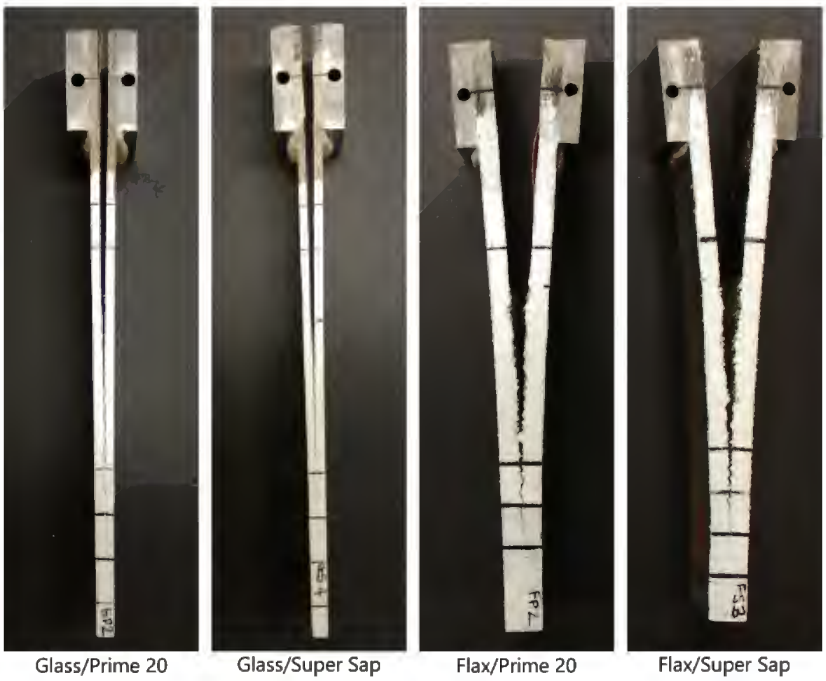

Figure 6-26: Photographs of different DCB tested specimens

The average values of G_{Ic} determined for the different composites is shown in Table 6-9. The fracture toughness at initiation, $G_{Ic,init}$, was visually determined based on the change in crack length from the initial vertical line. The data then starts to deviate as the crack propagated (see Figure 6-24). From this region, the average value for the propagation fracture toughness $G_{Ic,prop}$ was determined. The results

for the jute fibre reinforced composites were taken using a similar method. Pinto et al [202] found that plain weave 330 g/m^2 jute fibre reinforced epoxy composites had an $G_{Ic,init}$ of approximately 1400 J/m^2. Therefore, it should be noted that the values for the jute fibre reinforced composites could be higher than the values listed.

Table 6-9: Average values of the fracture toughness at initiation and propagation

	$G_{Ic,init}$ [J/m^2]	$G_{Ic,prop}$ [J/m^2]
Glass /Prime 20LV	819	918
Glass /SuperSap	531	618
Flax /Prime 20LV	2272	2334
Flax /SuperSap	2388	2474
Jute /Prime 20LV	1257[a]	1356[a]
a – based on the small dataset available. Results were inconclusive as through thickness cracking occurred.		

The highest values obtained for the interlaminar fracture toughness was for the flax fibre reinforced composites. Similar results for $G_{Ic,init}$ were found for the woven 500 g/m^2 flax fibre reinforced epoxy composites where $G_{Ic,init}$ and $G_{Ic,prop}$ were approximately 2000 J/m^2 and 3500 J/m^2 respectively [203]. Glass fibre reinforced SuperSap composites had a lower interlaminar fracture toughness than the glass fibre reinforced Prime 20LV composites. However, the opposite results were observed for the flax fibre reinforced composites with the two resin systems. The initial and propagation values for G_{Ic} were very similar for the all the laminates tested. It was possible that high values found interlaminar toughness for the natural fibres because the crack did not stay within the interlaminar zone but crossed the reinforcement layer. Therefore, it was more likely that through-thickness cracks rather than large amounts of delamination would occur in the natural fibre laminates. In comparison, GFRP would delaminate.

6.4 Through-thickness testing for Supawood

Two types of quasi-static tests were performed on Supawood to determine some characteristics of the internal bond of the material. Considering that Supawood is not a traditional laminated composite and is manufactured from compressed short wood fibres and a binder, tensile and compression tests through the thickness of specimen were performed. SANS 6016 [204] specification was used as a basis to determine test procedures and geometries. All specimens were cut from the same 16 mm thick board that was used for the blast tested specimens.

6.4.1 Overview of through-thickness tensile tests

Five square 40 x 40 mm test specimens were tested at a crosshead speed of 1 mm/min. T-shaped steel loading blocks were glued onto specimen using a high strength Spabond epoxy to form the test specimen, illustrated in Figure 6-27. The assembly was placed into grips of the Zwick 1484 testing machine. The crossheads moved apart causing a tensile force on the specimen through its thickness. The test was performed until specimen failure occurred when the measured force dropped significantly.

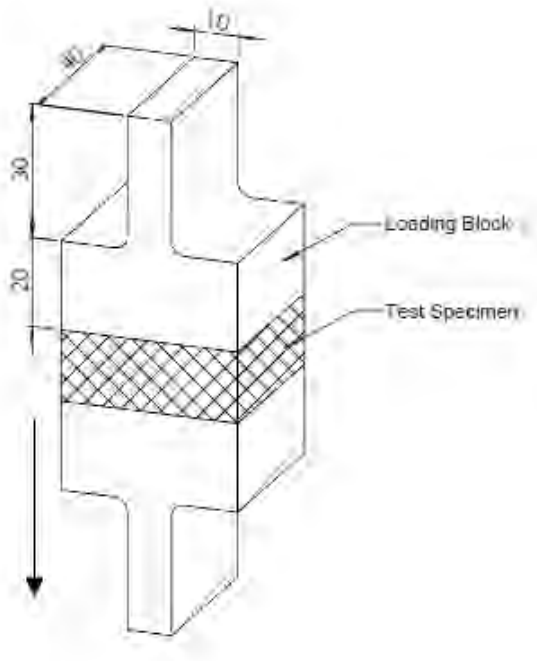

Figure 6-27: Test specimen and loading blocks assembly

The test was used to determine the through thickness (transverse) tensile strength or internal bond strength of the 16 mm Supawood panel used for blast testing. The force and displacement were recorded. The resulting tensile stress was determined using Equation 6-8. According to SANS 6016 [204], the transverse tensile strength of the board was defined as the mean value obtained for the maximum tensile strength for five specimens.

$$\sigma = \frac{P_{max}}{b\,w} \qquad 6\text{-}10$$

Where P_{max}= maximum applied tensile force before the specimen fails, w = average width of the specimen, and b = average length of the specimen.

Five specimens were tested, and results are shown in Table 6-10. The transverse tensile strength was found to be 0.38 MPa which was lower than stipulated in the data sheet for Supawood at 0.5 MPa

[190]. However, determining the tensile strength perpendicular to a surface was found to be troublesome, especially gluing loading blocks and inserting the specimen onto the machine.

Table 6-10: Transverse tensile testing results and cross-sectional area geometry for Supawood 16mm board

	Transverse tensile strength, σ_T [MPa]
MDF 16mm -1	0.36
MDF 16mm -2	0.19
MDF 16mm -3	0.33
MDF 16mm -4	0.69
MDF 16mm -5	0.34
Average	0.38

As the specimen failed, a crack would form through the Supawood. The position where the crack was formed is shown in Figure 6-28. Cracks tended to occur near the mid-plane of the specimen, as expected, because the outer surfaces of Supawood board were denser compared to the centre of the material.

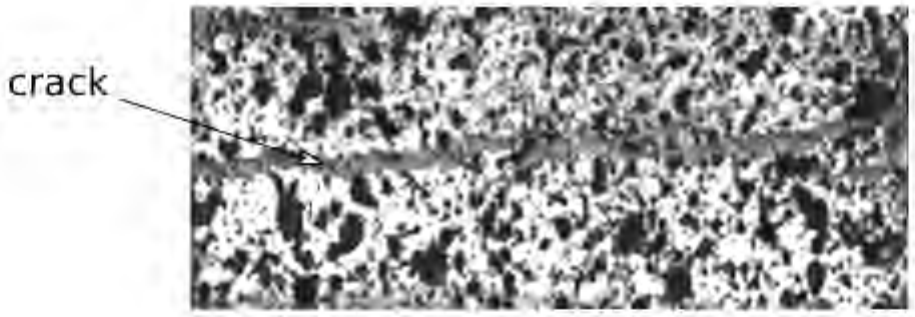

Figure 6-28: Photograph of a transverse tensile Supawood 16mm board specimen

6.4.2 Overview of through-thickness compression tests

No standards were found for transverse compression tests in the South African National Standard for uncoated fibreboard products [205] or ASTM standards for evaluating properties of wood-based fibre and particle panel materials [206]. Therefore, similar to the square geometry used in SANS 6016 [204], 16mm thick boards were cut into 25 mm x 25 mm blocks and were tested under compressive loading.

The specimen was placed between a cylindrical loading block and flat bottom plate. The flat bottom plate was set to move towards the stationary cylindrical loading block, loading the specimen in compression through the thickness. The specimen was compressed until the measured force dropped. The transverse compressive strength was calculated using Equation 6-8, where P_{max} was the measured maximum compressive force onto the specimen instead.

The stress-strain curves obtained from the compression tests are shown in Figure 6-29. The curves were all similar, confirming the consistency of the material. Initially, the curves exhibited an elastic response up to about 0.007 strain, followed by a steep non-linear increase in strength. This was possibly due to the compression of less dense internal mid-section of the specimen.

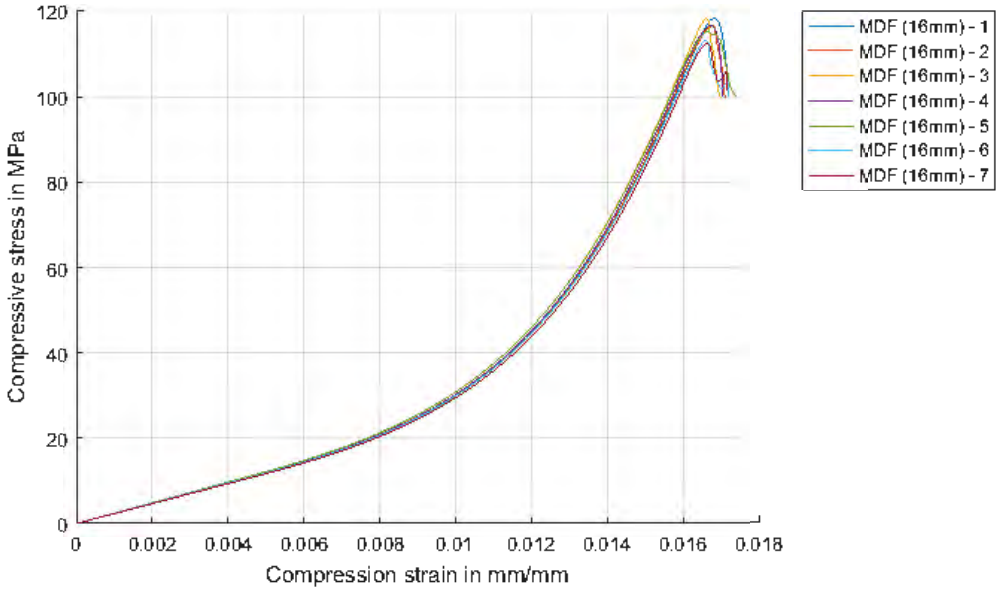

Figure 6-29: Through-thickness compression stress and strain curves for Supawood 16mm board

The transverse compression test results of the Supawood 16mm board are listed in Table 6-11. The resulting transverse compression strength and strain at failure of the Supawood panel was found to be 115.5 MPa and 0.0172 respectively.

Table 6-11: Transverse compression testing results for Supawood 16mm board

	Transverse compressive strength, σ_c [MPa]	Compressive strain at failure, ε^c_{fail} [mm/mm]
MDF 16mm -1c	118.05	0.0172
MDF 16mm -2c	116.23	0.0171
MDF 16mm -3c	117.95	0.0170
MDF 16mm -4c	116.36	0.0170
MDF 16mm -5c	114.93	0.0174
MDF 16mm -6c	112.71	0.0172
MDF 16mm -7c	112.20	0.0171
Average	115.5	0.0172

6.4.3 Overview on through-thickness tests

Based on these experiments, it was found that the transverse strength of 16 mm Supawood panel was far greater in compression than tensile, as expected. The low internal (tensile) bond strength of the panel could be due to its low-density structure with lots of voids within the panel.

6.5 Summary of chapter

A summary of the properties of the different materials used is in Table 6-12. In terms of flexural and tensile strength, the glass fibre reinforced composites were superior to the natural fibres tested. However, the interlaminar fracture toughness was lower for the glass fibre reinforced composites. The flax FRPs were the strongest natural fibre composites tested, followed by jute FRP and then Supawood. The shear stress of the jute fibre reinforced composites was lower than its interlaminar fracture toughness. In general, this composite behaved in a brittle manner for all the different tests. Supawood had very consistent repeatable results but were found to have low strength.

The resin, whether SuperSap or Prime 20LV, could significantly influence the results depending on the type of fibre. Moreover, the modulus of the glass fibre reinforced composites tended to be similar with no significant differences for the two resin types. However, in the flax fibre reinforced composites, since the fibre was weak in comparison to glass fibre, the effect of the resins was more noticeable. Additionally, similar curves were observed for the jute and flax fibre reinforced composites manufactured using the same resin, Prime 20LV. The relationship between the stress and strain of the specimens, for the most part, were linear for the glass fibre reinforced composites but non-linear for the natural fibre composites.

Manufacturing and fibre orientation also affected the different properties tested. Strength properties were higher for the VI manufactured flax fibre reinforced specimens than the hand lay-up counterpart. Loading fibres in a different orientation affected the stress and strain curves because of the load bearing capacity of the fibre. However, it seemed that the properties were most influenced by the fibre type. For weaker fibres, the influence of the resin dominated the properties.

Based on the tensile and flexural strength values, it is likely that the blast resistance would be greatest for the GFRPs, then flax FRP followed by jute FRP and Supawood. As the stress/strain curves were linear for the GFRPs, depending on the size of the charge mass (especially if it is tested at low charges as the NFCs), the blast panel would behave elastically, and little damage would be expected. The jute FRPs would mostly likely behave in a brittle manner and fragmentation could occur, which has been consistently observed in all quasi-static tests. Delamination is more unlikely to occur in the NFCs as a form of damage in blast loading due to high interlaminar strength values compared to the GFRPs.

Table 6-12: Properties of the selected composites based on the quasi-static tests performed

	Flexural properties				Tensile properties				Mode I interlaminar properties	
	σ^f_{max} [MPa]	$\varepsilon^f_{\sigma max}$ [m/m]	E^f_{chord} [GPa]	ε^f_{fail} [m/m]	E^T [GPa]	σ^T_Y [MPa]	σ^T_U [MPa]	ε^T_{fail} [m/mx10^3]	$G_{Ic,init}$ [J/m^2]	$G_{Ic,prop}$ [J/m^2]
Glass/ Prime 20LV	399 (17) 452 (19)	0.025 (19) 0.026 (17)	21.9 (17) 21.3 (19)	0.032 (17) 0.029 (19)	20 (0/90°) 7(45°)	164 (0/90°) 46(45°)	359 (0/90°) 110(45°)	20 (0/90°) >80 (45°)	819	918
Glass/ SuperSap	276	0.015	20.2	0.023	20 (0/90°) 9 (45°)	219 (0/90°) 46 (45°)	448 (0/90°) 147 (45°)	24 (0/90°) >110 (45°)	531	618
Flax/ Prime 20	112	0.030	6.3	0.030	4.3 (0/90°) 3.8 (45°)	31 (0/90°) 23 (45°)	65 (0/90°) 40 (45°)	25 (0/90°) 22 (45°)	2272	2334
Hand lay-up Flax/ Prime 20[a]	58	0.045	3.4	0.050	3.8	28	66	25		
Flax/ SuperSap	77	0.042	3.9	0.044	3.3 (0/90°) 2.9 (45°)	26 (0/90°) 20 (45°)	62 (0/90°) 39 (45°)	33 (0/90°) 33 (45°)	2388	2474
Jute/ Prime 20	89	0.019	6.2	0.019	6 (0/90°) 3.8 (45°)	12 (0/90°) 10 (45°)	56 (0/90°) 41 (45°)	14 (0/90°) 18 (45°)	1257	1356
Supawood	30	0.015	27.6	0.017	2.7	8	17	10	(0.38 [c])	(115.5 [c])

a – similar results were found for the different tensile hand lay-up flax FRPs, therefore the mean value was taken

b – reported mean result for combined plain 3mm and 12 mm boards as they were similar (shaven boards omitted as it is not indicative of the plain 16 mm boards)

c – transverse properties (tensile, compression) of Supawood in MPa

7 Experimental blast loading methodology

Based on the numerical models, described in Chapter 4, physical blast experiments were performed on the six different materials described in chapter 5. Small-scale blast experiments were conducted in a blast chamber located at the BISRU Laboratory, University of Cape Town. The panels were clamped along the boundary and subjected to blast loads by detonating different masses of plastic explosive to obtain a range of panel responses. The stand-off distance for the explosive was set at 200mm using a square tube, similar to the ones used in the blast testing of fibre metal laminate panels [181], [185], [207]. The square tube directed the blast load onto the exposed area of the specimen, ensuring that all the impulse measured from the pendulum was applied through the blast panel.

PE4 plastic explosives were shaped into cylindrical discs using a mould and detonated to generate the blast load impacting the specimen. A detonator was attached to the disc by using a small amount of PE4 plastic explosive (either 0.5 g or 1 g), known as the leader, in a similar fashion conducted by Langdon et al [185]. Initial charge mass and diameter values were selected based on simulation results. These were adjusted during the testing phase on the basis of the experimental results. The diameter of the explosive disc was usually 30 mm, but in some cases, this was changed. For example, the diameter was reduced to 20 mm for charges less than 4 g (used for some Supawood tests due to the low blast resistance of the material) and increased to 40 mm for charges greater than 18 g (used in some GFRP tests as the GFRP was more blast resistant than the other materials). The charge diameter, charge mass range and number of tests per materials are shown in Table 7-1.

A total of 58 tests were performed: 40 were conducted on a composite that contained some form of a sustainable constituent, and 18 were performed on GFRP with a Prime 20LV resin system of two nominal thicknesses as a baseline. Twenty experiments used high-speed imaging to capture the transient deformation using optical means of non-contact measurement of macroscopic parameters, such as back face surface strain and displacement. Details of the transient response measurement instrumentation used in the blast tests are presented in section 7.4.

Table 7-1: Testing parameters for the performed experiments

Material	Charge Mass Range (g)	Charge Diameter Range (mm)	Total Tests
Glass FRP (Prime 20LV)	4 - 40	30 - 40	18
Glass FRP (Super Sap)	6 - 18	30	6
Flax FRP (Prime 20LV)	5 - 11	30	14
Flax FRP (Super Sap)	5 - 11	30	5
Jute FRP (Prime 20LV)	4 - 11	30	6
Supawood	2 – 6	20 - 30	9

7.1 Clamping arrangement

The target (test) panel was clamped as shown in Figure 7-1, where a square tube clamp was positioned in the front end to direct the blast load onto the target panel. This provided a semi-confined environment where the explosive products were directed towards the target panel. Both the square tube clamp and the back-panel clamp allowed the target panel to have a central exposed area of 200 x 200 mm. To minimise variability of the results due to boundary conditions, all the panels had the same clamping conditions, which is consistent with prior work on composites reported by Langdon and co-workers[207]–[209].

The square tube had a small recess at the open end to locate the polystyrene pad. The nominally 10 mm thick polystyrene pad was marked to facilitate positioning of the PE4 cylindrical charge, shown in red on Figure 7-1. The charge was placed at the centre of the polystyrene pad using double-sided tape. The effect of the polystyrene pad on the blast load was not determined for this project. Previous work has shown that the polystyrene pad has little effect at this SOD [135]. Moreover, each polystyrene pad was of similar thickness and density to minimise any variation.

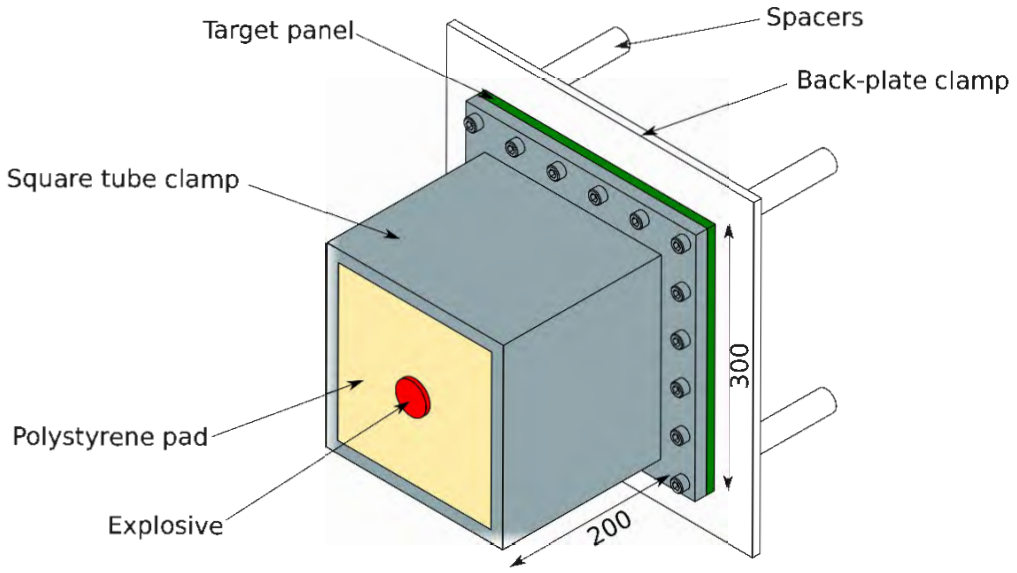

Figure 7-1: Schematic of the square tube clamping rig

7.2 Ballistic pendulum

The clamping rig was mounted to a ballistic pendulum, which was used to infer the impulse transfer to the target panel due to the blast load. For this project, two different ballistic pendula, shown in Figure 7-2 and Figure 7-3, were used. The "I-Beam" pendulum, shown in Figure 7-2, was used to capture the impulse imparted onto the target plates. The "closed" pendulum equipped with high-speed stereo-imaging, shown in Figure 7-3, was used to capture both the impulse imparted onto the target panels and the transient response of the target panels.

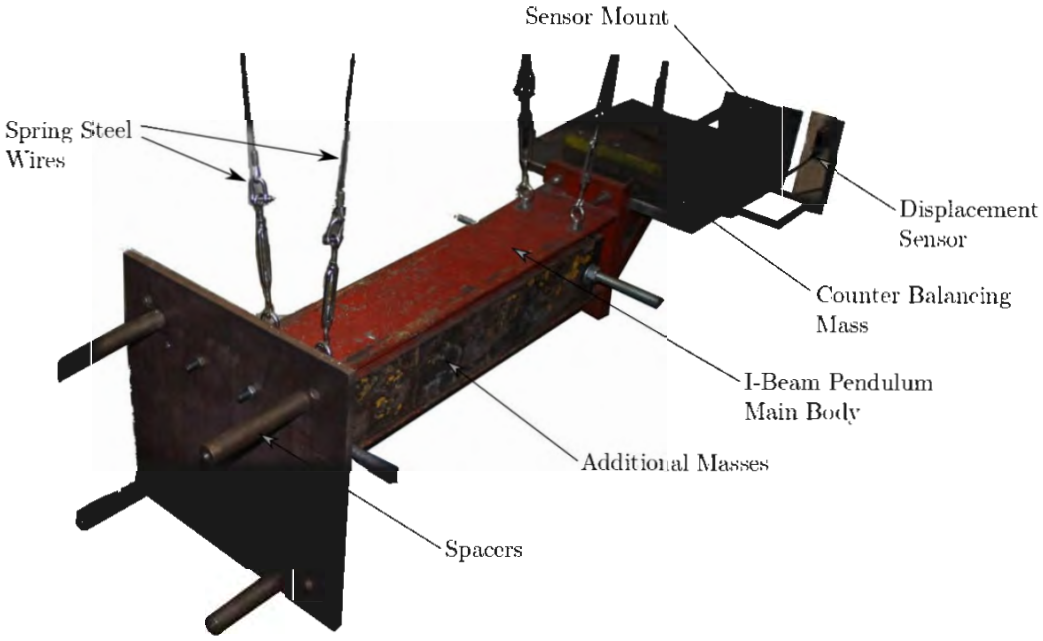

Figure 7-2: I-beam ballistic pendulum

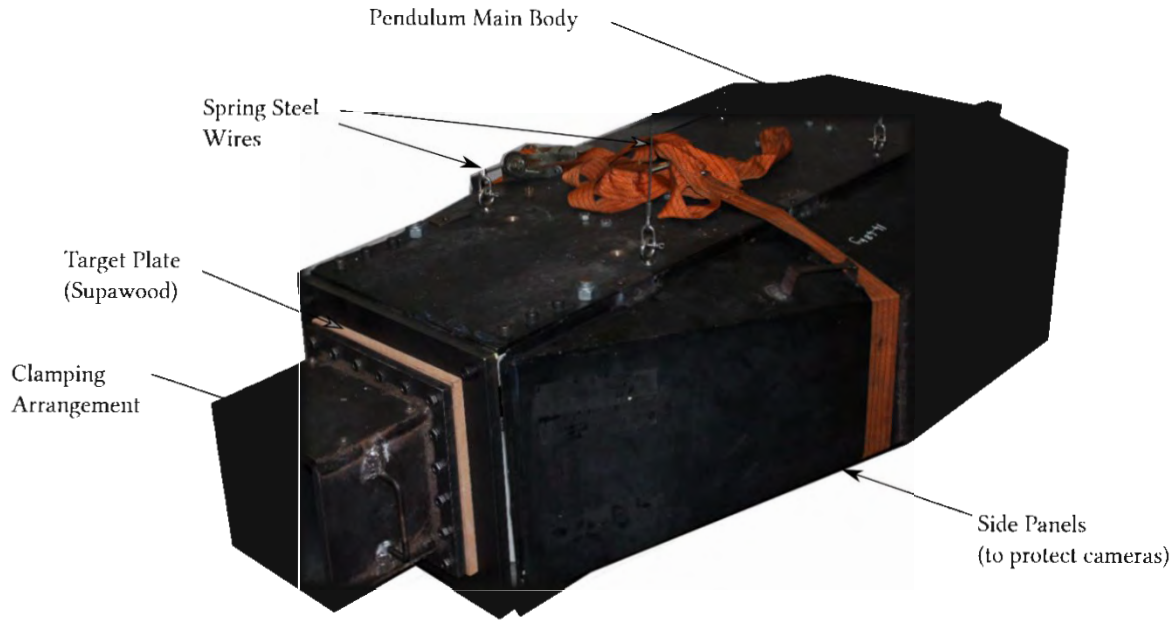

Figure 7-3: Closed pendulum modified for stereo-imaging

In general, a ballistic pendulum consists of a main body suspended by four spring wires that allow free movements on its longitudinal axis. After setting up the clamping arrangement and attaching it to the pendulum, the system was balanced using counterweights. Additional masses were also used, particularly at high charge masses, to avoid large oscillations, and to minimise the rotational effects and lateral sway of the ballistic pendulum. A laser distance sensor mounted to the wall near the rear end of the pendulum captured the horizontal displacement of the pendulum swing during each test. The initial velocity of the pendulum and consequently, impulse imparted onto the target plate, was determined using pendulum theory from the measured displacement.

7.3 Pendulum theory

Upon detonation of the explosive, the blast impulse transferred to the pendulum caused it to undergo damped harmonic motion. A simplified 2-D model of the system, and the subsequent free-body diagram of the system as displaced, are illustrated in Figure 7-4.

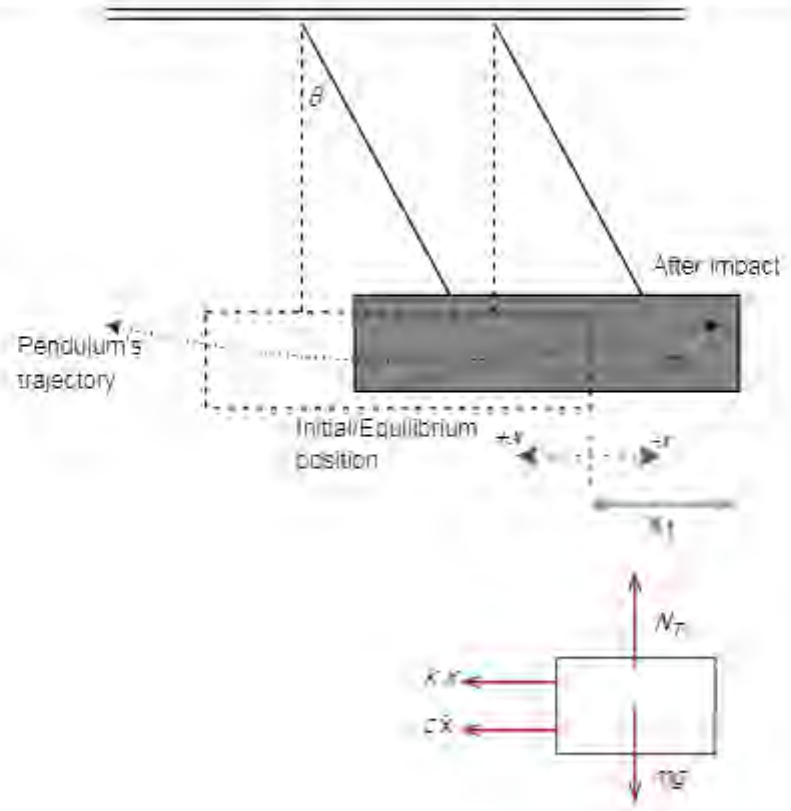

Figure 7-4: Model of the ballistic pendulum and free-body diagram

As the pendulum oscillated, the motion (x) was significantly smaller than the height at which the system was suspended from resulting in a small maximum angle. Applying small angle approximations, where $\sin\theta = \theta$, the system was reduced to a linearized single degree of freedom vibrational problem.

The equation of motion for the system was determined from the free body diagram with Equation 7-1. Using the parameters shown in Figure 7-4, Equation 7-2 was determined.

$$\ddot{x} + c\dot{x} + kx = 0 \qquad 7\text{-}1$$

$$\ddot{x} + 2\beta\dot{x} + \omega_n^2 x = 0 \qquad 7\text{-}2$$

where,

$$\beta = \frac{c}{2m_p} \qquad 7\text{-}3$$

where c is the viscous damping coefficient [N·s/m], m_p is the mass of the pendulum and ω_n is the natural circular frequency [Hz].

From the initial condition where the system was stationary (x = 0), the solution for the displacement against time was given by Equation 7-4.

$$x(t) = \frac{(e^{-\beta t})\dot{x}_0 \sin(\omega_d t)}{\omega_d} \qquad 7\text{-}4$$

where $\dot{x}_0$ is the initial velocity and $\omega_d$is the damped natural frequency of the pendulum.

Figure 7-5 shows the resulting displacement (x) versus time (t) retrieved from the displacement sensor from a blast test. The key points of interest (T, x_1 and x_2) which were used to calculate the impulse exerted onto the target panel are indicated on Figure 7-5.

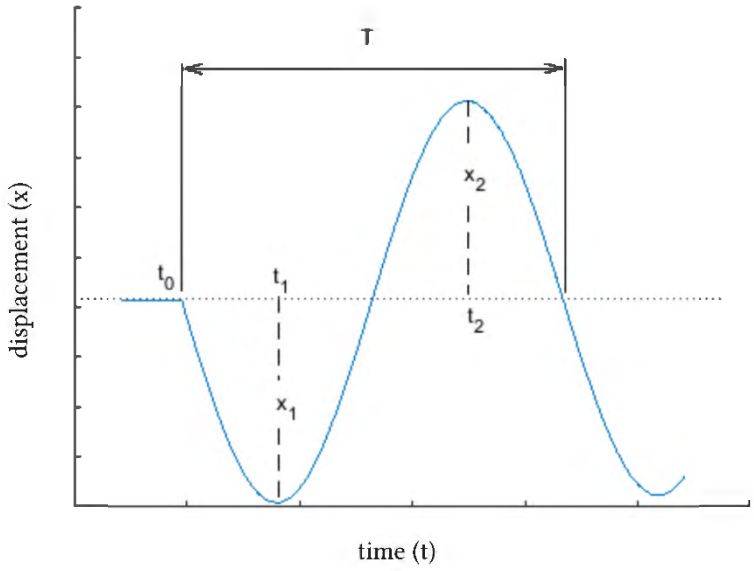

Figure 7-5: Smoothed data graph from the displacement sensor for a blast test

The maximum negative displacement x_1 and maximum positive displacement x_2 were measured and their ratio was computed to give Equation 7-5. However, any two observed amplitudes and corresponding times with respect to the full cycle period (T) could have been used.

$$\frac{x_1}{x_2} = \frac{\left(e^{-\beta(t_1 - t_0)}\right)\dot{x}_0 / \omega_d}{(e^{-\beta(t_2 - t_0)})\dot{x}_0/\omega_d} = e^{\frac{1}{2}\beta T} \qquad 7\text{-}5$$

where $(t_1 - t_0) = \frac{1}{4}T$ and $(t_2 - t_0) = \frac{3}{4}T$.

Using Equation 7-5, β was calculated. Rearranging Equation 7-4, the initial velocity was determined using any displacement (x) value and the corresponding time value (t) from t_0. Equation 7-6 shows the value for the initial velocity to when using the position of the maximum negative displacement x_1.

$$\dot{x}_0 = \frac{2\pi}{T} x_1 e^{\frac{1}{4}\beta T} \qquad 7\text{-}6$$

Finally, the impulse transferred onto the panel was calculated using Equation 7-7.

$$I = m_p \dot{x}_0 \qquad 7\text{-}7$$

For some of the tests, a pen was attached to the bottom of the red I-beam ballistic pendulum to measure the movement of the pendulum. The principle to determine the impulse was similar to the laser-based system. However, the positioning of the pen did not directly give the horizontal displacement of the oscillation. This was compensated for by using the position and geometry of the pen relative to the pendulum. Derivations can be found in Refs [181] and [180] where this type of measurement was also used for blast tests conducted in the same facility.

7.4 Transient response measurements

Most tests were conducted on the basic pendulum (shown in Figure 7-2), where the primary goal was to ascertain the damage levels in specimens for increasing explosive charge mass. For some tests at low charge masses that were expected to inflict minor damage (that is, with no risk of panel rupture), tests were performed on the stereo-imaging pendulum as shown in Figure 7-3 and Figure 7-6. These charge masses were chosen to ensure no damage occurred to the stereo-imaging equipment. Within the modified pendulum, the stereo-imaging set-up comprises two IDT vision NR4 S3 high-speed cameras mounted on an aluminium rail system and diffused LED lighting fixtures as shown in Figure 7-6. The cameras used in blast measurements were positioned at a safe distance in order to avoid damage by fragment impact. A laser displacement sensor was used to measure the motion of the pendulum. Similar equipment and testing method was used by Curry and Langdon [210] to determine the transient behaviour of steel plates subjected to localised blast loading.

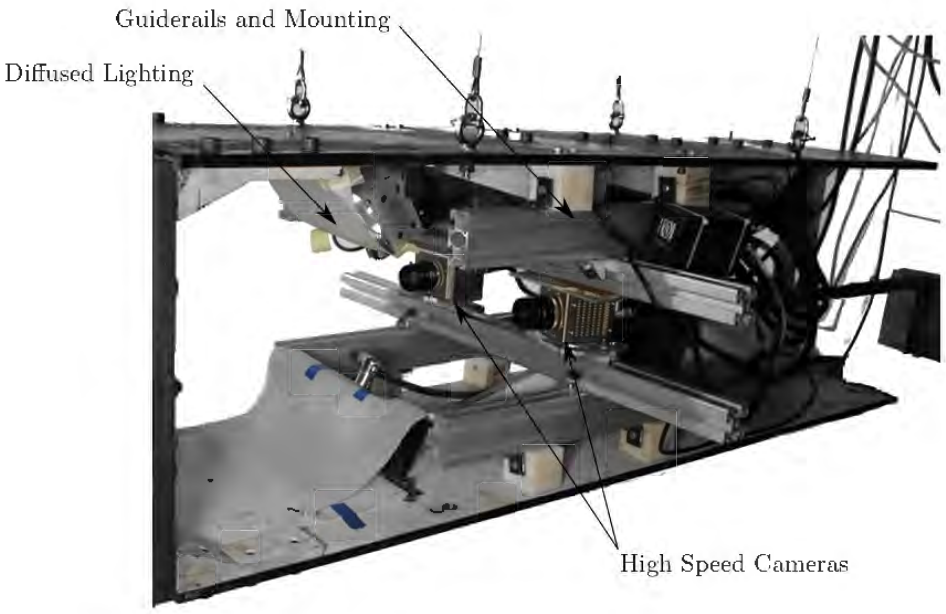

Figure 7-6: Internal view of the stereo-imaging pendulum showing the cameras and lighting system

Similar to the work by Curry and Langdon [210], only a full width strip along the mid-line on the rear surface was recorded shown in Figure 7-7. A frame rate of 30 kfps was used during filming of the rear surface. A high frame rate, such as this one, influences the image lighting, which in turn affects the choice of exposure time. The exposure time should therefore be kept as small as possible to reduce motion blur that can occur as an object moves through the frame during filming. In this experimental arrangement, the exposure time was set at 31 µs which represented a compromise between reducing motion blur and enabled sufficient lighting for a high-quality image. The diffused LED lighting, visible in Figure 7-6, was developed to ensure adequate illumination for the very short exposure times required.

Figure 7-7: Example of a captured image during DIC testing from one of the cameras

During testing, the cameras were triggered instantaneously by the detonation of the explosive using an aluminium foil break-wire circuit placed on the polystyrene pad shown in Figure 7-1. This break wire was made using a piece of foil glued onto the pad with two wires to a triggering device that was linked to the camera.

7.4.1 Measurement principles of digital image correlation

Digital Image Correlation (DIC) uses optical methods, such as image matching, and highly specialised algorithms to resolve the motion on the surface of deforming structures [211]. In order to compute deformation using DIC, unique features in two images are required. Without this, it would be difficult to determine motion vectors on a texture-less structure and repeated structures can lead to misinterpretation[211]. A non-periodic, quasi-random, speckled pattern is often used in DIC avoid misinterpretation. The patterns used, need to adhere to the surface and deform with the surface to ensure that no loss of correlation occurs [211].

From an image of a well speckled structure, pattern matching between parts of the image, known as subsets or windows, are used to estimate motion from the grey value distribution between a small subset in the template image and a displaced copy in another image [211]. This is illustrated in Figure 7-8 [212], where pattern matching, and pixel tracking are implemented to obtain the displacement vectors.

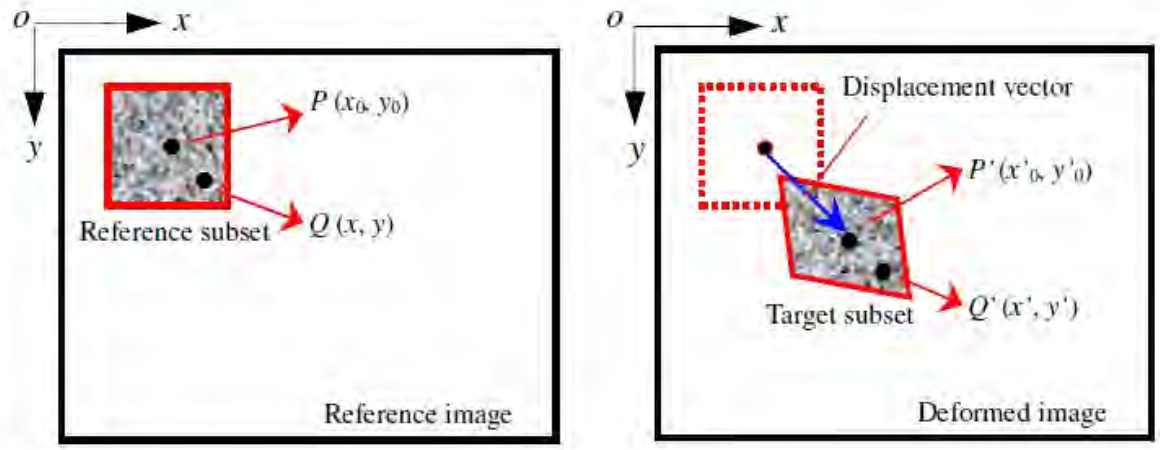

Figure 7-8: Illustration describing the basic principle of subset based DIC method

7.4.2 Specimen preparation

A speckled pattern was applied to the back surface of the panels by spraying a quick-drying matt lacquer spray paint using the following method:

- Wipe clean with a cloth to remove any dust and contaminants off the back surface
- Apply an opaque layer, along the region of interest, on the surface of the panel using a flat white spray paint
- Once dry, lightly overspray the layer to create a mist using the matt black spray paint
- Continue to mist the surface, interchanging between the white and black spray, until the desired speckled pattern was achieved.

For the GFRP panels, additionally the full front surface of the panel had an opaque black layer painted so that no information would be lost due to the light flash emitted during detonation. The position of the centre of the plate and the horizontal mid-line were marked off on each plate as gauge points of interest (indicated by the yellow cross and line in Figure 7-7).

A range of factors could cause distortions in the measured deformation. Noise in the results is random and unavoidable, but it can be minimised with a good speckle pattern. As similar spacing between the stereovision system and the panel was used for Curry and Langdon [210], therefore the same speckle pattern was mimicked for the materials tested in this project. While the inside of the stereo-imaging pendulum was cleaned then closed, it was possible that contaminants and dust could affect the captured images, creating noise issues in the data analysis.

7.4.3 Calibration of stereovision system and post processing data

Istra 4D software, available from Dantec Dynamics [213], was used to analyse the captured images for the stereo-video system shown in Figure 7-6 and render the full-field deformation measurements for the visible strip for the blast tests. However, prior to each blast test, the system had to be calibrated for use.

A customised Dantec Dynamics checkerboard calibration target plate [214] was used during the calibration process. Images were recorded while the calibration target was moved from the four corners of the open area where the specimen would be attached (at the same distance from the camera), then moved to the centre where the target was titled and rotated in different orientations. Approximately ten images were used to determine the calibration parameters. Figure 7-9 shows an example of three image pairs and circled grid points found using a calibration grid spacing of 15 mm.

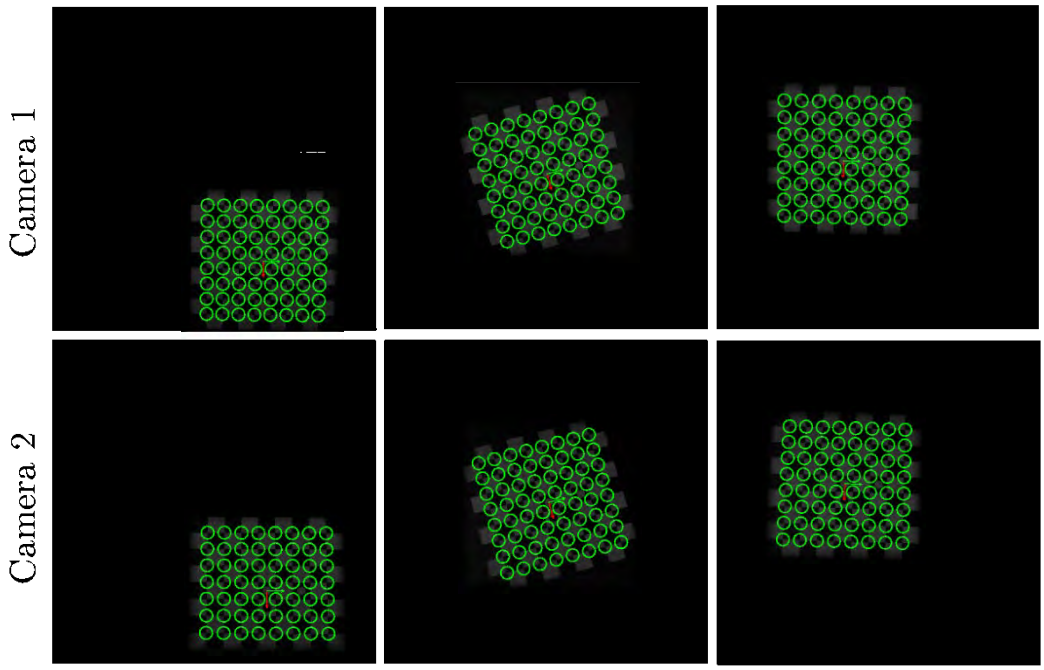

Figure 7-9: Image pairs in different positions used during the calibration process

The calibration process determined the intrinsic and extrinsic parameters of the camera and, the positioning of the target plate. Table 7-2 shows an example of the calibration process results from the images shown in Figure 7-9. These parameters are used within Istra 4D to determine the displacements without any further input, apart from the test images, from the user.

Table 7-2: Example of calibration results of the set of data shown in Figure 7-9

Stereo Parameters:		
Angle (deg)	29.44	
Baseline (mm)	408.692	
Corrected Residual (pixels)	0.0555	
Camera Parameters:		
Parameter	Camera 1	Camera 2
Principle Point x (pixels)	479 ± 5	513 ± 5
Principle Point y (pixels)	493.8 ± 0.9	481.1 ± 0.9
Focal Length x (pixels)	2765 ± 7	2777 ± 7
Focal Length y (pixels)	2764 ± 7	2776 ± 7

While post-processing the images, all analyses were performed using a subset size of 19 x 19 pixels and a grid spacing of 2 pixels, similar to large deformation measurements captured using high speed stereovision system and DIC by Sutton et al [211], [215], and Curry and Langdon [210]. The z-

displacement for the centre of the panel and the mid-line at each time step were obtained in reference to an image prior to detonation. The results from the DIC are discussed further in Chapter 9.

7.5 Summary of chapter

The experimental method for blast testing square test plates comprising different sustainable materials was presented in this chapter. The plates had an exposed square area with a length of 200 mm and were mounted to a square picture-frame clamp. A square tube was used to position the explosive 200 mm away from the centre of the plate and provide a semi-confined blast arrangement, enabling certainty that all impulse was directed onto the front surface of the target plate.

The clamped test plates were mounted to two types of ballistic pendula, one with a high-speed camera system for determining transient deformations. For the tests performed on the ballistic pendulum with cameras, a horizontal strip through the mid-line of the rear surface of the plate was recorded to obtain the transient z-displacement. The impulse transferred to the test plate by the blast was measured from the swing of the ballistic pendulum. The results from these experiments can be found in chapters 8 and 9.

8 Qualitative results and observations

Table 8-1 lists the types of tests and results such as panel thickness, charge mass and diameter, calculated impulse and whether transient data was available. Values are presented according to material type in ascending order according to the total charge mass used (which is the sum of leader and cylindrical charge). The relationship between the charge mass and impulse was derived. Subsequently, the results were described in terms of impulse rather than charge mass. Therefore, from section 8.2, the qualitative results and observations made in this chapter have been presented in terms of impulse.

After each test, the front and back surfaces of the target plates were visually inspected and photographed. Due to the transparent nature of the glass fibre reinforced polymer composites, paint used on DIC panels was removed around the exposed area so that it was possible to identify any delamination damage. The paint was not removed for any of the natural fibre composites (Supawood, flax and jute fibre reinforced laminates) tested, due to the natural opacity of the panel. Thereafter, plates were sectioned along the mid-line for further inspection. The failure modes were identified from observations on the surfaces and midpoint cross sections. Moreover, microscopy images were taken of the different composite materials.

Table 8-1: Uniform blast test parameters and impulse

Material Description	Specimen Name	Thickness (mm)	Charge mass (g)	Charge Φ (mm)	Impulse (Ns)	DIC data avail.
Glass fibre –19 layers Prime 20LV VI	G19/P20-10	6.2	5	30	19.3	
	G19/P20-8	6.1	7	30	25.2	X
	G19/P20-4	6.0	11	30	31.7	X
	G19/P20-9	6.2	11	30	33.7	X
	G19/P20-1	6.3	25	30	54.3	
	G19/P20-3	6.2	25	40	64.8	
	G19/P20-5	6.2	30	40	71.3	
	G19/P20-6	6.1	35	40	84.4	
	G19/P20-2	6.2	40	40	82.7	
Glass fibre – 17 layers Prime 20LV VI	G17/P20-7	5.0	4	30	15.5	
	G17/P20-10	4.8	5	30	17.9	
	G17/P20-5	5.0	6	30	21.6	X
	G17/P20-8	5.1	6	30	22.2	X
	G17/P20-4	5.0	7	30	23.5	
	G17/P20-2	5.1	9	30	28.1	X
	G17/P20-9	5.0	11	30	30.9	
	G17/P20-6	5.0	15	30	37.6	
	G17/P20-1	5.1	20	30	48.5	
Glass fibre – 17 layers Super Sap VI	G17/SS-3	5.1	6	30	21.5	X
	G17/SS-4	5.1	9	30	28	
	G17/SS-1	5.2	10	30	30.9	
	G17/SS-5	5.1	11	30	30.7	X
	G17/SS-2	5.1	15	30	46.6	
	G17/SS-6	5.1	18	30	43.2	X
Supawood Ready to use fibreboard 16 mm	MDF-3.1	16.2	2	20	10.4	
	MDF-3.2	16.2	3	20	14.1	
	MDF-6	16.2	3	20	11.5	
	MDF-7	16.1	3	20	11.8	X
	MDF-2	16.1	3.5	30	17.2	
	MDF-4	16.1	3.5	20	17.2	
	MDF-8	16.2	4	20	15.7	X
	MDF-5	16.1	4.5	20	19.5	
	MDF-1	16.1	6	30	20	
Jute fibre – 13 layers Prime 20LV VI	J13/P20-5	10	4	30	15.6	X
	J13/P20-4	10.2	5	30	17.8	
	J13/P20-6	10.1	5	30	19.9	X
	J13/P20-1	10.1	6	30	19.0	
	J13/P20-3	10	7	30	21.3	
	J13/P20-2	10	11	30	33.2	
Flax fibre – 9 layers Prime 20LV VI	F9/P20-3	10.1	5	30	19.5	X
	F9/P20-1	10.1	6	30	22.8	
	F9/P20-4	10.1	7	30	23.5	X
	F9/P20-5	10	9	30	25.5	X
	F9/P20-2	10	11	30	39.5	
Flax fibre – 8 layers Prime 20LV Hand lay up	F8/P20H-5	10.1	5	30	17.2	
	F8/P20H-9	10.2	6	30	23.3	X
	F8/P20H-7	9.7	7	30	22.9	X
	F8/P20H-8	10.2	8	30	23.8	
	F8/P20H-3	10.2	9	30	29	
	F8/P20H-4	10.3	10	30	28.1	
	F8/P20H-6	10.3	10	30	34	
	F8/P20H-1	9.5	11	30	27.1	
Flax fibre – 9 layers Super Sap VI	F9/SS-3	9.9	5	30	21	X
	F9/SS-1	10	6	30	21	
	F9/SS-6	10	7	30	24.1	X
	F9/SS-5	9.9	9	30	28.3	X
	F9/SS-2	9.9	11	30	36.6	

8.1 Charge versus impulse

Figure 8-1 shows the relationship between charge mass and impulse for all the tests irrespective of the materials used. The results showed some experimental variations due to the nature of blast testing. Overall, the relationship between the charge mass and calculated impulse followed a generally increasing linear trend, as shown in Figure 8-1, as expected. The impulses obtained correlated with previous experimental work on glass fibre metal laminates [207] and GLARE [185] using a similar set-up at charges lower than 15 g. The impulses calculated at greater charge masses, exceeding 15 g, were higher than those obtained by Langdon et al [207], however, the charge diameters used in that study were 20 mm and 25 mm. The aspect ratio of a cylindrical charge mass has been shown to affect the impulse imparted onto a specimen [216]. The results given in this chapter are subsequently presented and discussed in terms of the impulse calculated.

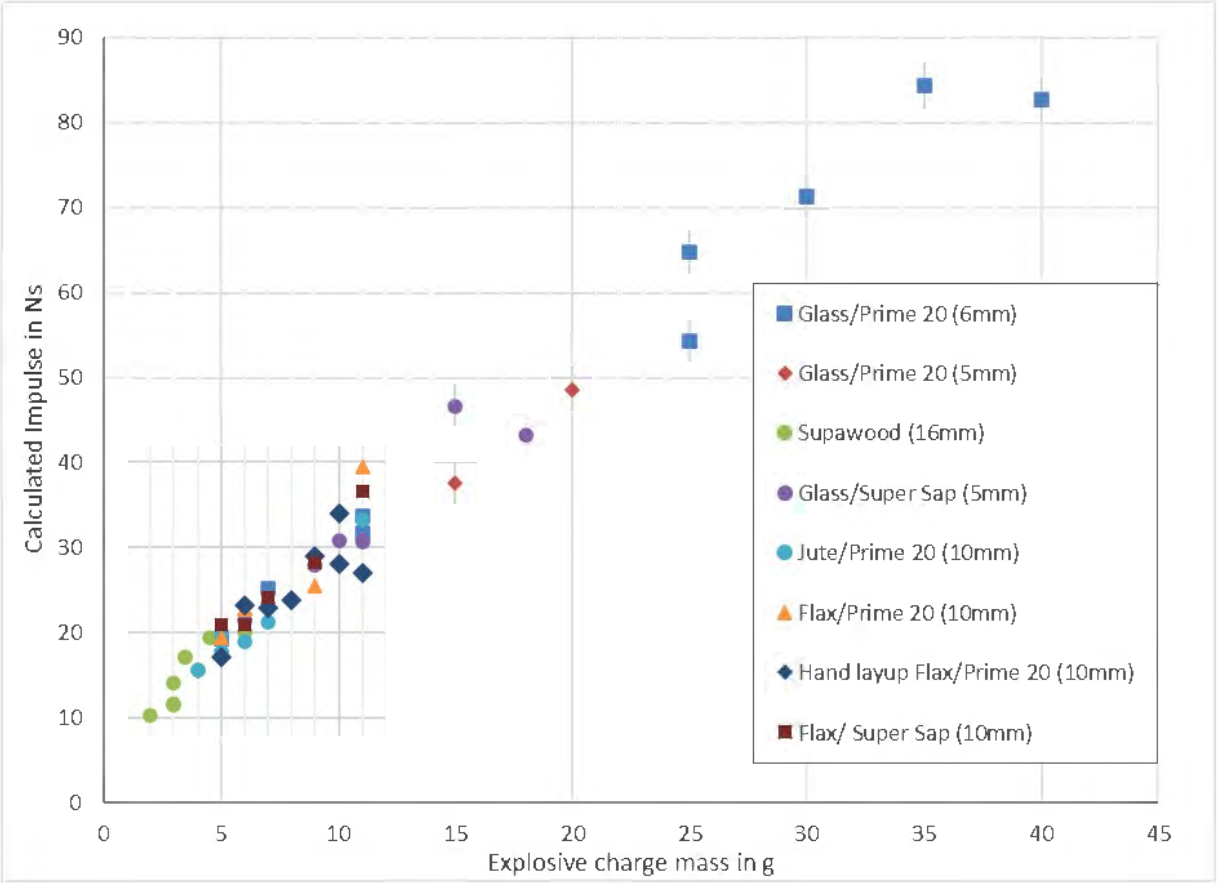

Figure 8-1: Graph of impulse versus charge mass for the blast tests

8.2 Glass fibre reinforced Prime 20LV composites

The progression for the damage observed on the front and back surfaces of the two thicknesses of GFRPs are shown in Figure 8-2 and Figure 8-3 for Glass 19/Prime 20LV (nominally 6 mm thick) and Glass 17/Prime 20LV (nominally 5 mm thick) panels, respectively. For simplicity, the two thicknesses of GFRPs were denoted as Glass 19/Prime 20LV for the nominally 6 mm GFRPs and Glass 17/Prime 20LV for the nominally 5mm GFRPs. The number adjacent to the fibre refers to the number of plies in the laminate alongside the resin system. This naming convention was used for the rest of the materials presented. Images of the surfaces of the remaining glass fibre reinforced composite Prime 20LV panels can be found in Appendix C.

In general, the Glass 19/Prime 20LV panels, shown in Figure 8-2, had less damage in comparison to Glass 17/Prime 20LV panels. At an impulse ranging from 19.3 Ns to 33.7 Ns, little damage was observed on the Glass 19/Prime 20LV panels. The damage observed typically was found at the clamped edge boundary. In comparison, a similar amount of damage was observed on Glass 17/Prime 20LV panels at a lower impulse of 23.5 Ns.

Apart from the damage at the clamped edge boundary, delamination was a prominent mode of failure for the glass fibre reinforced Prime 20LV panels and was identified by the opaque white areas that were larger than a weave unit as shown in Figure 8-4. The through thickness position where delamination occurred could not be determined by observing the front and back surfaces of the panels. However, it was possible to observe on some panels that that multiple layers had delaminated, particularly on the back surface of G19/P20-2 in Figure 8-2. Delamination was also found within the clamped area which can be clearly observed in G17/P20-5 in Figure 8-3. Within the exposed area of the panel, very small amounts of delamination were initially observed at an impulse of 33.7 Ns and 21.6 Ns for the 6 mm and Glass 17/Prime 20LV panels respectively.

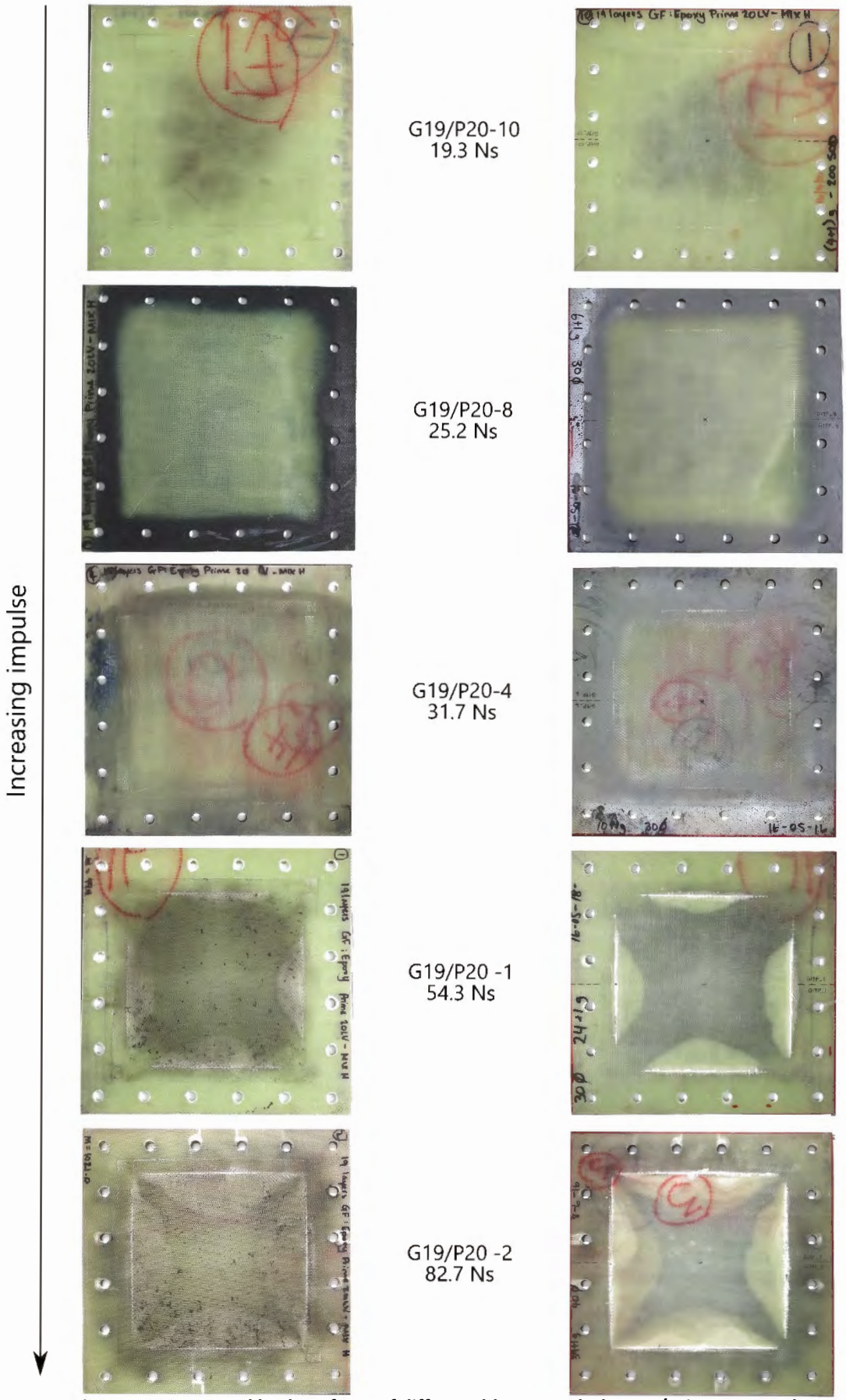

Figure 8-2: Front and back surfaces of different blast tested Glass 19/Prime 20 panels

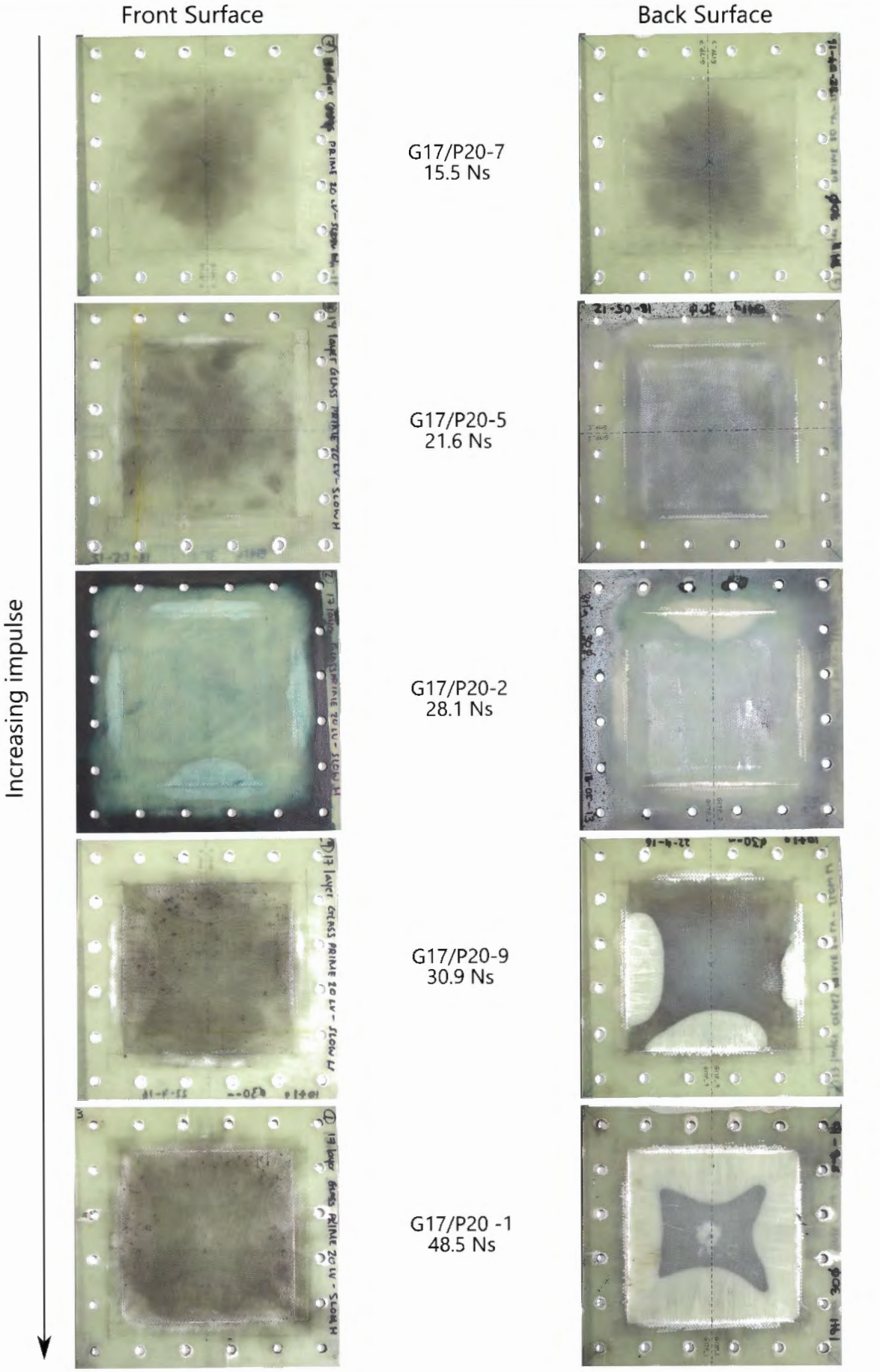

Figure 8-3: Front and back surfaces of different blast tested Glass 17/Prime 20 panels

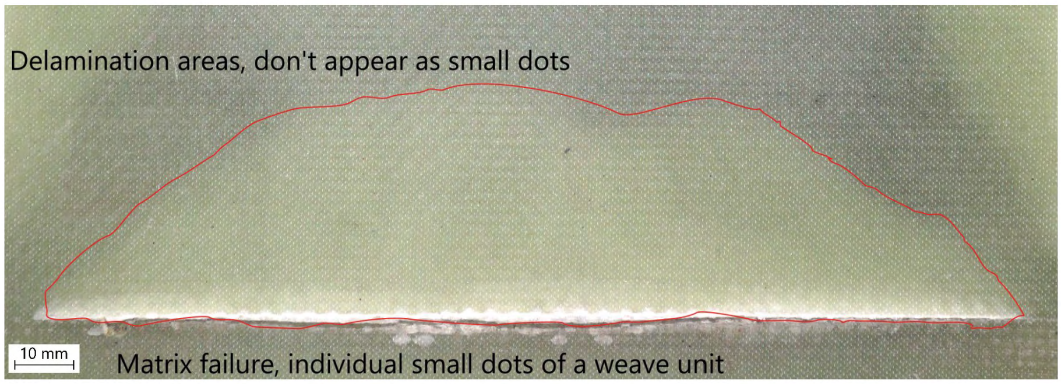

Figure 8-4: Damage size for large amounts of delamination and observed matrix failure at the clamped edges

With increasing impulse, a delamination pattern was observed on the glass fibre reinforced Prime 20LV panels. The delamination pattern occurred along the four boundary edges and expanded towards the centre of the panel with increasing impulse. Similar to previous work investigating the blast response of glass fibre metal laminates [207] and GLARE [185] to uniform blast loads, formation of yield lines on glass fibre metal laminates and GLARE were similar to the delamination pattern presented in the Glass/Prime 20LV panels. At highest impulse of 48.5 Ns tested on the nominal 5 mm Glass/Prime 20LV panels, the delamination occurred at the centre of the panel as shown in Figure 8-3.

Cracking, which was considered as a form of fibre failure in addition to matrix failure, was observed on four 6 mm thick Glass/ Prime 20LV panels, where the impulse was greater than 64.8 Ns, as depicted by the example shown in Figure 8-5. No cracking was observed on the tests performed on Glass 17/Prime 20LV panels. The cracking observed in the exposed area of the glass fibre reinforced panels, namely G19/P20-3, G19/P20-5, G19/P20-6 and G19/P20-2, is highlighted in on Figure 8-6. The cracking extended from the boundary towards the centre of the panel the front surface as a straight line.

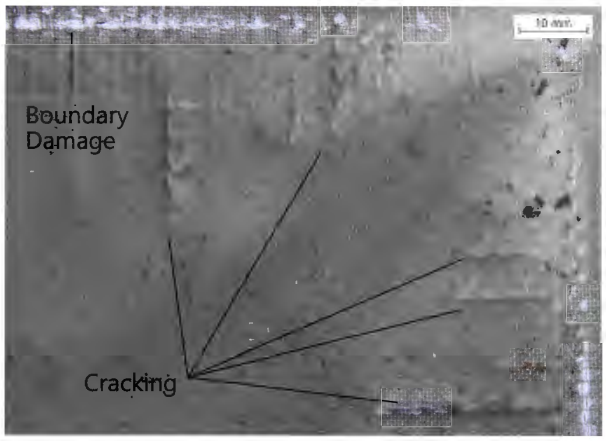

Figure 8-5: Close up image of fibre cracking

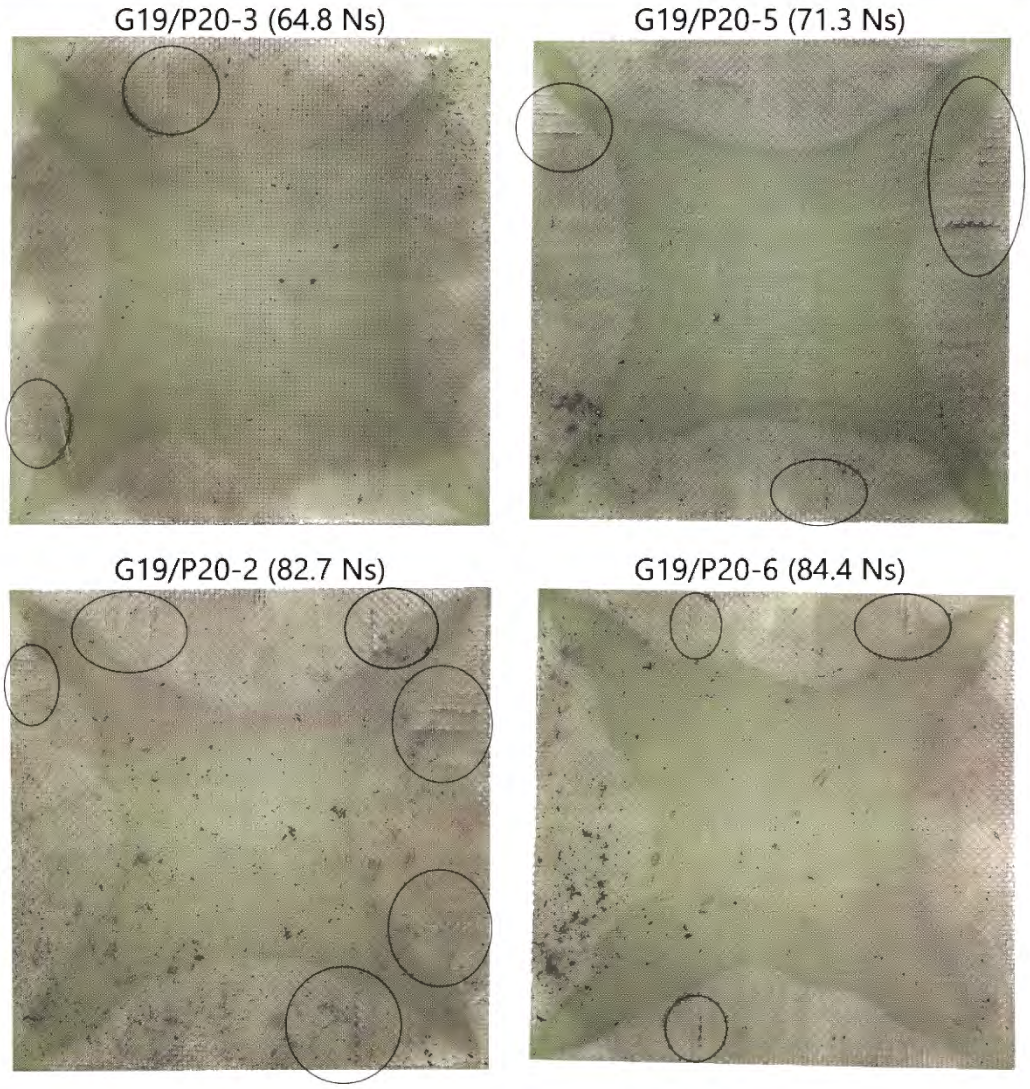

Figure 8-6: Photographs showing fibre cracking highlighted by circles observed on the exposed area (200 mm x 200 mm) front surface of 6 mm thick Glass/Prime 20LV panels

Upon further visual inspection of the clamped edge boundary and clamped area, various types of failures were found depending on the severity of the impulsive load. Initially at lower impulses, the damage was fibre failure with cracks formed along the clamped edge boundary as shown in Figure 8-7. However, as the impulse increased, additional failures such as matrix failure and delamination extending towards the edge of the panel were observed. Furthermore, damage (which was a combination of fibre and matrix failure) was also observed around the clamping holes caused by the panel pulling at the bolt holes. The observations of cracking and pull in around the bolt holes is shown in Figure 8-7.

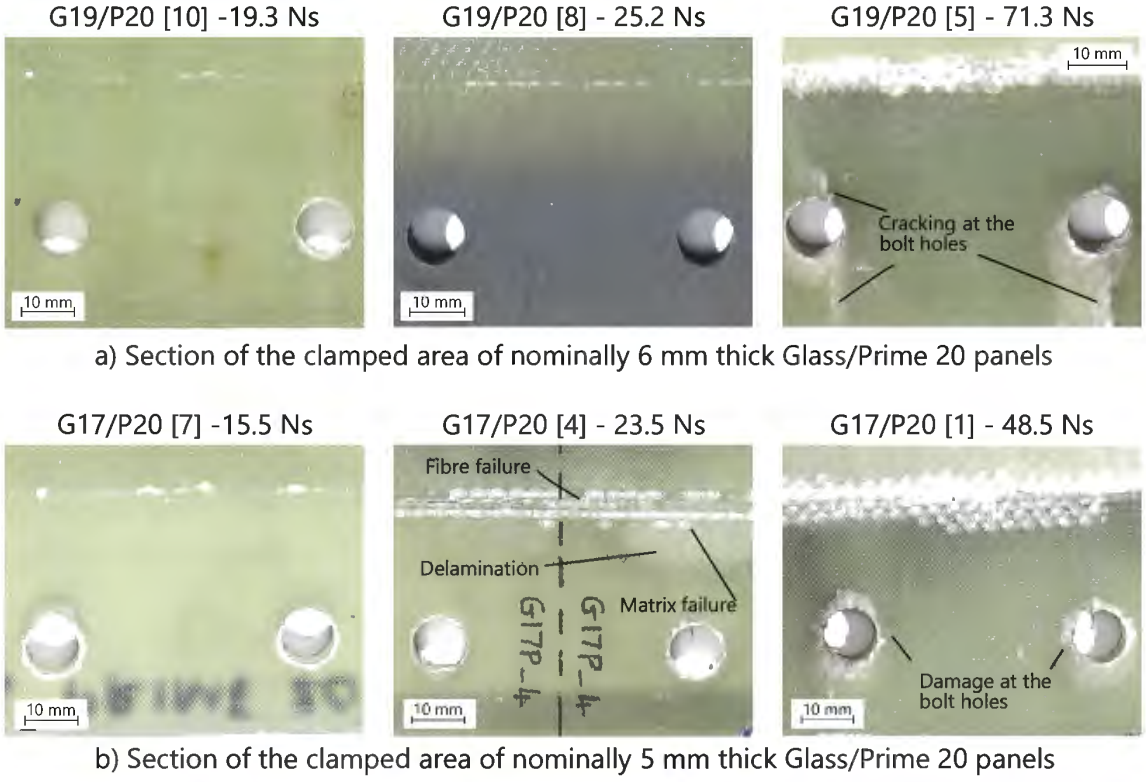

Figure 8-7: Photographs showing boundary damage on glass fibre reinforced Prime 20LV composite panels

The cross-sections were wiped with a damp cloth after sectioning and photographed to seek any visible signs of damage in the cross-sectional surface and to observe the permanent deformation profile. The cross-section images of the two kinds of Glass/ Prime 20LV panels are shown in Figure 8-8. Minimal damage was observed through the thickness of the panels. Where delamination occurred, faint visible cracks parallel to the face were observed. Microscope images of these cracks are shown in section 8.8.2. The profile of the glass fibre reinforced seemed to dome slightly, particularly with increasing impulse. The maximum midpoint deflection measure was 1.2 mm and 0.6 mm for the 6 mm and 5 mm thick glass fibre reinforced Prime 20LV composite panels respectively. However, in general, the panels were considered relatively flat as the permanent deflection was very small compared to the thickness of the panel.

Figure 8-8: Cross-sectional photographs of blast tested glass fibre reinforced Prime 20LV panels

8.3 Glass fibre reinforced Super Sap composites

The progression for the damage observed on the front and back surfaces of 5 mm thick glass fibre reinforced Super Sap (Glass 17/Super Sap) panels is shown in Figure 8-9. Images of the front and back surfaces of G17/SS-5 can be found in Appendix C.

Similar failure modes were observed on the Glass 17/Super Sap panels as those described for the GFRPs with Prime 20LV. In comparison to the Glass 17/Prime 20LV panels, the cracking and matrix failure observed on the Glass 17/Super Sap panels were more severe for similar impulses. Delamination was also a prominent mode of failure with similar delamination pattern. Delamination occurred at the centre of two Glass/Super Sap panels, namely G17/SS-2 and G17/P20-1 at an impulse of 43.2 Ns and 48.5 Ns, respectively.

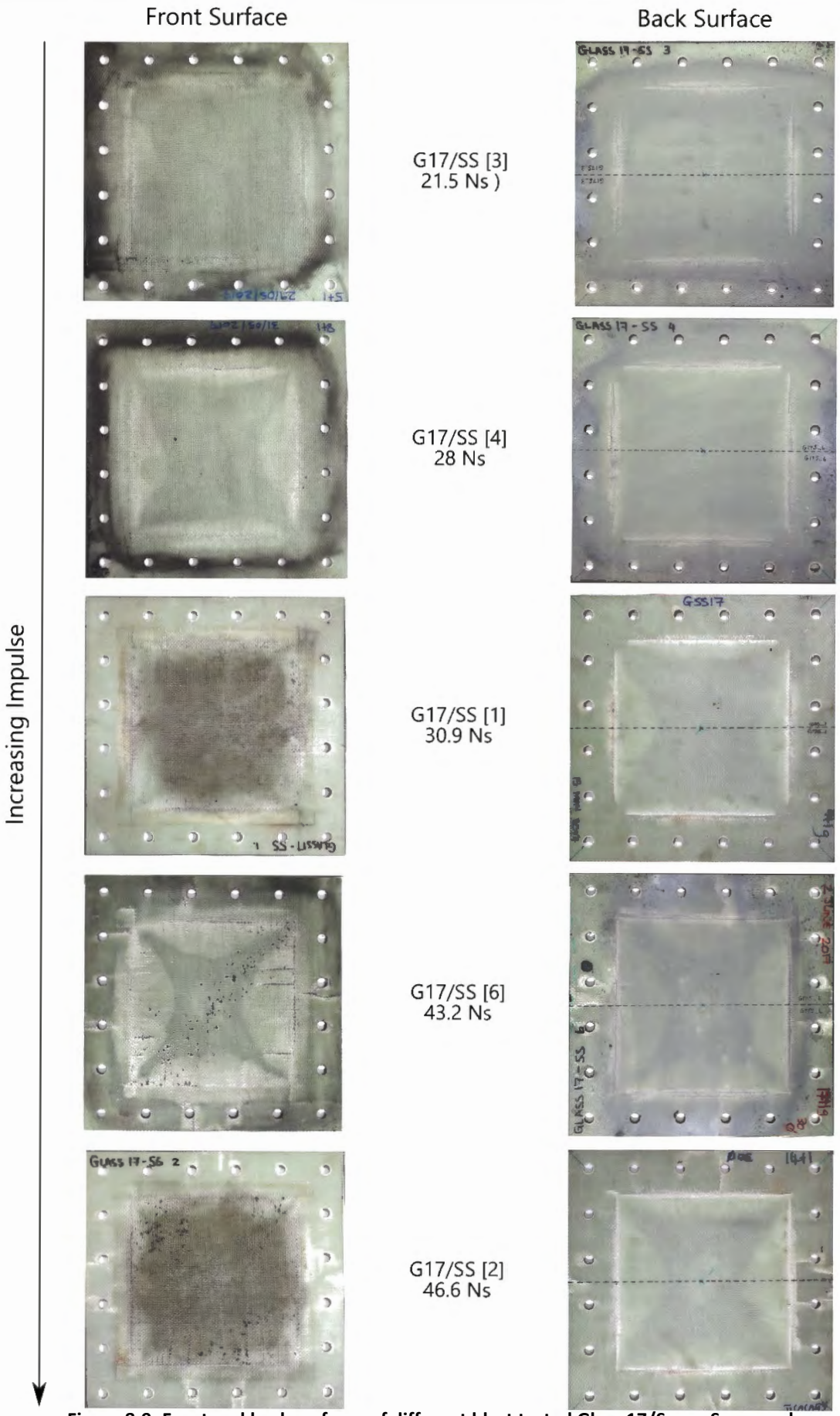

Figure 8-9: Front and back surfaces of different blast tested Glass 17/Super Sap panels

Fibre cracking that extended from the clamped boundary towards the centre occurred. This was similar to cracks found in the Glass 19/Prime 20LV panels subjected to impulse greater than 64.8 Ns. A detailed view of the cracking is shown in Figure 8-10. Cracking withing the exposed area was straight along the weave. However, cracks within the clamping area deviated from the weave pattern and was askew.

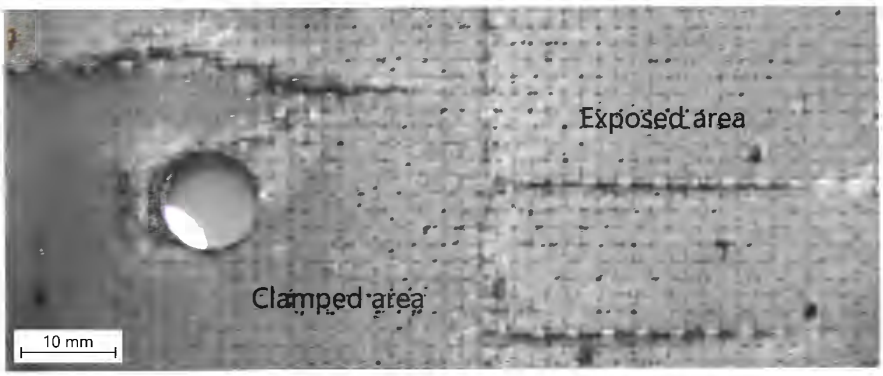

Figure 8-10: Photographs showing cracking on a blast tested Glass 17/ Super Sap panel

Increased levels of damage were noted at the boundary for the Glass 17/Super Sap panels compared to Glass 17/Prime 20LV panels of similar thickness. Furthermore, for similar impulses (for example G17/P20-4 at 23.5 Ns and G17/SS-3 at 21.5 Ns) the amount of damage along the clamped edge, primarily matrix failure was more severe. On panels G17/SS-6 and G17/SS-2, significant cracking around the bolt holes was observed as shown in Figure 8-11.

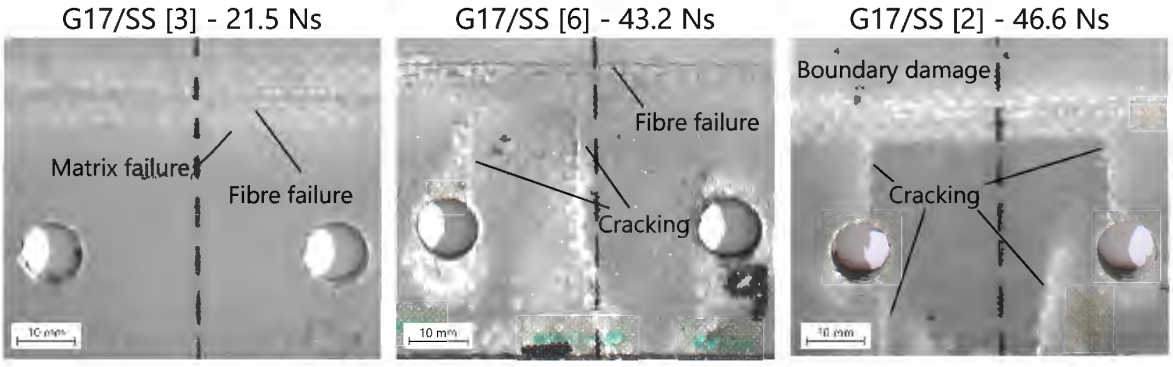

Figure 8-11: Photographs showing damage observed along the clamped area and clamped edge boundary on Glass 17/Super Sap panels

Around the centre of the Glass 17/Super Sap panels small white dots of the size of a weave unit were found on either front (at impulses greater than 30.9) or back surface (at impulses less than 30.7) of the panel as shown in Figure 8-12. The small dots observed were not large enough to be considered as delamination. The fibre surrounding the dots appeared intact. Therefore, it was likely that this damage was localised matrix cracking or interface damage. This damage was not observed on either

Glass 17/Prime 20LV or Glass 19/Prime 20LV panels. The area where matrix failure was concentrated, circled in blue in Figure 8-13, tended to increase with increasing impulse. Figure 8-13 also shows panels where cracking was observed circled in black. Despite minimal delamination occurring in the exposed area of the G17/SS-3 at 21.5 Ns, the white dots were still visible.

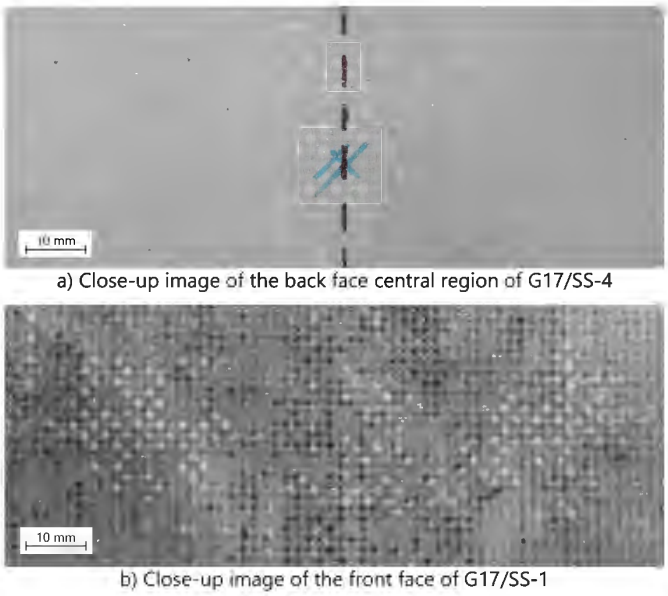

a) Close-up image of the back face central region of G17/SS-4

b) Close-up image of the front face of G17/SS-1

Figure 8-12: Photographs showing Matrix or interface damage on Glass 17/Super Sap panels

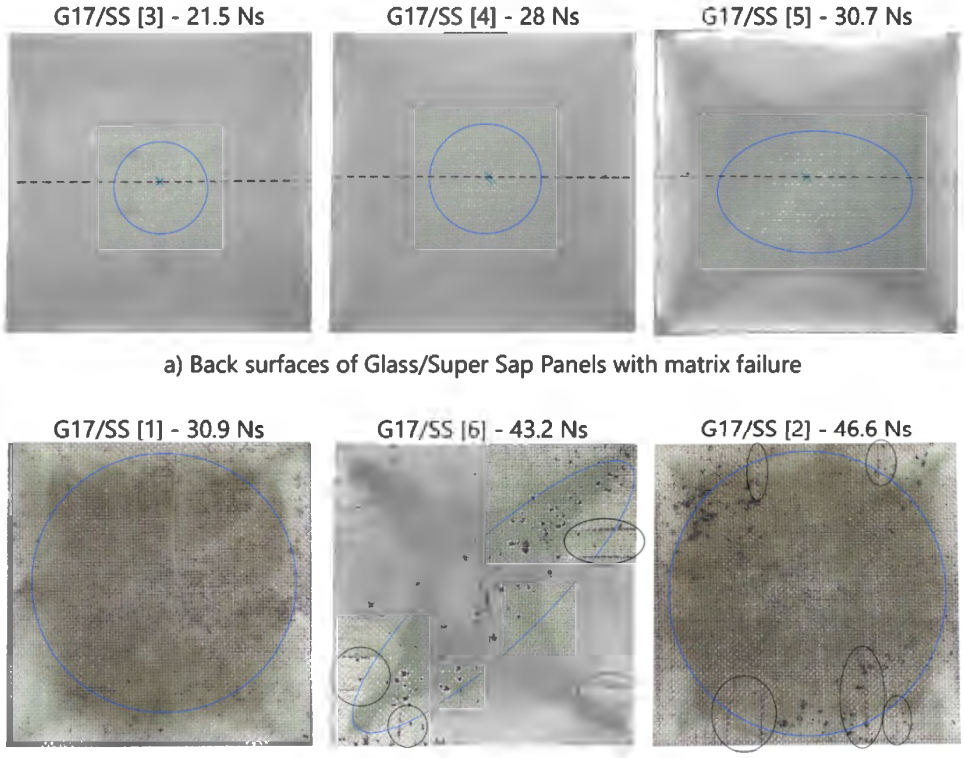

a) Back surfaces of Glass/Super Sap Panels with matrix failure

b) Front surfaces of Glass/Super Sap Panels with matrix failure and fibre cracking

Figure 8-13: Photographs of exposed areas of different blast tested Glass 17/Super Sap panels showing matrix failure and cracking

Furthermore, part of the matrix was missing on the front surface of G17/SS-6. Indents was found diagonally across the panel in addition to matrix failure as shown on a detailed view in Figure 8-14. It is not clear if this was a surface feature that was made more prominent from the paint. However, it is possible that the indents occurred after testing as result of fragments from the metal jacket of the detonator impacting the panel. In combination with this, the panel was painted, subjected to an impulse of 43.2 Ns and infused with Super Sap resin, all of which could have contributed to the indents.

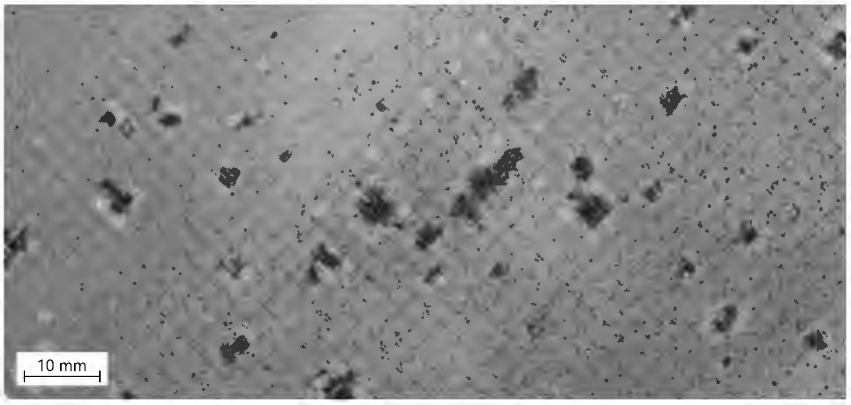

Figure 8-14: Photographs showing indents (black spots) found on G17/SS-6 at 43.2 Ns

The damage and final profile observed on the Glass 17/Super Sap panels was similar to those observed in the GRFPs with Prime 20LV composites. The maximum midpoint deflection measured was 0.6 mm, similarly to the Glass 17/Prime 20LV. The profile was also considered flat. Images of the cross-sectioned panels are shown in Figure 8-15.

Figure 8-15: Cross-sectional photographs of blast tested Glass 17/Super Sap panels

8.4 Supawood

Supawood panels were the weakest of all the materials tested. Smaller masses of explosive (ranging from 2 g – 6 g) were used in the test series. Consequently, the impulse ranged from 10.4 Ns to 20 Ns. Photographs showing the progression of damage with increasing impulse, on the front and back

surfaces of the panels, is shown in Figure 8-16. Images of the remaining Supawood panels tested in the series can be found in Appendix D. Initially, no visible damage was observed on the surfaces at impulses lower than 14.1 Ns except for MDF-6 at 11.5 Ns. Cracks appeared at higher impulses until a panel (MDF-1) completely failed at an impulse of 20 Ns.

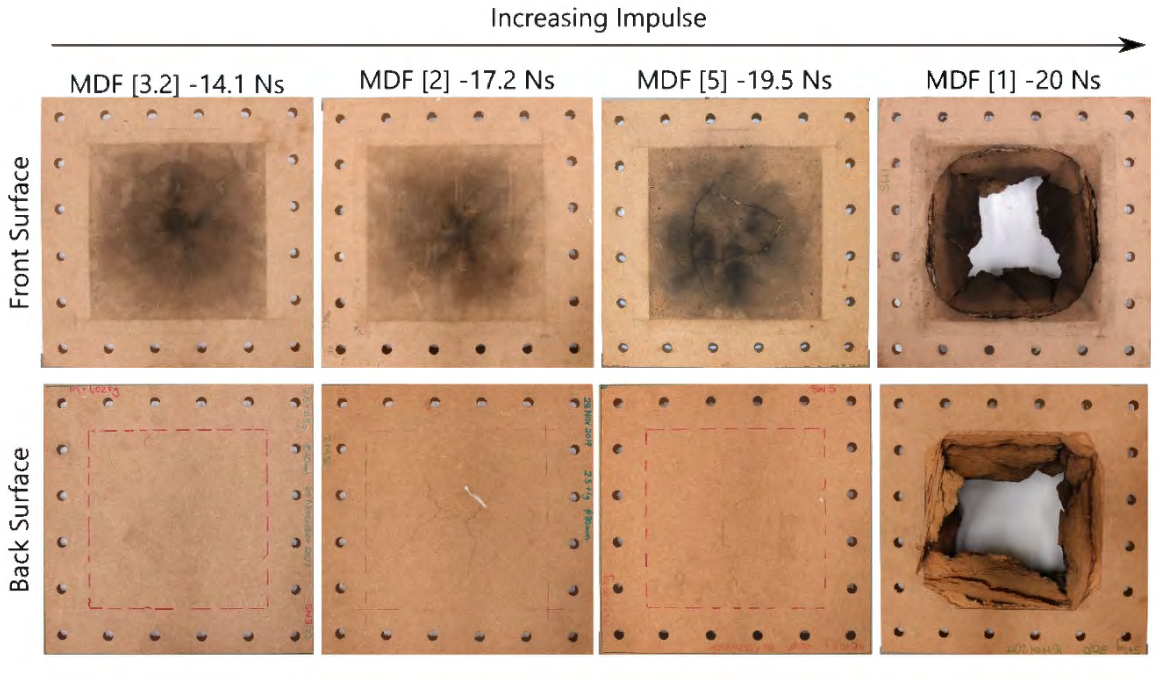

Figure 8-16: Front and back surfaces of different blast tested Supawood panels

Typically, cracks were found on the back surface of the Supawood panels and not on the front surface, except for MDF-5 at an impulse of 19.5 Ns. The cracks formed were traced and are highlighted in Figure 8-17. While the crack grew from MDF-6 to MDF-8, the crack for MDF-8, MDF-2 and MDF-4 did not appear to significantly change in length when the impulse increased from 15.7 Ns to 17.2 Ns. There also appeared to be little consistency with regards to crack pattern.

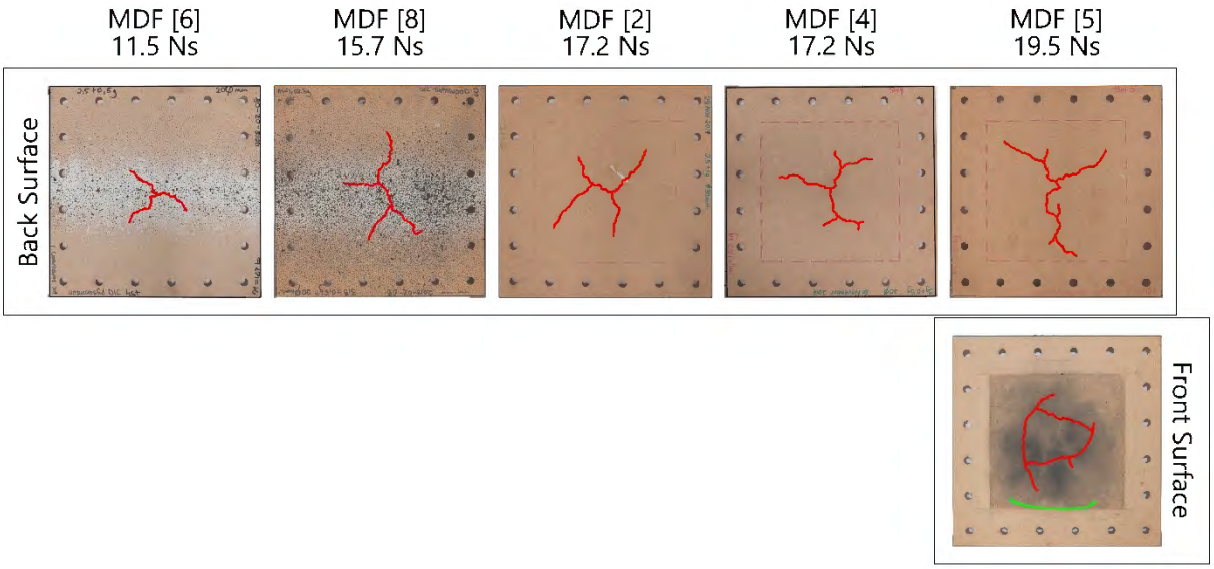

Figure 8-17: Cracks on the surfaces of blast tested Supawood Panels.

On the front surface of MDF-5, the crack pattern suggested that a hole might form at the centre of the panel. A crack was also formed at the boundary. There was no damage observed at the boundary for any panels tested at a lower impulse. The exposed areas of MDF-5, without tracings, show how the cracks appeared in Figure 8-18.

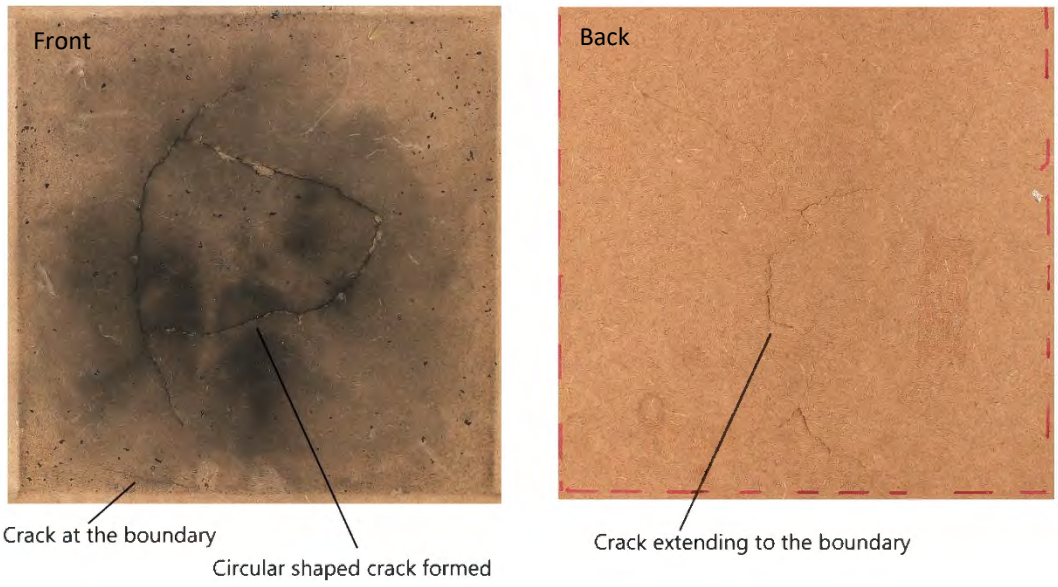

Figure 8-18: Photographs showing the exposed area of MDF-5 subjected to 19.5 Ns

For the nominal impulse of 20 Ns (MDF-5 subjected to a charge mass of 4.5 g and 20 mm in diameter, and MDF-1 at 6 g and 30 mm) there were significant differences in damage observed as shown in Figure 8-16. MDF-5 had large amounts of cracks on the front and back surface, however the panel remained intact. MDF-1 ruptured and fragments of the Supawood panel scattered in the blast chamber. The behaviour was not like rupture and damage observed in metals as the centre did not

punch out in a singular piece. Instead, multiple fragments were formed. These fragments resulted from fractures through the thickness as well as parallel to the surfaces. These fragments varied in sizes and thicknesses. The fragments, alongside the panel (MDF-1), are shown in Figure 8-19.

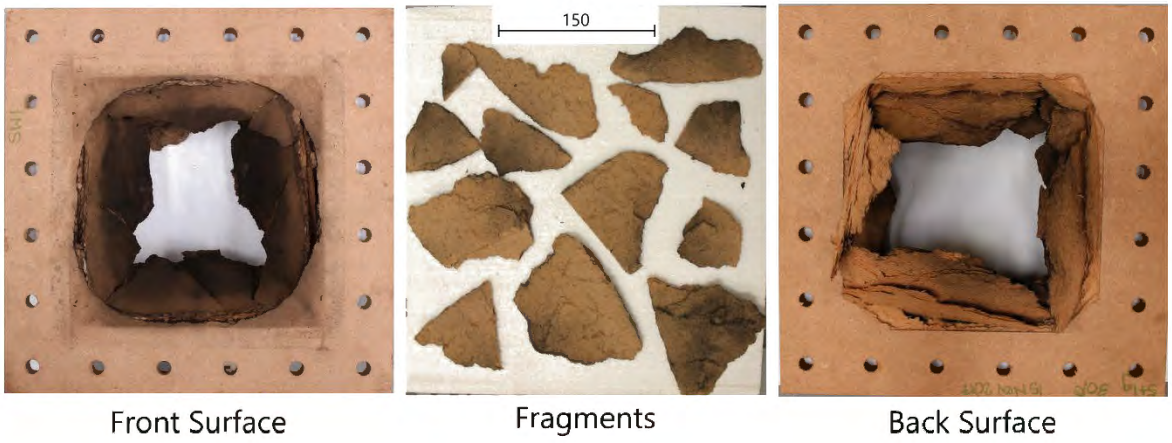

Figure 8-19: Fragments from blast tested Supawood panel MDF-1 blast tested at 20 Ns

A schematic is shown in Figure 8-20 to differentiate the types of cracking that could occur on the cross-section of the composites. Supawood panels showed signs of damage, in the form of cracks, on the cross-sectional area as shown in Figure 8-21. The cracks developed were predominately parallel to the surfaces (which was termed as through-width cracks). Despite the lack of back-surface cracks on MDF-7 and MDF-3.2, more internal cracks were observed on the two Supawood panels compared to MDF-6. Sectioning MDF-1 was difficult as the panel was very fragile, and parts of the panel came loose. The profile of the panels shows a slight bulge for MDF-5, MDF-2, and MDF-8 where there appeared to be significant cracks. The other panels, excluding MDF-1, remained fairly flat.

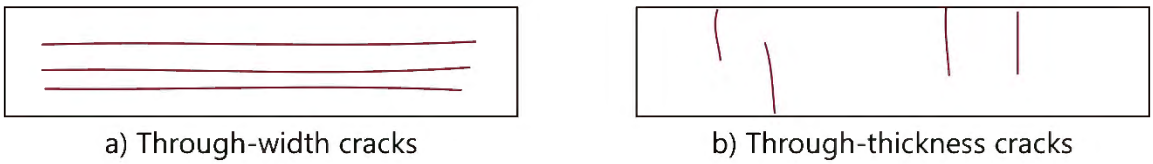

Figure 8-20: Schematic of cracks orientated a) parallel and b) perpendicular to the surfaces

Figure 8-21: Cross section photographs for blast tested Supawood panels

8.5 Flax fibre reinforced Prime 20LV composites

The observations found on the flax fibre reinforced Prime 20LV composites were divided into two sections. Section 8.5.1 discusses the qualitative results on the Flax 9/Prime 20LV panels manufactured using VI, whereas section 8.5.2 discusses the results on the Flax 8/Prime 20LV manufactured using hand lay-up. The differences between the two flax fibre reinforced Prime 20LV panels, including manufacturing practices, were elaborated in section 5.

8.5.1 Flax FRP panels manufactured using VI

The front and back surfaces of the VI flax fibre reinforced Prime 20LV composite (Flax 9/Prime 20LV) panels tested are shown in Figure 8-22 in ascending order of exposed impulsive loads. Due to the paint on DIC panels and black burn mark left on the front surfaces of panels, cracks were traced and highlighted in Figure 8-22. Original images can be found in Appendix E. Red traces indicated cracks found in the exposed area of the panel and green traces were at the clamped edge boundary. Cracking was found to be the most significant failure observed. Detailed images of cracks on unpainted specimens are shown in Figure 8-23.

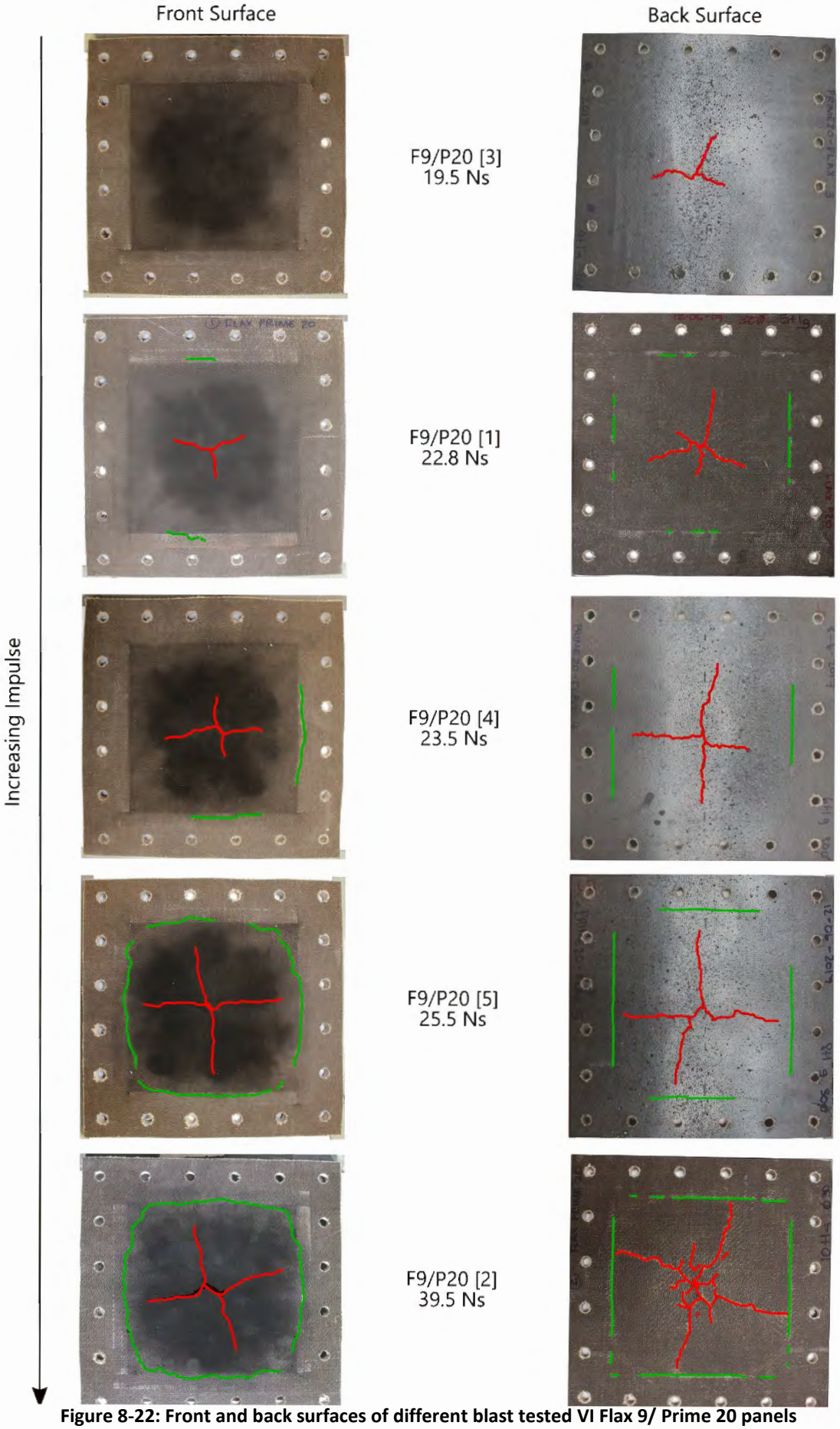

Figure 8-22: Front and back surfaces of different blast tested VI Flax 9/ Prime 20 panels

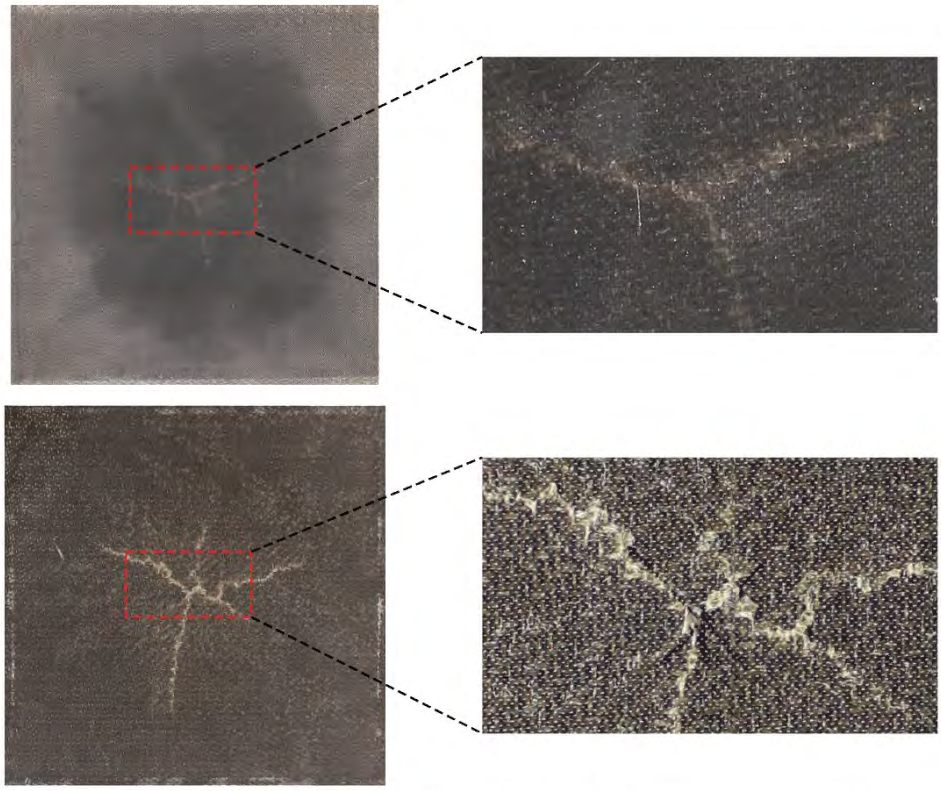

a) Detailed view of the front and back surfaces of F9/P20-1 subjected to 22.8 Ns

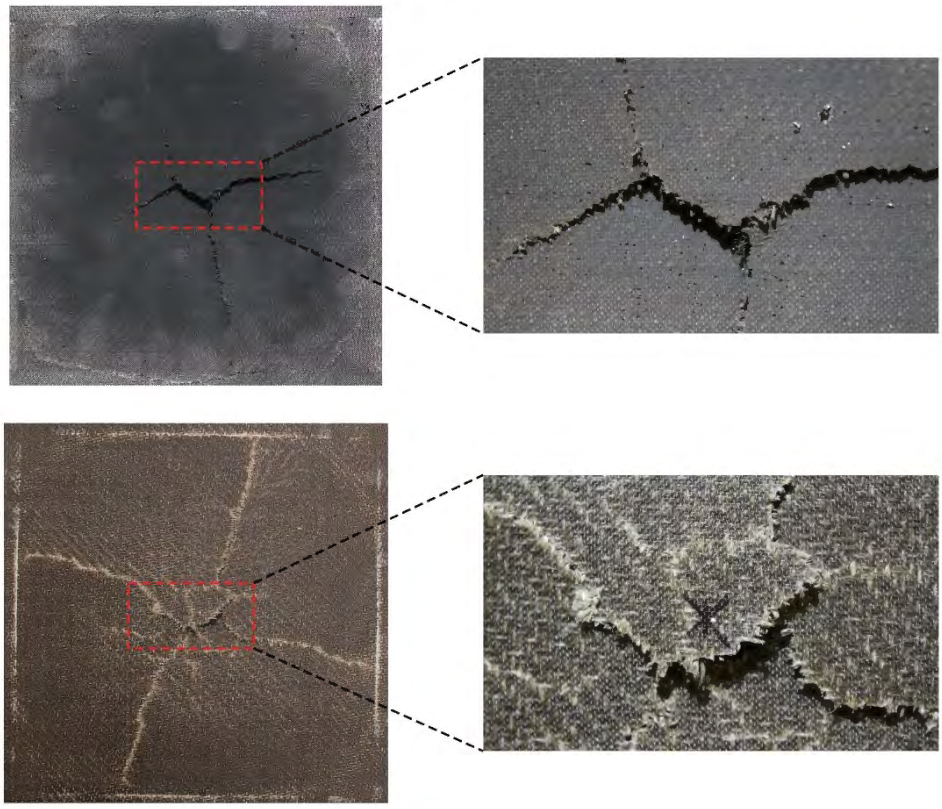

b) Detailed view of the front and back surfaces of F9/P20-2 subjected to 39.5 Ns

Figure 8-23: Detailed view of the cracks formed on the exposed area of VI Flax 9/Prime 20LV panels

Initially, no cracks were observed on the front surface of F9/P20-3 at an impulse of 19.5 Ns. Cracks were, however, observed on the back surface indicating a tensile mode of failure. In general, the cracking appeared to be extending from the centre, increasing in length and number with increasing impulse on both faces. At an impulse of 25.5 Ns, the cracks on panel F9/P20-5 had reached the edge of the clamped edge. The crack pattern was consistently cross-shaped. Similar cross-shaped cracks were observed on carbon fibre reinforced epoxy composites tested under uniform blast loading conditions by Yahya et al [140]. Note that the exposed area for the carbon reinforced composites was circular instead of square [140]. The damage near boundary on the flax fibre reinforced panels seemed to form a slight circular pattern on the front surface.

As observed with the cracks, the damage at the boundary increased, shown in Figure 8-24, with increasing impulse and was a combination of matrix and fibre cracking was observed on the front and back surfaces. At low impulses below 23.5 Ns, the boundary damage observed along the front and back surfaces were similar. Slight scuffing likely occurred during clamping as the surfaces of the panel are not completely smooth. At higher impulses, the boundary damage on the back surface was more severe but typically only at the clamped edge. On the front surface, open cracks were observed. The cracks formed were not at the apex of the clamp corners.

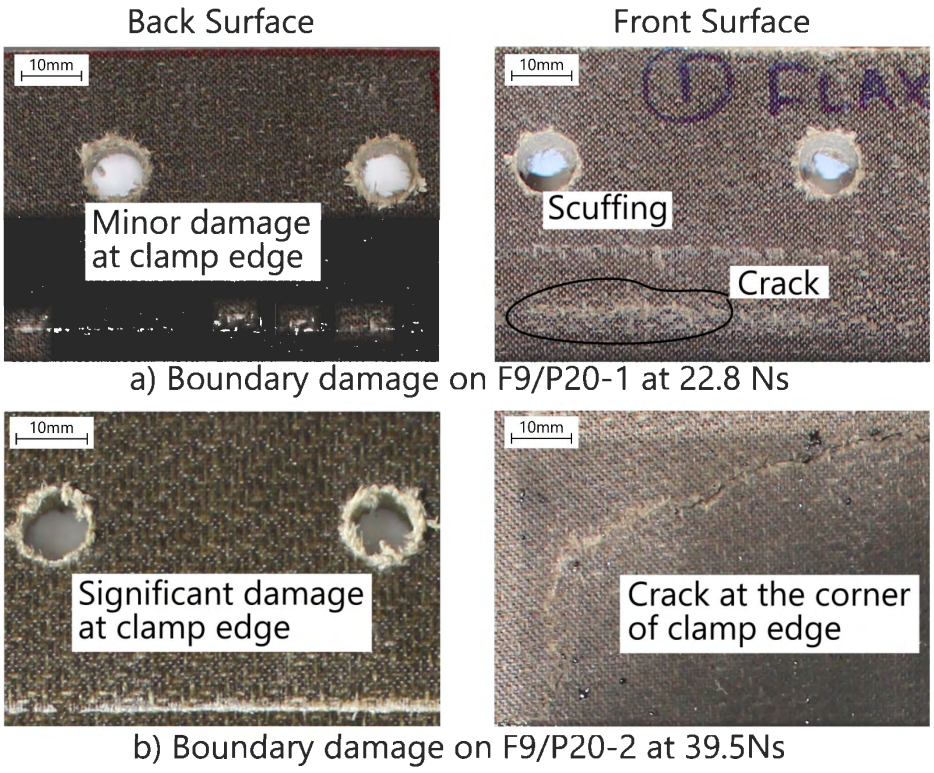

Figure 8-24: Damage observed along the clamped area and clamped edge boundary on VI Flax 9/Prime 20LV panels

The images of the cross-sections for the VI Flax 9/Prime 20LV panels are shown in Figure 8-25. Through-thickness cracking was observed with no signs of delamination. The profile for the panels F9/P20-4, F9/P20-1, F9/P20-3 appeared flat. A slight dome was then observed on F9/P20-5, followed by a shallow triangular-shaped profile which formed for F9/P20-2.

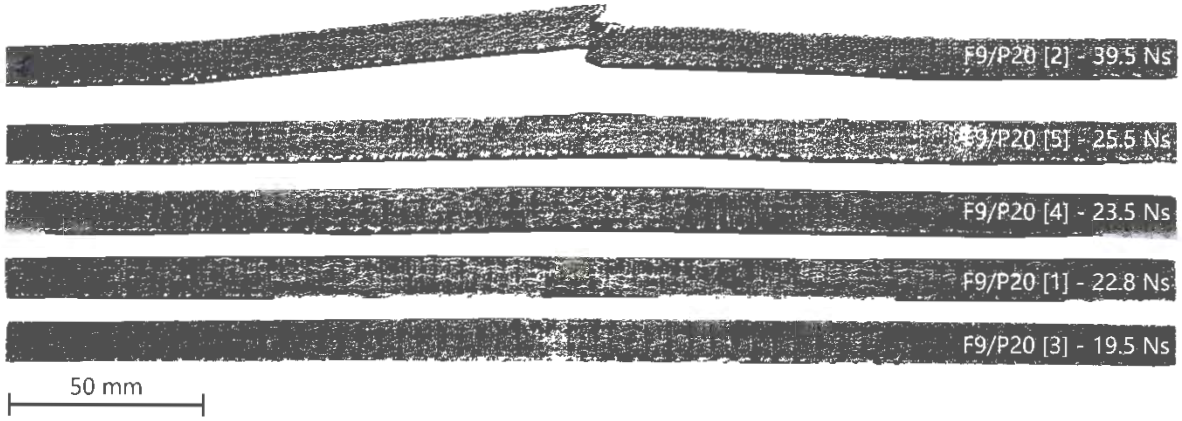

Figure 8-25: Cross section photographs for blast tested VI Flax 9/Prime 20LV panels

8.5.2 Flax FRP panels manufactured using hand lay-up

The front and back surfaces, with highlighted cracks, for the hand lay-up flax fibre reinforced panels (Flax 8/Prime 20LV), tested at a similar nominal impulse as the VI Flax 9/Prime 20LV panels, are shown in Figure 8-26. The remaining panels, both traced and non-traced, and original images of the panels displayed in Figure 8-26 can be found in Appendix E.

Cracks were a prominent failure mode for the flax fibre reinforced panels manufactured using hand lay-up. The edges of the cracks were not smooth. More fibre pull-out and fracture were observed compared to the VI Flax 9/Prime 20LV panels as depicted in Figure 8-27. Overall, the crack length quantity increased with increasing impulse, despite less damage observed on F8/P20H-9 as shown in Figure 8-26. On panel F8/P20H-8, at an impulse of 23.8 Ns. The cracks on the back surface had reached the clamped edge of the panel. While the crack pattern was not as well-defined and consistent as the VI Flax 9/Prime 20LV panels, a cross pattern was observed on some of the hand lay-up panels.

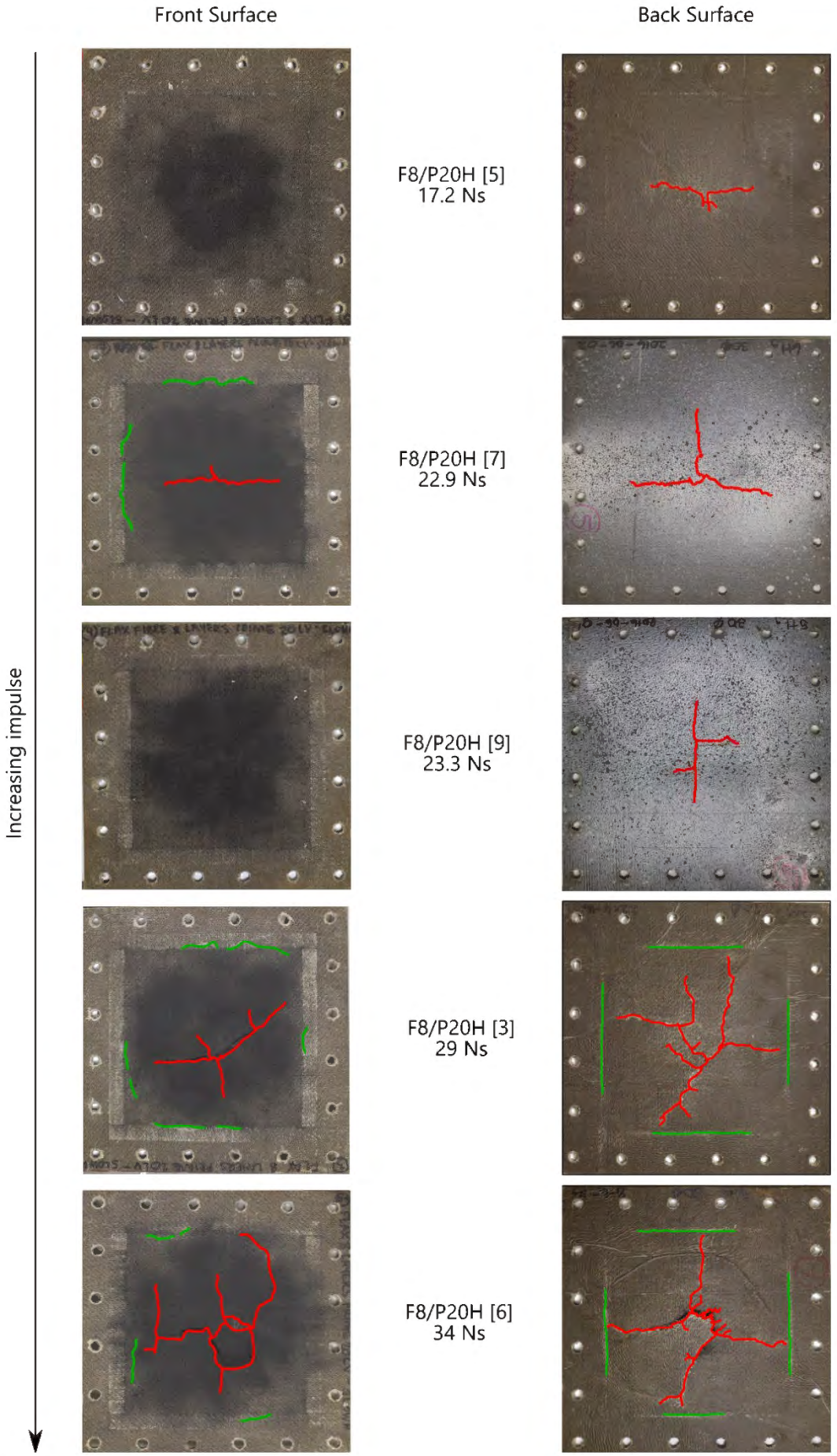

Figure 8-26: Front and back surfaces of different blast tested hand lay-up Flax 8/Prime 20 panels

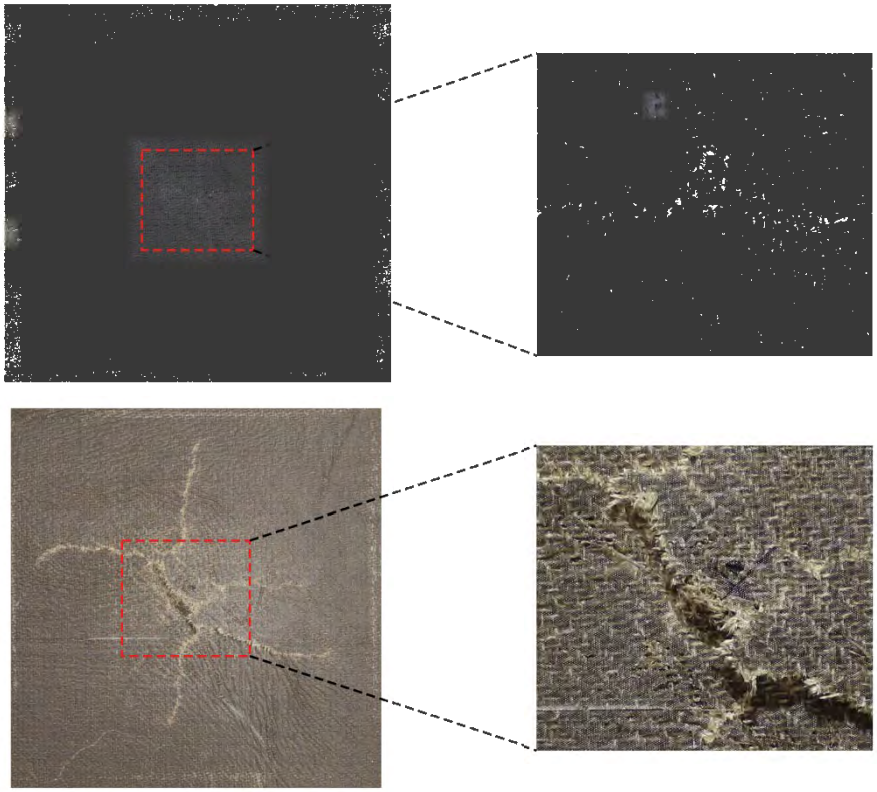

a) Detailed view of the front and back surfaces of F8/P20H-8 subjected to 23.8 Ns

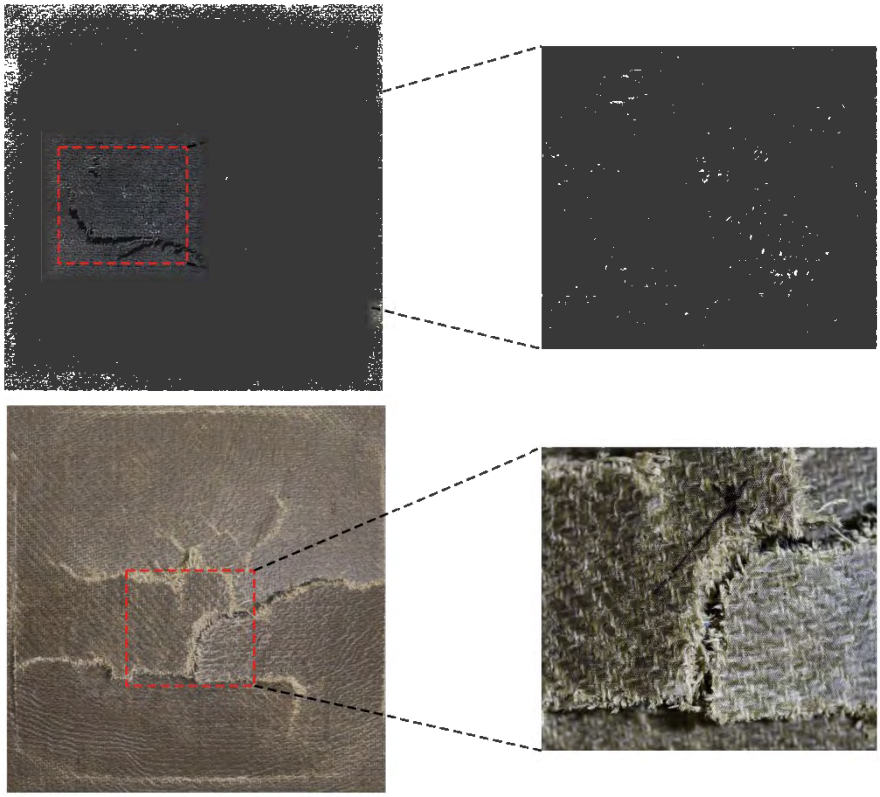

b) Detailed view of the front and back surfaces of F8/P20H-4 subjected to 28.1 Ns

Figure 8-27: Detailed view of the cracks formed on the exposed area of hand lay-up Flax 8/Prime 20LV panels

There were similarities between the VI and hand lay-up flax fibre reinforced Prime 20LV composite panels in the type of damage observed on the clamped edge boundaries of the panels as shown in Figure 8-28. Additionally, two hand lay-up Flax 8/Prime 20LV panels, F08/P20-4, shown in Figure 8-29, and F08/P20 [1], had sheared at the boundary. This was similar to a shear or punched cutting process and possibly a result of the significant difference in elastic response between the flax fibre reinforced composite panel and the steel clamp frame.

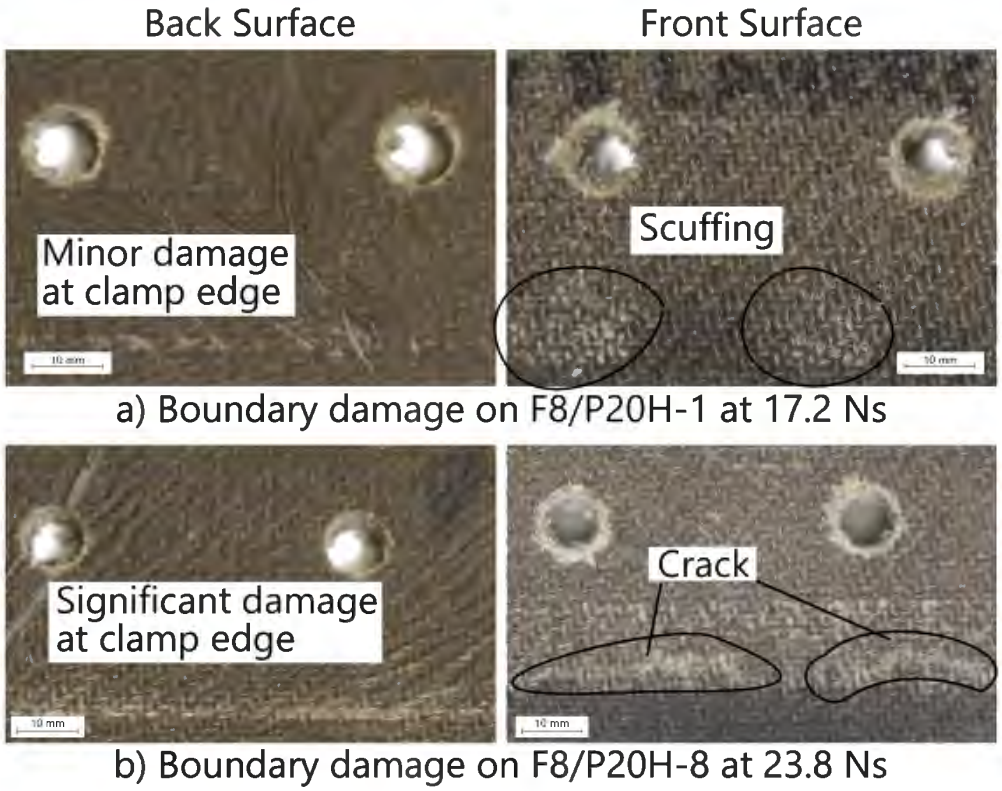

Figure 8-28: Damage observed along the clamped area and clamped edge boundary on hand lay-up Flax/Prime 20LV panels

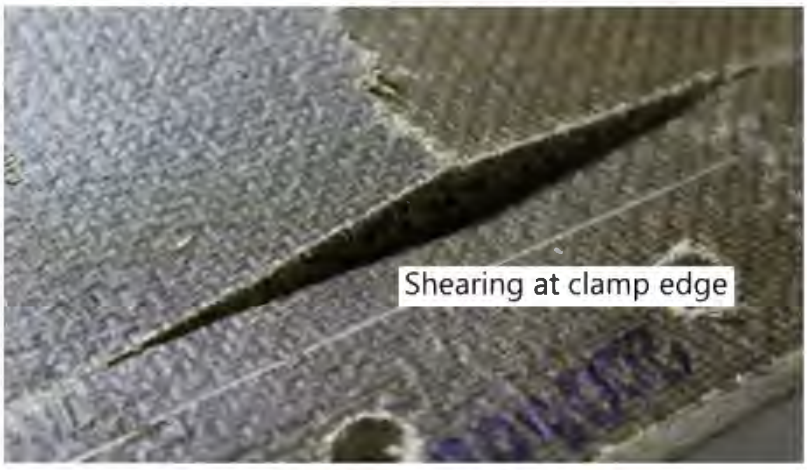

Figure 8-29: Shearing along the boundary on the back face of F8/P20H-4 at 28.1 Ns

While significant permanent deformation was observed and accounted for using midpoint displacement measurements, the surface of some the hand lay-up flax fibre reinforced panels seemed to be irregular as shown in Figure 8-30. This was not observed on the VI Flax 9/Prime 20LV panels where the surfaces were relatively smooth and straight. This suggested that delamination occurred in those panels due to the weak interfacial adhesion within the panels caused by the less consistent manufacturing process. This delamination could thus be identified without sectioning the panel.

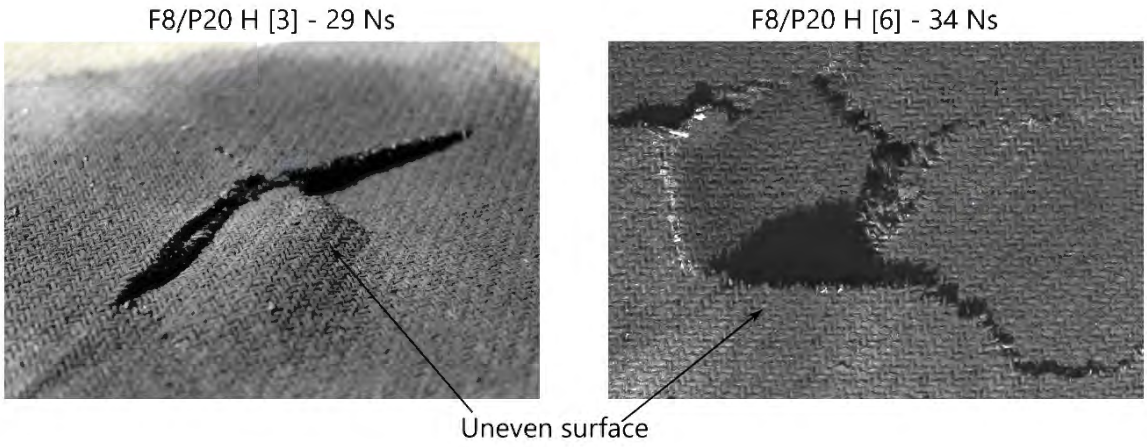

Figure 8-30: Photographs of the surface of hand lay-up Flax8/Prime 20LV panels

Delamination was observed on the six hand lay-up flax fibre reinforced panels, namely F8/P20H-1, F8/P20H-6, F8/P20H-4, F8/P20H-3, F8/P20H-8 and F8/P20H-9, as shown in Figure 8-31. Within every panel, the first layer closest to the blast loaded face had separated from the panel and appeared as through-width cracks. Through-thickness cracking was also observed. The through-thickness cracks, however, appeared to be skew and jagged in comparison to ones observed on the VI Flax 9/Prime 20LV panels. Additionally, on F8/P20H-1, through-width cracks had propagated through the thickness. F8/P20H-5 seemed flat without much deformation at low impulse of 17.2 Ns. The profiles for the other hand lay-up flax fibre reinforced panels seemed random with uneven surfaces (delamination effect).

Figure 8-31: Cross section photographs for blast tested hand lay-up Flax/Prime 20LV panels

8.6 Flax fibre reinforced Super Sap composites

The front and back surfaces, with highlighted cracks, for all of the VI flax fibre reinforced Super Sap (Flax 9/Super Sap) composite panels tested are shown in Figure 8-32. Original images can be found in Appendix E. Detailed views of the cracks observed on Flax 9/Super Sap panels are shown in Figure 8-33 and were found to be similar to the cracks observed on VI Flax 9/Prime 20LV panels.

Less cracking was observed on the Flax/Super Sap panels compared to the Flax/Prime 20LV panels. Cracking on the front face was only observed on F9/SS-5 at 28.3 Ns (which was also the same panel where the crack had reached the edge of the clamped edge). On F9/SS-2, capping and cracks formed (detailed image found on Figure 8-33b). In comparison to the VI Flax/Prime 20LV panels, the crack patterns observed on Flax/Super Sap panels appeared random. It was difficult to determine whether a cross-shaped pattern had formed as significant crack damage occurred at higher impulses.

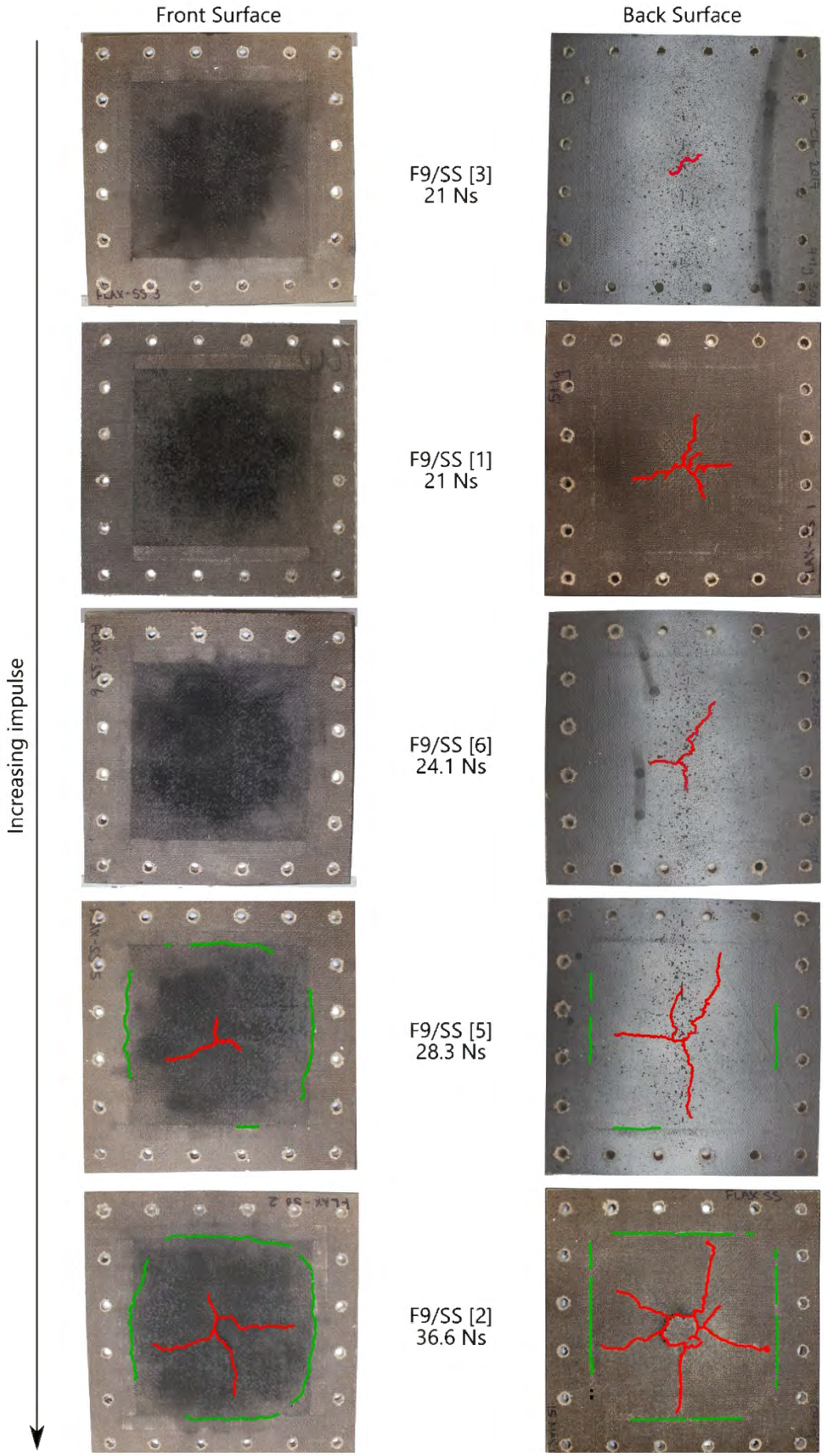

Figure 8-32: Front and back surfaces of different blast tested Flax 9/Super Sap panels

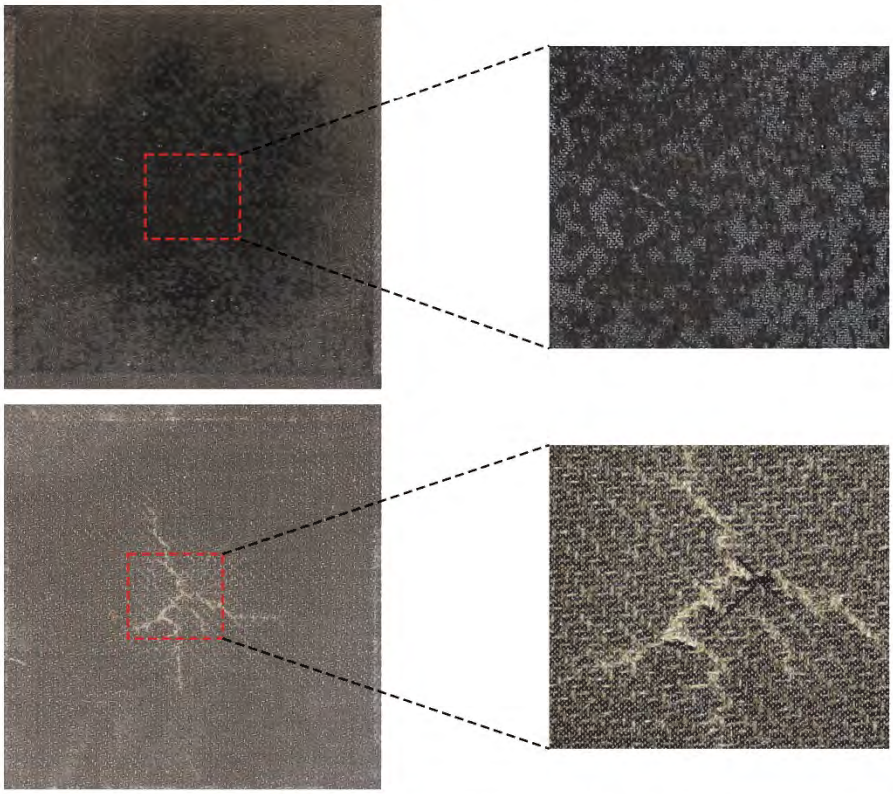

a) Detailed view of the front and back surfaces of F9/SS-1 subjected to 21 Ns

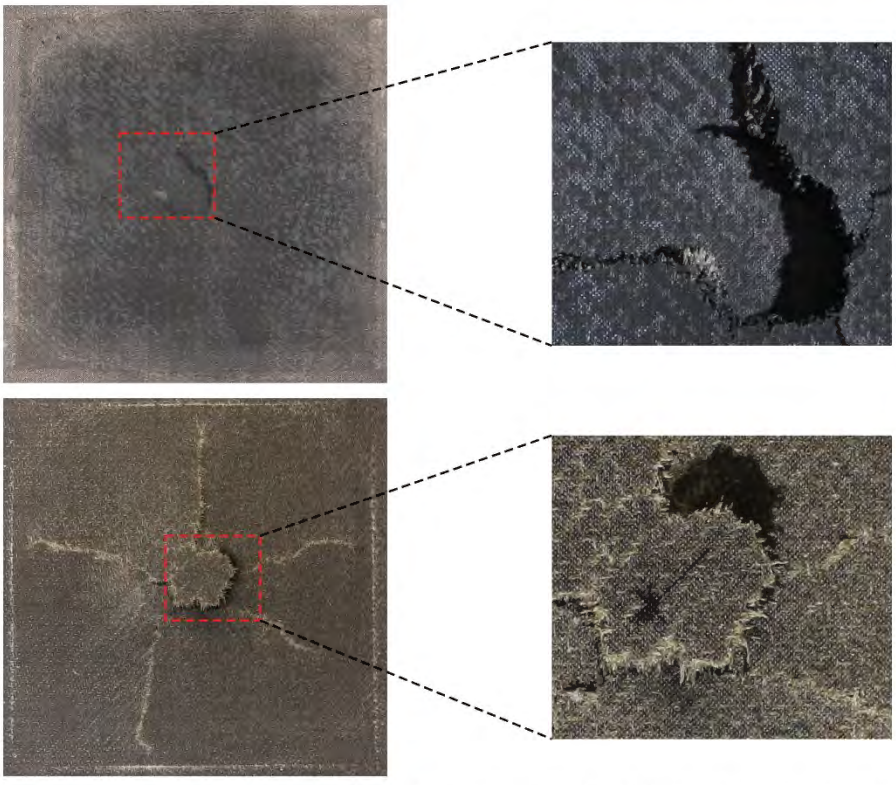

b) Detailed view of the front and back surfaces of F9/SS-2 subjected to 36.6 Ns

Figure 8-33: Detailed view of the cracks formed on the exposed area of VI Flax 9/Super Sap 20 panels

The damage observed at the boundaries was similar to Flax 9/Prime 20LV panels. Fibre and matrix failure occurred at high impulses. Cracking along the clamped edge was also observed. Examples of the damage at the boundary is shown in Figure 8-34.

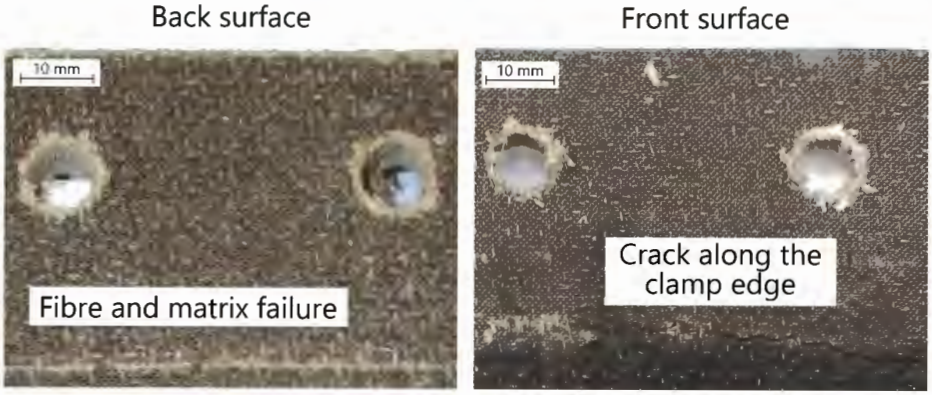

Figure 8-34: Damage observed at the boundaries of F9/SS-2 at 36.6 Ns

Similar observations were made on the Flax 9/Super Sap panels with regards to the cross-section. Delamination and through-thickness cracking was not observed. Panels F9/SS-1, F9/SS-6 and F9/SS-3 were fairly flat. A slight dome was observed on F9/SS-5. As observed on F9/P20-2, at the highest impulse tested at 36.6 Ns for FP/SS-2, the profile was a shallow triangular shape.

Figure 8-35: Cross section photographs for blast tested Flax 9/Super Sap panels

It did appear that, in general, the two VI flax fibre reinforced panels (one infused with Prime 20LV and the other with Super Sap) behaved similarly. The type of damage and cross-section profile was similar for the two materials. However, the amount of damage observed was less for the Flax/Super Sap panels which was contrary to the observations found for the glass fibre reinforced Super Sap and Prime 20LV composites tested.

8.7 Jute fibre reinforced Prime 20LV composites

The front and back surfaces, with highlighted cracks, for all the jute fibre reinforced composite (Jute 13/Prime 20LV) panels tested, except J13/P20-2 is shown in Figure 8-36. Original images can be found in Appendix F. The damage observed on the different panels ranged from insignificant at lower impulse (J13/P20-5 at 15.6 Ns) to severe with a hole having been formed in the central region of the panels with accompanying cracks having been developed from the formed holes to the boundary (J13/P20-6 at 19.9 Ns).

A detailed view of the cracks on Jute/Prime 20LV panels are shown in Figure 8-37. Cracks were first observed at 17.8 Ns on J13/P20-4 as faint crack lines formed on the back and front surface of the panel. The cracks had also reached the clamped edge. The amount and length of cracks increased with increasing impulses. In panel J13/P20-1, cracks extended to the boundary with shearing also occurring at the boundary. A hole formed at the panel centre of J13/P20-6 and J13/P20-3. It seemed that there was a single fragment after testing (shown for J13/P20-3 in Figure 8-37 (b)), which was not observed in any of the flax fibre reinforced composites. The crack pattern appeared random. However, for J13/P20-1 and J13/P20-3 circular arc cracks had formed. The cracks formed on the jute fibre reinforced composite panels suggested brittle behaviour. It was likely that the properties of the jute fibre reinforced composites were resin dominated.

On the back surface of panels J13/P20-1 and J13/P20-3, shearing along the boundary had occurred. Furthermore, it appeared that cracks on the clamped boundary stemmed from the centre of the panel as shown in Figure 8-38. Therefore, when tracing the panels, these cracks were considered part of the cracks originating in the exposed area (as shown in Figure 8-36 on the back surface of J13/P20-5). On the clamp edge appeared to be a line of damage considered as boundary failure which was a combination of fibre and matrix failure. On the front surface, open cracks had occurred along the boundary which were increasing severity with increasing impulse.

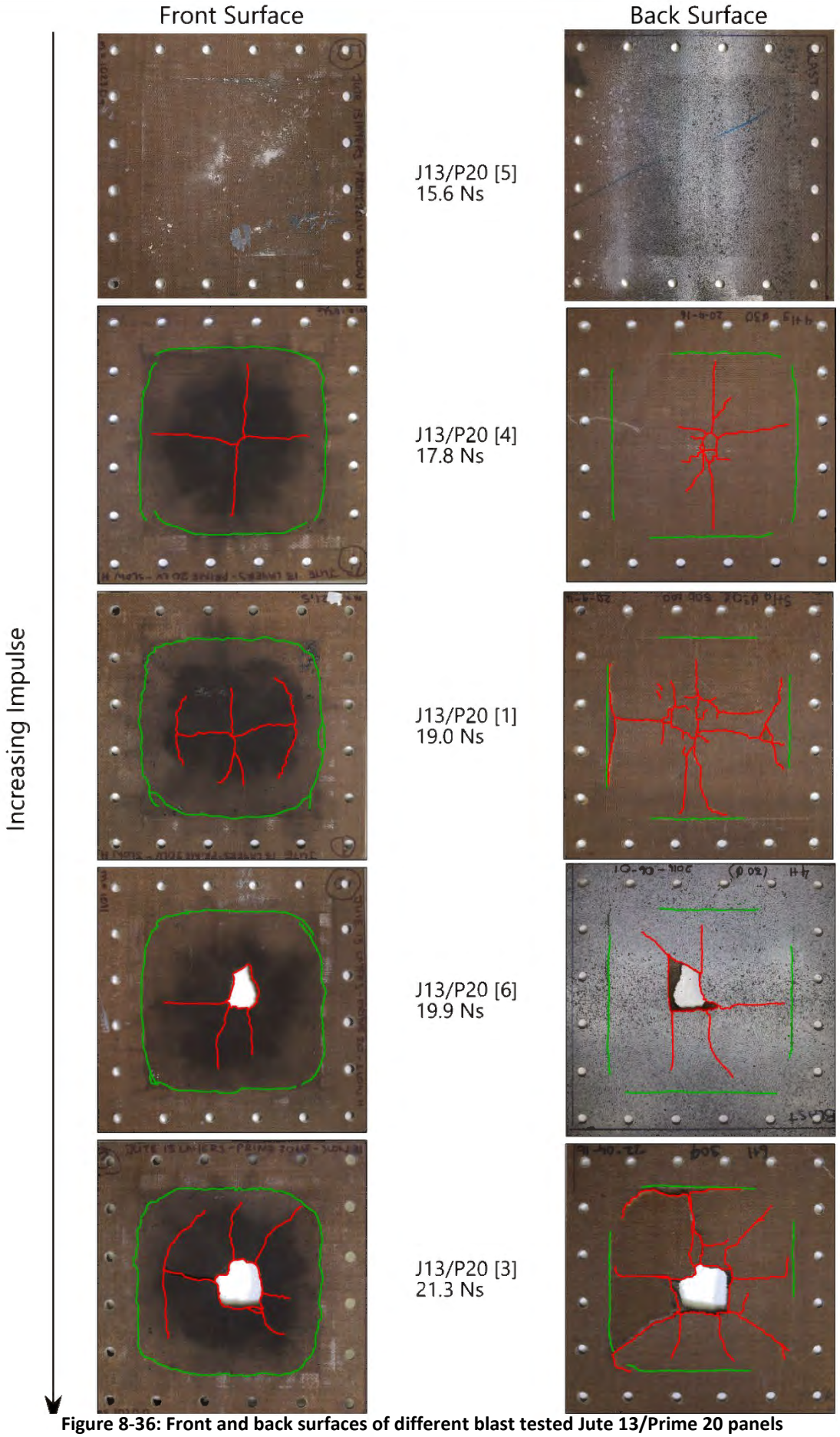

Figure 8-36: Front and back surfaces of different blast tested Jute 13/Prime 20 panels

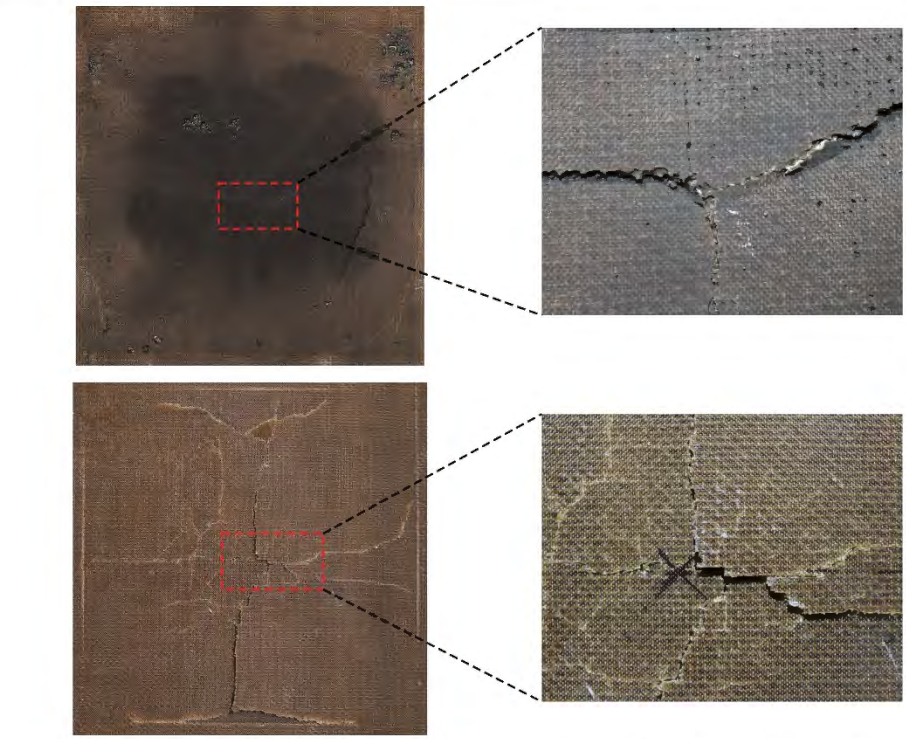

a) Detailed view of the front and back surfaces of J13/P20-1 subjected to 19 Ns

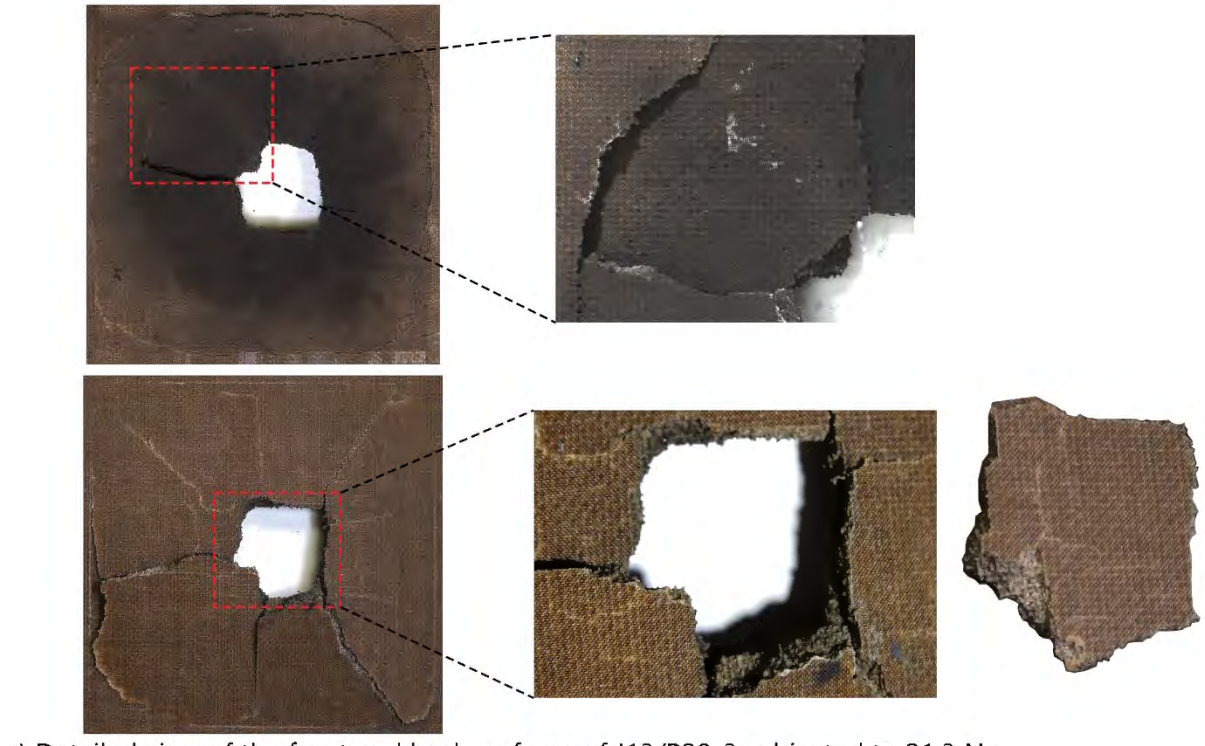

a) Detailed view of the front and back surfaces of J13/P20-3 subjected to 21.3 Ns

Figure 8-37: Detailed view of the cracks formed on exposed area of Jute 13/Prime 20LV panels

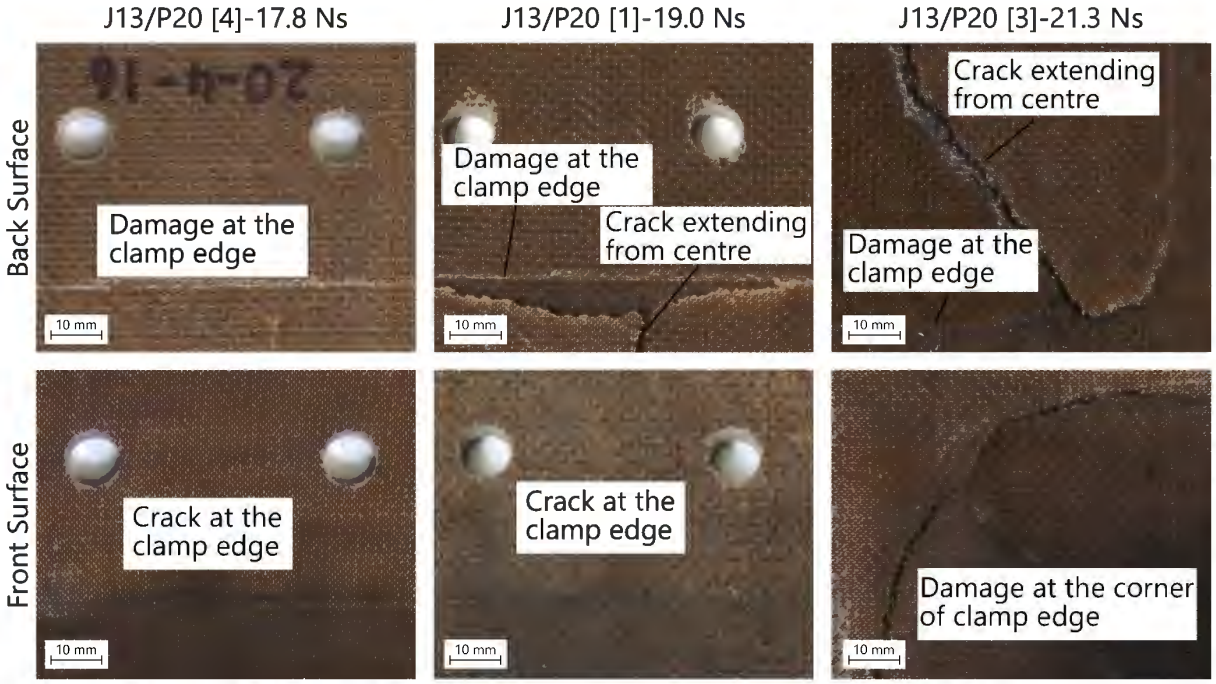

Figure 8-38:Damage at observed at the boundaries of Jute 13/Prime 20LV panels

At an impulse of 33.2 Ns, the exposed area of panel J13/P20-2, shown in Figure 8-39, was completely destroyed leaving only the clamped area intact. Most of the fragments retrieved after the test were as thick as the panel showing no evidence of delamination. It was likely that shearing occurred along the four edges as the panel shattered. Surface cracks were also observed on some of the fragments.

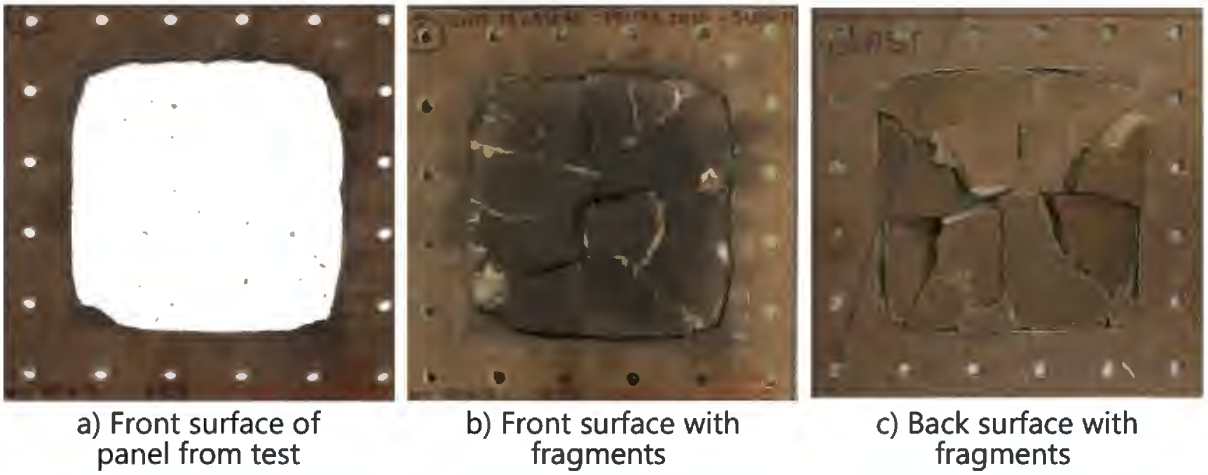

Figure 8-39: Destroyed jute fibre reinforced composite blasted tested at an impulse of 33.2 Ns

The photographs for the cross section of the jute fibre reinforced panels excluding J13/P20-2 are shown in Figure 8-40. The surface was found to be smoother compared to all flax fibre reinforced panels. Through-thickness cracking was observed on panels J13/P20-3, J13/P20-1 and J13/P20-6. Additionally, through-thickness cracking was observed at the boundary of the clamped edge for the

same panels. On J13/P20-4 at the centre of the panel, cracks formed parallel to the surface. The profile of J13/P20-6 was fairly flat despite part of the panel missing. Yet both J13/P20-3 and J13/P20-1 have a triangular shaped profile. The profile for the panels tested at impulses lower that 17.8 Ns were generally flat.

Figure 8-40: Cross section photographs for blast tested jute fibre reinforced panels

8.8 Results from microscopy

Stereomicroscope and scanning electronic microscope (SEM) images were also taken to further investigate the damage and fracture surfaces sustained by the different composites. This was used to describe the general surface characteristics of the different composite material and to identify how well the individual fibres bonded with the resin.

Stereomicroscopes are useful in analysing details of the three-dimensional structure of a specimen [217]. Typically, stereomicroscopes provide a wide field of view and variable magnification which could be a quick and useful manner to observe the fracture surfaces. It is considered suitable in applications where larger depth of fields and high contrasts are required [218]. SEM micrographs have been used in various natural fibre composite studies [219]–[221] to determine the interfacial adhesion between fibre and matrix and perform morphological analyses. SEM images of these studies were found to be similar as the ones presented in this work and were used to help describe the fibre- matrix adhesion. Furthermore, the SEM images were used as qualitative observations of the volume fraction of the composites. With reference to test method ASTM D3171, determining the constituent content of the composite by removing the matrix by digestion or ignition would be unsuitable for the NFCs. The alternative method suggested, which calculates the fibre content based on the measured thickness, does not consider voids. Based on the structure of the natural fibre (non-uniform cross section and cores), the value obtained would not give an accurate representation.

8.8.1 Observations from SEM images

Samples for SEM were obtained by removing a small piece, about 10 x 10 mm, from a section of a tested panel where no damage within the clamped area could be identified. Each specimen was prepared by sanding and polishing prior to taking SEM images. For each composite material, three SEM image are presented that show the arrangement of the fibres where one layer of the fibre is perpendicular to another layer, the circular and vertical cross-section of the fibre. Figure 8-41 shows a schematic of the idealised laminate and the three sections observed under SEM with the SEM parameters used.

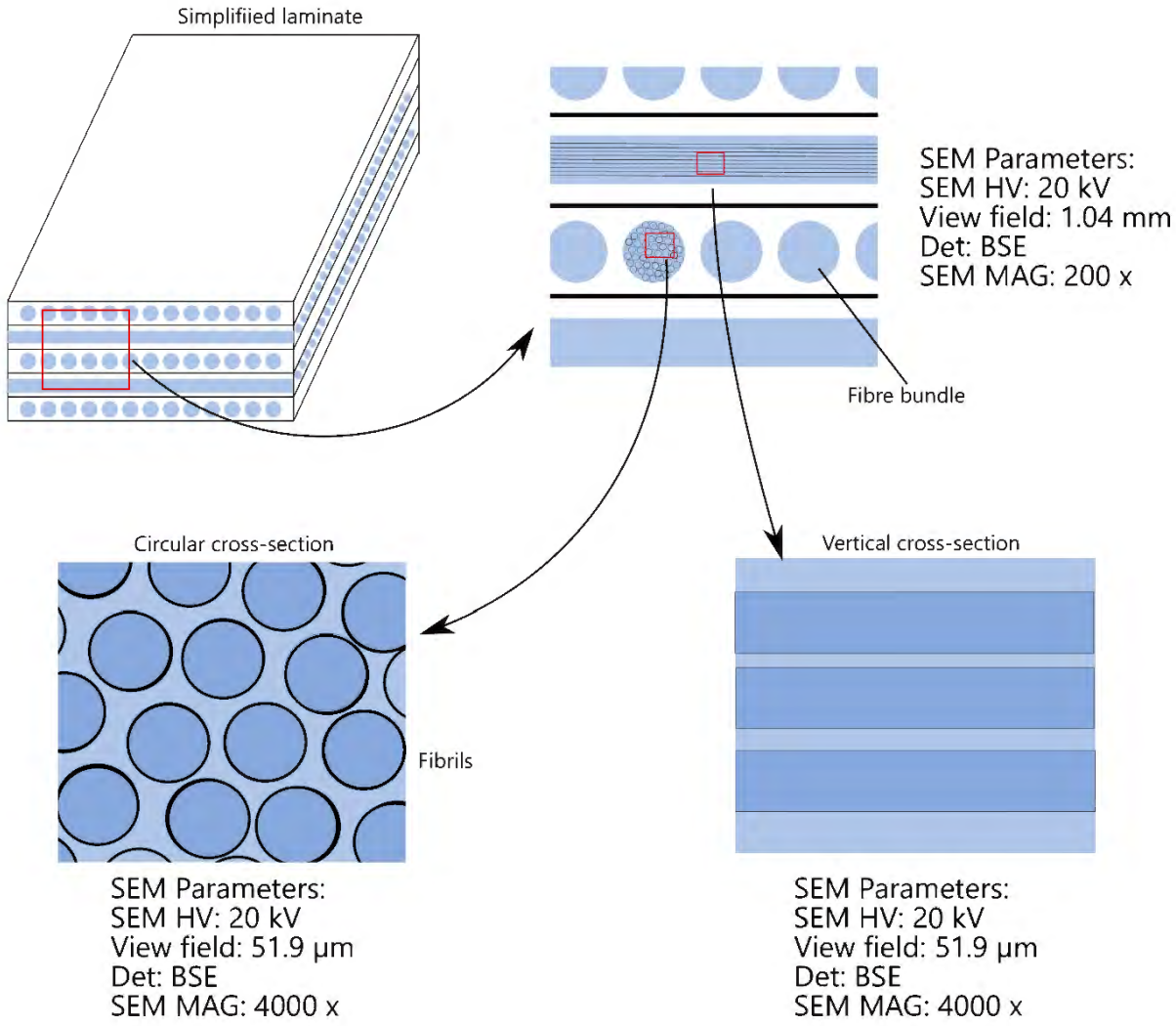

Figure 8-41: Simplified illustration of the SEM images and respective parameters

Examples for the glass fibre reinforced composite materials are shown in Figure 8-42. The individual fibres in the glass fibre bundle appeared to be of similar shape and size to one another. They also appeared to be well packed as shown in Figure 8-42. From circular and vertical cross-section images in Figure 8-42, fibres appeared fractured. This was likely due to the polishing process. In general, the different resins seemed well bonded to the individual fibres and seemed indistinguishable.

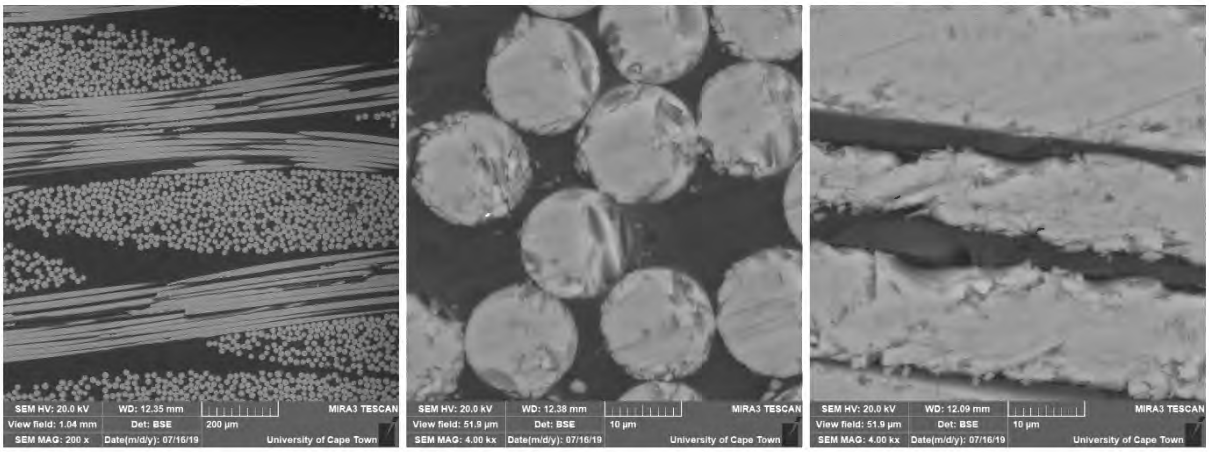

a) Glass/ Prime 20 (nominal thickness = 6 mm)

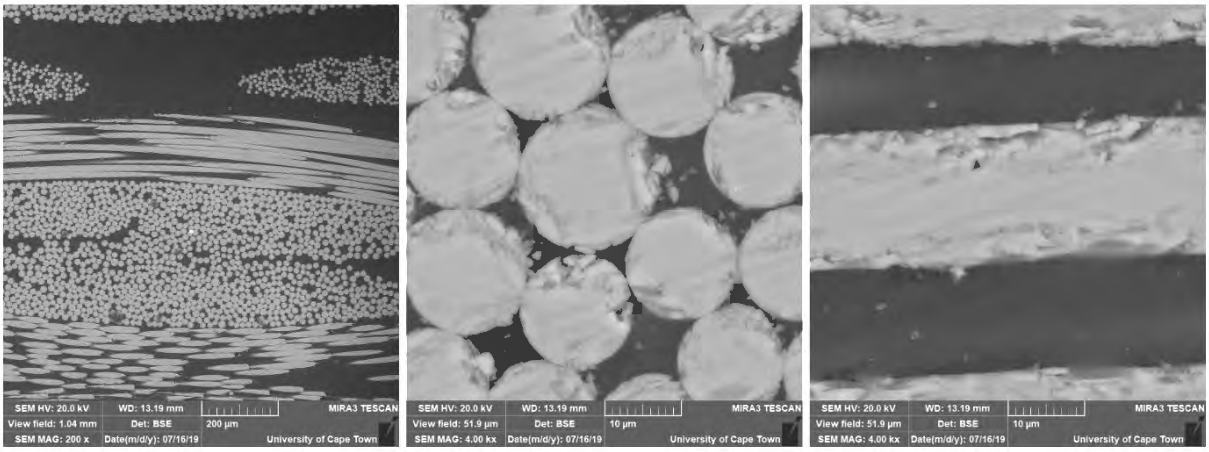

b) Glass/ Prime 20 (nominal thickness = 5 mm)

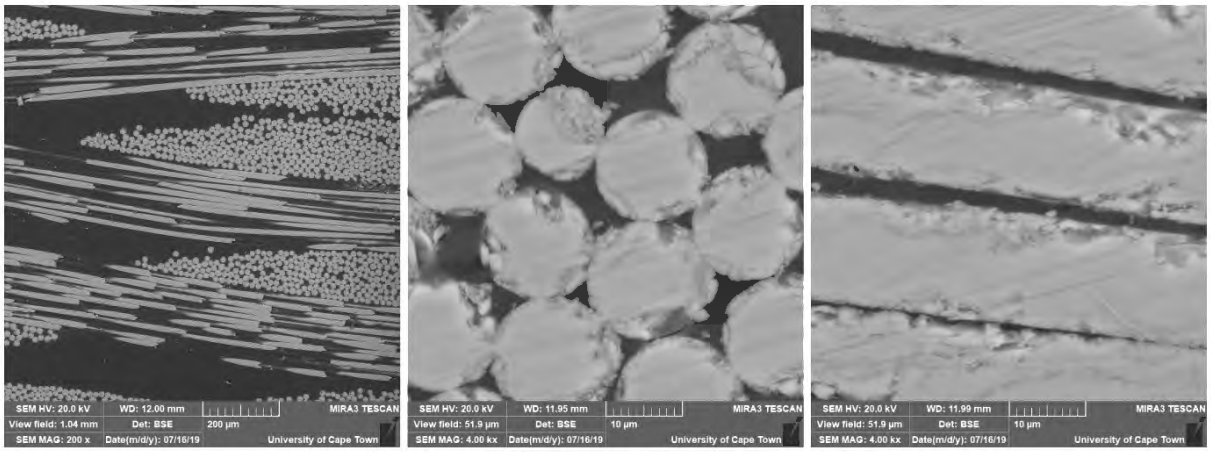

c) Glass/ Super Sap (nominal thickness = 5 mm)

Figure 8-42: SEM images of different glass fibre reinforced composite samples

Considering how Supawood is manufactured, the fibres were found to be randomly orientated yet densely packed, as expected, and shown in Figure 8-43. There were several air gaps observed in the material. Little amounts of resin were observed. In Figure 8-43, the fibres appeared to be fluffed. It is uncertain how much polishing the specimen contributed to this effect.

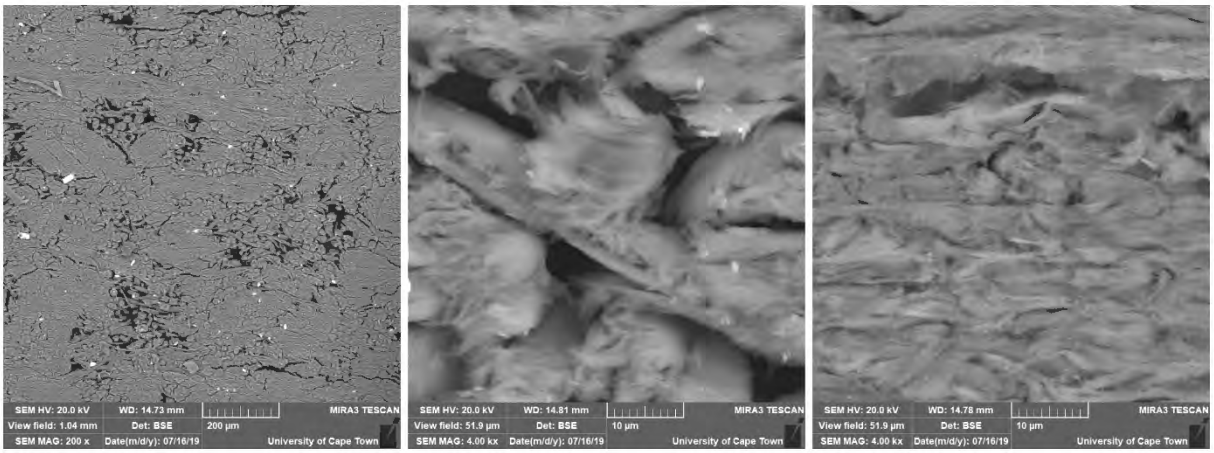

Figure 8-43: SEM Images of a Supawood sample

The SEM images for the flax-based composites, like the stereomicroscope images, were separated based on the manufacturing method. SEM images of the VATM flax fibre reinforced composite samples are shown in Figure 8-44 and the hand lay-up ones are shown in Figure 8-45. The flax fibre structure was not uniform or circular like glass fibre as observed in Figure 8-44. The individual fibres had a flattened core. The shape of circular cross-section of the fibres on the VI Flax/Prime 20LV sample seemed less elongated in comparison to the Flax/Super Sap. However, this can be expected as natural fibres are not as consistent in size and shape as synthetic fibres like glass or carbon fibre. Between the fibrils in a bundle were air gaps or cracks. Nevertheless, interfacial adhesion between fibre and resin was observed in some areas.

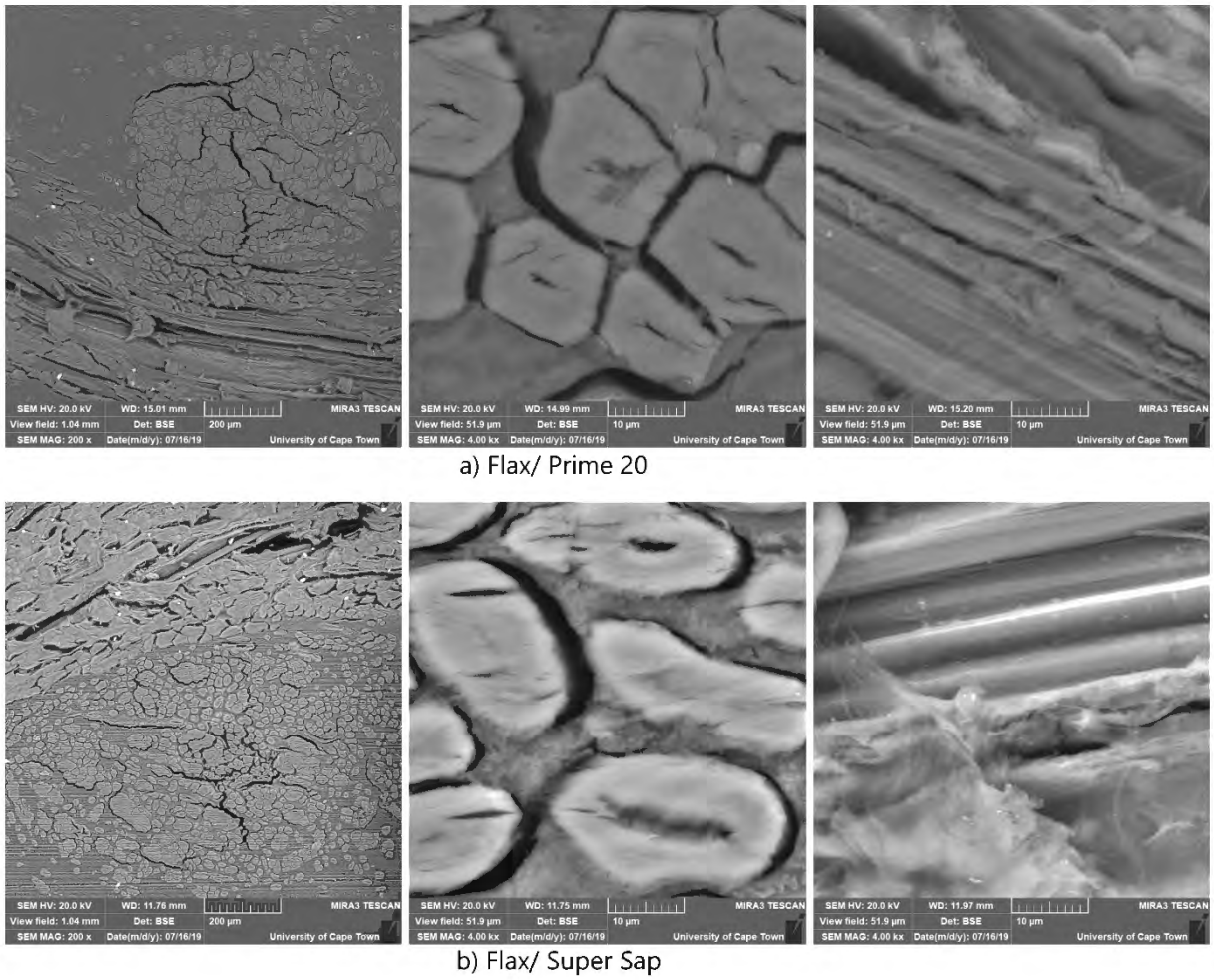

Figure 8-44: SEM images of different VI flax fibre reinforced composite samples

In section area A, shown in Figure 8-45a, similar observations can be made for the VI flax fibre reinforced samples. Some areas had good interfacial adhesion. Airgaps were also observed between individual fibrils. In section area B of the same sample, shown in Figure 8-45b, a pool of resin sitting on top of a fibre bundle was observed near a dry spot where fibres running perpendicular looking dry. Large airgaps and part where the resin was oversaturated were observed.

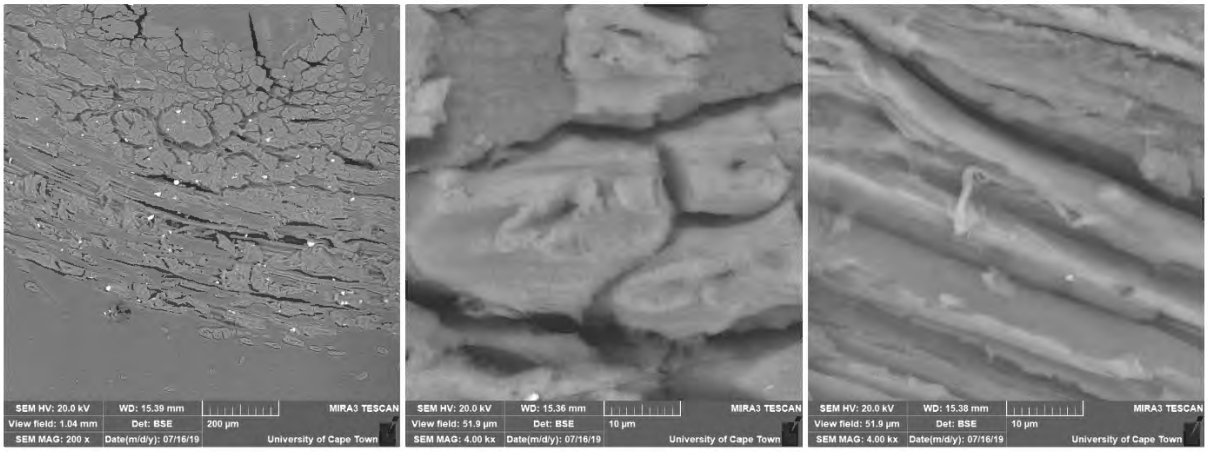

a) Section area A

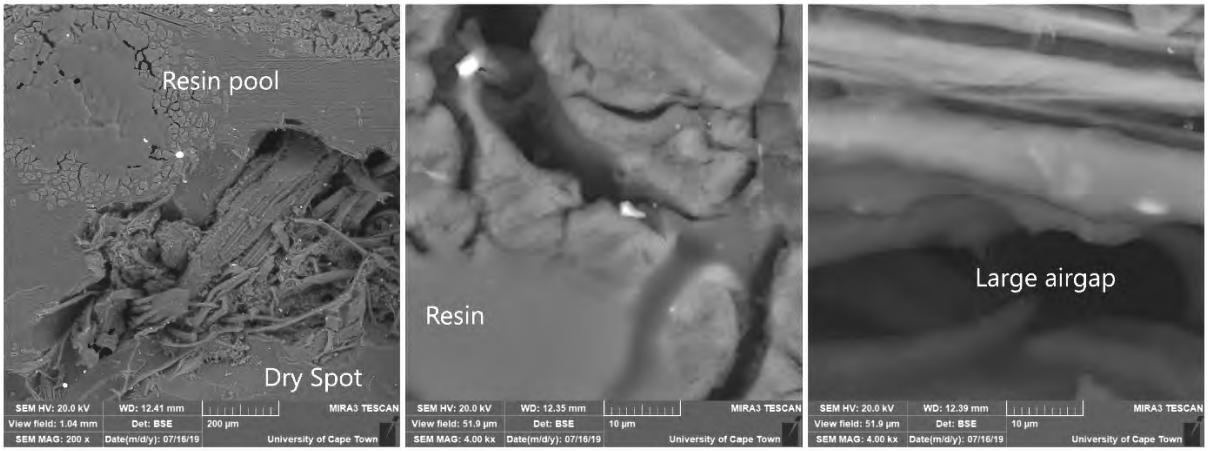

a) Section area B

Figure 8-45: SEM images of different area on a hand lay-up flax fibre reinforced composite sample

Similar observations were made on the jute fibre reinforced samples, shown in Figure 8-46. The core of jute fibre was significantly larger and rounder than those on flax fibre, yet the size of the fibre was smaller. Despite the fact that the resin filled the cores there were areas between the resin and the inner wall of the fibre that were not well bonded as shown in Figure 8-46.

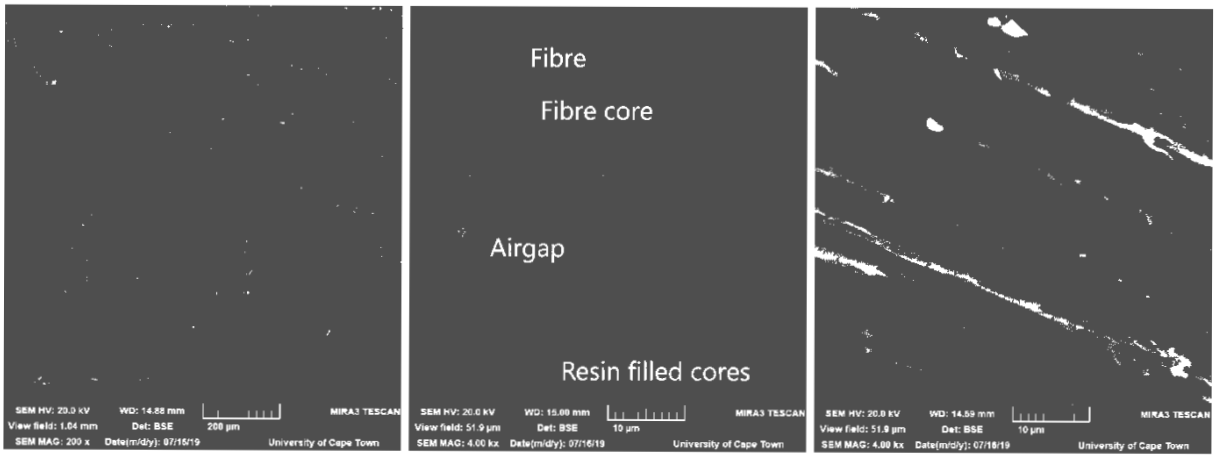

Figure 8-46: SEM Images of a jute fibre reinforced composite sample

Despite manufacturing the VI natural fibre laminates with care and using the same method used on the glass fibre reinforced composites, it did appear that consistent and complete fibre encapsulation was not as prominent as in the glass fibre reinforced composites. However, there was a more uniform distribution of fibres and resin for the VI composites in comparison to the hand lay-up flax fibre reinforced composite.

8.8.2 Observations from stereomicroscope images

Stereomicroscope images of samples cut from areas such as the boundary or delaminated area where damage was observed are shown in Figure 8-47. Sample A in Figure 8-47a shows a though-thickness crack angled at the boundary of the panel tested where through thickness cracking was observed. The through-width crack on Figure 8-47b indicated that two layers of fibre were separated. Voids of different sizes less than 200 µm, shown in Figure 8-47c, were scattered on different glass fibre reinforced composites samples. A crack formed on the front surface of Sample D is shown in Figure 8-47d. The top view of a delaminated surface is shown in Figure 8-47e. Sample F on Figure 8-47f shows the front surface where the matrix or interface failure occurred around the clamped edge boundary as the fibre remained intact.

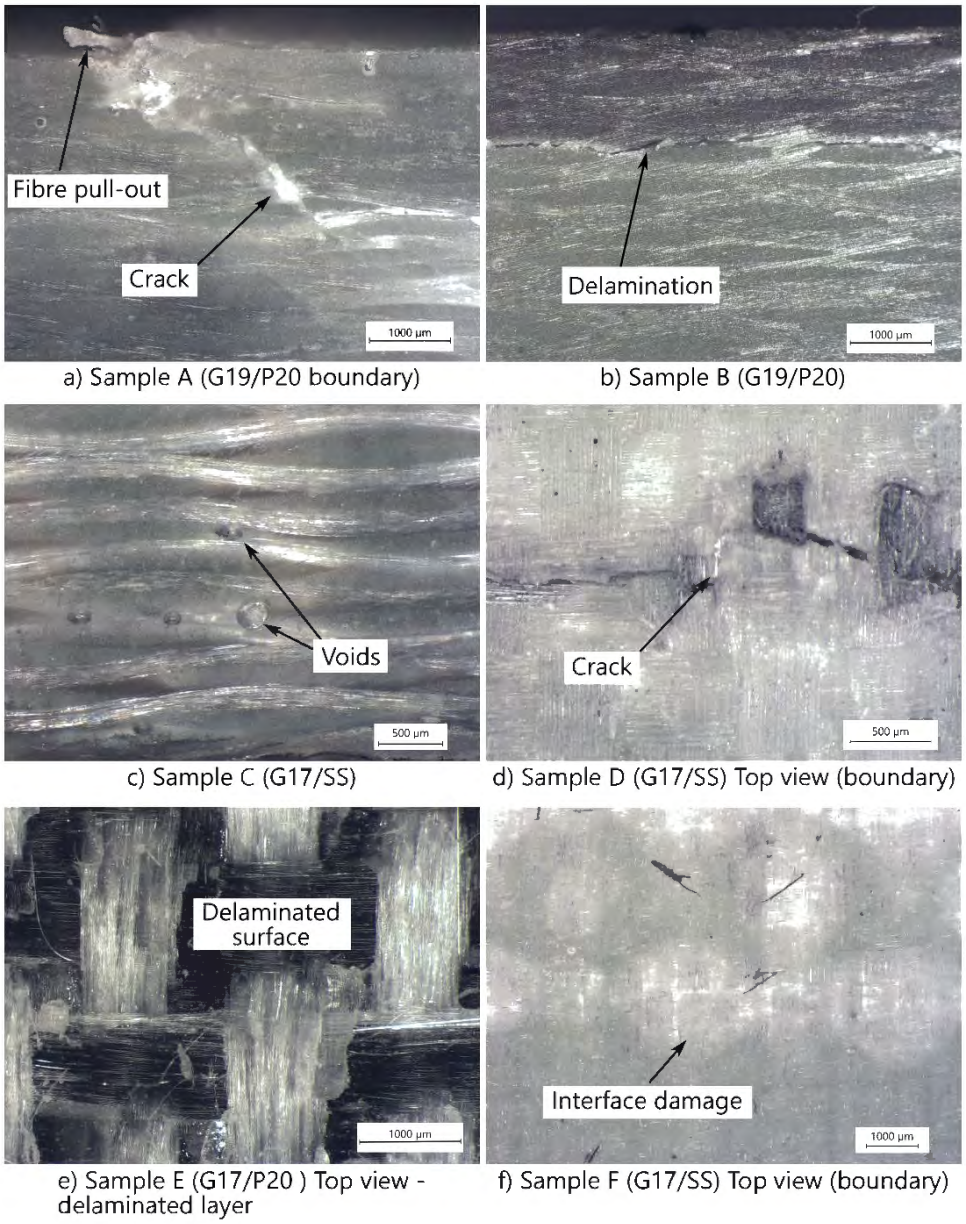

Figure 8-47: Stereomicroscope images of different glass fibre reinforced composite samples

An untested Supawood sample (Figure 8-48a) is shown alongside images of the cross-section of the fractured surface (Figure 8-48b) and front surface of a fragment (Figure 8-48c). Prior to blast testing, as observed in Figure 8-48a, the edges of the Supawood sample are more compressed compared to the centre of panel as expected. The fracture surface, shown in Figure 8-48b, was uneven with many frayed fibres. On the fracture surface, the fibres appeared to have remained tightly packed, short in length and are randomly orientated in the horizontal plane. On the front surface of the sample taken from a fragment, shown in Figure 8-48c, although fibres were randomly orientated, they were more orientated parallel for the surfaces.

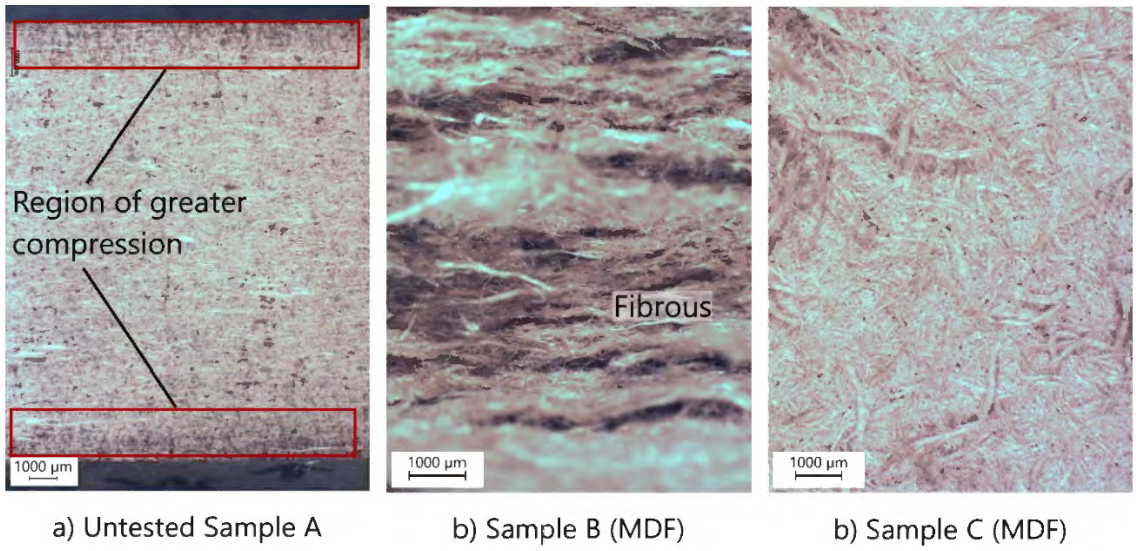

Figure 8-48: Stereomicroscope images of Supawood samples

The stereomicroscope images of the flax fibre reinforced samples were separated by manufacturing method. The two types of VI flax fibre reinforced composites were found to be very similar. A number of small voids of less than 100 µm diameter and less were found in both Sample A and Sample B, as shown in Figure 8-49a and Figure 8-49b. Images of the fractured surfaces are shown on Figure 8-49c –Figure 8-49f where out-of-plane fibre fracture and cracking and in-plane fibre pull-out were observed.

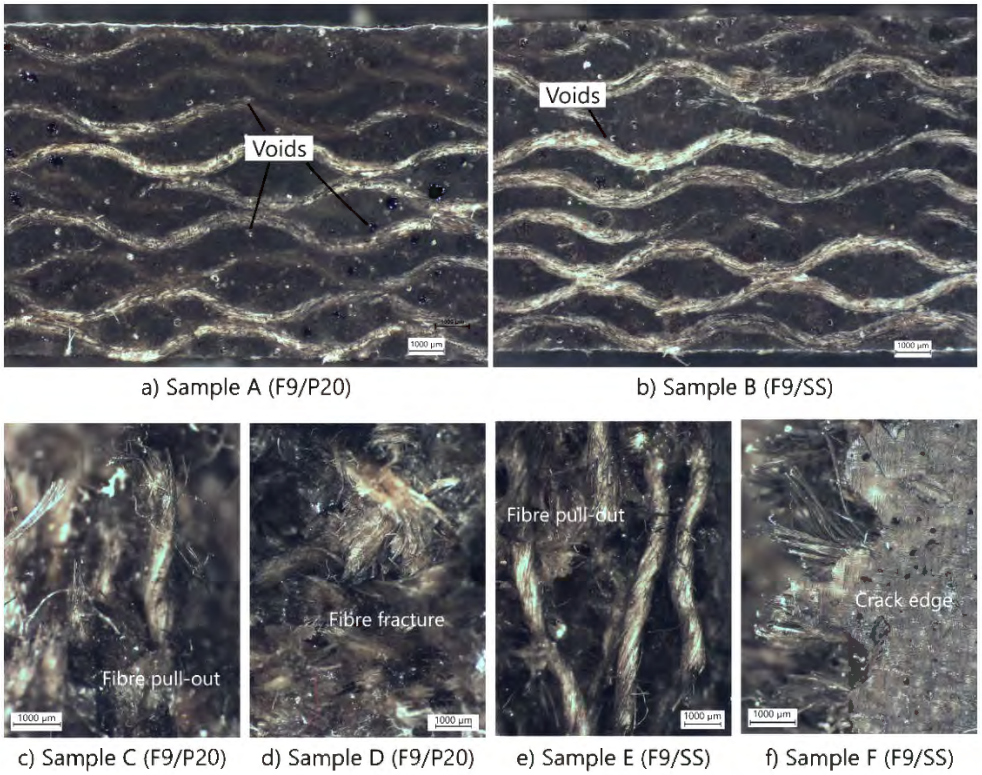

Figure 8-49: Stereomicroscope images of VI flax fibre reinforced samples

The resin distribution for the hand lay-up flax fibre composite samples, shown in Figure 8-50a seemed to be less uniform in comparison to VI samples in Figure 8-49a and Figure 8-49b. Dry areas and a bumpy surface, shown in Figure 8-50b was observed on the face exposed to air with a plastic sheet covering it during manufacturing. At the top face, large airgaps and dry spots were found, some as large as 600 µm as shown in Figure 8-50b and decreased significantly in size towards the bottom face.

In comparison to the VI flax samples, there appeared to be an uneven distribution of resin. Some areas had more resin than others in the samples. Blobs of resin were found on the fracture surfaces as shown in Figure 8-50c and Figure 8-50d. However, like the VI flax fibre reinforced panels, fibre fracture and pull-out were also observed on Figure 8-50c and Figure 8-50d.

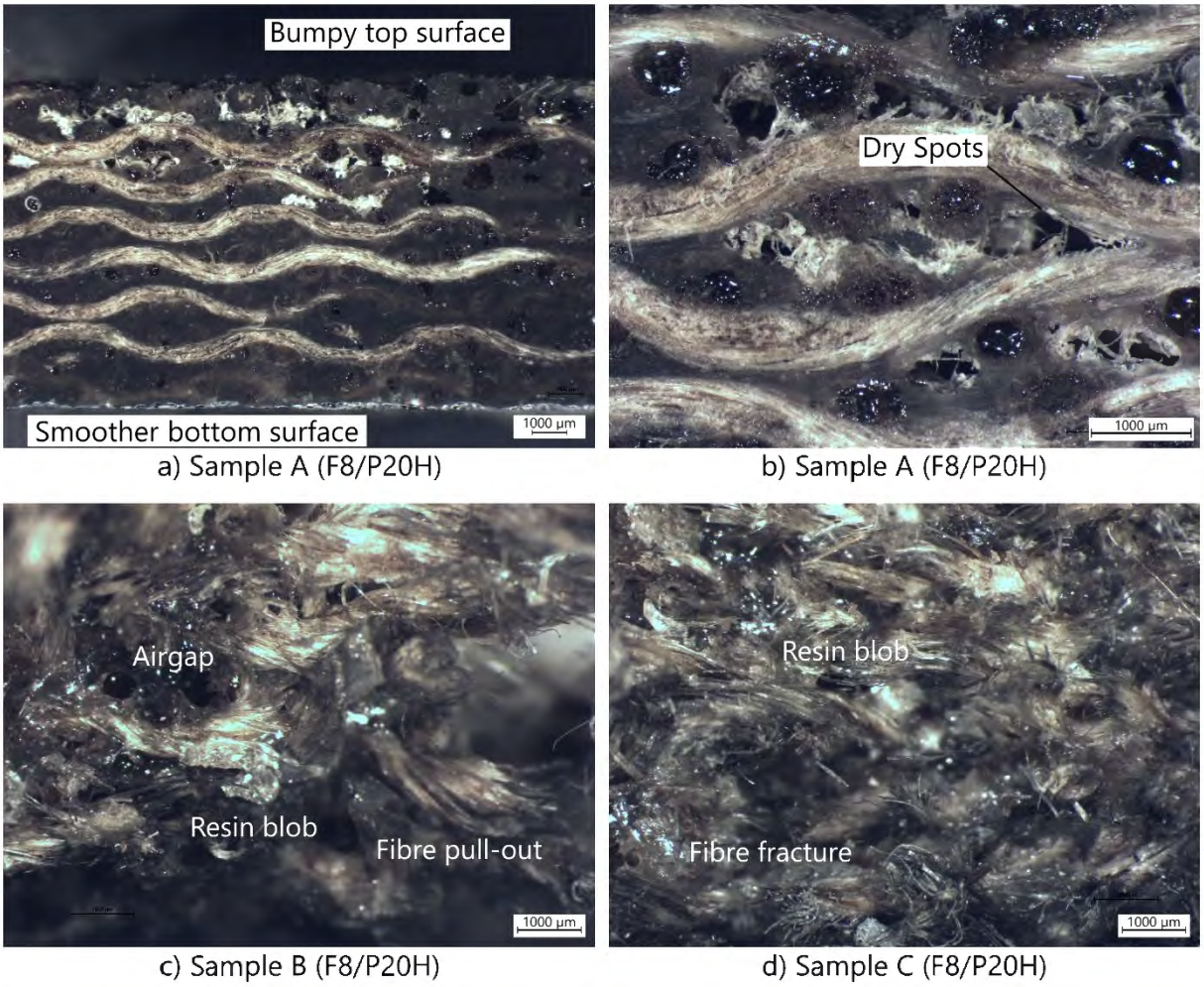

Figure 8-50: Stereomicroscope images of hand lay-up flax fibre reinforced samples

Voids shown in Figure 8-51a, similar to that found on the VI flax fibre reinforced composites, were also found in the jute fibre reinforced samples. They were of a slightly greater in size, approximately 200 µm. The quantity seemed widespread. The fracture surfaces of the jute fibre reinforced fragments were smoother than those observed on the flax fibre reinforced composites as shown in Figure 8-51b.

Brittle failure was observed in the matrix adjacent to the fibres. Moreover, an through-thickness crack can be observed on Figure 8-51b. Virtually no fibre pull-out (like that observed on the flax fibre composite samples) was observed and the fibres had fractured as shown in Figure 8-51c.

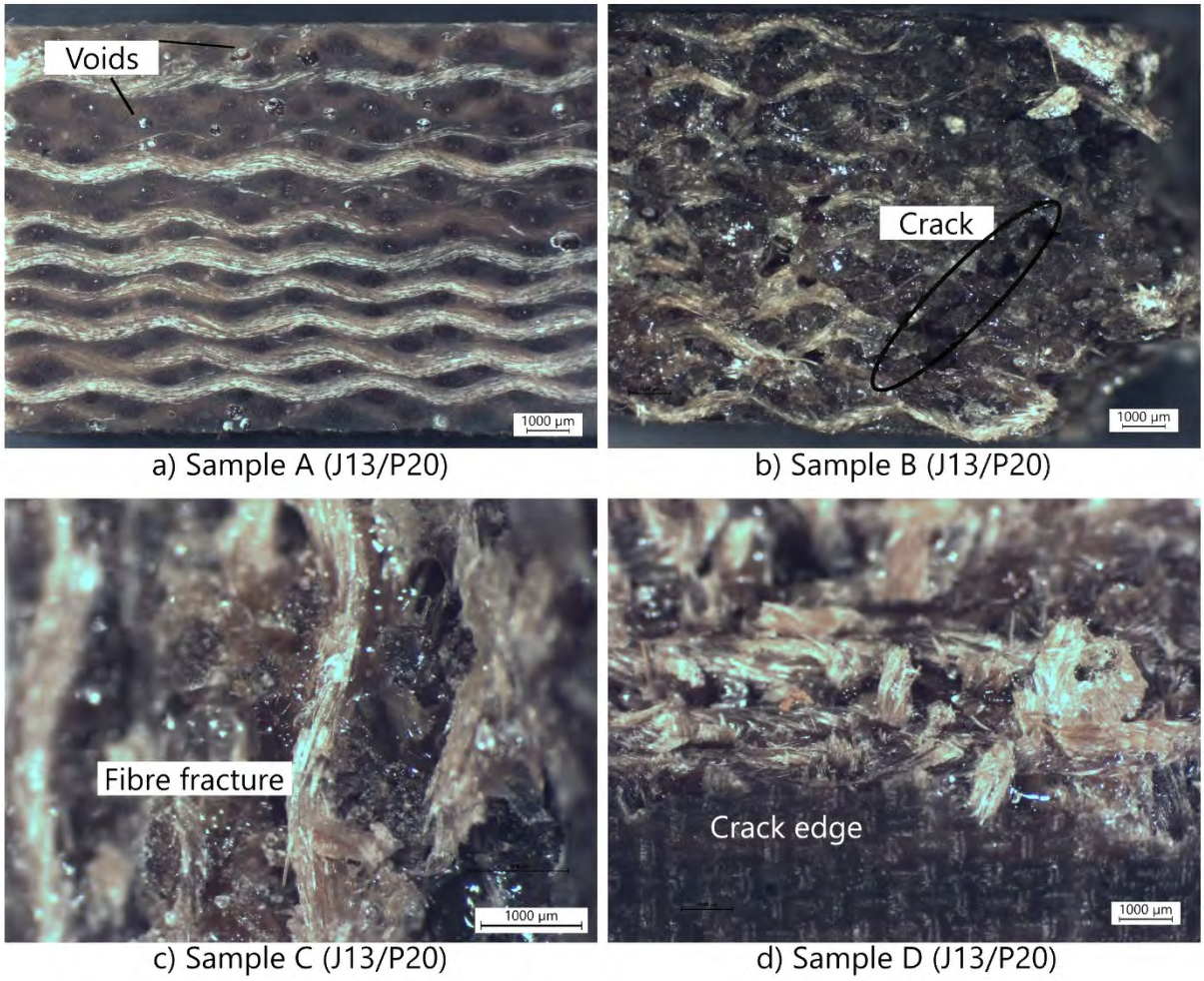

Figure 8-51: Stereomicroscope images of the fracture surfaces of a 13-layer jute fibre reinforced composite

8.9 Summary of chapter

Different failure modes were found on the different materials tested. On the glass fibre reinforced composite panels, delamination, cracking, failure around the clamp holes and boundary were observed. Matrix or interface failure was also observed on glass fibre reinforced Super Sap panels which was not apparent on glass fibre reinforced Prime 20LV panels. The damage found on the blast tested Supawood panels were cracking, significant permanent deformation, and failure at the boundary. Similar failure modes were observed on the flax and jute fibre reinforced panel. The jute fibre reinforced composites behaved in a more brittle manner. Delamination was also found on the hand lay-up flax fibre reinforced composites; however, this failure mode was not found on the VI manufacture natural fibre composites. Additionally, none of the glass fibre reinforced composite

panels had ruptured in the charge mass range tested, yet rupture was observed in the Supawood and jute fibre reinforced panels.

Upon further investigation on a micro-scale, airgaps were found on all the materials tested of various sizes. Fewer airgaps were found in the glass fibre reinforced composites in comparison to natural fibre composites. There were significant differences in the structure of the fibres, where both flax and jute fibre had a core which was not present in the glass fibre. The interfacial adhesion between glass fibre and resin, irrespective of resin type, was better in comparison to the interfacial adhesion between the natural fibre (flax or jute) and resin. As expected, Supawood was found to be a very dry material with randomly orientated fibres, yet the structure was similar to fibre reinforced polymer laminates. Lastly, the resin distribution was more uniform for the VI composites in comparison to the hand lay-up flax fibre reinforced composite.

9 Quantitative results

This chapter reports the quantitative results from the blast test programme, including measurements of crack length, delamination, mass loss due to fragmentation and the transient deformation of the panels. Table 9-1 lists the failure mode progression of the composite panels tested according to increasing charge impulse (together with the charge parameters such as charge mass in g and diameter in mm given in brackets). From the failure modes, the following damage: permanent midpoint deflection (permanent deformation is not listed in Table 9-1), mass loss due to fragmentation, delamination in GFRPs, and amount and length of cracks, was quantified and described in this chapter. Furthermore, the results obtained from DIC are given in section 9.6.

Table 9-1:Failure mode progression of blasted composite panels

Panel	Impulse in Ns, Charge(g,mm)	Failure modes	Panel	Impulse in Ns, Charge(g,mm)	Failure modes
Glass fibre reinforced Prime 20LV (A)			Glass fibre reinforced Prime 20LV (B)		
G19/P20-10	19.3 (5, 30)		G17/P20-7	15.5 (4, 30)	
G19/P20-8	25.2 (7, 30)		G17/P20-10	17.9 (5, 30)	D^{B}
G19/P20-4	31.7 (11, 30)	D^{B}	G17/P20-5	21.6 (6, 30)	$D^{B/C}$
G19/P20-9	33.7 (11, 30)	Del, D^{B}	G17/P20-8	22.2 (6, 30)	$D^{B/C}$
G19/P20-1	54.3 (25, 30)	Del, $D^{B/C}$	G17/P20-4	23.5 (7, 30)	$D^{B/C}$
G19/P20-3	64.8 (25, 40)	C^{F}, Del, $D^{B/C}$	G17/P20-2	28.1 (9, 30)	Del, $D^{B/C}$
G19/P20-5	71.3 (30, 40)	C^{F}, Del, $D^{B/C}$	G17/P20-9	30.9 (11, 30)	Del, $D^{B/C}$
G19/P20-2	82.7 (40, 40)	C^{F}, Del, $D^{B/C}$	G17/P20-6	37.6 (15, 30)	Del, $D^{B/C}$
G19/P20-6	84.4 (35, 40)	C^{F}, Del, $D^{B/C}$	G17/P20-1	48.5 (20, 30)	Del, $D^{B/C}$
Glass fibre reinforced Super Sap			Jute fibre reinforced Prime 20LV		
G17/SS-3	21.5 (6, 30)	Del, D^{B}, M	J13/P20-5	15.6 (4, 30)	
G17/SS-4	28 (9, 30)	Del, D^{B}, M	J13/P20-4	17.8 (5, 30)	C^{F}, D^{B}
G17/SS-5	30.7 (11, 30)	Del, D^{B}, M	J13/P20-1	19.0 (6, 30)	C^{F}, D^{B}
G17/SS-1	30.9 (10, 30)	Del, D^{B}, M	J13/P20-6	19.9 (5, 30)	C^{F}, Frag, D^{B}
G17/SS-6	43.2 (18, 30)	C^{F}, Del, $D^{B/C}$, M	J13/P20-3	21.3 (7, 30)	C^{F}, Frag, D^{B}
G17/SS-2	46.6 (15, 30)	C^{F}, Del, $D^{B/C}$, M	J13/P20-2	33.2 (11, 30)	Frag
Supawood			Hand lay-up flax fibre reinforced Prime 20LV		
MDF-3.1	10.4 (2, 20)	C^{I}	F8/P20H-5	17.2 (5, 30)	C^{F}
MDF-6	11.5 (3, 20)	$C^{B/I}$	F8/P20H-7	22.9 (7, 30)	C^{F}
MDF-7	11.8 (3, 20)	C^{I}	F8/P20H-9	23.3 (6, 30)	C^{F}, Del
MDF-3.2	14.1 (3, 20)	C^{I}	F8/P20H-8	23.8 (8, 30)	C^{F}, Del
MDF-8	15.7 (4, 20)	$C^{B/I}$	F8/P20H-1	27.1 (11, 30)	C^{F}, Del, $D^{B}{}_{S}$
MDF-4	17.2 (3.5, 20)	$C^{B/I}$	F8/P20H-4	28.1 (10, 30)	C^{F}, Del, $D^{B}{}_{S}$
MDF-2	17.2 (3.5, 30)	$C^{B/I}$	F8/P20H-3	29 (9, 30)	C^{F}, Del, D^{B}
MDF-5	19.5 (4.5, 20)	$C^{B/F/I}$	F8/P20H-6	34 (10, 30)	C^{F}, Del, D^{B}
MDF-1	20 (6, 30)	Frag			
VI flax fibre reinforced Prime 20LV			VI flax fibre reinforced Super Sap		
F9/P20-3	19.5 (5, 30)	C^{F}	F9/SS-3	21 (5, 30)	C^{F}
F9/P20-1	22.8 (6, 30)	C^{F}, D^{B}	F9/SS-1	21 (6, 30)	C^{F}
F9/P20-4	23.5 (7, 30)	C^{F}, D^{B}	F9/SS-6	24.1 (7, 30)	C^{F}
F9/P20-5	25.5 (9, 30)	C^{F}, D^{B}	F9/SS-5	28.3 (9, 30)	C^{F}, D^{B}
F9/P20-2	39.5 (11, 30)	C^{F}, D^{B}	F9/SS-2	36.6 (11, 30)	C^{F}, D^{B}

C – cracking in the exposed area; superscript F -front surface, B -back surface, I – internal (through-width unique to Supawood panels)

Del - delamination

D – damage (can be cracking, delamination or other failures) found around the boundary or clamp area, superscript B -boundary, C – clamped region, subscript S – panel sheared at the boundary

Frag – fragmentation, destroyed panel

M – matrix/interface failure, unique to Glass/Super Sap panels

9.1 Impulse versus midpoint deflection

The centre of each panel was measured to note any visible permanent deformation which was termed as midpoint deflection. For panels where rupture occurred at the centre of the panel, namely MDF-1, J13/P20-2 and J13/P20-3, the highest remaining point on the panel was noted. The full set values can be found in Appendix G. Figure 9-1 shows the midpoint deflection versus impulse for each of the different composites tested with the exception of panel J13/P20-3. The data set presented was limited to 60 Ns for impulse and 40 mm for deflection as the impulse tested on the GFRPs were greater than natural fibre reinforced composites. Best fit trendlines based on all data points for a set material are included in Figure 9-1. The trendlines were used to evaluate the damage progression with increasing impulse for the different composites.

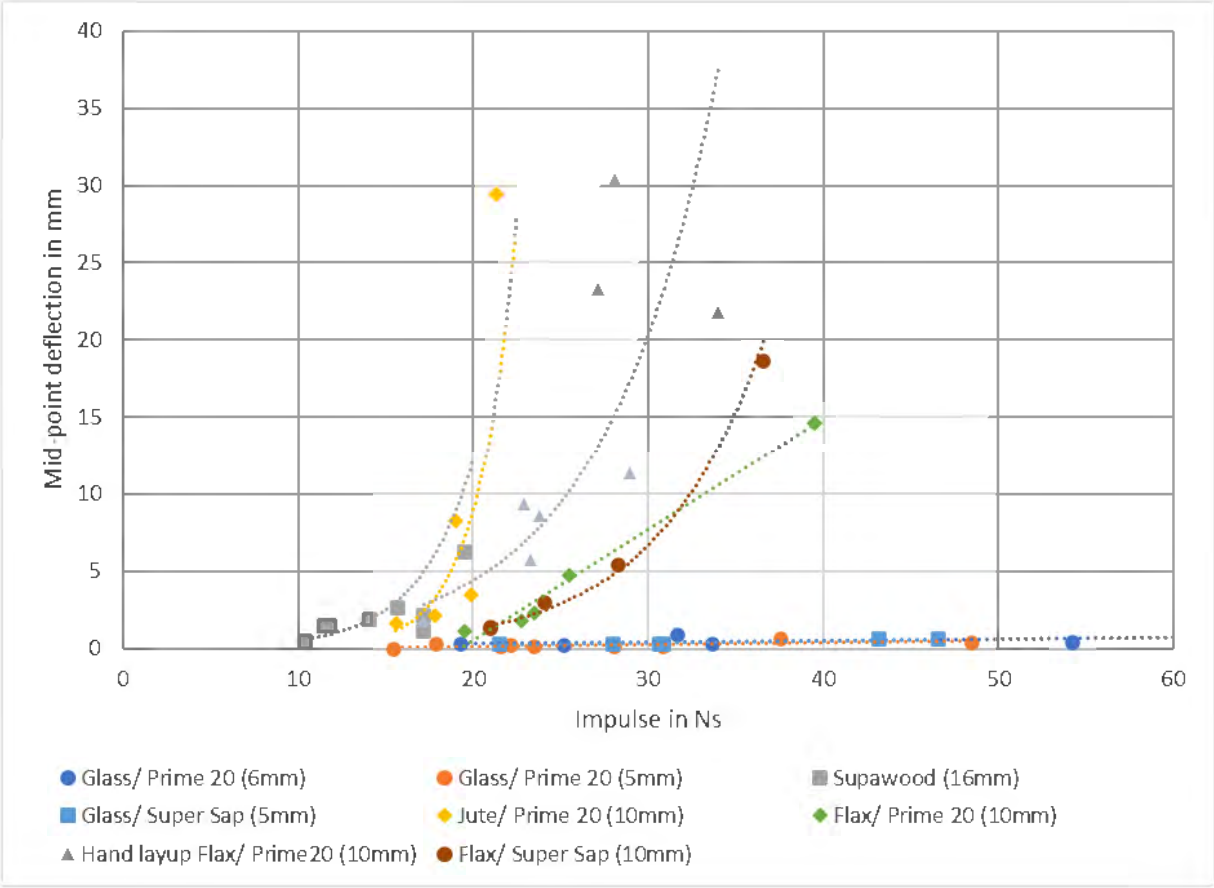

Figure 9-1: Graph of midpoint displacement versus impulse for the blast tests

GFRP exhibited almost no measurable permanent deformation in the range of blast tests performed. There was also no noticeable difference between the two resin systems (Prime 20LV and Super Sap) and nominal thicknesses (17 or 19 layers of glass fibre reinforcement) when considering the glass fibre reinforced panels. In comparison, the panels with natural fibres as reinforcements were far weaker, sustaining significant damage and permanent deformation with for similar applied impulses.

Supawood and jute fibre reinforced panels were the weakest materials tested, exhibiting an exponential increase in permanent deformation. The flax fibre reinforced panels performed better than the jute fibre reinforced and Supawood panels. The midpoint deflection for the hand lay-up flax fibre reinforced panel was greater than the VI flax fibre reinforced panels at similar impulses. There was also more variation in the hand lay-up panel results in comparison to all other materials. In terms of permanent midpoint deflection, there was initially little difference between the resin systems in the VI flax fibre reinforced composite for impulses lower than 30 Ns. Thereafter, there seemed to be a significant increase in the damage where F9/P20-2 sustained a lower midpoint deflection at 39.5 Ns than F9/SS-2 at 36.6 Ns which affected the trendline for the two materials.

9.2 Mass loss from blast testing

As shown in Table 9-1, one Supawood panel (MDF-1 at 20 Ns) and three jute fibre reinforced Prime 20LV panels (J13/P20-6, J13/P20-3 and J13/P20-2 at 19.9, 21.3 and 33.2 Ns respectively) had ruptured. This occurred at impulses greater than 19.5 Ns. At lower impulses, the panels remained intact, and no fragmentation was observed. For the Supawood panel, the percentage of mass lost in MDF-1 was 17 % at 20 Ns. For the jute fibre reinforced panels, the percentage of the mass lost was 1 % for J13/P20-6 at 19.9 Ns, 2 % for J13/P20-3 at 21.3 Ns and 43 % (which accounted for most of the exposed area) for the J13/P20-2. While there is a significant difference between J13/P20-3 and J13/P20-2 which could be attributed to the brittle nature of the panel, the impulse where rupture was initially observed was considered the point of complete failure.

9.3 Delamination in GFRP

Due to the transparency of the GFRPs, it is possible to observe delamination from the surfaces of the panel. Delamination could not be observed for the natural fibre reinforced composites tested because of their opaque nature.

The total affected area of the panel that had delaminated was measured. This was calculated as a percentage of the exposed area of 200 x 200 mm. Only the sections that had delaminated in the exposed region were considered as shown in Figure 9-2. A similar procedure was also conducted by Langdon et al [168].

The surfaces of the GFRP panels were photographed using a lightbox which illuminated the exposed area, highlighting the delamination. The damage on the panel was then traced as indicated in Figure 9-2 where the red sections indicated delamination that occurred within the clamping region. The blue region was calculated as the delamination percentage for the exposed area.

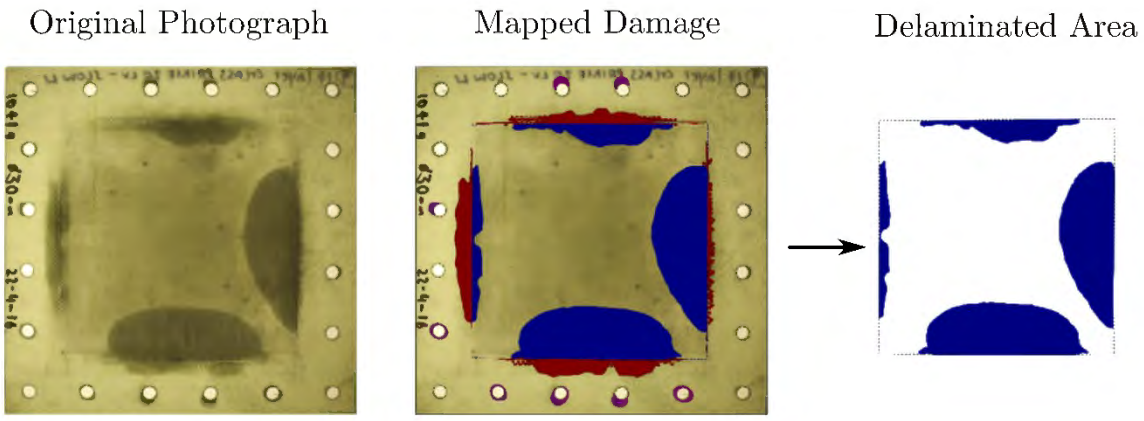

Figure 9-2: Photographs of G17/P20-9, using a lightbox, illustrating the mapped damage and the delaminated sections in the exposed area(blue)

9.3.1 Delamination versus impulse

The calculated delamination area percentages are listed in Table 9-2. Panels where no delamination, in either the clamping or exposed area, was observed have been omitted from Table 9-2. Panels where delamination occurred only in the clamped region was given a 0 for the delaminated area percentage.

Table 9-2: Delamination percentage on the blast tested glass fibre reinforced composites

Panel Name	Impulse, Ns	Delaminated Area, %
G19/P20-9	33.7	0.3
G19/P20-1	54.3	25
G19/P20-3	64.8	51
G19/P20-5	71.3	54
G19/P20-2	82.7	59
G19/P20-6	84.4	47
G17/P20-5	21.6	0
G17/P20-8	22.2	0
G17/P20-4	23.5	0
G17/P20-2	28.1	11
G17/P20-9	30.9	31
G17/P20-6	37.6	59
G17/P20-1	48.5	75
G17/SS-3	21.5	16
G17/SS-4	28	40
G17/SS-5	30.7	45
G17/SS-1	30.9	41
G17/SS-6	43.2	65
G17/SS-2	46.6	54

Despite delamination observed on Glass17/Prime 20LV panels at an impulse between 21.6 and 23.5 Ns, the damage was only found in the clamping region. The tracings of the Glass17/ Prime 20LV panels are shown in Figure 9-3.

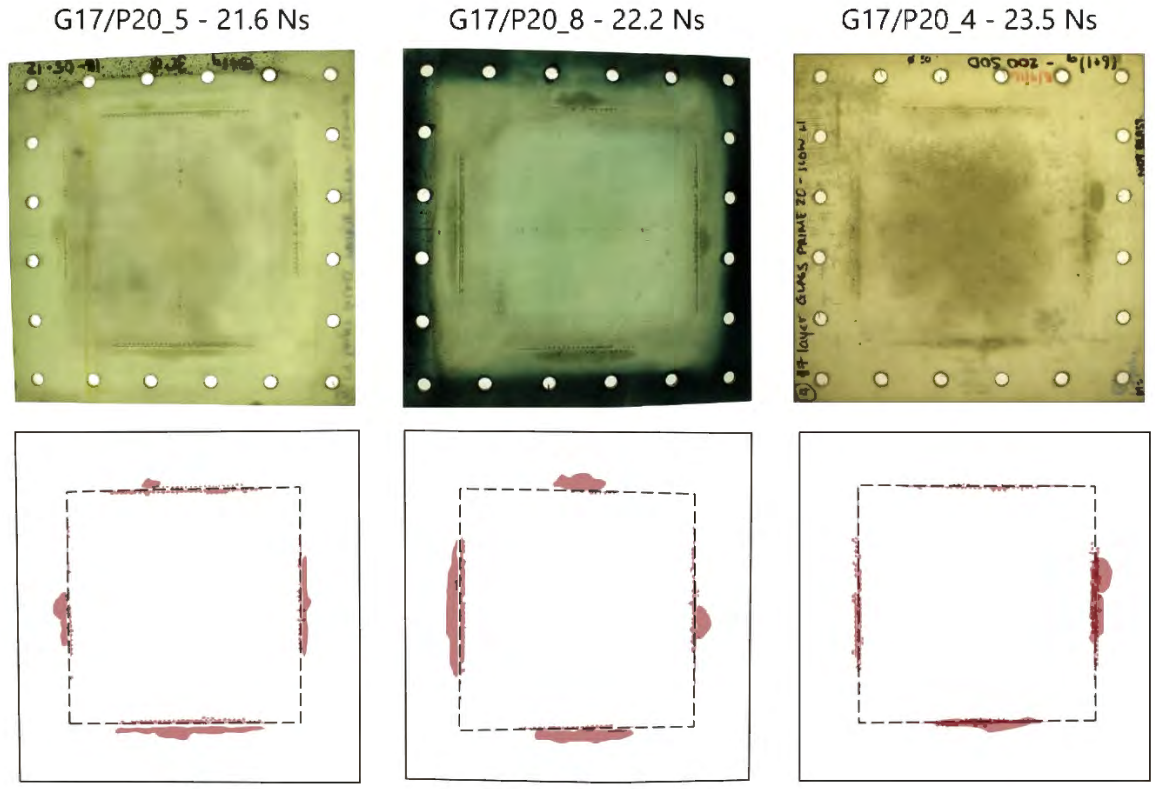

Figure 9-3: Highlighted damage showing delaminated areas found within the clamped region in Glass17/Prime 20LV panels

Figure 9-4 shows a graph of the delamination area non-zero results found for the delamination percentage against impulse of the GFRPs. Higher values of delamination were observed at lower impulses for both Glass 17/Prime 20LV and Glass 17/Super Sap panels when compared to the Glass 19/Prime 20LV panels. The values for the Glass 17/Prime 20LV and Glass 17/Super Sap panels were in a similar range. Initially within 40 Ns, the results for the Glass 17/Prime 20LV and Glass 17/Super Sap had relatively similar values.

A general trend of increasing delamination with increasing impulse was observed for the three materials. Considering the values for the Glass 17/Prime 20LV and Glass 17/Super Sap were similar, the combination of the results of the two materials was observed. From the data points shown in Figure 9-4, and considering variability due to the nature of the tests and material, the trend appears to be relatively linear. A steeper gradient was observed on the combined Glass 17/Prime 20LV and Glass 17/Super Sap panels in comparison to Glass 19/Prime 20LV due to the lower panel thickness.

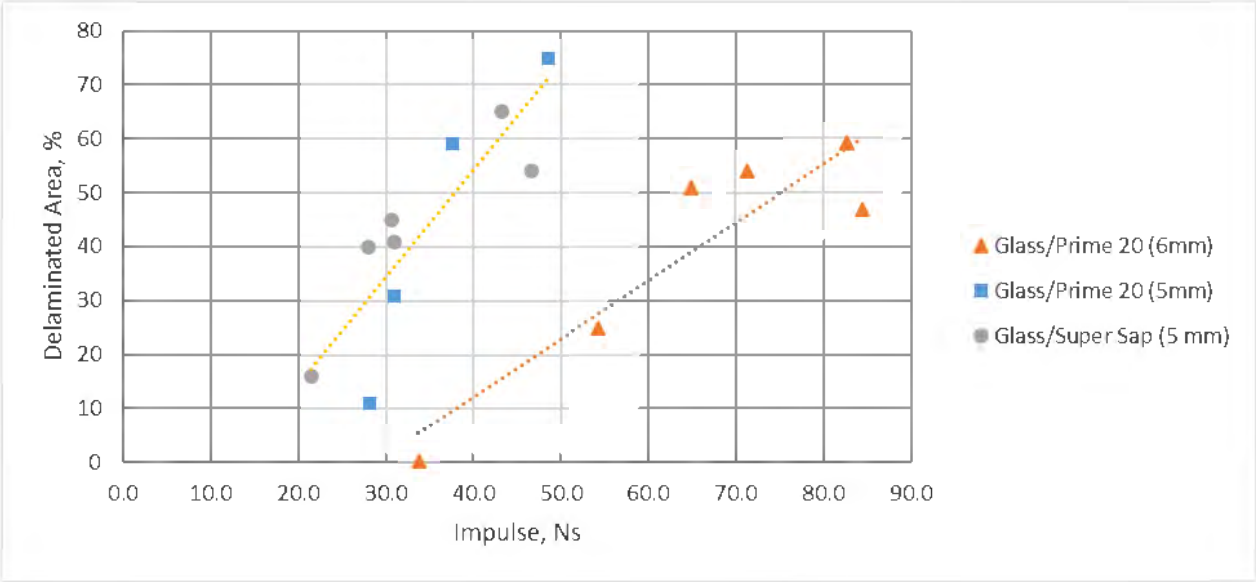

Figure 9-4: Graph of delaminated area versus impulse found on different GFRPs tested

9.4 Cracking along the front and back surfaces

As presented in chapter 8, in some panels, cracking occurred either on the front or back surface, both along the boundary and within the exposed area of the panel. This type of damage was more prominent in the natural fibre composites tested but cracking was also observed on some of the GFRP panels.

Most of the natural fibre laminates and Supawood panels appeared to have a crack in the central region. The cracking in the natural fibre composites appeared to radially branch out from the centre, often extending through the thickness, and increased with increasing charge mass. In comparison to the GFRPs, cracking within the exposed area of the panel had a different appearance. The cracking on the GFRPs had extended perpendicular to the clamped edge out from the boundary and appeared as surface cracking.

The total crack lengths of the back face and the front face were measured from traces made on photographs as shown in examples depicted in Figure 9-5. The total crack length was calculated from determining the pixel size to millimetres ratio based on the length of the panel. Red was used to indicate cracks within the exposed area while green was considered as cracks along the boundary. The cracks were separated in terms of front and back surfaces, and further separated into non-boundary (cracks within the exposed area), and clamped boundary region as listed in Appendix H.

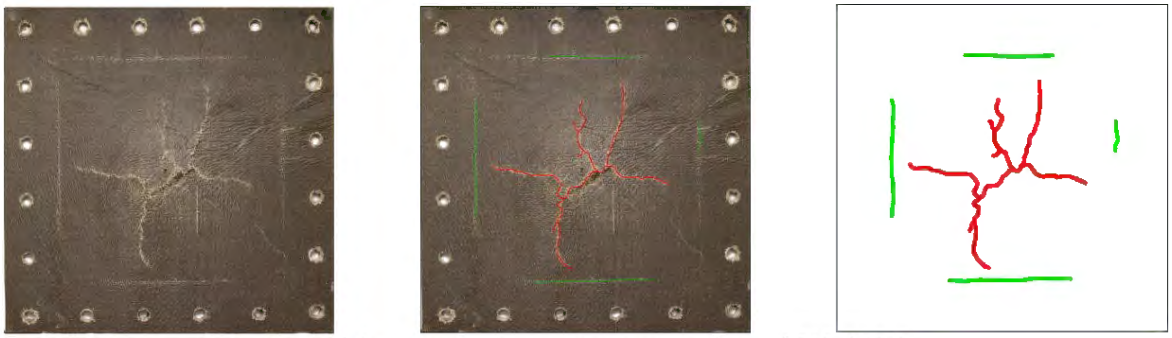

a) Crack lengths tracing on the back surface of F08/P20-8

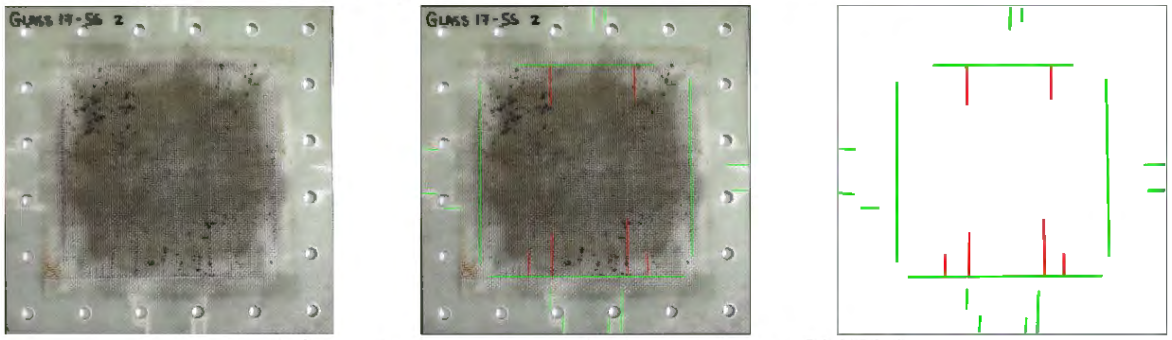

b) Crack lengths tracing on the front surface of G17/SS-2

Figure 9-5: Tracings of crack lengths within the exposed area (red), and boundary and clamped region (green) on a a) Flax 8/Prime 20LV, and b) Glass 17/Super Sap panel

9.4.1 Crack length versus impulse

The crack lengths determined in the exposed areas on the front and back surfaces were plotted against impulse and shown in Figure 9-6. To compare the two surfaces, the x-axis was set to 10 – 50 Ns and y-axis from 0 – 1400 mm. The results for the Glass 19/Prime 20LV panels were outside this range and are excluded from Figure 9-6.

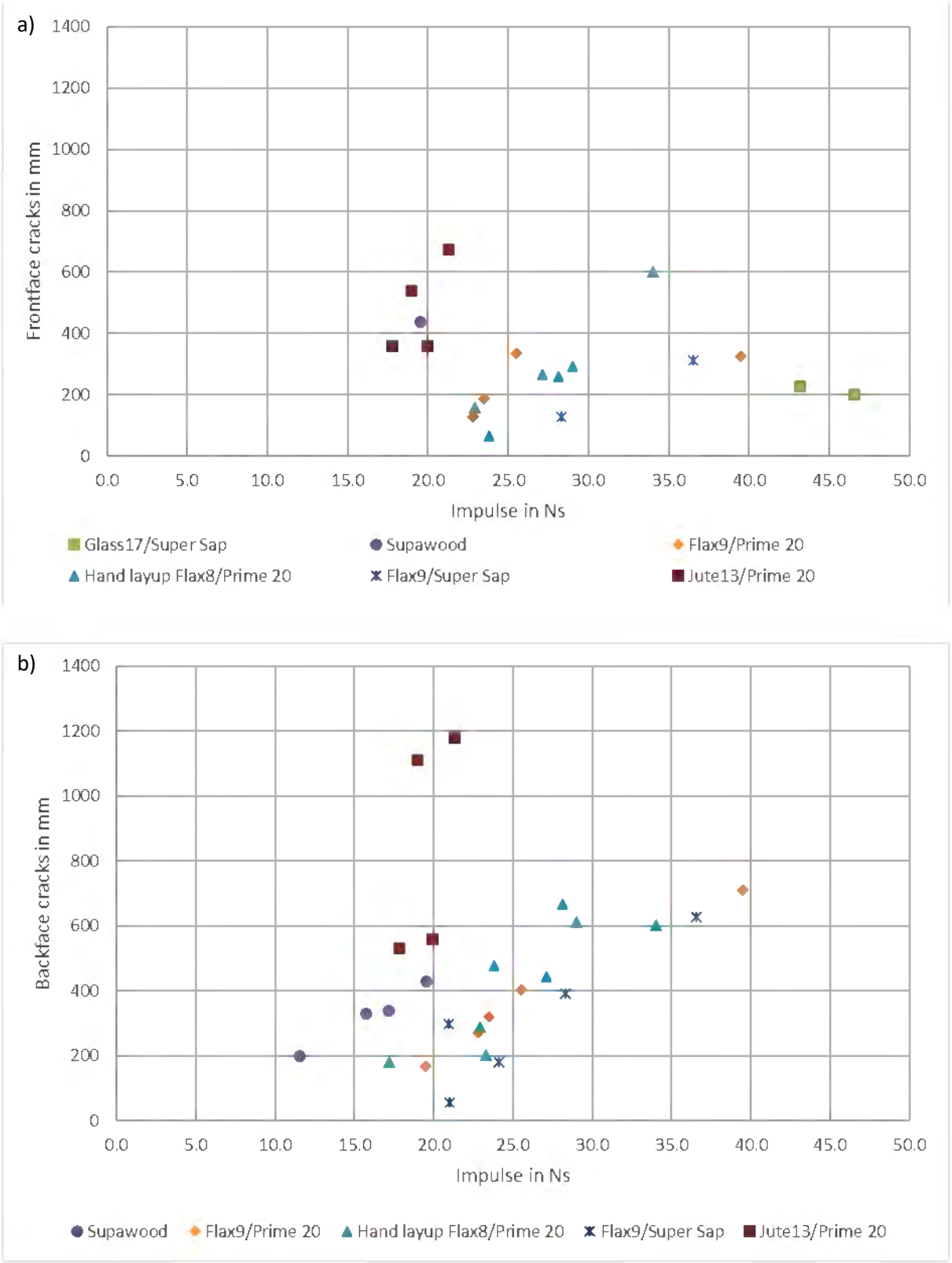

Figure 9-6: Graphs of crack length measured on a) front surfaces and b) back surfaces versus impulse

For the natural fibre composites, more cracks were visible on the back surface than the front surface. On the back surface, cracks found on Supawood, Flax 9/Prime 20LV and Flax 9/Super Sap panels appeared to increase linearly with increasing impulses. The data on Jute 13/Prime 20LV appeared

scattered. Cracks were only observed on the front surface of the GFRPs (particularly on Glass 19/Prime 20LV at higher impulses and Glass 17/ Super Sap). In the tested charge masses range, the GFRPs did not sustain as much cracking as the natural fibre composites, therefore trendlines could not be determined. On the front surface on the hand lay-up Flax 8/Prime 20LV panels, the trend seemed linear and within the same band of results found on the back surface.

The impulse versus the total (back and front) measured crack lengths (including those found at the boundary and clamped region) for all the different panels tested is shown in Figure 9-7. As expected, the total crack lengths found on Glass 19/Prime 20LV was lower compared to the other materials tested at similar impulses. The Flax 9/Super Sap exhibited less cracking than its Prime 20LV counterparts. However, for the GFRPs, Glass 17/Prime 20LV exhibited less cracking than Glass 17/ Super Sap. The total surface cracks observed for the VI Flax 9/Prime 20LV and hand lay-up Flax 8/Prime 20LV appeared to be in a similar range. Supawood initiated cracking at the lowest impulses compared to the other panel types. Apart from Jute 13/Prime 20LV, all other materials exhibited a linear increase, with variation in crack length with increasing impulse.

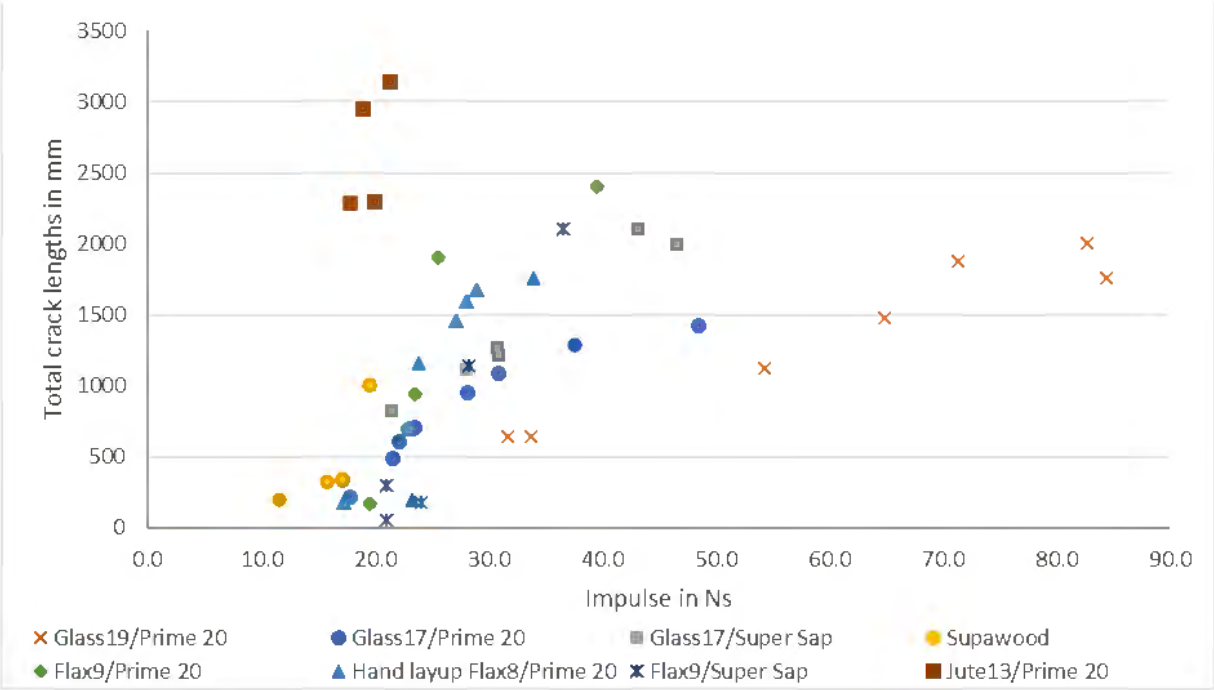

Figure 9-7: Graph of impulse versus total crack lengths measured

9.5 Through width cracking in Supawood

As stated in section 8.4, internal damage was observed in the Supawood panels, even in instances where no damage was visible on the front and back surfaces of panels MDF_3.1, MDF_3.2 and MDF_7. This internal damage, referred to as through width cracking, was considered separate to the cracking

found on the front and back surfaces of panels. The cracks were traced from photographs of the cross section, as shown in Figure 9-8, and measured using the similar method described in section 9.4. The crack lengths were used as indication for the damage sustained.

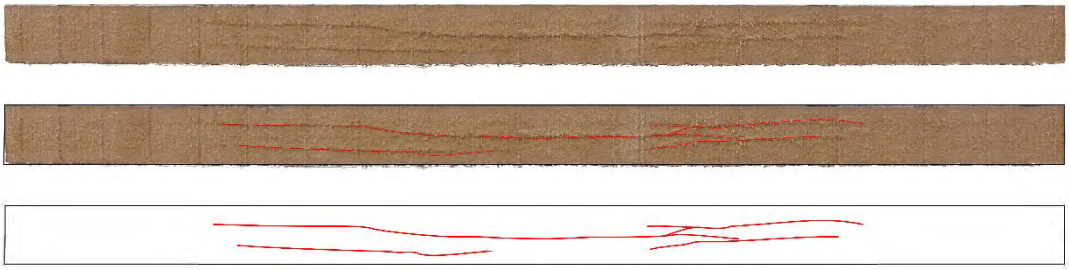

Figure 9-8: Traced cracks at the mid-plane of a Supawood panel

These through-thickness crack lengths were plotted against impulse and are shown in Figure 9-9. The data values used can be found in Appendix H. Despite the lack of visible damage on the front or back surfaces (highlighted orange datapoints in Figure 9-9), three Supawood panels exhibited significant through thickness cracking.

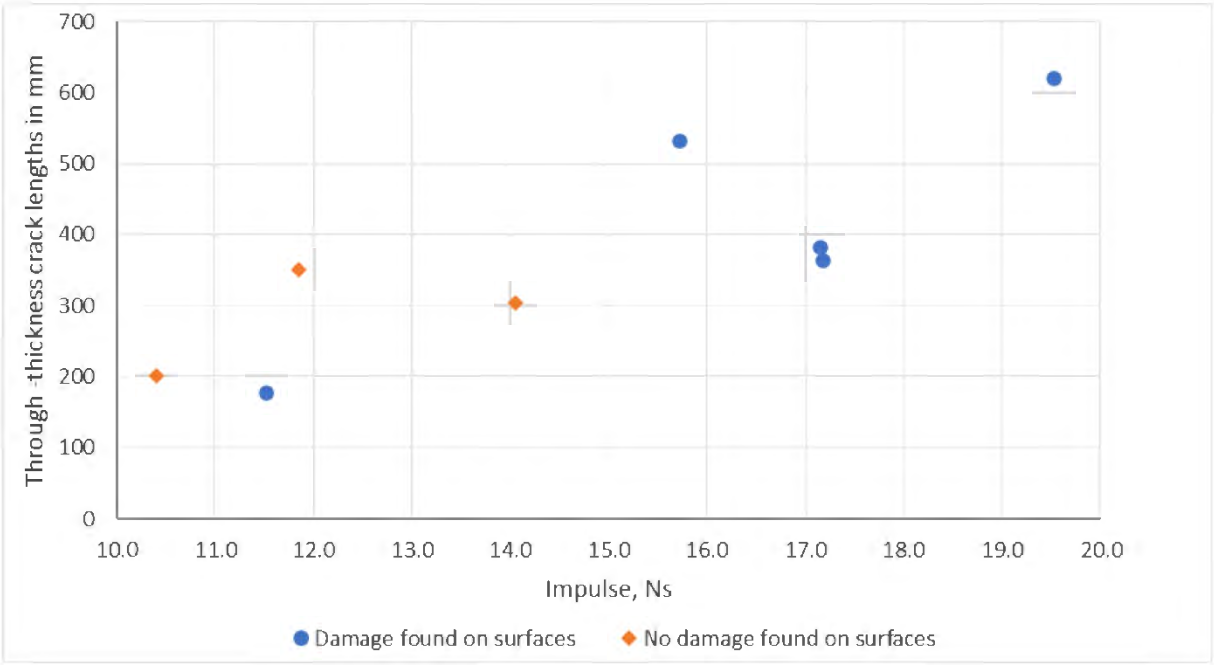

Figure 9-9: Graph of through-thickness cracking versus impulse on MDF panels

9.6 Transient results

Twenty blast tests were performed using the modified stereo-imaging pendulum. Results were taken from images of the central strip across the panel which was tracked optically. From these images, the mid-point displacement time history and horizontal mid-plane deformed profile evolution over time were generated using DIC.

Upon examination of the mid-point displacement time histories (further detailed in section 9.6.1), it was found that the panels, irrespective of the composite type, often initially behaved like a viscously damped harmonic vibration, with an exponentially decaying displacement magnitude. Therefore, vibration parameters, such as natural frequency and damping ratio, were calculated based on the free response of a single-degree-of-freedom system, for the first two full oscillations where possible. The damping ratio was found by taking the natural log of the ratio of the positive or negative successive amplitudes, also known as the logarithmic decrement, from the test data using Equation 9-1. The natural frequency for the panel could be calculated using Equation 9-2.

$$\zeta = \frac{\delta}{\sqrt{(2\pi)^2 + \delta^2}} \qquad 9\text{-}1$$

where δ is the log decrement.

$$\omega_n = \frac{\omega_d}{\sqrt{1-\zeta^2}} = \frac{2\pi}{\tau_d\sqrt{1-\zeta^2}} \qquad 9\text{-}2$$

ω_n is the natural frequency, τ_d is the measured damping period and $\zeta$is the damping ratio?

The midpoint often deflected significantly both in the directions, i.e., towards and away from the camera. An idealised curve of the midpoint displacement time history is shown in Figure 9-10. As the displacement cycles, the minimum displacement (Point 6 in Figure 9-10) found was termed as rebound deflection value.

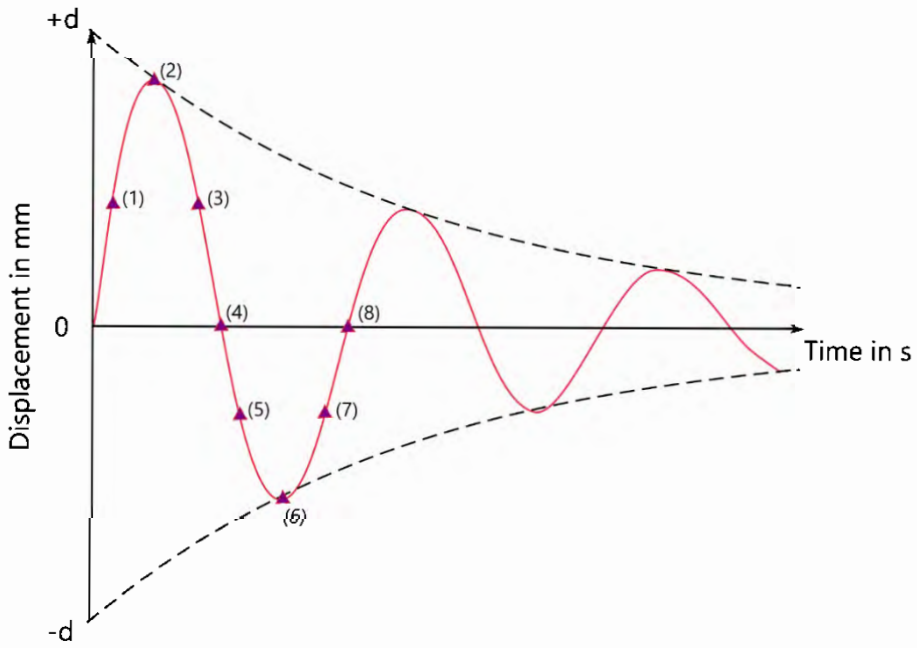

Figure 9-10: Idealised curve showing the points of interest used to display the mid-plane profiles

Using the idealised curve shown in Figure 9-10, the first full cycle was analysed at the 8 points indicated unless stated otherwise. The midpoint deflection datapoint of (0,0) was not chosen as this state was chosen as the reference points. Points chosen include the maximum and minimum values measured for the midpoint within in the first cycle (Point 2 and 6), the points where the mid-point returned to near zero (Point 4 and 8) and approximately half the displacement towards either the maximum or minimum value (Point 1,3,5 and 7). The out-of-plane deformation (referred as z-displacements on graphs) from these points were extracted and plotted to observe the evolution of the profile of the panel from a horizontal strip at the centre of the panel. The profiles can be found in section 9.6.2.

9.6.1 Transient mid-point deflection

The transient midpoint deflection time histories for the glass fibre reinforced specimens tested are shown in Figure 9-11. Dotted horizontal lines of the same colour as a transient midpoint deflection correspond to the same panel and represent the permanent deformation measured. The x axis has been limited to 10 microseconds.

In general, the midpoint deflection appeared to behave as a viscously damped harmonic vibration for at least three cycles for any of the GFRPs tested. Thereafter, the deflection deviated from the harmonic motion due to the effect of internal damage and noise. Higher values were observed for the maximum amplitudes with increasing impulse. On G17/P20-5, the few deformation oscillations were missing for this test because the flash transmitted through the translucent panel. The absence of paint on the front surface was problem. Consequently, the front surface exposed area of the remaining GFRPs had been painted. The panels did not sustain a significant permanent deformation in comparison to the maximum midpoint deflection found suggesting that the panels tested behaved elastically.

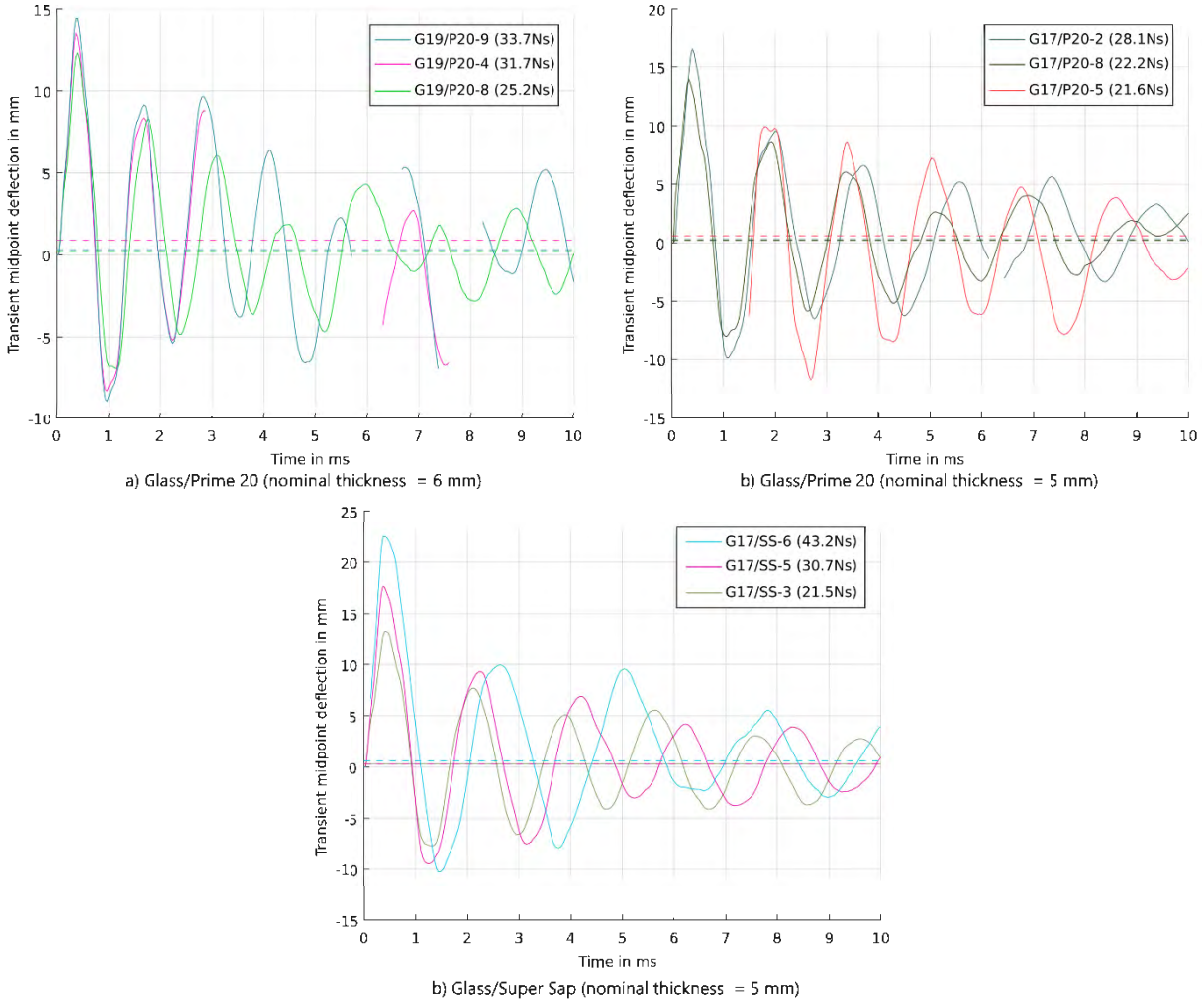

Figure 9-11: Midpoint deflection time histories for different glass fibre reinforced composites panels

The transient midpoint deflection time histories for the Supawood panels tested are shown in Figure 9-12. Very low masses of explosive were required to ensure that the panel would not rupture. However, due to this limitation, only two panels were tested using the high-speed camera system. From the two panels, transient midpoint deflection oscillated in a viscously damped harmonic vibration for at least 3 cycles, similar to the GFRPs. However, the period of the cycle was longer. On MDF-8, discontinuities were found at the maximum deflection. This was due to cracks forming at the centre which had consequently affected the speckled pattern. The crack on the panel is shown in the photographs taken by the same camera at different times in Figure 9-13. The clamp has been cropped out so that the crack can be more noticeable.

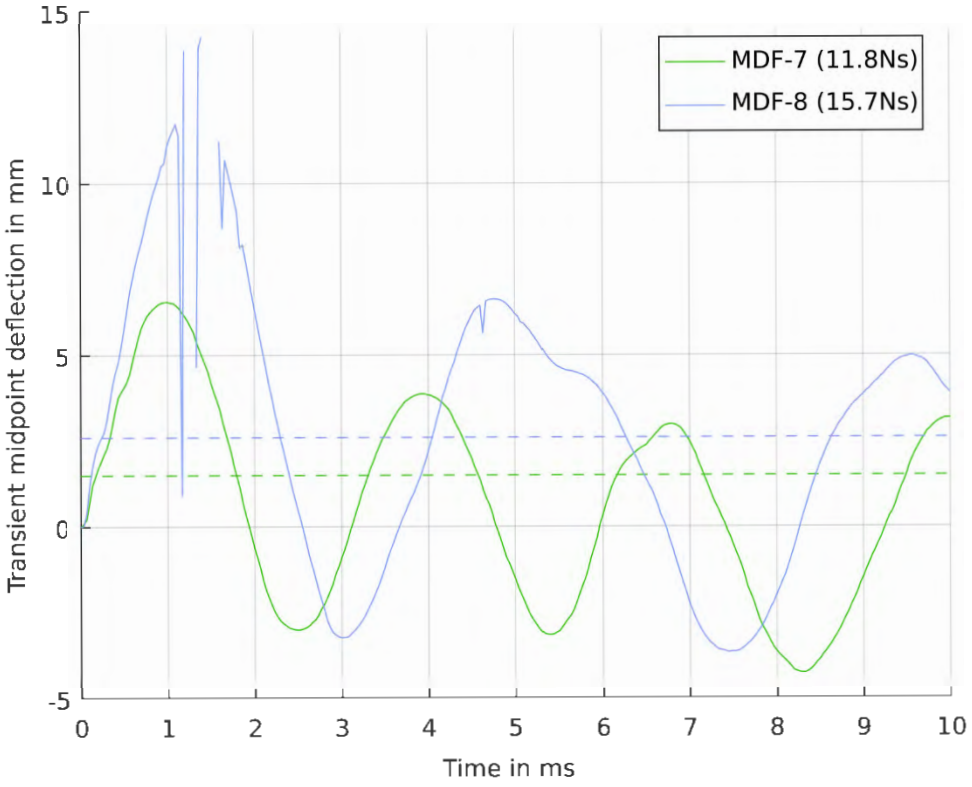

Figure 9-12: Midpoint deflection time histories for Supawood panels

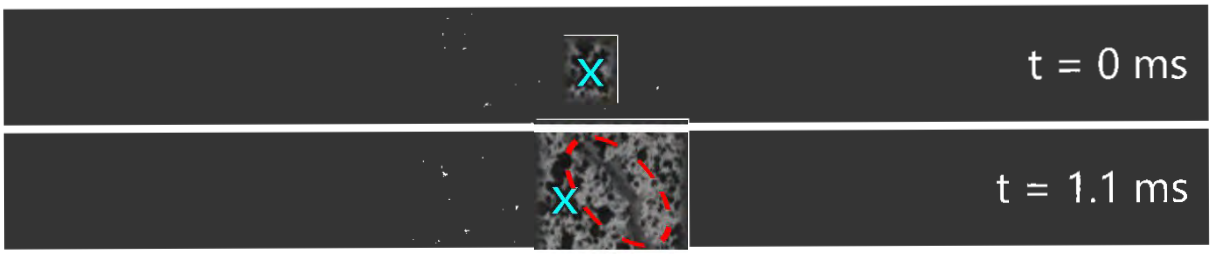

Figure 9-13: Crack found on MDF-8 during testing

The transient midpoint deflection time histories for the flax and jute fibre reinforced composite panels are shown in Figure 9-14. Viscously damped harmonic vibration behaviour was also observed on all the panels except F9/P20-5 and J13/P20-6 (which is further explained). In general, due to the damage (mostly cracking) that occurred on the back surface of the panels, decorrelation occurred fairly early on. There were periods, especially as the crack opened at large deflections, where information was lost. Depending on the severity of the crack, correlation would resume as the crack closed as it rebounded.

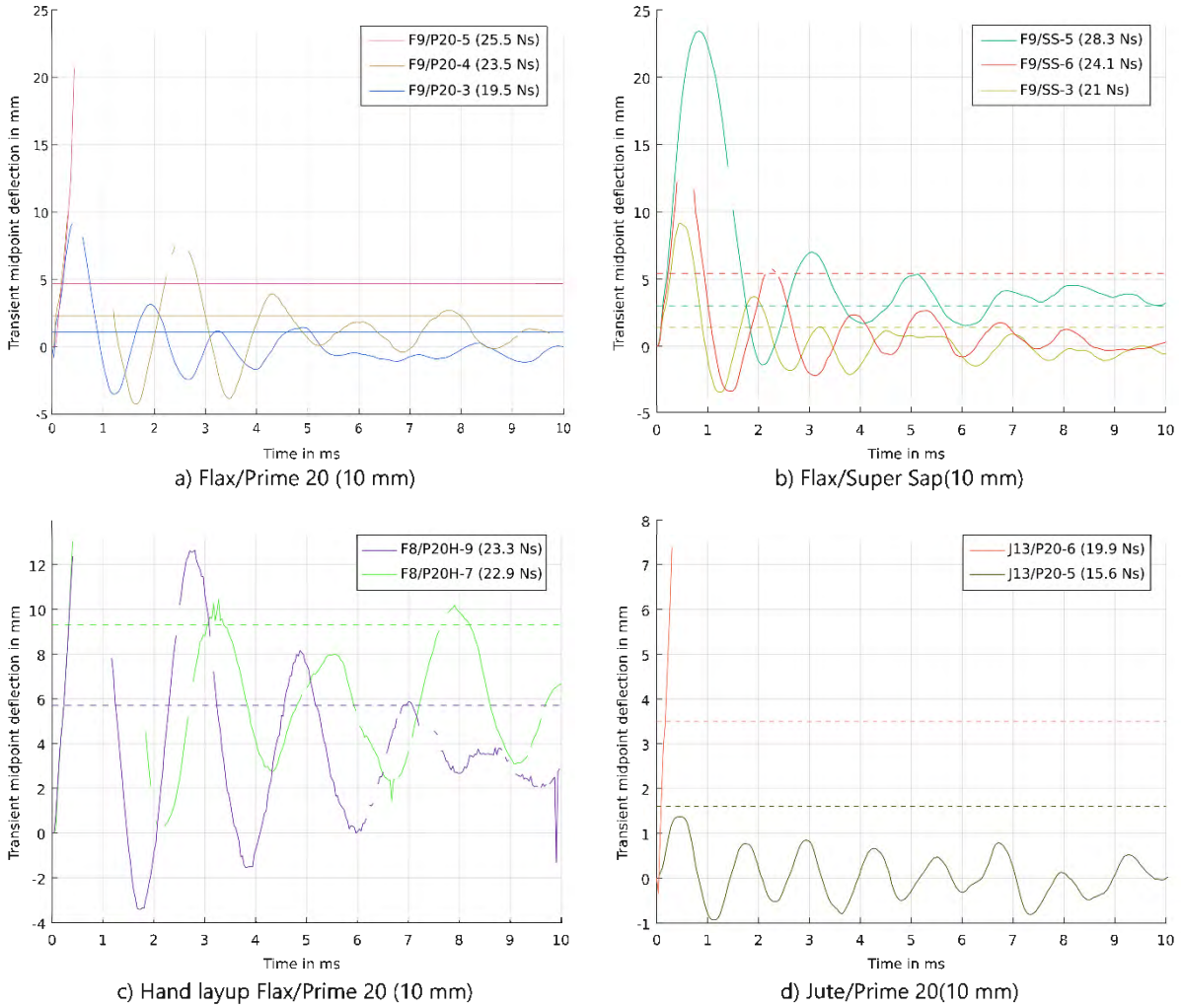

Figure 9-14: Midpoint deflection time histories for different natural fibre laminates

On F9/P20-5, explosive by-products in the form of a dark cloud exited through the crack that had formed at the centre of the panel as shown in Figure 9-15. Within one frame (0.03 microseconds), the crack had formed. The midpoint was, however, not directly on the crack and some data was obtained. At t = 0.13 microseconds, the crack was wide enough to allow some explosive by-products through the opening and would progressively expand and cover the midpoint. The gas escaping through the crack continued to expand towards the clamped edge boundary, as shown at t = 0.47microseconds in Figure 9-15, leading to the decorrelation of data.

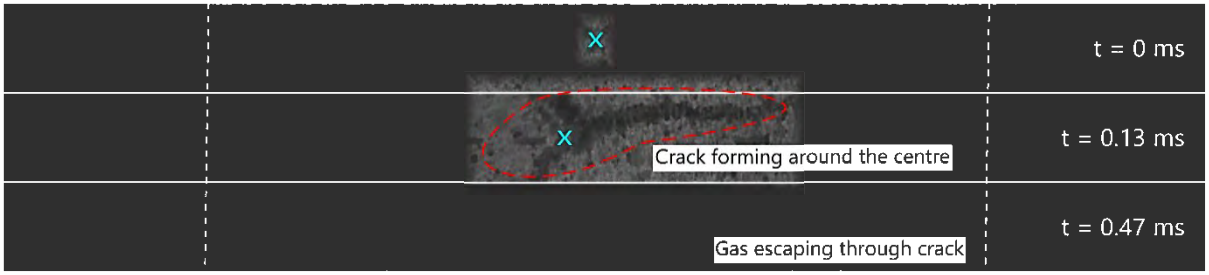

Figure 9-15: Gaseous substances exiting the crack on F9/P20-5

For J13/P20-6, the panel had fragmented during testing as shown in Figure 9-16. As the fragment moves towards the camera, a similar dark cloud of explosive by-products as observed in F9/P20-5 exited through the opening. Both the fragment and by-products caused decorrelation around the central region of the panel.

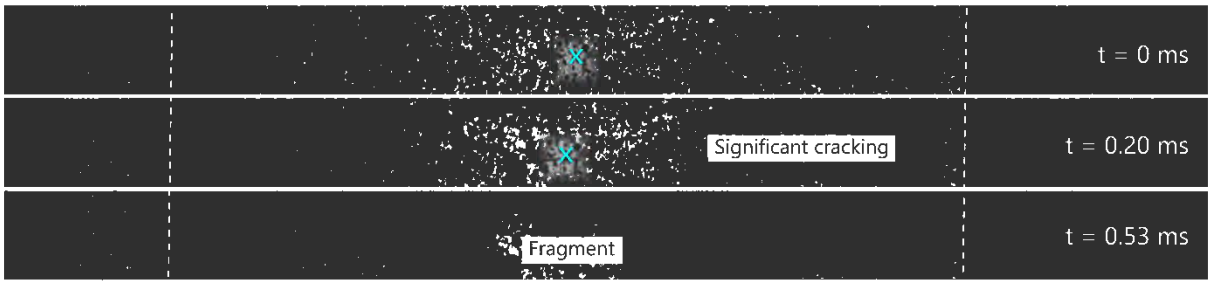

Figure 9-16: Fragment forming in J13/P20 -6

9.6.2 Transient displacement profiles

The transient displacement profiles are presented according to the type of fibre. As stated previously, if possible, the eight profiles displayed for each panel represent particular points on the midpoint deflection within the first cycle. These points have been indicated by a number and an arrow showing the direction of movement. The centre of the panel was marked on each graph. Any additional points or deviations (marked with an asterisk) from the eight points indicated on Figure 9-10 is further detailed.

Glass Fibre Reinforced Composites

The transient displacement profiles for the GFRP panels tested with a high speed camera system are shown in Figure 9-17, Figure 9-18 and Figure 9-19 for the Glass 19/Prime 20LV, Glass 17/Prime 20LV and Glass 17/Super Sap panels respectively. As the initial cycle could not be recorded on G17/P20-5,

the profiles were taken from the second cycle in a similar manner with an additional profile taken at the start of the oscillation where the midpoint deflection was zero.

In general, a global dome-shaped profile was observed. There appeared to be a slight flattening of the profile in the centre during the early stages of deformation (point 1). Points 4 and 8 show that the profiles return to a flat profile. For most panels, the peak was in the central region. The profiles appeared similar, often overlapping on top of each other. Additionally, the profiles seemed symmetric about the y-axis of the centre of the panel.

For some panels, the peak of the profile was slightly off centre. These included panels G19/P20-9 (Figure 9-17c), G17/P20-2 (Figure 9-18c) and G17/SS-3 (Figure 9-19a). This caused the curves for point 1 and 3, and point 5 and 7, to have peaks on different sides (i.e., if the peak on point 1 was towards the left, the peak for point 3 would be towards the right). Moreover, the profiles for points 4 and 8 tended to have a slight sinusoidal shape.

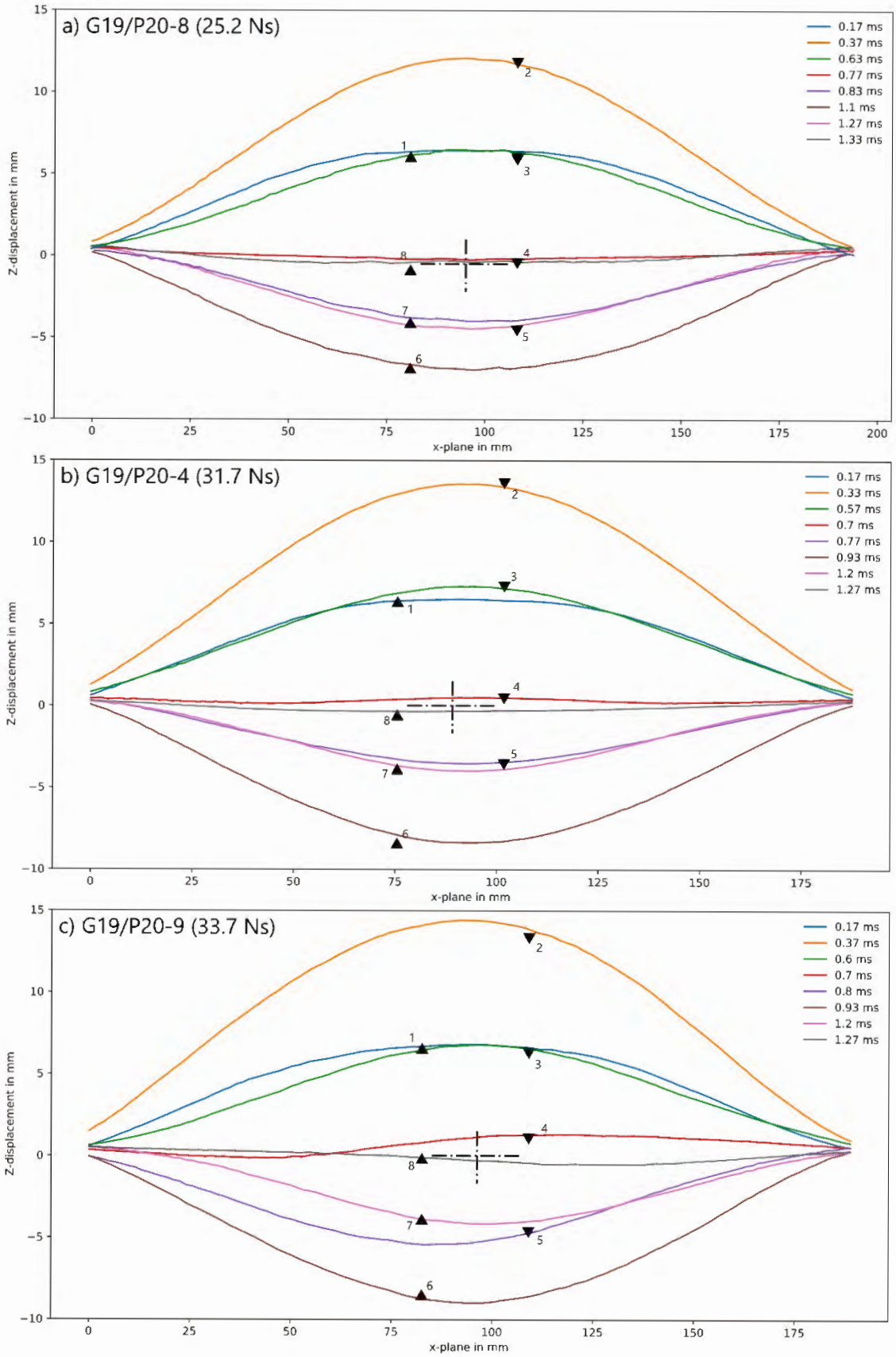

Figure 9-17: Transient displacement profiles for Glass 19/Prime 20LV panels

As previously mentioned, for G17/P20-5 (Figure 9-18c), the profiles from the second cycle were plotted due to data lost from the light flash during detonation. Some profiles appeared more localised which could be a result of damage from the initial cycle.

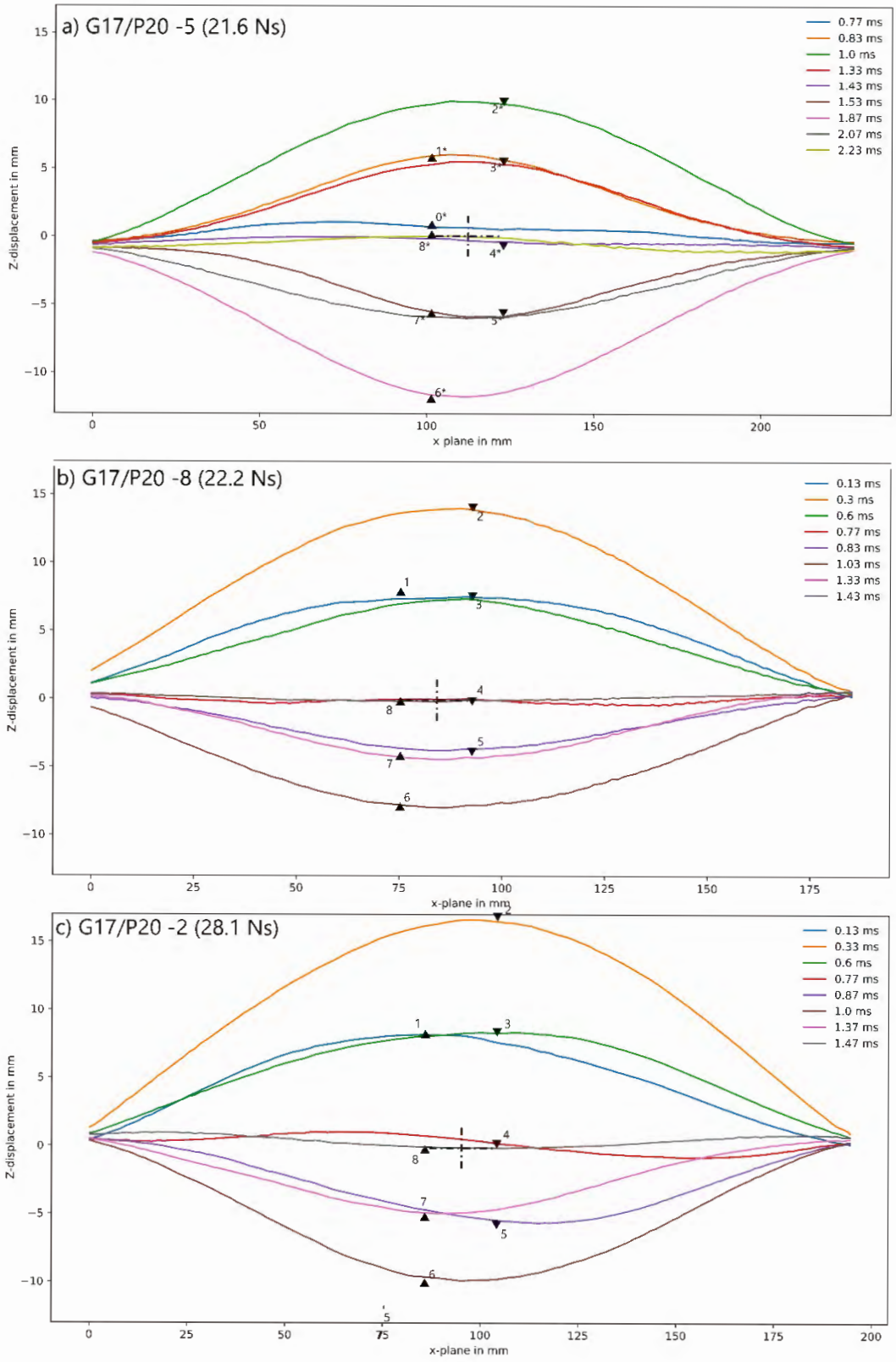

Figure 9-18: Transient displacement profiles for Glass 17/Prime 20LV panels

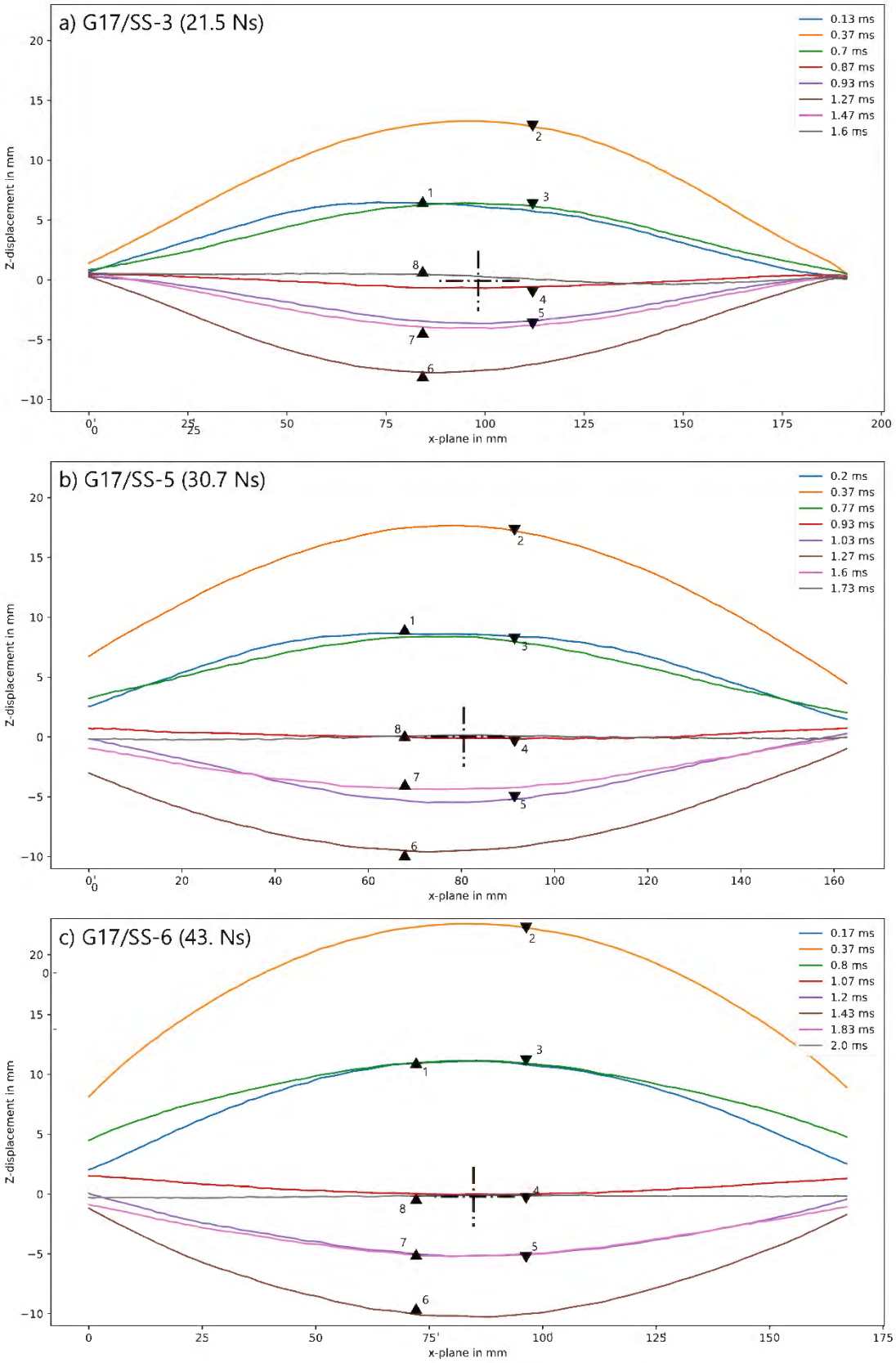

Figure 9-19: Transient displacement profiles for Glass 17/Super Sap panels

Supawood

The transient displacement profiles for the two Supawood panels tested are shown in Figure 9-20. The profile evolution of MDF-7 was similar to the GFRP panels, being dome-shaped and similar in shapes almost overlaying each other. For MDF-8, shown in Figure 9-20b, the crack caused a discontinuity in the speckle pattern on the panel surface, meaning that the measurements could not be correlated around the crack for point 2. As the panel rebounded, around the centre, it was possible to observe a kink on points 3 to 8 which decreased in size indicating that the crack was closing during this time period.

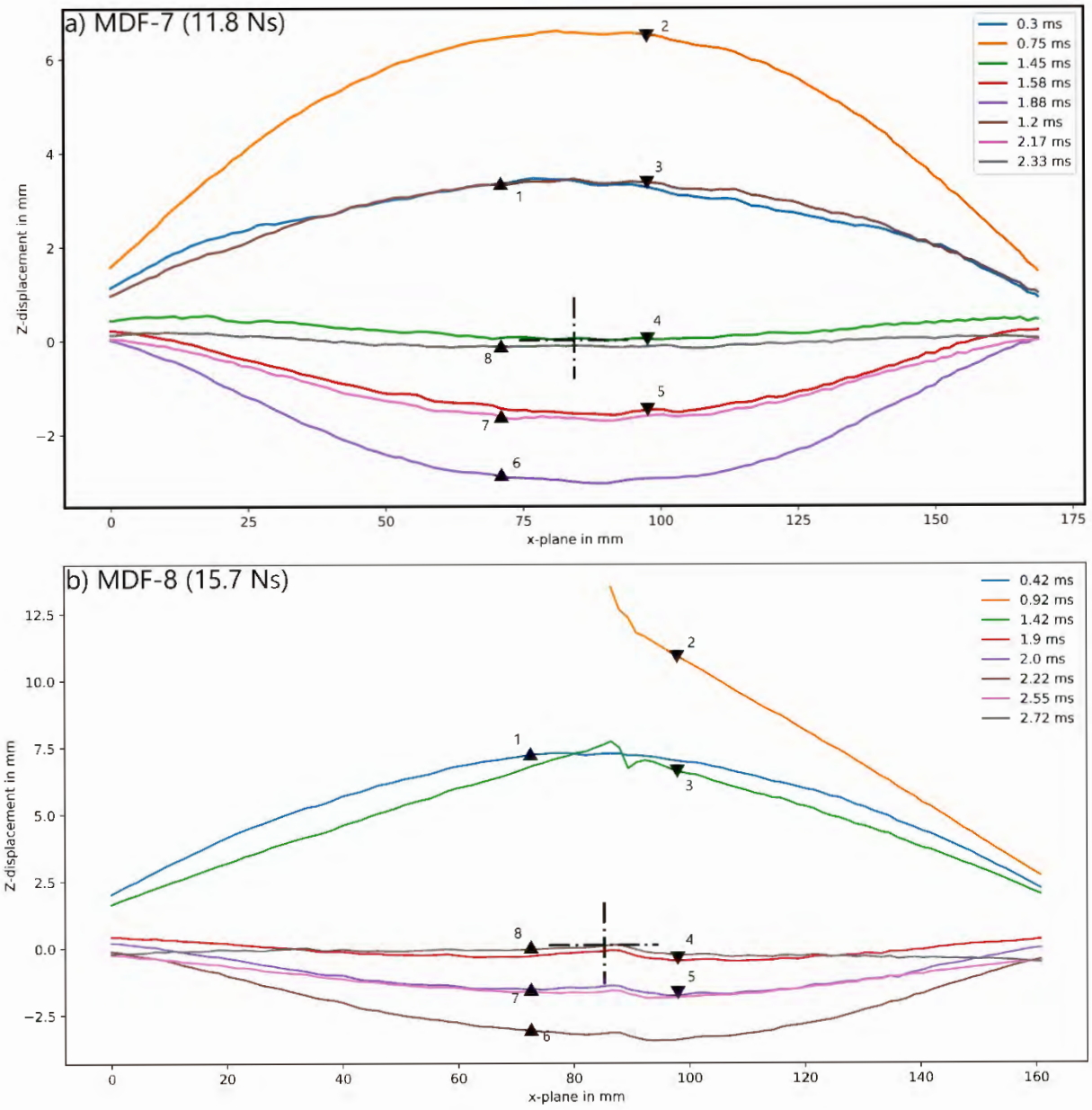

Figure 9-20: Transient displacement profiles for Supawood panels

Jute Fibre Reinforced Composites

The transient displacement profiles for the tested jute fibre reinforced composites panels are shown in Figure 9-21. J13/P20-5, shown in Figure 9-21a, behaved similarly to Supawood and glass fibre reinforced composite panels. However, on J13/P20-5, because the z-displacement was low (less than 2 mm), the noise in the data was more noticeable. For a similar set-up, Curry [182] found that the uncertainty was approximately 0.3 mm. The transient mid-line profiles of panel J13/P20-6 are shown in Figure 9-21b. In the early stages (times before 300 microseconds, points 1* and 2*) the profile resembled a dome-shape. At t = 300 microseconds, some of the DIC data is missing, indicating possible crack formation. This is confirmed by checking the camera footage directly, where cracking was clearly evident (see Figure 9-16). The profile shape seemed to change to more conical shape, although this is difficult to ascertain as much of the data is missing due to decorrelation. Fragmentation was observed in this panel (Figure 8-36).

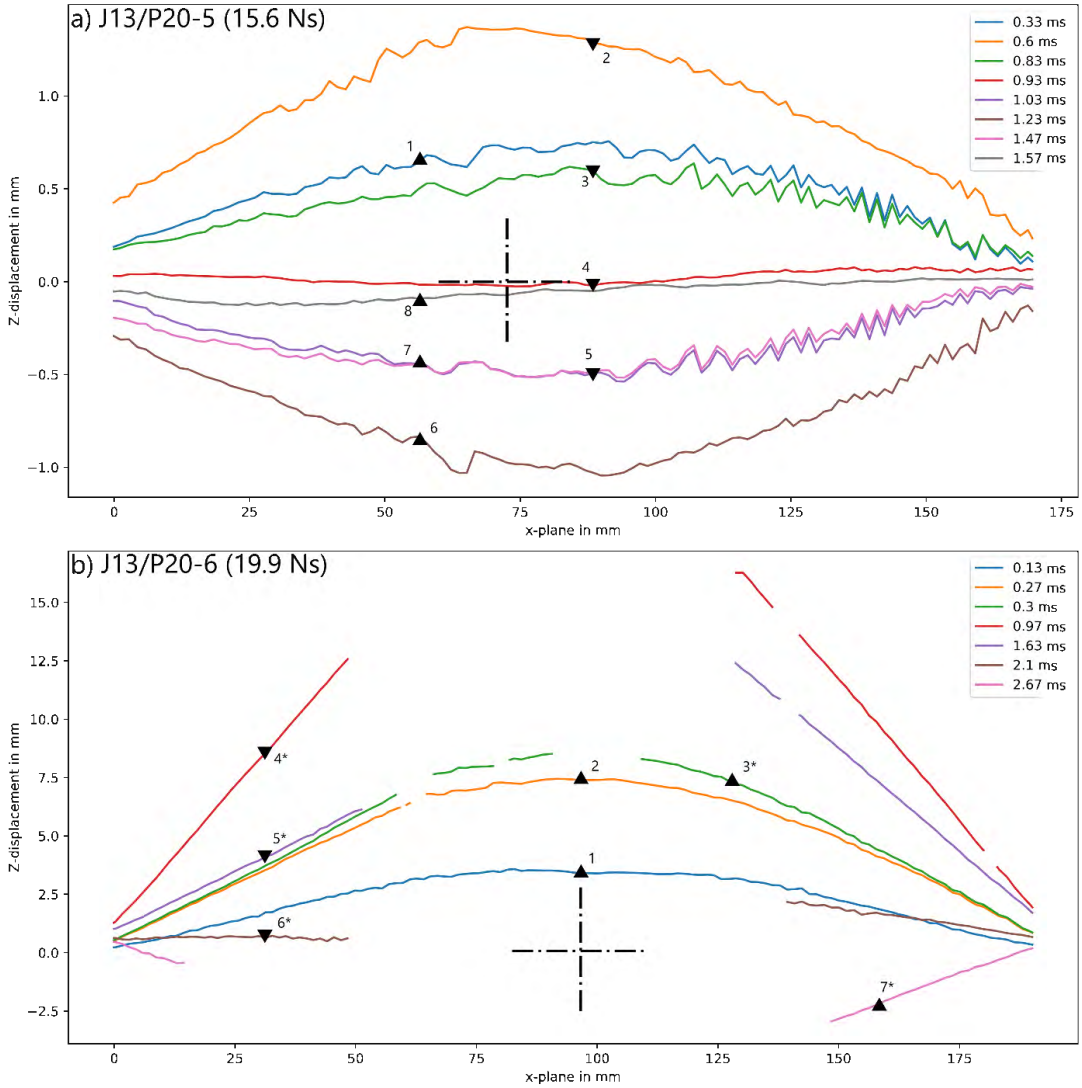

Figure 9-21: Transient displacement profiles for Jute 13/Prime 20LV panels

Flax Fibre Reinforced Composites

The transient displacement profiles for the flax fibre reinforced composites panels are shown in Figure 9-22 – Figure 9-24. As damage often occurred around the centre of the flax fibre reinforced specimens, profiles were included in the graphs to show that the maximum deflection was higher than the data obtained for the midpoint deflection in section 9.6.1.

Initially, the resulting profile for the F8/P20H panel (point 1 and 2) was similar to the GFRPs where the profile was dome-like in shape. However, after damage and cracking had occurred, the sides were straighter, with one side higher than the other.

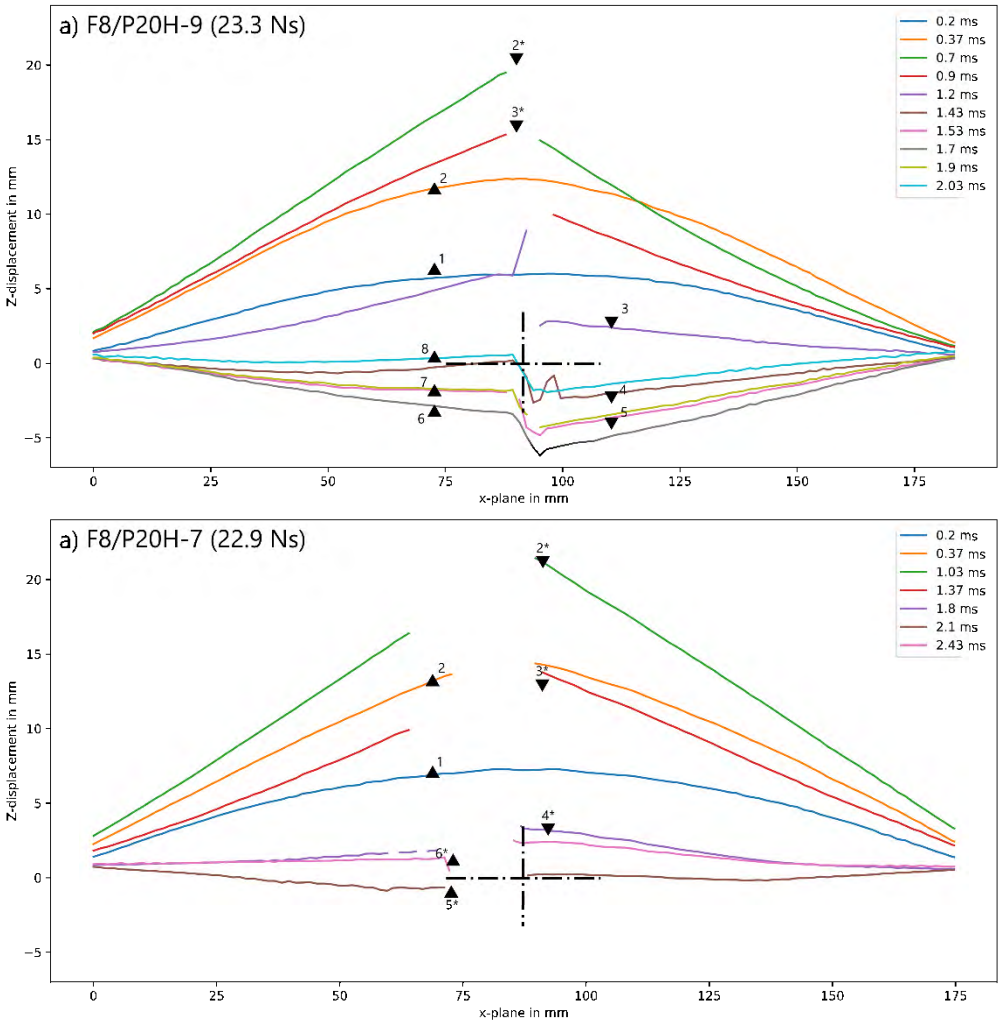

Figure 9-22: Displacement profiles for hand lay-up Flax 8/Prime 20LV panels

In some cases where the damage was not as severe, namely on the VI manufactured flax fibre reinforced composites subjected to an impulse less than 24.1 Ns, the profile was dome shaped prior to cracking. The deformed shape thereafter transitioned to a cone-like shape when cracking was initiated at the centre before returning to a dome-shaped on rebound when the crack closed up. At

higher impulses, the behaviour was similar to that observed for the hand lay-up flax fibre reinforced composites. On F9/P20-5 (Figure 9-23c), a large spike was observed at t = 0.5 microseconds. However, by checking the panel after testing, the panel had not fragmented but cracking was observed in the central region (Figure 8-22). The spike was likely due to a misinterpretation as the speckling changed due to the cracking and explosive by-products "cloud" (see Figure 9-15).

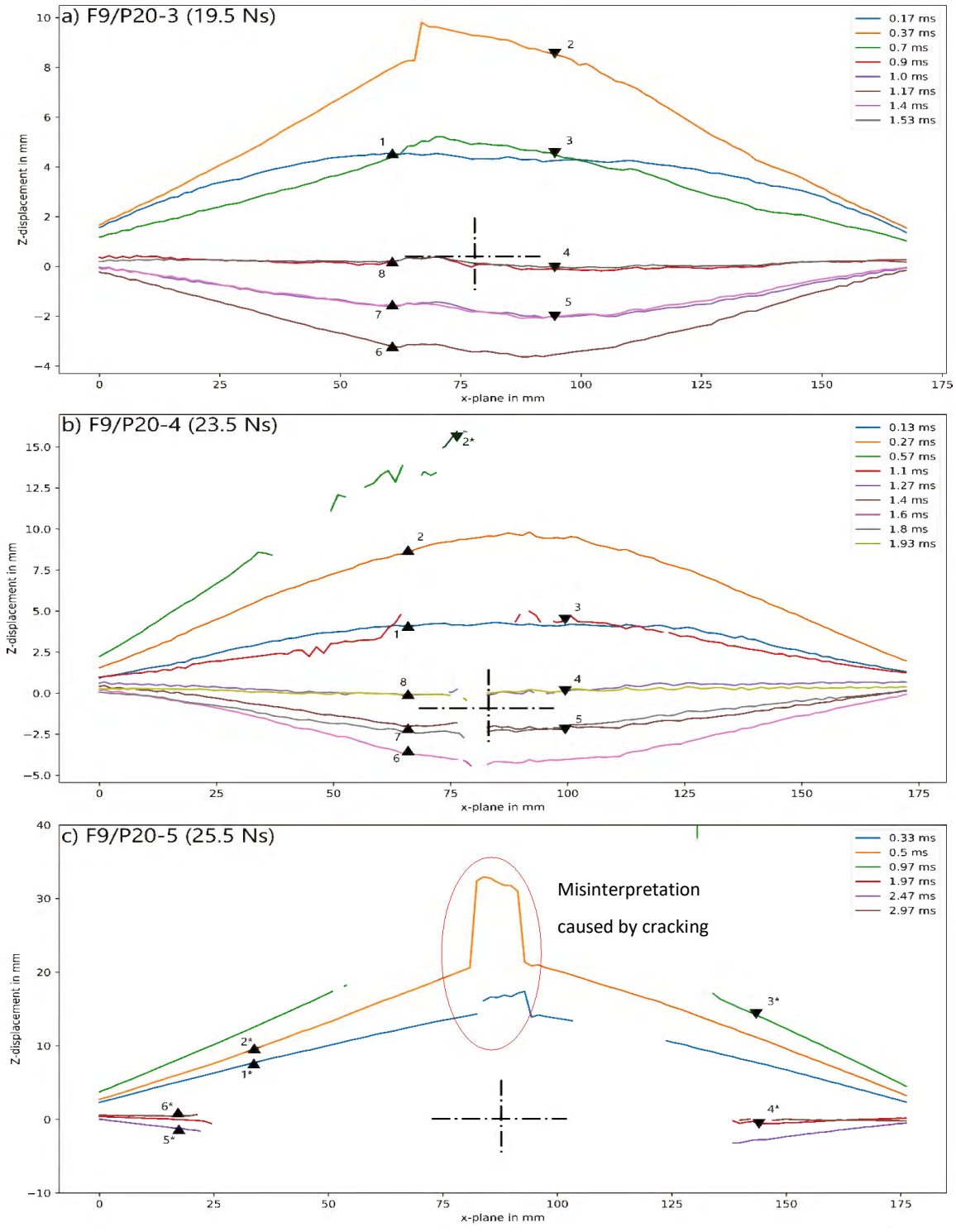

Figure 9-23: Displacement profiles of Flax 9/Prime 20LV panels

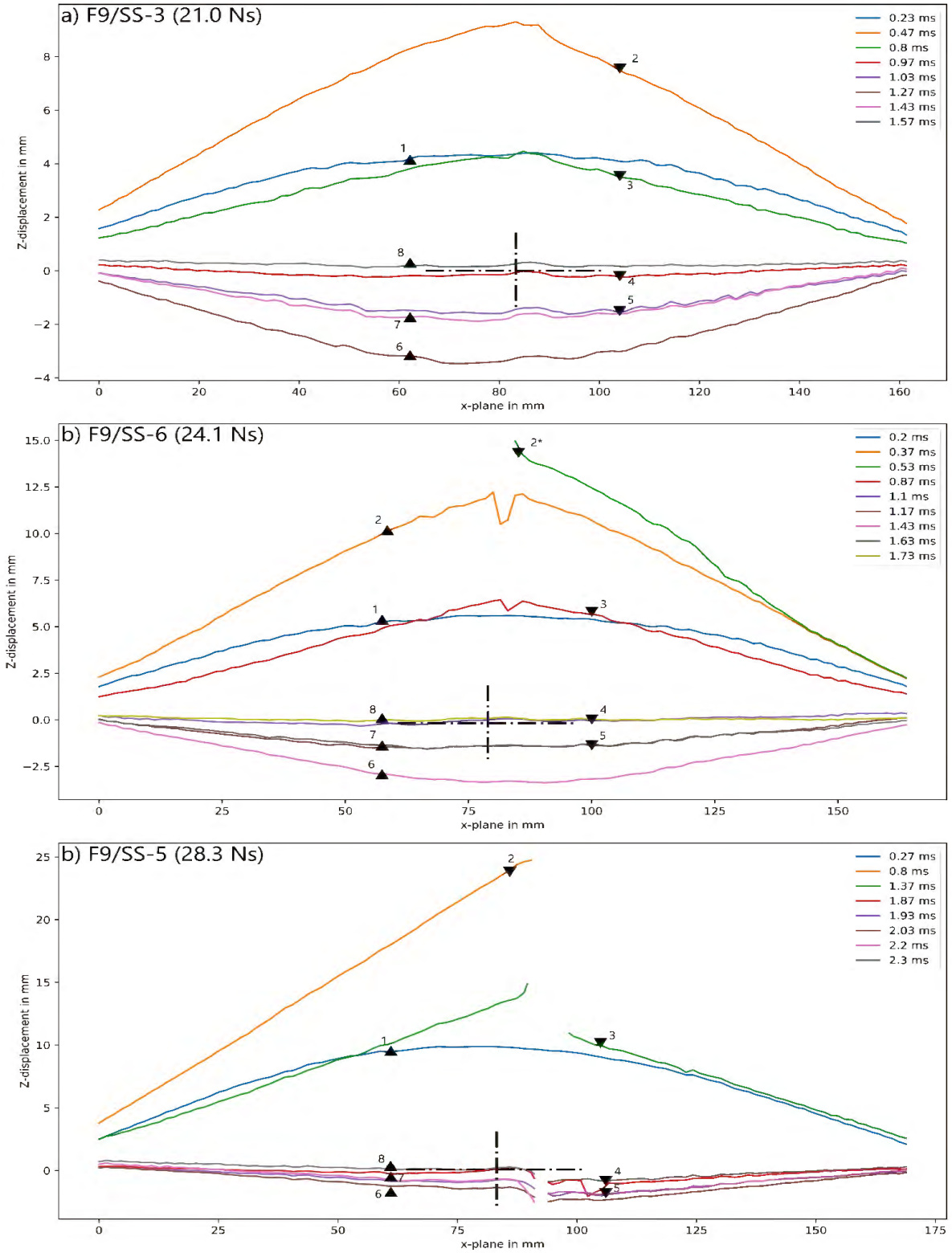

Figure 9-24: Displacement profiles of Flax 9/Super Sap panels

9.6.3 Overview of transient test results

A summary of the transient results is listed in Table 9-3. It includes the measured maximum (d_{max}) and rebound (d_{min}) deflection and the respective times at which they occurred, as well as the calculated damping coefficients of the panel. Panels where data was missing and the values found were likely to be higher, due to image blur or particulates obscuring the vision of the camera during capturing, are indicated with an asterisk on Table 9-3. Additionally, it was not possible, based on the results of the graph shown in section 9.6.1, to determine vibrational parameters for F9/P20-5 and J13/P20-6.

Table 9-3: DIC results based on the mid-point deflection

Specimen Name	Impulse (Ns)	d_{max} (mm)	t_{dmax} (ms)	d_{min} (mm)	t_{dmin} (ms)	ζ	τ_d (ms)	ω_n (rad/s)
G19/P20-8	25.2	12.3	0.40	-7.0	1.13	0.160	1.31	4855
G19/P20-4	31.7	13.5	0.37	-8.3	0.97	0.177	1.30	4911
G19/P20-9	33.7	14.4	0.40	-8.9	0.97	0.105	1.27	4975
G17/P20-5[a]	21.6	> 9.9	-	< -11.8	-	0.037	1.58	3972
G17/P20-8	22.2	13.9	0.33	-8.0	1.07	0.065	1.58	3977
G17/P20-2	28.1	16.6	0.40	-9.9	1.07	0.089	1.65	3823
G17/SS-3	21.5	13.3	0.43	-7.7	1.33	0.065	1.65	3816
G17/SS-5	30.7	17.6	0.37	-9.5	1.27	0.076	1.87	3376
G17/SS-6	43.2	22.6	0.40	-10.2	1.47	0.099	2.27	2786
MDF-7	11.8	6.6	1	-4.3	8.33	0.056	2.90	2170
MDF-8	15.7	14.2	1.4	-3.7	7.43	0.227	4.20	1536
F9/P20-3	19.5	9.2	0.40	-3.5	1.20	0.168	1.43	4447
F9/P20-4	23.5	*9.8	*0.30	-4.2	1.63	0.029	1.97	3211
F9/P20-5	25.5	*20.7	*0.43	-	-	-	-	-
F8/P20H-9	23.3	*12.6	*2.80	-3.4	1.73	0.101	2.07	3056
F8/P20H-7	22.9	*13.0	*0.4	*0.0	*0	0.342	2.46	2723
F9/SS-3	21.0	9.2	0.47	-3.4	1.27	0.157	1.37	4655
F9/SS-6	24.1	*12.2	*0.40	-3.3	1.47	0.149	1.70	3738
F9/SS-5	28.3	23.4	0.83	-1.4	2.07	0.304	2.10	3141
J13/P20-5	15.6	1.3	0.43	-1.2	1.82	0.083	1.22	5158
J13/P20-6	19.9	7.4	0.30	-0.3	0.033	-	-	-

* - data was missing and actual values are likely higher

a – data based on the oscillations observed after the light obscuring the recordings

There was little consistency in the damping coefficient and natural frequencies. The 17-layer GFRP panels (both Prime 20LV and Super Sap) had lower damping coefficients than the Glass 19/Prime 20LV panels indicating that increasing thickness increases the damping capacity of the panel. The data for the natural fibre composites either had a large range or too few data points to draw a meaningful conclusion. However, it was expected that the natural frequency would decrease with increasing impulse because the internal damage, which reduces the stiffness of the panel, was greater.

Figure 9-25 shows a graph of the maximum and rebound midpoint deflection versus impulse for the different composite panels. The maximum deflection appeared to increase with increasing impulse for all the panels tested. Similarly, for G19/P20 and G17/SS panels, the minimum mid-point displacement followed a similar trend for the glass fibre reinforced composite panels. There appeared to be significant amounts of scatter for the natural fibre composites tested, particular for the rebound deflection.

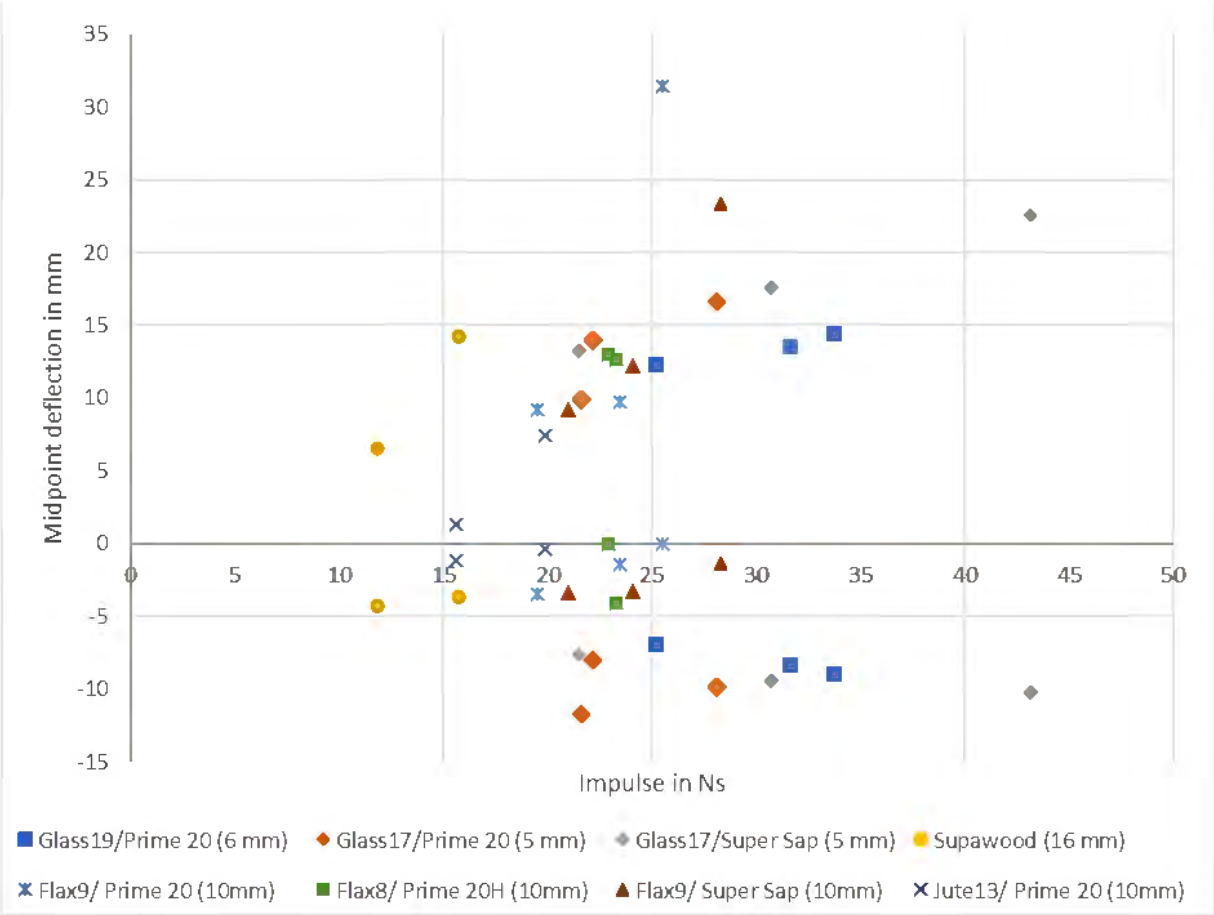

Figure 9-25: Graph of maximum and minimum DIC midpoint deflections versus impulse for blast tests

The time at which the maximum deflection had been reached seemed fairly consistent, between 0.33 – 0.43 microseconds, for the different GFRPs. From all the materials tested, Supawood panels had the longest time to peak deflection for the maximum deflection which can be a result of the significantly lower charge masses and impulses. The time to the rebound deflection from zero was shorter for the Glass/Prime 20LV panels than the Glass/Super Sap. It was difficult to observe trends from the other panels, with regards for the time to reach of the maximum and rebound deflection.

9.7 Summary of chapter

In general, the permanent midpoint deflection and surface cracking exhibited by the GFRP panels was lower than the damage exhibited by the natural fibre composites at similar impulses. Depending on the fibre (flax or glass), the resin had some influence on the cracking observed. For the flax FRPs, Super Sap based composites performed slightly better than the Prime 20LV counterparts. This was likely because the Super Sap resin is stronger than Prime 20LV (based on the flexural strength listed in Table 3-2) and the effect is more apparent in the flax fibres because of the relative fibre weakness. However, in the GFRPs, in terms of cracking, Prime 20LV based composites performed better by ~40 % at applied impulses over 40 Ns. However, delamination was found to be similar for the for the GFRPs of a similar thickness. Increasing the number of plies and consequently the thickness of the panel had a greater effect on the amount of delamination areas observed. Less delamination was observed on Glass 19/Prime 20LV tested at a similar nominal impulse as the Glass 17/Prime 20LV and Glass 17/Super Sap.

Initially, most of the panels underwent a viscously damped harmonic vibrational motion. As the impulse increased, the movement that the panel underwent caused damage which was more notable for the natural fibre composites tested. Depending on the severity of the damage, the profile of a natural fibre reinforced composite panel changed from dome-shaped, which was observed on the glass fibre reinforced composite panels, to a conical shape. The cyclic movement and consequent damage added to the complexity of composites where manufacturing, fibre, matrix choice and interaction between the two, affected the mechanical properties.

10 Discussion

In this chapter, influence of fibre type, resin type, and manufacturing method, as well as the transient behaviour of the panels are discussed. Results from the quasi-static testing (chapter 5) are used to gain insight how the different materials behaved under a blast load. The relative strength of the natural fibre laminates and glass fibre reinforced Super Sap composites versus the control materials, namely glass fibre reinforced Prime 20LV composites and Supawood, are discussed. This is further evaluated against metallic materials. Lastly, a sustainability assessment for the different composites is conducted, in terms of mechanical performance and natural or sustainable materials usage, to determine opportunities for sustainable materials as replacements.

10.1 Failure modes and mechanisms

10.1.1 Permanent deflection

In the range of blast tests performed, the permanent midpoint deflection of the natural fibre composites increased with increasing impulse whereas no measurable permanent deformation was exhibited by all GFRPs. Irreversible deflection occurred due to damage in the natural fibre composites such as cracking, fragmentation and delamination. In Figure 10-1, the cross-sections taken from a representative panel for the different materials, tested at high impulses within their material system, show how damage (or lack thereof) affected the permanent deflection and resulting profile of the panel.

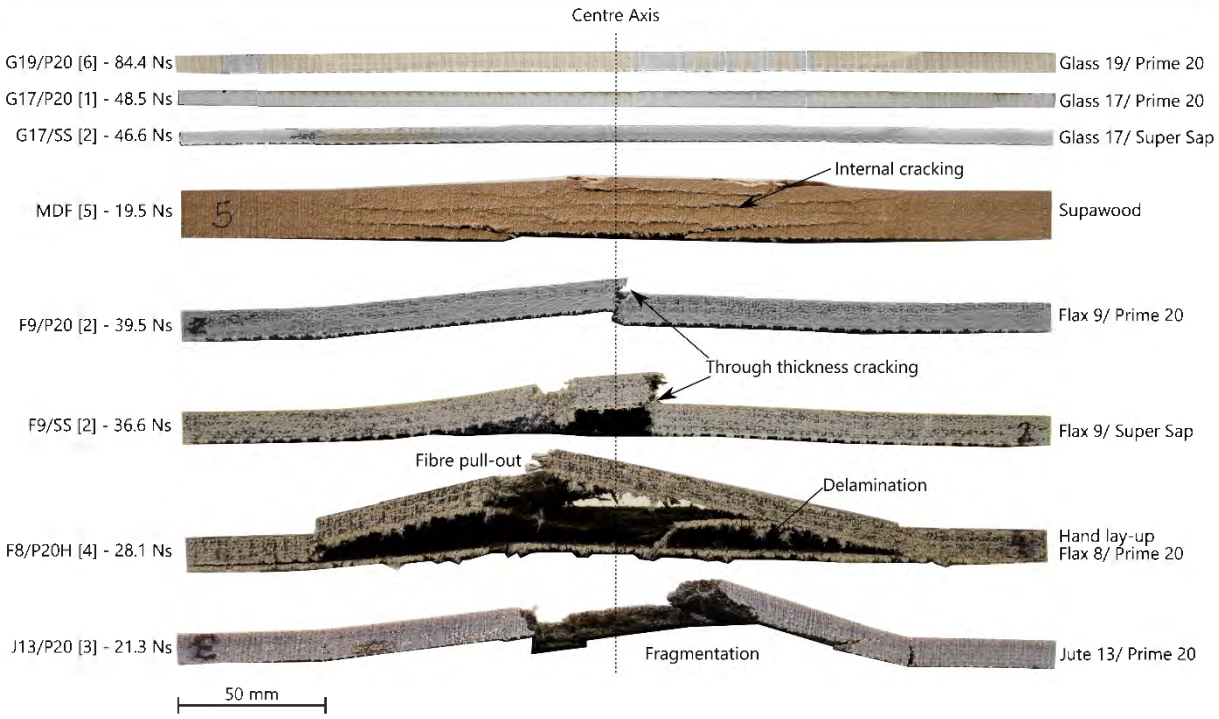

Figure 10-1: Representative images of the damage observed on cross-section of different blast tested panels

The negligible values of permanent deflection for GFRPs and results from the transient data indicated that the panels elastically deformed and gradually returned to their original state. Similar behaviour was observed for natural fibre composite panels tested at low impulse where low amounts of damage occurred.

10.1.2 Delamination

Delamination was observed on all the GFRPs which increased with increasing impulse. However, none of the natural fibre laminates delaminated except for the hand lay-up flax fibre reinforced composites. This correlated with the higher interlaminar properties values found for the flax and jute fibre reinforced composites as the delamination resistance would be higher for those materials. For convenience, the results of the interlaminar properties from chapter 6 are reshown in Table 10-1 to illustrate the significant differences in toughness between the glass and natural fibre laminates.

Table 10-1: Average values of the interlaminar fracture toughness at initiation and propagation

	$G_{Ic,init}$ [J/m^2]	$G_{Ic,prop}$ [J/m^2]
Glass / Prime 20LV	819	918
Glass/ SuperSap	531	618
Flax/ Prime 20LV	2272	2334
Flax/ SuperSap	2388	2474
Jute/ Prime 20LV	1257	1356

For the GFRPs, delamination was likely initiated as fine-scale microstructural damage, such as fibre-matrix interfacial cracks and short matrix cracks before developing into delamination with increasing impulse as observed by Franz et al [136] and Comtois et al [137]. According to Kerber et al [222], the failure modes (which extends to the results of the natural fibre composites tested) are caused by interlaminar and membrane (flexural) stresses generated as the panel bends under the blast wave. At similar impulses, less delamination was observed on the Glass 19/Prime 20LV compared to Glass 17/Prime 20LV as shown in Figure 10-2. Similar results were found between the two 17-layer GFRP despite the difference in resin. The flexural strength for Glass 19/Prime 20LV was greater than the 17-layer GFRPs.

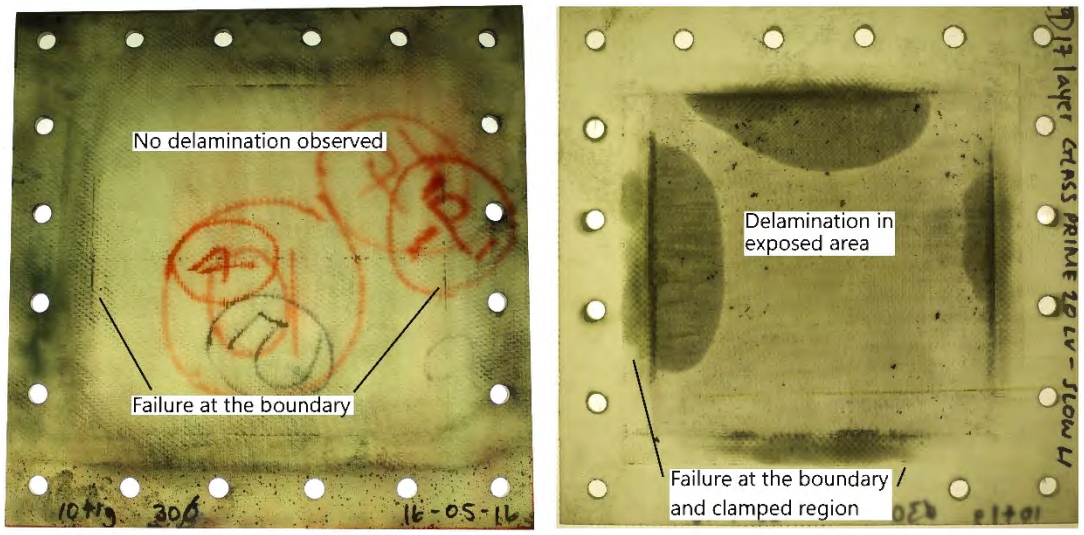

a) G19/P20-4 (31.7 Ns) b) G17/P20-9 (30.9 Ns))

Figure 10-2: Comparison of a G19/P20 panel and G17/P20 panel at similar impulses

Most of the delamination occurred at the boundary of the GFRPs, increasing towards the centre of the panel. This was relatively similar to the results reported by Comtois et al [137] where the major area of delamination was associated with the fixing arrangements. In contrast, delamination was observed around the central region of the panel for results reported by Yahya et al [139]. In that work, while the specimens were clamped onto a similar ballistic pendulum, circular plates were used, and the bolt positions were differently spaced. Moreover, the Mode I interlaminar fracture energy for the GFRP was 1708 J/m^2 [139], significantly higher than those presented in this work. Comtois et al [137] attributed the pattern of delamination to the boundary conditions of the panel when compared to other GFRPs. Therefore, it seemed that both the interlaminar fracture properties and boundary conditions appeared to have an impact on the pattern of delamination. A higher I value in the thicker panels resulted in less deformation and thus less delamination. Therefore, it was possible that more layers through its thickness distributed the stress at the interface between the layers. Considering testing conditions and other panel dimensions (apart from the thickness) are the same, the impulse of the Glass 19/Prime 20LV was multiplied by the square of the ratio of the average thickness between the 17-layer GFRP and 19-layer GFRP panels. The comparison of the delamination for the new adjusted impulse of Glass 19/Prime 20LV and the 17-layer GFRP panels is shown in Figure 10-3. From Figure 10-3, it seemed that the data aligns with each other, suggesting that simile scaling laws could predict delamination damage in composites. However, this is a limited set of data and delamination would likely be dependent on multiple factors (such as the influence of the other failure modes, clamping and constituent materials) due to the complexities associated with blast loading.

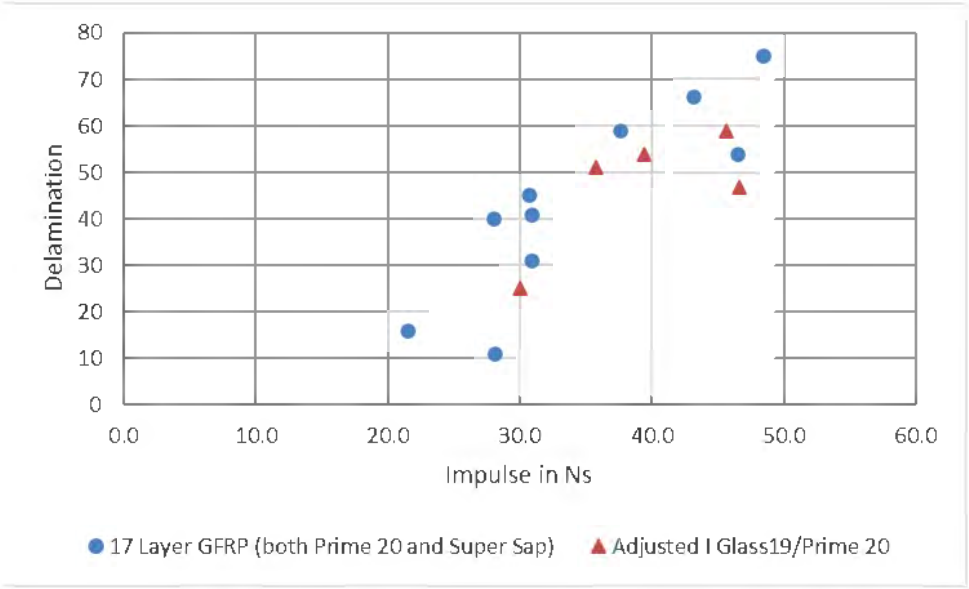

Figure 10-3: Graph of delaminated area versus impulse where the impulse was adjusted for Glass 19/Prime 20LV

In comparison, the main reason for the delamination in the hand lay-up flax fibre reinforced composites was likely due to the manufacturing method described in further detail in section 10.7. As the panel deflected, the top layer (which coincidently was position facing the explosive) had separated from the rest of the panel. Scarponi [148] showed that poor interfacial adhesion results in large amounts of delamination and splitting on natural fibre composites tested under impact loading. Hence, this delamination was caused by the poor adhesion between the layers. Where the fibres were more saturated, similar observations were made as the VI flax fibre reinforced composites. It is likely that for a well manufactured flax fibre reinforced epoxy composite, tested under similar conditions, the more probable mode of failure will be cracking rather than delamination, due to their high interlaminar fracture toughness properties.

10.1.3 Cracking and fragmentation

Cracking was the main failure mode observed in the natural fibre composites. Initially, it was observed on the back surface. With increasing impulse, cracks also developed on the front surface. For some of the different natural fibre composites tested, particularly the VI manufactured composites, some cracks on the front surface matched the cracks found on the back surface as shown in Figure 10-3 suggesting that through-thickness cracking occurred which was confirmed by inspecting the cross-section of the panels. Through thickness cracking was not as clear on the hand lay-up composite or in the Supawood (due to the structure).

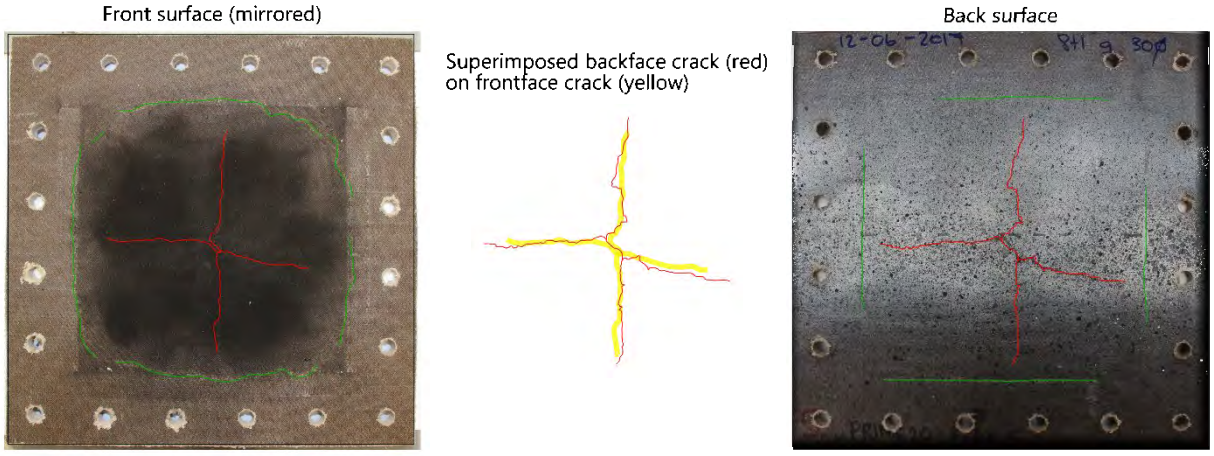

Figure 10-4: Comparison of the front and back surface cracks on F9/P20 at 25.5 Ns

The cracking eventually led to fragmentation in the jute fibre reinforced composites and Supawood. It was likely that the flax fibre reinforced composites would have fragmented if tested at a slightly greater impulse. A similar behaviour for the laminates was found by Huang et al [146] on flax fibre reinforced composites due to the brittle epoxy resin and strong interfacial adhesion. The cracking was caused by interlaminar, and membrane (flexural) stresses generated as the panel deformed similar to

delamination. This suggested that the properties are resin dominated as opposed to fibre dominated. The geometry and size of fragments of the composite panels are complicated due to the competing damage mechanisms, material heterogeneity, interfacial effects and failure modes. Furthermore, pre-existing internal flaws and cracks will contribute to fracture and fragmentation.

Surface cracking was also observed on the front surface of Glass 19/Prime 20LV and Glass 17/Super Sap at high impulses. The flexural properties found for the Glass 17/Super Sap were considerably lower than Glass 17/Prime 20LV, as listed in Table 10-2. This could have contributed to the lack of cracking on Glass 17/Prime 20LV as it was tested at a similar impulse range as Glass 17/Super Sap. At higher impulses similar to Glass 19/Prime 20LV, it is likely that cracking would be observed on the Glass 17/Prime 20LV.

Table 10-2: Mean values for the flexural properties of Glass 17/Prime 20LV and Glass 17/Super Sap

	Flexural strength, σ^f_{max} [MPa]	Strain at σ^f_{max} , $\varepsilon^f_{\sigma max}$ [m/m]	Flexural chord of elasticity, E^f_{chord} [GPa]	Strain at failure, ε^f_{fail} [m/m]
Glass 17/Prime 20LV	399	0.025	21.9	0.032
Glass 17/ Super Sap	276	0.015	20.2	0.023

In addition to cracking on the front and back surfaces, through width cracking was observed on the cross section of the Supawood panels. On some panels, no damage was observed on the surfaces of the panel which remained relatively flat. This showed that the compressed section of the panel offering some resistance towards damage caused by blast loading. However, considering the damage would be internal, observing the exterior surfaces of Supawood may not be enough and the extent of the damage may be more severe than expected.

10.1.4 Matrix failure in glass fibre reinforced Super Sap composites

It was difficult to determine what caused the matrix or interface failure found on the glass fibre reinforced Super Sap composites. While the obvious difference was the change of resin, which is discussed further in section 10.6, it was unclear why the failure would initially occur on the back surface until a threshold impulse of 30.9 Ns before appearing on the front surface. However, it was possible that the matrix failures were more widespread through the thickness of the panel. Additionally, the matrix failure appeared to have negligible impact on the delamination as similar results were found on Glass 17/ Prime 20LV.

10.1.5 Damage along the boundary

It was likely that stress concentration effects at the clamped boundary caused some of damage at the boundaries of all composites. Initially, the damage would be minor fibre and matrix failure along the clamp edge except in the Supawood (where no boundary damage observed). As the impulse increased, through thickness cracking at the boundaries was observed. For the GFRP, cracking also extended into the clamped region.

Damage at the boundary was the first failure mode observed for GFRP, yet the last mode of failure observed for the natural fibre composites as cracking was observed prior to damage to the boundary. The damage sustained in the exposed area in the natural fibre composites could have dissipated part of the energy, thus reducing the damage at the boundary.

It was also possible that the damage at boundaries were caused due to slight variations in drilling causing bolt holes to not be perfectly aligned, manufacturing inconsistences (like thickness varying across the panel), variations on the clamping forces and loading. This would explain why the boundary damage was not distributed evenly and scuffing was observed.

In general, boundary conditions influence the behaviour of the panel and in turn, this could affect the failure mode initiation and location of the damage on a panel. Similar observations were found by Nurick et al[223] on metallic plates where the boundary conditions had a significant effect on the damage observed on panels (such as large inelastic deformation) when subjected to uniform air blast loading conditions. Quantifying the relationship between the effect of the boundary condition on the response of the panel is challenging as other factors, such as testing conditions (charge mass and stand-off distance), constituent materials, and panel properties (including the existence of small defects and variability due to composite manufacture), influence the response as well.

10.2 Failure mode initiation and thresholds

A failure initiation chart, shown in Figure 10-4, was constructed, using the data from Table 9-1. Similar charts were drawn by Langdon et al [168] based on the work performed by Sinclair [224]. These charts were used as an indicator of the onset of a failure mode for range of charge masses. Similar to charts observed [168], [224], dotted lines were used to show the combination of failure modes at higher charge masses.

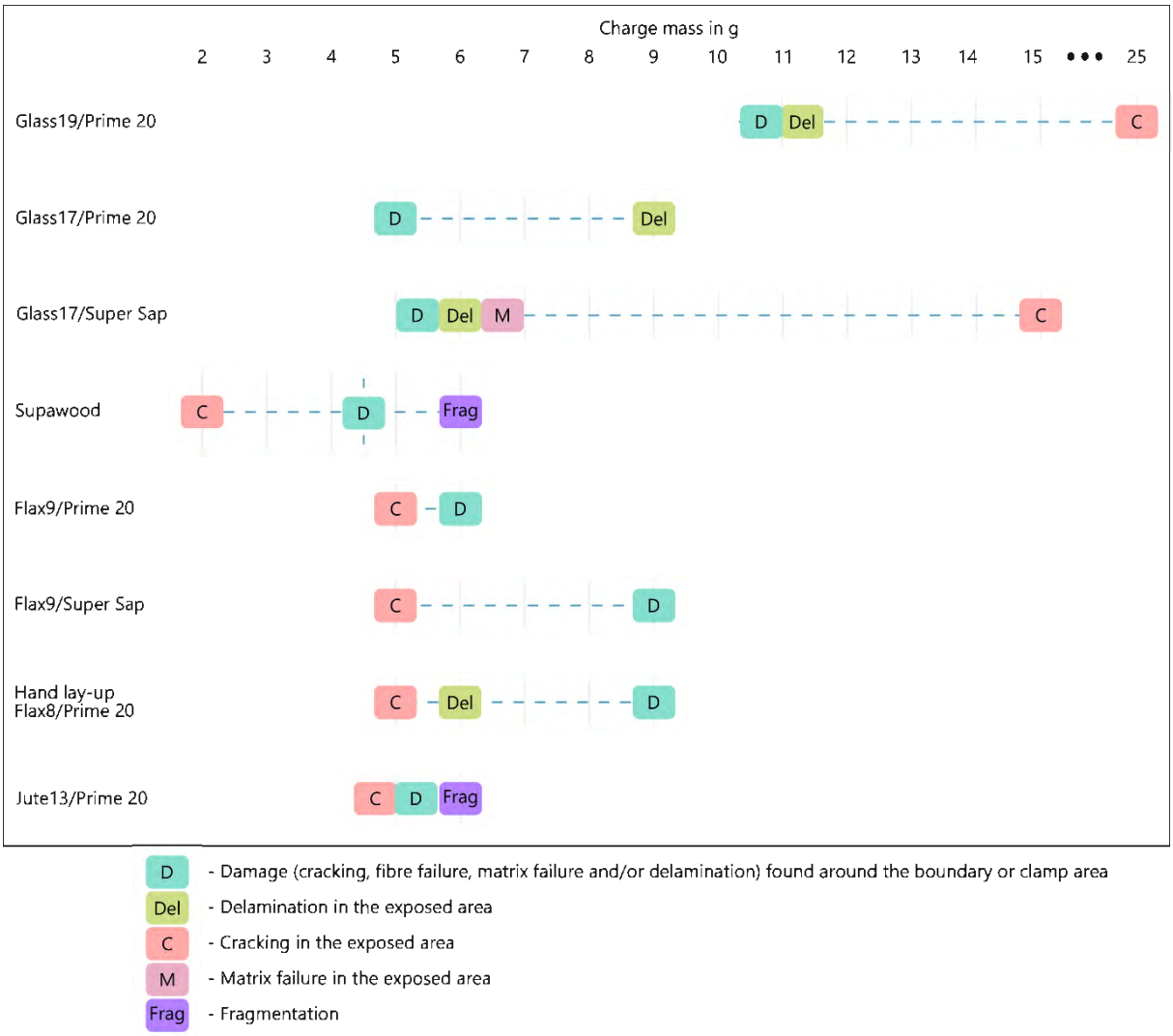

Figure 10-5: Failure initiation chart of the different blast tested materials

By increasing the number of plies of the glass fibre reinforced composites by two (Glass 17/Prime 20LV – Glass 19/Prime 20LV), it was observed that damage was initiated at double the charge mass, as indicated in Figure 10-4. The charge mass to onset failure was similar for Glass 17/Prime 20LV and Glass17/Super Sap. Initially, additional failure modes on Glass 17/Super Sap were found (such as damage at the boundary, matrix failure and delamination) compared to Glass 17/Prime 20LV where only damage at the boundary was observed. The charge mass of 5 g to initiate damage for all the natural fibre laminates was the same as Glass 17/Prime 20LV. Supawood was the weakest material as only 2 g of explosive caused (internal) cracking in the panels.

The corresponding impulse that caused the damage shown in Figure 10-4, is found in Figure 10-5. In addition, square markers were used for the natural fibre composites to indicate the impulse where the panels were considered to have completely failed. For the Supawood, hand lay-up flax fibre reinforced composites, and jute fibre reinforced composites, shearing and fragmentation was chosen

as indicators of complete failure. While the VI flax fibre reinforced composites had neither fragmented nor sheared at the boundary, examinations on the panels tested at their highest impulse indicated, in chapter 8, that these panels were close to complete failure. For the GFRPs, none of the panels had fractured in the impulse range tested. Moreover, given that Glass 19/Prime 20LV had not completely failed at an impulse of 84.4 Ns, it was likely that the impulse required to cause fragmentation and complete failure in a glass fibre reinforced panel was well above the range of the natural fibre composites tested.

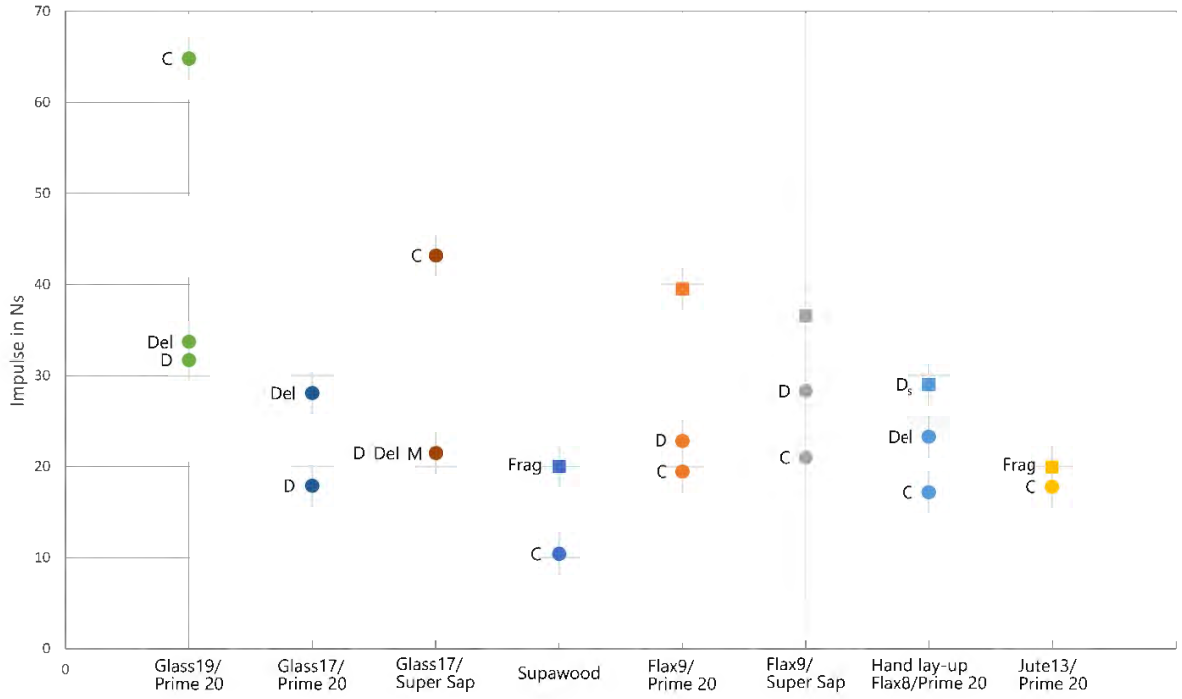

Figure 10-6: Impulse required to cause damage and failed (squares) composites

The difference between the impulse required to initiate damage and complete failure was, in general, small for the natural fibre composites. These differences were approximately 10 Ns, 20 Ns, 17 Ns, 12 Ns and 2 Ns for Supawood, Flax 9/Prime 20LV, Flax 9/Super Sap, hand lay-up Flax 8/Prime 20LV and Jute 13/Prime 20LV respectively. The best performing flax fibre reinforced composite tested was the VI Flax 9/Prime 20LV followed by Flax 9/Super Sap and lastly hand lay-up Flax 8/Prime 20LV. The results were relatively similar Flax 9/Prime 20LV and Flax 9/Super Sap, but lower for hand lay-up Flax 8/Prime 20LV suggesting that the manufacturing method may have a greater role than the resin. The response of the jute fibre reinforced composites was extremely sensitive within a narrow impulsive range. Similar results were found on carbon fibre reinforced composites [139] and like those carbon fibre reinforced composites, cracking was likely a precursor to complete failure of the panel. In this way, Supawood can be considered to be superior to the jute fibre reinforced composites despite failing at similar impulses.

10.3 Transient behaviour of materials

For the transient displacement profiles, the highest displacement was, for most panels, located at the centre of the panel with the displacement decreasing symmetrically on both sides away from the centre prior to any significant damage (usually cracking in the natural fibre composites) that occurred. This suggested that the impulse imparted onto those panels was evenly distributed over the surface of the panel. Asymmetric profiles that were occasionally observed were likely due to the detonation occurring slightly off-centre, as well as the internal damage occurring off-centre in the panel.

The dynamic response of the different composites was similar; the panels had all initially deformed in the direction of the blast wave before deflected in the opposite direction (rebound deformation). This motion was due to the inertia of the panel following the blast load and elastic behaviour of the panel. A global dome shape profile was observed on the different composites at impulses where little damage was sustained as shown in Figure 10-6. A similar response was observed by Gargano et al [141] on glass and carbon reinforced composites under their low intensity blast load testing.

The profile of the natural composites changed from dome-shaped to cone-shaped when cracking occurred (as shown on Figure 10-6b). However, the rebound deformation helped keep the panel together, particularly at lower impulses as the profile returned to a global dome shape. For the natural fibre composites, the opposite trend compared to the GFRPs was observed where the minimum displacement decreased with increasing impulse. This was likely due to the panels breaking during testing and the mechanical properties, particularly elastic modulus, reducing as damage (such as cracking, fibre and matrix failure) occurred. It also possible that longer damping periods measured for the natural fibre composites were due to the significant damage and cracking which occurred.

In general, the failure modes (delamination, cracking, and matrix failure) affected the overall behaviour of the laminate. In addition, the cyclic deformation was similar to low cycle fatigue. While most of the damage was likely caused by the initial response to the blast, cyclic loading could have increased crack growth and delamination.

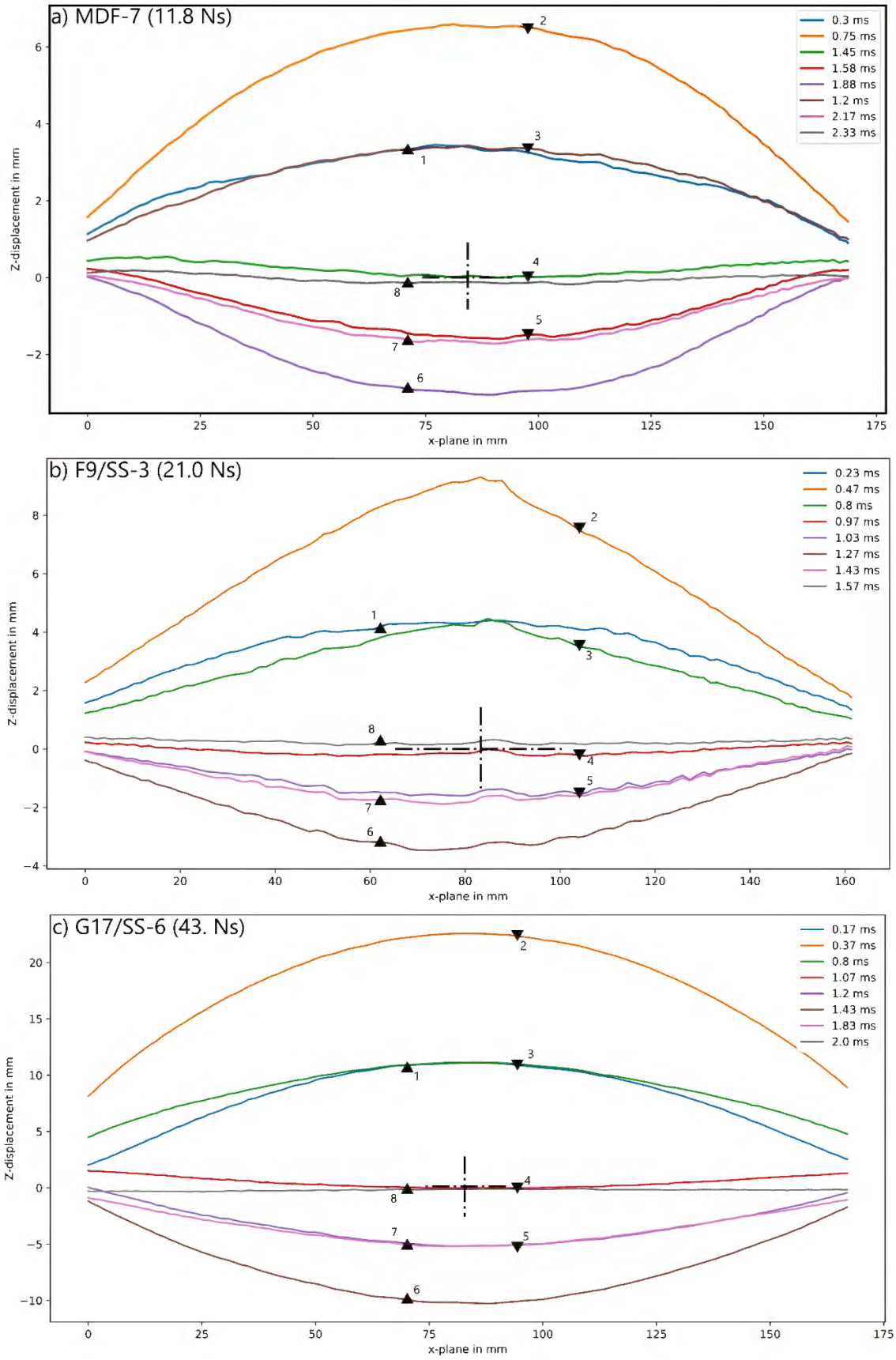

Figure 10-7: Comparison of the transient midplane profiles observed for a) Supawood, b) Flax 9/Super Sap and c) Glass 17/Super Sap

10.4 Non dimensional analysis approach

As there were differences in the material properties, and panel and charge geometry, non-dimensional analysis was implemented to compare the response of the different composite materials tested. The non-dimensional impulse, φ_q, was calculated using Equation 10-1 for quadrangular plates tested [225]. It should be noted that Equation 10-1 was obtained empirically for metal plates subjected to large inelastic response where tearing was not observed.

$$\varphi_q = \frac{I}{2t^2(BL\rho\sigma)^{1/2}} \qquad 10\text{-}1$$

Where I is the measure impulse, t panel thickness, L panel length, B panel width, ρ density and σ characteristic material stress.

The mean value for 0/90^o quasi-static tensile yield stress was taken as the characteristic material stress as quasi-static yield strength is used for monolithic metal plates [225]. The panel density was simply determined as mass over volume. The permanent deflection-thickness (δ/t) ratio was plotted against the calculated non-dimensional impulse and shown in Figure 10-7 - Figure 10-9 for the glass fibre reinforced composites, natural fibre composites and all the materials tested respectively.

The results for the glass fibre reinforced Prime 20LV composites were scattered compared to the glass fibre reinforced Super Sap composites making it difficult to determine if there were any trends in the data. However, the residual displacement was low, and non-dimensional analysis could be more appropriate for large deformation responses and ductile materials.

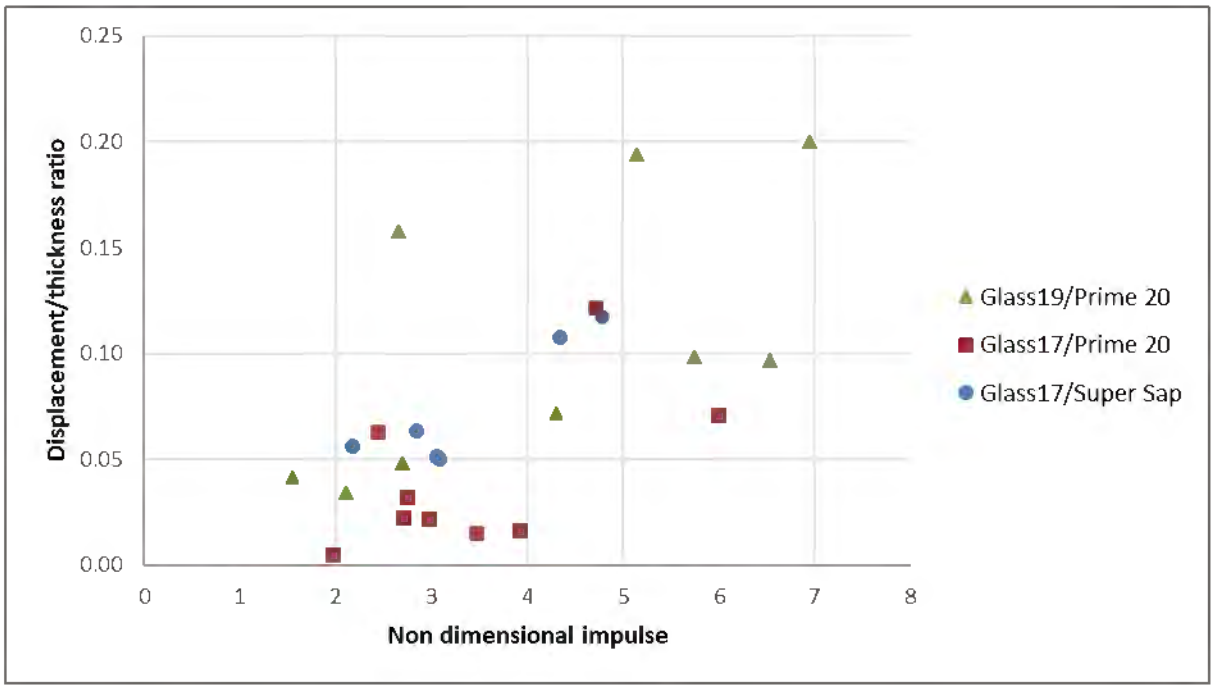

Figure 10-8: Graph of displacement/thickness ratio versus dimensionless impulse for GFRPs tested

Natural fibre composites were more consistent than the glass fibre reinforced composites as shown in Figure 10-8. Linear trend can be observed for the Supawood, Flax9/Prime 20LV, Flax9/Super Sap and Jute13/Prime 20LV. The results for the hand lay-up Flax8/Prime 20LV were more scattered, likely due to the manufacturing process.

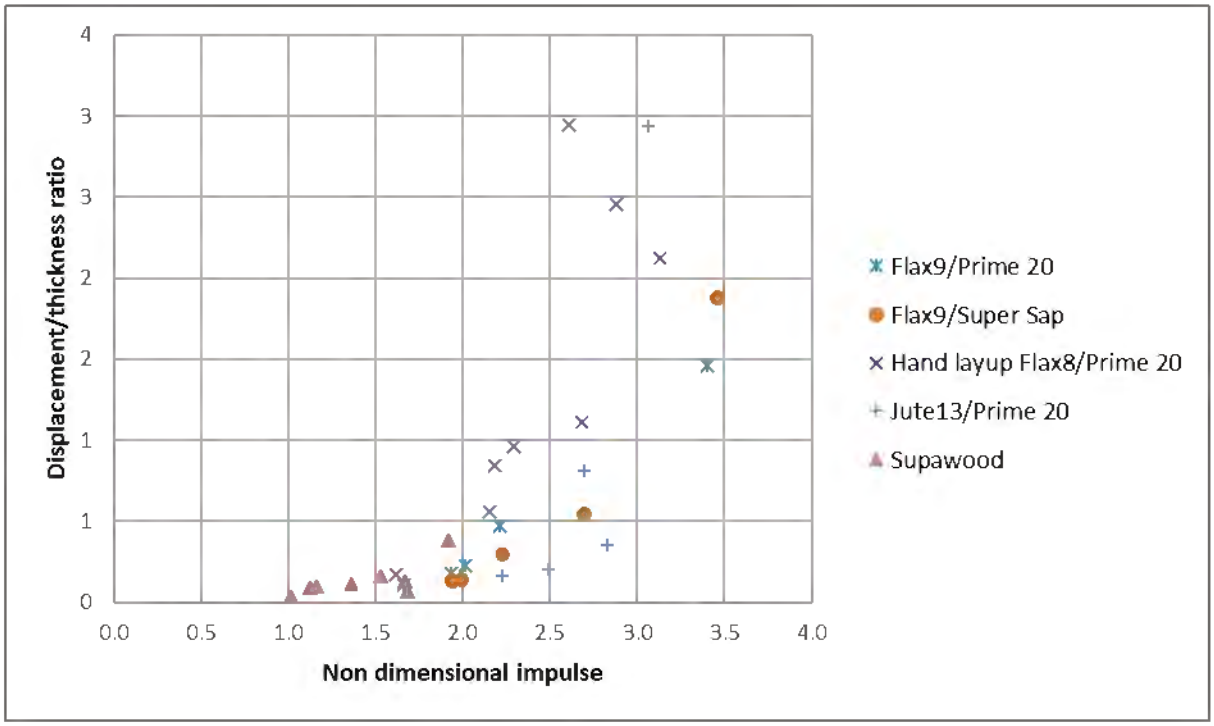

Figure 10-9: Graph of displacement/thickness ratio and dimensionless impulse for NFCs tested

Among the plotted results for all the blast tested panels, an empirical relationship obtained using a regression analysis on 356 data points of quadrangular plates subjected to uniform and localised blast loads [225] was drawn. A significant portion of the results were below the empirical relationship, suggesting that less permanent displacement would be observed for a given impulse especially for GFRP.

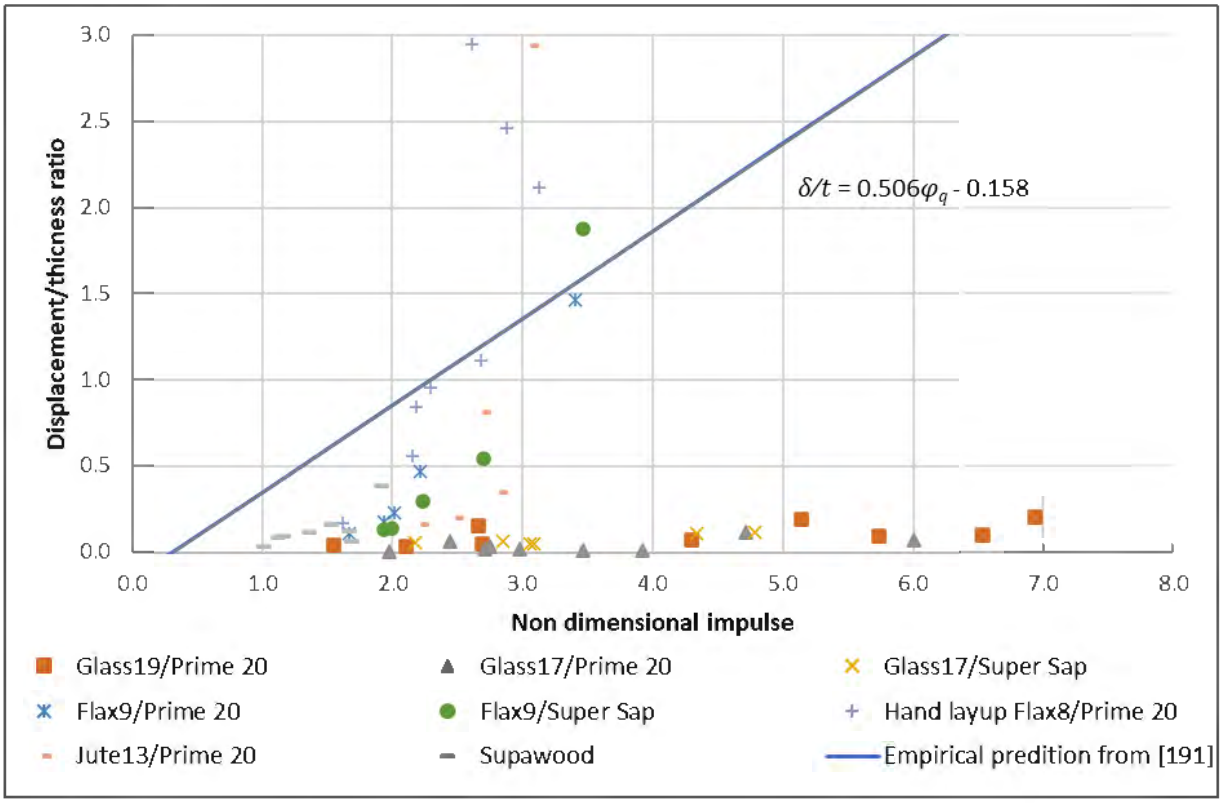

Figure 10-10: Graph of displacement/thickness ratio and dimensionless impulse for all tests

Figure 10-9 shows this sort of approach is unsuitable for composite materials, due to their low permanent displacements. Unfortunately, finding a more suitable method was quite challenging as the failure modes observed can be very different between different composites. The difficulties in using non-dimensional analysis approaches with a single performance metric (e.g., delaminated area, normalised crack) are apparent in FRPs which exhibit multiple complex and varied failure modes depending on their constituent materials, lay-up and manufacturing method. Therefore, several approaches that partitions composites into different failure or material categories would be necessary.

As shown from Figure 10-9, it may not be appropriate to use the same non-dimensional approach used on metallic materials for these composites, especially when considering the permanent displacement and tensile strength as defining parameters. Therefore, the peak transient displacement was normalised instead. Additionally, the peak flexural stress as a characteristic stress as the blast

tests seemed similar to the bending response. A linear relationship can be observed when the composites tested are plotted using this modified non-dimensional approach as shown in Figure 10-10. The R^2 correlation coefficient found using a linear regression fit on the data was 0.85. While this value is lower than that found for metals, it still indicated a strong correlation. Further work should be conducted to determine whether this approach will enable comparison of panels with different geometries (exposed area and thickness) and composites.

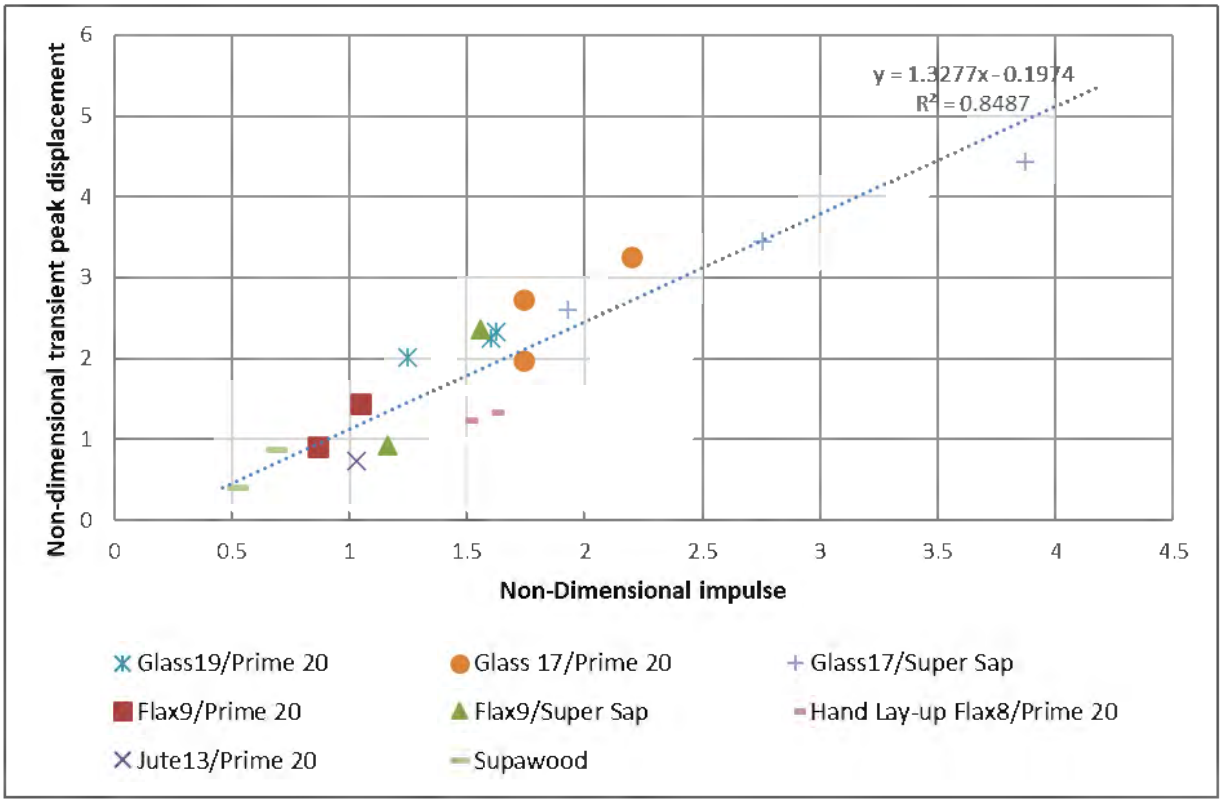

Figure 10-11: Graph of non-dimensional transient displacement and dimensionless impulse for all tests with DIC data

10.5 Influence of fibre type

The superior tensile and flexural strength reflected on the blast behaviour of the GFRPs. In comparison to the natural fibre composites tested, the GFRPs were found to have better blast resistant properties because:

1. Negligible permanent midpoint deflections were measured, and panels tested in the same range as the natural fibre composites behaved elastically,
2. Smaller amounts of fibre failure were observed, most of which were at the boundaries,
3. A continuous (linear) damage progression was observed for various failure modes (such as delamination, total cracking, and matrix failure on Glass 17/Super Sap) and,
4. None of the panels had ruptured in their impulse range tested

While the manufacturing method did play an important role in the flax fibre reinforced composites, the results showed that composites reinforced with flax fibre were stronger than jute fibre and Supawood because:

1. Smaller permanent midpoint deflections and cracking were measured at similar impulses, and
2. A relative continuous progression was observed for midpoint deflection and total cracking provided the panels were manufactured using VI.

The jute fibre reinforced composites behaved in a brittle manner throughout all the tests (both quasi-static and blast). Apart from the low flexural and tensile properties, the shear stress was also found to be lower than the interlaminar fracture toughness. In the blast tests, the jute fibre reinforced composites generally showed a non-continuous progressive cracking (where the amount of the cracks were unpredictable, and no trend was observed). In some case, the jute fibre reinforced composites fragmented. The difference between the onset of damage and complete failure was fairly insignificant. Therefore, the ability to absorb the blast energy was considered very low. It was possible that the jute fibre could benefit from an additional treatment that would improve the interfacial adhesion, however microscope images do suggest that there is a good bond between the jute fibres and the resin. Considering the size of the core of the fibre, as shown in Figure 10-10, the composite would have remained resin rich. The behaviour of the composite would consequently still be resin dominated and brittle.

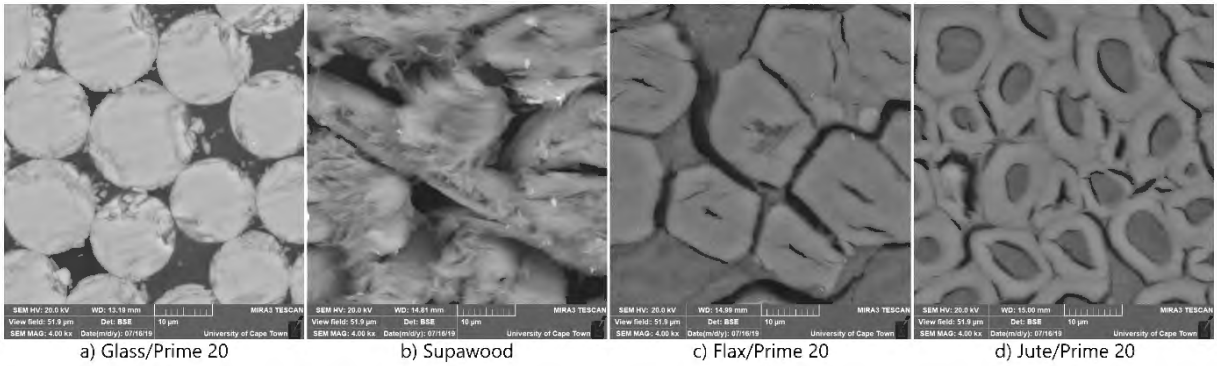

Figure 10-12: Comparison of fibre structure on SEM images for a) glass fibre, b) short wood fibres in Supawood, c) flax fibre and d) jute fibre (SEM MAG: 4000x)

The Supawood failed at a similar impulse as the jute fibre reinforced composites despite having lower flexural and tensile properties. However, this may be more indicative of structure of the panel rather than the fibre type. Furthermore, significantly less resin was used to manufacture Supawood.

10.6 Influence of type of epoxy resin used

In the quasi-static tests, both flexural and interlaminar properties reported for the glass fibre reinforced Super Sap composites, were significantly lower than the glass fibre reinforced Prime 20LV composites. This, in turn, did not appear to increase the percentage of delamination observed or the permanent midpoint deflection measured. The only noticeable difference between the two GFRPs, with the same number of plies, was the matrix failure and cracking observed on the Glass 17/Prime 20LV panels.

Extensive cracking within and along the clamped edge of the Glass 17/Super Sap panels was observed at high impulses. Yet, on Glass 17/Prime 20LV, less cracking was observed in the clamped region and no cracking in the exposed area at similar impulses as shown in Figure 10-11. The increased cracking in the clamped region indicates that Glass 17/Super Sap were more susceptible to pulling in at the bolt holes and the effects of a (bolt) hole in the composite.

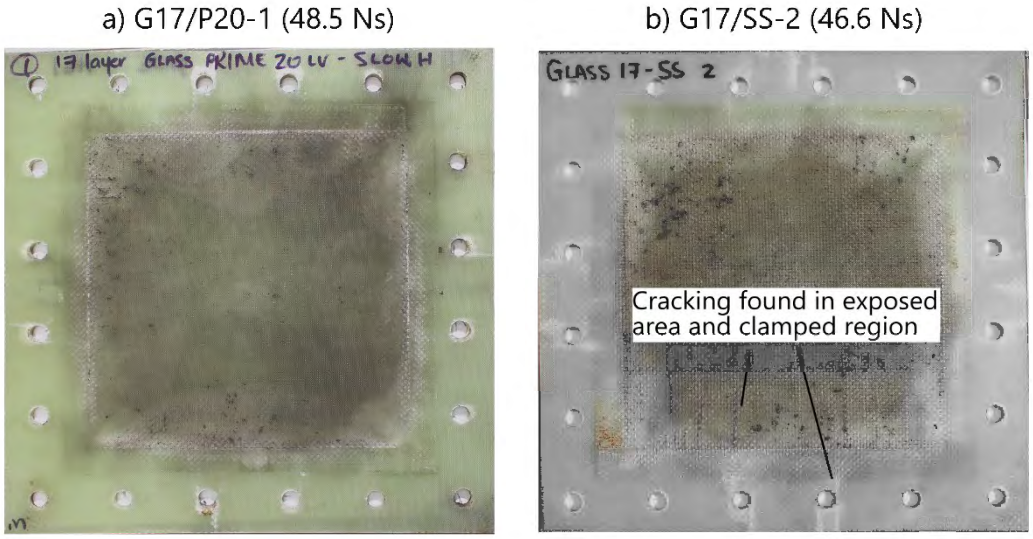

Figure 10-13: Comparison of the front surface of a) Glass 17/Prime 20LV and b) Glass 17/ Super Sap

A possible reason for the cracking could be because Glass 17/Super Sap was less flexible than Glass 17/Prime 20LV. Okoli et al [226] found that, for a given fibre content, the failure modes in laminates changed from fibre brittle failure (at quasi-static testing conditions) to brittle failure with high amounts of matrix damage at intermediate to high strain rates. This strain rate sensitivity could have also influenced the matrix failure observed. The effects of strain rate were, however, not determined in this thesis prior to blast testing but could be considered in future work.

It was possible that the compatibility between the resin and fibre, coupled with the shock loading and deformation, caused the matrix failure, as good adhesion between was observed on SEM images as shown in Figure 10-12. In addition, considering that the bolt holes had an influence on the cracking

observed, voids within the composite may have led to matrix failure as the panel deformed. Voids were found to degrade the matrix mechanical properties (such as hardness) and interface. Fibre dominated properties showed a lower sensitivity to voids [106], [227]–[229]. This could explain the juxtaposition of the presence of the matrix failure with little influence on delamination or midpoint deflection as the properties of the GFRPs were fibre dominated. Additionally, there were no significant voids seen in the SEM images of the GFRPs.

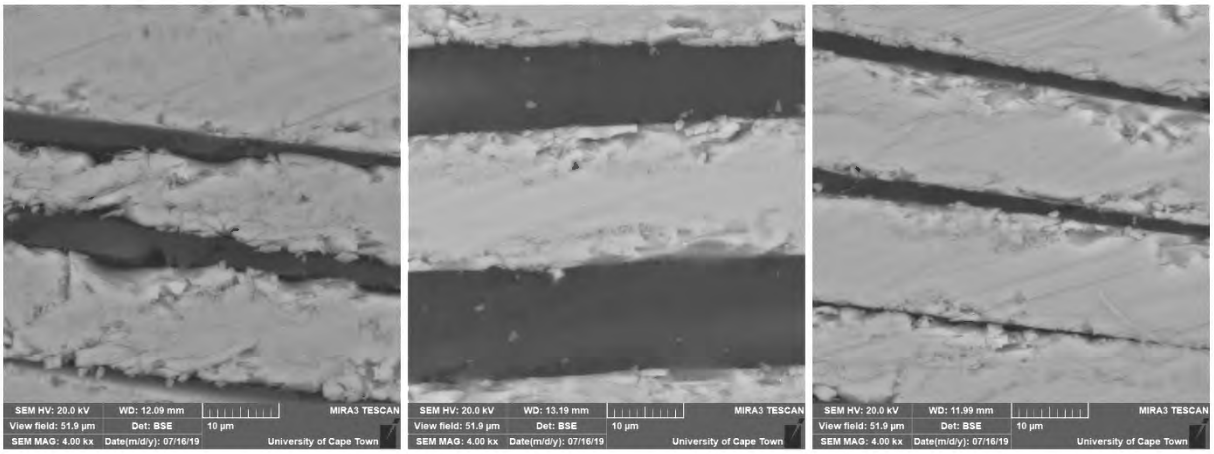

a) Glass 19/ Prime 20 b) Glass 17/ Prime 20 c) Glass 17/ Super Sap

Figure 10-14: SEM images of glass fibre reinforced composites (SEM MAG: 4000x)

In the flax fibre reinforced composites, slightly less cracking and midpoint deflection was observed in Flax 9/Super Sap compared to Flax 9/Prime 20LV, possibly because the interlaminar strengths of the flax fibre reinforced Super Sap composites were higher. In general, because the panels were opaque, it was more difficult to determine any significant differences in the flax fibre reinforced composites. The effects of the resin (such as cracking and matrix failure) seemed more apparent for GFRP where matrix failure was visible. A possible reason could be because the mechanical properties (such as strength, ductility, and impact resistance) of the glass fibre and matrix were very different. Yet for the flax fibre, the properties are similar. Furthermore, both resins were epoxies with relatively similar mechanical properties. However, the overall blast resistant properties (in terms of delamination and cracking in the exposed area) appeared to be more dependent on fibre type rather than resin when comparing epoxy resins. A greater influence would likely occur if different types of resins (for example, polypropylene versus epoxy or vinyl ester versus polyester) were tested as shown by studies on different GFRPs and flax FRPs [141], [146].

10.7 Influence of hand lay-up versus VI on flax fibre reinforced composites

When comparing the VI and hand lay-up manufacturing methods for the flax fibre reinforced composites, a reduction in defects such as voids, inconsistent resin distribution and airgaps were

noted in the VI panel. This was observed using microscope and SEM images as shown in Figure 10-13 and Figure 10-14 respectively.

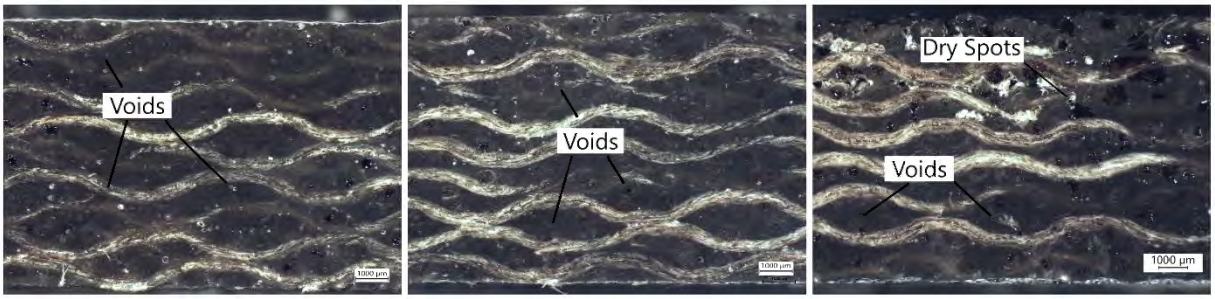

Figure 10-15: Comparison of the through thickness of a) Flax9 /Prime 20LV, b) Flax9 /Super Sap and c) hand lay-up Flax 8/Prime 20LV panels

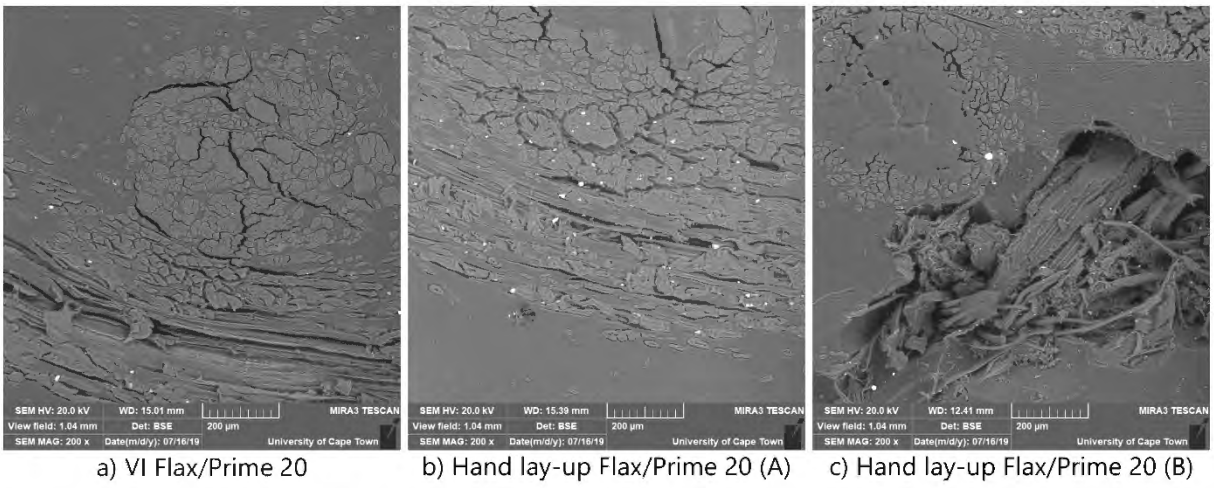

Figure 10-16: Comparison of the fibre-matrix interface on SEM images for a) VI manufactured Flax/Prime 20LV, and b and c) hand lay-up Flax/Prime 20LV specimen (SEM 200 x)

Delamination occurred in some of the hand lay-up composites as the crack growth would have been initiated and exacerbated by the defects. In the glass fibre reinforced composites, delamination was a dominant mode of failure absorbing most of the blast energy with little permanent mid-point deflection was sustained. For the hand lay-up flax fibre composites, little energy absorption due to delamination would have taken place unlike in the GFRPs. More blast energy exerted onto the hand lay-up Flax 8/Prime 20LV panels was dissipated via cracking, compared to the VI counterparts. This was due to the significant number of defects which would have easily allowed the ply to separate from the resin rich section which can be observed in Figure 10-13.

It was clear that a better wettability and homogeneous compaction was achieved with VI. Results with less variation was observed for the VI flax fibre reinforced composites compared to the hand lay-up

composites. Less back surface cracking, as shown in Figure 10-15, and midpoint displacement was obtained for the VI flax fibre reinforced composites.

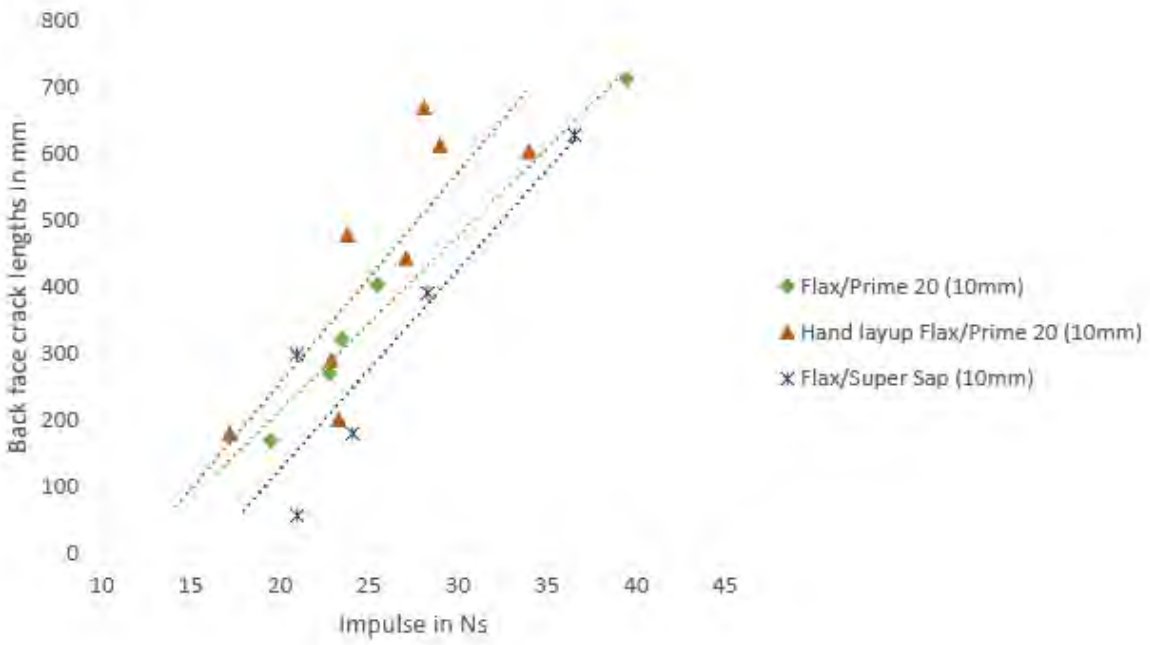

Figure 10-17: Graph of impulse versus back face crack lengths for the flax fibre reinforced composites

Similar results, such as the increased number of defects in hand lay-up specimens and decreased tensile and flexural strengths, were also found on comparative manufacturing methods studies on kenaf/polyester [115], jute/epoxy [116] and cotton/epoxy [113] composites. Therefore, manufacturing natural fibre composite components using VI, or at the very least including a compaction method with hand lay-up, could provide more consistent results and better mechanical properties that would consequently improve blast resistant properties.

10.8 Sustainability of materials

The results obtained from this project describe the blast behaviour of different materials and demonstrate the viability of replacing petroleum-based epoxies with bio-based epoxy resin in blast-related applications. While, as expected, these natural fibres cannot completely replace glass fibres in blast-resistant applications, as discussed in the literature survey, current market trends have seen a growth of the use of natural fibres in automotive and construction applications and understanding their blast performance is still useful. In comparison to jute fibre, flax fibre had better blast protection. Furthermore, it was found that a “fully environmentally friendly” natural fibre composite (flax fibre reinforced Super Sap laminates) produced similar results as a natural fibre composite with a fossil-fuel

based resin. In addition, the Supawood had a formidable response to blast loading despite very low mechanical properties.

The results of a simple sustainability assessment on the materials tested is listed in Table 10-3. All costs are given in South African Rands and include a 14 % consumption tax. The cost calculated was based on a 300 x 300mm panel at the time of purchase (between years 2016 – 2017) and approximate costs were given for the materials donated. The environmental level was based on the constituent materials described in the literature survey and materials chapter (chapter 2 and 3 respectively).

Table 10-3: Sustainability assessment of the materials tested

Composite	Cost per panel	Positive environmental impact	Blast performance level
Glass fibre/ Prime 20LV	R 73.00[a] – R 84.00[b]	Low	High
Glass fibre/ Super Sap	R 108.00	Moderate	High
Supawood	R 7.00	Moderate to High[c]	Low
Flax fibre/ Prime 20LV	R 260.00[d] - 282.00[e]	Moderate	Moderate
Flax fibre/ Super Sap	R 396.00	High	Moderate
Jute fibre/ Prime 20LV	R 115.00	Moderate	Very Low

a – cost for Glass 17/Prime 20LV
b – cost of Glass 19/Prime 20LV
c – depends on the UF resin used (undisclosed by manufacturer)
d – cost of Flax 8/Prime 20LV
e – cost of Flax 9/Prime 20LV

Considering that the flax textile was produced in Belgium and jute textile in the United Kingdom, the price of each per square metre was R 313.00 and R 74.00 respectively. Should South Africa produce similar materials, the cost would be lower considering the cost of hessian fabric is around R 25.00 per square meter [230] (in 2020) as a low baseline. A big contributing factor to the higher prices for the natural fibre composite was resin, as approximately double the amount of resin was required compared to the GFRPs.

The glass fibre reinforced Super Sap composite was, overall, the best sustainable composite tested as it offered good blast performance levels with moderate environmental impact at a fairly low cost. It is easy to see why Supawood is used extensively for household applications as it is very inexpensive. While Supawood may not offer much blast resistance, for such a cheap material, it performs well. If the market for sustainable epoxies and natural fibres continues to grow, it could potentially become

economically more favourable for consumers, as well as environmentally conscience, as the demand increases, and prices reduce.

11 Conclusions

The aim of this thesis was to understand the blast response of a range of composites containing materials deemed sustainable and to compare it to baseline FRP composites. The objectives were to determine the influence of fibre, resin type, and blast behaviour of the different composites. The influence of manufacturing method on flax fibre reinforced composites was also investigated. The results of the numerical simulations were used to determine panel dimensions for the natural fibre composites and blast test parameters. The failure modes and transient response of fully clamped, square, fibre reinforced composites under a uniform air blast loading condition were reported. The composites were characterised by quasi-static tests, namely tensile, flexural and Mode I interlaminar fracture toughness tests. These tests also provided additional understanding about the blast behaviour of the composites.

As expected, the glass fibre reinforced composites had superior blast response to the natural fibre composites. The response of the glass and natural fibre reinforced composites were reflective of the results from quasi-static testing. This was because both the tensile and flexural strengths of the glass fibre reinforced composites, and energy-absorbing capacity was better due to lower interlaminar properties. Furthermore, the addition of additional plies in the composites showed a significant improvement in mechanical properties and blast performance.

When subjected to blast loading, all glass fibre reinforced composites showed continuous damage progression in the form of delamination. The failure modes observed included delamination, surface cracking on the front face, and matrix and fibre failure along the along the boundary. Some of the failure modes observed extended into the clamped region of the panel. Additionally, matrix failure was observed in the glass fibre reinforced Super Sap composites. The influence of the resin on GFRP presented matrix failure and increased surface cracking on the glass fibre reinforced Super Sap composites. However, this did not appear to have any significant impact on the overall blast resistance of the GFRP panels with a Super Sap matrix.

In contrast, the predominate failure mode in the natural fibre composites was cracking. In comparison to the glass fibre, the mechanical properties of the natural fibres and resin were comparable and natural fibres are weaker than glass fibres. Additionally, based on the structure of the natural fibres, there were more resin in the panels. These factors would contribute to the difference in failure mechanism. In the flax FRP composites, resin type had an influence as less back face cracking was observed on the Super Sap infused panels compared to the Prime 20LV counterparts. A continuous damage progression was observed on the VI flax fibre reinforced composites. Hand lay-up flax fibre

reinforced composite results were often scattered. Furthermore, the top layer of the composite separated due to the large dry spots and voids caused by the manufacturing method.

The jute fibre reinforced composites were very brittle and weak. At very low impulses, little to no signs of external and through-thickness damage was observed prior to crack initiation. The range between panel failure and initial damage was very limited, making the materials unpredictable when subjected to blasts. Surprisingly, despite Supawood having the weakest mechanical properties, their ability to absorb energy was considered better than the jute fibre reinforced composites. This ability was likely due to the structure of the composites as parallel cracks along the through thickness were observed.

Considering sustainability, the best performing material was the glass fibre reinforced Super Sap composites as it offered good blast performance with fewer environmental impacts (compared to glass fibre reinforced Prime 20LV composites), and at a decent price point. However, the flax fibre reinforced composites may be more promising in the future. Furthermore, while Supawood was very weak, it performed better than the jute fibre reinforced composites at a significantly lower cost.

12 Recommendations

The work performed provided some insights to the blast performance of different composites, some of which contain a sustainable constituent, under a uniform blast loading condition. However, there remain gaps in understanding the blast response on fibre reinforced composites, especially with sustainability and sustainable materials in mind. As a result of the findings and conclusions of this thesis, the following recommendations are made:

- The effects of loading conditions on composites could be further investigated. Localised blast loading could be considered, as currently there is a lack of information on this loading condition as also highlighted by Mouritz [133]. Therefore, consider extending the tests on the Glass/Bio-resin and Glass/"conventional"-resin series to fully quantity the effect of resin type over a large range of test conditions, including localised blast loading with higher load intensities in a local region. Further studies could also be conducted to investigate the effect of different clamping conditions and size of panels.
- The effects of strain rate on the blast response of composites containing sustainable resins could be investigated. This could determine if there is a significant difference for the strain-rate effect on similarly formulated resins where one is derived from sustainable sources and the other petroleum based.
- The influence of the number of plies with respect to the textile areal density (for example, comparing a 10-layer 400 g/m^2 GFRP to a 20-layer 200 g/m^2 GFRP) could be investigated.
- An in-depth numerical model could be developed that can be used to predict the blast behaviour of the different materials tested. This will need to include modelling extensive through-width and thickness cracking, perforation and multiple fragmentation failures.
- The blast performance of other natural fibres (such as hemp and sisal) and plant-based resins could be carried out including multiple repeated tests under various testing conditions. With more information on different natural fibres and plant-based resins a non-dimensional analysis approach could then be developed. This non-dimensional analysis approach should consider material type and common failure mode as a basis.
- The use of hybrid composites, which contains both natural fibre and glass fibre, could yield a more sustainable product in comparison to conventional glass fibre reinforced composites. Research shows that natural fibre/glass fibre hybrid composites typically have better material properties, such as flexural, tensile and interlaminar strength, compared to only using the natural fibre [231]–[235]. While the performance of natural fibres in composites is lower than glass fibre, Ramesh et al [234] found that hybrid composites were suitable for medium

strength applications. Additionally, the adoption of hybrid composites was found to reduce costs and mass compared to current commercial pipe solutions [235]. Further tests could be carried out to investigate the blast response of these hybrid composites.

- The development of appropriate material characterisation approaches for materials that behave in a brittle manner, similar to the jute FRPs.

References

[1] A. Wilkinson, M. Hill, and P. Gollan, “The sustainability debate,” International Journal of Operations and Production Management, vol. 21, no. 12, pp. 1492–1502, 2001, doi: 10.1108/01443570110410865.

[2] L. P. Thiele, Sustainability. Wiley, 2013.

[3] J. A. Du Pisani, “Sustainable development – historical roots of the concept,” Environmental Sciences, vol. 3, no. 2, pp. 83–96, Jun. 2006, doi: 10.1080/15693430600688831.

[4] S. Dresner, The Principles of Sustainability. Earthscan, 2008.

[5] G. Lori, C. Morison, M. Larcher, and J. Belis, “Sustainable facade design for glazed buildings in a blast resilient urban environment,” Glass Structures & Engineering, vol. 4, no. 2, pp. 145–173, 2019, doi: 10.1007/s40940-018-0088-3.

[6] K. Kim and Y. Park, “Development of Design Considerations as a Sustainability Approach for Military Protective Structures: A Case Study of Artillery Fighting Position in South Korea,” Sustainability, vol. 12, no. 16, p. 6479, Aug. 2020, doi: 10.3390/su12166479.

[7] Institute for Economics & Peace, “Global Terrorism Index 2020: Measuring the Impact of Terrorism, Sydney, November 2020,” 2020. http://visionofhumanity.org/reports (accessed Feb. 25, 2021).

[8] N. Osseiran and I. Coles, “Beirut Explosion: What Happened in Lebanon and Everything Else We Know,” The Wall Street Journal, 2020.

[9] S. V Joshi, L. T. Drzal, A. K. Mohanty, and S. Arora, “Are natural fiber composites environmentally superior to glass fiber reinforced composites?,” Composites Part A: Applied Science and Manufacturing, vol. 35, no. 3, pp. 371–376, Mar. 2004, doi: 10.1016/j.compositesa.2003.09.016.

[10] J. Liu, S. Wang, Y. Peng, J. Zhu, W. Zhao, and X. Liu, “Advances in sustainable thermosetting resins: From renewable feedstock to high performance and recyclability,” Progress in Polymer Science, vol. 113, p. 101353, Feb. 2021, doi: 10.1016/j.progpolymsci.2020.101353.

[11] D. Puglia, J. Biagiotti, and J. M. Kenny, “A Review on Natural Fibre-Based Composites—Part II,” Journal of Natural Fibers, vol. 1, no. 3, pp. 23–65, Apr. 2005, doi: 10.1300/J395v01n03_03.

[12] A. M. Cunha, A. R. Campos, C. Cristovão, C. Vila, V. Santos, and J. C. Parajó, “Sustainable materials in automotive applications,” Plastics, Rubber and Composites, vol. 35, no. 6–7, pp. 233–241, Sep. 2006, doi: 10.1179/174328906X146487.

[13] A. Unni and G. Anjali, “Cost-benefit analysis of conventional and modern building materials for sustainable development of social housing,” Materials Today: Proceedings, Dec. 2021, doi: 10.1016/J.MATPR.2021.12.113.

[14] A. F. Al-Mudhaffer, S. K. Saleh, and G. I. Kadhum, “The role of sustainable materials in reducing building temperature,” Materials Today: Proceedings, Sep. 2021, doi: 10.1016/J.MATPR.2021.08.249.

[15] F. Asdrubali, S. Schiavoni, and K. v Horoshenkov, “A Review of Sustainable Materials for Acoustic Applications,” Building Acoustics, vol. 19, no. 4, pp. 283–311, Dec. 2012, doi: 10.1260/1351-010X.19.4.283.

[16] A. C. Pereira et al., “Evaluation of the projectile’s loss of energy in polyester composite reinforced with fique fiber and fabric,” Materials Research, vol. 22, 2019.

[17] F. D. C. Garcia Filho and S. N. Monteiro, “Piassava fiber as an epoxy matrix composite reinforcement for ballistic armor applications,” Jom, vol. 71, no. 2, pp. 801–808, 2019.

[18] F. S. da Luz, F. da C. Garcia Filho, M. S. Oliveira, L. F. C. Nascimento, and S. N. Monteiro, “Composites with natural fibers and conventional materials applied in a hard armor: A comparison,” Polymers (Basel), vol. 12, no. 9, p. 1920, 2020.

[19] M. Y. Khalid, A. al Rashid, Z. U. Arif, W. Ahmed, H. Arshad, and A. A. Zaidi, “Natural fiber reinforced composites: Sustainable materials for emerging applications,” Results in Engineering, vol. 11, p. 100263, Sep. 2021, doi: 10.1016/J.RINENG.2021.100263.

[20] J. H. Lora and W. G. Glasser, “Recent Industrial Applications of Lignin: A Sustainable Alternative to Nonrenewable Materials,” Journal of Polymers and the Environment, vol. 10, no. 1, pp. 39–48, 2002, doi: 10.1023/A:1021070006895.

[21] K. Fic, A. Platek, J. Piwek, and E. Frackowiak, “Sustainable materials for electrochemical capacitors,” Materials Today, vol. 21, no. 4, pp. 437–454, May 2018, doi: 10.1016/J.MATTOD.2018.03.005.

[22] F. C. Campbell, Structural Composite Materials. Ohio: ASM International, 2010.

[23] P. K. Mallick, Fiber-Reinforced Composites: Materials, Manufacturing, and Design, Third Edition, 3rd ed. Boca Raton: CRC Press, 2007.

[24] Textile Technologist, “Difference Between Natural Fiber And Synthetic Fiber | Textile Fashion Study,” 2012. http://textilefashionstudy.com/difference-between-natural-fiber-and-synthetic-fiber/ (accessed Mar. 06, 2015).

[25] S. Kalpakjian and S. R. Schmid, Manufacturing Engineering and Technology, 6th ed. Singapore: Prentice Hall, 2010.

[26] B. Sabuncuoglu, S. Orlova, L. Gorbatikh, S. V Lomov, and I. Verpoest, “Micro-scale finite element analysis of stress concentrations in steel fiber composites under transverse loading,” Journal of Composite Materials, vol. 49, no. 9, pp. 1057–1069, Apr. 2015, doi: 10.1177/0021998314528826.

[27] M. E. Alves Fidelis, T. V. C. Pereira, O. D. F. M. Gomes, F. De Andrade Silva, and R. D. Toledo Filho, “The effect of fiber morphology on the tensile strength of natural fibers,” Journal of Materials Research and Technology, vol. 2, no. 2, pp. 149–157, 2013, doi: 10.1016/j.jmrt.2013.02.003.

[28] D. U. Shah, “Natural fibre composites: Comprehensive Ashby-type materials selection charts,” Materials & Design (1980-2015), vol. 62, pp. 21–31, Oct. 2014, doi: 10.1016/j.matdes.2014.05.002.

[29] B. Philip, E. Abraham, L. Pothan, and S. Thomas, “Plant Fiber-Based Composites,” in Green Composites from Natural Resources, V. Thakur, Ed. Boca Raton: CRC Press, 2013, pp. 95–124. doi: 10.1201/b16076-6.

[30] R. M. Rowell, “Natural fibres: types and properties,” in Properties and Performance of Natural-Fibre Composites, Elsevier, 2008, pp. 3–66. doi: 10.1533/9781845694593.1.3.

[31] D. Gay, S. V Hoa, and S. W. Tsai, “Composite Materials.” CRC Press, 2002. doi: 10.1201/9781420031683.

[32] Tubecon, “Mechanical Properties of Steel,” Technical Info. http://www.tubecon.co.za/en/technical-info/tubecon-wiki/mechanical-properties-of-common-steel.html (accessed Feb. 23, 2021).

[33] M. Fogorasi and I. Barbu, “The potential of natural fibres for automotive sector - Review,” IOP Conference Series: Materials Science and Engineering, vol. 252, p. 012044, Oct. 2017, doi: 10.1088/1757-899X/252/1/012044.

[34] P. Morgan, Carbon Fibers and Their Composites. CRC Press, 2005. doi: 10.1201/9781420028744.

[35] T. Karthik and R. Rathinamoorthy, “Sustainable synthetic fibre production,” in The Textile Institute Book Series, Ed. Woodhead Publishing, 2017, pp. 191–240. doi: https://doi.org/10.1016/B978-0-08-102041-8.00008-1.

[36] V. V Vasiliev and E. V Morozov, Mechanics and Analysis of Composite Materials. Elsevier Science, 2001.

[37] M. M. Kabir, H. Wang, K. T. Lau, and F. Cardona, “Chemical treatments on plant-based natural fibre reinforced polymer composites: An overview,” Composites Part B: Engineering, vol. 43, no. 7, pp. 2883–2892, Oct. 2012, doi: 10.1016/j.compositesb.2012.04.053.

[38] S.-J. Park and M.-K. Seo, “Chapter 6 - Element and Processing,” in Interface Science and Composites, vol. 18, S.-J. Park and M.-K. B. T.-I. S. and T. Seo, Eds. Elsevier, 2011, pp. 431–499. doi: https://doi.org/10.1016/B978-0-12-375049-5.00006-2.

[39] M. Fan and B. Weclawski, “Long natural fibre composites,” in Advanced High Strength Natural Fibre Composites in Construction, Elsevier, 2017, pp. 141–177. doi: 10.1016/B978-0-08-100411-1.00006-6.

[40] L. C. Bank, Composites for Construction. John Wiley & Sons, Inc., 2006. doi: 10.1002/9780470121429.

[41] Chemical Retrieval on the Web, “Polymer Properties Database,” 2015. http://polymerdatabase.com/polymer classes/UreaFormaldehyde type.html (accessed Oct. 03, 2018).

[42] M. A. Rahman, F. Parvin, M. Hasan, and M. E. Hoque, “Introduction to Manufacturing of Natural Fibre-Reinforced Polymer Composites,” in Manufacturing of Natural Fibre Reinforced Polymer Composites, Springer International Publishing, 2015, pp. 17–43. doi: 10.1007/978-3-319-07944-8_2.

[43] Performance Composites Inc., “Technical Information, Fibreglass and Composite Material Design Guide.” http://www.performancecomposites.com/about-composites-technical-info/122-designing-with-fiberglass.html (accessed Jun. 10, 2018).

[44] D. Cripps, “Wet/Hand Lay-up.” https://netcomposites.com/guide-tools/guide/manufacturing/wethand-lay-up/ (accessed Jun. 13, 2018).

[45] G. Eckold, Design and Manufacture of Composite Structures. Woodhead Publishing Limited, 1994. doi: 10.1533/9781845698560.

[46] D. Cripps, T. J. Searle, and J. Summerscales, “Open Mold Techniques for Thermoset Composites,” in Comprehensive Composite Materials, Elsevier, 2000, pp. 737–761. doi: 10.1016/b0-08-042993-9/00188-1.

[47] L. Calabrese, G. Di Bella, and V. Fiore, “Manufacture of marine composite sandwich structures,” in Marine Applications of Advanced Fibre-Reinforced Composites, Elsevier, 2016, pp. 57–78. doi: 10.1016/B978-1-78242-250-1.00003-X.

[48] M. R. M. Jamir, M. S. A. Majid, and A. Khasri, “Natural lightweight hybrid composites for aircraft structural applications,” in Sustainable Composites for Aerospace Applications, Elsevier, 2018, pp. 155–170. doi: 10.1016/B978-0-08-102131-6.00008-6.

[49] R. A. Shenoi and A. R. Dodkins, “Design of Ships and Marine Structures Made from FRP Composite Materials,” in Comprehensive Composite Materials, Elsevier, 2000, pp. 429–449. doi: 10.1016/B0-08-042993-9/00117-0.

[50] L. P. Ramos, N. Uddin, and U. Vaidya, “DEVELOPMENT OF COST-EFFECTIVE VARTM TECHNOLOGY FOR REPAIR AND HARDENING DESIGN METHOD AND SPECIFICATIONS FOR ALDOT CONTRACTOR PHASE 3,” Birmingham, 2013.

[51] F. A. Kamke, “Wood: Nonstructural Panel Processes,” in Encyclopedia of Materials: Science and Technology, Elsevier, 2001, pp. 9673–9678. doi: 10.1016/B0-08-043152-6/01754-X.

[52] PG Bison, “How PG Bison’s SUPAWOOD is made,” Youtube, 2016. https://www.youtube.com/watch?v=BhBCKKTH4uQ (accessed Mar. 20, 2018).

[53] ETA, “Medium Density Fiberboard Manufacturing,” Wood Products Industry, 2002. https://www3.epa.gov/ttnchie1/ap42/ch10/final/c10s0603.pdf (accessed Oct. 15, 2018).

[54] W. Gul, Dr. A. Khan, and Dr. A. Shakoor, “Impact of Hot Pressing Pressure on Medium Density Fiberboard (MDF) Performance,” HAL Archives, vol. 1, p. hal-01612472, Oct. 2017.

[55] V. Thakur, M. Thakur, R. Gupta, R. Prasanth, and M. Kessler, “Green Composites,” in Green Composites from Natural Resources, {CRC} Press, 2013, pp. 1–10. doi: 10.1201/b16076-2.

[56] T. Nishino, “Natural fibre sources,” in Green Composites, Elsevier, 2004, pp. 49–80. doi: 10.1016/b978-1-85573-739-6.50007-5.

[57] L. Mohammed, M. N. M. Ansari, G. Pua, M. Jawaid, and M. S. Islam, “A Review on Natural Fiber Reinforced Polymer Composite and Its Applications,” International Journal of Polymer Science, vol. 2015, pp. 1–15, 2015, doi: 10.1155/2015/243947.

[58] S. Thomas and L. A. Pothan, “Natural fibre composites - State of the art, new challenges and opportunities,” in Natural Fibre Reinforced Polymer Composites: From Macro to Nanoscale, Old City Publishing Inc. & Editions des Archives Comtemporaines Ltd, 2009, pp. 3–6.

[59] Grand View Research, “Natural Fiber Composites (NFC) Market Size, Share & Trends Analysis Report By Raw Material, By Matrix, By Technology, By Application, And Segment Forecasts, 2018 - 2024,” Market Analysis Report, 2018. https://www.grandviewresearch.com/industry-analysis/natural-fiber-composites-market (accessed Dec. 26, 2020).

[60] Food and Agriculture Organization of the United Nations, “Jute, Kenaf, Sisal, Abaca, Coir and Allied Fibres STATISTICS,” Rome, 2012.

[61] Food and Agriculture Organization of the United Nations, “Application of Natural Fibre Composites in the Development of Rural Societies,” 2013. http://www.fao.org/docrep/007/ad416e/ad416e06.htm (accessed Apr. 25, 2016).

[62] Statista, “Gross domestic product (GDP) distribution across economic sectors South Africa 2019 Published by H. Plecher, Nov 18, 2020 This statistic shows the distribution of the gross domestic product (GDP) across economic sectors in South Africa from 2009 to 2019.,” Economy & Politics > International, 2020. https://www.statista.com/statistics/371233/south-africa-gdp-distribution-across-economic-sectors/ (accessed Dec. 26, 2020).

[63] SouthAfrica.co.za, “Agriculture in South Africa - Crop Farming,” Products of Origin > Farming in South Africa, 2020. http://southafrica.co.za/agriculture-in-south-africa.html#:~:text=South Africa’s agricultural sector is,to the country’s agricultural economy. (accessed Dec. 26, 2020).

[64] A. Le Duigou, P. Davies, and C. Baley, “Environmental Impact Analysis of the Production of Flax Fibres to be Used as Composite Material Reinforcement,” Journal of Biobased Materials and Bioenergy, vol. 5, no. 1, pp. 153–165, Mar. 2011, doi: 10.1166/jbmb.2011.1116.

[65] K. Wötzel, R. Wirth, and M. Flake, “Life cycle studies on hemp fibre reinforced components and ABS for automotive parts,” Die Angewandte Makromolekulare Chemie, vol. 272, no. 1, pp. 121–127, Dec. 1999, doi: 10.1002/(sici)1522-9505(19991201)272:1<121::aid-apmc121>3.0.co;2-t.

[66] W.-P. Schmidt and H.-M. Beyer, “Life Cycle Study on a Natural Fibre Reinforced Component,” Nov. 1998. doi: 10.4271/982195.

[67] N. Dissanayake and J. Summerscales, “Life Cycle Assessment for Natural Fiber Composites,” in Green Composites from Natural Resources, CRC Press, 2013, pp. 157–186. doi: 10.1201/b16076-9.

[68] N. I. Huth, P. J. Thorburn, B. J. Radford, and C. M. Thornton, “Impacts of fertilisers and legumes on N2O and CO2 emissions from soils in subtropical agricultural systems: A simulation study,” Agriculture, Ecosystems & Environment, vol. 136, no. 3–4, pp. 351–357, Mar. 2010, doi: 10.1016/j.agee.2009.12.016.

[69] PlasticsEurope Epoxy Resins Committee (ERC), “EPOXY RESINS AND CURING AGENTS, Toxicology, Health, Safety and Environmental Aspects,” 2006. https://www.plasticseurope.org/en/resources/publications/428-epoxy-resins-and-curing-agents (accessed Jun. 12, 2018).

[70] M. Yang, K. A. Rosentrater, Y. Minliang, and K. A. Rosentrater, “Environmental effects and economic analysis of adhesives: a review of life cycle assessment (LCA) and techno-economic analysis (TEA),” Jul. 2015. doi: 10.13031/aim.20152189933.

[71] European Chemicals Agency, “Epoxy/Phenolic Resin,” Substance Infocard, 2018. https://echa.europa.eu/substance-information/-/substanceinfo/100.122.923 (accessed Oct. 10, 2018).

[72] European Chemicals Agency, “Iso-Butylated Urea Formaldehyde Resin,” Substance Infocard, 2018. https://echa.europa.eu/substance-information/-/substanceinfo/100.117.257 (accessed Oct. 10, 2018).

[73] J. E. McDevitt and W. J. Grigsby, “Life Cycle Assessment of Bio- and Petro-Chemical Adhesives Used in Fiberboard Production,” Journal of Polymers and the Environment, vol. 22, no. 4, pp. 537–544, Jun. 2014, doi: 10.1007/s10924-014-0677-4.

[74] Minnesota Department of Health, “Volatile Organic Compounds in Your Home.” http://www.health.state.mn.us/divs/eh/indoorair/voc/ (accessed Feb. 16, 2018).

[75] W. D. Kerns, K. L. Pavkov, D. J. Donofrio, E. J. Gralla, and J. A. Swenberg, “Carcinogenicity of Formaldehyde in Rats and Mice after Long-Term Inhalation Exposure,” Cancer Research, vol. 43, no. 9, pp. 4382 LP – 4392, Sep. 1983.

[76] Z. He, Y. Zhang, and W. Wei, “Formaldehyde and VOC emissions at different manufacturing stages of wood-based panels,” Building and Environment, vol. 47, pp. 197–204, Jan. 2012, doi: 10.1016/j.buildenv.2011.07.023.

[77] United Nations General Assembly, “The Sustainable Development Goals Report,” New York, 2020. doi: 10.18356/2282dd98-en.

[78] Spolchemie, “Innovation and Solutions,” 2014. https://www.spolchemie.cz/en/homepage/News/Innovation-and-Solutions/2014/09/04/FACT-SHEET-20146-Spoleks-Environmental-Certification-Renewed (accessed Oct. 10, 2018).

[79] Entropy Resins Inc, “Why Super Sap.” https://entropyresins.com/why-use-super-sap/ (accessed Mar. 20, 2018).

[80] Healthy Building Network, “Alternative Resin Binders for Particleboard, Medium Density Fiberboard (MDF), and Wheatboard,” 2008. https://s3.amazonaws.com/hbnweb.dev/uploads/files/alternative-resin-binders-for-particleboard-medium-density-fiberboard-mdf-and-wheatboard.pdf (accessed Oct. 10, 2018).

[81] R. A. Shanks, “Alternative solutions: recyclable synthetic fibre-thermoplastic composites,” in Green Composites, Elsevier, 2004, pp. 100–122. doi: 10.1016/b978-1-85573-739-6.50009-9.

[82] Y. Yang, R. Boom, B. Irion, D.-J. van Heerden, P. Kuiper, and H. de Wit, “Recycling of composite materials,” Chemical Engineering and Processing: Process Intensification, vol. 51, pp. 53–68, 2012, doi: https://doi.org/10.1016/j.cep.2011.09.007.

[83] N. Tucker, “Clean production,” in Green Composites, Elsevier, 2004, pp. 207–232. doi: 10.1016/b978-1-85573-739-6.50013-0.

[84] Peebles Media Group Limited, “Firm claims breakthrough in recycling of MDF waste,” Envirotec Magazine, 2017. https://envirotecmagazine.com/2017/01/16/firm-claims-breakthrough-in-recycling-of-mdf-waste/ (accessed Oct. 10, 2018).

[85] N. Hancox, “An overview of the impact behaviour of fibre-reinforced composites,” in Impact Behaviour of Fibre-reinforced Composite Materials and Structures, {CRC} Press, 2000. doi: 10.1201/9781439822814.ch1.

[86] A.-H. M.R and Z. Chwei, “Effect the stacking sequences of composite laminates under low velocity impact on failure modes by using carbon fiber reinforced polymer,” vol. 5, pp. 1813–2319, Feb. 2016.

[87] B. R. Souza, R. M. Di Benedetto, D. Hirayama, O. de Andrade Raponi, L. C. M. Barbosa, and A. C. A. Junior, “Manufacturing and Characterization of Jute/PP Thermoplastic Commingled Composite,” Materials Research, vol. 20, no. suppl 2, pp. 458–465, Oct. 2017, doi: 10.1590/1980-5373-mr-2017-0104.

[88] D. A. Hernandez, C. A. Soufen, M. O. Orlandi, U. E. Paulista, and U. E. Paulista, “Carbon Fiber Reinforced Polymer and Epoxy Adhesive Tensile Test Failure Analysis Using Scanning Electron Microscopy,” Materials Research, vol. 20, no. 4, pp. 951–961, 2017.

[89] M. Z. R. Khan, S. K. Srivastava, and M. K. Gupta, “Tensile and flexural properties of natural fiber reinforced polymer composites: A review,” Journal of Reinforced Plastics and Composites, vol. 37, no. 24, pp. 1435–1455, Sep. 2018, doi: 10.1177/0731684418799528.

[90] W. D. Callister, “Composites,” in Materials Science and Engineering: An Introduction, 7th ed., Danvers: John Wiley & Sons, Incorporated, 2007, pp. 577–619.

[91] M. Poletto, “Assessment of the thermal behavior of lignins from softwood and hardwood species,” Maderas. Ciencia y tecnología, 2017, doi: 10.4067/S0718-221X2017005000006.

[92] BGF Industries, “Glass properties,” BGF Industries, Inc., 2012. http://www.bgf.com/technical/glass-properties/ (accessed Jun. 13, 2020).

[93] C. W. Nguong, S. N. B. Lee, and D. Sujan, “A Review on Natural Fibre Reinforced Polymer Composites,” International Journal of Materials and Metallurgical Engineering, vol. 7, no. 1, pp. 52–59, 2013.

[94] W. Kaufmyn, “Fiber-reinforced composites,” Fog.ccsf.edu. https://fog.ccsf.edu/~wkaufmyn/ENGN45/CourseHandouts/14_CompositeMaterials/03_Fiber-reinforcedComposites.html (accessed Mar. 05, 2018).

[95] X. Li, Y. Wu, Z. Cai, and J. E. Winandy, “Primary properties of MDF using thermomechanical pulp made from oxalic acid pretreated rice straw particles,” Industrial Crops and Products, vol. 41, no. 1, pp. 414–418, Jan. 2013, doi: 10.1016/J.INDCROP.2012.04.039.

[96] J. T. Benthien, S. Heldner, and M. Ohlmeyer, “Investigation of the interrelations between defibration conditions, fiber size and medium-density fiberboard (MDF) properties,” European Journal of Wood and Wood Products 2016 75:2, vol. 75, no. 2, pp. 215–232, Aug. 2016, doi: 10.1007/S00107-016-1094-2.

[97] P. Widsten, S. Tuominen, P. Qvintus-Leino, and J. E. Laine, “The influence of high defibration temperature on the properties of medium-density fiberboard (MDF) made from laccase-treated softwood fibers,” Wood Science and Technology 2004 38:7, vol. 38, no. 7, pp. 521–528, Sep. 2004, doi: 10.1007/S00226-003-0206-4.

[98] M. Khonakdar Dazmiri, M. Valizadeh Kiamahalleh, M. Valizadeh Kiamahalleh, H. R. Mansouri, and V. Moazami, “Revealing the impacts of recycled urea–formaldehyde wastes on the physical–mechanical properties of MDF,” European Journal of Wood and Wood Products 2018 77:2, vol. 77, no. 2, pp. 293–299, Dec. 2018, doi: 10.1007/S00107-018-1375-Z.

[99] H. A. Aisyah, M. T. Paridah, M. H. Sahri, U. M. K. Anwar, and A. A. Astimar, “Properties of medium density fibreboard (MDF) from kenaf (Hibiscus cannabinus L.) core as function of refining conditions,” Composites Part B: Engineering, vol. 44, no. 1, pp. 592–596, Jan. 2013, doi: 10.1016/J.COMPOSITESB.2012.02.029.

[100] S. Halvarsson, H. Edlund, and M. Norgren, “Properties of medium-density fibreboard (MDF) based on wheat straw and melamine modified urea formaldehyde (UMF) resin,” Industrial Crops and Products, vol. 28, no. 1, pp. 37–46, Jul. 2008, doi: 10.1016/J.INDCROP.2008.01.005.

[101] V. J. Popovska, B. Iliev, and I. Spiroski, “Characteristics of Medium Density Fiberboards for Furniture Production and Interior Application,” South East European Journal of Architecture and Design, vol. 2016, no. 0, pp. 1–5, Mar. 2016, doi: 10.3889/seejad.2016.10013.

[102] J. A. Halip, L. S. Hua, Z. Ashaari, P. M. Tahir, L. W. Chen, and M. K. Anwar Uyup, “8 - Effect of treatment on water absorption behavior of natural fiber–reinforced polymer composites,” in Woodhead Publishing Series in Composites Science and Engineering, M. Jawaid, M. Thariq, and N. B. T.-M. and P. T. of B. Saba Fibre-Reinforced Composites and Hybrid Composites, Eds. Woodhead Publishing, 2019, pp. 141–156. doi: https://doi.org/10.1016/B978-0-08-102292-4.00008-4.

[103] H. Dhakal and Z. Zhang, “Properties and Characterization of Natural Fiber-Reinforced Polymeric Composites,” in Green Composites from Natural Resources, CRC Press, 2013, pp. 321–354. doi: 10.1201/b16076-16.

[104] K. Sever, M. Sarikanat, Y. Seki, H. A. Gülec, M. Mutlu, and İ. H. Tavman, “Improvement of Interfacial Adhesion of Glass Fiber/Epoxy Composite by Using Plasma Polymerized Glass Fibers,” The Journal of Adhesion, vol. 86, no. 9, pp. 915–938, Aug. 2010, doi: 10.1080/00218464.2010.506160.

[105] Z. Xu, Y. Huang, C. Zhang, L. Liu, Y. Zhang, and L. Wang, “Effect of γ-ray irradiation grafting on the carbon fibers and interfacial adhesion of epoxy composites,” Composites Science and Technology, vol. 67, no. 15–16, pp. 3261–3270, Dec. 2007, doi: 10.1016/j.compscitech.2007.03.038.

[106] M. Mehdikhani, L. Gorbatikh, I. Verpoest, and S. V Lomov, “Voids in fiber-reinforced polymer composites: A review on their formation, characteristics, and effects on mechanical performance,” Journal of Composite Materials, vol. 53, no. 12, pp. 1579–1669, May 2019, doi: 10.1177/0021998318772152.

[107] H. Zhu, B. Wu, D. Li, D. Zhang, and Y. Chen, “Influence of Voids on the Tensile Performance of Carbon/epoxy Fabric Laminates,” Journal of Materials Science & Technology, vol. 27, no. 1, pp. 69–73, Jan. 2011, doi: 10.1016/S1005-0302(11)60028-5.

[108] X. Liu and F. Chen, “A review of void formation and its effects on the mechanical performance of carbon fiber reinforced plastic,” Engineering Transactions, vol. 64, no. 1, pp. 33–51, 2016.

[109] J. N. Zalameda and B. T. Smith, “Measurement of Composite Fiber Volume Fraction Using Thermal and Ultrasonic Inspection Techniques BT - Nondestructive Characterization of Materials VI,” R. E. Green, K. J. Kozaczek, and C. O. Ruud, Eds. Boston, MA: Springer US, 1994, pp. 741–748. doi: 10.1007/978-1-4615-2574-5_94.

[110] A. Amiri and C. Ulven, Advanced Method for Void Fraction Evaluation of Natural Fiber Composites using Micro-Ct Technology. SAMPE CONFERENCE AND EXHIBITION, California, 2016. doi: 10.13140/RG.2.1.3397.9763.

[111] M. Amirkhosravi, M. Pishvar, Y. K. Hamidi, and M. C. Altan, “Accurate characterization of fiber and void volume fractions of natural fiber composites by pyrolysis in a nitrogen atmosphere,” in AIP Conference Proceedings, Jan. 2020, vol. 2205, no. 1, p. 20032. doi: 10.1063/1.5142947.

[112] A. McIlhagger, E. Archer, and R. McIlhagger, “Manufacturing processes for composite materials and components for aerospace applications,” in Polymer Composites in the Aerospace Industry, Cambridge: Elsevier, 2015, pp. 53–75. doi: 10.1016/B978-0-85709-523-7.00003-7.

[113] C. L. Tafur, E. E. Mora, and R. R. Baracaldo, “Effects of the Vacuum Moulding Process on the Mechanical Properties of Cotton/Epoxy Composite,” Fibres and Textiles in Eastern Europe, vol. 26, no. 3(129), pp. 93–97, Jun. 2018, doi: 10.5604/01.3001.0011.7309.

[114] A. Donnell, M. A. Dweib, and R. P. Wool, “Natural fiber composites with plant oil-based resin,” Composites Science and Technology, vol. 64, no. 9, pp. 1135–1145, Jul. 2004, doi: 10.1016/j.compscitech.2003.09.024.

[115] M. Yuhazri and P. Phongsakorn, “A Comparison Process Between Vacuum Infusion And Hand Lay up Method Toward Kenaf/Polyester Composites,” International Journal of Basic & Applied, vol. 10, no. 33, pp. 63–66, 2010.

[116] H. B. An, H. Takagi, and Y. H. Kim, “A comparison of mechanical property of jute/styrene by vartm and hand-lay up methods,” ICCM International Conferences on Composite Materials, pp. 1–4, 2011.

[117] M. Sharba, S. Salman, Z. Leman, M. Sultan, M. Ishak, and M. Hanim, “Effects of Processing Method, Moisture Content, and Resin System on Physical and Mechanical Properties of Woven Kenaf Plant Fiber Composites,” Bioresources, vol. 11, pp. 1466–1476, Feb. 2016, doi: 10.15376/biores.11.1.1466-1476.

[118] D. C. Weggel, “Blast threats and blast loading,” in Blast Protection of Civil Infrastructures and Vehicles Using Composites, Great Abington Cambridge: Elsevier, 2010, pp. 3–43. doi: 10.1533/9781845698034.1.3.

[119] G. F. Kinney and K. J. Graham, Explosive Shocks in Air. Berlin, Heidelberg: Springer Berlin Heidelberg, 1985. doi: 10.1007/978-3-642-86682-1.

[120] P. W. Cooper, Explosive Engineering. New York: Wiley-VCH, 1996.

[121] R. E. Duff and E. Houston, "Measurement of the Chapman-Jouguet Pressure and Reaction Zone Length in a Detonating High Explosive", J. Chem. Phys. 23, 1955, pp. 1268-1273 doi: 10.1063/1.1742255

[122] D. Zou, “Explosives,” in Theory and Technology of Rock Excavation for Civil Engineering, Singapore: Springer Singapore, 2017, pp. 105–170. doi: 10.1007/978-981-10-1989-0_3.

[123] W. Fickett and W. C. Davis, Detonation: Theory and Experiments. Berkeley: University of California, 1979.

[124] P. Smith and G. Mays, Blast Effects on Buildings. London: Thomas Telford Publications, 1995.

[125] Unified Facilities Criteria (UFC), “Structures to resist the effects of Accidental Explosions UFC 3-340-02,” 2008.

[126] S. K. Lahiri, “Blast loading due to conventional weapons (conwep) simulation of rapid structural failure due to blast loads from conventional weapons (CONWEP) Dr,” Semantics Scholar, 2010. https://www.semanticscholar.org/paper/BLAST-LOADING-DUE-TO-CONVENTIONAL-WEAPONS-(-CONWEP-Lahiri/945507c666c7c34bb12665207c6a0ef3ea3da125?navId=extracted (accessed Feb. 18, 2019).

[127] T. Ngo, P. Mendis, A. Gupta, and J. Ramsay, “Blast loading and blast effects on structures - An overview,” Electronic Journal of Structural Engineering, vol. 7, pp. 76–91, Jan. 2007.

[128] C. Knock and N. Davies, “Blast Waves from Cylindrical Charges,” 28th International Symposium on Shock Waves. Springer Berlin Heidelberg, pp. 87–92, 2012. doi: 10.1007/978-3-642-25688-2_13.

[129] C. Johnson, P. Mulligan, K. Williams, M. Langenderfer, and J. Heniff, “Effect of explosive charge geometry on shock wave propagation,” in AIP Conference Proceedings 1979, 2018, p. 150021. doi: 10.1063/1.5044977.

[130] C. Knock, N. Davies, and T. Reeves, “Predicting Blast Waves from the Axial Direction of a Cylindrical Charge,” Propellants, Explosives, Pyrotechnics, vol. 40, no. 2, pp. 169–179, Apr. 2015, doi: 10.1002/prep.201300188.

[131] N. Uddin, Blast protection of civil infrastructures and vehicles using composites. Great Abington Cambridge: Woodhead Publishing Limited, 2010. doi: 10.1533/9781845698034.

[132] S. A. Tekalur, A. Shukla, and P. Ruggiero, “Blast loaded thin composite plates - An experimental study,” Proceedings of the 2006 SEM Annual Conference and Exposition on Experimental and Applied Mechanics 2006, vol. 4, pp. 1801–1807, Jan. 2006.

[133] A. P. Mouritz, “Advances in understanding the response of fibre-based polymer composites to shock waves and explosive blasts,” Composites Part A: Applied Science and Manufacturing, vol. 125, p. 105502, 2019, doi: https://doi.org/10.1016/j.compositesa.2019.105502.

[134] University of Calgary, “Transport of NOx in Propulsion Systems,” Aerospace and Compressible Flow Research, 2015. http://www.ucalgary.ca/johansen/node/7 (accessed May 07, 2015).

[135] N. Jacob, G. N. Nurick, and G. S. Langdon, “The effect of stand-off distance on the failure of fully clamped circular mild steel plates subjected to blast loads,” Engineering Structures, vol. 29, no. 10, pp. 2723–2736, Oct. 2007, doi: 10.1016/j.engstruct.2007.01.021.

[136] T. Franz, G. N. Nurick, and M. J. Perry, “Experimental investigation into the response of chopped-strand mat glassfibre laminates to blast loading,” International Journal of Impact Engineering, vol. 27, no. 6, pp. 639–667, Jul. 2002, doi: 10.1016/s0734-743x(01)00158-0.

[137] J. L. R. Comtois, M. R. Edwards, and M. C. Oakes, “The effect of explosives on polymer matrix composite laminates,” Composites Part A: Applied Science and Manufacturing, vol. 30, no. 3, pp. 181–190, Mar. 1999, doi: 10.1016/s1359-835x(98)00172-9.

[138] S. A. Tekalur, K. Shivakumar, and A. Shukla, “Mechanical behavior and damage evolution in E-glass vinyl ester and carbon composites subjected to static and blast loads,” Composites Part B: Engineering, vol. 39, no. 1, pp. 57–65, Jan. 2008, doi: 10.1016/j.compositesb.2007.02.020.

[139] M. Y. Yahya, W. J. Cantwell, G. S. Langdon, and G. N. Nurick, “The Blast Behavior of Fiber Reinforced Thermoplastic Laminates,” Journal of Composite Materials, vol. 42, no. 21, pp. 2275–2297, Nov. 2008, doi: 10.1177/0021998308094968.

[140] M. Y. Yahya, W. J. Cantwell, G. S. Langdon, and G. N. Nurick, “The blast resistance of a woven carbon fiber-reinforced epoxy composite,” Journal of Composite Materials, vol. 45, no. 7, pp. 789–801, Feb. 2011, doi: 10.1177/0021998310376103.

[141] A. Gargano, K. Pingkarawat, M. Blacklock, V. Pickerd, and A. P. Mouritz, “Comparative assessment of the explosive blast performance of carbon and glass fibre-polymer composites used in naval ship structures,” Composite Structures, vol. 171, pp. 306–316, Jul. 2017, doi: 10.1016/j.compstruct.2017.03.041.

[142] D. Lacroix, C. Viau, D. Côté, M. Poulin, A. Lopez, and G. Doudak, “Overview on the structural performance of timber structures under the effects of blast loading & research and design considerations,” Structures and Architecture. CRC Press, pp. 67–74, 2016. doi: 10.1201/b20891-8.

[143] J. Buchar, L. Severa, M. Havlicek, and S. Rolc, “Response of wood to the explosive loading,” Journal De Physique. IV : JP, vol. 10, no. 9, pp. 529–534, 2000, doi: 10.1051/jp4:2000988.

[144] J. Buchar and L. Slonek, “Evaluation of wood–based members response to the explosive loading,”, 2000. https://www.semanticscholar.org/paper/Evaluation-of-wood-%E2%80%93-based-members-response-to-the-Buchar-Slonek/b98413665d56325a05344b0506124b3be97060ac (accessed Jun. 28, 2018).

[145] A. P. Bol'shakov et al., "Damping Properties of Sequoia, Birch, Pine, and Aspen under Shock Loading," Journal of Applied Mechanics and Technical Physics, vol. 42, no. 2, pp. 202–210, 2001, doi: 10.1023/A:1018859432046.

[146] K. Huang, A. V. Rammohan, U. Kureemun, W. S. Teo, L. Q. N. Tran, and H. P. Lee, "Shock wave impact behavior of flax fiber reinforced polymer composites," Composites Part B: Engineering, vol. 102, pp. 78–85, 2016, doi: 10.1016/j.compositesb.2016.07.014.

[147] S. Li, A. Poudel, and T. Chu, "An Image Enhancement Method for Ultrasonic NDE of CFRP Panels," Mar. 2012.

[148] C. Scarponi, "Impact behavior of natural fiber composite laminates," in Interface Engineering of Natural Fibre Composites for Maximum Performance, Elsevier, 2011, pp. 341–382. doi: 10.1533/9780857092281.2.341.

[149] E. Marsyahyo, Jamasri, H. S. B. Rochardjo, and Soekrisno, "Preliminary Investigation on Bulletproof Panels Made from Ramie Fiber Reinforced Composites for {NIJ} Level {II}, {IIA}, and {IV}," Journal of Industrial Textiles, vol. 39, no. 1, pp. 13–26, Feb. 2009, doi: 10.1177/1528083708098913.

[150] P. Wambua, B. Vangrimde, S. Lomov, and I. Verpoest, "The response of natural fibre composites to ballistic impact by fragment simulating projectiles," Composite Structures, vol. 77, no. 2, pp. 232–240, Jan. 2007, doi: 10.1016/j.compstruct.2005.07.006.

[151] L. Koene and F. Broekhuis, "Bullet Penetration into Medium Density Fibreboard Targets," 2019.

[152] D. Bachtiar, S. M. Sapuan, and M. M. Hamdan, "The Influence of Alkaline Surface Fibre Treatment on the Impact Properties of Sugar Palm Fibre-Reinforced Epoxy Composites," Polymer-Plastics Technology and Engineering, vol. 48, no. 4, pp. 379–383, Apr. 2009, doi: 10.1080/03602550902725373.

[153] J. Gassan and A. K. Bledzki, "Possibilities for improving the mechanical properties of jute/epoxy composites by alkali treatment of fibres," Composites Science and Technology, vol. 59, no. 9, pp. 1303–1309, Jul. 1999, doi: 10.1016/s0266-3538(98)00169-9.

[154] C. Santulli and A. P. Caruso, "Effect of Fibre Architecture on the Falling Weight Impact Properties of Hemp/Epoxy Composites," Journal of Biobased Materials and Bioenergy, vol. 3, no. 3, pp. 291–297, Sep. 2009, doi: 10.1166/jbmb.2009.1037.

[155] W. Nuthong, P. Uawongsuwan, W. Pivsa-Art, and H. Hamada, “Impact Property of Flexible Epoxy Treated Natural Fiber Reinforced (PLA) Composites,” Energy Procedia, vol. 34, pp. 839–847, 2013, doi: 10.1016/j.egypro.2013.06.820.

[156] C. Santulli, “Impact properties of glass/plant fibre hybrid laminates,” Journal of Materials Science, vol. 42, no. 11, pp. 3699–3707, Jun. 2007, doi: 10.1007/s10853-006-0662-y.

[157] P. E. Irving and C. Soutis, Polymer Composites in the Aerospace Industry. Elsevier Science, 2019.

[158] Aerontec, “Product Data Sheet: AEROTEX WR- 400 PW,” Cape Town, 2017.

[159] LINEO, “LINEO - Flax Fabrics Technical Fabrics made of Flax Fibers,” Mont Saint Aignon, 2010.

[160] Composites Evolution Ltd, “Biotex Jute 400g/m2 2x2 Twill,” Chesterfield, 2015.

[161] AMT Composites, “Wovitex 400 P Glass Fabric - Technical Datasheet,” Maitland, 2018.

[162] PG Bison, “3MM SINGLE FACE WHITE AND 3MM SUPAWOOD HIGH DENSITY FIBRE BOARD (HDF).”

[163] Gurit, "Prime(TM) 20LV," Document Number PDS-PRIME20LV-13-1215. Available: https://www.gurit.com/-/media/Gurit/Datasheets/prime-20lv.pdf

[164] Entropy Resins Inc, “Super Sap CLR.” https://entropyresins.com/product/super-sap-clr-clear-epoxy-resin/ (accessed Mar. 20, 2018).

[165] S. Ekşi and K. Genel, “Comparison of mechanical properties of unidirectional and woven carbon, glass and aramid fiber reinforced epoxy composites,” in Acta Physica Polonica A, Sep. 2017, vol. 132, no. 3, pp. 879–882. doi: 10.12693/APhysPolA.132.879.

[166] D. Das, O. P. Dubey, M. Sharma, R. K. Nayak, and C. Samal, “Mechanical properties and abrasion behaviour of glass fiber reinforced polymer composites – A case study,” Materials Today: Proceedings, no. xxxx, pp. 1–6, 2019, doi: 10.1016/j.matpr.2019.07.644.

[167] S. Pichandi, S. Rana, D. Oliveira, and R. Fangueiro, “Fibrous and composite materials for blast protection of structural elements: A state-of-the-art review,” Journal of Reinforced Plastics and Composites, vol. 32, no. 19, pp. 1477–1500, Aug. 2013, doi: 10.1177/0731684413498297.

[168] G. S. Langdon, C. J. von Klemperer, and G. M. Sinclair, “Blast response of sandwich structures: The influence of curvature,” in Dynamic Deformation, Damage and Fracture in Composite Materials

and Structures, Woodhead Publishing, 2016, pp. 365–389. doi: 10.1016/B978-0-08-100080-9.00013-0.

[169] I. Ghoor, “The Response of Concave Singly Curved Fibre Reinforced Moulded Sandwich and Laminated Composite Panels to Blast Loading,” University of Cape Town, MSc Thesis, 2017.

[170] C. Baley, A. Le Duigou, C. Morvan, and A. Bourmaud, “Tensile properties of flax fibers,” in Handbook of Properties of Textile and Technical Fibres, 2nd ed., Elsevier, 2018, pp. 275–300. doi: 10.1016/B978-0-08-101272-7.00008-0.

[171] A. Moudood, A. Rahman, A. Öchsner, M. Islam, and G. Francucci, “Flax fiber and its composites: An overview of water and moisture absorption impact on their performance,” Journal of Reinforced Plastics and Composites, vol. 38, no. 7, pp. 323–339, Apr. 2019, doi: 10.1177/0731684418818893.

[172] C. Baley, M. Gomina, J. Breard, A. Bourmaud, and P. Davies, “Variability of mechanical properties of flax fibres for composite reinforcement. A review,” Industrial Crops and Products, p. 111984, Nov. 2019, doi: 10.1016/J.INDCROP.2019.111984.

[173] D. E. Akin, “Flax Fiber,” in Kirk-Othmer Encyclopedia of Chemical Technology, Hoboken, NJ, USA: John Wiley & Sons, Inc., 2003. doi: 10.1002/0471238961.0612012401110914.a01.

[174] LINEO, “Advanced Flax - Discovery,” LINEO, 2015. https://www.lineo.eu/discovery# (accessed Mar. 16, 2018).

[175] M. S. Aly-Hassan, “A new perspective in multifunctional composite materials,” in Multifunctionality of Polymer Composites, Elsevier, 2015, pp. 42–67. doi: 10.1016/B978-0-323-26434-1.00002-7.

[176] PG Bison, “SupaWood | PG Bison,” 2020. https://pgbison.co.za/products/supawood (accessed Dec. 28, 2020).

[177] PG Bison, “Supawood Material Safety Data Sheet,” Boksburg, 2010.

[178] M. Hamilton and S. Severinghaus, “Entropy Resins’ Project,” Huntington, 2020.

[179] Livermore Software Technology Corporation, “LS-DYNA,” 2018. http://www.lstc.com/products/ls-dyna (accessed Mar. 07, 2016).

[180] V. Shekhar, “The effect of bend radius on the impulse transfer characteristics of V-hulls,” University of Cape Town, MSc thesis, 2015.

[181] G. Volschenk, “The response of aluminium and glass fibre FMLs subjected to blast loading,” University of Cape Town, MSc thesis, 2015.

[182] R. Curry, “Response of plates subjected to air-blast and buried explosions,” University of Cape Town, PhD thesis, 2017.

[183] Livermore Software Technology Corporation, LS-DYNA Keyword User’s Manual Volume II R7.1, no. 5442. Livermore, California, 2014. doi: 10.1007/978-3-540-69451-9.

[184] R. J. Curry and G. S. Langdon, “The effect of explosive charge backing in close-proximity air-blast loading,” International Journal of Impact Engineering, vol. 151, p. 103822, May 2021, doi: 10.1016/j.ijimpeng.2021.103822.

[185] G. S. Langdon, Y. Chi, G. N. Nurick, and P. Haupt, “Response of GLARE© panels to blast loading,” Engineering Structures, vol. 31, no. 12, pp. 3116–3120, 2009, doi: 10.1016/j.engstruct.2009.07.010.

[186] B. M. Dobratz and L. L. N. Laboratory., LLNL explosives handbook: properties of chemical explosives and explosive simulants. Livermore, Calif.; Springfield, Va.: Lawrence Livermore National Laboratory, University of California; Available from National Technical Information Service, 1985.

[187] D. Bogosian, M. Yokota, and S. Rigby, “TNT equivalence of C-4 and PE4: A review of traditional sources and recent data,” 24th International Symposium on Military Aspects of Blast and Shock (MABS 24), no. September, pp. 1–15, 2016.

[188] E. C. Botelho, R. S. Almeida, L. C. Pardini, and M. C. Rezende, “Elastic properties of hygrothermally conditioned glare laminate,” International Journal of Engineering Science, vol. 45, no. 1, pp. 163–172, Jan. 2007, doi: 10.1016/J.IJENGSCI.2006.08.017.

[189] A. Pozzi and R. Sepe, “Mechanical properties of woven natural fiber reinforced composites,” ECCM 2012 - Composites at Venice, Proceedings of the 15th European Conference on Composite Materials, no. June, pp. 24–28, 2012.

[190] PG Bison, “Panel Products DATA SHEET | TECHNICAL DATA | SUPAWOOD,” Boksburg, 2016.

[191] MakeItFrom.com, “Material Properties of Medium Density Fibreboard,” Medium Density Fibreboard, 2018. https://www.makeitfrom.com/material-properties/Medium-Density-Fiberboard-MDF (accessed Mar. 13, 2016).

[192] W. Wang, X. Zhang, N. Chouw, Z. Li, and Y. Shi, “Strain rate effect on the dynamic tensile behaviour of flax fibre reinforced polymer,” Composite Structures, vol. 200, no. May, pp. 135–143, Sep. 2018, doi: 10.1016/j.compstruct.2018.05.109.

[193] Entropy Resins Inc, “CLR Clear Resin: Technical Data Sheet,” Hayward, 2015.

[194] W. Wang, “Re: FW: Manufacturing Process.” Email correspondence, 2015.

[195] ASTM International, “D5528 - 13 Standard test method for mode I interlaminar fracture toughness of unidirectional fiber-reinforced polymer matrix composites,” West Conshohocken, PA, 2014. doi: 10.1520/D5528-13.2.

[196] Gurit, “Spabond 340 Epoxy adhesive system (PDS-Spabond 340-8-0208).”

[197] ASTM International, “D3039/D3039M- 17 Standard test method for Tensile Properties of Polymer Matrix Composite Materials,” West Conshohocken, PA, 2014. doi: 10.1520/D3039.

[198] V. Shekhar, “Response of composite V-structures to air blast loading - Numerical and Experimental,” University of Cape Town, MSc Thesis, 2021.

[199] ASTM International, “D7264/D7264M-15 Standard Test Method for Flexural Properties of Polymer Matrix Composite Materials,” West Conshohocken, PA, 2015. doi: 10.1520/D7264.

[200] N. Nasuha, A. I. Azmi, and C. L. Tan, “A review on mode-I interlaminar fracture toughness of fibre reinforced composites,” Journal of Physics: Conference Series, vol. 908, no. 1, pp. 0–8, 2017, doi: 10.1088/1742-6596/908/1/012024.

[201] R. Zulkifli, K. Su Pei, and C. Husna Azhari, “Interlaminar Fracture Properties of Multi-Layer Woven Silk Fibre/Polyester Composites,” Asian Journal of Applied Sciences, vol. 1, no. 2. pp. 177–184, 2008. doi: 10.3923/ajaps.2008.177.184.

[202] M. Pinto, V. B. Chalivendra, Y. K. Kim, and A. F. Lewis, “Improving the strength and service life of jute/epoxy laminar composites for structural applications,” Composite Structures, vol. 156, pp. 333–337, Nov. 2016, doi: 10.1016/j.compstruct.2015.10.005.

[203] M. Ravandi, W. S. Teo, L. Q. N. Tran, M. S. Yong, and T. E. Tay, “The effects of through-the-thickness stitching on the Mode I interlaminar fracture toughness of flax/epoxy composite laminates,” Materials & Design, vol. 109, pp. 659–669, Nov. 2016, doi: 10.1016/j.matdes.2016.07.093.

[204] South African National Standard, “SAN 6016: 2005 Transverse tensile (internal bond) strength of wood-based panels,” Groenkloof, 2011.

[205] South African National Standard, “SANS 540-1: 2009 Fibreboard products Part 1: Uncoated fibreboard,” Groenkloof, 2009.

[206] ASTM International, “D1037-12 Standard test methods for evaluating Properties of Wood-Based Fiber and Particle Panel Materials,” West Conshohocken, PA, 2012. doi: 10.1520/D1037-12.1.

[207] G. S. Langdon, C. J. von Klemperer, G. F. Volschenk, T. van Tonder, and R. A. Govender, “The influence of interfacial bonding on the response of lightweight aluminium and glass fibre metal laminate panels subjected to air-blast loading,” Proceedings of the Institution of Mechanical Engineers, Part C: Journal of Mechanical Engineering Science, vol. 232, no. 8, pp. 1402–1417, 2018, doi: 10.1177/0954406217718859.

[208] G. S. Langdon, D. Karagiozova, C. J. von Klemperer, G. N. Nurick, A. Ozinsky, and E. G. Pickering, “The air-blast response of sandwich panels with composite face sheets and polymer foam cores: Experiments and predictions,” International Journal of Impact Engineering, vol. 54, pp. 64–82, Apr. 2013, doi: 10.1016/j.ijimpeng.2012.10.015.

[209] G. S. Langdon, C. J. von Klemperer, B. K. Rowland, and G. N. Nurick, “The response of sandwich structures with composite face sheets and polymer foam cores to air-blast loading: Preliminary experiments,” Engineering Structures, vol. 36, pp. 104–112, Mar. 2012, doi: 10.1016/j.engstruct.2011.11.023.

[210] R. J. Curry and G. S. Langdon, “Transient response of steel plates subjected to close proximity explosive detonations in air,” International Journal of Impact Engineering, vol. 102, pp. 102–116, Apr. 2017, doi: 10.1016/J.IJIMPENG.2016.12.004.

[211] H. Schreier, J.-J. Orteu, and M. A. Sutton, Image Correlation for Shape, Motion and Deformation Measurements. Boston, MA: Springer US, 2009. doi: 10.1007/978-0-387-78747-3.

[212] B. Pan, Z. Wang, and Z. Lu, “Genuine full-field deformation measurement of an object with complex shape using reliability-guided digital image correlation,” Optics Express, vol. 18, no. 2, p. 1011, 2010, doi: 10.1364/oe.18.001011.

[213] Dantec Dynamics A/S, “Istra 4D - Shearography.” https://www.dantecdynamics.com/istra-4d-shearography (accessed Jun. 16, 2019).

[214] Dantec Dynamics A/S, “DIC Standard 3D,” Nova Instruments, 2020. https://www.dantecdynamics.com/solutions-applications/solutions/stress-strain-espi-dic/digital-image-correlation-dic/dic-standard-3d/ (accessed Jan. 02, 2020).

[215] M. A. Sutton, “Three-dimensional digital image correlation to quantify deformation and crack-opening displacement in ductile aluminum under mixed-mode I/III loading,” Optical Engineering, vol. 46, no. 5, p. 051003, May 2007, doi: 10.1117/1.2741279.

[216] S. Mahoi, “Influence of Shape of Solid Explosives on the Deformation of Circular Steel Plates – Experimental and Numerical Investigations,” University of Cape Town, Cape Town, PhD thesis, 2006.

[217] P. E. Nothnagle, W. Chambers, and M. W. Davidson, “Introduction to Stereomicroscopy,” Nikon Instruments Inc., 2019.

[218] M.M. Houck, “Analytical Light Microscopy,” Encyclopedia of Forensic Sciences (Second Edition), Academic Press, 2013, pp. 609-611, ISBN 9780123821669, doi: 10.1016/B978-0-12-382165-2.00251-8.

[219] K. Lau, P. Hung, M.-H. Zhu, and D. Hui, “Properties of natural fibre composites for structural engineering applications,” Composites Part B: Engineering, vol. 136, pp. 222–233, 2018, doi: https://doi.org/10.1016/j.compositesb.2017.10.038.

[220] B. Vijaya Ramnath et al., “Evaluation of mechanical properties of abaca–jute–glass fibre reinforced epoxy composite,” Materials & Design, vol. 51, pp. 357–366, 2013, doi: https://doi.org/10.1016/j.matdes.2013.03.102.

[221] V. S. Srinivasan, S. Rajendra Boopathy, D. Sangeetha, and B. Vijaya Ramnath, “Evaluation of mechanical and thermal properties of banana–flax based natural fibre composite,” Materials & Design, vol. 60, pp. 620–627, 2014, doi: https://doi.org/10.1016/j.matdes.2014.03.014.

[222] A. Kerber, A. Gargano, K. Pingkarawat, and A. P. Mouritz, “Explosive blast damage resistance of three-dimensional textile composites,” Composites Part A: Applied Science and Manufacturing, vol. 100, pp. 170–182, Sep. 2017, doi: 10.1016/j.compositesa.2017.05.005.

[223] G. N. Nurick, M. E. Gelman, and N. S. Marshall, “Tearing of blast loaded plates with clamped boundary conditions,” International Journal of Impact Engineering, vol. 18, no. 7, pp. 803–827, 1996, doi: https://doi.org/10.1016/S0734-743X(96)00026-7.

[224] G. M. Sinclair, “The response of singly curved fibre reinforced sandwich and laminate composite panels subjected to localised blast loads,” University of Cape Town, Cape Town, MSc thesis, 2014.

[225] S. Chung Kim Yuen, G. N. Nurick, G. S. Langdon, and Y. Iyer, “Deformation of thin plates subjected to impulsive load: Part III – an update 25 years on,” International Journal of Impact Engineering, vol. 107, pp. 108–117, Sep. 2017, doi: 10.1016/j.ijimpeng.2016.06.010.

[226] O. I. Okoli and G. Smith, “Failure modes of fibre reinforced composites: The effects of strain rate and fibre content,” Journal of Materials Science, vol. 33, pp. 5415–5422, Jan. 1998, doi: 10.1023/A:1004406618845.

[227] P. Olivier, J. P. Cottu, and B. Ferret, “Effects of cure cycle pressure and voids on some mechanical properties of carbon/epoxy laminates,” Composites, vol. 26, no. 7, pp. 509–515, Jul. 1995, doi: 10.1016/0010-4361(95)96808-J.

[228] H. Huang and R. Talreja, “Effects of void geometry on elastic properties of unidirectional fiber reinforced composites,” Composites Science and Technology, vol. 65, no. 13, pp. 1964–1981, Oct. 2005, doi: 10.1016/j.compscitech.2005.02.019.

[229] S. F. M. de Almeida and Z. dos S. N. Neto, “Effect of void content on the strength of composite laminates,” Composite Structures, vol. 28, no. 2, pp. 139–148, Jan. 1994, doi: 10.1016/0263-8223(94)90044-2.

[230] Box Shop and Packaging, “Hessian Bags | Hessian Cloth,” 2020. https://www.boxshopsa.net/shop-online/buy-hessian-fabric/hessian-fabric-for-sale/hessian-cloth-for-sale/ (accessed Dec. 29, 2020).

[231] E. H. Saidane, D. Scida, M. Assarar, H. Sabhi, and R. Ayad, “Hybridisation effect on diffusion kinetic and tensile mechanical behaviour of epoxy-based flax–glass composites,” Composites Part A: Applied Science and Manufacturing, vol. 87, pp. 153–160, Aug. 2016, doi: 10.1016/j.compositesa.2016.04.023.

[232] M. R. Sanjay and B. Yogesha, “Studies on Mechanical Properties of Jute/E-Glass Fiber Reinforced Epoxy Hybrid Composites,” Journal of Minerals and Materials Characterization and Engineering, vol. 04, no. 01, pp. 15–25, 2016, doi: 10.4236/jmmce.2016.41002.

[233] S. Mishra et al., “Studies on mechanical performance of biofibre/glass reinforced polyester hybrid composites,” Composites Science and Technology, vol. 63, no. 10, pp. 1377–1385, Aug. 2003, doi: 10.1016/S0266-3538(03)00084-8.

[234] M. Ramesh, K. Palanikumar, and K. H. Reddy, “Comparative Evaluation on Properties of Hybrid Glass Fiber- Sisal/Jute Reinforced Epoxy Composites,” Procedia Engineering, vol. 51, pp. 745–750, 2013, doi: 10.1016/j.proeng.2013.01.106.

[235] G. Cicala, G. Cristaldi, G. Recca, G. Ziegmann, A. El-Sabbagh, and M. Dickert, “Properties and performances of various hybrid glass/natural fibre composites for curved pipes,” Materials & Design, vol. 30, no. 7, pp. 2538–2542, Aug. 2009, doi: 10.1016/j.matdes.2008.09.044.

List of Publications

Journal articles

- Langdon, GS; von Klemperer, CJ; Gabriel, S; Chung Kim Yuen, S. "Transient response and failure of medium density fibreboard panels subjected to air-blast loading" Composite Structures, ***Submission being processed***

International Conference Proceedings (full papers and extended abstracts)

- von Klemperer, CJ; Langdon, GS; Gabriel, S; Chung Kim Yuen, S "Blast response of panels containing sustainable materials" 22nd International Conference on Composite Materials (ICCM-22), July 2019, Melbourne, Australia.
- Gabriel, S; Langdon, GS; von Klemperer, CJ; Chung Kim Yuen, S "The effect of Blast Loading on Composites containing sustainable materials" 3rd International Conference on Composites, Biocomposites and Nanocomposites (ICCBN 2018), November 2018, Port Elizabeth, South Africa.

National workshops and conferences

- Gabriel, S; Langdon, GS; von Klemperer, CJ; Chung Kim Yuen, S "Blast Loading on Composites containing Sustainable Materials" South African Ballistic Organisation (SABO) Symposium, September 2019, Somerset West, South Africa.
- Gabriel, S; Langdon, GS; von Klemperer, CJ; Chung Kim Yuen, S "The effects of Blast Loading on Composites that contain Sustainable Materials" South African Institution of Mechanical Engineering (SAIMechE) Western Cape Postgraduate Conference on Mechanical, Manufacturing, Materials & Biomedical Engineering, November 2017, Stellenbosch, South Africa.
- Gabriel, S; Langdon, GS; von Klemperer, CJ; Chung Kim Yuen, S "The effect of Blast Loading on Composites that contain Sustainable Materials" South African Ballistic Organisation (SABO) Symposium, September 2016, Somerset West, South Africa.
- Gabriel, S; Langdon, GS; von Klemperer, CJ; Chung Kim Yuen, S "The effect of Blast Loading on Composites which contain Sustainable Materials" South African Institution of Mechanical Engineering (SAIMechE) Western Cape Postgraduate Conference on Mechanical, Manufacturing, Materials & Biomedical Engineering, November 2016, Rondebosch, South Africa.
- Gabriel, S; Langdon, GS; von Klemperer, CJ; Chung Kim Yuen, S "The effect of Blast Loading on Composites which contain Sustainable Materials" South African Institution of Mechanical Engineering (SAIMechE) Western Cape Postgraduate Conference on Mechanical, Manufacturing, Materials & Biomedical Engineering, November 2015, Bellville, South Africa.

Appendix A Numerical simulation input deck

```
$# LS-DYNA Keyword file created by LS-PrePost(R) V4.5.25 - 07Nov2018
$# Created on Mar-08-2019 (18:20:18)
*KEYWORD MEMORY=500000000 NCPU=4
*TITLE
$#                                                 title
LS-DYNA keyword deck by LS-PrePost
$=========================================================================
$ Control Cards
$=========================================================================
*CONTROL_ALE
$#    dct     nadv     meth     afac     bfac     cfac     dfac     efac
     -1        1        3     -1.0      0.0      0.0      0.0      0.0
$#  start      end    aafac    vfact     prit      ebc     pref   nsidebc
    0.01.00000E20      1.01.00000E-6        0        0    0.1013        0
$#   ncpl     nbkt   imascl   checkr   beamin   mmgpref   pdifmx   dtmufac
      1       50        0      0.0
*CONTROL_ENERGY
$#   hgen     rwen    slnten     rylen
      1        2        1        1
*CONTROL_SOLUTION
$#   soln      nlq     isnan     lcint
      0        0        1      100
*CONTROL_TERMINATION
$# endtim    endcyc     dtmin    endeng    endmas     nosol
   0.35        0      0.0      0.01.000000E8
*CONTROL_TIMESTEP
$# dtinit    tssfac     isdo    tslimt     dt2ms     lctm     erode     ms1st
1.00000E-4      0.67        0      0.0      0.0        0        0        0
$# dt2msf   dt2mslc    imscl    unused    unused    rmscl
    0.0        0        0                   0.0
$=========================================================================
$ Database Cards
$=========================================================================
*DATABASE_GLSTAT
$#     dt    binary     lcur     ioopt
   0.001        0        0        1
*DATABASE_MATSUM
$#     dt    binary     lcur     ioopt
   0.001        0        0        1
*DATABASE_TRHIST
$#     dt    binary     lcur     ioopt
   0.001        0        0        1
```

```
*DATABASE_BINARY_D3PLOT
$#     dt     lcdt     beam     npltc    psetid
   0.001        0        0        0        0
$#   ioopt
       0
*DATABASE_FSI
$#     dt
   0.001
$#dbsfi_id      sid     stype      swid    convid   ndsetid      cid
     200      200        1        0        0        0        0
$=========================================================================
$ Boundary conditions for air
$=========================================================================
*BOUNDARY_NON_REFLECTING
$#   ssid       ad       as
     100      0.0      0.0
*BOUNDARY_SPC_SET_ID
$#     id                                      heading
      11XOZ symmetry air
$#   nsid      cid     dofx     dofy     dofz    dofrx    dofry    dofrz
     100        0        0        1        0        1        0        1
*BOUNDARY_SPC_SET_ID
$#     id                                      heading
      12YOZ symmetry air
$#   nsid      cid     dofx     dofy     dofz    dofrx    dofry    dofrz
     101        0        1        0        0        0        1        1
$ For uniform loading condition, reflective boundary is needed
*BOUNDARY_SPC_SET_ID
$#     id                                      heading
      12YOZ reflective boundary
$#   nsid      cid     dofx     dofy     dofz    dofrx    dofry    dofrz
     101        0        1        1        1        1        1        1
$=========================================================================
$ Boundary conditions for plates
$=========================================================================
*BOUNDARY_SPC_SET_ID
$#     id                                      heading
      21XOZ Symmetry for Plate
$#   nsid      cid     dofx     dofy     dofz    dofrx    dofry    dofrz
     201        0        0        1        0        1        0        1
*BOUNDARY_SPC_SET_ID
$#     id                                      heading
      22YOZ Symmetry for Plate
$#   nsid      cid     dofx     dofy     dofz    dofrx    dofry    dofrz
     202        0        1        0        0        0        1        1
```

```
*BOUNDARY_SPC_SET_ID
$#     id                                        heading
      23Fixed Boundary for Plate
$#   nsid      cid     dofx     dofy     dofz    dofrx    dofry    dofrz
    203       0       1        1        1       1        1        1
$=========================================================================
$ Initial cards for explosive
$=========================================================================
*INITIAL_VOLUME_FRACTION_GEOMETRY
$#   fmsid   fmidtyp    bammg    ntrace
     100       1        1        5
$# conttyp   fillopt    fammg       vx       vy       vz    radvel    unused
      4        0        2       0.0      0.0      0.0       0
$#     x1       y1       z1       x2       y2       z2       r1       r2
   100.0    100.0    41.25    100.0    100.0     50.0     15.0     15.0
*INITIAL_DETONATION
$#    pid        x        y        z       lt
     50    100.0    100.0     43.0      0.0
$=========================================================================
$ Parts and relevant descriptions
$=========================================================================
*PART
$#                                          title
Explosive
$#    pid    secid      mid    eosid     hgid     grav   adpopt     tmid
     50     1050       50       50     1050        0        0        0
*SECTION_SOLID_TITLE
Air and Explosive section
$#   secid    elform      aet
    1050       11        0
*MAT_HIGH_EXPLOSIVE_BURN_TITLE
Explosive material
$#    mid       ro        d      pcj     beta        k        g     sigy
     50  0.001601    8193.0   28000.0      0.0      0.0      0.0      0.0
*EOS_JWL_TITLE
Explosive EOS
$#   eosid        a        b       r1       r2     omeg       e0       vo
     50  609800.0   12950.0      4.5      1.4     0.25    9000.0      1.0
*HOURGLASS_TITLE
Air and Explosive Hourglass
$#    hgid      ihq       qm      ibq       q1       q2    qb/vdc       qw
    1050        21.00000E-6        0      1.5     0.06      0.1      0.1
*PART
$#                                          title
Localised Airblock
```

```
$#    pid    secid      mid    eosid     hgid     grav   adpopt     tmid
    100     1050      100      100     1050        0        0        0
*MAT_NULL_TITLE
Air Material
$#    mid       ro       pc       mu    terod    cerod       ym       pr
    1001.18400E-6      0.0      0.0      0.0      0.0      0.0      0.0
*EOS_LINEAR_POLYNOMIAL_TITLE
Air EOS
$#  eosid       c0       c1       c2       c3       c4       c5       c6
    100      0.0      0.0      0.0      0.0      0.4      0.4      0.0
$#     e0       v0
  0.2533      1.0
*PART
$#                                                  title
Composite Plate
$#    pid    secid      mid    eosid     hgid     grav   adpopt     tmid
    200      200      210        0      200        0        0        0
*SECTION_SOLID_TITLE
Composite Plate Section
$#  secid   elform      aet
    200        1        0
*MAT_ISOTROPIC_ELASTIC_FAILURE_TITLE
Flax Material
$#    mid       ro        g     sigy     etan     bulk
    210   0.00122   12700.0    264.0      0.0   46700.0
$#    epf      prf      rem     trem
   0.018      0.0      0.0      0.0
*HOURGLASS_TITLE
Plate Hourglass (Default)
$#   hgid      ihq       qm      ibq       q1       q2    qb/vdc       qw
    200        1      0.1        0      1.5     0.06      0.1      0.1
$=========================================================================
$ Plate/air/explosive interaction
$=========================================================================
*CONSTRAINED_LAGRANGE_IN_SOLID_TITLE
$#  coupid                                          title
    1200Plate Air interaction
$#  slave   master    sstyp    mstyp    nquad    ctype    direc    mcoup
    200      100        1        1        2        4        3     -100
$#  start      end     pfac     fric   frcmin     norm   normtyp     damp
    0.01.00000E10      0.1      0.0      0.5        0        0      0.0
$#     cq     hmin     hmax    ileak    pleak   lcidpor    nvent  blockage
    0.0      0.0      0.0        1      0.1        0        0        0
$#  iboxid   ipenchk   intforc   ialesof   lagmul    pfacmm     thkf
      0        0        0        0      0.0        0      0.0
```

```
*CONSTRAINED_LAGRANGE_IN_SOLID_TITLE
$#  coupid                                          title
     520Explosive Plate interaction
$#   slave    master    sstyp    mstyp    nquad    ctype    direc    mcoup
     200       50        1        1        2        4        3      -50
$#   start      end     pfac     fric    frcmin     norm   normtyp     damp
     0.01.00000E10      0.1      0.0      0.5        0        0      0.0
$#      cq     hmin     hmax    ileak    pleak   lcidpor    nvent  blockage
     0.0      0.0      0.0        1      0.1        0        0        0
$#  iboxid   ipenchk   intforc   ialesof    lagmul    pfacmm     thkf
       0        0        0        0       0.0        0       0.0
*CONSTRAINED_LAGRANGE_IN_SOLID_TITLE
$#  coupid                                          title
    1250Plate All Interaction
$#   slave    master    sstyp    mstyp    nquad    ctype    direc    mcoup
     200      1050        1        0        2        4        3     -150
$#   start      end     pfac     fric    frcmin     norm   normtyp     damp
     0.01.00000E10      0.1      0.0      0.5        0        0      0.0
$#      cq     hmin     hmax    ileak    pleak   lcidpor    nvent  blockage
     0.0      0.0      0.0        1      0.1        0        0        0
$#  iboxid   ipenchk   intforc   ialesof    lagmul    pfacmm     thkf
       0        0        0        0       0.0        0       0.0
$=========================================================================
$ Combining the air and plate
$=========================================================================
*DEFINE_TRANSFORMATION_TITLE
Plate Transformation
$#  tranid
     200
$#  option       a1       a2       a3       a4       a5       a6       a7
TRANSL          0.0      0.0    250.0      0.0      0.0      0.0      0.0
$ TRANSL          0.0      0.0     50.0      0.0      0.0      0.0      0.0 for local
*INCLUDE_TRANSFORM
$#
plate.k
$#  idnoff    ideoff    idpoff    idmoff    idsoff    idfoff    iddoff
       0         0         0         0         0         0         0
$#  idroff
       0
$#  fctmas    fcttim    fctlen    fcttem   incout1    unused
     1.0       1.0      1.01.0             1
$#  tranid
     200
```

```
*INCLUDE
$#
uniform_air.k
```

Appendix B Quasi-static data (flexural and tensile)

B.1 Experimental flexural test results

Glass fibre reinforced Prime 20LV

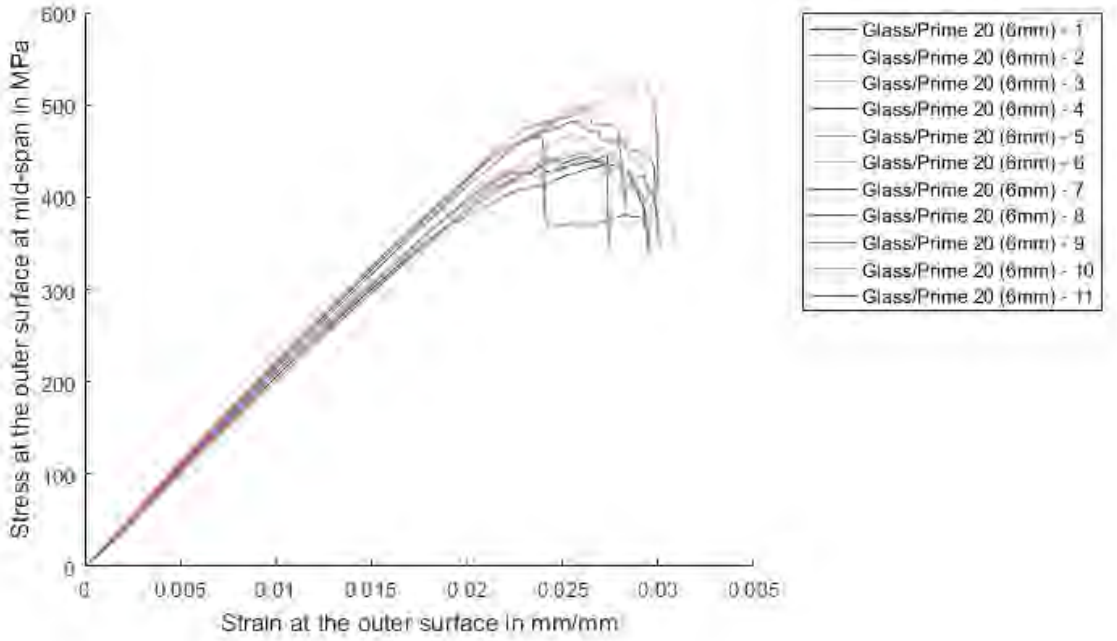

Figure B-1: Plot curves for the flexural stress against strain for Glass 19/Prime 20LV specimens

Table B-1: Flexural geometry and properties for Glass 19/Prime 20LV specimens

	h [mm]	w [mm]	L [mm]	σ^f_{max} [MPa]	$\varepsilon^f_{\sigma max}$ [m/m]	E^f_{chord} [MPa]	E^f_{secant} [MPa]	ε^f_{fail} [m/m]
GP6-1	6.13	32.40	98	483.57	0.026	22444.17	18982.84	0.030
GP6-2	6.10	32.55	98	498.20	0.026	22693.18	17467.53	0.028
GP6-3	6.17	32.23	98	467.44	0.025	21737.10	17068.89	0.028
GP6-4	6.26	32.43	100	444.86	0.027	21277.45	12613.56	0.027
GP6-5	6.19	31.92	100	445.08	0.026	21049.30	11486.67	0.029
GP6-6	6.19	31.15	100	451.14	0.027	21349.64	9373.08	0.030
GP6-7	6.43	31.73	102	435.85	0.027	20713.79	11577.43	0.029
GP6-8	6.30	31.93	100	443.77	0.026	19952.23	15509.02	0.030
GP6-9	6.12	32.50	98	522.42	0.029	22448.70	11755.29	0.030
GP6-10	6.23	32.55	100	458.37	0.028	20227.45	14702.37	0.030
GP6-11	6.13	32.45	98	468.52	0.023	21810.73	19088.09	0.024

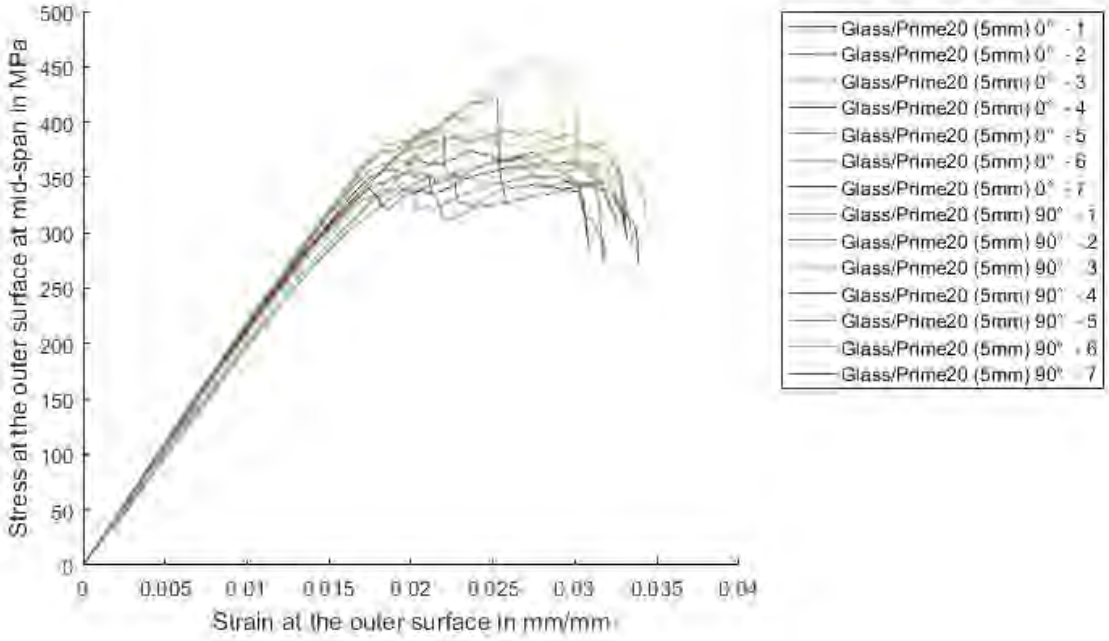

Figure B-2: Plot curves for the flexural stress against strain for Glass 17/Prime 20LV specimens

Table B-2: Flexural geometry and properties for Glass 17/Prime 20LV specimens

	h [mm]	w [mm]	L [mm]	σ^f_{max} [MPa]	$\varepsilon^f_{\sigma max}$ [m/m]	E^f_{chord} [MPa]	E^f_{secant} [MPa]	ε^f_{fail} [m/m]
GP5.1-1	4.89	30.29	78	393.89	0.021	22259.61	21346.13	0.032
GP5.1-2	4.94	30.03	79	393.39	0.028	22162.57	16478.45	0.033
GP5.1-3	4.91	30.47	79	410.13	0.023	22094.20	21105.16	0.031
GP5.1-4	4.86	30.19	78	421.38	0.025	22133.68	18960.10	0.025
GP5.1-5	4.88	30.24	78	393.05	0.022	22754.77	21108.11	0.033
GP5.1-6	4.89	30.32	78	387.50	0.025	22543.01	20141.01	0.034
GP5.1-7	4.90	30.20	78	374.71	0.024	21377.31	20034.24	0.033
GP5.2-1	4.92	30.27	79	356.38	0.020	22239.99	21016.32	0.031
GP5.2-2	4.97	30.29	80	351.44	0.029	21920.14	10857.45	0.032
GP5.2-3	4.88	30.23	78	454.79	0.027	21897.47	15005.13	0.029
GP5.2-4	4.94	30.10	79	351.28	0.022	20494.43	19130.57	0.034
GP5.2-5	4.96	30.28	79	362.54	0.031	20576.06	7047.11	0.033
GP5.2-6	4.94	30.21	79	455.69	0.028	21157.39	14575.65	0.030
GP5.2-7	4.90	30.40	78	361.15	0.027	22262.14	15990.56	0.031

Glass fibre reinforced Super Sap

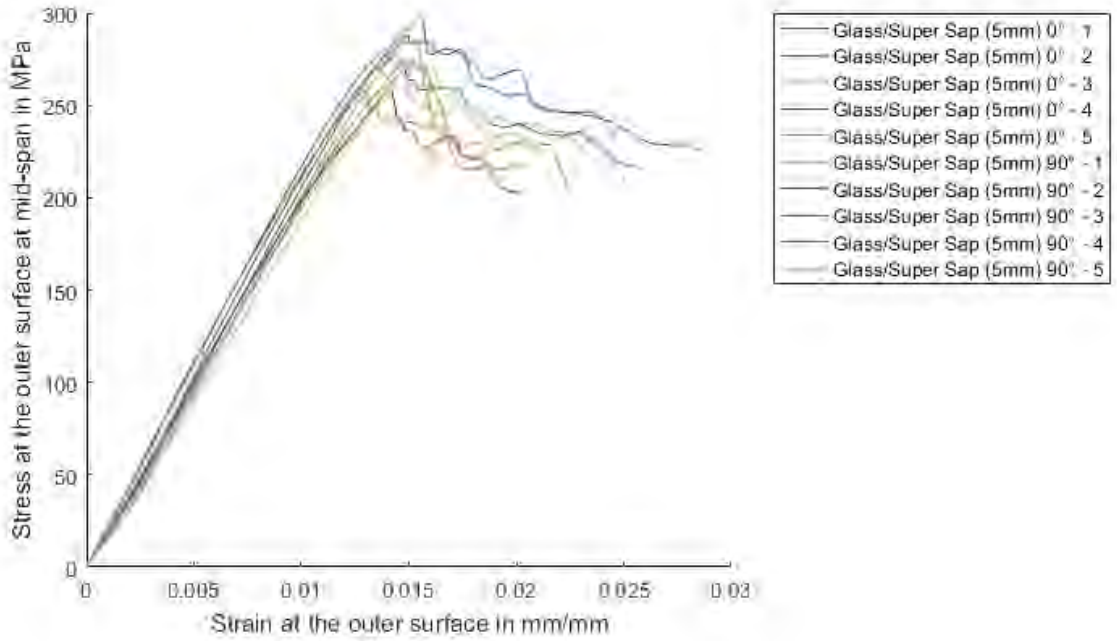

Figure B-3: Plot curves for the flexural stress against strain for Glass 17/Super Sap specimens

Table B-3: Flexural geometry and properties for Glass 17/Super Sap specimens

	h [mm]	w [mm]	L [mm]	σ^f_{max} [MPa]	$\varepsilon^f_{\sigma max}$ [m/m]	E^f_{chord} [MPa]	E^f_{secant} [MPa]	ε^f_{fail} [m/m]
GS5.1-1	5.05	35.07	81	297.22	0.015	19847.98	19276.63	0.019
GS5.1-2	4.92	34.36	79	275.19	0.015	20064.54	18415.00	0.017
GS5.1-3	5.04	35.51	81	274.65	0.015	20659.38	16831.57	0.016
GS5.1-4	5.08	35.62	81	288.10	0.015	22451.40	18846.92	0.021
GS5.1-5	5.09	35.02	81	286.50	0.015	19826.49	18938.63	0.016
GS5.2-1	5.05	30.28	81	268.98	0.015	18978.92	17226.65	0.023
GS5.2-2	5.01	30.02	79	258.09	0.014	20776.44	16702.46	0.018
GS5.2-3	5.00	29.07	79	276.35	0.014	21073.02	19459.68	0.021
GS5.2-4	5.02	30.04	80	258.28	0.013	22356.04	19197.54	0.018
GS5.2-5	5.02	30.44	80	271.88	0.016	17593.45	17403.57	0.019

VI manufactured flax fibre reinforced Super Sap

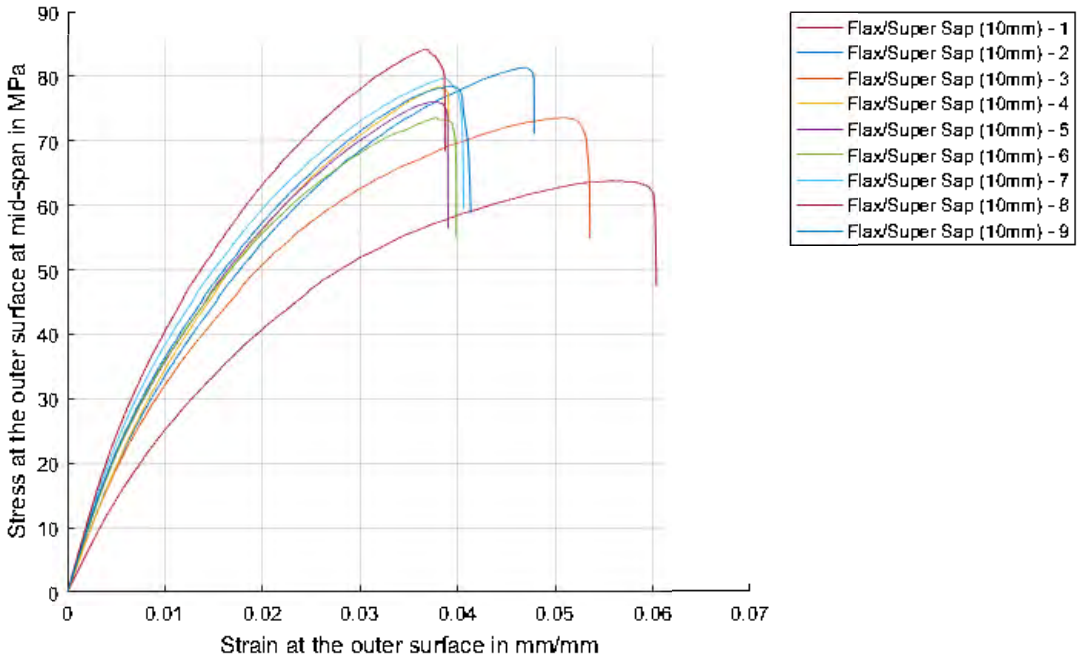

Figure B-4: Plot curves for the flexural stress against strain for VI manufactured Flax 9/Super Sap specimens

Table B-4: Flexural geometry and properties for VI manufactured Flax 9/Super Sap specimens

	h [mm]	w [mm]	L [mm]	σ^f_{max} [MPa]	$\varepsilon^f_{\sigma max}$ [m/m]	E^f_{chord} [MPa]	E^f_{secant} [MPa]	ε^f_{fail} [m/m]
FS10-1	9.89	29.18	158	63.82	0.056	2932.96	330.21	0.060
FS10-2	10.12	29.28	162	81.38	0.047	3854.49	723.68	0.048
FS10-3	9.83	29.49	159	73.64	0.051	3511.83	429.25	0.054
FS10-4	9.94	28.78	159	78.42	0.038	3736.35	1052.48	0.039
FS10-5	9.86	29.88	158	76.06	0.038	4026.76	1016.74	0.039
FS10-6	9.86	29.93	158	73.62	0.038	4108.72	845.44	0.040
FS10-7	9.94	29.64	159	79.70	0.039	4205.21	896.22	0.041
FS10-8	9.97	29.59	159	84.18	0.037	4470.60	1179.76	0.039
FS10-9	9.94	29.83	159	78.52	0.039	4047.82	927.83	0.041

VI manufactured flax fibre reinforced Prime 20LV

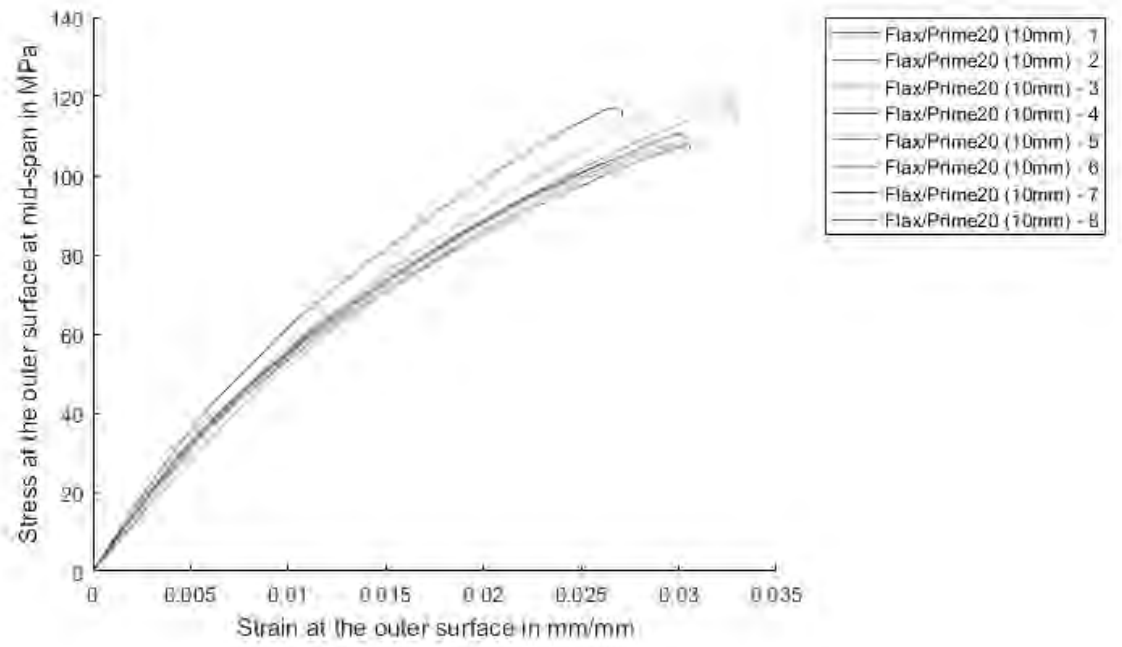

Figure B-5: Plot curves for the flexural stress against strain for VI manufactured Flax 9/Prime 20LV specimens

Table B-5: Flexural geometry and properties for VI manufactured Flax 9/Prime 20LV specimens

	h [mm]	w [mm]	L [mm]	σ^f_{max} [MPa]	$\varepsilon^f_{\sigma max}$ [m/m]	E^f_{chord} [MPa]	E^f_{secant} [MPa]	ε^f_{fail} [m/m]
FP10-1	9.86	23.89	158	107.91	0.031	6327.60	2150.70	0.031
FP10-2	9.88	23.78	158	117.81	0.033	6320.78	2088.97	0.033
FP10-3	9.75	24.27	156	108.40	0.030	6492.04	2132.51	0.030
FP10-4	9.89	23.75	158	110.66	0.030	6538.10	2149.71	0.030
FP10-5	9.74	24.00	156	121.83	0.032	6744.06	2225.31	0.032
FP10-6	9.76	24.02	156	107.73	0.029	5614.75	2398.09	0.030
FP10-7	9.69	24.25	155	117.26	0.027	7247.14	2898.10	0.027
FP10-8	9.91	23.71	158	103.09	0.026	6712.61	2410.93	0.026

Hand lay-up flax fibre reinforced Prime 20LV

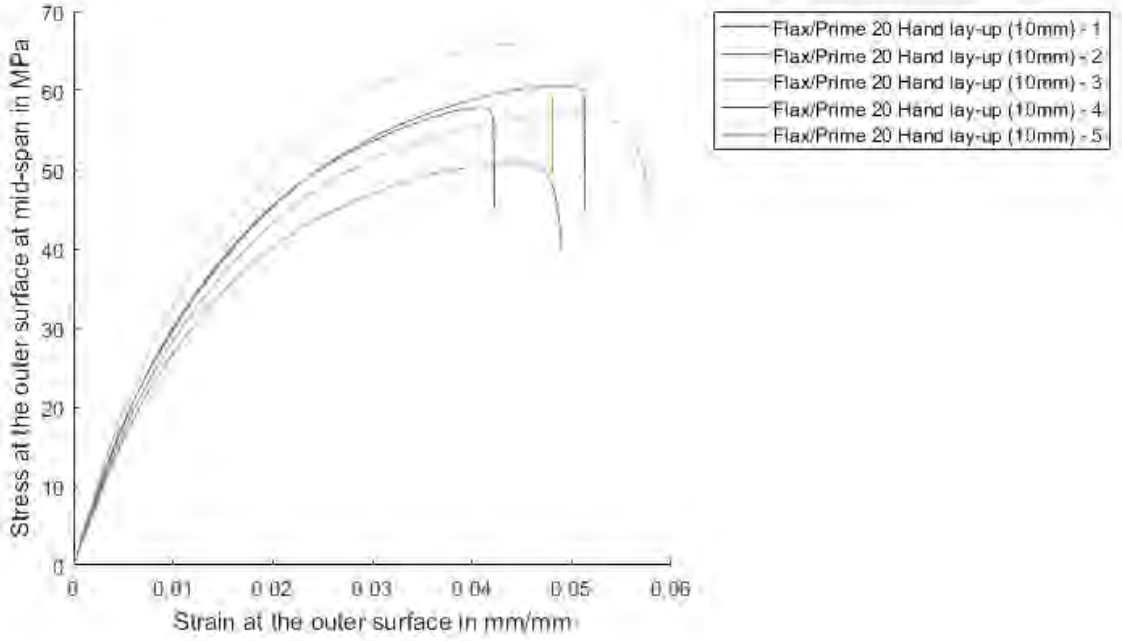

Figure B-6: Plot curves for the flexural stress against strain for hand lay-up Flax 8/Prime 20LV specimens

Table B-6: Flexural geometry and properties for hand lay-up Flax 8/Prime 20LV specimens

	h [mm]	w [mm]	L [mm]	σ^f_{max} [MPa]	$\varepsilon^f_{\sigma max}$ [m/m]	E^f_{chord} [MPa]	E^f_{secant} [MPa]	ε^f_{fail} [m/m]
FP10H.4-1	9.66	33.68	154	57.83	0.0412	3472.53	441.54	0.042
FP10H.4-2	9.74	33.57	156	50.97	0.0441	3133.79	263.13	0.049
FP10H.4-3	9.61	33.48	154	65.90	0.0435	3778.48	447.07	0.048
FP10H.4-4	9.84	33.45	158	60.60	0.0491	3481.40	255.27	0.051
FP10H.4-5	9.75	33.97	156	57.12	0.0500	3322.28	256.65	0.057

Jute fibre reinforced Prime 20LV

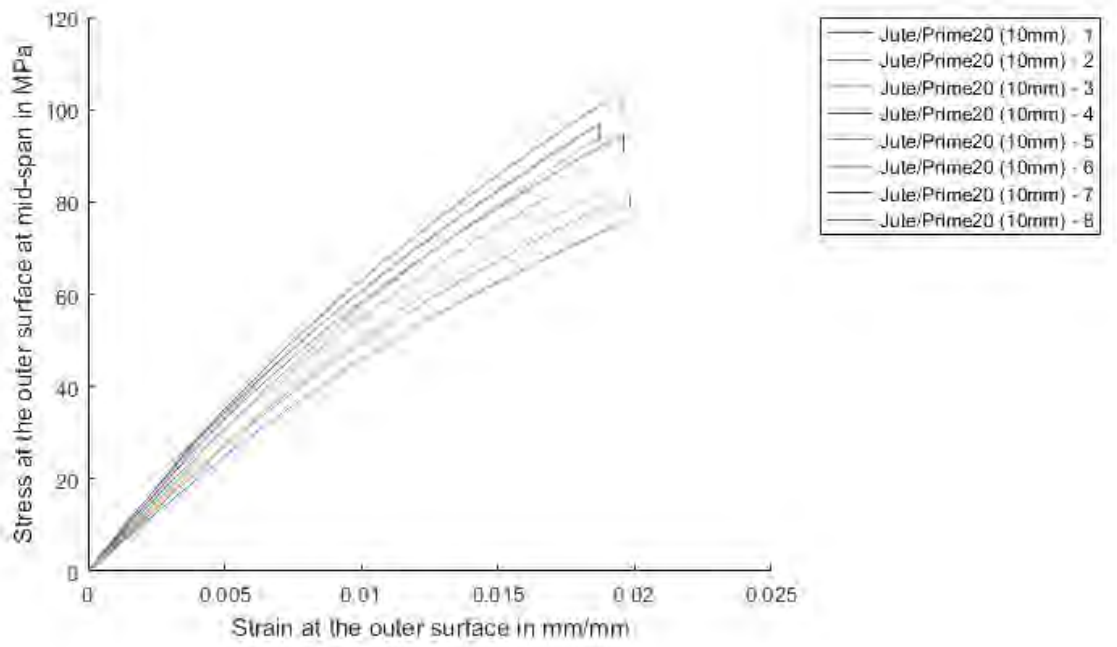

Figure B-7: Plot curves for the flexural stress against strain for Jute 13/Prime 20LV specimens

Table B-7: Flexural geometry and properties for Jute 13/Prime 20LV specimens

	h [mm]	w [mm]	L [mm]	σ^f_{max} [MPa]	$\varepsilon^f_{\sigma max}$ [m/m]	E^f_{chord} [MPa]	E^f_{secant} [MPa]	ε^f_{fail} [m/m]
JP10-1	9.97	36.17	159	76.64	0.020	4959.96	3089.91	0.020
JP10-2	9.87	35.91	158	81.38	0.020	5338.60	3318.72	0.020
JP10-3	9.93	36.09	159	81.56	0.019	5459.87	3809.22	0.019
JP10-4	9.87	36.07	158	94.66	0.020	6717.67	3872.76	0.020
JP10-5	10.01	36.17	160	82.47	0.017	6297.76	4101.49	0.017
JP10-6	9.85	36.16	158	93.57	0.019	6250.36	4391.30	0.019
JP10-7	9.87	36.10	158	96.84	0.019	6956.04	4293.38	0.019
JP10-8	9.88	36.17	158	103.97	0.020	7164.27	4352.45	0.020

Supawood 16mm board

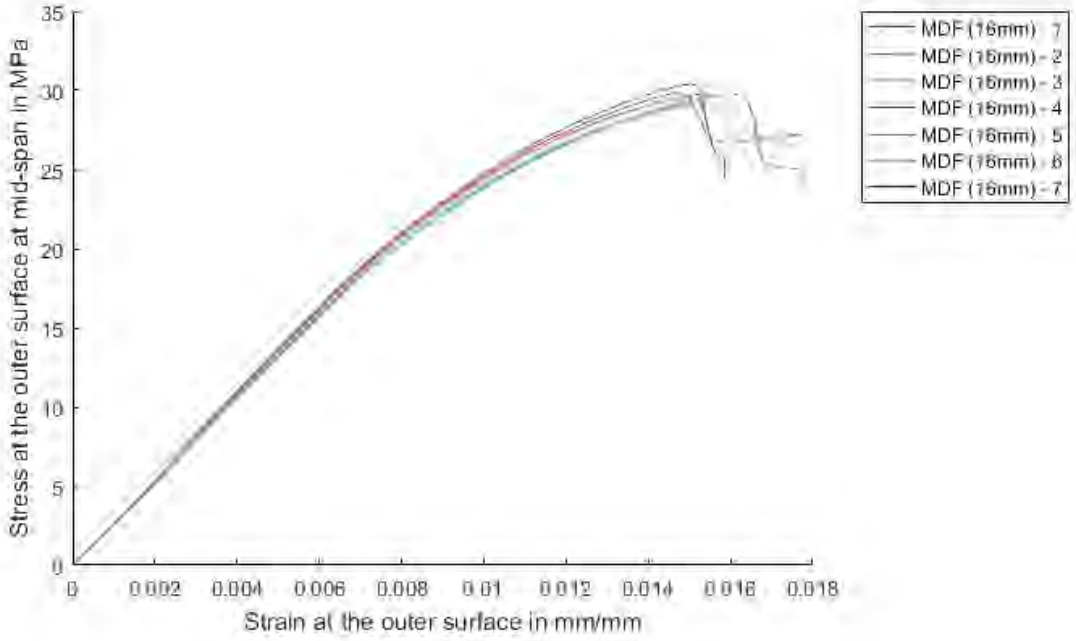

Figure B-8: Plot curves for the flexural stress against strain for Supawood 16mm specimens

Table B-8: Flexural geometry and properties for Supawood 16mm specimens

	h [mm]	w [mm]	L [mm]	σ^f_{max} [MPa]	$\varepsilon^f_{\sigma max}$ [m/m]	E^f_{chord} [MPa]	E^f_{secant} [MPa]	ε^f_{fail} [m/m]
MD16-1	16.19	55.17	260	29.74	0.016	2745.21	1610.96	0.017
MD16-2	16.06	54.91	258	29.83	0.015	2800.59	1697.27	0.016
MD16-3	16.05	55.00	258	29.43	0.015	2796.10	1788.97	0.018
MD16-4	16.08	55.05	258	29.83	0.015	2818.09	1912.19	0.018
MD16-5	16.03	54.27	258	29.13	0.015	2784.49	1740.29	0.016
MD16-6	16.13	54.41	258	29.17	0.015	2761.13	1729.98	0.015
MD16-7	16.09	54.89	258	30.39	0.015	2832.61	1868.36	0.016

B.2 Tensile test algorithm flow chart

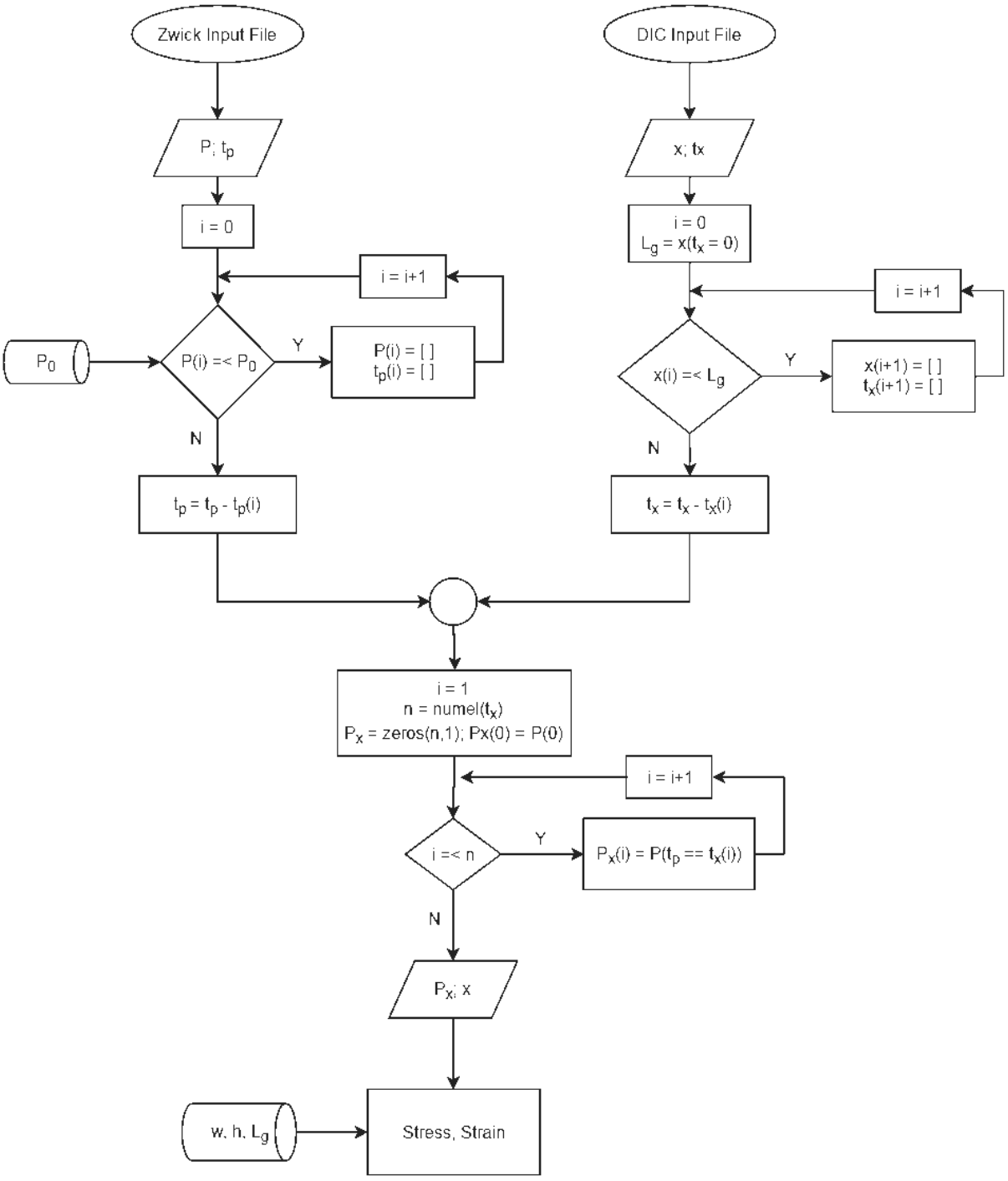

B.3 Experimental tensile test results

Glass fibre reinforced Super Sap

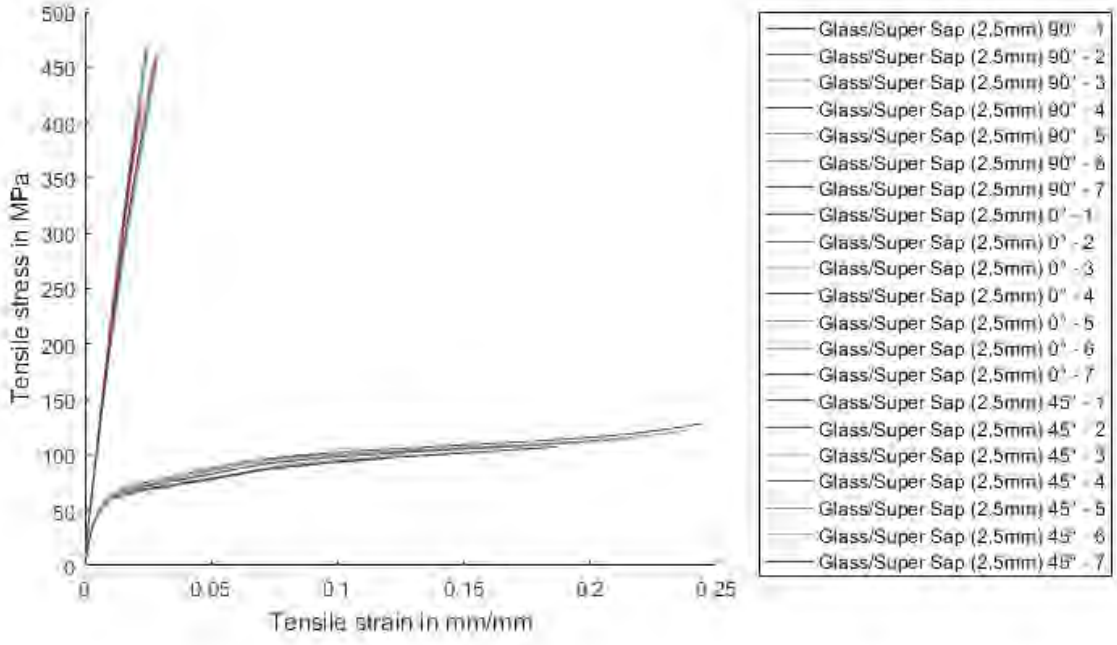

Figure B-9: Plot curves for the tensile stress against strain for glass reinforced Super Sap composites

Table B-9: Tensile geometry and properties for glass fibre reinforced Super Sap composites

	h [mm]	w [mm]	E [MPa]	σ_Y [MPa]	$\sigma_{0.2Y}$ [MPa]	σ_U [MPa]	ε_{fail} [m/m]	Failure Code
GSS_90-1	2.47	26.32	30362.1	257.85	448.02	467.67	0.025	XWT
GSS_90-2	2.65	26.72	29706.6	189.12	389.41	420.01	0.024	MWB
GSS_90-3	2.49	26.41	30019.9	214.39	411.30	457.05	0.025	AWT
GSS_90-4	2.48	26.37	29028.6	239.85		443.34	0.024	AWB
GSS_90-5	2.48	26.44	30668.8	216.70	432.10	468.41	0.025	AWB
GSS_90-6	2.47	26.44	29396.9			449.47	0.010	LWT
GSS_90-7	2.50	25.98	26907.6	225.34	413.53	413.68	0.022	AAB
GSS_0-1	2.48	26.21	27841.3	211.54	339.99	427.69	0.027	A(X)WT
GSS_0-2	2.50	26.36	30472.5	193.97	329.65	462.40	0.029	LGB
GSS_0-3	2.49	26.32	29221.2	209.27		445.87	0.028	LGT
GSS_0-4	2.50	26.42	29603.8	211.64	328.21	448.26	0.028	AWB
GSS_0-5	2.53	26.46	29891.4	217.29		445.93	0.017	LGM
GSS_0-6	2.52	26.36	29942.3	219.90	350.33	451.29	0.029	MGM
GSS_0-7	2.46	26.34	29991.6	238.22	358.05	463.49	0.028	LGM
GSS_45-1	2.44	26.30	9609.2	48.07	58.21	149.76	>0.244	AWT
GSS_45-2	2.57	25.92	9560.3	44.40	53.03	143.35	>0.117	LWT
GSS_45-3	2.54	26.21	9673.2	46.36	55.81	145.49	>0.219	LWB
GSS_45-4	2.50	26.29	9870.5	46.87	56.15	150.36	>0.198	AGB
GSS_45-5	2.53	26.20	9215.7	45.82	56.12	138.85	>0.239	AWB
GSS_45-6	2.52	26.38	9934.0	44.92	54.09	149.24	>0.125	LWB
GSS_45-7	2.54	26.22	10016.0	44.81	54.19	150.59	>0.186	AGT

VI manufactured flax fibre reinforced Super Sap

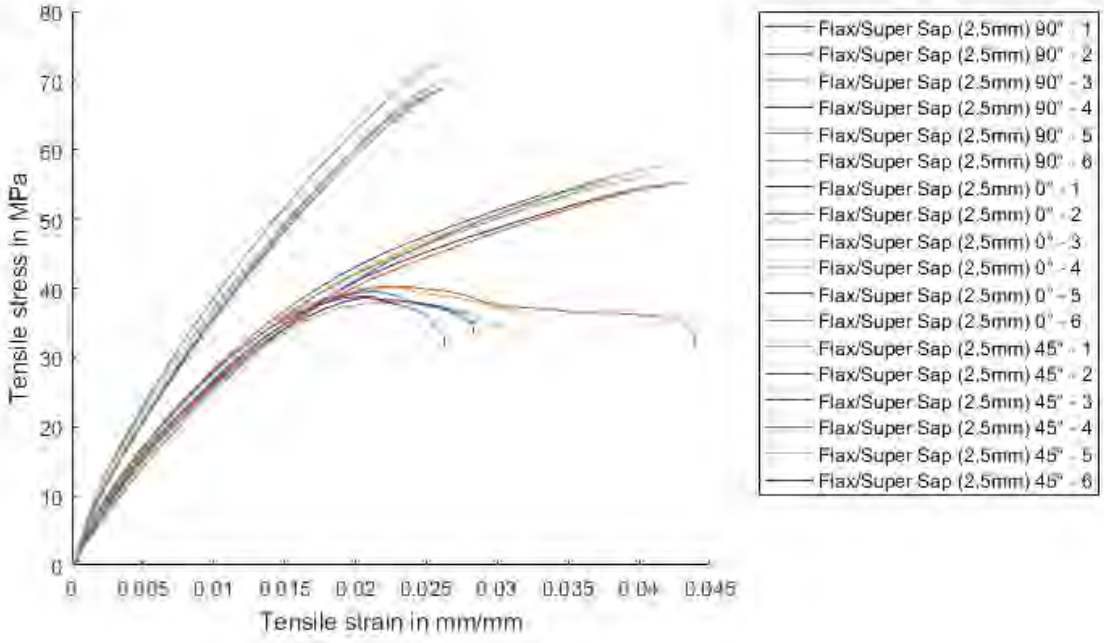

Figure B-10: Plot curves for the tensile stress against strain for flax reinforced Super Sap composites

Table B-10: Tensile geometry and properties for flax fibre reinforced Super Sap composites

	h [mm]	w [mm]	E [MPa]	σ_Y [MPa]	$\sigma_{0.2Y}$ [MPa]	σ_U [MPa]	ε_{fail} [m/m]	Failure Code
FSS_90-1	2.40	26.39	3764.97	32.38	50.71	72.81	0.027	LWB
FSS_90-2	2.51	26.00	3709.85	31.39	49.78	68.64	0.025	LGM
FSS_90-3	2.46	26.44	3575.56	31.42	48.92	70.08	0.027	LIB
FSS_90-4	2.46	26.51	3633.66	31.62	48.90	68.83	0.027	LGB
FSS_90-5	2.46	26.46	3633.81	30.98	48.64	67.60	0.025	LIB
FSS_90-6	2.51	26.40	3598.35	31.19	48.31	67.36	0.026	LAT
FSS_0-1	2.48	26.47	2948.92	20.44	30.78	54.66	0.042	LWB
FSS_0-2	2.50	26.27	2701.89	18.42	32.18	56.99	0.038	LAT
FSS_0-3	2.51	26.29	2920.61	20.04	30.08	55.23	0.044	LWB
FSS_0-4	2.41	26.42	3039.95	21.53	32.01	57.64	0.042	LGT
FSS_0-5	2.37	26.41	3085.68	22.10	32.66	53.40	0.033	LGB
FSS_0-6	2.41	26.43	2984.48	21.32	31.33	55.85	0.041	LGT
FSS_45-1	2.47	26.29	2801.63	19.23	30.18	38.02	0.035	LGM
FSS_45-2	2.49	26.28	2852.75	19.27	30.86	38.59	0.029	AWB
FSS_45-3	2.42	26.38	2853.56	19.41	31.24	39.48	0.030	AGT
FSS_45-4	2.44	26.20	2879.82	20.25	31.69	40.29	0.044	AAT
FSS_45-5	2.37	26.32	2915.35	19.52	31.45	40.12	0.035	LWB
FSS_45-6	2.46	26.33	2907.36	20.36	31.26	38.85	0.026	LWB

VI manufactured flax fibre reinforced Prime 20LV

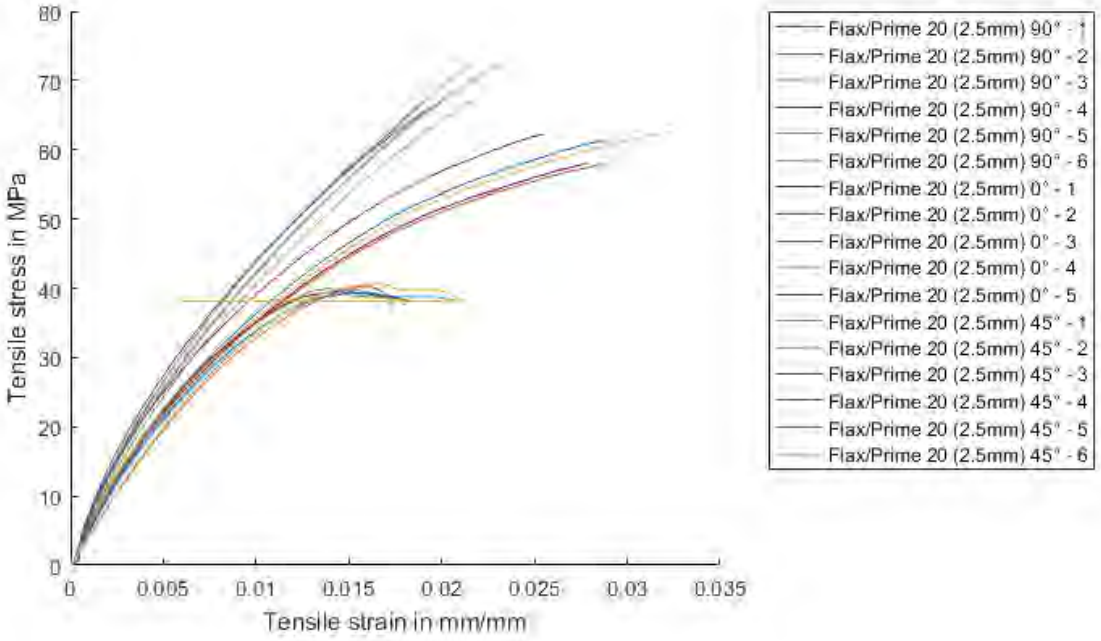

Figure B-11: Plot curves for the tensile stress against strain for VI manufactured flax reinforced Prime 20LV composites

Table B-11: Tensile geometry and properties for VI manufactured flax fibre reinforced Prime 20LV composites

	h [mm]	w [mm]	E [MPa]	σ_Y [MPa]	$\sigma_{0.2Y}$ [MPa]	σ_U [MPa]	ε_{fail} [m/m]	Failure Code
FP20_90-1	2.31	26.17	4690.3	34.69		72.09	0.022	LWB
FP20_90-2	2.34	26.31	4466.6	32.60	50.38	72.70	0.023	LGB
FP20_90-3	2.39	26.47	4716.3	34.71	51.57	71.88	0.022	LWB
FP20_90-4	2.35	26.40	4532.2	33.56	49.70	66.38	0.021	LWT
FP20_90-5	2.44	26.21	4398.0	31.92	48.05	67.04	0.022	LGB
FP20_90-6	2.37	26.40	4528.7	33.07	50.07	69.22	0.021	LWB
FP20_0-1	2.36	26.25	3966.0	27.49	38.79	58.05	0.028	LGT
FP20_0-2	2.29	26.12	4096.9	28.16	40.24	61.42	0.029	LWB
FP20_0-3	2.35	26.06	3918.4	27.11	38.36	57.94	0.029	LWB
FP20_0-4	2.35	26.09	4042.1	27.29	39.12	62.59	0.033	LGM
FP20_0-5	2.34	26.05	4380.3	30.91	42.46	62.20	0.026	LGB
FP20_45-1	2.44	26.39	3987.0	26.89	36.76	39.97	0.022	LGB
FP20_45-2	2.48	26.24	3847.4	23.73	35.51	39.80	0.023	LAB
FP20_45-3	2.45	26.43	4242.0	22.92	35.16	39.58	0.021	LGB
FP20_45-4	2.48	26.30	3694.5	22.99	34.88	39.31	0.021	LWB
FP20_45-5	2.39	26.41	3748.1	20.86	34.81	40.36	0.022	LWT
FP20_45-6	2.43	26.28	3753.7	20.48	35.54	40.61	0.021	LWT

Hand lay-up flax fibre reinforced Prime 20LV

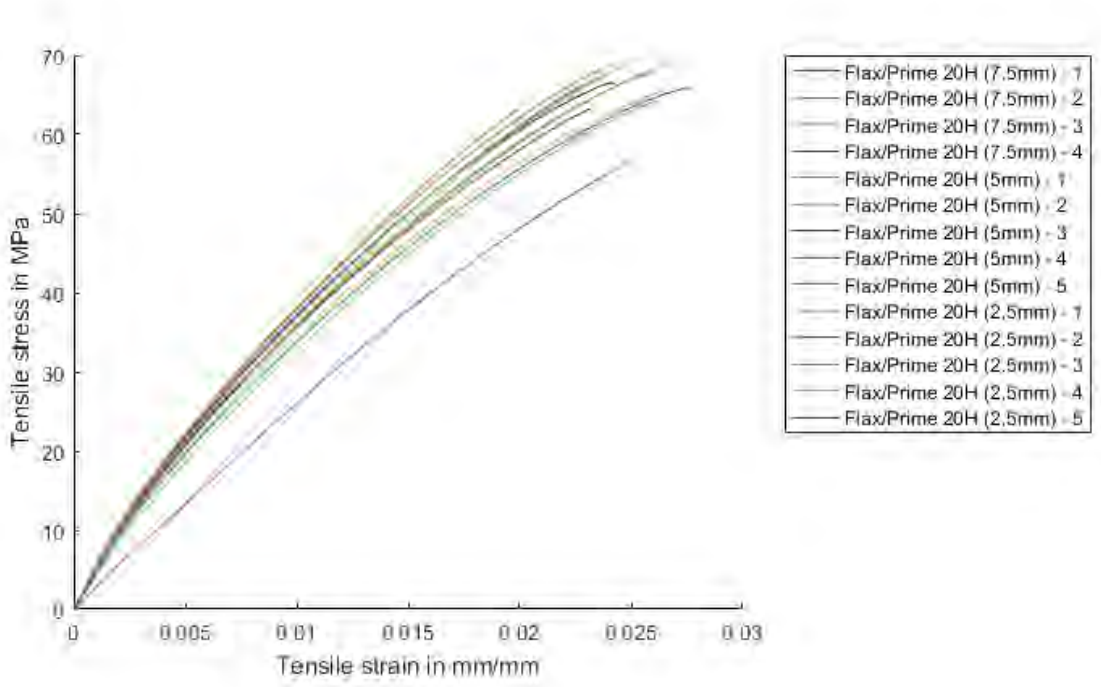

Figure B-12: Plot curves for the tensile stress against strain for hand lay-up flax reinforced Prime 20LV composites

Table B-12: Tensile geometry and properties for hand lay-up flax fibre reinforced Prime 20LV composites

	h [mm]	w [mm]	E [MPa]	σ_Y [MPa]	$\sigma_{0.2Y}$ [MPa]	σ_U [MPa]	ε_{fail} [m/m]	Failure Code
FP20(h)_7.5-1	7.41	29.94	3814.4	28.81	47.98	66.38	0.023	LWT
FP20(h)_7.5-2	7.58	29.88	3844.1	27.89	49.92	63.27	0.020	LGT
FP20(h)_7.5-3	7.34	29.89	3755.6	29.76	48.80	67.47	0.024	LGT
FP20(h)_7.5-4	7.32	29.83	3899.3	28.89	47.53	62.32	0.021	LGT
FP20(h)_5-1	5.02	25.43	3805.2	27.45	45.61	67.82	0.026	LGM
FP20(h)_5-2	4.99	25.34	3480.2	24.56	43.49	64.31	0.027	LGB
FP20(h)_5-3	4.98	25.43	3910.8	29.16	47.23	66.56	0.024	LWB
FP20(h)_5-4	5.03	25.28	3599.1	26.45	43.37	65.78	0.028	LWT
FP20(h)_5-5	5.05	25.31	4004.3	28.72	48.06	68.95	0.025	LWT
FP20(h)_2.5-1	2.61	25.36	3706.1	25.95	43.29	65.72	0.027	LGT
FP20(h)_2.5-2	2.62	25.36	2514.2	38.25	54.50	63.50	0.025	LGT
FP20(h)_2.5-3	2.54	25.32	3906.0	25.24	44.09	69.32	0.028	LGM
FP20(h)_2.5-4	2.51	25.36	3980.0	27.75	46.72	69.40	0.026	LWB
FP20(h)_2.5-5	2.62	25.01	3830.8	25.41	43.42	63.18	0.024	LWB

Jute fibre reinforced Prime 20LV

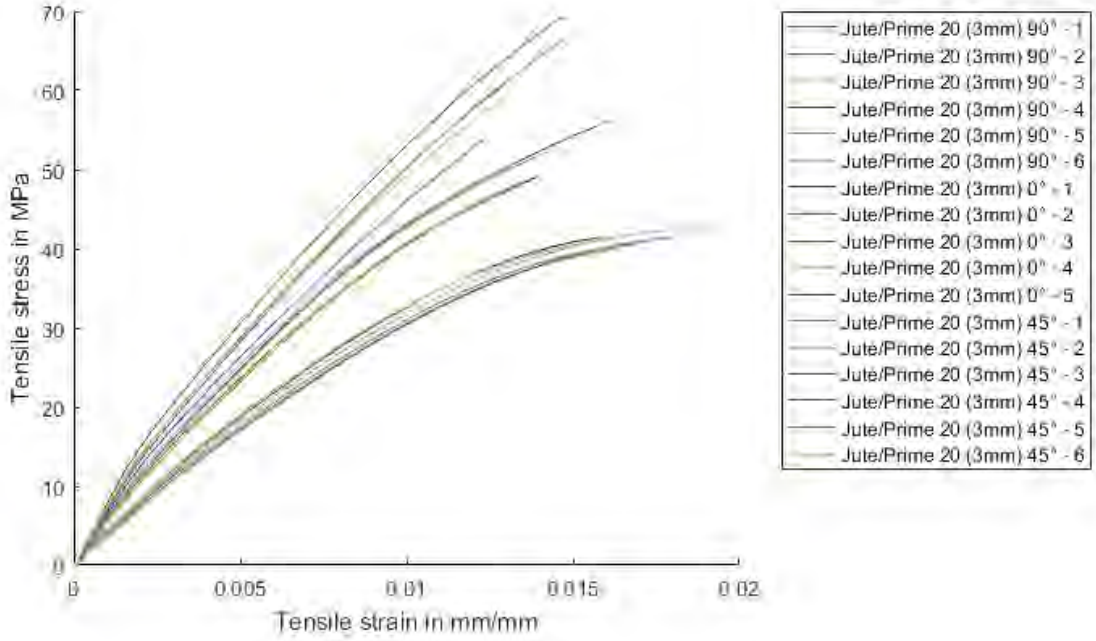

Figure B-13: Plot curves for the tensile stress against strain for jute reinforced Prime 20LV composites

Table B-13: Tensile geometry and properties for jute fibre reinforced Prime 20LV composites

	h [mm]	w [mm]	E [MPa]	σ_Y [MPa]	$\sigma_{0.2Y}$ [MPa]	σ_U [MPa]	ε_{fail} [m/m]	Failure Code
JP20_90-1	3.17	25.59	5358.8	10.56	36.80	49.08	0.014	LAB
JP20_90-2	3.10	25.16	5243.3	9.84	38.01	49.27	0.014	LAB
JP20_90-3	3.28	25.58	5133.7	11.41	39.47	47.46	0.013	LAB
JP20_90-4	3.16	24.48	5672.6	11.28	39.78	56.15	0.016	LWT
JP20_90-5	3.19	24.37	5502.5	11.04	39.86	52.36	0.015	LWT
JP20_90-6	3.21	25.01	5724.1	10.97		50.81	0.013	LAT
JP20_0-1	3.10	24.31	6810.4	12.21	44.06	69.53	0.016	LAB
JP20_0-2	3.23	24.18	6506.3	11.84	44.94	66.57	0.015	LAT
JP20_0-3	3.30	24.38	6653.0	13.34	43.72	60.81	0.013	LWB
JP20_0-4	3.27	24.66	6510.0	12.74	41.16	58.95	0.013	LAB
JP20_0-5	3.39	24.66	6137.4	12.98	40.22	53.80	0.013	LGM
JP20_45-1	3.21	24.29	3594.8	10.95	32.54	39.99	0.017	AWB
JP20_45-2	3.14	24.37	4003.1	8.57	30.90	42.67	0.020	AWT
JP20_45-3	3.12	24.41	4169.6	9.00	30.92	41.38	0.016	AWB
JP20_45-4	3.17	24.21	3700.6	8.66	31.49	41.51	0.018	LAB
JP20_45-5	3.23	24.33	3835.8	9.62	30.77	40.55	0.017	AGB
JP20_45-6	3.12	24.41	3760.8	10.35	32.81	41.38	0.017	AWT

Supawood

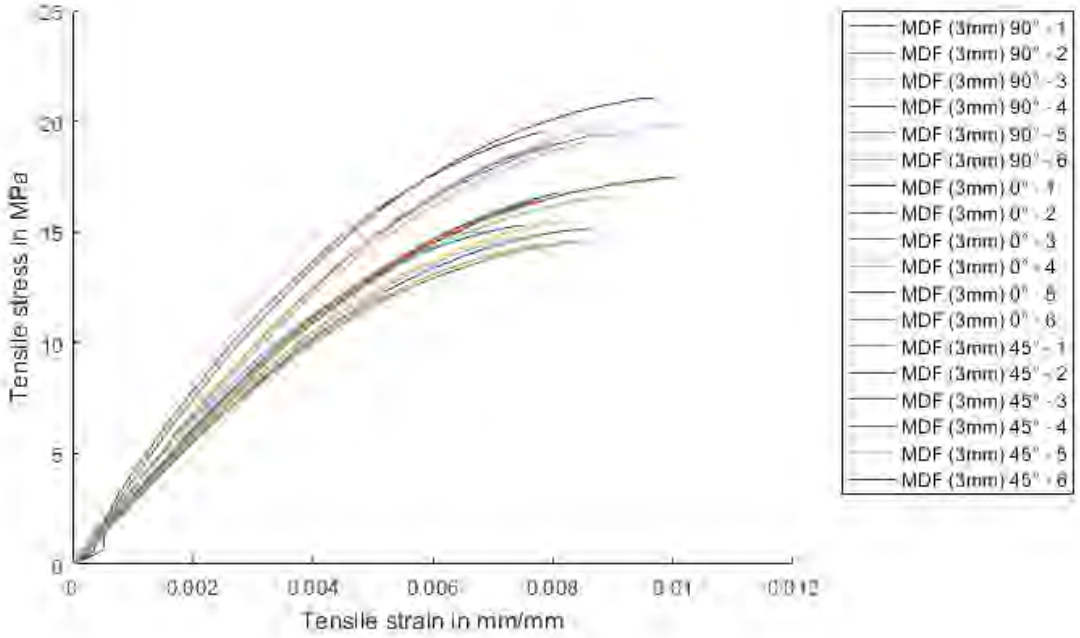

Figure B-14: Plot curves for the tensile stress against strain for 3 mm Supawood

Table B-14: Tensile geometry and properties for 3 mm Supawood

	h [mm]	w [mm]	E [MPa]	σ_Y [MPa]	$\sigma_{0.2Y}$ [MPa]	σ_U [MPa]	ε_{fail} [m/m]	Failure Code
MDF3_90-1	3.11	25.16	2792.5	7.03	14.77	15.29	0.008	LGM
MDF3_90-2	3.10	24.85	2689.5	7.03	13.89	14.62	0.009	LGM
MDF3_90-3	3.10	25.06	2866.6	6.57	14.86	15.53	0.009	LGT
MDF3_90-4	3.09	25.18	2765.4	6.66	14.45	15.12	0.009	LGB
MDF3_90-5	3.09	24.98	2735.7	7.10	14.06	14.39	0.008	LWT
MDF3_90-6	3.09	25.03	2836.7	6.77	14.59	14.82	0.008	AGM
MDF3_0-1	3.12	24.87	2904.2	7.40	16.12	17.45	0.010	LGB
MDF3_0-2	3.11	24.94	2967.6	7.55	16.24	16.76	0.008	LAB
MDF3_0-3	3.11	24.88	2993.2	6.78	15.95	17.31	0.010	LGB
MDF3_0-4	3.12	24.87	2919.5	7.65	16.17	16.47	0.008	LWT
MDF3_0-5	3.11	24.91	3021.3	6.83	16.02	16.34	0.008	LGM
MDF3_0-6	3.11	24.83	2921.4	7.41	15.67	16.55	0.009	AGM
MDF3_45-1	3.10	25.02	3223.8	8.00	18.21	19.87	0.010	LGT
MDF3_45-2	3.10	24.98	3362.3	9.06	18.74	19.52	0.009	LWT
MDF3_45-3	3.10	24.87	3317.6	8.68	18.61	18.89	0.008	AAT
MDF3_45-4	3.09	24.93	3320.4	8.11	18.37	19.42	0.009	LGT
MDF3_45-5	3.10	24.94	3337.6	8.20	18.70	19.66	0.009	LAT
MDF3_45-6	3.10	24.84	3418.5	8.05	19.28	21.03	0.010	LWB

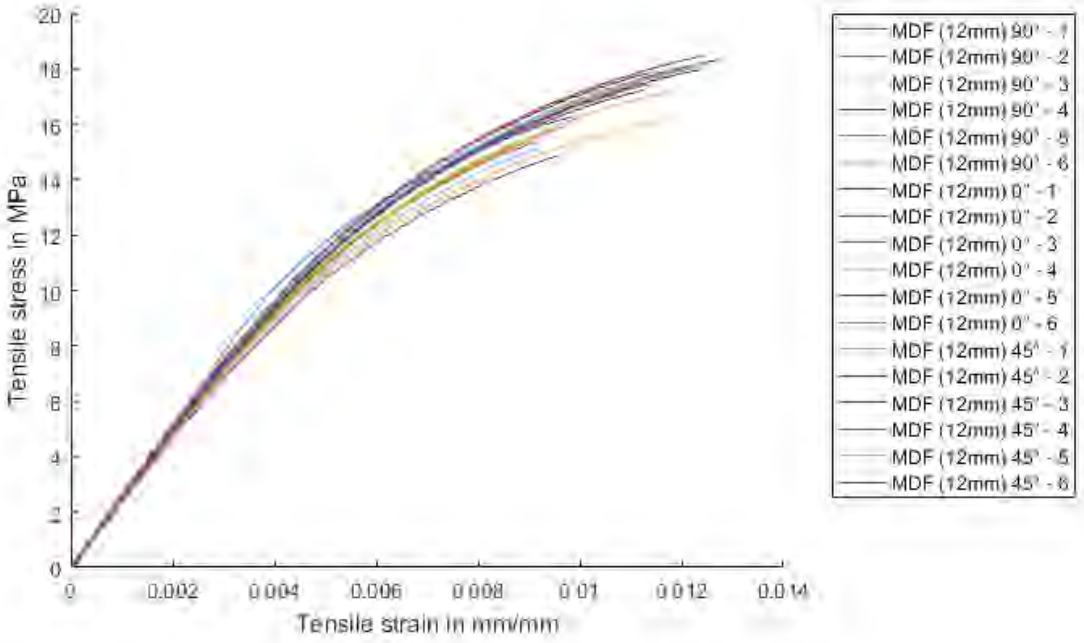

Figure B-15: Plot curves for the tensile stress against strain for 12 mm Supawood

Table B-15: Tensile geometry and properties for 12 mm Supawood

	h [mm]	w [mm]	E [MPa]	σ_Y [MPa]	$\sigma_{0.2Y}$ [MPa]	σ_U [MPa]	ε_{fail} [m/m]	Failure Code
MDF12_90-1	12.20	24.91	2531.8	10.17	15.01	16.32	0.010	LGM
MDF12_90-2	12.15	24.92	2390.7	7.48	14.51	15.35	0.009	LGM
MDF12_90-3	12.12	24.87	2327.8	7.52	13.90	16.23	0.012	LWT
MDF12_90-4	12.10	24.69	2333.9	6.49	13.51	14.95	0.010	LGM
MDF12_90-5	12.15	24.67	2485.8	6.49	14.54	15.80	0.009	LGM
MDF12_90-6	12.15	24.70	2404.7	6.59	14.05	15.09	0.009	LGM
MDF12_0-1	12.16	24.76	2556.3	7.69	15.38	17.87	0.011	LGM
MDF12_0-2	12.18	24.76	2549.8	6.77	15.10	18.34	0.013	LAT
MDF12_0-3	12.16	24.94	2479.7	7.23	15.03	17.43	0.011	LWB
MDF12_0-4	12.15	24.80	2477.8	8.31	15.33	18.23	0.013	LGM
MDF12_0-5	12.15	24.69	2552.8	6.94	15.50	18.49	0.012	LGB
MDF12_0-6	12.19	24.93	2501.9	6.92	15.13	17.35	0.011	LGM
MDF12_45-1	12.16	24.37	2509.8	7.81	15.17	18.12	0.012	LAT
MDF12_45-2	12.15	24.61	2461.4	8.31	15.25	17.98	0.012	LGM
MDF12_45-3	12.14	24.70	2445.1	8.17	15.29	16.50	0.010	LGB
MDF12_45-4	12.15	24.86	2390.2	8.12	14.68	15.93	0.010	LAB
MDF12_45-5	12.16	24.75	2402.0	7.19	14.77	17.27	0.012	LWT
MDF12_45-6	12.15	27.73	2443.3	8.54	15.17	17.25	0.011	LWB

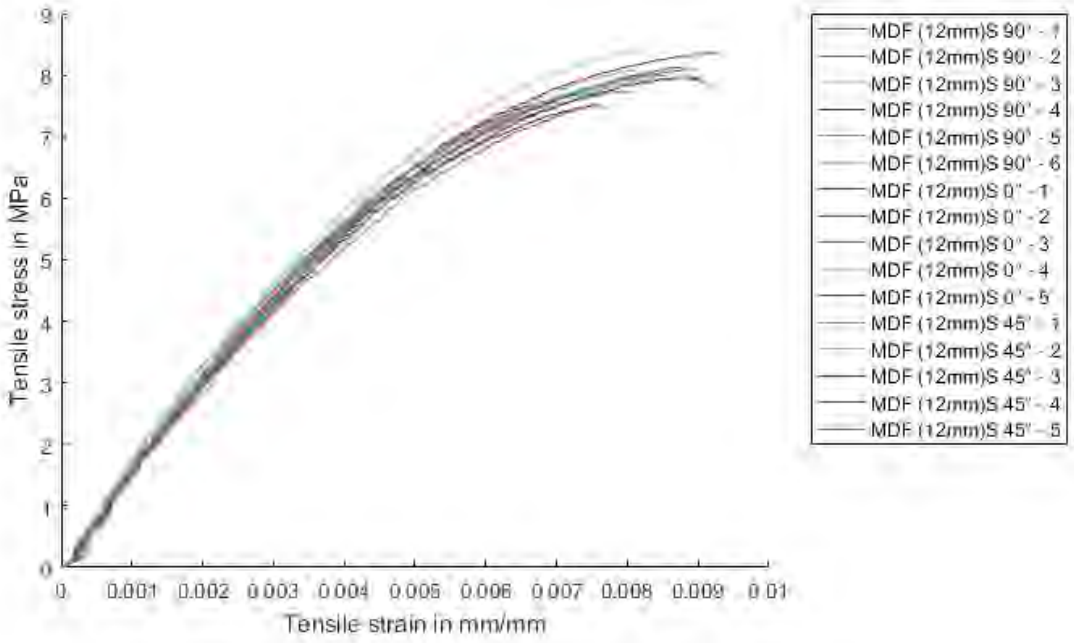

Figure B-16: Plot curves for the tensile stress against strain for shaven 12 mm Supawood

Table B-16: Tensile geometry and properties for shaven 12 mm Supawood

	h [mm]	w [mm]	E [MPa]	σ_Y [MPa]	$\sigma_{0.2Y}$ [MPa]	σ_U [MPa]	ε_{fail} [m/m]	Failure Code
MDF12(s)_90-1	12.05	25.01	1491.7	4.84	7.64	8.13	0.0088	LWT
MDF12(s)_90-2	12.41	24.70	1491.3	4.22	7.63	8.08	0.0090	LWB
MDF12(s)_90-3	12.18	24.82	1522.8	4.53	7.77	8.07	0.0082	LWT
MDF12(s)_90-4	12.35	24.83	1568.9	3.79	7.74	8.36	0.0094	LWT
MDF12(s)_90-5	12.04	24.72	1673.6	3.72	7.35	8.00	0.0086	LGT
MDF12(s)_90-6	12.09	24.61	1711.5	3.22	7.81	8.39	0.0083	LWT
MDF12(s)_0-1	12.20	24.94	1496.5	3.50	7.35	7.50	0.0078	LWB
MDF12(s)_0-2	12.07	24.68	1602.0	3.89		7.07	0.0056	LAB
MDF12(s)_0-3	12.20	24.84	1526.3	4.03	7.45	7.73	0.0081	LGT
MDF12(s)_0-4	11.89	24.88	1555.3	3.95		7.40	0.0066	LWB
MDF12(s)_0-5	12.01	24.83	1563.2	4.07	7.54	7.55	0.0067	LWB
MDF12(s)_45-1	12.09	25.16	1526.5	4.95	7.62	7.83	0.0076	LAB
MDF12(s)_45-2	12.33	25.02	1486.0	3.76	7.53	7.94	0.0085	LWB
MDF12(s)_45-3	12.17	24.84	1527.5	3.50	7.44	7.96	0.0093	LGB
MDF12(s)_45-4	11.98	24.90	1562.8	3.02	7.51	7.70	0.0075	LGB
MDF12(s)_45-5	11.95	25.00	1428.2	4.11	7.40	7.52	0.0076	LWT

Appendix C Outstanding GFRP blast images

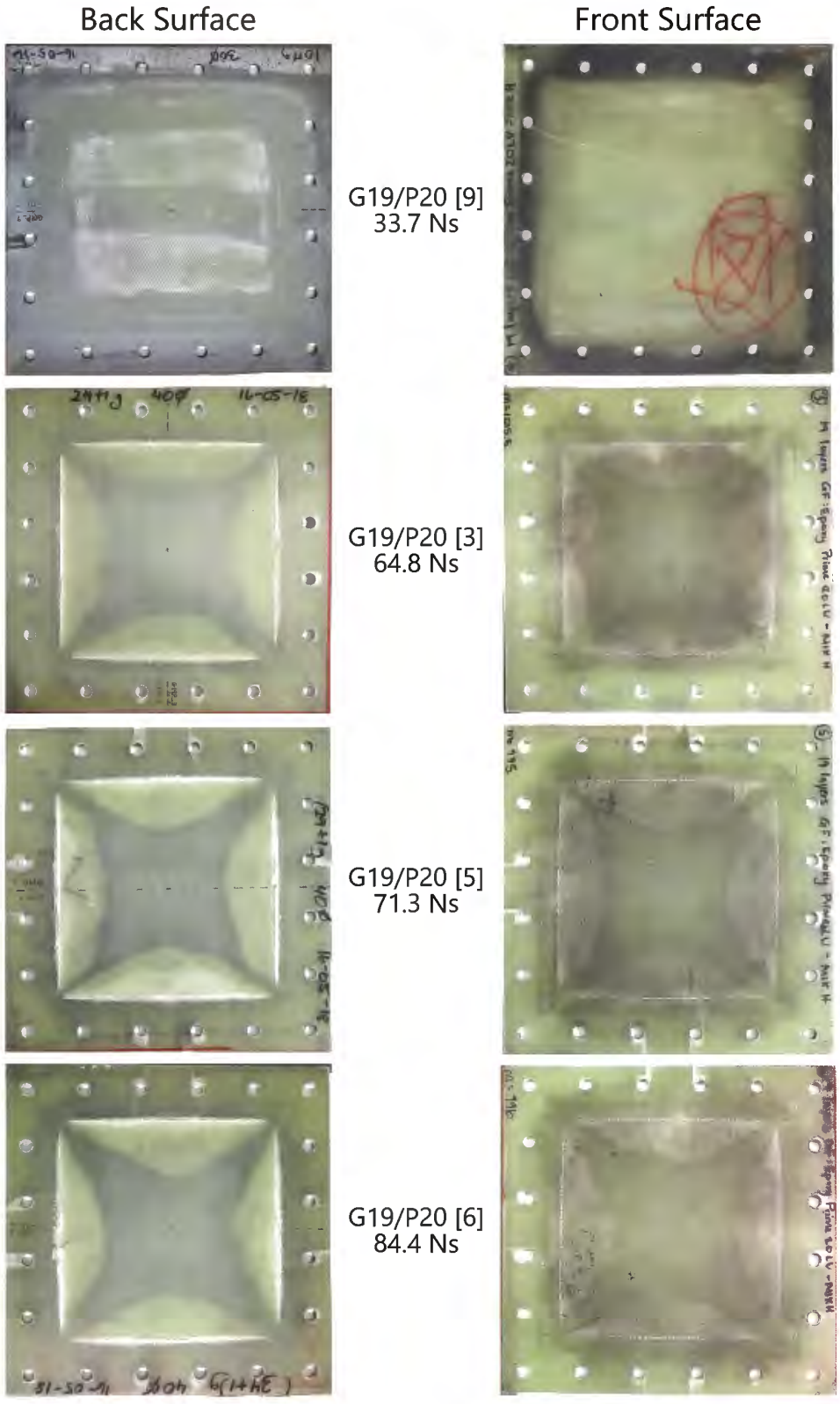

Figure C-1: Outstanding photographs of the front and back surfaces of different blast tested Glass 19/Prime 20LVpanels

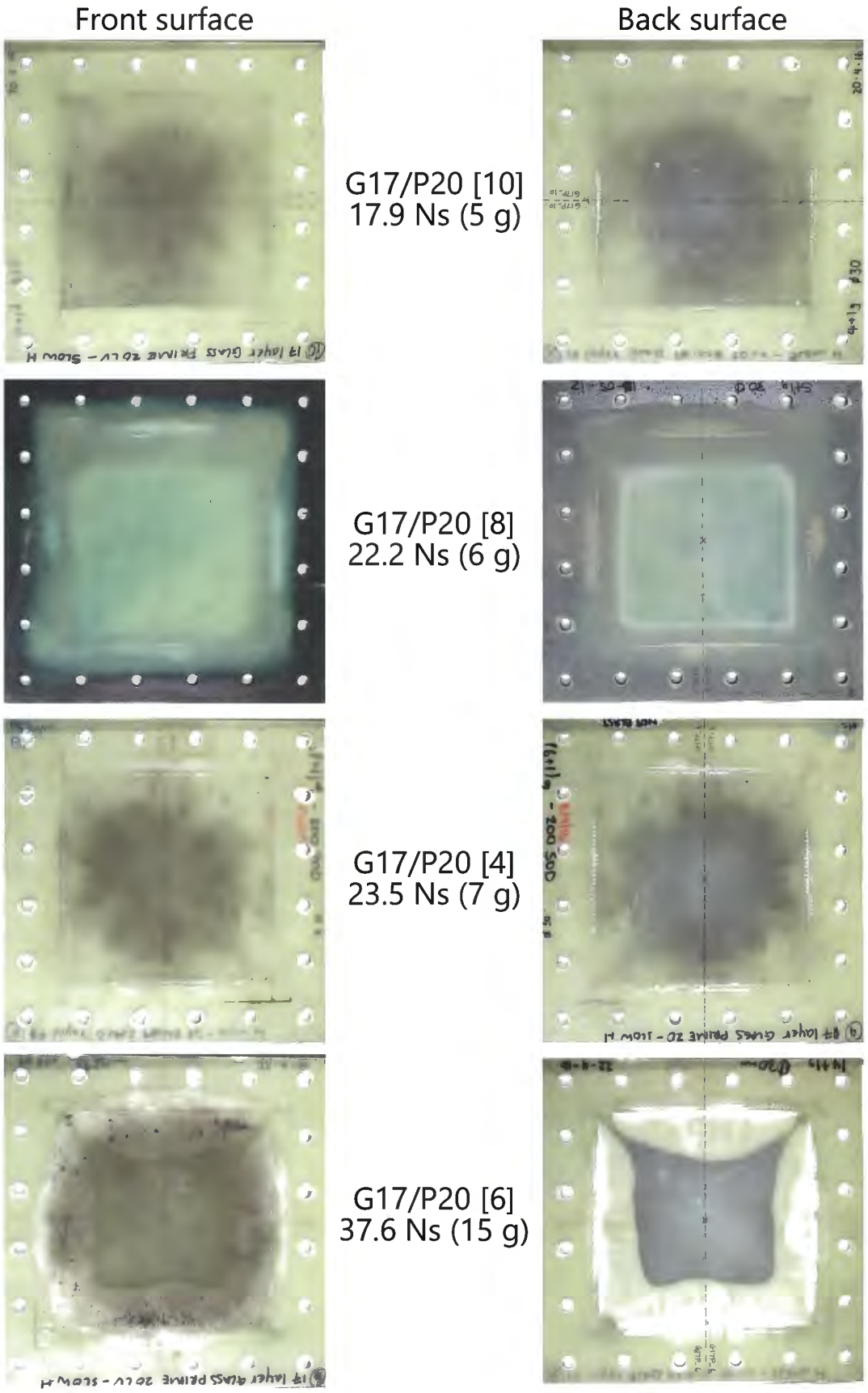

Figure C-2: Outstanding photographs of the front and back surfaces of different blast tested Glass 17/Prime 20LVpanels

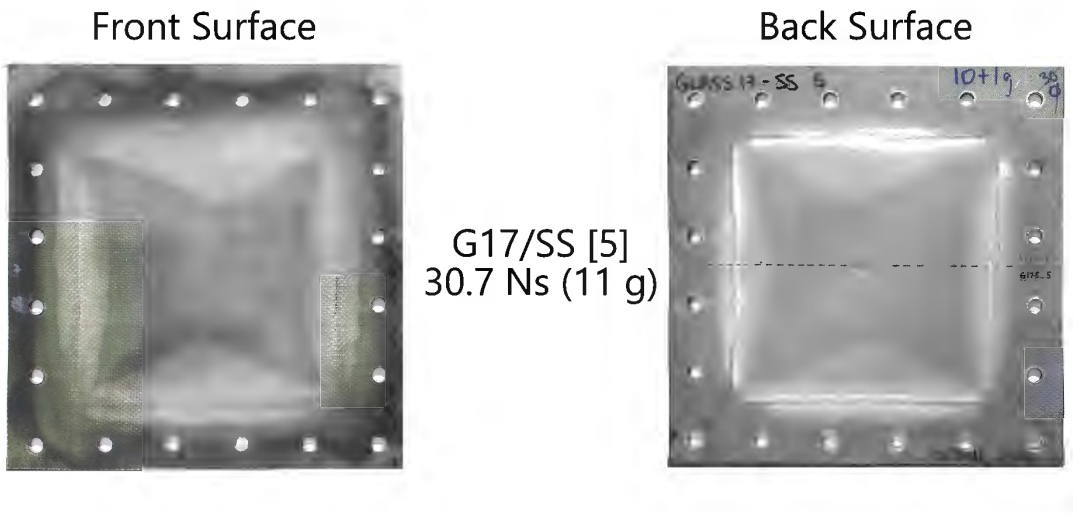

Figure C-3: Outstanding photographs of the front and back surface of G17/SS-5

Appendix D Outstanding Supawood blast images

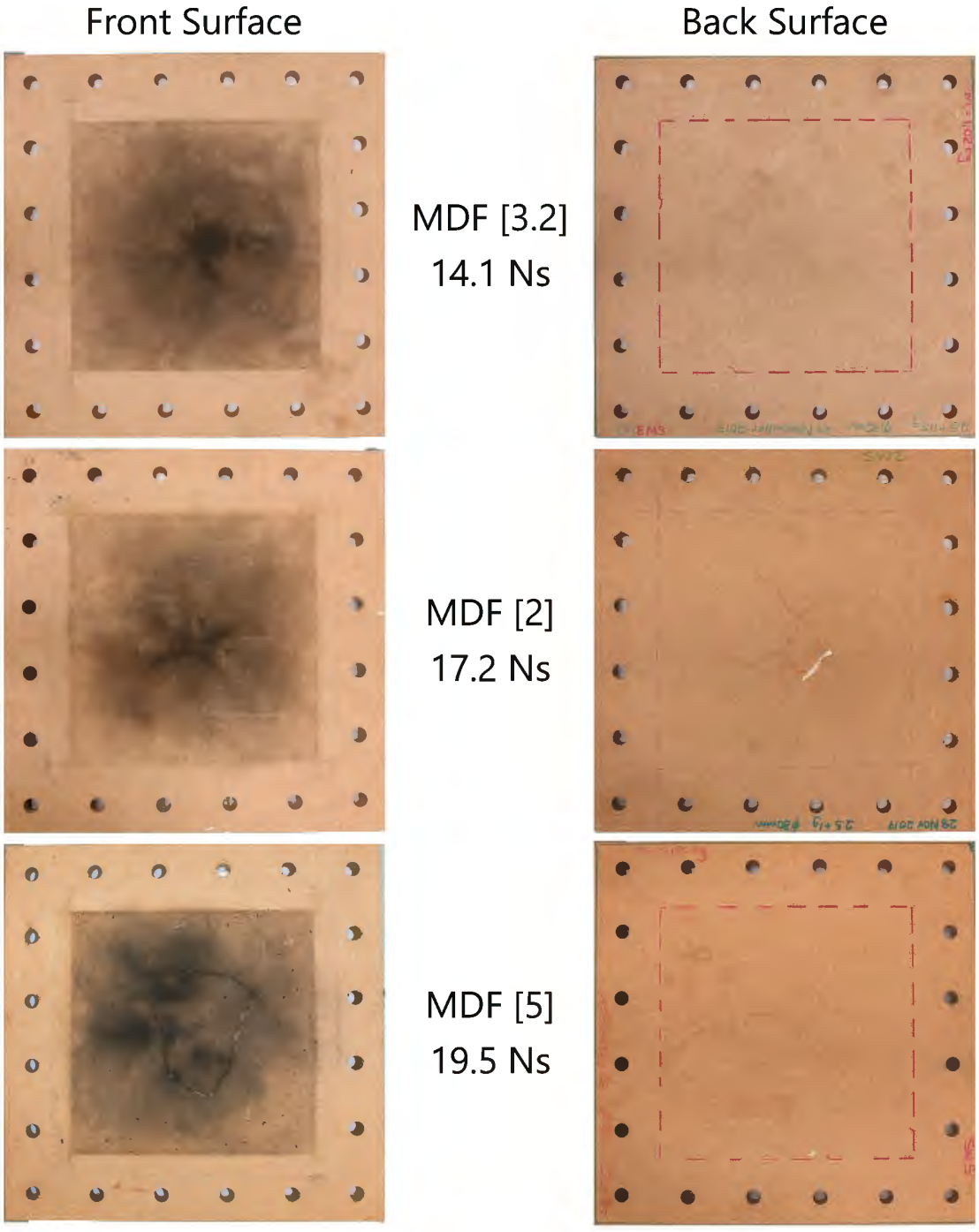

Figure D-1: Outstanding photographs of the front and back surfaces of different Supawood panels

Appendix E Outstanding flax FRP blast images and images with no crack outline

Hand lay-up flax fibre reinforced Prime 20LV

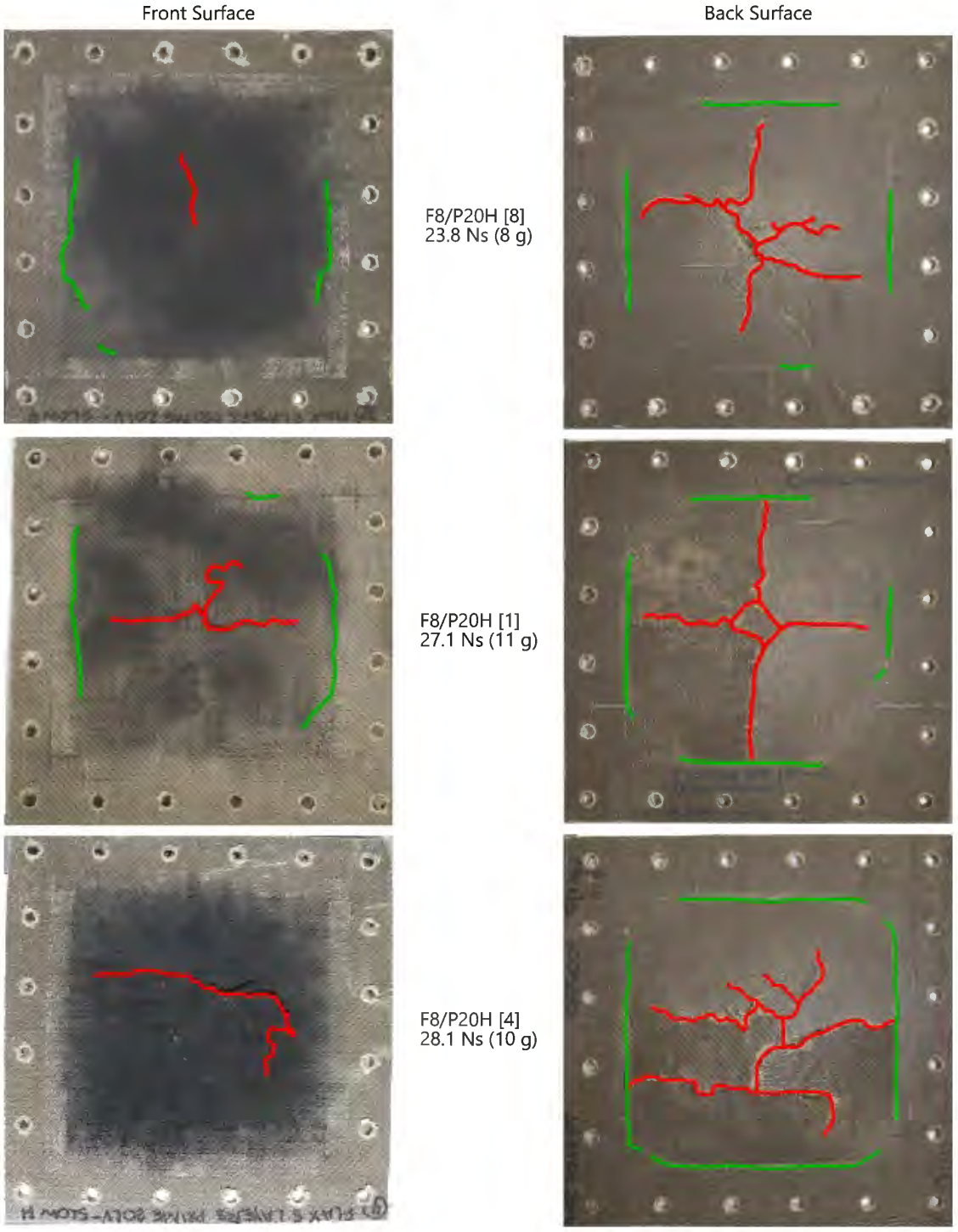

Figure E-1: Outstanding photographs of the front and back surfaces, with crack tracings, of different blast tested hand lay-up Flax 8/Prime 20LVpanels

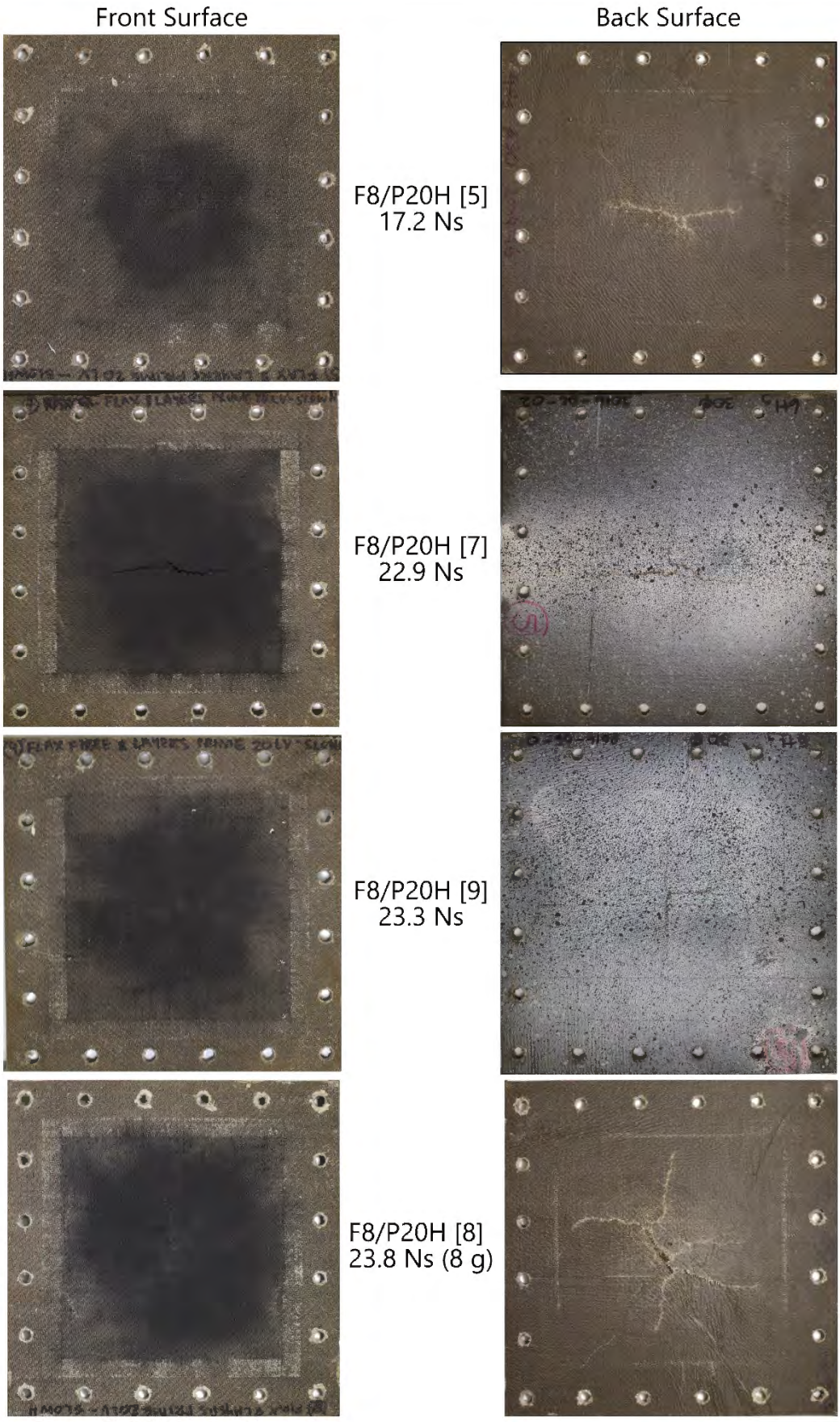

Figure E-2: Front and back surfaces of different blast tested hand lay-up Flax 8/Prime 20LVpanels subjected to an impulse below 25 Ns (with no crack tracings)

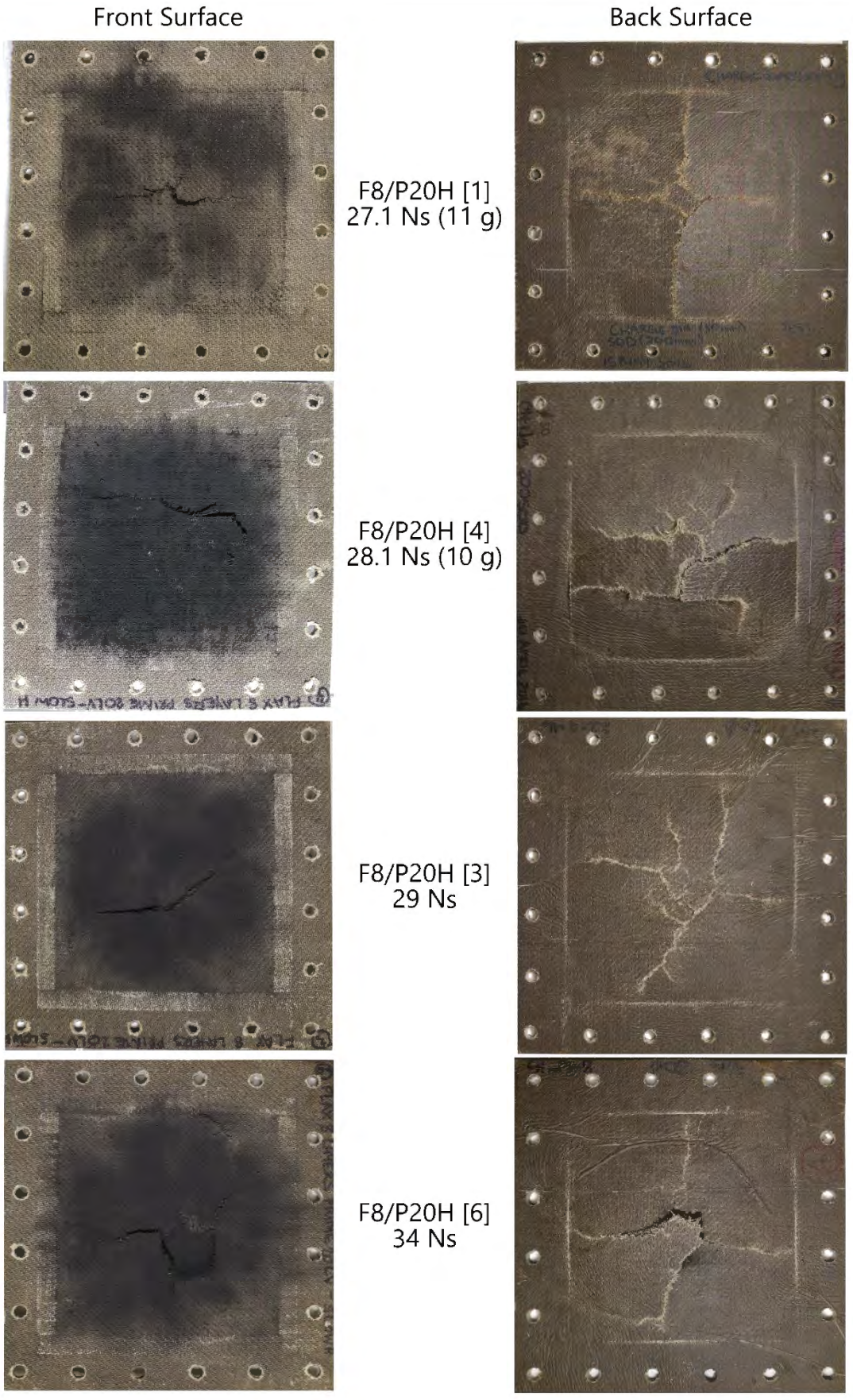

Figure E-3: Front and back surfaces of different blast tested hand lay-up Flax 8/Prime 20LVpanels subjected to an impulse above 25 Ns (with no crack tracings)

VI manufactured flax fibre reinforced Prime 20LV

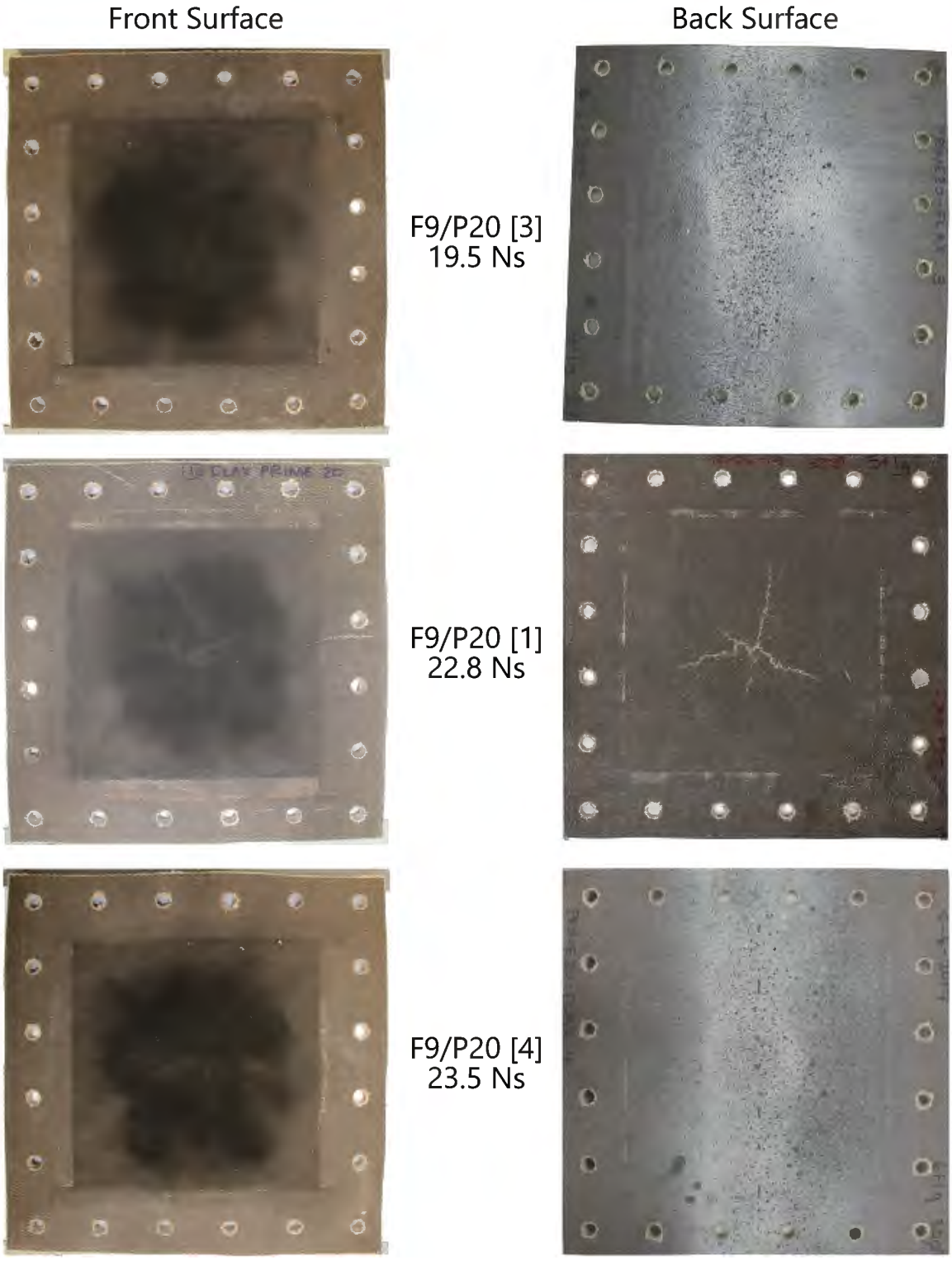

Figure E-4: Front and back surfaces of different blast tested VI Flax 9/Prime 20LVpanels subjected to an impulse below 25 Ns (with no crack tracings)

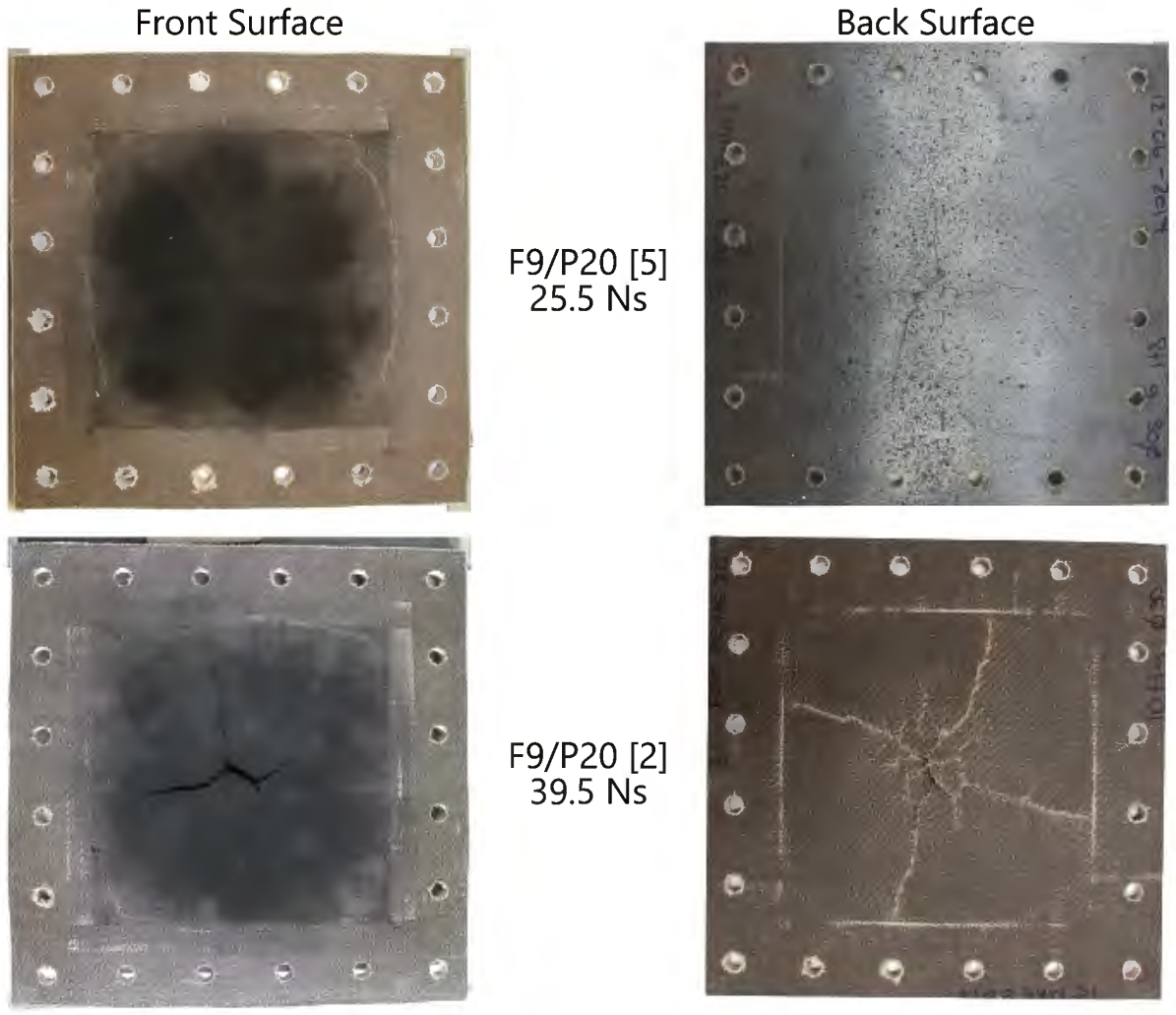

Figure E-5: Front and back surfaces of different blast tested VI Flax 9/Prime 20LV panels subjected to an impulse above 25 Ns (with no crack tracings)

VI manufactured flax fibre reinforced Super Sap

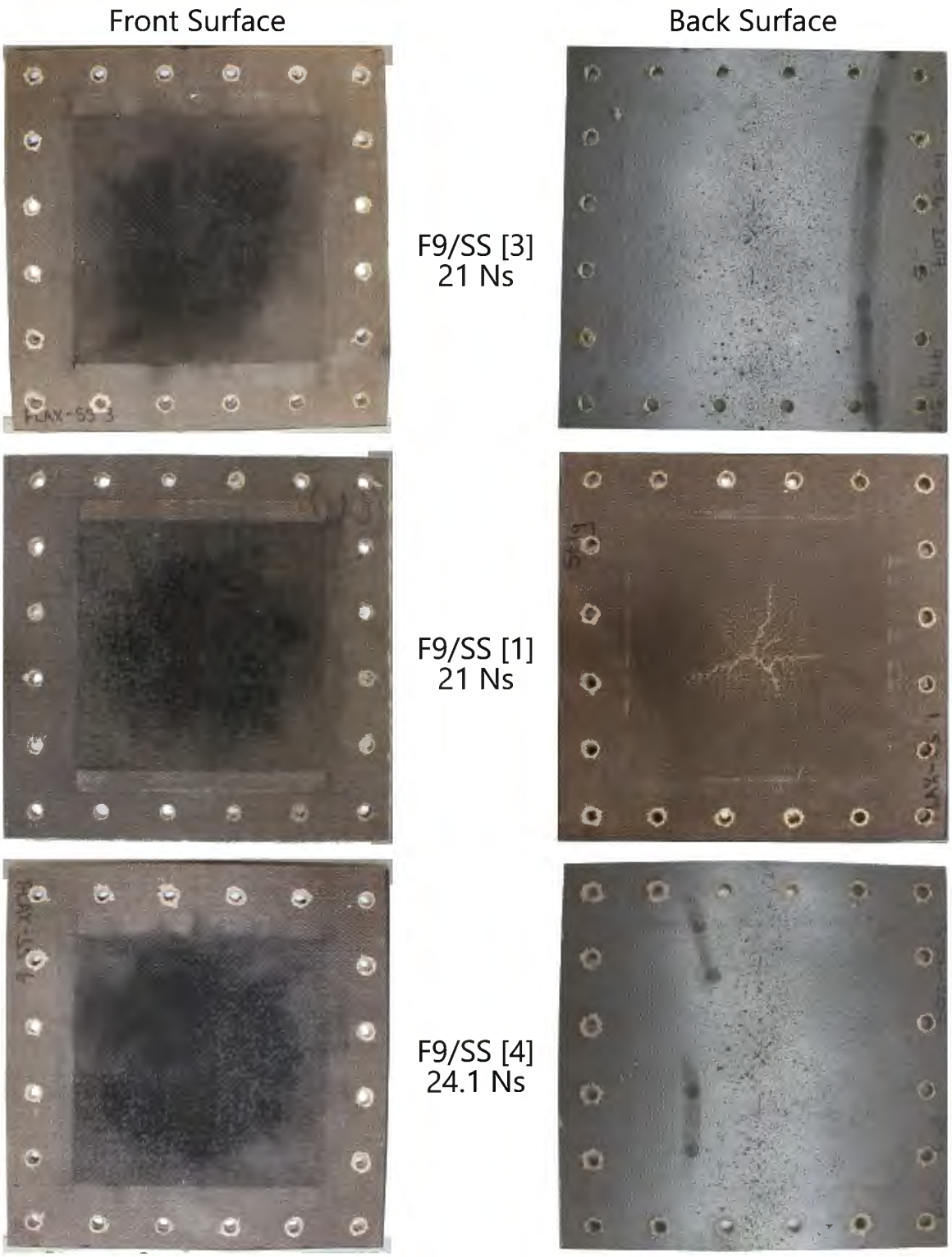

Figure E-6: Front and back surfaces of different blast tested VI Flax 9/Super Sap panels subjected to an impulse below 25 Ns (with no crack tracings)

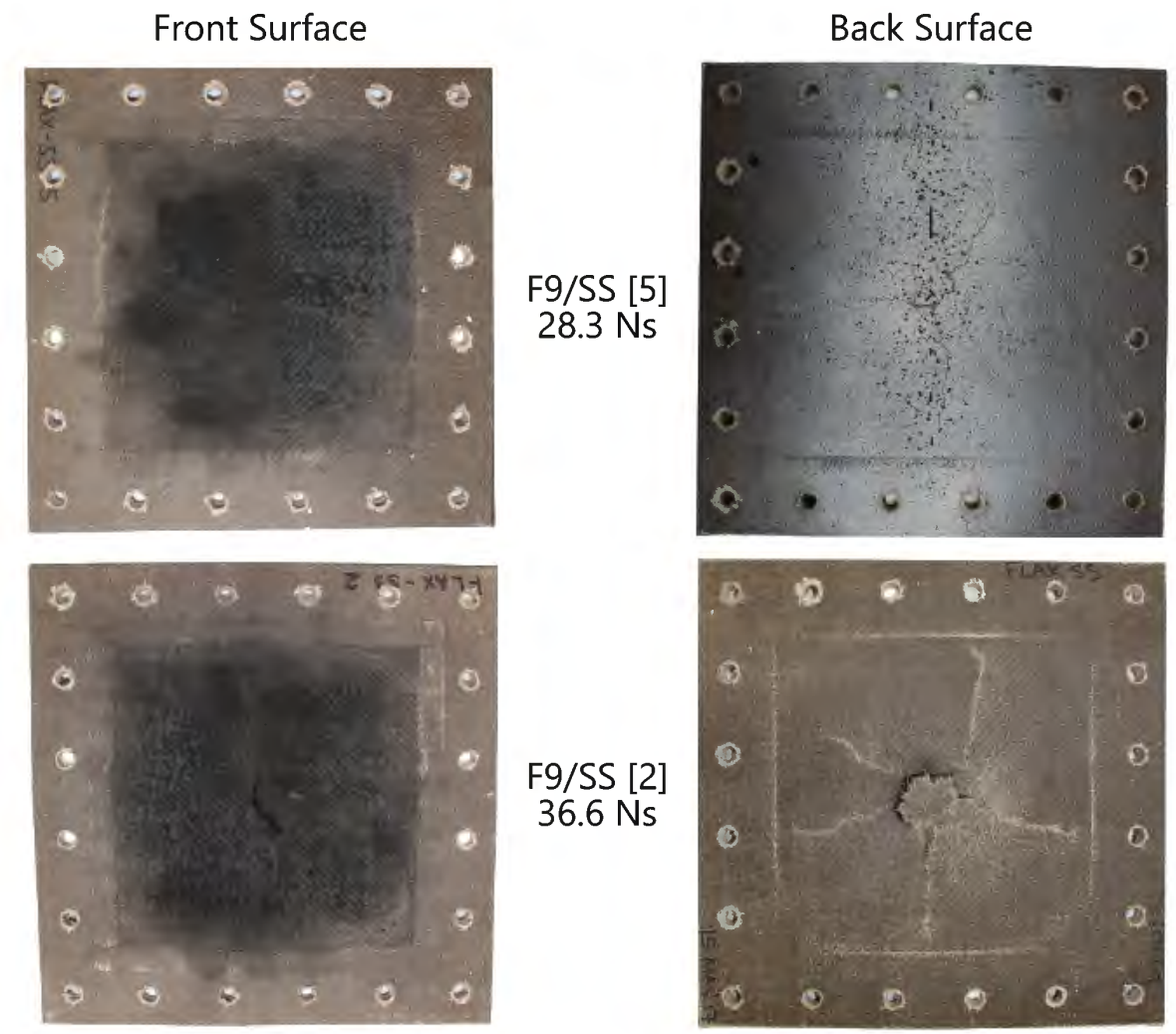

Figure E-7: Front and back surfaces of different blast tested VI Flax 9/Super Sap panels subjected to an impulse above 25 Ns (with no crack tracings)

Appendix F Jute FRP blast images with no crack outline

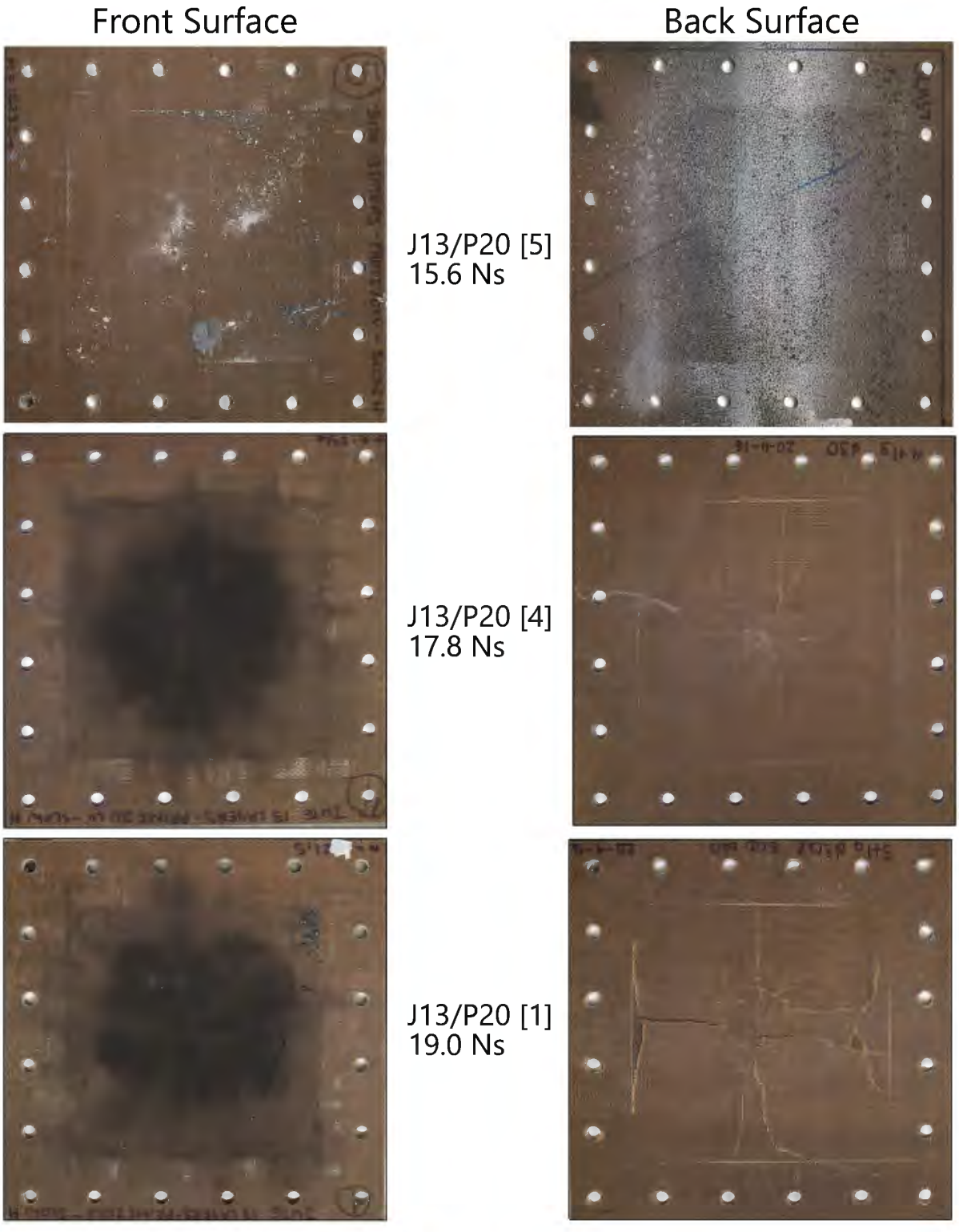

Figure F-1: Front and back surfaces of different blast tested Jute 13/Super Sap panels subjected to an impulse below 19.5 Ns (with no crack tracings)

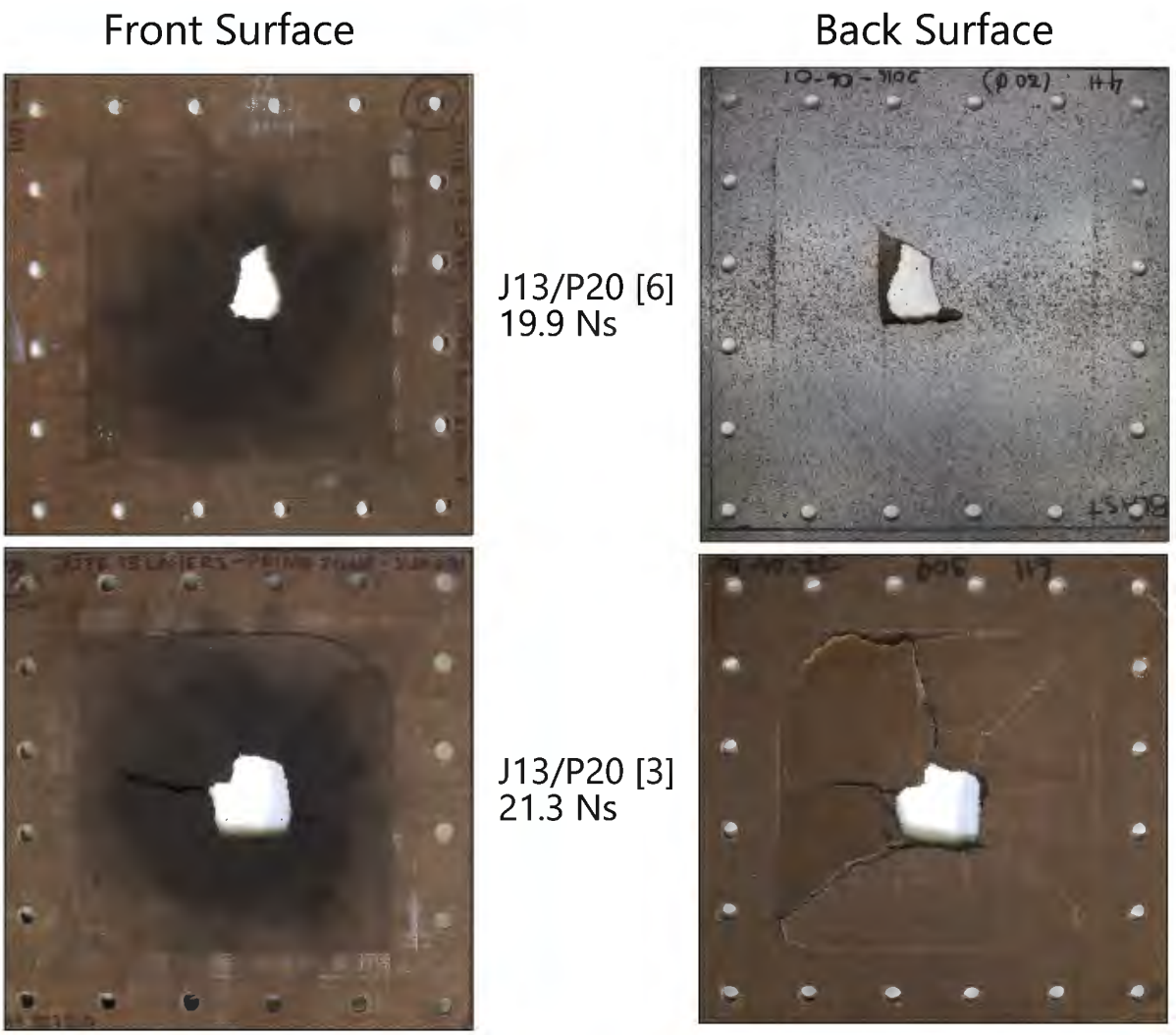

Figure F-2: Front and back surfaces of different blast tested Jute 13/Super Sap panels subjected to an impulse above 19.5 Ns (with no crack tracings)

Appendix G Blast impulse versus midpoint deflection data

Table G-1: Panel thickness and mass, explosive charge parameters and measured midpoint deflection for control GFRP materials tested

Material Description	Specimen Name	Panel t (mm)	Pre-test mass (kg)	Post-test mass (kg)	Charge mass (g)	Charge Φ (mm)	Impulse (Ns)	Mid-point defl. (mm)
Glass Fibre 19 Layer Prime 20LV VARTM	G19/P20-10	6.2	0.99	0.99	5	30	19.3	0.3
	G19/P20-8	6.1	0.97	0.97	7	30	25.2	0.2
	G19/P20-4	6.0	1.01	1.01	11	30	31.7	0.9
	G19/P20-9	6.2	1.01	1.01	11	30	33.7	0.3
	G19/P20-1	6.3	0.99	0.99	25	30	54.3	0.4
	G19/P20-3	6.2	1.01	1.01	25	40	64.8	1.2
	G19/P20-5	6.2	0.97	0.97	30	40	71.3	0.6
	G19/P20-6	6.1	0.99	0.99	35	40	84.4	1.2
	G19/P20-2	6.2	1.02	1.02	40	40	82.7	0.6
Glass Fibre 17 Layer Prime 20LV VARTM	G17/P20-7	5.0	0.76	0.76	4	30	15.5	0
	G17/P20-10	4.8	0.75	0.75	5	30	17.9	0.3
	G17/P20-5	5.0	0.77	0.76	6	30	21.6	0.1
	G17/P20-8	5.1	0.76	0.76	6	30	22.2	0.2
	G17/P20-4	5.0	0.76	0.76	7	30	23.5	0.1
	G17/P20-2	5.1	0.77	0.77	9	30	28.1	0.1
	G17/P20-9	5.0	0.76	0.76	11	30	30.9	0.1
	G17/P20-6	5.0	0.76	0.76	15	30	37.6	0.6
	G17/P20-1	5.1	0.77	0.76	20	30	48.5	0.4

Table G-2: Panel thickness and mass, explosive charge parameters and measured midpoint deflection for Supawood panels tested

Material Description	Specimen Name	Panel t (mm)	Pre-test mass (kg)	Post-test mass (kg)	Charge mass (g)	Charge Φ (mm)	Impulse (Ns)	Mid-point defl. (mm)
Supawood 16 mm Ready to use	MDF-3.1	16.2	1.01	1.02	2	20	10.4	0.5
	MDF-3.2	16.2	1.01	1.02	3	20	14.1	1.9
	MDF-6	16.2	1.01	1.01	3	20	11.5	1.5
	MDF-7	16.1	1.02	1.02	3	20	11.8	1.5
	MDF-2	16.1	1.01	1.02	3.5	30	17.2	1.1
	MDF-4	16.1	1.02	1.02	3.5	20	17.2	2.1
	MDF-8	16.2	1.02	1.02	4	20	15.7	2.6
	MDF-5	16.1	1.01	1.02	4.5	20	19.5	6.2
	MDF-1	16.1	1.02	0.85	6	30	20	102.7

Table G-3: Panel thickness and mass, explosive charge parameters and measured midpoint deflection for glass fibre reinforced Super Sap composites tested

Material Description	Specimen Name	t (mm)	Pre-test mass (kg)	Post-test mass (kg)	Charge mass (g)	Charge Φ (mm)	Impulse (Ns)	Mid-point defl. (mm)
Glass fibre 17 layers Super Sap VARTM	G17/SS-3	5.1	0.84	0.84	6	30	21.5	0.3
	G17/SS-4	5.1	0.82	0.82	9	30	28	0.3
	G17/SS-1	5.2	0.83	0.83	10	30	30.9	0.3
	G17/SS-5	5.1	0.86	0.86	11	30	30.7	0.3
	G17/SS-2	5.1	0.83	0.83	15	30	46.6	0.6
	G17/SS-6	5.1	0.85	0.85	18	30	43.2	0.6

Table G-4: Panel thickness and mass, explosive charge parameters and measured midpoint deflection for natural fibre laminates tested

Material Description	Specimen Name	t (mm)	Pre-test mass (kg)	Post-test mass (kg)	Charge mass (g)	Charge Φ (mm)	Impulse (Ns)	Mid-point defl. (mm)
Jute fibre 13 layers Prime 20 VARTM	J13/P20-5	10	1.04	1.04	4	30	15.6	1.6
	J13/P20-4	10.2	1.02	1.02	5	30	17.8	2.1
	J13/P20-6	10.1	1.03	1.02	5	30	19.9	3.5
	J13/P20-1	10.1	1.02	1.02	6	30	19.0	8.2
	J13/P20-3	10	1.02	1.00	7	30	21.3	29.5
	J13/P20-2	10	1.02	0.58	11	30	33.2	0.5
Flax fibre 9 layers Prime 20 VARTM	F9/P20-3	10.1	1.1	1.1	5	30	19.5	1.1
	F9/P20-1	10.1	1.10	1.10	6	30	22.8	1.8
	F9/P20-4	10.1	1.08	1.08	7	30	23.5	2.3
	F9/P20-5	10	1.08	1.08	9	30	25.5	4.7
	F9/P20-2	10	1.1	1.1	11	30	39.5	14.6
Flax fibre 8 layers Prime 20 Hand lay up	F8/P20H-5	10.1	0.97	0.97	5	30	17.2	1.8
	F8/P20H-9	10.2	0.98	0.98	6	30	23.3	5.7
	F8/P20H-7	9.7	0.96	0.96	7	30	22.9	9.3
	F8/P20H-8	10.2	0.98	0.98	8	30	23.8	8.6
	F8/P20H-3	10.2	0.97	0.97	9	30	29	11.3
	F8/P20H-4	10.3	0.94	0.94	10	30	28.1	30.4
	F8/P20H-6	10.3	0.97	0.97	10	30	34	21.8
	F8/P20H-1	9.5	0.92	0.92	11	30	27.1	23.3
Flax fibre 9 layers Super Sap VARTM	F9/SS-3	9.9	1.08	1.08	5	30	21	1.4
	F9/SS-1	10	1.1	1.1	6	30	21	1.3
	F9/SS-6	10	1.1	1.1	7	30	24.1	3
	F9/SS-5	9.9	1.08	1.08	9	30	28.3	5.4
	F9/SS-2	9.9	1.08	1.08	11	30	36.6	18.6

Appendix H Cracking data measured from blast testing

Table H-1: Cracks measured on the blast tested GFRP panels

	Back surface		Front		
	Exposed	Boundary	Exposed	Boundary	Total surface crack
	mm	mm	mm	mm	mm
G17/P20-7	-	-	-	-	-
G17/P20-10	-	220	-	-	220
G17/P20-5	-	472	-	20	492
G17/P20-8	-	461	-	143	604
G17/P20-4	-	475	-	236	711
G17/P20-2	-	611	-	338	949
G17/P20-9	-	588	-	500	1088
G17/P20-6	-	699	-	590	1289
G17/P20-1	-	741	-	680	1421
G19/P20-10	-	-	-	-	0
G19/P20-8	-	-	-	-	0
G19/P20-4	-	360	-	281	641
G19/P20-9	-	404	-	235	639
G19/P20-1	-	602	-	523	1125
G19/P20-3	-	767	94	616	1477
G19/P20-5	-	864	146	865	1875
G19/P20-6	-	870	68	821	1759
G19/P20-2	-	861	312	828	2001
G17/SS-3	-	617	-	208	825
G17/SS-4	-	713	-	400	1113
G17/SS-1	-	674	-	543	1217
G17/SS-5	-	706	-	566	1272
G17/SS-2	-	951	201	841	1993
G17/SS-6	-	991	226	891	2108

Table H-2: Cracks measured on the blast tested natural fibre laminates tested

	Back surface		Front surface		Total surface crack
	Exposed	Boundary	Exposed	Boundary	
	mm	mm	mm	mm	mm
F8/P20H-5	180	-	-		180
F8/P20H-9	201	-	-		201
F8/P20H-7	290	-	159	249	698
F8/P20H-8	478	349	66	265	1158
F8/P20H-3	612	445	293	329	1679
F8/P20H-4	669	671	261	0	1601
F8/P20H-6	603	401	601	152	1757
F8/P20H-1	443	424	266	331	1464
F9/P20-3	169	-	-	-	169
F9/P20-1	270	208	128	94	700
F9/P20-4	321	222	189	209	941
F9/P20-5	403	503	335	663	1904
F9/P20-2	712	633	326	736	2407
F9/SS-3	57	-	-	-	57
F9/SS-1	298	-	-	-	298
F9/SS-6	180	-	-	-	180
F9/SS-5	391	218	130	403	1142
F9/SS-2	628	547	314	612	2101
J13/P20-5	-	-	-	-	0
J13/P20-4	530	629	360	764	2283
J13/P20-6	559	585	357	797	2298
J13/P20-1	1110	480	539	824	2953
J13/P20-3	1180	520	674	769	3143
J13/P20-2[a]	2410	768	2410	768	6356

a – Significant damage and fragmentation was observed

Table H-3: Cracks measured on the blast tested Supawood panels

	Back surface		Front surface		Total surface crack	Cross-section
	Exposed	Boundary	Exposed	Boundary		
	mm	mm	mm	mm	mm	mm
MDF-3.1	-	-	-	-	-	201
MDF-3.2	-	-	-	-	-	304
MDF-6	198	-	-	-	198	177
MDF-7	-	-	-	-	-	351
MDF-2	340	-	-	-	340	382
MDF-4	338	-	-	-	338	364
MDF-8	329	-	-	-	329	532
MDF-5	430	-	436	136	1002	621
MDF-1[a]	1720	744	1720	744	4928	N/A

a – Significant damage and fragmentation was observed